

---

# Entwicklung neuer Strategien zur spezifischen Hemmung humaner Histondeacetylase 8

Vom Fachbereich Chemie  
der Technischen Universität Darmstadt



TECHNISCHE  
UNIVERSITÄT  
DARMSTADT

zur Erlangung des Grades

*Doctor rerum naturalium (Dr. rer. nat.)*

**Dissertation**

von

**Niklas Jänsch, M. Eng.**

aus Darmstadt

Erstgutachter:  
Zweitgutachter:  
Drittgutachter:

Prof. Dr. Harald Kolmar  
Prof. Dr. Franz-Josef Meyer-Almes (Hochschule Darmstadt)  
Prof. Dr. Wolfgang Sippl (Martin-Luther-Universität Halle-Wittenberg)

Darmstadt 2023

---

---

Jäsch, Niklas: Entwicklung neuer Strategien zur spezifischen Hemmung humaner Histondeacetylase 8  
Darmstadt, Technische Universität Darmstadt  
Jahr der Veröffentlichung der Dissertation auf TUpriints: 2023

URN: urn:nbn:de:tuda-tuprints-244343

URL: <https://tuprints.ulb.tu-darmstadt.de/id/eprint/24434>

Tag der Einreichung: 24.Mai 2023

Tag der mündlichen Prüfung: 10.Juli 2023

Urheberrechtlich geschützt / In Copyright  
<https://rightsstatements.org/page/InC/1.0/>

---

---

Die vorliegende Arbeit wurde in der Arbeitsgruppe von Prof. Dr. Franz-Josef Meyer-Almes an der Hochschule Darmstadt im Fachbereich Chemie- und Biotechnologie in Kooperation mit Prof. Dr. Harald Kolmar am Clemens-Schöpf-Institut für Organische Chemie und Biochemie der Technischen Universität Darmstadt von Dezember 2018 bis Juli 2023 angefertigt.

---

---

## Publikationen zur Redoxregulation und Entwicklung kovalenter Inaktivatoren von HDAC8

---

### The enzyme activity of histone deacetylase 8 is modulated by a redox-switch

Jänsch, N.; Meyners, C.; Muth, M.; Kopranovic, A.; Witt, O.; Oehme, I.; Meyer-Almes, F. J.  
Redox Biology (doi.org/10.1016/j.redox.2018.09.013)

### Covalent inhibition of histone deacetylase 8 by 3,4-dihydro-2H-pyrimido[1,2-c][1,3]benzothiazin-6-imine

Muth, M.; Jänsch, N.; Kopranovic, A.; Krämer, A.; Wössner, N.; Jung, N.; Kirschhöfer, F.; Brenner-Weiss, G.; Meyer-Almes, F. J.  
Biochimica et Biophysica Acta (BBA) – General Subjects (doi.org/10.1016/j.bbagen.2019.01.001)

### Switching the Switch: Ligand Induced Disulfide Formation in HDAC8

Jänsch, N.; Sugiarto, W.O.; Muth, M.; Kopranovic, A.; Desczyk, C.; Ballweg, M.; Kirschhöfer, F.; Brenner-Weiss, G.; Meyer-Almes, F. J.  
Chemistry – A European Journal (doi.org/10.1002/chem.202001712)

### Assessment of Tractable Cysteines for Covalent Targeting by Screening Covalent Fragments

Petri, L.; Ábrányi-Balogh, P.; Imre, T.; Pálffy, G.; Perczel, A.; Knez, D.; Hrast, M.; Gobec, M.; Sosič, I.; Nyíri, K.; Vértessy, B.G.; Jänsch, N.; Desczyk, C.; Meyer-Almes, F. J.; Ogris, I.; Golič Grdadolnik, S.; Giacinto Iacovino, L.; Binda, C.; Gobec, S.; Keserü, G. M.  
ChemBioChem (doi.org/10.1002/cbic.202000700)

### 3-Chloro-5-Substituted-1,2,4-Thiadiazoles (TDZs) as Selective and Efficient Protein Thiol Modifiers

Jänsch, N.; Frühauf, A.; Schweipert, M.; Debarnot, C.; Erhardt, M.; Brenner-Weiss, G.; Kirschhöfer, F.; Jasionis, T.; Capkauskaitė, E.; Zubriene, A.; Matulis, D.; Meyer-Almes, F. J.  
ChemBioChem (doi.org/10.1002/cbic.202200417)

---

## Publikationen zu Dithiocarbamaten als HDAC8 Inhibitoren

---

### Synthesis and structure activity relationship of 1,3-benzo-thiazine-2-thiones as selective HDAC8 inhibitors

Wolff, B.; Jänsch, N.; Sugiarto, W.O.; Frühschulz, S.; Lang, M.; Altintas, R.; Oehme, I.; Meyer-Almes, F. J.  
European Journal of Medicinal Chemistry (doi.org/10.1016/j.ejmech.2019.111756)

### Thiocarbonyl Surrogate via Combination of Potassium Sulfide and Chloroform for Dithiocarbamate Construction

Tan, W.; Jänsch, N.; Öhlmann, T.; Meyer-Almes, F. J.; Jiang, X.  
Organic Letters (doi.org/10.1021/acs.orglett.9b02784)

---

## Publikationen zu Thiazolidindionen als HDAC8 Inhibitoren

---

### Discovery of 5-nathylidene-2,4-thiazolidinedione derivatives as selective HDAC8 inhibitors and evaluation of their cytotoxic effects in leukemic cell lines

Tilekar, K.; Upadhyay, N.; Jänsch, N.; Schweipert, M.; Mrowka, P.; Meyer-Almes, F. J.; Ramaa, C. S.  
Bioorganic Chemistry (doi.org/10.1016/j.bioorg.2019.103522)

### Discovery of novel N-substituted thiazolidinediones (TZDs) as HDAC8 inhibitors: in-silico studies, synthesis, and biological evaluation

Upadhyay, N.; Tilekar, K.; Jänsch, N.; Schweipert, M.; Hess, J. D.; Henze Macias, L.; Mrowka, P.; Aguilera, R. J.; Choe, J.Y.; Meyer-Almes, F. J.; Ramaa, C. S.  
Bioorganic Chemistry (doi.org/10.1016/j.bioorg.2020.103934)

---

---

---

## Publikationen zu anderen Themen während der Doktorarbeit

---

### **Mechanistic Insights into Binding of Ligands with Thiazolidinedione Warhead to Human Histone Deacetylase 4**

Schweipert, S.; \* [Jänsch, N.](#); \* Upadhyay, N.; Kalpana, T.; Wozny, E.; Basheer, S.; Wurster, E.; Müller, M.; Ramaa, CS.; Meyer-Almes, F.J.

Pharmaceuticals ([dor.org/10.3390/ph14101032](https://doi.org/10.3390/ph14101032))

### **Kinetically selective and potent inhibitors of HDAC8**

Schweipert, M.; [Jänsch, N.](#); Sugiarto, WO.; Meyer-Almes, F. J.

Biological Chemistry ([doi.org/10.1515/hsz-2018-0363](https://doi.org/10.1515/hsz-2018-0363))

### **Using design of experiment to optimize enzyme activity assays**

[Jänsch, N.](#); Colin, F.; Schröder, M.; Meyer-Almes, F. J.

ChemTexts ([doi.org/10.1007/s40828-019-0095-2](https://doi.org/10.1007/s40828-019-0095-2))

### **Methionine 274 Is Not the Determining Factor for Selective Inhibition of Histone Deacetylase 8 (HDAC8) by L-Shaped Inhibitors**

[Jänsch, N.](#); Lang, K. L.; Meyer-Almes, F. J.

International Journal of Molecular Sciences ([doi.org/10.3390/ijms231911775](https://doi.org/10.3390/ijms231911775))

\*geteilte Erstautorenschaft

---

## Posterbeiträge an Fachkonferenzen

---

### **Disulfide dependent Regulation of HDAC8**

[Jänsch, N.](#); Kopranovic, A.; Sugiarto, WO.; Meyer-Almes, F. J.

Functional Disulfides in Health and Disease, Weizmann Institute of Science, 2021

### **From Redox-Regulation to Covalent Inactivators of HDAC8**

[Jänsch, N.](#); Kopranovic, A.; Sugiarto, WO.; Meyer-Almes, F. J.

Frontiers in Medicinal Chemistry, Technische Universität Darmstadt, 2021

---

---

*„Ich bin überzeugt, dass wir nicht in erster Linie arbeiten, um Reichtum oder gar Ehre zu erlangen, sondern weil wir an der Aufgabe interessiert sind, Spaß daran haben und sehr stark fühlen, dass es erstrebenswert ist.“*

Frederick Sanger  
(1918 – 2013)

---

---

---

## Zusammenfassung

---

Die Deacetylierung von Histonen ist ein wichtiger Mechanismus für die Regulation von Genen und der daraus resultierenden Transkription und Translation in funktionelle Proteine. Die Deacetylierung von Histonen wird durch die sogenannten Histondeacetylasen (HDACs) katalysiert, welche sich in vier Untergruppen aufteilen. Die Einteilung erfolgt hauptsächlich anhand struktureller Unterschiede. Humane Histondeacetylase 8 (HDAC8) gehört der Klasse I der zinkabhängigen Histondeacetylasen an. Namensgebend ist die Deacetylierung N-terminaler Lysinreste an Histonen. In Folge einer Deacetylierung liegen diese überwiegend protoniert vor und gehen eine verstärkte Wechselwirkung zu dem negativ geladenen Phosphatrückgrat der DNA ein. Durch diesen Mechanismus wird die Expression spezifischer Gene in Abhängigkeit des Acetylierungsstatus erhöht oder verringert. Diese epigenetische Regulation hat damit tiefgreifende physiologische Folgen. Eine erhöhte Expression von HDACs wird in Verbindung gesetzt mit der Entstehung neurodegenerativer Erkrankungen und der Entstehung von verschiedenen Krebsarten. Neben Histonen werden viele weitere Proteine als potenzielle Substrate von HDACs beschrieben, was die Komplexität der Regulation durch posttranslationale Modifikationen verdeutlicht. Die Acetylierung von Lysinen an Proteinen hat wahrscheinlich eine ähnliche Bedeutung, wie die Phosphorylierung proteingebundener Serine und Threonine durch Kinasen. Für die Entwicklung neuer Wirkstoffe, welche sich gegen HDACs richten, ist es daher entscheidend in diese Mechanismen eingreifen zu können. Ein besseres Verständnis über die molekularen Grundlagen der Regulation und Aufbau von HDACs ist daher essenziell und bietet eine große Chance bei der Behandlung verschiedener Krankheitstypen.

Die meisten gegen HDACs gerichteten Inhibitoren, wie zum Beispiel Vorinostat, Panobinostat und Belinostat verfügen über eine Zink-komplexierende Kopfgruppe, einen hydrophoben, linearen Linker und eine abschließende, variable, Cap-Region. Aufgrund der hohen Konservierung des Aktivzentrums von HDACs verfügen diese kompetitiven Inhibitoren in der Regel über keine nennenswerte Selektivität unter den Isoformen. Um Nebenwirkungen, hervorgerufen durch unerwünschte off-target Effekte, zu vermeiden, ist es erstrebenswert sich der Thematik der Entwicklung spezifischer Inhibitoren anzunehmen und Mechanismen zu identifizieren, welche dies ermöglichen. Erste HDAC8 spezifische Inhibitoren wie PCI-34051 wurden bereits entwickelt. Dennoch stellt die gezielte Hemmung einzelner HDACs innerhalb ihrer strukturverwandten Isoenzyme Wissenschaftler vor große Herausforderungen. Die Manipulation und Ausnutzung Isoenzym-spezifischer Regulationsmechanismen, wie das Adressieren von Inhibitoren an allosterisch regulative Regionen, stellt daher einen vielversprechenden Ansatz für die Hemmung der Enzymaktivität und Funktion von HDAC8 dar.

Die Ergebnisse dieser Doktorarbeit sind im kumulativen Teil aufgeführt und näher erörtert. Dieser Teil setzt sich aus dreizehn in begutachteten Zeitschriften veröffentlichten Artikeln zusammen, welche in vier Unterkapitel gegliedert sind. Das erste Unterkapitel befasst sich mit der Entdeckung und Aufklärung der cysteinabhängigen Redoxregulation von HDAC8 und der Nutzung dieser Mechanismen für die Entwicklung zielgerichteter kovalenter Inaktivatoren. Genauer wurde mittels Methoden der Redoxbiologie festgestellt, dass die Enzymaktivität von HDAC8 durch eine Disulfidbrücke zwischen Cys<sub>102</sub> und Cys<sub>153</sub> reguliert wird. Diese Disulfidbrücke kann sowohl durch die Zugabe von Wasserstoffperoxid als auch durch redox-aktive, kleine Moleküle induziert werden. Im besten Fall nähern sich solche Wirkstoffe in einem vorgelagerten nicht-kovalenten Gleichgewicht den redox-aktiven Cysteinen an, um dann in einem zweiten Schritt die kovalente Verbrückung zu induzieren. Einem solchen Wirkstoff mit dem Namen PD-404,182, welcher aus einer Wirkstofffindungskampagne entstammt, widmen sich zwei Publikationen innerhalb des ersten Kapitels des kumulativen Teils dieser Dissertation. Dort wird der genaue Mechanismus der Interaktion und die daraus hervorgehenden Erkenntnisse genauer beschrieben.

Neben der gefundenen Disulfidbrücke zwischen Cys<sub>102</sub> und Cys<sub>153</sub> wird zusätzlich beschrieben, dass HDAC8 durch drei weitere Disulfidbrücken, nämlich zwischen Cys<sub>244</sub> und Cys<sub>287</sub>, Cys<sub>275</sub> und Cys<sub>352</sub> sowie zwischen Cys<sub>125</sub> und Cys<sub>131</sub>, reguliert werden kann. Somit wird verdeutlicht, dass HDAC8 über ein unter den humanen Histondeacetylasen einzigartiges Muster an regulativen Disulfidbrücken verfügt. Diese Erkenntnisse dienen im weiteren als Grundlage für die Findung und Entwicklung erster kovalenter Inaktivatoren von HDAC8. Mittels einer Kampagne für die Findung gegen Cystein gerichteter kovalenter Wirkstoffe konnten erste Fragmente identifiziert werden. Diese Ergebnisse sind in den beiden letzten Publikationen des ersten Kapitels zusammengefasst.

Somit beschreibt das erste Kapitel dieser Dissertation eine vielversprechende Strategie für die Entwicklung HDAC8 selektiver Inhibitoren, durch die Ausnutzung von spezifischen, cysteinabhängigen Regulationsmechanismen. Probleme, die bei der Entwicklung von Inhibitoren normalerweise durch die stark

---

---

konservierte Bindetasche von HDACs auftreten, werden durch die Ausnutzung solcher spezifischer Regulationsmechanismen umgangen. Jedoch sei nicht zu vergessen, dass die Entwicklung zielgerichteter kovalenter Inaktivatoren Wissenschaftler vor andere, nicht zu unterschätzende Herausforderungen stellt. Eine davon ist die genaue Abwägung der Reaktivität. Es besteht ein schmaler Grat zwischen der gezielten kovalenten Modifikation spezifischer Cysteine auf Proteinen und einer unspezifischen Reaktion, mit jedem zur Verfügung stehenden Cystein.

Das zweite Kapitel des kumulativen Teils greift die Entdeckung des Disulfidbrücken-induzierenden Inhibitors PD-404,182 auf und beschreibt die Weiterentwicklung dieses Wirkstoffes in Richtung unreaktiver Moleküle, um die molekulare Erkennung der reversiblen Interaktion im Aktivzentrum in den Vordergrund zu rücken. Dieses Vorgehen dient dazu, eine Alternative zu den gängigen Zink-komplexierenden kompetitiven Inhibitoren zu entwickeln. Bei PD-404,182 handelt es sich um ein zyklisches Benzothiazinimin, welches nach Annäherung an ein Cystein ein gemischtes Disulfid, unter Ringöffnung, eingeht. Im folgenden Schritt wird im Rahmen einer Substitutionsreaktion mit einem weiteren, proteingebundenen Cystein die Formierung einer intermolekularen Disulfidbrücke eingeleitet.

Durch Substitution des Imin Stickstoffes innerhalb von PD-404,182 gegen einen Schwefel hin zum Thion gelingt es, die Reaktion gegenüber Cystein zu unterdrücken, was in einer Fülle an verschiedenen Derivaten mit hoher Potenz und Spezifität gegen HDAC8 resultiert. Diese Strukturen entfalten ihre inhibitorische Wirkung allein durch die molekulare Erkennung am Aktivzentrum durch Verdrängung des Substrates.

Durch eine Kooperation mit Ina Oehme vom Deutschen Krebsforschungszentrum (DKFZ) in Heidelberg wurde zusätzlich gezeigt, dass diese Molekülklasse vergleichbare inhibitorische Aktivität auf das Wachstum von Zellkulturen ausübt, wie der selektive Referenzinhibitor PCI-34051. Somit wurde eine von PD-404,182 abgeleitete zweite Generation an Inhibitoren geschaffen, welche über eine völlig neuartige Zink-komplexierende Funktion verfügen.

Neben den in der Arbeitsgruppe von Prof. Dr. Meyer-Almes entwickelten Inhibitoren wurden auch Moleküle mit gleicher Funktionalität im Rahmen einer Kooperation mit Xuefeng Jiang von der East China Normal University (ECNU) auf inhibitorische Wirkung gegenüber HDAC8 getestet. Dabei wurden nicht nur vielversprechende neue Leitstrukturen identifiziert, sondern auch ein Ansatz für eine schnellere, einfachere und vor allem nachhaltigere Synthese dieser Wirkstoffgruppe publiziert. Somit wurde, ausgehend von den anfänglichen Entdeckungen, eine bisher unbeschriebene Klasse an HDAC8 Inhibitoren entwickelt. Diese könnten zukünftig als Alternative zu den gängigen Zink-komplexierenden HDAC-Inhibitoren fungieren und können schnell und nachhaltig synthetisiert werden.

Von einer möglichen Alternative zu gängigen HDAC-Inhibitoren handelt das dritte Unterkapitel des kumulativen Teils dieser Doktorarbeit. Im Rahmen einer Kooperation mit C. S. Ramaa vom Bharati Vidyapeeth's College of Pharmacy wird bereits bekannten und seit Jahrzehnten erforschten Molekülen eine neue Rolle als HDAC8 Inhibitoren zugeschrieben. Bei diesen Wirkstoffen handelt es sich um Derivate von Thiazolidindionen, welche einst als potenzielle Antidiabetika Erwähnung in verschiedenen Publikationen fanden. Aufgrund von Langzeitnebenwirkungen sank das kommerzielle Interesse an dieser Wirkstoffklasse wieder. Jedoch wurde herausgefunden, dass die untersuchten Thiazolidindione eine starke strukturelle Ähnlichkeit zu HDAC-Inhibitoren aufweisen. Im Grunde verfügen diese über eine Zink-komplexierende Gruppe, einen hydrophoben Linker und eine variable Cap-Region, welche die Bindetasche am Enzym verschließt. Durch den Kooperationspartner wurden mehrere hundert Strukturen mit der funktionellen Thiazolidindion Gruppe breitgestellt und im Rahmen dieser Dissertation auf inhibitorische Wirkung gegen HDAC8 getestet. Daraus ergaben sich mehrere strukturelle Untergruppen mit  $IC_{50}$  Werten im Bereich von 1 – 50  $\mu$ M. Die identifizierten Wirkstoffe wurden anschließend auf Isoenzymselektivität gegen andere HDACs getestet und die thermodynamische Stabilisierung von HDAC8 durch die Wirkstoffbindung untersucht. Die hervorgehenden Publikationen wurden durch molekulares Docking und Testung der Wirkung auf Zellkulturmodelle vervollständigt. Aus dieser Kooperation gingen zwei Publikationen hervor, welche eine bislang völlig neue Leitstruktur für die Entwicklung möglicher HDAC8 Inhibitoren identifizieren und somit die Grundlage für weitere Optimierung dieser Wirkstoffe schaffen.

Das letzte Kapitel des kumulativen Teils der vorliegenden Dissertation fasst vier Publikationen zusammen, welche keinem der vorherigen Kapitel zuzuordnen sind, jedoch auch der Überthematik der Wirkstoffentwicklung gegen

---



---

HDACs angehören. Zwei davon entschlüsseln näher die Wichtigkeit einer transienten Bindetasche in HDAC8. Diese ist direkt neben dem Aktivzentrum gelegen und wird durch Bindung von spezifischen Inhibitoren ausgebildet.

In der ersten Publikation wurde ein Inhibitor beschrieben, welcher durch die zusätzliche Bindung in dieser Nebentasche über eine außerordentlich hohe Verweilzeit auf dem Enzym verfügt. Die zweite befasst sich mit der Rolle von Met<sub>274</sub> und der Wichtigkeit dieser Aminosäure bei der Bindung selektiver HDAC8 Inhibitoren.

Zusätzlich ist eine Publikation entstanden, welche eine weitere Untergruppe der zuvor erwähnten Thiazolidindione als HDAC4 Inhibitoren näher beschreibt. Der Fokus bei dieser Publikation liegt auf dem empirischen Austausch verschiedener Aminosäuren innerhalb der Binderegion der Inhibitoren an HDAC4 und der Untersuchung, welche Aminosäuren für die Interaktion von entscheidender Rolle sind.

Zuletzt ist innerhalb des letzten Kapitels des kumulativen Teils eine Publikation zur Anwendung von statistischer Versuchsplanung im Rahmen einer Lehrveranstaltung entstanden. In dieser Publikation wird beschrieben, wie sich die Michealis-Menten Theorie und die der kompetitiven Hemmung durch statistische Versuchsplanung in ein studentisches Lehrpraktikum integrieren lassen.

Neben den publizierten Fachaufsätzen wurden Teile dieser Arbeit an zwei internationalen Fachkonferenzen im Rahmen von Posterbeiträgen präsentiert. Somit leistet die vorliegende Arbeit einen großen Beitrag für die Entwicklung neuer HDAC8-spezifischer Inhibitoren. Ein besonderer Schwerpunkt der Arbeit ist es, Alternativen zu aktuellen Bemühungen zu identifizieren, welche sich zukünftig zu ausgereiften Inhibitoren entwickeln könnten.

---

---

---

## Abstract

---

The deacetylation of histones is an important mechanism for regulating genes and the resulting transcription and translation into proteins. Histone deacetylation is catalyzed by histone deacetylases (HDACs), which are divided into four subgroups primarily based on structural differences. Human histone deacetylase 8 (HDAC8) belongs to the class I zinc-dependent histone deacetylases, named for the deacetylation of N-terminal lysine residues on histones. As a result of deacetylation, these residues are predominantly protonated and interact more strongly with the negatively charged phosphate backbone of DNA. This mechanism increases or reduces the expression of specific genes depending on the acetylation status, leading to profound physiological consequences. Increased expression of HDACs is associated with the development of neurodegenerative diseases and various types of cancer. Besides histones, many other proteins are described as potential substrates of HDACs, highlighting the complexity of regulation through post-translational modifications. Acetylation of lysines on proteins likely has a similar importance as the phosphorylation of serines and threonines by kinases. Therefore, a better understanding of the molecular basis of HDAC regulation and structure is essential and offers a significant opportunity in combating various disease types.

Most HDAC inhibitors, such as Vorinostat, Panobinostat, and Belinostat, have a zinc-chelating head group, a hydrophobic linear linker, and a variable cap region. Due to the high conservation of the HDAC active site, these competitive inhibitors generally lack significant selectivity among the isoforms. To avoid side effects caused by unwanted off-target effects, it is desirable to develop specific inhibitors and identify mechanisms that enable this. First HDAC8-specific inhibitors, such as PCI-34051, have already been developed. However, targeting individual HDACs within their structurally related isoforms presents significant challenges for scientists. Manipulation and exploitation of isoenzyme-specific regulatory mechanisms, such as addressing inhibitors to allosteric regulatory regions, therefore represent a promising approach to inhibit the enzyme activity and function of HDAC8.

The results of this doctoral thesis are presented and discussed in the cumulative part. This part consists of thirteen peer-reviewed articles published in scientific journals, which are divided into four sub-chapters. The first sub-chapter deals with the discovery and elucidation of the cysteine-dependent redox regulation of HDAC8 and the use of these mechanisms for the development of targeted covalent inactivators. More specifically, using methods of redox biology, it was found that HDAC8 activity is regulated by a disulfide bond between Cys<sub>102</sub> and Cys<sub>153</sub>. This disulfide bond can be induced by both the addition of hydrogen peroxide and redox-active small molecules. In the best case, such drugs approach the redox-active cysteines in a pre-existing non-covalent equilibrium and then induce covalent bridging in a second step. One such drug, called PD 404,182, which originates from a drug discovery campaign, is the subject of two publications within the first chapter of the cumulative part of this dissertation. The exact mechanism of interaction and the resulting findings are described in more detail there. In addition to the disulfide bond found between Cys<sub>102</sub> and Cys<sub>153</sub>, it is described that HDAC8 can be regulated by three other disulfide bonds, namely between Cys<sub>244</sub> and Cys<sub>287</sub>, Cys<sub>275</sub> and Cys<sub>352</sub>, and between Cys<sub>125</sub> and Cys<sub>131</sub>. Thus, it is highlighted that HDAC8 has a unique pattern of regulatory disulfide bonds among human histone deacetylases. These findings serve as a basis for the discovery and development of the first covalent inhibitors of HDAC8 by a screening campaign for the discovery of cysteine-targeted covalent drugs, first fragments have been identified. These results are summarized in the last two publications of the first chapter.

Thus, the first chapter of this dissertation describes a promising strategy for the development of HDAC8 selective inhibitors by exploiting specific, cysteine-dependent regulatory mechanisms. Problems that normally arise in inhibitor development due to the highly conserved binding pocket of HDACs are circumvented by exploiting such specific regulatory mechanisms. However, it should not be forgotten that the development of targeted covalent inhibitors presents scientists with other challenges that cannot be underestimated. One of these challenges is the precise balancing of reactivity. There is a fine line between the targeted covalent modification of specific cysteines on proteins and a non-specific reaction with any available cysteine.

The second chapter of the cumulative part addresses the discovery of the disulfide bond-inducing inhibitor PD 404,182 and describes the further development of this drug towards unreactive molecules in order to focus on the molecular recognition of reversible interaction in the active site. This approach aims to develop an alternative to the common zinc-complexing competitive inhibitors. PD 404,182 is a cyclic benzothiazinimine, which forms a mixed disulfide upon approaching a cysteine, followed by ring opening. In the next step, an intermolecular disulfide bond formation is initiated through a substitution reaction with another protein-bound cysteine. By

---

---

substituting the imine nitrogen within PD-404,182 for sulfur towards the thion, it is possible to suppress the reaction towards cysteine, resulting in a plethora of different derivatives with high potency and specificity against HDAC8. These structures exert their inhibitory effect solely through molecular recognition at the active site by displacement of the substrate.

In cooperation with Ina Oehme from the German Cancer Research Centre (Deutschen Krebsforschungszentrum, DKFZ) in Heidelberg, it was additionally shown that this class of molecules exerts effects on cell cultures comparable to the selective reference inhibitor PCI 34051. Thus, a second generation of inhibitors derived from PD-404,182 was created, which has a completely novel zinc-complexing function.

In addition to the inhibitors developed in the research group of Prof. Dr. Meyer Almes, molecules with the same functionality were also tested for inhibitory effects on HDAC8 in a cooperation with Xuefeng Jiang from the East China Normal University (ECNU). This not only identified promising new lead structures but also published an approach for a faster, simpler, and above all more sustainable synthesis of this class of drugs. Thus, a previously undescribed class of HDAC8 inhibitors has been developed based on the initial discoveries. These could serve as an alternative to common zinc-complexing HDAC inhibitors and can be synthesized quickly and sustainably.

The third subchapter of the cumulative part of this doctoral thesis discusses an possible alternative to common HDAC inhibitors. In collaboration with C. S. Ramaa from the Bharati Vidyapeeth's College of Pharmacy, previously known and extensively researched molecules have been attributed a new role as HDAC8 inhibitors. These molecules are derivatives of thiazolidinediones, which were once mentioned in various publications as potential antidiabetic drugs. Due to long-term side effects, commercial interest in this class of drugs declined. However, it was found that the investigated thiazolidinediones have a strong structural similarity to HDAC inhibitors. Essentially, they possess a zinc complexing group, a hydrophobic linker, and a variable cap region that closes the binding pocket of the enzyme. Through the cooperation partner, several hundred structures with the functional thiazolidinedione group were provided and tested for inhibitory activity against HDAC8 in this dissertation. This resulted in several structural subgroups with  $IC_{50}$  values in the micromolar range. The identified compounds were subsequently tested for isoenzyme selectivity against other HDACs and the thermodynamic stabilization of HDAC8 through drug binding was investigated. The resulting publications were completed by molecular docking and testing the effect on cell culture models. This collaboration resulted in two publications that identified a completely new lead structure for the development of possible HDAC8 inhibitors and thus provide a basis for further optimization of these drugs.

The last chapter of the cumulative part of this thesis summarizes four publications that do not belong to any of the previous chapters, but are also part of the overarching theme of drug development against HDACs. Two of them explore the importance of a transient binding pocket in HDAC8. This is located directly next to the active center and is formed by binding specific inhibitors.

In the first publication, an inhibitor was described that has an exceptionally long residence time on the enzyme due to additional binding in this side pocket. The second deals with the role of Met<sub>274</sub> and the importance of this amino acid in binding selective HDAC8 inhibitors.

In addition, a publication has emerged that describes another subgroup of the aforementioned thiazolidinediones as HDAC4 inhibitors. The focus of this publication is on the empirical exchange of various amino acids within the binding region of inhibitors on HDAC4 and the investigation of which amino acids are crucial for the interaction.

Finally, within the last chapter of the cumulative part, a publication on the application of statistical experimental design in a teaching course was created. This publication describes how the Michaelis-Menten theory and that of competitive inhibition can be integrated into a student teaching practical through statistical experimental design.

In addition to the published articles, parts of this work were presented at international scientific conferences in the form of poster presentations. Thus, the present work makes a significant contribution to the development of new HDAC8-specific inhibitors, particularly in identifying alternatives to current efforts that could develop into mature inhibitors in the future.

---

---

---

## Inhaltsverzeichnis

---

1	Einleitung	1
1.1	Humane Histondeacetylasen	1
1.2	Histondeacetylase 8	3
1.3	Cysteinabhängige Redoxbiologie	4
1.4	HDAC-Inhibitoren	6
1.5	Kovalente Inaktivatoren	7
2	Literaturverzeichnis	9
3	Abbildungsverzeichnis	13
4	Abkürzungsverzeichnis	14
5	Kumulativer Teil	15
5.1	Untersuchung der cysteinabhängigen Redoxregulation von HDAC8 und Entwicklung erster kovalenter Inaktivatoren	15
5.2	Wirkstoffe mit Dithiocarbamat Funktionalität als potenzielle HDAC8 Inhibitoren	63
5.3	Umnutzung von Thiazolidindionen als HDAC8 Inhibitoren	91
5.4	Publikationen zu anderen Themen während der Doktorarbeit	148
6	Danksagung	238
7	Erklärungen	239

---

---

# 1 Einleitung

---

## 1.1 Humane Histondeacetylasen

Warum sind Menschen so unterschiedlich, obwohl sie eine Übereinstimmung von etwa 99,9% Ihres Erbguts untereinander aufweisen?<sup>1</sup> Selbst zu den nächsten Verwandten des Menschen, den Schimpansen, besteht noch eine genetische Übereinstimmung von mehr als 98,5%.<sup>2</sup> Warum entwickeln eineiige Zwillinge unterschiedliche Krankheiten, obwohl sie sich so ähnlich sind? Dachte man noch mit der Entschlüsselung des menschlichen Genoms<sup>3</sup>, welches ein Meilenstein der modernen Biowissenschaften darstellt, dass man die Antwort zur Bekämpfung jeglicher Krankheiten und den „Schlüssel zum Leben“ finden könnte, so stellte sich schnell Ernüchterung ein. Es ist, wie so oft in der Wissenschaft, komplexer als ursprünglich angenommen. Im Laufe der folgenden Jahre entwickelte sich ein tiefgreifenderes Verständnis darüber, wie Gene reguliert werden, wann diese an und ab geschaltet werden und warum Organismen mit einem nahezu identischen Genom, doch so unterschiedlich sind.

Das Teilgebiet der Biowissenschaften, welches sich mit der Regulation von Genen aufgrund äußerer Einflüsse befasst ist die Epigenetik.<sup>4</sup> Im Kern geht es darum, dass regulatorisch wirkende Proteine, wie zum Beispiel Transkriptionsfaktoren, durch Mechanismen wie posttranslationale Modifikationen (PTMs) oder andere Effekte ihre Aktivität, Struktur und Bindeeigenschaften verändern. Dadurch kann das Binden von RNA-Polymerasen oder Transkriptionsfaktoren verbessert oder verschlechtert werden. Dies führt zu einer veränderten Konzentration an synthetisierten Proteinen, welche auf diesem spezifischen Abschnitt der DNA kodiert sind. Auf der anderen Seite, kann auch die DNA direkt modifiziert werden, wodurch das Binden von RNA-Polymerasen verhindert wird.<sup>5</sup>

Die vorliegende Arbeit fokussiert sich auf die Untersuchung von Histondeacetylasen (HDACs). Namensgebend ist das erste und wohl am meisten untersuchte Substrat der HDACs, die Histone.<sup>6</sup> Histone sind grundlegend für die Struktur und Organisation der DNA. Sie sind kleine, globuläre Proteine, welche sich zu einem Oktamer verbinden. Um dieses Oktamer windet sich die DNA und es bildet sich das sogenannte Nukleosom, welches eine ungefähre Größe von 10 nm besitzt. Wie an einer Perlenkette reihen sich nun Nukleosomen zu einem großen DNA-Protein-Komplex auf, dem Chromatin. Dieses bildet schlussendlich das Chromosom.<sup>7</sup> Dieser Prozess ist dynamisch und das Bindungsgleichgewicht zwischen Histonen und DNA verändert sich stetig. Besteht eine schwache Bindung der DNA mit Histonen, spricht man vom sogenannten Euchromatin, welches eine aufgelockerte Struktur darstellt. Im Gegensatz dazu weist das Heterochromatin eine starke Bindung zwischen DNA und den Histonen auf. Es wird auch kondensiertes Chromatin genannt. Das Bindungsgleichgewicht zwischen DNA und Histon wird unter anderem durch die Acetylierungen von Lysinresten an der N-terminalen Region der Histone beeinflusst.<sup>8,9</sup> Durch diese PTM wird der Ladungszustand der Oberfläche der Histone derartig beeinflusst, dass sie das Bindungsgleichgewicht zwischen DNA und Histon negativ beeinflusst. Innerhalb von Histonen sind Lysinreste an der freien  $\epsilon$ -Aminofunktion positiv geladen. Deshalb werden diese generell auch als basische Proteine bezeichnet. DNA hingegen verfügt, aufgrund der Phosphatgruppe des Phosphat-Ribose Rückgrates, über einen Überschuss an negativen Ladungen. Diese ionische Wechselwirkung ist wesentlich für die Interaktion zwischen DNA und Histonen. Liegen die Lysine des Histons an der  $\epsilon$ -Aminofunktion acetyliert vor, wird die positive Ladung ausgeglichen und die Bindung lockert sich auf. Die Acetylierung erfolgt durch die sogenannten Histonacetyltransferasen (HATs), welche die Gegenspieler der HDACs darstellen (Abbildung 1).<sup>10</sup>

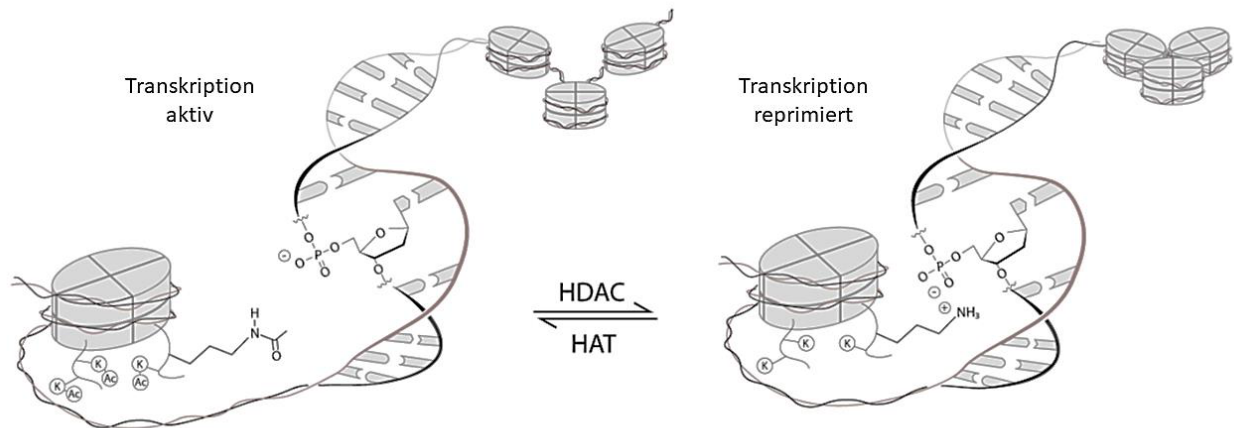


Abbildung 1: Illustration des Acetylierungsgleichgewichtes, hervorgerufen durch die entgegengesetzten Aktivitäten von Histondeacetylase (HDAC) und Histonacetyltransferasen (HAT), welches die Wechselwirkung zwischen Histonen und DNA steuert und somit die Transkription von Genen aktiviert oder hemmt. Die Abbildung ist abgewandelt aus.<sup>11</sup>

HDACs nehmen demnach eine integrale Rolle für die Regulation von Genen ein. Die Schaffung von Wissen über diese Enzyme liefert ein besseres Verständnis epigenetischer Prozesse.<sup>12</sup> Schon heute zeigt sich, dass eine Hemmung von HDACs, mittels kleiner Moleküle, ein vielversprechender Ansatz für die Behandlung verschiedener, HDAC assoziierter, Krankheiten ist.<sup>13</sup> Auch zeigt sich, dass HDACs eine wichtige Rolle bei der Entwicklung von Lebewesen und Stoffwechselfunktionen spielen.<sup>14,15</sup>

HDACs gehören im weitesten Sinne zur Enzymklasse der Hydrolasen und lassen sich in vier Klassen einteilen, die  $\text{NAD}^+$  abhängigen Sirtuine<sup>16,17</sup> der HDAC Klasse III und die zinkabhängigen HDACs der Klassen I, II und IV (Abbildung 2).<sup>18</sup>

		Größe	Lokalisation	
Klasse I	HDAC1	AA 9-321	482	Kern
	HDAC2	AA 9-322	488	Kern
	HDAC3	AA 3-316	428	Kern / Zytoplasma
	HDAC8	AA 14-324	377	Kern
Klasse IIa, IIb	HDAC4	AA 655-1084	1084	Kern / Zytoplasma
	HDAC5	AA 684-1028	1122	Kern / Zytoplasma
	HDAC6	AA 87-404   AA 482-800	1215	Zytoplasma
	HDAC7	AA 518-865	952	Kern / Zytoplasma
	HDAC9	AA 631-978	1011	Kern / Zytoplasma
	HDAC10	AA 1-323	669	Zytoplasma
Klasse IV	HDAC11	AA 14-326	347	Kern

**Katalytische Domäne**

Abbildung 2: Einteilung der Zink-abhängigen humanen Histondeacetylase. Die Abbildung ist abgewandelt aus.<sup>11</sup>

Die katalytische Aktivität der zinkabhängigen HDACs entfaltet sich durch die Polarisierung eines Wassermoleküls innerhalb des Aktivzentrums (AZ). Die Polarisierung wird hervorgerufen durch ein gebundenes Zinkion, welches anschließend an den Carbonyl-Kohlenstoff des  $\epsilon$ -Aminoacetylrestes des acetylierten Lysins addiert. Über eine nachgeschaltete Substitutionsreaktion mit tetragonalem Übergangszustand ( $\text{S}_{\text{N}}2\text{t}$ -

Mechanismus) werden Essigsäure und ein Lysinrest frei. Bei den  $\text{NAD}^+$  abhängigen Sirtuinen erfolgt die Deacetylierung über einen mehrstufigen Mechanismus, durch eine Übertragung der Essigsäure auf die Ribose des  $\text{NAD}^+$ .<sup>19,20</sup>

Die folgenden Kapitel sollen einen tieferen Einblick in die in dieser Arbeit hauptsächlich untersuchte Histondeacetylase 8 geben.

## 1.2 Histondeacetylase 8

HDAC8 besteht aus 377 Aminosäuren mit einem Molekulargewicht von 41,8 kDa. Der Kern des Proteins wird durch eine typische  $\alpha/\beta$ -fold Domäne aus acht  $\beta$ -Faltblätter gebildet, welche durch 13  $\alpha$ -Helices umrandet werden und somit das Aktivzentrum mit einem von den Aminosäuren Asp<sub>178</sub>, Asp<sub>267</sub> und His<sub>180</sub> komplexierten Zinkion bilden.<sup>21</sup> Als Mechanismus wird ein Säure-Base Mechanismus, bei welchem His<sub>142</sub>, His<sub>143</sub> und Tyr<sub>306</sub> beteiligt sind, postuliert. His<sub>143</sub> fungiert hierbei als Base und Säure. Im ersten Schritt deprotoniert His<sub>143</sub> das vom Zink komplexierte Wasser, welches darauffolgend nukleophil das Carboxyl-Kohlenstoff der Amidbindung angreift. Das tetragonale Zwischenprodukt wird von Tyr<sub>306</sub> stabilisiert. HDACs, welche anstelle des Tyr<sub>306</sub> ein Histidin haben, können den Übergangszustand nicht stabilisieren und verfügen dementsprechend über keine *in vitro* Enzymaktivität. In einem zweiten Schritt fungiert His<sub>143</sub> als Base und protoniert das sekundäre Amin. Infolgedessen kommt es zur Deacetylierung, worauf Acetat und proteingebundenes Lysin werden freigegeben.<sup>22</sup>

Im Gegensatz zu den anderen Vertretern der HDAC Klasse I fehlt HDAC8 eine C-terminale Domäne mit einer Länge von 50 – 111 Aminosäuren (Abbildung 2), welche bei HDAC1, 2 und 3 für die Rekrutierung von Interaktionspartnern zuständig ist.<sup>23</sup> Dadurch wird die enzymatische Aktivität und Lokalisation innerhalb der Zelle moduliert. Zusätzlich wird bei HDAC1, 2 und 3 die Enzymaktivität durch PTMs innerhalb dieser Domäne reguliert.<sup>23</sup>

Neben dem verkürzten C-Terminus ist ein Alleinstellungsmerkmal von HDAC8 eine besonders flexible Bindungstasche, welche durch Konformationsänderungen des L1 Loops zwischen den Aminosäuren 30 und 36 hervorgerufen wird.<sup>24</sup> Ein Vergleich von Kristallstrukturen mit unterschiedlichen Inhibitoren, welche im Aktivzentrum gebunden sind, verdeutlicht diese Flexibilität (Abbildung 3). Auf der gegenüberliegenden Seite ist die Flexibilität zwischen Loop 2 und 6 hervorzuheben, welche eine Furche bilden, die für die Bindung Isoenzym-selektiver Inhibitoren verantwortlich gemacht wird.<sup>25</sup>

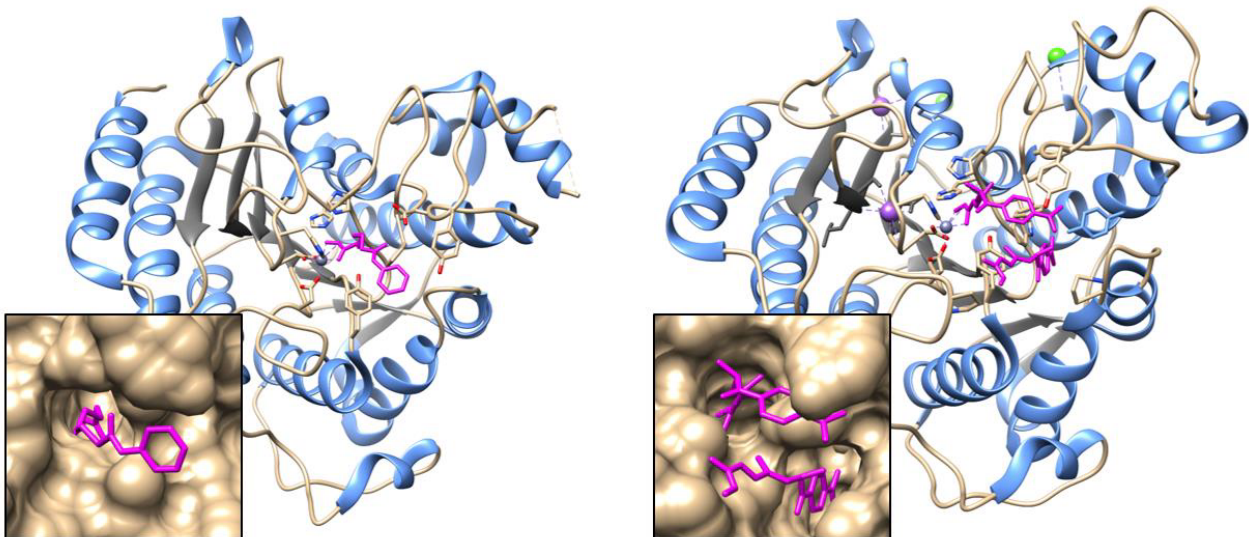


Abbildung 3: Illustration der strukturellen Flexibilität der Bindungstasche von HDAC8. Die linke Abbildung (1T69) zeigt den Inhibitor (Magenta) SAHA gebunden am katalytischen Zinkion (Grau). Die rechte Abbildung (1T64) zeigt den Inhibitor (TSA) gebunden im Aktivzentrum von HDAC8. Im ersten Schritt öffnet sich die transiente Seitentasche, in welcher dann ein weiterer Ligand binden kann.

Durch diese gegebene Flexibilität kann HDAC8 seine Struktur an verschiedene Substrate anpassen.<sup>26</sup> Studien zeigen, dass die Enzymaktivität nicht nur auf die Deacetylierung von Lysinen beschränkt ist, sondern auch Fettsäureacyllysine<sup>27,28</sup>, Laktat und Pyruvatreste<sup>29</sup> sowie Thioacetyllysine<sup>30</sup> werden als Substrate erkannt und gespalten. Neben den namensgebenden Histonen haben sich in letzter Zeit unzählige nicht-Histonproteine als denkbare Substrate gezeigt.<sup>31-34</sup> Diese Beobachtungen lenken den Fokus von einem Histon-fokussierten Modell,

---

hin zu einem Protein-Acetylom-Modell, mit zur Zeit mehr als 3600 potentiell acetylierten Proteinen, welche für essentielle Funktionen in zellulären Prozessen zuständig sind.<sup>31</sup> Zu den bekanntesten Substraten von HDAC8 zählen SMC3, ERRalpha und p53.<sup>33</sup> Zur Zeit werden auch Peroxiredoxin 6, Phosphoglyceratmutase 1 und Parkinson Protein 7 als mögliche Substrate diskutiert, der eindeutige Nachweis steht allerdings noch aus.

Über die Regulation von HDAC8 ist wenig bekannt. Als Interaktionspartner wurden durch Co-Immunopräzipitationsexperimente CREB (cAMP response element binding protein) und Proteinphosphatase 1 identifiziert.<sup>35</sup> Zusätzlich zeigt eine erhöhte HDAC8-Expression eine verringerte CREB-Aktivität. Des Weiteren konnte gezeigt werden, dass die Enzymaktivität von HDAC8 abhängig vom katalytischen Metallion ist.<sup>36,37</sup> Die Autoren der Studie verweisen hierbei auf einen potentiell reversiblen Metallaustausch im Aktivzentrum, um in Abhängigkeit der Ionenkonzentration die Enzymaktivität und Substraterkennung anzupassen.

Abschließend ist an dieser Stelle noch aufzuführen, dass HDAC8 an Ser<sub>39</sub> durch Protein Kinase A phosphoryliert wird und dadurch die Enzymaktivität allosterisch beeinflusst wird.<sup>38</sup> Ser<sub>39</sub> liegt innerhalb der Helix H2 neben der Helix H1. Durch die Phosphorylierung ändert sich die Ladung an Ser<sub>39</sub> und die beiden Loops werden durch eine ionische Wechselwirkung näher zusammengezogen. Diese Konformationsänderung hat wiederum einen Einfluss auf die Struktur des L1 Loops, welcher bereits als integraler Bestandteil der besonderen Flexibilität des Aktivzentrum beschrieben wurde.<sup>39</sup> Die HDAC8-spezifische allosterische Regulation innerhalb der H<sub>1</sub>L<sub>1</sub>H<sub>2</sub>-Domäne macht diese Region besonders interessant für zukünftige Untersuchungen, da sie eine Besonderheit unter den Histondeacetylasen ist und so in den anderen HDACs nicht vorkommt.<sup>40-42</sup>

Als therapeutisches Zielprotein kommt HDAC8 bei der Entstehung und Behandlung von vielen Krankheitsbildern in Frage.<sup>43</sup> Es hat sich gezeigt, dass HDAC8 in vielen Krebsgeweben überexprimiert wird.<sup>44</sup> Als Beispiel sind Leberkarzinome, Bauchspeicheldrüsen-Tumore, metastasierende Melanome, die akute myeloische Leukämie (AML) sowie die akute lymphatische Leukämie (ALL) zu nennen.<sup>45-47</sup> Eine besondere Rolle wird HDAC8 bei der Entstehung von Neuroblastomen zugeschrieben.<sup>48</sup> Neuroblastome sind mit etwa 7% aller Krebserkrankungen die häufigsten soliden Tumore im frühen Kindesalter und betreffen mit 40% besonders Neugeborene bis zum ersten Lebensjahr. Erste Studien konnten zeigen, dass es unter Zugabe der HDAC8-spezifischen Inhibitoren PCI-34051 und CPD2 in Kombination mit ATRA (all-trans Retinsäure) zu einem drastischen Absterben von Neuroblastomzellen kommt.<sup>48</sup> Laut den Autoren ist CREB für das Zusammenspiel von HDAC8 und ATRA zuständig. Die spezifische Hemmung von HDAC8 ist somit eine vielversprechende Herangehensweise für die Behandlung von Neuroblastomen.

Im weiteren Verlauf dieser Dissertation wird auf die Struktur und das Design von HDAC-Inhibitoren eingegangen und ihre Wirkweise beschrieben. Doch zunächst soll auf die besonderen Aspekte der cysteinabhängigen Redoxbiologie eingegangen werden, um eine Wissensgrundlage für hervorgebrachte Erkenntnisse dieser Doktorarbeit zu liefern.

### 1.3 Cysteinabhängige Redoxbiologie

Die Grundlage der Redoxbiologie beruht auf der Vorstellung, dass ein Gleichgewicht zwischen Oxidantien und Antioxidantien existiert, welches durch den Einfluss reaktiver Sauerstoffspezies (ROS) wie Superoxiden, Hydroxylradikalen und Wasserstoffperoxid gestört wird. Es wurde angenommen, dass es aufgrund dieses Ungleichgewichtes zwischen Oxidantien und Antioxidantien zu schwerwiegenden physiologischen Änderungen, wie der Entstehung von Krebs kommt.

Heute haben wir ein besseres Verständnis darüber, welchen Einfluss ROS auf molekularer Ebene haben. Allerdings ist immer noch weiteres, tiefergreifenderes Wissen nötig. Im Mittelpunkt stehen hierbei Cysteinthiole, welche aufgrund ihrer, unter den Aminosäuren einzigartigen Reaktivität, verschiedene PTMs haben können.<sup>49</sup> Diese PTMs beeinflussen nicht nur die Struktur von Proteinen, sondern können zu Veränderungen der Enzymaktivität und Lokalisation führen, sowie die Interaktion zwischen Proteinen einleiten oder unterbrechen.<sup>50</sup> Bei solchen, regulativen Cysteinen, spricht man auch von Redoxschaltern.<sup>51</sup> Durch die direkte Reaktion mit H<sub>2</sub>O<sub>2</sub> bildet sich unter Wasserabspaltung Sulfensäure, welche durch eine erneute Oxidation mit H<sub>2</sub>O<sub>2</sub> zur Sulfinensäure und schließlich irreversibel zur Sulfonsäure oxidiert wird (Abbildung 4).



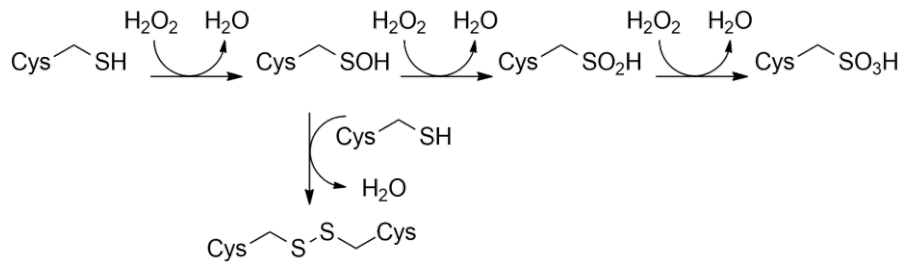


Abbildung 4: Oxidation von Cysteinen durch Wasserstoffperoxid. Im ersten Schritt wird das Cysteinthiol zur Sulfensäure oxidiert, welche dann unter Wasserabspaltung ein Disulfid eingehen kann. Eine Überoxidation führt zur Sulfinsäure und schlussendlich zur Sulfonsäure.

Des Weiteren kann sich aus der Sulfensäure durch die Reaktion mit einem weiteren Cysteinthiol ein inter- oder intramolekulares Disulfid, bilden.<sup>52</sup> Auch kleine, thiolhaltige Moleküle wie Glutathion (GSH), welche als Redoxpartner Glutathion:Glutathiondisulfid (GSH:GSSG,  $E^{0'} = -230 \text{ mV}$ ) als zellulärer Redoxpuffer fungieren, können mit Sulfensäure reagieren und somit ein gemischtes Disulfid bilden.<sup>53</sup> Neben der Reaktion mit  $\text{H}_2\text{O}_2$  können Cysteinthiole auch mit dem Gasotransmitter  $\text{H}_2\text{S}$  zum Persulfid reagieren. Neueste Studien entdeckten die sogenannte SONOS Brücke, bei welcher zwei Cysteine mit einem benachbarten Lysin eine kovalente, redoxabhängige Dreifachverbindung eingehen.<sup>54,55</sup> Entdeckungen wie diese zeigen, wie vielfältig cysteinabhängige Redoxmodifikationen sind und wie viel es auf diesem wissenschaftlichen Feld noch zu entdecken gibt.

Neben Cystein gibt es unter den 20 kanonischen Aminosäuren nur noch Methionin als schwefelhaltige Aminosäure. Jedoch ist hier aufgrund der Thioetherstruktur des Methionins die Reaktivität erheblich geringer als bei Cystein. In Lösung hat die Thiofunktion von freiem Cystein einen  $\text{pK}_\text{S}$  Wert von ca. 8,5.<sup>49</sup> Das Gleichgewicht zwischen Thiol und Thiolat wird durch die Proteinumgebung, zum Beispiel durch proximale basische Aminosäuren wie Histidin, Lysin und Arginin, oder durch Wasserstoffbrückenbindungen zum Peptidrückgrat, in Richtung Thiolat, verschoben und somit die Reaktivität erhöht.<sup>53</sup> Einzig Selenocystein (Sec) hat aufgrund seines größeren Elektronenradius eine noch höhere Reaktivität ( $\text{pK}_\text{S}$  ca. 5,3). Selenocystein kommt zum Beispiel in Thioreduktasen vor, welche am Ende einer Disulfidaustauschkaskade oxidiertes Thioredoxin reduzieren und unter NADPH Verbrauch rereduziert werden.<sup>56,57</sup> Aufgrund des Gleichgewichtes zwischen Thiol und Thiolat und dem daraus resultierenden  $\text{pK}_\text{S}$ -Wert ergibt sich das Redoxpotential einer Disulfidbrücke, welches von Disulfid zu Disulfid unterschiedlich ausfällt.<sup>58</sup> Das Redoxpotential ist hierbei die Triebkraft für Oxidation und Reduktion von Thiolen und Disulfiden. Regulatorische Disulfide haben ein Redoxpotential von -200 bis -300 mV, da eine zelluläre Reduktion durch Thioredoxine oder GSH gewährleistet sein muss. Strukturelle Disulfide hingegen weisen ein wesentlich geringeres Redoxpotential auf, um auch in Anwesenheit disulfidreduzierender Enzyme und freier Thiole intakt zu bleiben.<sup>59</sup>

Schließlich stellt sich die Frage, wie die Oxidationsäquivalente von Wasserstoffperoxid bis hin zum Redox regulierten Enzym gelangen. Lange galten Peroxidasen und Peroxiredoxine als Enzyme, welche die Spaltung von  $\text{H}_2\text{O}_2$  in Wasser übernehmen und einzig dem Schutz der Zelle vor einer Überexposition an ROS dienen.<sup>60</sup> Heute vermutet man, dass Oxidationsäquivalente über Disulfidaustauschkaskaden bis hin zum Zielprotein gelangen (Abbildung 5).<sup>61</sup>

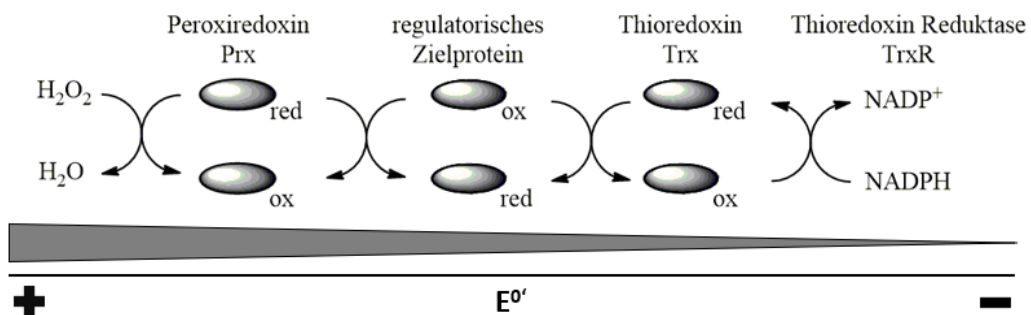


Abbildung 5: Schematische Darstellung einer Disulfidaustauschkaskade, auch Redox-Relay genannt.

Peroxiredoxine werden anhand der Anzahl der katalytischen Cysteine in Ein- und Zweicystein-Peroxiredoxine eingeteilt. Bei ersteren wird ein Cystein durch  $\text{H}_2\text{O}_2$  zur Sulfensäure oxidiert und das benachbarte Cystein bildet

darauf eine Disulfidbrücke unter Wasserabspaltung aus. Diese Disulfidbrücke wird von einem Cystein des Empfängerproteins nukleophil attackiert, worauf sich eine intermolekulare Disulfidbrücke zwischen zwei Proteinen bildet. Ein weiteres Cystein im Empfängerprotein attackiert nun die intermolekulare Disulfidbrücke und es bildet sich eine intramolekulare Verknüpfung zweier Thiole. Bei den Ein-Cystein-Peroxiredoxinen dient die initial gebildete Sulfensäure als Elektrophil für die direkte Disulfidbildung zwischen zwei Proteinen.<sup>62</sup>

Das in beiden Fällen oxidierte Empfängerprotein wird wiederum durch Thioredoxine oder GSH reduziert und kann seiner normalen Funktion nachgehen. Ein prominentes Beispiel für eine Peroxiredoxin-vermittelte Redoxkaskade zur Signaltransduktion wurde von Sobotta *et. al* für Peroxiredoxin 2 und STAT3 beschrieben.<sup>63</sup> Die Regulation von redoxsensitiven Proteinen erfolgt somit nicht durch direkte Reaktion mit H<sub>2</sub>O<sub>2</sub>, sondern steht vielmehr unter kinetischer Kontrolle, vermittelt durch Peroxiredoxine und hochspezifische Interaktionen zwischen Donor- und Empfängerprotein. H<sub>2</sub>O<sub>2</sub> und andere ROS sind somit viel mehr als nur zellschädigende Moleküle.<sup>64</sup> Sie haben vermutlich weitreichende regulatorische Funktionen innerhalb der verschiedenen Zellkompartimente und die aktuelle Forschung dürfte noch viele neue Erkenntnisse offenlegen.

#### 1.4 HDAC-Inhibitoren

HDAC-Inhibitoren (HDACis) verfügen in der Regel über eine Cap-Gruppe, welche für die Erzeugung von Selektivität variiert werden kann, einem hydrophoben Linker und einer Zink-bindenden Kopfgruppe, für die Chelatisierung.<sup>11</sup> Heutzutage sind fünf HDACis für die Behandlung von Krebs zugelassen. Zum Beispiel Vorinostat (SAHA), Romidepsin (FK228) und Belinostat (PDX-101) für die Behandlung von T-Zell Lymphomen<sup>65-67</sup>. Panobinostat (LBH-589) ist für die Behandlung von multiplen Myelomen zugelassen.<sup>68</sup> Erst vor kurzem wurde in China der HDACis Chidamide für die Behandlung von T-Zell Lymphomen zugelassen.<sup>69</sup> In der folgenden Abbildung sind die Strukturen dieser Inhibitoren illustriert (Abbildung 6).

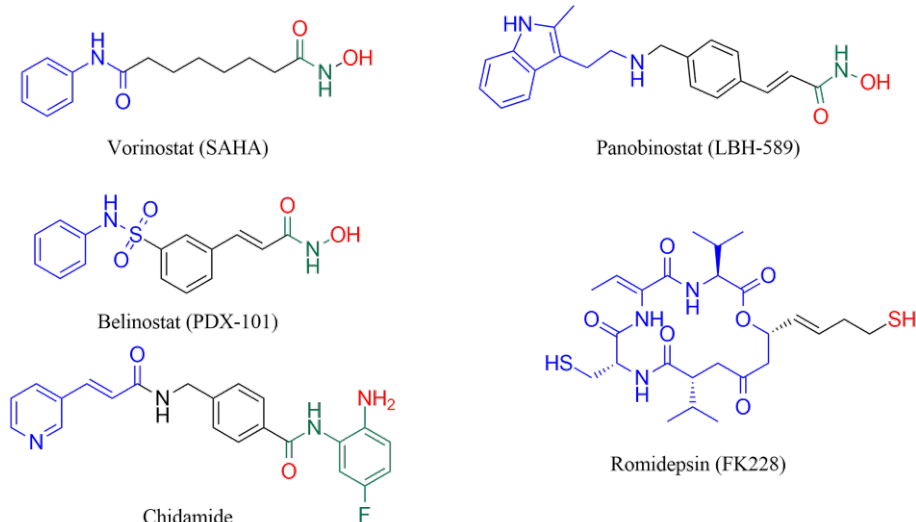


Abbildung 6: Strukturformeln von zugelassenen HDACis für die Behandlung verschiedener Krebsarten. Die Cap-Gruppe ist blau gefärbt, der verbindende Linker ist schwarz, die Zink-bindende Gruppe ist grün und die chelatisierenden Atome sind rot dargestellt. Die Abbildung ist abgewandelt aus.<sup>11</sup>

Es gibt HDACis, welche mehr oder weniger spezifisch gegen einzelne HDACs wirken (Isoenzym-selektive Inhibitoren). Allerdings richten sich die meisten HDACis sich unspezifisch gegen alle Isoenzyme richten (pan-Inhibitoren).<sup>13</sup> Diese lassen sich in drei gut erforschte Untergruppen einteilen: (1) Hydroxamsäuren, (2) kurzkettige Fettsäuren und (3) Benzamide.<sup>70</sup> Die erste gelöste Struktur war die des *histone deacetylase-like protein* (HDLP) mit der Hydroxamsäure SAHA und TSA.<sup>71</sup> Aufgrund der starken Konservierung des Aktivzentrums unter den Histondeacetylasen stellte dieser Moment einen entscheidenden Schritt für das Verständnis der molekularen Interaktion zwischen HDACs und ihren Inhibitoren dar. Dadurch war es möglich einzelne Aminosäuren, welche eine entscheidende Rolle für die Interaktion spielen, zu identifizieren und neuere Inhibitoren anhand der dreidimensionalen Struktur passgenau zu entwerfen. Für die Bindung eines Hydroxamsäure-Inhibitors spielen die beiden katalytischen Histidine His<sub>141</sub> und His<sub>142</sub> sowie Tyr<sub>304</sub> eine wesentliche Rolle. Diese Aminosäuren komplexieren die Hydroxamat-Gruppe des Inhibitors in ähnlicher Weise, wie das Carbonsäureamid von acetyliertem Lysin bei der Substratumsetzung. Der Weg zum Aktivzentrum wird durch einen hydrophoben Kanal gebildet, welcher durch die beiden Phe<sub>151</sub> und Phe<sub>206</sub> flankiert wird. In diesen Kanal legt sich der hydrophobe

---

Linker der Inhibitoren, welcher an beiden Seiten von den beiden aromatischen Resten der Phenylalanine gefestigt wird. Weiter von entscheidender Rolle ist das oberflächengebundene Asp<sub>100</sub>, welches mit dem Inhibitor eine Wasserstoffbrücke ausbildet.<sup>11</sup> All diese genannten Eigenschaften teilen sich die verschiedenen HDACs untereinander. Allerdings weisen sie dabei geringe aber durchaus entscheidenden Unterschiede auf. So unterscheiden sie sich beispielsweise in der Flexibilität der Bindetasche.

Für die Entwicklung HDAC8-spezifischer Inhibitoren haben sich andere molekulare Eigenschaften, wie die anfänglich erwähnte, besondere Flexibilität der Bindetasche, als wichtig herauskristallisiert. Der zur Zeit potenteste HDAC8-Inhibitor ist PCI-34051.<sup>72</sup> Dieser Inhibitor zählt zu den sogenannten L-förmigen HDAC8-Inhibitoren. Diese L-Form kann sich besonders gut an das Aktivzentrum von HDAC8 anpassen, weswegen diese als Isoenzym selektiv angesehen werden. Eine bislang wenig untersuchte Möglichkeit, um Selektivität für HDAC8 zu erlangen, ist die Entwicklung von kovalenten Inhibitoren, denen sich das folgende Kapitel grundlegend widmet.

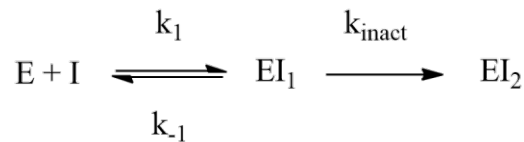
## 1.5 Kovalente Inaktivatoren

Kovalente Inaktivatoren entfalten Ihre Wirkung durch die kovalente Modifikation spezifischer Aminosäurereste an Proteinen. Dadurch verlieren sie ihre Enzymaktivität oder sind nicht mehr in der Lage, eine Bindung mit Interaktionspartnern einzugehen. Die Hemmung der Enzymaktivität kann durch die Blockierung des Aktivzentrums oder durch allosterische Effekte erfolgen, welche die Struktur des Zielproteins, hervorgerufen durch die kovalente Modifikation, verändern. Diese allosterischen Effekte können auch die Bindeeigenschaften von Proteinen untereinander beeinflussen, sowohl positiv als auch negativ. Für die kovalente Modifikation kommen aufgrund ihrer nukleophilen Eigenschaften vor allem Serin, Lysin und Cystein in Frage. Der unter den Medikamenten am meisten verbreitete kovalente Inaktivator ist vermutlich Aspirin, welcher ein Serin im Aktivzentrum der Prostaglandin-Synthetase irreversibel acetyliert und damit die Aktivität dieses Enzyms hemmt. Aspirin wurde bereits 1899 erstmals vermarktet und wird bis heute vielseitig angewendet. Ein weiteres prominentes Beispiel ist das Antibiotikum Penicillin, welches 1928 entdeckt wurde und einen unumstrittenen Einfluss auf die Bekämpfung mikrobieller Krankheiten hatte und noch immer hat. Modernere Beispiele sind der Protonenpumpenhemmer Omeprazol aus dem Jahre 1988 oder der Bruton-Tyrosinkinase Hemmer Ibrutinib, welcher 2013 für die Behandlung von B-Zell Lymphomen zugelassen wurde.<sup>73,74</sup> Erfolge wie die Entwicklung von Ibrutinib legen das Fundament für einen regelrechten Trend in der Entwicklung kovalenter Inaktivatoren für Kinasen und auch als Antiinfektiva.<sup>75,76</sup>

Trotz dieser erfolgreichen Beispiele werden kovalente Inhibitoren oft kritisch betrachtet. Zum Beispiel können sie, aufgrund unvorhergesehener Modifikationen von anderen Proteinen, unerwartete toxische Nebeneffekte aufweisen oder führen zu einer Arzneimittelüberempfindlichkeit. Des Weiteren eignen Sie sich nicht für Proteine mit einer schnellen „turn over“ Rate und die kovalent modifizierte Aminosäure kann mutieren, was zu einer Resistenz führen kann.<sup>77</sup> Ungeachtet der zu Recht angebrachten Bedenken, haben kovalente Inaktivatoren einige interessante und nicht zu unterschätzende Vorteile. Aufgrund der irreversiblen Bindung kovalenter Inhibitoren und der sich daraus ergebenden hohen Verweilzeit am Protein, müssen diese zum Beispiel in geringeren täglichen Dosierungen, im Vergleich zu reversiblen Inhibitoren verabreicht werden. Zusätzlich ermöglichen kovalente Inhibitoren die Hemmung von bisher als „undruggable“ geltenden Proteinen. Diese können beispielsweise aufgrund ihrer Oberflächeneigenschaften, wie das Fehlen einer Bindetasche, keine Bindung mit Inhibitoren eingehen. Ein gutes Beispiel für ein therapeutisch nicht zugängliches Protein ist die onkogene G12C Mutante von KRAS.<sup>78</sup> Des Weiteren bieten kovalente Inhibitoren eine Möglichkeit, Proteine durch die Bindung an allosterischen Domänen zu inhibieren und somit die kompetitive Bindung im Aktivzentrum zu umgehen, welches oft stark konserviert unter den Isoenzymen ist.

Ziel der Entwicklung kovalenter Inaktivatoren ist es also, deren Spezifität zu erhöhen bei gleichzeitiger Verringerung der Reaktivität. Dies wird erreicht, indem die Bindungskonstante des vorgelagerten Gleichgewichts zwischen Inhibitor und Protein erhöht wird und danach, zielgerichtet eine kovalente Bindung zwischen Aminosäurerest und Inhibitor, mit geringer Reaktivität, eingeleitet wird. Das Konzept der sogenannten zielgerichteten kovalenten Inaktivatoren (*targeted covalent inactivators*, TCI) bedarf einer sorgfältigen Abwägung der Reaktivität, ist aber ein weitestgehend akzeptierter Ansatz.<sup>79</sup>

Kinetisch wird dieses Konzept durch folgende Gleichung beschrieben.



$$k_1/k_{-1} = K_i$$

Der erste Schritt beschreibt das reversible Gleichgewicht zwischen Enzym und Inhibitor, ausgedrückt durch die Gleichgewichtskonstante  $K_i$ , gefolgt von einem irreversiblen Inaktivierungsschritt  $k_{\text{inact}}$ .<sup>76</sup> Für die rationale Entwicklung kovalenter Inaktivatoren wird der Ausdruck  $k_{\text{inact}}/K_i$ , anstelle einer Einteilung nach  $IC_{50}$  Werten herangezogen, mit dem Ziel diesen Wert zu erhöhen.<sup>80</sup>

Neben dem vorgestellten Mechanismus gibt es noch kovalente Inhibitoren, welche an und für sich unreaktiv sind und erst nach Bindung im Aktivzentrum des Enzyms aktiviert werden. Diese Art von kovalenten Inaktivatoren nennt man „*quiescent affinity labels*“ zu denen auch Aspirin, Omeprazol und Penicillin gehören.

Aufgrund des geringen Vorkommens von Cystein innerhalb von Proteinen und der einzigartigen Chemie von Schwefel ist Cystein besonders attraktiv für die Entwicklung zielgerichteter kovalenter Inaktivatoren.<sup>81</sup> Die am besten untersuchte reaktive Gruppe sind Michael-Akzeptoren wie Maleimide oder  $\alpha,\beta$ -ungesättigte Carbonylverbindungen wie das Acrylamid Ibrutinib oder generell andere aktivierte ungesättigte Verbindungen wie Alkene und Alkine. Daneben finden Heteroaromaten, welche über eine nukleophile aromatische Substitution reagieren, Alkylhalide wie  $\alpha$ -Halo-Acetamide, Aldehyde,  $\alpha$ -Diketone sowie Epoxide als potenziell reaktive Gruppen beim Design von Cystein-reaktiven kovalenten Inaktivatoren Verwendung.

---

## 2 Literaturverzeichnis

---

1. Lander, E. S. Initial impact of the sequencing of the human genome. *Nature* 470, 187–197; 10.1038/nature09792 (2011).
2. Initial sequence of the chimpanzee genome and comparison with the human genome. *Nature* 437, 69–87; 10.1038/nature04072 (2005).
3. Finishing the euchromatic sequence of the human genome. *Nature* 431, 931–945; 10.1038/nature03001 (2004).
4. Peixoto, P., Cartron, P.-F., Serandour, A. A. & Hervouet, E. From 1957 to Nowadays: A Brief History of Epigenetics. *International journal of molecular sciences* 21; 10.3390/ijms21207571 (2020).
5. Zhang, L., Lu, Q. & Chang, C. Epigenetics in Health and Disease. *Advances in experimental medicine and biology* 1253, 3–55; 10.1007/978-981-15-3449-2\_1 (2020).
6. Gregoret, I. V., Lee, Y.-M. & Goodson, H. V. Molecular evolution of the histone deacetylase family: functional implications of phylogenetic analysis. *Journal of molecular biology* 338, 17–31; 10.1016/j.jmb.2004.02.006 (2004).
7. Grunstein, M. Histone acetylation in chromatin structure and transcription. *Nature* 389, 349–352; 10.1038/38664 (1997).
8. Kouzarides, T. Acetylation: a regulatory modification to rival phosphorylation? *The EMBO journal* 19, 1176–1179; 10.1093/emboj/19.6.1176 (2000).
9. PHILLIPS, D. M. The presence of acetyl groups of histones. *The Biochemical journal* 87, 258–263; 10.1042/bj0870258 (1963).
10. Yang, X.-J. & Seto, E. HATs and HDACs: from structure, function and regulation to novel strategies for therapy and prevention. *Oncogene* 26, 5310–5318; 10.1038/sj.onc.1210599 (2007).
11. Frühauf, A. & Meyer-Almes, F.-J. Non-Hydroxamate Zinc-Binding Groups as Warheads for Histone Deacetylases. *Molecules (Basel, Switzerland)* 26; 10.3390/molecules26175151 (2021).
12. Turner, B. M. Histone acetylation and an epigenetic code. *Bioessays* 22, 836–845; 10.1002/1521-1878(200009)22:9<836::AID-BIES9>3.0.CO;2-X (2000).
13. Eckschlager, T., Plch, J., Stiborova, M. & Hrabeta, J. Histone Deacetylase Inhibitors as Anticancer Drugs. *International journal of molecular sciences* 18; 10.3390/ijms18071414 (2017).
14. Zhao, S. et al. Regulation of cellular metabolism by protein lysine acetylation. *Science (New York, N.Y.)* 327, 1000–1004; 10.1126/science.1179689 (2010).
15. Liu, X., Yang, S., Yu, C.-W., Chen, C.-Y. & Wu, K. Histone Acetylation and Plant Development. *The Enzymes* 40, 173–199; 10.1016/bs.enz.2016.08.001 (2016).
16. Sauve, A. A. Sirtuin chemical mechanisms. *Biochimica et biophysica acta* 1804, 1591–1603; 10.1016/j.bbapap.2010.01.021 (2010).
17. Singh, C. K. et al. The Role of Sirtuins in Antioxidant and Redox Signaling. *Antioxidants & redox signaling* 28, 643–661; 10.1089/ars.2017.7290 (2018).
18. Seto, E. & Yoshida, M. Erasers of histone acetylation: the histone deacetylase enzymes. *Cold Spring Harbor perspectives in biology* 6, a018713; 10.1101/cshperspect.a018713 (2014).
19. Lombardi, P. M., Cole, K. E., Dowling, D. P. & Christianson, D. W. Structure, mechanism, and inhibition of histone deacetylases and related metalloenzymes. *Current opinion in structural biology* 21, 735–743; 10.1016/j.sbi.2011.08.004 (2011).
20. Marmorstein, R. Structure of histone deacetylases: insights into substrate recognition and catalysis. *Structure (London, England : 1993)* 9, 1127–1133; 10.1016/s0969-2126(01)00690-6 (2001).
21. Somoza, J. R. et al. Structural snapshots of human HDAC8 provide insights into the class I histone deacetylases. *Structure (London, England : 1993)* 12, 1325–1334; 10.1016/j.str.2004.04.012 (2004).
22. Gantt, S. M. L. et al. General Base-General Acid Catalysis in Human Histone Deacetylase 8. *Biochemistry* 55, 820–832; 10.1021/acs.biochem.5b01327 (2016).
23. Moser, M. A., Hagelkruys, A. & Seiser, C. Transcription and beyond: the role of mammalian class I lysine deacetylases. *Chromosoma* 123, 67–78; 10.1007/s00412-013-0441-x (2014).
24. Kunze, M. B. A. et al. Loop interactions and dynamics tune the enzymatic activity of the human histone deacetylase 8. *Journal of the American Chemical Society* 135, 17862–17868; 10.1021/ja408184x (2013).
25. Marek, M. et al. Characterization of Histone Deacetylase 8 (HDAC8) Selective Inhibition Reveals Specific Active Site Structural and Functional Determinants. *Journal of medicinal chemistry* 61, 10000–10016; 10.1021/acs.jmedchem.8b01087 (2018).

26. Toro, T. B., Swanier, J. S., Bezue, J. A., Broussard, C. G. & Watt, T. J. Lysine Deacetylase Substrate Selectivity: A Dynamic Ionic Interaction Specific to KDAC8. *Biochemistry* 60, 2524–2536; 10.1021/acs.biochem.1c00384 (2021).
27. Aramsangtienchai, P. et al. HDAC8 Catalyzes the Hydrolysis of Long Chain Fatty Acyl Lysine. *ACS chemical biology* 11, 2685–2692; 10.1021/acscchembio.6b00396 (2016).
28. Yoo, H. & Polsinelli, G. A. Kinetic Characterization of Human Histone Deacetylase 8 With Medium-Chain Fatty Acyl Lysine. *Epigenetics insights* 14, 25168657211065685; 10.1177/25168657211065685 (2021).
29. Zessin, M. et al. Uncovering Robust Delactoylase and Depyruvoylase Activities of HDAC Isoforms. *ACS chemical biology* 17, 1364–1375; 10.1021/acscchembio.1c00863 (2022).
30. Fatkins, D. G., Monnot, A. D. & Zheng, W. Nepsilon-thioacetyl-lysine: a multi-facet functional probe for enzymatic protein lysine Nepsilon-deacetylation. *Bioorganic & medicinal chemistry letters* 16, 3651–3656; 10.1016/j.bmcl.2006.04.075 (2006).
31. Narita, T., Weinert, B. T. & Choudhary, C. Functions and mechanisms of non-histone protein acetylation. *Nature reviews. Molecular cell biology* 20, 156–174; 10.1038/s41580-018-0081-3 (2019).
32. Toro, T. B. & Watt, T. J. Critical review of non-histone human substrates of metal-dependent lysine deacetylases. *FASEB journal : official publication of the Federation of American Societies for Experimental Biology* 34, 13140–13155; 10.1096/fj.202001301RR (2020).
33. Alam, N. et al. Structure-Based Identification of HDAC8 Non-histone Substrates. *Structure (London, England : 1993)* 24, 458–468; 10.1016/j.str.2016.02.002 (2016).
34. Wolfson, N. A., Pitcairn, C. A. & Fierke, C. A. HDAC8 substrates: Histones and beyond. *Biopolymers* 99, 112–126; 10.1002/bip.22135 (2013).
35. Gao, J., Siddoway, B., Huang, Q. & Xia, H. Inactivation of CREB mediated gene transcription by HDAC8 bound protein phosphatase. *Biochemical and biophysical research communications* 379, 1–5; 10.1016/j.bbrc.2008.11.135 (2009).
36. Kim, B., Pithadia, A. S. & Fierke, C. A. Kinetics and thermodynamics of metal-binding to histone deacetylase 8. *Protein science : a publication of the Protein Society* 24, 354–365; 10.1002/pro.2623 (2015).
37. Wu, R., Wang, S., Zhou, N., Cao, Z. & Zhang, Y. A proton-shuttle reaction mechanism for histone deacetylase 8 and the catalytic role of metal ions. *Journal of the American Chemical Society* 132, 9471–9479; 10.1021/ja103932d (2010).
38. Lee, H., Rezai-Zadeh, N. & Seto, E. Negative regulation of histone deacetylase 8 activity by cyclic AMP-dependent protein kinase A. *Molecular and cellular biology* 24, 765–773; 10.1128/MCB.24.2.765-773.2004 (2004).
39. Dowling, D. P., Gantt, S. L., Gattis, S. G., Fierke, C. A. & Christianson, D. W. Structural studies of human histone deacetylase 8 and its site-specific variants complexed with substrate and inhibitors. *Biochemistry* 47, 13554–13563; 10.1021/bi801610c (2008).
40. Shukla, V. K., Siemons, L., Gervasio, F. L. & Hansen, D. F. Aromatic side-chain flips orchestrate the conformational sampling of functional loops in human histone deacetylase 8. *Chemical science* 12, 9318–9327; 10.1039/d1sc01929e (2021).
41. Welker Leng, K. R. et al. Phosphorylation of Histone Deacetylase 8: Structural and Mechanistic Analysis of the Phosphomimetic S39E Mutant. *Biochemistry* 58, 4480–4493; 10.1021/acs.biochem.9b00653 (2019).
42. Werbeck, N. D. et al. A distal regulatory region of a class I human histone deacetylase. *Nature communications* 11, 3841; 10.1038/s41467-020-17610-w (2020).
43. Chakrabarti, A. et al. HDAC8: a multifaceted target for therapeutic interventions. *Trends in pharmacological sciences* 36, 481–492; 10.1016/j.tips.2015.04.013 (2015).
44. Johnstone, R. W. Histone-deacetylase inhibitors: novel drugs for the treatment of cancer. *Nature reviews. Drug discovery* 1, 287–299; 10.1038/nrd772 (2002).
45. Chakrabarti, A. et al. Targeting histone deacetylase 8 as a therapeutic approach to cancer and neurodegenerative diseases. *Future medicinal chemistry* 8, 1609–1634; 10.4155/fmc-2016-0117 (2016).
46. Lopez, G. et al. HDAC8, A Potential Therapeutic Target for the Treatment of Malignant Peripheral Nerve Sheath Tumors (MPNST). *PloS one* 10, e0133302; 10.1371/journal.pone.0133302 (2015).
47. Mormino, A. et al. Histone-deacetylase 8 drives the immune response and the growth of glioma. *Glia* 69, 2682–2698; 10.1002/glia.24065 (2021).
48. Rettig, I. et al. Selective inhibition of HDAC8 decreases neuroblastoma growth in vitro and in vivo and enhances retinoic acid-mediated differentiation. *Cell death & disease* 6, e1657; 10.1038/cddis.2015.24 (2015).

49. Chauvin, J.-P. R. & Pratt, D. A. On the Reactions of Thiols, Sulfenic Acids, and Sulfinic Acids with Hydrogen Peroxide. *Angewandte Chemie (International ed. in English)* 56, 6255–6259; 10.1002/anie.201610402 (2017).
50. Garrido Ruiz, D., Sandoval-Perez, A., Rangarajan, A. V., Gunderson, E. L. & Jacobson, M. P. Cysteine Oxidation in Proteins: Structure, Biophysics, and Simulation. *Biochemistry* 61, 2165–2176; 10.1021/acs.biochem.2c00349 (2022).
51. Klomsiri, C., Karplus, P. A. & Poole, L. B. Cysteine-based redox switches in enzymes. *Antioxidants & redox signaling* 14, 1065–1077; 10.1089/ars.2010.3376 (2011).
52. Nagy, P. Kinetics and mechanisms of thiol-disulfide exchange covering direct substitution and thiol oxidation-mediated pathways. *Antioxidants & redox signaling* 18, 1623–1641; 10.1089/ars.2012.4973 (2013).
53. Poole, L. B. The basics of thiols and cysteines in redox biology and chemistry. *Free radical biology & medicine* 80, 148–157; 10.1016/j.freeradbiomed.2014.11.013 (2015).
54. Rabe von Pappenheim, F. et al. Widespread occurrence of covalent lysine-cysteine redox switches in proteins. *Nature chemical biology* 18, 368–375; 10.1038/s41589-021-00966-5 (2022).
55. Wensien, M. et al. A lysine-cysteine redox switch with an NOS bridge regulates enzyme function. *Nature* 593, 460–464; 10.1038/s41586-021-03513-3 (2021).
56. Meyer, Y., Buchanan, B. B., Vignols, F. & Reichheld, J.-P. Thioredoxins and glutaredoxins: unifying elements in redox biology. *Annual review of genetics* 43, 335–367; 10.1146/annurev-genet-102108-134201 (2009).
57. Ogata, F. T., Branco, V., Vale, F. F. & Coppo, L. Glutaredoxin: Discovery, redox defense and much more. *Redox biology* 43, 101975; 10.1016/j.redox.2021.101975 (2021).
58. Wouters, M. A., Fan, S. W. & Haworth, N. L. Disulfides as redox switches: from molecular mechanisms to functional significance. *Antioxidants & redox signaling* 12, 53–91; 10.1089/ars.2009.2510 (2010).
59. Bechtel, T. J. & Weerapana, E. From structure to redox: The diverse functional roles of disulfides and implications in disease. *Proteomics* 17; 10.1002/pmic.201600391 (2017).
60. Sies, H. Hydrogen peroxide as a central redox signaling molecule in physiological oxidative stress: Oxidative eustress. *Redox biology* 11, 613–619; 10.1016/j.redox.2016.12.035 (2017).
61. Stöcker, S., van Laer, K., Mijuskovic, A. & Dick, T. P. The Conundrum of Hydrogen Peroxide Signaling and the Emerging Role of Peroxiredoxins as Redox Relay Hubs. *Antioxidants & redox signaling* 28, 558–573; 10.1089/ars.2017.7162 (2018).
62. Ismail, T., Kim, Y., Lee, H., Lee, D.-S. & Lee, H.-S. Interplay Between Mitochondrial Peroxiredoxins and ROS in Cancer Development and Progression. *International journal of molecular sciences* 20; 10.3390/ijms20184407 (2019).
63. Sobotta, M. C. et al. Peroxiredoxin-2 and STAT3 form a redox relay for H<sub>2</sub>O<sub>2</sub> signaling. *Nature chemical biology* 11, 64–70; 10.1038/nchembio.1695 (2015).
64. Antunes, F. & Brito, P. M. Quantitative biology of hydrogen peroxide signaling. *Redox biology* 13, 1–7; 10.1016/j.redox.2017.04.039 (2017).
65. Duvic, M. & Vu, J. Vorinostat in cutaneous T-cell lymphoma. *Drugs of today (Barcelona, Spain : 1998)* 43, 585–599; 10.1358/dot.2007.43.9.1112980 (2007).
66. Campas-Moya, C. Romidepsin for the treatment of cutaneous T-cell lymphoma. *Drugs of today (Barcelona, Spain : 1998)* 45, 787–795; 10.1358/dot.2009.45.11.1437052 (2009).
67. Lee, H.-Z. et al. FDA Approval: Belinostat for the Treatment of Patients with Relapsed or Refractory Peripheral T-cell Lymphoma. *Clinical cancer research : an official journal of the American Association for Cancer Research* 21, 2666–2670; 10.1158/1078-0432.CCR-14-3119 (2015).
68. Raedler, L. A. Farydak (Panobinostat): First HDAC Inhibitor Approved for Patients with Relapsed Multiple Myeloma. *American Health & Drug Benefits* 9, 84–87 (2016).
69. Lu, X., Ning, Z., Li, Z., Cao, H. & Wang, X. Development of chidamide for peripheral T-cell lymphoma, the first orphan drug approved in China. *Intractable & rare diseases research* 5, 185–191; 10.5582/irdr.2016.01024 (2016).
70. Ceccacci, E. & Minucci, S. Inhibition of histone deacetylases in cancer therapy: lessons from leukaemia. *British journal of cancer* 114, 605–611; 10.1038/bjc.2016.36 (2016).
71. Finnin, M. S. et al. Structures of a histone deacetylase homologue bound to the TSA and SAHA inhibitors. *Nature* 401, 188–193; 10.1038/43710 (1999).

- 
72. Balasubramanian, S. et al. A novel histone deacetylase 8 (HDAC8)-specific inhibitor PCI-34051 induces apoptosis in T-cell lymphomas. *Leukemia* 22, 1026–1034; 10.1038/leu.2008.9 (2008).
  73. Boike, L., Henning, N. J. & Nomura, D. K. Advances in covalent drug discovery. *Nat Rev Drug Discov* 21, 881–898; 10.1038/s41573-022-00542-z (2022).
  74. Ghosh, A. K., Samanta, I., Mondal, A. & Liu, W. R. Covalent Inhibition in Drug Discovery. *ChemMedChem* 14, 889–906; 10.1002/cmdc.201900107 (2019).
  75. Lu, S. & Zhang, J. Designed covalent allosteric modulators: an emerging paradigm in drug discovery. *Drug discovery today* 22, 447–453; 10.1016/j.drudis.2016.11.013 (2017).
  76. Singh, J., Petter, R. C., Baillie, T. A. & Whitty, A. The resurgence of covalent drugs. *Nat Rev Drug Discov* 10, 307–317; 10.1038/nrd3410 (2011).
  77. Sutanto, F., Konstantinidou, M. & Dömling, A. Covalent inhibitors: a rational approach to drug discovery. *RSC Medicinal Chemistry* 11, 876–884; 10.1039/d0md00154f (2020).
  78. Naim, N., Moukheiber, S., Daou, S. & Kourie, H. R. KRAS-G12C covalent inhibitors: A game changer in the scene of cancer therapies. *Critical Reviews in Oncology/Hematology* 168, 103524; 10.1016/j.critrevonc.2021.103524 (2021).
  79. Baillie, T. A. Zielgerichtete kovalente Inhibitoren für das Wirkstoffdesign. *Angew. Chem.* 128, 13606–13619; 10.1002/ange.201601091 (2016).
  80. Strelow, J. M. A Perspective on the Kinetics of Covalent and Irreversible Inhibition. *SLAS discovery : advancing life sciences R & D* 22, 3–20; 10.1177/1087057116671509 (2017).
  81. Huang, F., Han, X., Xiao, X. & Zhou, J. Covalent Warheads Targeting Cysteine Residue: The Promising Approach in Drug Development. *Molecules (Basel, Switzerland)* 27; 10.3390/molecules27227728 (2022).



---

### 3 Abbildungsverzeichnis

---

Abbildung 1: Illustration des Acetylierungsgleichgewichtes, hervorgerufen durch die entgegengesetzten Aktivitäten von Histondeacetylase (HDAC) und Histonacetyltransferase (HAT), welches die Wechselwirkung zwischen Histonen und DNA steuert und somit die Transkription von Genen aktiviert oder unterdrückt. Die Abbildung ist abgewandelt aus. <sup>11</sup> .....	2
Abbildung 2: Einteilung der Zink-abhängigen humanen Histondeacetylasen. Die Abbildung ist abgewandelt aus. <sup>11</sup> .....	2
Abbildung 3: Illustration der strukturellen Flexibilität der Bindungstasche von HDAC8. Die Linke Abbildung (1T69) zeigt den Inhibitor (Magenta) SAHA gebunden am katalytischen Zinkion (Grau). Die rechte Abbildung (1T64) zeigt den Inhibitor (TSA) gebunden im Aktivzentrum von HDAC8. Im ersten Schritt öffnet sich die transiente Seitentasche, in welcher dann ein weiterer Ligand binden kann.....	3
Abbildung 4: Oxidation von Cysteinen durch Wasserstoffperoxid. Im ersten Schritt wird das Cysteinthiol zur Sulfensäure oxidiert, welche dann unter Wasserabspaltung ein Disulfid eingehen kann. Eine Überoxidation führt zur Sulfinsäure und schlussendlich zur Solfonsäure .....	5
Abbildung 5: Schematische Darstellung einer Disulfidaustauschkaskade, auch Redox-Relay genannt. ....	5
Abbildung 6: Strukturformeln von zugelassenen HDACis für die Behandlung verschiedener Krebsarten. Die Cap-Gruppe ist blau gefärbt, der verbindende Linker ist schwarz, die Zink-bindende Gruppe ist grün und die chelatisierenden Atome sind rot gefärbt. Die Abbildung ist abgewandelt aus. <sup>11</sup> .....	6

---

## 4 Abkürzungsverzeichnis

---

ALL	Akute lymphatische Leukämie
AML	Akute myeloische Leukämie
Asp	Asparaginsäure
ATRA	<i>All-trans retinoic acid</i>
AZ	Aktivzentrum
cAMP	Zyklisches Adenosinmonophosphat
CREB	<i>cAMP response element binding protein</i>
Cys	Cystein
DKFZ	Deutsches Krebsforschungszentrum
DNA	<i>Deoxyribonucleic acid</i>
DOE	<i>Design of experiments</i>
ERRα	Estrogen related receptor alpha
ESI	Elektronensprayionisation
GSH	Glutathion
GSSG	Glutathiondisulfid
H	<i>Helix</i>
HAT	Histonacetyltransferase
HDAC	Histondeacetylase
HDLp	<i>Histone deacetylase-like protein</i>
His	Histidin
HPLC	<i>High performance liquid chromatography</i>
L	<i>Loop</i>
Met	Methionin
MS	<i>Mass spectrometry</i>
NAD	Nicotinamidadenindinukleotid
NADPH	Nicotinamidadenindinukleotidphosphat
NEM	N-Ethylmaleinimid
NOX	NADPH-Oxidase
p53	Humaner Tumorsuppressor p53
PTM	Posttranslationale Modifikation
ROS	<i>Reactive oxygen species</i>
SAHA	<i>Suberoylanilide hydroxamid acid</i>
SDS-PAGE	Natriumdodecylsulphat Polyacrylamid Gelelektrophorese
Sec	Selenocystein
Ser	Serin
SMC3	<i>Structural maintenance of chromosomes 3</i>
STAT	<i>signal transducer and activator of transcription</i>
TCEP	Tris-(2-caroxyethyl)-phosphin
TCI	<i>Targeted covalent inactivator</i>
TDZ	Thiadiazol
TOF	<i>Time of flight</i>
TSA	Trichostatin A
Tyr	Tyrosin
TZD	Thiazolidindion

---

## 5 Kumulativer Teil

---

### 5.1 Untersuchung der cysteinabhängigen Redoxregulation von HDAC8 und Entwicklung erster kovalenter Inaktivatoren

Das erste Unterkapitel des kumulativen Teils dieser Dissertation befasst sich mit der Entdeckung und der weiterführenden Untersuchung der cysteinabhängigen Redoxregulation von HDAC8 und dem Versuch der Anwendung dieser Erkenntnisse als Grundlage für die Entwicklung von kovalenten Inhibitoren.

Am Anfang dieses Unterkapitels steht die Beobachtung, dass rekombinant exprimierte HDAC8 bereits nach wenigen Tagen Lagerung an Enzymaktivität verliert. Durch die Zugabe von TCEP lässt sich diese wiedergewinnen. Unter Verwendung einer nicht-reduzierenden SDS-PAGE wurde herausgefunden, dass HDAC8 während der Lagerung oxidiert und somit zu einem Großteil inaktiv vorliegt. Dies legt die Vermutung nahe, dass es sich hierbei um einen Verlust der Enzymaktivität durch disulfidabhängige Redoxprozesse handeln könnte. Durch den gezielten Austausch von Cystein gegen Serin wurde empirisch herausgefunden, dass Cys<sub>102</sub> und Cys<sub>153</sub> notwendig für diese Regulation von HDAC8 sind. Genauer wurde herausgefunden, dass durch die Zugabe von H<sub>2</sub>O<sub>2</sub> Cys<sub>102</sub> und Cys<sub>153</sub> eine reversible, regulative Disulfidbrücke bilden. Diesem Redoxschalter widmet sich die erste Publikation dieses Unterkapitels.

Parallel zu diesen Befunden wurde der Wirkmechanismus eines kleinen potenziellen Wirkstoffes auf HDAC8 genauer untersucht. Bei diesem Wirkstoff handelt es sich um PD-404,182, welcher in einer vergangenen Wirkstofffindungs-Kampagne als potenter und HDAC8-selektiver Inhibitor mit unbekanntem Wirkmechanismus, identifiziert wurde. Bei PD-404,182 handelt es sich um ein zyklisches Benzothiazininin, und Studien zeigten bereits, dass dieses mit dem Thiol von Glutathion ein kovalentes Produkt bilden kann. Daraufhin wurde vermutet, dass PD-404,182 auf ähnliche Weise, seine Wirkung auf HDAC8 entfalten könnte. Mittels hochaufgelöster HPLC-MS/MS wurde der genaue Reaktionsmechanismus von PD-404,182 aufgeschlüsselt und gezeigt, dass dieses Molekül gemischte Disulfide mit freien Thiolen bilden und Glutathion zum Glutathiondisulfid oxidieren kann. Des Weiteren ist die Inhibition von HDAC8 durch die Zugabe von TCEP als Reduktionsmittel reversibel. Somit wurde gezeigt, dass PD-404,182 der erste Inhibitor seiner Art ist, welcher die zuvor entdeckten Redoxmechanismen von HDAC8 ausnutzt, um als kovalenter, cysteinreaktiver Inhibitor zu fungieren. Genauere Details sind in der zweiten Publikation dieses Unterkapitels beschrieben.

Die dritte Publikation geht auf die genauere Entschlüsselung des Wirkmechanismus zwischen PD-404,182 und HDAC8 ein. Durch die Verwendung von HPLC-MS/MS und der Massenanalyse von Peptidfragmenten wurde detailliert gezeigt, dass PD-404,182 nicht nur gemischte Disulfide zwischen Cysteinthiolen bilden kann, sondern bei HDAC8 verschiedene Disulfidbrücken induziert. Von den 10 Cysteinen in HDAC8 bilden acht untereinander vier Disulfidbrücken, welche konzentrationsabhängig durch die Zugabe von PD-404,182 als Oxidationsmittel induziert werden. Diese Erkenntnisse erweiterten die Anzahl regulativer Disulfidbrücken in HDAC8 von einer Disulfidbrücke auf vier mögliche Disulfidbrücken, welche durch allosterische Konformationsänderungen die Enzymaktivität von HDAC8 jede für sich und vermutlich auch im Zusammenspiel untereinander regulieren.

Als nächster logischer Schritt stand im Raum, sich die erlangten Erkenntnisse über die cysteinabhängige Redoxregulation von HDAC8 für die Entwicklung von kovalenten Inhibitoren zunutze zu machen. Zusammen mit Kooperationspartnern um die Forschungsgruppe von György Keserü am Research Centre of Natural Science in Budapest wurde HDAC8 auf kovalente Fragmente getestet und eine Fülle an potenziellen Strukturen identifiziert, welche sich als Startpunkt für die Entwicklung kovalenter Inaktivatoren eignen könnten. Eine genauere Beschreibung ist der vierten Publikation dieses Unterkapitels zu entnehmen.

Zum Schluss ist diesem Unterkapitel eine Studie zu entnehmen, welche einen anfänglich als HDAC8 identifizierten Inhibitor als schnelle und selektive Molekülklasse für das Blockieren freier Cysteine beschreibt. Diese Sulfinyl-substituierten Thiadiazole eignen sich als schnellere Alternative für das gängig eingesetzte NEM, und die mögliche Verwendung wurde am Beispiel von massenanalytischen Anwendungen gezeigt. Zusätzlich eignet sich diese Molekülklasse für Biotin-Switch Assays, welche häufig in der Zellkultur zur Untersuchung cysteinabhängiger Regulationsmechanismen Verwendung finden. Abschließend wird diese Molekülklasse als möglicher Startpunkt für die Entwicklung kovalenter Inaktivatoren diskutiert.

---

**Titel:**

The enzyme activity of histone deacetylase 8 is modulated by a redox-switch

**Autoren:**

Niklas Jansch, Christian Meyners, Marius Muth, Aleksandra Koprancovic, Olaf Witt, Ina Oehme, Franz-Josef Meyer-Almes

**Bibliographische Daten:**

Redox Biology (doi.org/10.1016/j.redox.2018.09.013)

**Zusammenfassung:**

Enzyme aus der Familie der Histon-Deacetylasen (HDAC) werden durch verschiedene Mechanismen reguliert. Über die Regulierung von HDAC8, einem etablierten Zielmolekül für die Behandlung verschiedener Krebsarten, ist jedoch nur sehr wenig bekannt. In einer früheren Studie über Enzyme der HDAC-Klasse I wurde kein redoxsensitives Cysteinylthiol in HDAC8 identifiziert. Dies steht im Gegensatz zu der Beobachtung, dass HDAC8 durch Zugabe von Reduktionsmitteln unterschiedliche Enzymaktivitäten aufweist. Angesichts der Bedeutung von HDAC8 in der Tumorentstehung wurde eine mögliche Redox-Regulation durch biochemische und biophysikalische Methoden in Kombination mit gerichteter Mutagenese untersucht. Das Auftreten einer charakteristischen Disulfidbindung, unter oxidierenden Bedingungen, ist mit einem vollständigen, aber reversiblen Verlust der Enzymaktivität verbunden. Die Cysteine 102 und 153 wurden als integraler Bestandteil des Redox-Schalters identifiziert. Eine mögliche intrazelluläre Regulation von HDAC8 hervorgerufen durch Redox-Signaltransduktion wird durch die beobachtete Beziehung zwischen der Hemmung von reaktiven Sauerstoffspezies, welche durch NADPH-Oxidasen (NOX) erzeugt werden, und der gleichzeitig erhöhten HDAC8-Aktivität in Neuroblastom-Tumorzellen nahegelegt. Die langsame Kinetik für die direkte Oxidation von HDAC8 durch Wasserstoffperoxid deutet darauf hin, dass Transmitter von oxidativen Äquivalenten erforderlich sind, um das H<sub>2</sub>O<sub>2</sub>-Signal an HDAC8 zu übertragen.



# The enzyme activity of histone deacetylase 8 is modulated by a redox-switch

Niklas Jansch<sup>a</sup>, Christian Meyners<sup>a</sup>, Marius Muth<sup>a</sup>, Aleksandra Koprancovic<sup>a</sup>, Olaf Witt<sup>b,c,d,e</sup>, Ina Oehme<sup>b,c,e</sup>, Franz-Josef Meyer-Almes<sup>a,\*</sup>

<sup>a</sup> Department of Chemical Engineering and Biotechnology, University of Applied Sciences Darmstadt, Haardtring 100, 64295 Darmstadt, Germany

<sup>b</sup> Preclinical Program, Hopp Children's Cancer Center at NCT Heidelberg (KITZ), Germany

<sup>c</sup> Clinical Cooperation Unit Pediatric Oncology, German Cancer Research Center (DKFZ), INF 280, D-69120 Heidelberg, Germany

<sup>d</sup> Department of Pediatric Oncology, Hematology and Immunology, University Hospital Heidelberg, Heidelberg, Germany

<sup>e</sup> German Cancer Research Consortium (DKTK), Germany

## ARTICLE INFO

### Keywords:

HDAC8 stability  
Redox kinetics  
Redox signaling  
NOX  
Disulfide bond  
ROS  
Hydrogen peroxide

## ABSTRACT

Enzymes from the histone deacetylase (HDAC) family are highly regulated by different mechanisms. However, only very limited knowledge exists about the regulation of HDAC8, an established target in multiple types of cancer. A previous dedicated study of HDAC class I enzymes identified no redox-sensitive cysteinyl thiol in HDAC8. This is in contrast to the observation that HDAC8 preparations show different enzyme activities depending on the addition of reducing agents. In the light of the importance of HDAC8 in tumorigenesis a possible regulation by redox signaling was investigated using biochemical and biophysical methods combined with site directed mutagenesis. The occurrence of a characteristic disulfide bond under oxidizing conditions is associated with a complete but reversible loss of enzyme activity. Cysteines 102 and 153 are the integral components of the redox-switch. A possible regulation of HDAC8 by redox signal transduction is suggested by the observed relationship between inhibition of reactive oxygen species generating NOX and concomitant increased HDAC8 activity in neuroblastoma tumor cells. The slow kinetics for direct oxidation of HDAC8 by hydrogen peroxide suggests that transmitters of oxidative equivalents are required to transfer the H<sub>2</sub>O<sub>2</sub> signal to HDAC8.

## 1. Introduction

Histone deacetylases (HDACs) have emerged as promising targets for chemotherapeutic intervention in cancer, neurodegenerative and immune disorders [1–3]. The HDAC enzyme family is subdivided into class I (HDAC1–3 and 8), class IIa (HDAC4,5,7 and 9), class IIb (HDAC6 and 10), class III (sirtuins SIRT1–7) and class IV (HDAC11). The zinc dependent HDACs of class I, IIa/b and IV operate with a different mechanism than the sirtuins in class III which require NAD<sup>+</sup> for catalysis. HDAC8 is an established target for T-cell lymphoma and neuroblastoma and overexpressed in other tumors [4]. HDAC8 is found in the nucleus as well as the cytoplasm which is in line with an increasing number of identified substrates (SMC3, ERR- $\alpha$ (SMC3, E, RAI1, MLL2, p53, Cortactin) [5–7] and interaction partners (CREB/PP1, hEST1B, Inv(16) fusion protein, DEC-1, Hsp20,  $\alpha$ -actin) [8–12] in both compartments. Consequently, the physiological role of HDAC8 in cells is complex and needs further elucidation but it is clearly linked to relevant cancer mechanisms. HDAC8 activity is negatively regulated upon phosphorylation by cyclic AMP dependent protein kinase at position serine 39 [13]. Moreover, Fierke et al. suggested that HDAC8 could be also

regulated by metal switching *in vivo* [14]. Redox control of epigenetic processes has been proposed as a general principle to allow the cell to adapt to a changing environment. During the last years, it became clear that redox-sensitive proteins like peroxiredoxins serve not only as cellular self-defense against oxidative stress but can also act as redox relay for specific H<sub>2</sub>O<sub>2</sub> signaling in cells [15]. Several HDACs were shown to be redox-regulated. The class IIa HDAC4 has a redox-switch that controls shuttling between the nucleus and the cytoplasm [16]. Moreover, HDAC6 has been shown to interact with peroxiredoxins [17]. In another study, class I HDACs -1, -2 and -3 but not HDAC8 were proposed to be redox-sensitive and a putative redox-switch was identified using chemical probes [18]. However, we and others observed that HDAC8 activity depends on the enzyme preparation conditions [19]. Inspired by the additional finding that inactive oxidized HDAC8 can be re-transformed into active enzyme by the addition of Tris(2-carboxyethyl) phosphine (TCEP) or  $\beta$ -mercaptoethanol ( $\beta$ -ME), we initiated a comprehensive study to elucidate the mechanism of the redox-switching behavior of HDAC8. We provide unambiguous evidence that HDAC8 has a reversible thiol/disulfide redox-switch involving C153 and C102 and that the oxidized state of HDAC8 is thermodynamically more stable

\* Corresponding author.

E-mail address: [franz-josef.meyer-almes@h-da.de](mailto:franz-josef.meyer-almes@h-da.de) (F.-J. Meyer-Almes).

<https://doi.org/10.1016/j.redox.2018.09.013>

Received 19 June 2018; Received in revised form 12 September 2018; Accepted 24 September 2018

Available online 27 September 2018

2213-2317/© 2018 The Authors. Published by Elsevier B.V. This is an open access article under the CC BY license (<http://creativecommons.org/licenses/by/4.0/>).

than the corresponding reduced state. The potential physiological relevance of redox-regulation of HDAC8 is demonstrated by the inhibition of endogenously produced  $H_2O_2$  in neuroblastoma cells.

## 2. Materials and methods

### 2.1. Materials

All reagents and solvents were purchased from Sigma, Bachem, Roth, and used with further purification only if necessary. 9,9,9-trifluoro-8-oxo-N-phenyl-nonanamide (SATFMK) was prepared as described [20]. To minimize artificial oxidation of free thiols all measurements were performed in degassed buffer solutions. To prevent oxidation of enzyme during storage, enzymes were stored in the presence of 1 mM TCEP. TCEP was removed immediately before measurements by gel permeation chromatography with Zeba Spin Desalting Columns 7K MWCO (Thermo Scientific).

### 2.2. HDAC8 mutant variants

Mutant HDAC8 variants were generated using splicing by overlap extension PCR (SOE-PCR) with the following Primers:

HD8\_BamHI\_rev: 5'-AGGTGGATCCTTAAACAACGTGCTTCAGATTGCC-3',  
 HD8\_NdeI\_for: 5'-GCGCATATGGAGGAGCCGGAGGAG-3',  
 HD8\_C102S\_for: 5'-GGGCTAGGTTATGACTCCCAGCCACTGAAGGATA-3',  
 HD8\_C102S\_rev: 5'-TATCCCTTCAGTGGCTGGGGAGTCATAACCTAGCCC-3',  
 HD8\_C153S\_for: 5'-GATGAAGCATCTGGTTTTTCTTATCTCAATGATGCT-3',  
 HD8\_C153S\_rev: 5'-AGCATCATTGAGATAAGAAAAACCATGCTTCATC-3'.

DNA sequencing was performed at the sequencing service at the LMU Munich with the cycle, clean and run (BigDye v3.1) protocol.

### 2.3. HDAC8 expression and purification

pET14b vector (Novagen, EMD Millipore) containing codon-optimized human HDAC8, fused to a His<sub>6</sub> SUMO tag, was used to express HDAC8 in *E. coli* (BL21) DE3 pLysS. Cells were harvested by centrifugation for 10 min at 8000g and 4 °C and resuspended in lysis buffer (pH 8.0) containing 150 mM KCl, 50 mM Tris, 5 mM imidazole, 5 mM DTT, 1x HALT protease inhibitor cocktail (Thermo Scientific) and 5 µg/mL DNaseI. The cell suspension was sonicated and lysates were clarified by centrifugation at 18,000g for 30 min at 4 °C and sterile filtration. The filtrate was subsequently added to a 5 mL column volume of cOmplete His tag purification resin (Roche), equilibrated with immobilized metal affinity chromatography (IMAC) buffer A (pH 8.0) containing 150 mM KCl, 50 mM Tris and 5 mM imidazole. After washing with 50 mL of the same buffer His<sub>6</sub>-SUMO-HDAC8 was eluted with IMAC buffer B (pH 8.0) containing 150 mM KCl, 50 mM Tris and 100 mM imidazole. Subsequently 10 µg/mL His<sub>6</sub> tagged SUMO-Protease was added to the eluted HDAC8 fusion protein. Cleavage of His<sub>6</sub>-SUMO tag occurred overnight whilst dialyzing against 25 mM Tris, 50 mM NaCl and 5 mM β-ME (pH 8.0) at 4 °C. Then His<sub>6</sub>-SUMO tag and SUMO-Protease were removed by a second IMAC with AIC buffer A (pH 8.0) containing 25 mM Tris and 50 mM NaCl and 5 mM imidazole. HDAC8 containing flow through was concentrated and further purified on a strong anion exchanger (Bio-Scale Mini Macro-Prep High Q 5 mL Cartridge, Biorad). After a washing step using AIC buffer A HDAC8 was eluted using AIC buffer B (pH 8.0) containing 25 mM Tris and 1 M NaCl. 5 mM DTT was added to prevent oxidation and remove possible β-ME cysteine adducts. The final purification step included size exclusion chromatography with a HiLoad Superdex 75 material (GE) equilibrated with GPC Puffer (pH

8.0) containing 150 mM KCl and 50 mM Tris. The protein containing fractions were collected and concentrated. Glycerol and TCEP were added to final concentrations of 25% and 1 mM and protein was stored at −20 °C. We typically obtained 3–5 mg HDAC8 from 1 L culture.

### 2.4. Enzyme activity assays

The activity of all HDAC8 variants was determined in black half area 96-well microplates (Greiner bio-one, Germany) by a colorimetric assay described by Wegener et al. [21]. HDAC8 (10 nM) was incubated with indicated concentrations of  $H_2O_2$  for 1 h at 30 °C in HDAC8 assay buffer containing 25 mM Tris-HCl, 75 mM KCl and 0.001% Pluronic F-127 pH 8.0. Excess  $H_2O_2$  was quenched by the addition of 5.6 µg/mL freshly dissolved catalase. The reaction was initiated by the addition of 10 µM of the substrate Boc-Lys(tri-fluoroacetyl)-7-amino-4-methylcoumarin (Boc-Lys(TFA)-AMC). After incubation for 60 min, the reaction was stopped by the addition of 1.67 µM SATFMK and the deacetylated substrate was converted into a fluorescent dye (AMC) by the addition of 0.42 mg/mL trypsin. Measurements were performed in a fluorescence microplate reader (PHERAstar FS, BMG LABTECH). The data was analyzed with GraphPad Prism version 6.01.

### 2.5. Electrophoretic mobility shift assay (EMSA)

For the analysis of disulfide bond formation via migration change on non-reducing SDS-PAGE 5 µM of the respective HDAC8 variant was treated with increasing concentrations of  $H_2O_2$  (0–10 mM) in redox buffer containing 20 mM  $NaH_2PO_4$ , 20 mM  $Na_2HPO_4$ , 150 mM NaCl and 5 mM EDTA pH 7.0. After 1 h incubation at room temperature excess  $H_2O_2$  was quenched by the addition of 10 µg/mL catalase and free thiole groups were blocked by the addition of 8.3 mM NEM to prevent unwanted rearrangements of disulfide bonds followed by an incubation period of 30 min at room temperature. Finally, 4x non-reducing sample buffer was added containing 8% SDS, 250 mM Tris-HCl (pH 6.8), 40% Glycerol and 0.02% Bromophenol blue. The samples were denaturated for 5 min at 95 °C and cooled on ice. Subsequently, SDS-PAGE was performed on 12.5% gels at 200 V. Gels were stained with Coomassie brilliant blue solution.

### 2.6. Determination of the redox-potential between Cys<sub>102</sub> and Cys<sub>153</sub>

A codon optimized gene was purchased, with every cysteine (C28, C125, C131, C244, C275, C287, C314 and C352) changed to serine except Cys<sub>102</sub> and Cys<sub>153</sub>. This HDAC8<sub>lowC</sub> variant was expressed and purified as described above. At first a 2-fold serial dilution of 20 mM GSH was performed by keeping GSSG constant at 2 mM in a volume of 20 µL in buffers with three different pH-values (HEPES 100 mM, EDTA 100 µM, pH 7.0; Tris 100 mM, EDTA 100 µM, pH 8.0; CHES 100 mM, EDTA 100 µM, pH 9.0). Immediately after preparing the solutions 20 µL of the mutant HDAC8 was added to each mixture and kept overnight under nitrogen atmosphere to prevent oxygen oxidation. After reaching the equilibrium 5 µL TCA (100% (w/v)) was added to each sample and protein was precipitated for 20 min at −20 °C followed by 10 min centrifugation at 18,000g at 4 °C. The supernatant was removed, and the pellet resuspended by shaking in 30 µL redox-buffer containing 1 mM NEM for 30 min at 30 °C. After alkylation of nascent thiols 10 µL 4x non-reducing sample buffer was added to each sample followed by denaturation for 5 min at 95 °C. Samples were subjected to non-reducing SDS-PAGE and blotted on a PVDF Membrane (Merck, Millipore). Protein was detected using primary antibody for HDAC8 (E5, Santa Cruz biotechnology) and dye-labelled IRDye 800CW goat anti-mouse antibody (LiCor). Band intensities were quantified using the Image Studio Lite Software (LiCor). The redox-potential was determined at pH 7.0, 8.0 and 9.0. The dependency of the standard redox-potential from pH is described by the following general equation involving two protons:

## 2.7. Differential scanning fluorimetry to determine protein stability

Protein melting points were determined using a Prometheus NT.48 instrument from Nanotemper. 12  $\mu\text{M}$  of the respective HDAC8 variant was treated with increasing concentrations of  $\text{H}_2\text{O}_2$  (ranging from 0 to 5 mM) in redox buffer containing 20 mM  $\text{NaH}_2\text{PO}_4$ , 20 mM  $\text{Na}_2\text{HPO}_4$ , 150 mM NaCl and 5 mM EDTA pH 7.0. After 1 h incubation at room temperature, 10  $\mu\text{g}/\text{mL}$  catalase was added to eliminate excess  $\text{H}_2\text{O}_2$  and stop the oxidation process. The measurement was performed by increasing the temperature to 95  $^\circ\text{C}$  with a heating rate of 1  $^\circ\text{C}$  per minute and simultaneous detection of the fluorescence ratio of 350 nm/330 nm. The melting points were determined from the minimum of the first derivative of the function.

## 2.8. CD-spectroscopy

Spectra were collected by using a Jasco j-815cd spectropolarimeter (Easton, MD) equipped with a temperature controlling device in a quartz cell with a path length of 0.1 cm. Before experiments, HDAC8 was desalted by GPC with Zeba Spin Desalting Columns 7K MWCO (Thermo Scientific) equilibrated with CD buffer (pH 8.0) containing 5 mM Tris, 0.5% glycerol, 15 mM KCl and 0.1 mM DTT. Oxidized HDAC8 was generated by the addition of 5 mM  $\text{H}_2\text{O}_2$  for 1 h at room temperature and desalted against CD buffer without DTT. The final protein concentration was 5  $\mu\text{M}$ . Spectra were recorded in the far-UV from 260 to 195 nm and were the average of five scans.

## 2.9. Kinetics of HDAC8<sub>wt</sub> oxidation

To evaluate the kinetics of disulfide bond formation between the amino acids C102 and C153, 2.5  $\mu\text{M}$  HDAC8<sub>wt</sub> was treated with various concentrations of  $\text{H}_2\text{O}_2$  (ranging from 0 to 2.5 mM) and 200  $\mu\text{M}$  Fluoride-Lys HDAC substrate in potassium phosphate buffer (pH 7.6) containing 30 mM potassium phosphate, 100 mM KCl and 5% glycerol at 20  $^\circ\text{C}$ . Aliquots were removed at the indicated time periods and the reaction was quenched by the addition of 100  $\mu\text{M}$  N-hydroxy-N'-phenyloctanediamide (SAHA) and 0.04 mg/mL catalase after oxidation, 0.8 mg/mL Trypsin was added to generate fluorescent AMC for 15 min at 30  $^\circ\text{C}$ . The data was fitted using an exponential function in Graph Pad Prism and the observed pseudo first order rate constants were plotted against the different  $\text{H}_2\text{O}_2$  concentrations. The second order rate constant of oxidation was determined from the slope of the plot.

## 2.10. Reversible redox modulation of HDAC8<sub>wt</sub> activity

$\text{H}_2\text{O}_2$  and TCEP were added successively to a solution of fully reduced HDAC8<sub>wt</sub> (2.5 mg/ml in 25 mM Tris-HCl, 75 mM KCl and 0.001% Pluronic) to achieve alternating reducing and oxidizing conditions. HDAC8<sub>wt</sub> was incubated with  $\text{H}_2\text{O}_2$  for 45 min at 25  $^\circ\text{C}$  and TCEP for 60 min at 4  $^\circ\text{C}$ , respectively, while shaking at 650 rpm in a Thermomixer from Eppendorf. The oxidation process was stopped by adding 0.1 mg/mL catalase from bovine liver (Sigma-Aldrich). As control untreated HDAC8<sub>wt</sub> was supplemented by corresponding volumes of buffer. Aliquots were taken from each mixture to measure HDAC8<sub>wt</sub> activity. The samples for the enzyme activity assay (see above) of HDAC8<sub>wt</sub> were pretreated as follows: TCEP was removed and the buffer renewed using Zeba™ Spin Desalting Columns, 7K MWCO (Thermo Scientific). The redox modulation of HDAC8<sub>C102S/C153S</sub> activity was determined under the same conditions.

## 2.11. Western blot analysis

Western blot analysis was performed as described previously. [22] The following antibodies were used for detection: anti-acetyl-SMC3 (provided by Prof. K Shirahige, University of Tokyo, Tokyo, Japan) and

anti- $\beta$ -actin (clone AC-15; Sigma).

## 2.12. Determination of the Michaelis-Menten-parameters

10 nM (HDAC8<sub>wt</sub>, HDAC8<sub>C102S</sub>) and 100 nM (HDAC8<sub>C153S</sub>, HDAC8<sub>C102S/C153S</sub>) were incubated with increasing concentrations of Boc-Lys(TFA)-AMC for 5 min at 21  $^\circ\text{C}$  in HDAC8 assay buffer containing 25 mM Tris-HCl, 75 mM KCl and 0.001% Pluronic F-127 pH 8.0. After incubation 0.5 mg/mL Trypsin and 50  $\mu\text{M}$  SAHA was added to stop enzyme reaction and generate fluorescent AMC signal. Additionally, a series of varying concentrations AMC in the buffer described above was measured and RFU was plotted against AMC concentration. Resulting fluorescent signal per  $\mu\text{M}$  AMC was observed by the slope of linear regression.

## 2.13. NOX inhibition

BE(2)-C cells were incubated for 6 h with 5 and 10  $\mu\text{M}$  NADPH oxidase (NOX) inhibitor VAS2870 [23]. Whole cell lysates were blotted against SMC3 and normalized by the actin concentration of the same sample.

## 3. Results and discussion

### 3.1. Enzyme activity of HDAC8 correlates with its redox state

There is a large number of publications about the modulation of HDAC8 enzyme activity by inhibitors or incorporated metal ions [14,24]. In particular, the identification of N-acetylthiourea compounds as putative activators of HDAC8 raised considerable attention [25]. However, Toro et al. demonstrated that the activation effect was essentially due to enzyme preparations with inherently low activity [19]. Toro et al. suspected that the preparation conditions in the study of Singh et al. might have led to partially metal-depleted HDAC8 or stabilized a particular inactive conformation of the enzyme, which could be possibly activated by the N-acetylthiourea compounds. However, the authors did not identify the specific mechanism of activation, nor did they take into consideration possible redox effects as a causal factor for the postulated preparation effects.

We and others observed that the enzyme activity of HDAC8 decreases rapidly even if stored refrigerated at 4  $^\circ\text{C}$ . We also found that part of the activity of HDAC8<sub>wt</sub> can be recovered by the addition of reducing agents like DTT or TCEP. To elucidate a putative redox-sensitivity of HDAC8, we initiated a comprehensive study combining a variety of complementary biochemical, biophysical and cell-based approaches. Analysis of HDAC8<sub>wt</sub> under non-reducing conditions revealed that enzyme activity is lost depending on hydrogen peroxide ( $\text{H}_2\text{O}_2$ ) concentration (Fig. 1A). The oxidized form of HDAC8<sub>wt</sub> with disulfide bonds adopts a more constrained structure after denaturation and thus runs significantly faster in a non-reducing SDS-PAGE than the reduced form of HDAC8<sub>wt</sub> (lower panel of Fig. 1A). Increasing amounts of  $\text{H}_2\text{O}_2$  shift the redox-equilibrium progressively to the oxidized state of HDAC8<sub>wt</sub>. The percentage of the reduced state of HDAC8<sub>wt</sub> correlates perfectly with enzyme activity (Fig. 1A).

In contrast, the double mutant HDAC8<sub>C102S/C153S</sub> is essentially insensitive to  $\text{H}_2\text{O}_2$  (Fig. 1B). The enzyme activity remains unchanged in the presence of up to 10 mM  $\text{H}_2\text{O}_2$  and no additional band indicating a disulfide bridge becomes visible in the corresponding non-reducing gel.

### 3.2. The redox state-dependent enzyme activity of HDAC8 is reversible

The enzyme activity of oxidized HDAC8<sub>wt</sub> can be reversed repeatedly by adding reducing agent (Fig. 2A). However, overdosing and long exposure to  $\text{H}_2\text{O}_2$  produces overoxidation of HDAC8<sub>wt</sub> that cannot be reversed. During this process, thiol groups are in general irreversibly oxidized further to sulfinic and sulfonic acid [26,27]. Overoxidation

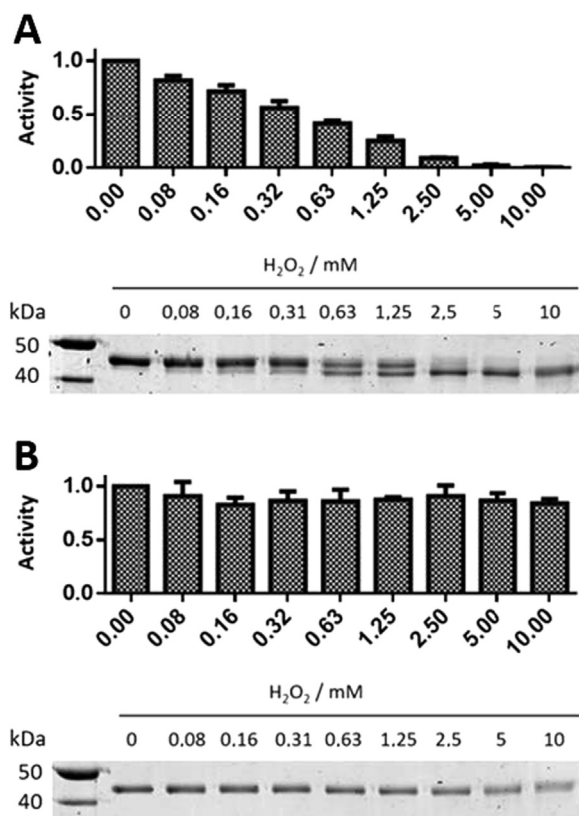


**Fig. 1.** Enzyme activity (upper panel) and EMSA (lower panel) of (A) HDAC8<sub>wt</sub> and (B) double-mutant HDAC8<sub>C102S/C153S</sub> in the presence of increasing amounts of H<sub>2</sub>O<sub>2</sub>. The enzyme activity test exploited the conversion of Boc-Lys(TFA)-AMC in the first step followed by the addition of trypsin to release fluorescent AMC. Gels were stained with Coomassie brilliant blue. The most left gel slot contains a ruler with indicated molecular weights. The upper band represents the reduced and the lower band the oxidized form of HDAC8<sub>wt</sub>. The mean and standard deviations were calculated from four independent experiments each performed in triplicates.

was prevented to a great extent by the addition of catalase immediately after H<sub>2</sub>O<sub>2</sub> mediated oxidation. Nevertheless, the maximum enzyme activity decreased significantly ( $p < 0.0001$ ) after each redox-cycle presumably due to unavoidable residual overoxidation (Fig. 2A). To determine whether the progressive loss of enzyme activity was due to oxidation elsewhere in the protein or specific for the C102/C153 redox switch, we repeated the experiment with HDAC8<sub>C102S/C153S</sub> double mutant protein (Fig. 2B). The progressive loss of enzyme activity during the redox cycles was clearly less pronounced for the HDAC8<sub>C102S/C153S</sub> variant lacking the redox switch than for HDAC8<sub>wt</sub> (71% remaining activity for HDAC8<sub>C102S/C153S</sub> and 27% remaining activity for HDAC8<sub>wt</sub>). Therefore, the postulated overoxidation process appears to be predominantly specific for the redox switch. However, other less dominant irreversible deactivation pathways cannot be completely ruled out.

The redox switch of HDAC8 consists of C102 and C153. In a previous study, no redox-sensitive cysteines were identified in HDAC8 using cyclopentenone prostaglandins as tool compounds to identify redox-sensitive cysteine residues by alkylation [18]. In contrast, HDAC1, -2 and -3 were shown to contain redox-responsive cysteine residues in the same study. The alkylated redox-sensitive cysteines in HDAC1 were found at two different positions, where HDAC8 showed no homologous cysteine. After that study, several X-ray structures of class I HDACs 1, -2 and -3 were published. A closer look for example at the crystal structures of HDAC1 (PDB-ID: 4BKX) reveals that C273 sits on the surface of HDAC1 and is more than 16 Å away from the closest

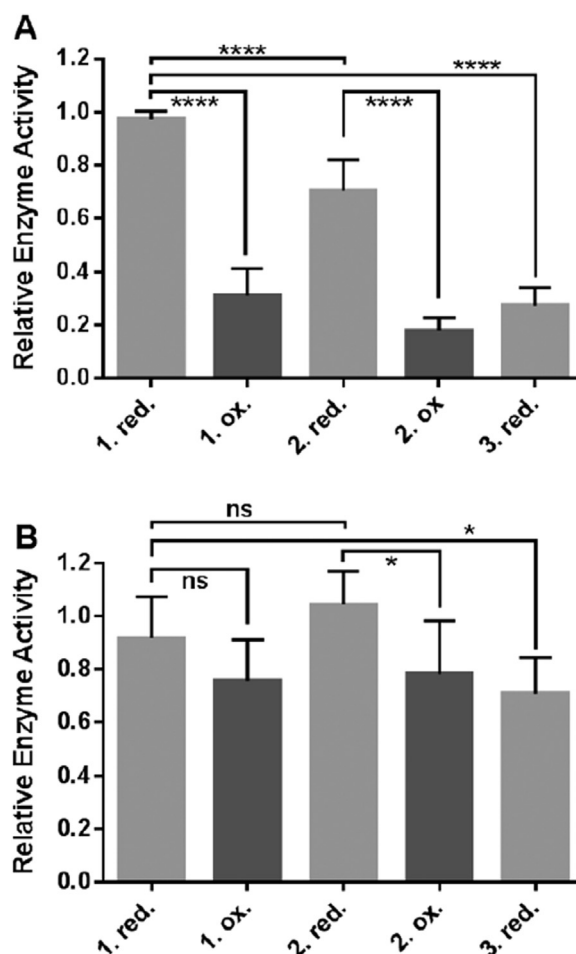


**Fig. 2.** Reversibility of redox modulation of the enzyme activity of (A) HDAC8<sub>wt</sub> and (B) HDAC8<sub>C102S/C153S</sub>. The enzyme activity of the same HDAC8 sample after subsequent alternating addition of slight stoichiometric excesses of TCEP (red.) and H<sub>2</sub>O<sub>2</sub> (ox.) is shown, respectively. The data represent means and standard deviations (HDAC8<sub>wt</sub>:  $n = 15$ , HDAC8<sub>C102S/C153S</sub>:  $n = 6$ ). Statistical significance was determined by an unpaired *t*-test. ns: not significant ( $p > 0.05$ ), \*:  $0.001 < p < 0.05$  and \*\*\*\*:  $p < 0.0001$ .

other cysteine. However, this cysteine might be involved in the formation of dimers upon oxidation. The second cysteine, C261, is buried in the interior of the properly folded protein and appears virtually inaccessible for larger alkylating agents such as cyclopentenone prostaglandins. It appears also reasonable that these bulky alkylating agents could have failed to modify the redox-sensitive C102 and C153 in HDAC8 due to sterical hindrance. The analysis of the X-ray structure of HDAC8 (PDB-ID: 1T64) reveals that C153 and C102 are in close proximity to each other (distance between C $\alpha$ -atoms: 6.7 Å) (Fig. 3) and in contact with the active site.

According to the crystal structure (PDB-ID: 1T64) at least one of these cysteines, located in the L3-loop lining the major active site binding pocket (C153) or the neighboring L2-loop (C102), should be accessible by H<sub>2</sub>O<sub>2</sub> and eventually form a disulfide bond with the other cysteine. Single exchange of C102 against serine has no significant influence on the catalytic efficiency of about  $13,000 \text{ M}^{-1} \text{ s}^{-1}$  in HDAC8<sub>wt</sub> (Table 1, Fig. S1). In contrast, the HDAC8<sub>C153S</sub> and HDAC8<sub>C102S/C153S</sub> mutants show a 4–9 fold lower catalytic efficiency than the wildtype enzyme indicating that C153 but not C102 plays a certain role in the catalytic mechanism of HDAC8 (Table 1, Fig. S1). However, substitution of C153 by serine does not abolish catalytic activity completely.

Furthermore, if the cysteines (C102, C153) involved in the putative redox-switch are exchanged with serine, the residual enzyme activity of



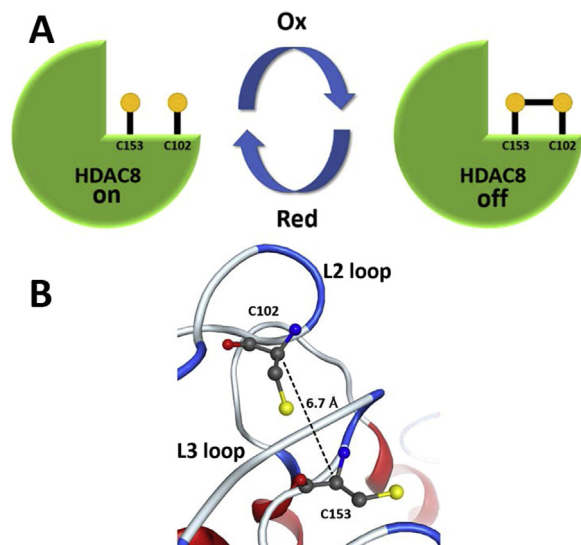


**Fig. 3.** A) Scheme of redox-switch: HDAC8<sub>wt</sub> is inactivated by H<sub>2</sub>O<sub>2</sub> induced reversible formation of a disulfide bridge between C153 and C102. B) Arrangement of C102 and C153 in two adjacent flexible loops, L2-loop containing C102 and L3-loop containing C153, showing a distance that enables the formation of a disulfide bond (PDB-ID: 1T64).

**Table 1**  
Michaelis-Menten-parameters of HDAC8 variants.

Enzyme	K <sub>M</sub> (μM)	k <sub>cat</sub> (s <sup>-1</sup> )	k <sub>cat</sub> K <sub>M</sub> <sup>-1</sup> (M <sup>-1</sup> s <sup>-1</sup> )
HDAC8 <sub>wt</sub>	96 ± 23	1.22 ± 0.14	13,000 ± 4400
HDAC8 <sub>C153S</sub>	179 ± 42	2.08 ± 0.24	3200 ± 1200
HDAC8 <sub>C102S</sub>	116 ± 27	0.58 ± 0.08	18,000 ± 6200
HDAC8 <sub>C102S/C153S</sub>	193 ± 32	0.38 ± 0.04	2000 ± 520

Means and standard deviations are provided, n = 3.

the double mutant HDAC8<sub>C102S/C153S</sub> becomes insensitive to treatment with H<sub>2</sub>O<sub>2</sub> (Fig. 1B). Consistently, no second band that is indicative for the oxidative state of HDAC8 occurs in the non-reducing SDS-PAGE gel upon treatment with hydrogen peroxide. Taken together, these results clearly prove that C102 and C153 constitute a redox-switch in HDAC8.

### 3.3. The reduced form of HDAC8<sub>wt</sub> is thermodynamically stabilized upon oxidation

The overall structure of oxidized HDAC8 shows no major deviations from its reduced form. The CD-spectra of the non-functional oxidized and the functional reduced form of HDAC8<sub>wt</sub> show no significant differences (Fig. S2). Similarly, the spectra of mutant proteins HDAC8<sub>C102S</sub>, HDAC8<sub>C153S</sub> and HDAC8<sub>C102S/C153S</sub> resemble that of wildtype HDAC8. Thus, oxidation of HDAC8 is not associated with major rearrangements of its overall structure. To investigate the effect of oxidation on protein stability, Differential Scanning Fluorimetry analyses of HDAC8<sub>wt</sub> were performed. Increasing H<sub>2</sub>O<sub>2</sub> concentrations cause a continuous shift of melting temperature from 42.27 °C of the reduced form to 44.14 °C (Table 2, Fig. S3A/B) indicating that the oxidized form of the protein is considerably more stable than the reduced form. This is in agreement with the formation of a stabilizing disulfide bond between C102 and C153. Consistently, the functional reduced HDAC8<sub>wt</sub> and mutant variants of HDAC8 with at least one of the cysteines C102 or C153 exchanged against serine show similar melting temperatures significantly distinct from that of inactive oxidized HDAC8<sub>wt</sub> (Table 2, Fig. S3C/D). The L2-loop is highly unordered in crystal structures of unbound HDAC8 and becomes more ordered upon binding to small molecule ligands [28]. Moreover, ligand binding

**Table 2**

Melting temperatures of HDAC8<sub>wt</sub> and mutant enzymes in the absence or in the presence of indicated concentrations of H<sub>2</sub>O<sub>2</sub>. Melting temperatures (T<sub>m</sub>) are shown as means with standard deviations, n = 3.

HDAC8 <sub>wt</sub>		T <sub>m</sub> (°C)
H <sub>2</sub> O <sub>2</sub> (mM)		
5.00		44.14 ± 0.33
2.50		43.96 ± 0.02
1.25		43.60 ± 0.08
0.63		43.26 ± 0.06
0.31		42.92 ± 0.03
0.16		42.57 ± 0.07
0.08		42.42 ± 0.05
0		42.27 ± 0.08
HDAC8 <sub>C102</sub>		
0	42.91 ± 0.05	
HDAC8 <sub>C153</sub>		
0	42.38 ± 0.01	
HDAC8 <sub>C102S/C153S</sub>		
0		42.26 ± 0.03

and the enzyme activity of HDAC8 largely depend on the conformation and flexibility of the L1- and L2-loops [29–32]. In fact, major movements of these loops and the side chain of F152 in the L3-loop are responsible for a transition from a wide-open state (PDB-ID: 1VKG) of the active site pocket into a sub-open state with a second transient binding pocket (PDB-ID: 1T64) and then into a closed state (PDB-ID: 1T69) [33]. These three representative crystal structures of HDAC8 were analyzed using the TRAnSient Pockets in Proteins (TRAPP) software platform developed in the laboratory of Rebecca Wade. The results confirmed that the L2- and L3-loop of HDAC8 are regions of increased flexibility (Fig. S4), which is in agreement with the experimentally observed large structural variations around the active site binding pocket of HDAC8. In a structurally highly related HDAC homolog HDAH from *Bordetella/Alcaligenes*, the L2- and L3-loop are interconnected and stabilized by a network of hydrogen bonds involving the pivotal amino acid T101. Substitution of T101 by alanine interrupts the strong interaction between both loops and leads to a dramatically increased flexibility of the L2-loop changing the mode of ligand interaction [34]. The formation of a disulfide bridge between C153 (L3-loop) and C102 (L2-loop) in HDAC8 introduces a covalent link between the L2- and L3-loop, which is also supposed to reduce the intrinsic flexibility of these loops adjacent to the catalytic site pocket. Wang et al. as well as Whitehead et al. postulated a mechanism of acetate release involving major conformational changes in the acetate release channel with R37 and W141 (numbering refers to HDAC8) acting as gate keepers [35,36]. The crucial importance of R37 for catalysis and function of the internal acetate release cavity of HDAC8 was experimentally confirmed by Haider et al. [37]. In summary, it can be concluded that the enzyme activity of HDACs and in particular HDAC8 is closely related with conformational flexibility at the active site binding pocket as well as the internal acetate release channel. The decreased flexibility at the active site upon oxidation of the redox-switch and covalent linkage of the L2- and L3-loop is suggested to contribute to the observed concomitant total loss in enzyme activity.

### 3.4. The amino acids C102 and C153 are conserved in class I HDACs

C153 in HDAC8 is conserved throughout all members of human HDACs from classes I, IIa and IIb, whereas C102 is only conserved in class I HDACs (Fig. S5). In class IIa HDACs 4, 5, and 9 this cysteine is replaced by serine with the exception of HDAC7, where cysteine is replaced by alanine. Although the multiple sequence alignment suggests also a cysteine in the second domain of HDAC6 at the position of C102 (HDAC8), this is clearly an artifact of the heuristic alignment algorithm, because an alignment of crystal structures of HDAC1, HDAC8 and

HDAC6 proves that I569 and no cysteine of HDAC6 matches C102 of HDAC8 (Fig. S6). Therefore, other HDAC class I members are also potentially regulated through a redox-switch corresponding to C102/C153 in HDAC8.

### 3.5. Standard redox-potential of C102/C153 switch

Since the ratio of the oxidized and reduced form of HDAC8 can be easily obtained from a non-reducing gel, the redox-potential of the molecular switch of HDAC8 could be determined from redox titrations (Fig. S7). The redox-potential of the C102/C153 redox-switch shows a linear dependency on pH and decreases from  $-218$  mV at pH 7.0 to  $-340$  mV at pH 9.0. These redox-potential differences per pH-unit are in excellent agreement with  $60.2$  mV calculated from the corresponding equation under Materials and Methods at  $30$  °C involving two protons. The very good correlation between the experimental and calculated pH-dependency of the redox-potentials in HDAC8<sub>lowC</sub> confirms that the C102/153 couple is exclusively responsible for redox-switching of HDAC8. Typical redox-potentials of the GSH/GSSG couple observed in cells range from  $-170$  mV [38,39] to  $-258$  mV [40].

HDAC8 can exist in both redox forms under these conditions. Interestingly, the standard redox potential of rapidly proliferating cells appears to be more negative than for differentiated, slowly proliferating cells [40]. Therefore, the ratio of the reduced active and the oxidized inactive form of HDAC8 in faster proliferating cancer cells ( $E = -258$  mV) would be about 20:1 according to the Nernst equation. In contrast, this ratio is inverted (ca. 1:40) for differentiated cells ( $E = -170$  mV). This is in agreement with previously referenced independent data proving that active (reduced) HDAC8 is involved in cancer. Moreover, a gene expression analysis found genes involved in antioxidant defense overexpressed associated with clinical resistance in a vorinostat phase 1 trial [41] and drug resistance can be overcome by a combination with redox-modulating compounds in leukemia cell lines and primary leukemia cells [42]. These findings highlight a significant role for the redox environment in cancer cells and particularly drug resistance. Moreover, our data suggest a positive relationship between cancer and enzyme activity of HDAC8. However, differences in redox-potentials of whole cells do not display the real redox conditions in particular subcellular compartments and are insufficient to predict the rate of interconversion between different redox partner molecules.

### 3.6. Oxidation kinetics of HDAC8

Having shown that redox-switching of HDAC8 involves amino acids C102 and C153, is reversible and characterized by a more stable and enzymatically inactive oxidized form, we analyzed the redox properties, kinetics and mechanism of the redox-switch in more detail (Fig. 4). For these experiments it was of utmost importance to stop the oxidation process after the indicated time by neutralizing excess  $H_2O_2$  by catalase. The observed oxidation rates,  $k_{obs}$ , were obtained from exponential fits to the time-dependent enzyme activity of HDAC8 and analyzed as a function of  $H_2O_2$  concentration. From the linear relationship, the specific rate constant of HDAC8 oxidation by  $H_2O_2$  was calculated to be  $0.51 \pm 0.01$   $M^{-1} s^{-1}$  (Fig. 4). This rate constant is much slower than for the antioxidants peroxiredoxins, glutathione peroxidase 1 or catalase ( $10^5$ – $10^7$   $M^{-1} s^{-1}$ ) and also slower than known redox-switches like PTP1B, SHP-2 or Keap1 ( $20$ – $140$   $M^{-1} s^{-1}$ ) [43]. The small oxidation rate requires the molecular interaction with a redox transfer molecule such as a redox-protein to enable efficient redox regulation of HDAC8 under physiological conditions. On the other side, such a mechanism ensures selectivity through molecular recognition.  $H_2O_2$  is a signaling messenger that can selectively modify cysteines in redox-regulated proteins, which react rather slowly with the free oxidant. Although thermodynamically favored, the oxidation of cysteines by  $H_2O_2$  is kinetically hindered. In principle, the oxidation reaction can be accelerated catalytically, e.g. by thiol peroxidases [15,44,45]. It is

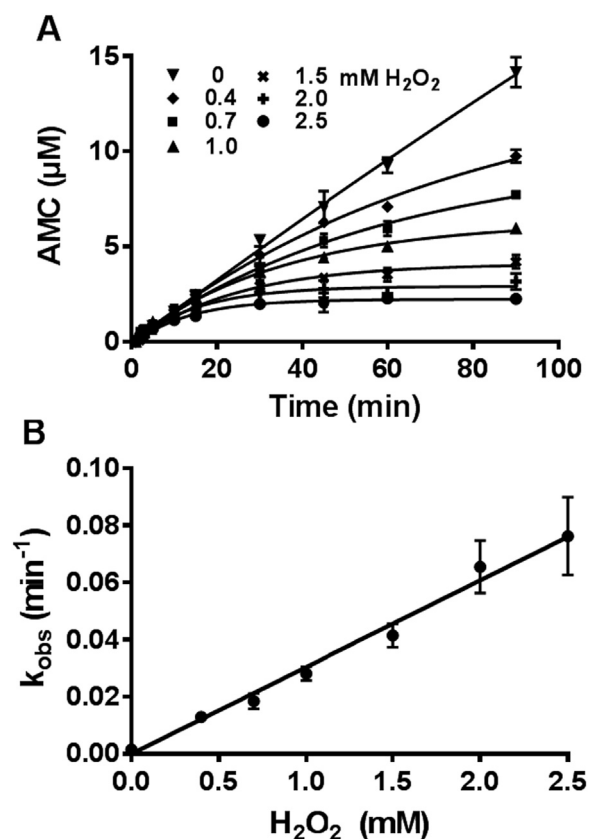


Fig. 4. Oxidation kinetics of HDAC8<sub>wt</sub>: A) Enzyme kinetics of HDAC8<sub>wt</sub> in the absence (filled down triangles) and in the presence of indicated concentrations of  $H_2O_2$ . Slow oxidation kinetics by  $H_2O_2$  causes a time-dependent decrease of enzyme activity. Smooth curved lines represent mono-exponential fits. B) The observed pseudo-first order rate constants ( $k_{obs}$ ) obtained from A) are plotted versus different indicated  $H_2O_2$  concentrations (ranging from 0 to 2.5 mM) used to oxidize HDAC8. The second order rate constant of the oxidation reaction is  $0.51 \pm 0.01$   $M^{-1} s^{-1}$ . Data means and standard deviations are shown,  $n = 3$ .

currently widely accepted that peroxiredoxins are not only key protectors against oxidative stress [44,46,47]. There is growing evidence that peroxiredoxins are major sensors and transmitters of  $H_2O_2$  signals [48]. It was shown that peroxiredoxins are able to transfer oxidizing equivalents to kinases, transcription factors and other redox-regulated proteins through specific protein-protein interactions [15,45,48,49].

### 3.7. Physiological relevance of redox-regulation of HDAC8

To analyze the cellular impact of redox regulation of HDAC8, we used the BE(2)-C neuroblastoma tumor cell line known to depend on HDAC8 for cell growth and survival [22,50,51]. We investigated the putative redox-regulation of HDAC8 under physiological conditions by modulating the concentration of endogenous  $H_2O_2$ . NOX family members are reactive oxygen species (ROS)-generating enzymes that regulate redox-sensitive signaling pathways involved in cancer development and progression [52]. They produce high levels of superoxide and  $H_2O_2$  in various cancer cell lines [52].

NOX activation and ROS production is also linked to the activation of oncogenes, such as RTKs (receptor tyrosine kinases) and their downstream signaling cascades (e.g. PI3K, mTOR, AKT) leading to tumor growth and survival [52]. In neuroblastoma, NOX enzymes are involved in retinoic acid-induced neuroblastoma cell differentiation [53]. Treatment of the BE(2)-C cells with NOX inhibitor VAS2870 reduces the intracellular production of  $H_2O_2$  and concomitantly the acetylation of SMC3 [5] (Fig. 5). This demonstrates a relationship between the intracellular levels of ROS including  $H_2O_2$  and HDAC8

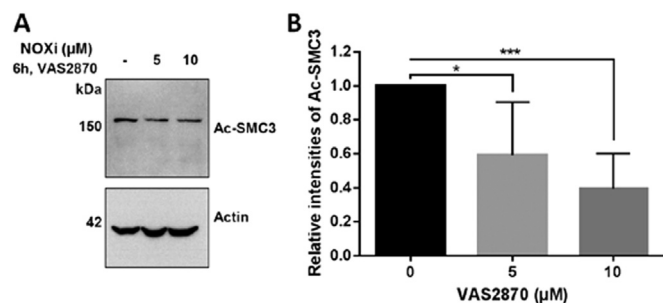


**Fig. 5.** Inhibition of NOX in BE(2)-C cells by different indicated concentrations of NOX inhibitor VAS2870 leads to a lower intracellular  $H_2O_2$ -level and decreased acetylation of SMC3. Immuno-blot results (A) and their respective quantification (B) are shown. The solvent (DMSO) control is indicated with a hyphen sign. Data here are the average  $\pm$  standard deviation of five independent repeats. Statistical significance was determined by Student's *t*-test. \*: *p*-value = 0.019 and \*\*\*: *p*-value = 0.0002.

activity. Together, these data suggest that HDAC8 could be redox-regulated under physiological conditions despite its very slow reaction kinetics with free  $H_2O_2$ . We hypothesize that the mechanism of redox regulation involves at least one  $H_2O_2$  sensor and transmitter enzyme to accelerate specific oxidation of HDAC8. Interestingly, peroxiredoxin 6 has been described as a putative interaction partner and substrate of HDAC8 using a proteomic approach [54]. This raises the possibility that both proteins may form a redox relay, where oxidative equivalents are transmitted from peroxiredoxin 6 to HDAC8. However, the exact mechanism of intracellular ROS/ $H_2O_2$  signaling to HDAC8 is unknown and currently under investigation.

#### 4. Conclusions

We provide evidence that the enzyme activity of HDAC8 depends strongly on its redox state. The occurrence of a characteristic disulfide bond under oxidizing conditions is associated with a transition into a significantly more stable protein resulting in a complete but reversible loss of enzyme activity. C102 and C153 are clearly identified to be the integral components of the redox-switch in HDAC8. The physiologically relevant regulation of HDAC8 by redox signal transduction is suggested by a clear connection between the activities of ROS/ $H_2O_2$  generating NOX and HDAC8 in neuroblastoma tumor cells. The redox-switch is only conserved among the members of HDAC class I suggesting that HDACs 1, 2 and 3 could also be regulated by a homologous switch. Further studies are required to obtain a full understanding of the redox-regulation network of human class I but also class II HDACs.

#### Acknowledgement

We acknowledge support by the Open Access Publishing Fund of Hochschule Darmstadt – University of Applied Sciences. We would also like to thank Michael Schröder for very helpful technical support. Additionally, we like to thank AG Fessner at the TU Darmstadt for the opportunity to use the Prometheus for the determination of the melting points and AG Hellmann at the University Mainz for support in acquiring the CD spectra. The kind gift of the anti-Ac-SMC3 antibody by Prof. K. Shirahige at the University of Tokyo is gratefully acknowledged.

#### Funding sources

Center for research and development (ZFE) of University of Applied Sciences.

#### Supporting information

- Determination of Michaelis-Menten Parameters of HDAC8 variants
- CD-spectra of reduced and oxidized form of HDAC8
- Differential scanning fluorimetric curves showing HDAC8wt stability in the presence of increasing hydrogen peroxide concentrations
- Dynamics simulations to demonstrate flexibility in HDAC8
- Multiple sequence alignment of L2- and L3-loop.
- Structural alignment of HDACs1, 6 and 8.
- Redox titration of HDAC8.

This material is available free of charge via the Internet at <http://pubs.acs.org>.

#### Appendix A. Supporting information

Supplementary data associated with this article can be found in the online version at [doi:10.1016/j.redox.2018.09.013](https://doi.org/10.1016/j.redox.2018.09.013).

#### References

- [1] K.J. Falkenberg, R.W. Johnstone, Histone deacetylases and their inhibitors in cancer, neurological diseases and immune disorders, *Nat. Rev. Drug Discov.* 13 (2014) 673–691.
- [2] A. Didonna, P. Opal, The promise and perils of HDAC inhibitors in neurodegeneration, *Ann. Clin. Transl. Neurol.* 2 (2015) 79–101.
- [3] L. Zhang, et al., Trend of histone deacetylase inhibitors in cancer therapy: isoform selectivity or multitargeted strategy, *Med. Res. Rev.* 35 (2015) 63–84.
- [4] A. Chakrabarti, et al., Targeting histone deacetylase 8 as a therapeutic approach to cancer and neurodegenerative diseases, *Future Med. Chem.* 8 (2016) 1609–1634.
- [5] M.A. Deardorff, et al., HDAC8 mutations in Cornelia de Lange syndrome affect the cohesin acetylation cycle, *Nature* 489 (2012) 313–317.
- [6] B.J. Wilson, A.M. Tremblay, G. Deblois, G. Sylvain-Drolet, V. Giguère, An acetylation switch modulates the transcriptional activity of estrogen-related receptor/alpha, *Mol. Endocrinol.* 24 (2010) 1349–1358.
- [7] D.E. Olson, et al., An unbiased approach to identify endogenous substrates of "histone" deacetylase 8, *ACS Chem. Biol.* (2014).
- [8] J. Gao, B. Siddoway, Q. Huang, H. Xia, Inactivation of CREB mediated gene transcription by HDAC8 bound protein phosphatase, *Biochem. Biophys. Res. Commun.* 379 (2009) 1–5.
- [9] H. Lee, N. Sengupta, A. Villagra, N. Rezaei-Zadeh, E. Seto, Histone deacetylase 8 safeguards the human ever-shorter telomeres 1B (hEST1B) protein from ubiquitin-mediated degradation, *Mol. Cell. Biol.* 26 (2006) 5259–5269.
- [10] K.L. Durst, B. Lutterbach, T. Kummalu, A.D. Friedman, S.W. Hiebert, The inv (16) fusion protein associates with corepressors via a smooth muscle myosin heavy-chain domain, *Mol. Cell. Biol.* 23 (2003) 607–619.
- [11] Y. Qian, J. Zhang, Y.S. Jung, X. Chen, DEC1 coordinates with HDAC8 to differentially regulate TAp73 and DeltaNp73 expression, *PLoS One* 9 (2014) e84015.
- [12] M. Karolczak-Bayatti, et al., Acetylation of heat shock protein 20 (Hsp20) regulates human myometrial activity, *J. Biol. Chem.* 286 (2011) 34346–34355.
- [13] H. Lee, N. Rezaei-Zadeh, E. Seto, Negative regulation of histone deacetylase 8 activity by cyclic amp-dependent protein kinase A, *Mol. Cell. Biol.* 24 (2004) 765–773.
- [14] C.A. Castaneda, et al., Active site metal identity alters histone deacetylase 8 substrate selectivity: a potential novel regulatory mechanism, *Biochemistry* 56 (2017) 5663–5670.
- [15] M.C. Sobotta, et al., Peroxiredoxin-2 and STAT3 form a redox relay for H2O2 signaling, *Nat. Chem. Biol.* 11 (2015) 64–70.
- [16] T. Ago, et al., A redox-dependent pathway for regulating class II HDACs and cardiac hypertrophy, *Cell* 133 (2008) 978–993.
- [17] R.B. Parmigiani, et al., HDAC6 is a specific deacetylase of peroxiredoxins and is involved in redox regulation, *Proc. Natl. Acad. Sci. USA* 105 (2008) 9633–9638.
- [18] K. Doyle, F.A. Fitzpatrick, Redox signaling, alkylation (carbonylation) of conserved cysteines inactivates class I histone deacetylases 1, 2, and 3 and antagonizes their transcriptional repressor function, *J. Biol. Chem.* 285 (2010) 17417–17424.
- [19] T.B. Toro, et al., KDAC8 with high basal velocity is not activated by N-acetylthioureas, *PLoS One* 11 (2016) e0146900.
- [20] R.R. Frey, et al., Trifluoromethyl ketones as inhibitors of histone deacetylase, *Bioorg. Med. Chem. Lett.* 12 (2002) 3443–3447.
- [21] D. Wegener, C. Hildmann, D. Rieger, A. Schwienhorst, Improved fluorogenic histone deacetylase assay for high-throughput-screening applications, *Anal. Biochem.* 321 (2003) 202–208.
- [22] I. Rettig, et al., Selective inhibition of HDAC8 decreases neuroblastoma growth in vitro and in vivo and enhances retinoic acid-mediated differentiation, *Cell Death Dis.* 6 (2015) e1657.
- [23] S. Altenhofer, et al., The NOX toolbox: validating the role of NADPH oxidases in physiology and disease, *Cell Mol. Life Sci.* 69 (2012) 2327–2343.
- [24] D.P. Dowling, S.G. Gattis, C.A. Fierke, D.W. Christianson, Structures of metal-substituted human histone deacetylase 8 provide mechanistic inferences on biological

- function, *Biochemistry* 49 (2010) 5048–5056.
- [25] R.K. Singh, et al., Histone deacetylase activators: N-acetylthioureas serve as highly potent and isozyme selective activators for human histone deacetylase-8 on a fluorescent substrate, *Bioorg. Med. Chem. Lett.* 21 (2011) 5920–5923.
- [26] M.C. Sobotta, et al., Exposing cells to H<sub>2</sub>O<sub>2</sub>: a quantitative comparison between continuous low-dose and one-time high-dose treatments, *Free Radic. Biol. Med.* 60 (2013) 325–335.
- [27] V.V. Loi, M. Rossius, H. Antelmann, Redox regulation by reversible protein S-thiolation in bacteria, *Front. Microbiol.* 6 (2015) 187.
- [28] D.P. Dowling, S.L. Gantt, S.G. Gattis, C.A. Fierke, D.W. Christianson, Structural studies of human histone deacetylase 8 and its site-specific variants complexed with substrate and inhibitors, *Biochemistry* 47 (2008) 13554–13563.
- [29] C. Decroos, et al., Biochemical and structural characterization of HDAC8 mutants associated with cornelia de lange syndrome spectrum disorders, *Biochemistry* 54 (2015) 6501–6513.
- [30] C. Decroos, et al., Compromised structure and function of HDAC8 mutants identified in cornelia de lange syndrome spectrum disorders, *ACS Chem. Biol.* (2014).
- [31] J.R. Somoza, et al., Structural snapshots of human HDAC8 provide insights into the class I histone deacetylases, *Structure* 12 (2004) 1325–1334.
- [32] C. Decroos, et al., Variable active site loop conformations accommodate the binding of macrocyclic largazole analogues to HDAC8, *Biochemistry* 54 (2015) 2126–2135.
- [33] N. Deschamps, C.A. Simões-Pires, P.-A. Carrupt, A. Nurisso, How the flexibility of human histone deacetylases influences ligand binding: an overview, *Drug Discov. Today* 20 (2015) 736–742.
- [34] C. Meyners, A. Kramer, O. Yildiz, F.J. Meyer-Almes, The thermodynamic signature of ligand binding to histone deacetylase-like amidohydrolases is most sensitive to the flexibility in the L2-loop lining the active site pocket, *Biochim. Biophys. Acta* 1861 (2017) 1855–1863.
- [35] L. Whitehead, et al., Human HDAC isoform selectivity achieved via exploitation of the acetate release channel with structurally unique small molecule inhibitors, *Bioorg. Med. Chem.* 19 (2011) 4626–4634.
- [36] D.F. Wang, O. Wiest, P. Helquist, H.Y. Lan-Hargest, N.L. Wiech, On the function of the 14 Å long internal cavity of histone deacetylase-like protein: implications for the design of histone deacetylase inhibitors, *J. Med. Chem.* 47 (2004) 3409–3417.
- [37] S. Haider, C.G. Joseph, S. Neidle, C.A. Fierke, M.J. Fuchter, On the function of the internal cavity of histone deacetylase protein 8: R37 is a crucial residue for catalysis, *Bioorg. Med. Chem. Lett.* 21 (2011) 2129–2132.
- [38] J. Cai, D.P. Jones, Superoxide in apoptosis. Mitochondrial generation triggered by cytochrome c loss, *J. Biol. Chem.* 273 (1998) 11401–11404.
- [39] D.P. Jones, E. Maellaro, S. Jiang, A.F. Slater, S. Orrenius, Effects of N-acetyl-L-cysteine on T-cell apoptosis are not mediated by increased cellular glutathione, *Immunol. Lett.* 45 (1995) 205–209.
- [40] W.G. Kirlin, et al., Glutathione redox potential in response to differentiation and enzyme inducers, *Free Radic. Biol. Med.* 27 (1999) 1208–1218.
- [41] G. Garcia-Manero, et al., Phase 1 study of the histone deacetylase inhibitor vorinostat (suberoylanilide hydroxamic acid [SAHA]) in patients with advanced leukemias and myelodysplastic syndromes, *Blood* 111 (2008) 1060–1066.
- [42] Y. Hu, et al., Overcoming resistance to histone deacetylase inhibitors in human leukemia with the redox modulating compound beta-phenylethyl isothiocyanate, *Blood* 116 (2010) 2732–2741.
- [43] F. Antunes, P.M. Brito, Quantitative biology of hydrogen peroxide signaling, *Redox Biol.* 13 (2017) 1–7.
- [44] D.E. Fomenko, et al., Thiol peroxidases mediate specific genome-wide regulation of gene expression in response to hydrogen peroxide, *Proc. Natl. Acad. Sci. USA* 108 (2011) 2729–2734.
- [45] R.M. Jarvis, S.M. Hughes, E.C. Ledgerwood, Peroxiredoxin 1 functions as a signal peroxidase to receive, transduce, and transmit peroxide signals in mammalian cells, *Free Radic. Biol. Med.* 53 (2012) 1522–1530.
- [46] L.B. Poole, K.J. Nelson, Discovering mechanisms of signaling-mediated cysteine oxidation, *Curr. Opin. Chem. Biol.* 12 (2008) 18–24.
- [47] E.A. Veal, A.M. Day, B.A. Morgan, Hydrogen peroxide sensing and signaling, *Mol. Cell* 26 (2007) 1–14.
- [48] S. Stocker, M. Maurer, T. Ruppert, T.P. Dick, A role for 2-Cys peroxiredoxins in facilitating cytosolic protein thiol oxidation, *Nat. Chem. Biol.* 14 (2018) 148–155.
- [49] M. Gutscher, et al., Proximity-based protein thiol oxidation by H<sub>2</sub>O<sub>2</sub>-scavenging peroxidases, *J. Biol. Chem.* 284 (2009) 31532–31540.
- [50] I. Oehme, et al., Histone deacetylase 8 in neuroblastoma tumorigenesis, *Clin. Cancer Res.* 15 (2009) 91–99.
- [51] J. Shen, et al., A kinome-wide RNAi screen identifies ALK as a target to sensitize neuroblastoma cells for HDAC8-inhibitor treatment, *Cell Death Differ.* (2018).
- [52] K. Block, Y. Gorin, Aiding and abetting roles of NOX oxidases in cellular transformation, *Nat. Rev. Cancer* 12 (2012) 627–637.
- [53] M. Nitti, et al., PKC delta and NADPH oxidase in retinoic acid-induced neuroblastoma cell differentiation, *Cell Signal.* 22 (2010) 828–835.
- [54] G. Lopez, et al., HDAC8, a potential therapeutic target for the treatment of malignant peripheral nerve sheath tumors (MPNST), *PLoS One* 10 (2015) e0133302.

---

**Titel:**

Covalent inhibition of histone deacetylase 8 by 3,4-dihydro-2H-pyrimido[1, 2-c][1,3]benzothiazin-6-imine

**Autoren:**

Marius Muth, Niklas Jänsch, Aleksandra Kopranovic, Andreas Krämer, Nathalie Wössner, Manfred Jung, Frank Kirschhöfer, Gerald Brenner-Weiß, Franz-Josef Meyer-Almes

**Bibliographische Daten:**

Biochimica et Biophysica Acta (BBA) – General Subjects (doi.org/10.1016/j.bbagen.2019.01.001)

**Zusammenfassung:****Hintergrund:**

HDAC8 ist ein etabliertes Zielmolekül für die Behandlung von T-Zell-Lymphomen und kindlicher Neuroblastome. Benzothiazin-Imine sind vielversprechende HDAC8-Inhibitoren mit unbekanntem Bindungsmechanismus, denen eine übliche Zink-Bindungsgruppe fehlt.

**Methoden:**

In dieser Studie werden hochauflösende und quantitative HPLC-gekoppelte ESI-MS/MS-Techniken mit der Bestimmung der Kristallstruktur und einer Reihe von biochemischen und Computer gestützten Methoden kombiniert, um den Wirkmechanismus zwischen Benzothiazin-Imin (1) und HDAC8 aufzuklären.

**Ergebnisse:**

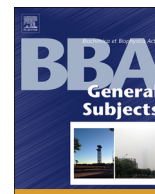
- 1) Benzothiazin-Imin (1) ist ein kovalenter Inhibitor von HDAC8
- 2) Die Hemmung ist in Gegenwart von Reduktionsmitteln reversibel
- 3) C153 im aktiven Zentrum und C102 sind am Hemmungsmechanismus beteiligt
- 4) Benzothiazin-Imin (1) modifiziert verschiedene Cysteine in HDAC8 und bildet dabei entweder Thiocyanate oder gemischte Disulfide mit dem freien Thiol (3)
- 5) Benzothiazin-Imin (1) und Sulfenamid (5) docken in unmittelbarer Nähe zu C153 im aktiven Zentrum an. Es wird angenommen, dass dies die kovalente Inaktivierung insbesondere in HDAC8 beschleunigt, und es wird vermutet, dass dies der Hauptgrund für die beobachtete nanomolare Potenz und Selektivität von Benzothiazin-Imin (1) ist.

**Schlussfolgerungen:**

(1) und seine Analoga sind interessante Modellverbindungen, die jedoch aufgrund ihrer hohen unselektiven Reaktivität gegenüber Thiolgruppen für eine therapeutische Behandlung nicht geeignet sind. Der postulierte vorangehende nicht-kovalente Bindungsmodus von (1) öffnet jedoch die Tür zu optimierten Verbindungen der nächsten Generation, die eine potente und selektive nicht-kovalente Erkennung mit einer geringen Reaktivität gegenüber C153 am aktiven Zentrum von HDAC8 kombinieren.

**Allgemeine Bedeutung:**

(1) stellt eine völlig neue Klasse von Inhibitoren für HDAC8 dar. Es wird vermutet, dass die anfängliche nicht-kovalente Interaktion am unteren Ende des aktiven Zentrums der Schlüssel für seine Selektivität ist. Eine weitere Optimierung der nicht-kovalenten Wechselwirkung und der Thiol-Reaktivität bietet Möglichkeiten zur Entwicklung therapeutisch nützlicher kovalenter HDAC8-Inhibitoren.



## Covalent inhibition of histone deacetylase 8 by 3,4-dihydro-2H-pyrimido[1,2-c][1,3]benzothiazin-6-imine

Marius Muth<sup>a,c</sup>, Niklas Jänsch<sup>a</sup>, Aleksandra Kopranovic<sup>a</sup>, Andreas Krämer<sup>b</sup>, Nathalie Wössner<sup>d</sup>, Manfred Jung<sup>d</sup>, Frank Kirschhöfer<sup>c</sup>, Gerald Brenner-Weiß<sup>c</sup>, Franz-Josef Meyer-Almes<sup>a,\*</sup>

<sup>a</sup> Department of Chemical Engineering and Biotechnology, University of Applied Sciences Darmstadt, Germany

<sup>b</sup> Institute of Pharmaceutical Chemistry, University Frankfurt, Germany

<sup>c</sup> Bioengineering and Biosystems, Institute of Functional Interfaces, Karlsruhe Institute of Technology, Germany

<sup>d</sup> Institute of Pharmaceutical Sciences, University of Freiburg, Germany

### ARTICLE INFO

#### Keywords:

HDAC8  
Selective inhibition  
Binding mechanism  
Non-hydroxamate inhibitor  
Covalent inhibitor  
Enzyme inhibition

### ABSTRACT

**Background:** HDAC8 is an established target for T-cell lymphoma and childhood neuroblastoma. Benzothiazine-imines are promising HDAC8 inhibitors with unknown binding mechanism lacking a usual zinc binding group. **Methods:** In this study high-resolution and quantitative HPLC-coupled ESI-MS/MS techniques are combined with crystal structure determination and a variety of biochemical and computational methods to elucidate the reaction mechanism between benzothiazine-imine **1** and HDAC8.

**Results:** 1) **1** is a covalent inhibitor of HDAC8; 2) inhibition is reversible in the presence of reducing agents; 3) C153 in the active site and C102 are involved in the inhibition mechanism; 4) **1** modifies various cysteines in HDAC8 forming either thiocyanates or mixed disulfides with **3**; 5) **1** and **5** dock in close proximity to C153 within the active site. This is supposed to accelerate covalent inactivation particularly in HDAC8 and suggested as major determinant for the observed nanomolar potency and selectivity of **1**.

**Conclusions:** **1** and its analogs are interesting model compounds but unsuitable for therapeutic treatment due to their high unselective reactivity towards thiol groups. However, the postulated preceding non-covalent binding mode of **1** opens a door to optimized next generation compounds that combine potent and selective non-covalent recognition with low reactivity towards C153 at the active site of HDAC8.

**General significance:** **1** represents a completely new class of inhibitors for HDAC8. Initial non-covalent interaction at the bottom of the active site is suggested to be the key for its selectivity. Further optimization of non-covalent interaction and thiol-reactivity provides opportunities to develop therapeutic useful covalent HDAC8 inhibitors.

### 1. Introduction

3,4-Dihydro-2H-pyrimido[1,2-c][1,3]benzothiazin-6-imine (PD 404,182, **1**) is a known inhibitor of bacterial 3-deoxy-D-manno-octulosonic acid 8-phosphate (KDO 8-P) synthase ( $K_i = 26$  nM) [1], Dimethylarginine dimethylaminohydrolase (DDAH1,  $IC_{50} = 9$   $\mu$ M) [2] and was also described to be effective against hepatitis C virus (HCV,  $IC_{50} = 11$   $\mu$ M) and human immunodeficiency virus (HIV,  $IC_{50} = 1$   $\mu$ M) [3], although the target and mechanism of anti-viral action is not completely clear. Searching the Pubchem BioAssay Database revealed 7 other proteins (histone lysine methyltransferase G9a, cytochrome P450 2C9, hydroxysteroid (17- $\beta$ ) dehydrogenase 4, 15-hydroxyprostaglandin dehydrogenase, human muscle pyruvate kinase,

aldehyde dehydrogenase 1, 15-human lipoxygenase 2) that were affected by **1** with bioactivity values in the range from 0.11 to 14  $\mu$ M [4]. **1** was inactive in 134 other bioassays. These findings suggest a certain potential for unselectivity of benzothiazin-6-imines. However, with the exception of KDO 8-P synthase, the reported activities for mentioned proteins are primarily in the micromolar range. Very recently, our group discovered **1** as an exceptional potent inhibitor ( $IC_{50} = 11$  nM) of human histone deacetylase 8 (HDAC8) and showed that it is highly selective against the human isoenzymes HDAC1–7 [5]. The most potent analog shows an  $IC_{50}$ -value of 2.9 nM against HDAC8. HDAC8 is an established target for T-cell lymphoma, childhood neuroblastoma and related to several other types of tumor [6]. Our finding was completely unexpected, since **1** lacks a classical zinc binding group that is a

\* Corresponding author.

E-mail address: [franz-josef.meyer-almes@h-da.de](mailto:franz-josef.meyer-almes@h-da.de) (F.-J. Meyer-Almes).

<https://doi.org/10.1016/j.bbagen.2019.01.001>

Received 31 August 2018; Received in revised form 25 November 2018; Accepted 2 January 2019

Available online 03 January 2019

0304-4165/© 2019 Elsevier B.V. All rights reserved.

common feature of most known inhibitors of zinc-dependent HDACs. Moreover, the structure-activity relationship of analog compounds appeared to be very broad suggesting great potential for further optimization using medicinal chemistry methods [5]. Okazaki et al. reported that the distinct S–N bond in the isothiazolopyrimidine scaffold was immediately cleaved in the presence of GSH or other reducing agents giving the thiophenol **3**, which was suggested to be the active anti-viral component [7]. Ghebremariam et al. observed that **1** is a long persistent inhibitor of DDAH and suggested that it may bind covalently to a cysteine residue in the catalytic site eventually forming the mixed disulfide **6** [2]. We also observed a long lasting inhibitory effect of **1** on HDAC8: About 90% of the enzyme remained inactive after 24 h dialysis. If the inhibitory mechanism involved covalent modification, what would explain the noteworthy selectivity for HDAC8 against other targets and even closely related HDAC isoenzymes? And what could be learned from the specific mode of action to develop optimized non-hydroxamate HDAC8 inhibitors? These considerations motivated us to study the inhibition mechanism of HDAC8 by **1** in great detail combining biochemical and biophysical methods with high-resolution HPLC-coupled ESI-MS/MS techniques.

## 2. Materials and methods

### 2.1. Materials

All reagents and solvents were purchased from Sigma, Fluka, Bachem, Roth or Tocris with a purity of 98% or higher. HPLC solvents were purchased from VWR with analytical grade or better. Sequencing grade modified Trypsin lyophilized was purchased at Promega. To minimize artificial oxidation of free thiols all measurements were performed in degassed buffer solutions. To prevent oxidation during storage, enzymes were stored in the presence of 1 mM TCEP. TCEP was removed immediately before measurements by GPC with Zeba Spin Desalting Columns 7 K MWCO (Thermo Scientific).

### 2.2. Mutagenesis

Mutant HDAC8 variants were generated using splicing by overlap extension PCR (SOE-PCR) with the following Primers:

```
HD8_BamHI_rev: 5'-AGGTGGATCCTTAAACAACGTGCTTCAGATT
GCC-3',
HD8_NdeI_for: 5'-GCGCATATGGAGGAGCCGGAGGAG-3',
HD8_C102S_for: 5'-GGGCTAGGTTATGACTCCCAGCCACTGAAGG
GATA-3',
HD8_C102S_rev: 5'-TATCCCTTCAGTGGCTGGGGAGTCATAACCTA
GCCC-3',
HD8_C153S_for: 5'-GATGAAGCATCTGGTTTTTCTTATCTCAATGAT
GCT-3',
HD8_C153S_rev: 5'-AGCATCATTGAGATAAGAAAAACAGATGCTT
CATC-3'.
```

DNA sequencing was performed at the sequencing service at the LMU Munich with the cycle, clean and run (BigDye v3.1) protocol.

#### 2.2.1. HDAC8 expression and purification

pET14b vector (Novagen, EMD Millipore) containing codon-optimized human HDAC8, fused to a His6 SUMO tag, was used to express HDAC8 in *E. coli* (BL21) DE3 pLysS. Cells were harvested by centrifugation for 10 min at 8000g and 4 °C and resuspended in lysis buffer (pH 8.0) containing 150 mM KCl, 50 mM Tris, 5 mM imidazole, 5 mM DTT, 1 x HALT protease inhibitor cocktail (Thermo Scientific) and 5 µg/ml DNaseI. The cell suspension was sonicated and lysates were clarified by centrifugation at 18000g for 30 min at 4 °C and sterile filtration. The filtrate was subsequently added to a 5 ml column volume of cOmplete His tag purification resin (Roche), equilibrated with IMAC buffer A

(pH 8.0) containing 150 mM KCl, 50 mM Tris and 5 mM imidazole. After washing with 50 ml of the same buffer His6-SUMO-HDAC8 was eluted with IMAC buffer B (pH 8.0) containing 150 mM KCl, 50 mM Tris and 100 mM imidazole. Subsequently 10 µg/ml His6 tagged SUMO-Protease was added to the eluted HDAC8 fusion protein. Cleavage of His6-SUMO tag occurred overnight whilst dialyzing against 25 mM Tris, 50 mM NaCl and 5 mM β-ME (pH 8.0) at 4 °C. Then His6-SUMO tag and SUMO-Protease was removed by a second IMAC with AIC buffer A (pH 8.0) containing 25 mM Tris and 50 mM NaCl and 5 mM imidazole. HDAC8 containing flowthrough was concentrated and further purified on a strong anion exchanger (Bio-Scale Mini Macro-Prep High Q 5 ml Cartridge, Biorad). After a washing step using AIC buffer A HDAC8 was eluted using AIC buffer B (pH 8.0) containing 25 mM Tris and 1 M NaCl. 5 mM DTT was added to prevent oxidation and remove possible β-ME cysteine adducts. The final purification step included size exclusion chromatography with a HiLoad Superdex 75 material (GE) equilibrated with GPC Puffer (pH 8.0) containing 150 mM KCl and 50 mM Tris. The protein containing fractions were collected and concentrated. Glycerol and TCEP were added to final concentrations of 25% and 1 mM and protein was stored at –20 °C. We typically obtained 3–5 mg HDAC8 from 1 l culture.

#### 2.2.2. Enzyme activity assay

All HDAC assays were executed in assay buffer (25 mM Tris-HCl pH 8.0, 50 mM NaCl and 0,001% (v/v) pluronic F-68) in black half area 96-well microplates (Greiner Bio-One, Germany). 1 nM of HDAC8<sub>WT</sub> or 10 nM of HDAC8 mutants were preincubated with a serial dilution of the compounds for 1 h at 30 °C, before initiating the enzyme reaction by addition of 10 µM Boc-Lys(TFA)-AMC. Some enzyme/compound mixtures were treated with either 1 mM TCEP or various concentrations of GSH for 1 h at 30 °C, before the enzyme reaction was started. The reaction was stopped after 60 min by adding 1.67 µM SATFMK. The deacetylated substrate was cleaved with 0.42 mg/ml Trypsin to release fluorescent AMC, which was detected with a microplate reader (PHERAstar FS, BMG LABTECH) with fluorescence excitation at 360 nm and emission at 460 nm. IC<sub>50</sub> values were calculated by generating dose-response curves in GraphPad Prism 6 and fitting those to a 4-parameter fit model. Sirtuin assays were performed according to a published procedure [8].

#### 2.2.3. Dialysis

HDAC8 (500 nM) was incubated with 100 µM **1** or buffer (control) for 1 h at room temperature and dialyzed (MEMBRA-CEL<sup>®</sup> dialysis membrane MWCO 3500, Serva, Germany) against 500-fold assay buffer with or without 50 mM β-mercaptoethanol (β-ME) for 22 h at 4 °C. Samples were taken before and after dialysis to determine the activity of the protein, by adding 20 µM Boc-Lys(TFA)-AMC and incubating for 30 min at 30 °C. The reaction was stopped by the addition of 1.7 µM SATFMK and 0,42 mg/ml Trypsin. Free AMC was detected in a microplate reader with fluorescence excitation at 360 nm and emission at 460 nm.

#### 2.2.4. Tryptic digestion

All tubes were cleaned with acetonitrile and water before use. 113 µM HDAC8 was treated with 300 µM **1** for 1 h at 25 °C in 10 mM ammonium bicarbonate buffer (ABC) while shaking at 400 rpm. A control sample was carried along without the addition of **1**. After treatment the samples were denatured at 90 °C for 30 min and alkylated with 14.5 mM iodoacetamide for 1 h at room temperature in the dark. All samples were diluted with ABC buffer to 56.6 µM HDAC8 to accomplish a pH value between 7 and 8. Tryptic digestion was started with 28.6 µg/ml sequencing grade modified trypsin (Promega, Germany) at 37 °C for 18 h while shaking at 400 rpm. The digestion process was stopped by freezing and storing the samples at –20 °C immediately after digestion till measurement.

### 2.2.5. Quantitative HPLC/ESI-QTOF-MS/MS

The liquid chromatography tandem mass spectrometry (LC-MS/MS) system consisted of an Agilent 1100 high performance liquid chromatograph (HPLC) equipped with a micro vacuum degasser, Multospher 120 RP 18-AQ, 250 × 4 mm (i.d.), 5 μm particle size coupled to an ABSciex X500R QTOF mass spectrometer equipped with an IonDrive TurboV ESI-source. HPLC separation was performed under gradient conditions with mobile phases of acetonitrile + 0.1% (v/v) formic acid (A) and Water + 0.1% (v/v) formic acid (B) at a flow rate of 0.5 ml/min. The gradient condition was set as follows: 0–5 min 10% A, 5–20 min linear increase to 70% A, 20–25 min 70% A, 25–26 min linear decrease to the initial condition of 10% A, 26–35 min 10% A for column equilibration. The injection volume was 10 μl. The parameters used for ESI-QTOF-MS/MS analysis in positive ion mode were as follows: nebulizer (gas 1), 50 arbitrary units; turbo gas (gas 2), 55 arbitrary units; curtain gas, 35 arbitrary units; source temperature, 500 °C; ionspray voltage + 5.5 kV, declustering potential (DP), 50 V; collision energy (CE), 10 V. TOF MS full scan and product ion Data were acquired by information dependent acquisition (IDA) scan mode in the mass range of 100–700 Da. The calibration delivery system (CDS) was set to perform an automatic external calibration every ten samples. Data acquisition and processing was performed with the Sciex OS 1.3 software.

The same system and mobile phases were used for peptide analysis but with different conditions as mentioned before. A 100 × 2 mm (i.d.), 2.3 μm particle size TSKgel Super-ODS C18 column with a flow rate of 0.2 ml/min was used with the gradient conditions set as follows: 0–5 min 5% A, 5–40 min linear increase to 80% A, 40–45 min 80% A, 45–55 min linear decrease to 5% A and 55–60 min 5% A for equilibration. The injection volume was 10 μl. ESI-QTOF-MS/MS parameters were as follows: gas 1, 45 arbitrary units; gas 2, 45 arbitrary units; curtain gas, 35 arbitrary units; source temperature, 400 °C; ionspray voltage + 5.5 kV, DP, 50 V; CE, 10 V. For data acquisition IDA scan mode was used in the mass range of 450–2000 Da. Dynamic collision energy mode was set active.

The software for Theoretical fragmentation and peptide fragment assignment were integrated in Sciex OS 1.3.

### 2.2.6. Protein crystallography

Protein expression and crystallization of HDAH was performed as described previously [9,10]. Briefly, crystals of HDAH were grown by hanging drop vapor diffusion against 500 μl reservoir, the reservoir solution contained 0.1 M malate-imidazole buffer (pH 5.25) and 3–6% PEG400. The reservoir solution and protein (10 mg/ml) were mixed in a 1:1 ratio to a final volume of 4 μl. Crystals grew in three to ten days at 20 °C. The obtained crystals of HDAH were soaked by adding of 2 μl of a 2 mM compound **1** dissolved in the reservoir solution directly to the drop and incubated for 24 h. Cryo-protection was achieved by washing the crystal in 0.1 M malate-imidazole buffer with a pH of 5.25 and 30% PEG400. The cryoprotected crystals were flash frozen in liquid nitrogen. Diffraction data were collected at 100 K on beamline PXII at the Swiss Light Source (SLS, Villigen, Switzerland).

### 2.2.7. Global fit analysis of reaction kinetics

The time courses of the relative concentrations of molecular species **1–9** were obtained from quantitative ESI-MS-measurements as described above. The simulation and modeling program COPASI was used to fit eligible models of the reaction mechanism to the set of time resolved concentrations [11]. In short, the model is described by a system of ordinary differential equations, which is determined by kinetic rate constants. These parameters were optimized by starting with randomized start values for all parameters and minimizing the total error sum of squares for the entire set of data curves by subsequently application of the implemented Evolution Strategy, Evolutionary Programming and Levenberg-Marquardt-algorithms. To estimate the absolute concentrations from relative concentrations, proportional factors were concurrently fitted to the data. Entering the determined rate constants and

proportional factors into the model allowed for the simulation of time-courses of all molecular species involved in the complex reaction mechanism.

### 2.2.8. Molecular docking

Modeling, preparation and visualization of structural data as well as molecular docking was performed using MOE 2016 software (Chemical Computing Group ULC, Canada). At first crystal structure data PDB-ID 1T64, 1T69, 1VKG, 3SFF representing significant conformations of HDAC8 in complex with various inhibitors were loaded into the program and subjected to structure preparation including 3D protonation for subsequent docking. The partial charges of all protein and ligand atoms were calculated using the implemented Amber12 force field. Molecular docking was performed choosing the triangle matcher for placement of the ligand in the binding site and ranked with the London dG scoring function. The best 30 poses were passed to the refinement and energy minimization in the pocket using the induced fit method and then rescored with the GBVI/WSA dG scoring function.

## 3. Results and discussion

### 3.1. Compound **1** and closely related analogs show similar activity against HDAC8

**1** been recently described as a novel, potent, and selective lead structure for HDAC8<sub>wt</sub> inhibitors [5]. Most interestingly, the compound contains no common zinc-chelating group characteristic for most HDAC inhibitors. Particularly the prevention of the ubiquitous hydroxamate group with a high potential for unspecific zinc ion binding and suspected mutagenicity let the pharmacophore of **1** appear an attractive alternative to existing HDAC8 inhibitors [12]. In light of its novel structure highly dissimilar to known HDAC inhibitors, we wondered about the mode of action of compound **1**. Since **1** was reported to exhibit anti-viral properties, Okazaki et al. investigated the chemical stability of the compound in greater detail and found out that **1** decomposes in the presence of glutathione (GSH) into thiophenol **3** which was believed to be the active anti-viral substance [7]. We confirmed the chemical instability of **1** in the presence of GSH, but besides **3** we also found considerable amounts of **5**, **6**, **8** and **9** using high-resolution ESI-MS. Next, we noticed that thiophenol **3** decomposes into sulfenamide **5** and thiourethane **8** immediately after dissolution in 10 mM ammonium carbonate buffer (pH 8.0) (Fig. S1). To identify the active substance that inhibits HDAC8<sub>wt</sub>, we determined IC<sub>50</sub>-values for analogs **1**, **3** and **5**, freshly dissolved in assay buffer (Fig. 1A). Surprisingly, all three compounds turned out to be similarly potent against HDAC8<sub>wt</sub> showing IC<sub>50</sub>-values of about 1 nM (Table S1). To simplify the reporting of next results, we will talk about HDAC8 inhibition by **1** when this compound is added to the enzyme, knowing that **1** can decompose into **3** and **5** in the presence of thiol groups such as those in the side chain of solvent-accessible cysteines at the surface of HDAC8.

### 3.2. Inhibition of HDAC8 is mediated by covalent modification of at least one cysteine

Since **1** inhibits in the concentration range of applied HDAC8<sub>wt</sub>, its binding is supposed to be very tight. To distinguish between a covalent and a reversible binding mode, we performed a dialysis of the complex formed by the interaction of HDAC8 and compound **1** (Fig. 2). After 22 h of dialysis in the absence of reducing agent, the enzyme activity of HDAC8<sub>wt</sub> remains substantially inhibited. In contrast, HDAC8 activity is completely recovered, if the protein-ligand complex is dialyzed against buffer including β-ME. This suggests covalent modification of HDAC8<sub>wt</sub> by **1** involving the formation and fission of a disulfide bridge between at least one accessible cysteine of the enzyme and the inhibitor. This conclusion is supported by the loss of activity of compounds **1**, **3** and **5** in the presence of the reducing agent TCEP that breaks disulfide bonds



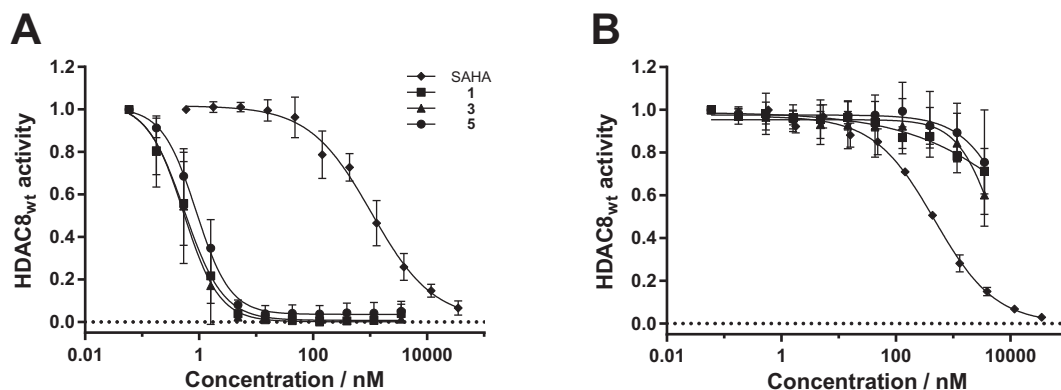


**Fig. 1.** Dose-response curve of **1**, **3**, **5** and control SAHA against indicated HDAC8<sub>wt</sub>. **1** nM HDAC8<sub>wt</sub> was A) in the absence and B) in the presence of TCEP incubated with varying concentrations of indicated inhibitor for 1 h at 30 °C. The remaining HDAC8<sub>wt</sub>-activity was determined using the standard enzyme activity assay. All data points represent means and standard deviations from 3 independent experiments. Solid lines are best-fit to a 4-parameter logistic.

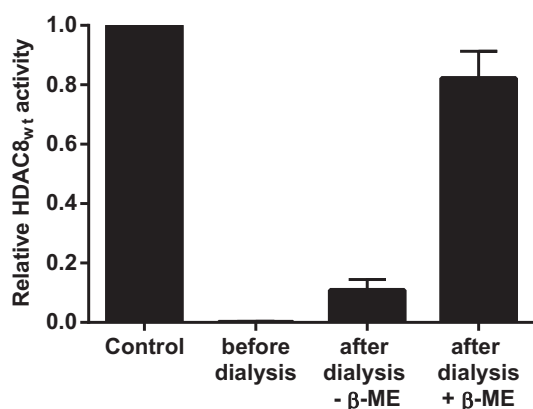


**Fig. 2.** Irreversible binding of **1** to HDAC8<sub>wt</sub> becomes reversible upon addition of reducing agent β-mercapto ethanol (β-ME). Enzyme activity is referred to 100% free HDAC8<sub>wt</sub>. After addition of 100 μM **1** to 500 nM HDAC8<sub>wt</sub> the enzyme is completely inhibited (before dialysis). After 24 h dialysis at 4 °C in the absence of β-ME only weak and in the presence of 50 mM β-ME almost the entire enzyme activity is recovered. Shown data are means and standard deviations of three independent experiments.

(Fig. 1B, Table S1). Moreover, addition of TCEP to preformed complexes between **1**, **3** and **5** and HDAC8<sub>wt</sub> reverses enzyme inactivation confirming the reversibility of the inhibitory mechanism that involves the formation and disruption of disulfide bonds. It should be noted that GSH at concentrations up to 1 mM is not able to reverse the inactivation of HDAC8<sub>wt</sub> once the disulfide with **1** is formed, possibly due to a less negative redox potential of GSH (−230 mV compared with −290 mV of TCEP) (Table S1).

### 3.3. Mechanism of GSH-modification by **1**

The reaction of GSH and **1** was investigated previously to learn about the corresponding transformations in aqueous solution. Okazaki et al. found that **1** was immediately cleaved in the presence of GSH producing **3** [7]. Similar to our results, **1** and **3** showed comparable EC<sub>50</sub>-values for the inhibition of HIV-1 infection. From these results, **1** was suggested as prodrug for the bioactive thiophenol **3** [7]. We applied the powerful technique of high-resolution ESI-MS to prove the existence of nine occurring molecular species in the reaction of GSH and **1** (Figs. 3, S2, S3, S5 and S6). In contrast to Okazaki, we verified only very small amounts of **3** immediately after mixing **1** and GSH. Similarly, purified **3** also disappears instantly after dissolution in ammonium carbonate buffer pH 8.0 generating significant amounts of sulfenamide

**5** and only minor amounts of **9** (Fig. S1). Therefore, we conclude that **3** is chemically unstable in aqueous solution. The concentration of every proven molecular entities involved in the reaction between GSH and **1** was quantified using LC-ESI-MS, and the corresponding time courses analyzed during a period of 15 h to elucidate the accurate mechanism of this unexpected complex reaction (Fig. 4 A, B). The decay of **1** shows two phases: a rapid drop within the first hour of reaction and a slow decrease over hours. In contrast, GSH disappears completely from the mixture within 30 min. Two intermediates, **5** and **6** are generated rather rapidly reaching their peak concentration at about 2 h and 0.5 h, respectively. While the mixed disulfide **6** vanishes after 3 h, the sulfenamide **5** is unexpected metastable and still present as one of the dominating species after 15 h. GSSG appears in conjunction with the rapid drop in GSH concentration and subsequently decreases slowly approaching a rather stable level. The occurrence of glutathione-thiocyanate (**4**) was unequivocally proven by ESI-MS/MS data (Fig. S2,S3), removal of the cyano group and the characteristic formation of a cyclic thiazolamine after reacting with a 5-fold excess concentration of cysteine (Fig. S4). Interestingly, **4** was shown to arise rapidly and be chemically stable for at least 15 h (Fig. 4A). Simulations suggest that cyanation is the predominant modification of GSH compared with disulfide formation (Fig. 4B). The whole complex reaction is superimposed by slowly emerging **8** and sulfinic acid **9** as final products. The array of time-dependent concentrations of all species was fit to a model taking all experimentally verified molecular entities into account (Fig. 4C).

The entire set of experimental time-dependent concentrations is well described by the reaction scheme in Fig. 4C). Comprehensive data analysis using COPASI provides the rate constants for every depicted elementary reaction steps (Table S2). The reaction mechanism postulates the formation of glutathione thiocyanate, **4**, proven by ESI-MS/MS, as suggested by Ghebremariam for the covalent inactivation of DDAH1 [2]. In the same step thiophenol **3** is generated that is instantly oxidized (see above) giving the central metastable sulfenamide **5**. The mixed disulfide **6** generated from **5** can react further with GSH giving GSSG and **3**. When GSH is consumed, the chemical equilibrium between **5**, **6** and **7** is established leading to a progressive drop in the concentration of **6** that is no longer produced from **5** and a slower moderate decrease of GSSG concentration. Simultaneously, two slow side reactions take place generating two chemically stable final products: Metastable **5** is oxidized to sulfinic acid **9**, and residual **1** is hydrolyzed to thiourethane **8**. The comprehensive analysis of quantitative and time-resolved data provide substantial insight into the accurate mechanism by which model compound GSH and **1** react. From these results we conclude that **1** is a general dual cysteine modifier in aqueous solution that can transfer cyano groups to thiol residues and also produces

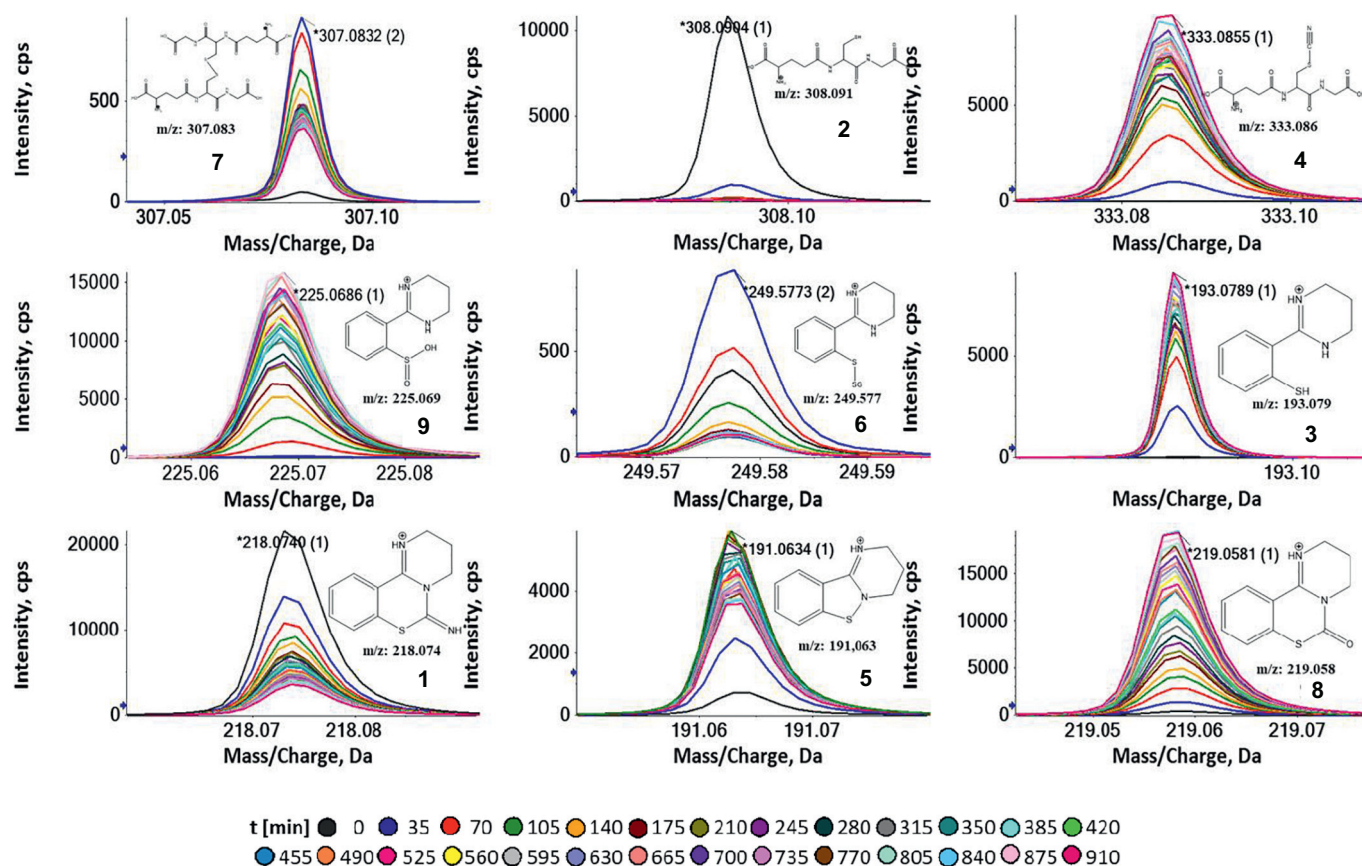


Fig. 3. Quantitative ESI-MS of all observed educts, intermediates and products of the reaction between compound 1 and GSH (2). The bold numbers under the  $m/z$  ratios correspond to those in Fig. 4 of the main text. The spectra are measured after indicated time periods.

mixed disulfides between cysteines and thiophenol 3.

### 3.4. Covalent modification of HDAC8<sub>wt</sub> by 1

In an attempt to elucidate the accurate binding mode of 1 to HDAC enzymes we tried to crystallize complexes of 1 with HDAC8 and HDAH, a bacterial homolog that crystallizes nicely in our hands [9,10]. We added 1 to a HDAH crystal in order to soak the ligand into the binding pocket. Unfortunately, we were not successful to obtain crystals of the HDAC8 complex with sufficient quality for structure determination. But we were able to determine the structure of the reaction product of HDAH and 1 at a very high spatial resolution of 1.47 Å. To our surprise, the binding site pocket was unoccupied. Instead, we found covalent modifications of two cysteines (C51 and C295) at the surface of HDAH.

Although no reducing agent was present during crystallization, both modifications were clearly visible as mixed disulfides between the respective cysteine and thiophenol 3 as shown exemplary for C51 (Fig. 5). The observed modifications of HDAH are in agreement with the reaction mechanism between 1 and GSH (Fig. 4C), which has been elucidated on the basis of quantitative ESI-MS data. The cysteine modification reaction seems to be rather unspecific and is supposed to be a common mechanism for unselective inhibition of other enzymes, if functional cysteines are hit.

To identify putatively modified cysteines in HDAC8<sub>wt</sub>, a reaction mixture of HDAC8<sub>wt</sub> and 1 was subjected to tryptic digestion followed by LC-ESI-MS/MS analysis. In fact, C153 in the catalytic site as well as various other cysteine residues were modified by 1 (Table S3). Five cysteines, including C28, C153, C244, C314 and C352 showed cyanation upon treatment with 1 (Fig. S3). These modifications are in agreement with the unspecific affinity labeling mechanism of GSH. Since the reaction of HDAC8<sub>wt</sub> with 1 was performed at high

concentrations of almost four orders of magnitude above the IC<sub>50</sub>-value of 1, only qualitative statements about the modified cysteines in HDAC8<sub>wt</sub> and no assessment of a preference for a particular cysteine can be made. However, it appears plausible that the effect of 1 or 5 responsible for the inhibition of HDAC8<sub>wt</sub> is mainly due to the modification of C153 in the catalytic site pocket thereby permanently blocking access to the catalytic center. In any case, 1 and most likely also related benzothiazine-imines are clearly able to modify solvent accessible thiol groups on protein surfaces and produce cysteine-thiocyanates as well as mixed disulfides between cysteine and 3. For the majority of enzyme targets including other HDAC isoenzymes that are effected by 1 only moderate activities in the micromolar range have been reported [2–5]. 1, 3 and 5 were also tested against Sirtuins, because Sirt1 was shown to respond to similar inhibitors [13]. The compounds show moderate micromolar activities against Sirt1 and Sirt2, but were virtually inactive against Sirt 3 (Table S7). This is in agreement with moderate activity on a variety of protein targets and our finding that 1 is a general cysteine modifier. Most recently, thiol reactive histone acetyltransferase (HAT) inhibitors have been considered as essentially nonselective interference compounds [13]. Typically, these HAT inhibitors show moderate IC<sub>50</sub>-values in the micromolar range. However, CPTH2, a thiol-reactive HAT (GCN5) inhibitor, does not inhibit HDAC8 (IC<sub>50</sub> > 50 μM, Fig. S13). Despite its unspecific cysteine reactivity, 1 is highly potent and selective against HDAC8 with an IC<sub>50</sub>-value of 11 nM [5]. Since C153 is conserved among all human HDAC isoenzymes and other cysteines in HDAC8 are also modified, another component had to be the major contributor to the observed selectivity of compound 1.

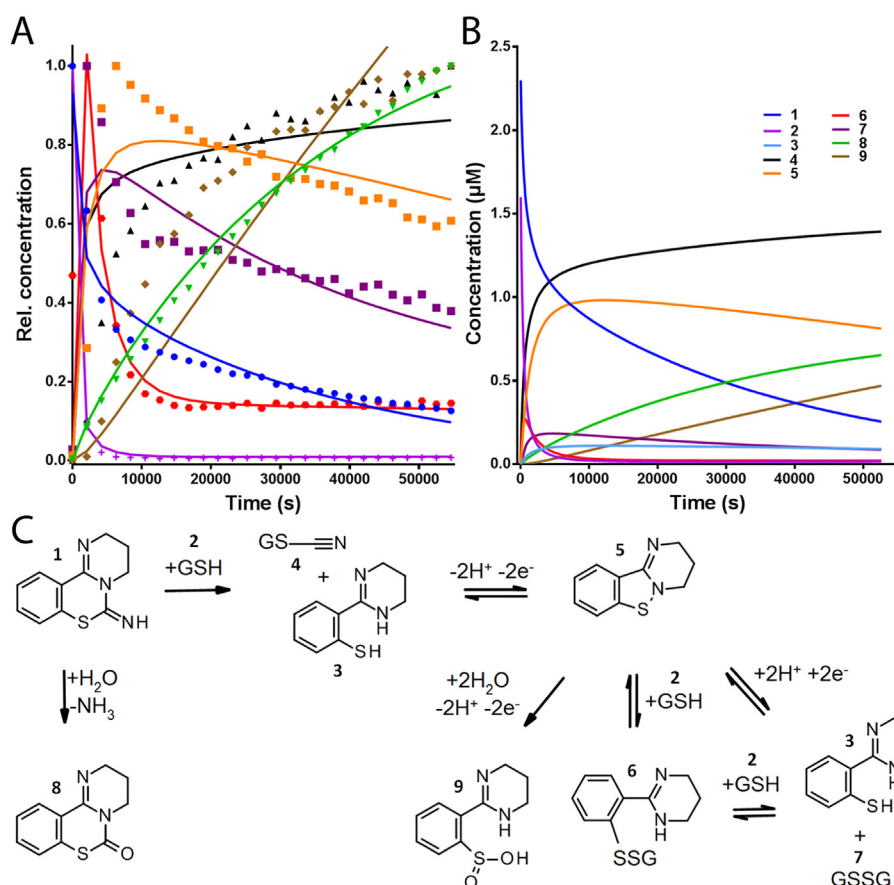


**Fig. 4.** A) Time courses of indicated species during the reaction between 2.3  $\mu\text{M}$  **1** and 1.6  $\mu\text{M}$  GSH in 10 mM ammonium carbonate buffer pH 8.0 at  $(26 \pm 1)^\circ\text{C}$ . Experimental relative concentrations as determined from ESI-MS. Solid lines represent a simultaneous fit of the reaction mechanism shown in C) to the data using COPASI. B) Simulated absolute concentrations on the basis of the reaction mechanism and rate constants determined in C) using COPASI. C) Proposed reaction mechanism of **1** with glutathione (GSH). GSSG is oxidized GSH and **4** is glutathione-thiocyanate. All chemical species have been identified and quantified using ESI-MS (Fig. S2).

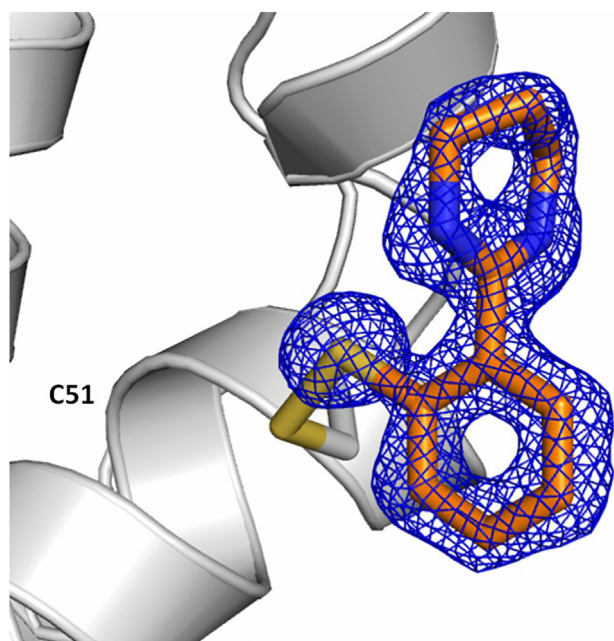


**Fig. 5.** Covalent modification of C51 in a crystal structure of HDAH (PDB-ID: 6GJK) after reaction with **1**. C51 forms a mixed disulfide bridge with thiophenol **3**. The blue mesh shows the  $2F_o - F_c$ -electron density map of the compound contoured at 1 sigma.

### 3.5. C102 and C153 are involved in the inhibition mechanism of HDAC8

Looking at available crystal structures of HDAC8 (e.g. PDB-ID: 1T69) reveals C153 in the active site and C102 in close proximity to be

eligible for a potential chemical modification by **1**. In the following, single mutants HDAC8<sub>C102S</sub> and HDAC8<sub>C153S</sub> and the double mutant HDAC8<sub>C102S/C153S</sub> were produced to elucidate the participation of the exchanged cysteines in the mechanism of inhibition. Since all HDAC8 variants were enzymatically active, the inhibitory efficacy of compounds **1**, **3** and **5** could be determined in terms of  $\text{IC}_{50}$ -values (Fig. 1A, Fig. S12). To demonstrate the reversibility of a putative disulfide bond involving C102 or C153, respectively, the concentration series were performed in the absence or after the addition of 1 mM TCEP to the preformed complex between HDAC8-variant and compound (Fig. S12). After the addition of the reducing agent, the enzyme activity of all HDAC8 variants is recovered confirming that the mechanism of HDAC8 inhibition by **1** and derivatives thereof involves the formation of disulfide bonds (Fig. S12). SAHA was used as control that shows absolutely no susceptibility to reducing agent TCEP.  $\text{IC}_{50}$ -values of SAHA varied slightly between 0.29 and 2.4  $\mu\text{M}$  among the 4 HDAC8 variants (Table S1). While SAHA behaves like a classical active site inhibitor against the double mutant HDAC8<sub>C102S/C153S</sub>, compounds **1**, **3** and **5** show a biphasic dose-response curve against the same enzyme (Fig. S12G). This finding suggests an allosteric interaction site at this HDAC8 variant. The  $\text{IC}_{50}$ -values of **1**, **3** and **5** for the more potent site is comparable with the  $\text{IC}_{50}$ -values against the single mutants of HDAC8. We hypothesize that other solvent accessible cysteines at the surface of HDAC8 may react with analogs of **1** enabling an indirect modulation of the catalytic efficiency of HDAC8<sub>C102S/C153S</sub>, which is not capable of full enzyme inactivation. Only at very high concentration of **1**, **3** or **5** ( $> 10 \mu\text{M}$ ) full inhibition is achieved probably by additional unselective modifications of the HDAC8 variant. These results suggest that HDAC8 contains at least two types of interaction sites: A high affinity site involving cysteines C102 and C153 in close proximity to the active site and at least one low affinity allosteric site where unselective disulfide modification can take place at higher concentrations of **1** analogs. There are only

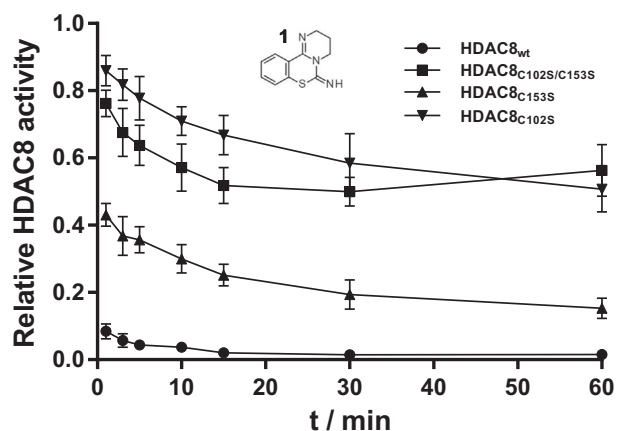


**Fig. 6.** Inhibition kinetics of different HDAC8 variants by compound **1**. 100 nM of the respective HDAC8 variant was incubated with 500 nM of freshly dissolved inhibitor at 30 °C. The residual enzyme activity was measured after varying incubation time periods. The data represent mean and standard deviation of at least four independent experiments.

rather small differences in  $IC_{50}$  values of **1**, **3** and **5** between HDAC8<sub>wt</sub> and HDAC8<sub>C153S</sub> and HDAC8<sub>C102S</sub> (Table S1). Due to the low enzyme activity of the HDAC8 mutant proteins as much as 10 nM enzyme concentration was chosen to measure and compare the dose-response curves of the inhibitors against all HDAC8 variants. Since particularly the  $IC_{50}$ -values with HDAC8<sub>wt</sub> approach the level of enzyme concentration, these  $IC_{50}$ -values only represent upper limits of the true inhibitory activity. This is also recognizable by the distinct steep shape of the dose-response curves of **1**, **3**, **5** on HDAC8<sub>wt</sub> indicating nearly stoichiometric tight binding of a ligand (Fig. S12A). Nevertheless, a clear differentiation between the inhibition of HDAC8<sub>wt</sub> and the mutant enzymes is not possible on the basis of these data. Unfortunately, it is not possible to lower the enzyme concentration of the mutant variants because of their weak enzyme activity. Moreover, it is more conclusive to investigate the inhibition kinetics of covalent inactivators such as cystine modifiers. In fact, the inhibition kinetics of HDAC8<sub>wt</sub> by **1** is clearly different from that of the mutant variants (Fig. 6). HDAC8<sub>wt</sub> is essentially completely inhibited after 2 min in striking contrast to HDAC8<sub>C102S</sub>, HDAC8<sub>C153S</sub> and HDAC8<sub>C102S/C153S</sub> indicating the pivotal role of both cysteines in the inhibition mechanism. **1** shows a slow inhibition of the double mutant HDAC8 approaching an equilibrium level of about 50% residual enzyme activity, which is in agreement with the corresponding dose-response curve (Fig. S12G). This finding suggests that the inhibition mechanism does not involve a continuing chemical inactivation but is rather maintained by non-covalent binding. In contrast, inhibition of HDAC8<sub>C153S</sub> and HDAC8<sub>C102S</sub> does not reach equilibrium but still continues even after 30 min of reaction suggesting a covalent modification of C102 and C153 (Fig. 6). Interestingly, C102 seems to be more rapidly hit by **1** than C153. The enzyme activity of HDAC8<sub>C153S</sub> drops instantly by about 50% and then shows a slow ongoing inhibition, whereas HDAC8<sub>C102S</sub> shows only the slow inhibition kinetics. The differential inhibition kinetics of the HDAC8 variants clearly demonstrates, that the presence of both cysteines, C102 and C153, is required for the rapid inhibition mechanism of HDAC8<sub>wt</sub>.

### 3.6. Non-covalent molecular recognition of **1** and **5** by HDAC8<sub>wt</sub>

The reactivity of **1** in the presence of GSH and the unselective modification of many proteins render benzothiazine-imines unsuitable for therapeutic applications. On the other hand, the significant increase in potency of **1** against HDAC8 by three orders of magnitudes cannot be explained by simple nonspecific affinity labeling. Therefore, we hypothesize that the experimentally observed high selectivity of

benzothiazine-imine analogs for HDAC8 is caused by an additional specific contribution to inhibition such as a beneficial non-covalent molecular recognition in the active site or another transient binding pocket that precedes covalent modification. Our hypothesis is supported by the inhibition kinetics of the HDAC8<sub>C102S/C153S</sub> double mutant that is in agreement with non-covalent binding (Fig. 6). The presumed non-covalent molecular recognition of **1** and **5** by HDAC8 was investigated further using computational methods, particularly molecular docking. It is known that the conserved binding pocket of HDAC8 is highly conserved among members of the HDAC family. However, HDAC8 is very special with respect to enhanced malleability of the region around the classical active site. There exist various X-ray structures that demonstrate the considerable flexibility of HDAC8 and a transition from closed (PDB-ID: 1T69) to sub-open (PDB-ID: 1T64) to wide-open (1VKG) binding pockets [14]. Most remarkable, the sub-open state shows a deep second binding pocket next to the conserved one, which is occupied with a second inhibitor molecule. The L1- and L2-loop are primarily responsible for ligand-induced conformational changes in HDAC8 [14–16]. Both loops display highly varying amino acid compositions in HDAC1 and HDAC8. In addition, the L1-loop of HDAC1 is 5 amino acids longer than that of HDAC8 causing a different flexibility profile in both isoenzymes [17]. Compounds **1** and **5** were docked into the binding pockets of above mentioned representative HDAC8 structures to determine the favored binding modes and identify putative beneficial contacts. Furthermore, **1** was also docked into available crystal structures of HDAC isoenzymes HDACs 1, 2, 4 and 6 to understand the observed selectivity in enzyme activity assays on a molecular basis (Fig. S9). The best docking score is obtained for HDAC8, thus confirming the experimental data (Table S4).

Docking of **1** into various crystal structures of HDAC8 revealed clearly different scores indicating different affinities to distinct conformations of HDAC8 (Table S5). The best docking pose of **1** at the bottom of the active site pocket in HDAC8 (PDB-ID: 1T69) is shown in Fig. 7A. A comparison of the docking result between HDAC8 (PDB-ID: 1T69) and **1** with the crystal structure of HDAC8 bound to an amino acid inhibitors (PDB-ID: 3SFF) shows a substantial overlap of both inhibitors binding to the transition area between the acetyl-lysine binding tunnel and the acetate release channel (Fig. 7B). The best docking pose of **1** in HDAC1 (PDB-ID: 5ICN) is located in the conserved active site binding pocket (Fig. S9). The closest distance between carbon atoms of F150 (matching F152 in HDAC8) and Y303 (matching Y306 in HDAC8) is 4.0 Å impeding access to the acetate release channel (Fig. S10). In addition, M30 located in the L1-loop of HDAC1 intrudes into the acetate release channel and clashes with superimposed compound **1** docked to HDAC8. In contrast, F152 and Y306 in the docked complex between HDAC8 and **1** are moved to the side allowing the aromatic moiety of **1** to protrude into the acetate release channel similar to the amino-acid derived inhibitors of Whitehead et al. [18] (Figs. 7 and S10). The dominating molecular interactions between HDAC8 and **1** are zinc binding through the imine nitrogen of **1** and a hydrogen bond between a nitrogen atom of the tetrahydropyrimidine ring of **1** and Y306. These are complemented by a cation- $\pi$ -interaction between the aromatic ring of **1** and R37 and mainly hydrophobic interactions to F152, F208, C153, I34 and G304. The aromatic ring of **1** forms a  $\pi$ - $\pi$  T-shaped interaction with W141 (Fig. S10). Acetate release is believed to be mediated by R37 stabilizing the charge of acetate in cooperation with W141 relocating its indole moiety to close the release channel [18,19]. The pivotal W141 is substituted by leucine in class I HDACs 1, 2 and 3, and has no counterpart in class II HDACs. This amino acid difference in the acetate release channel and also in the L1-loop (e.g. M30 in HDAC1 and 2 intrudes into the acetate release channel) as well as in the L2-loop are supposed to have significant impact on HDAC8 flexibility and the geometry of the internal binding cavity. In summary, differences in pivotal amino acids, protein malleability and the particular binding mode of **1** to HDAC8 is suggested to be the reason for the observed selectivity for HDAC8 and against class I HDACs 1 and 2 as well as class

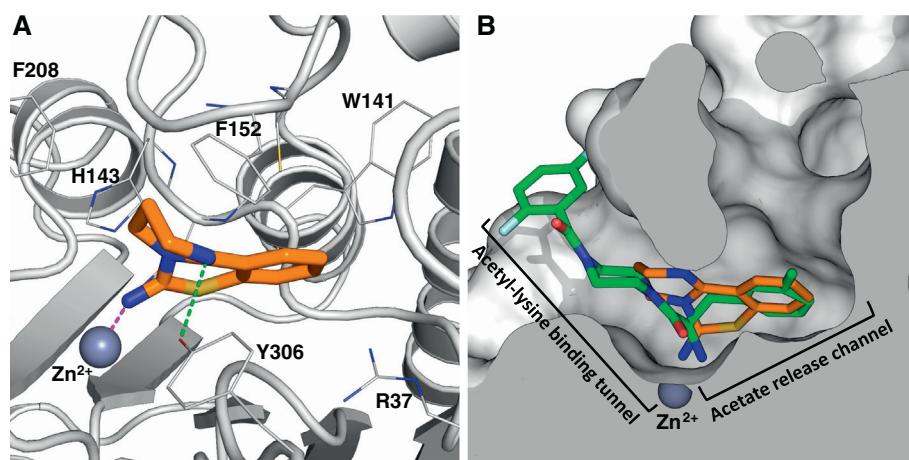


**Fig. 7.** Docking of **1** into the active site pocket of HDAC8 (PDB-ID: 1T69). A) **1** binds at the bottom of the active site pocket and protrudes into the acetate release channel. The green dashed line indicates a hydrogen bond to Y306 and the magenta dashed line a metal-binding interaction between the imine group and the catalytic zinc ion. B) Overlay of **1** (orange) docked into PDB-ID 1T69 and the complex between HDAC8 and amino-acid based inhibitor (PDB-ID: 3SFF, green) [18]. Both compounds show pronounced overlap, particularly in the transition area between the acetyl-lysine binding tunnel and the horizontal acetate release channel.

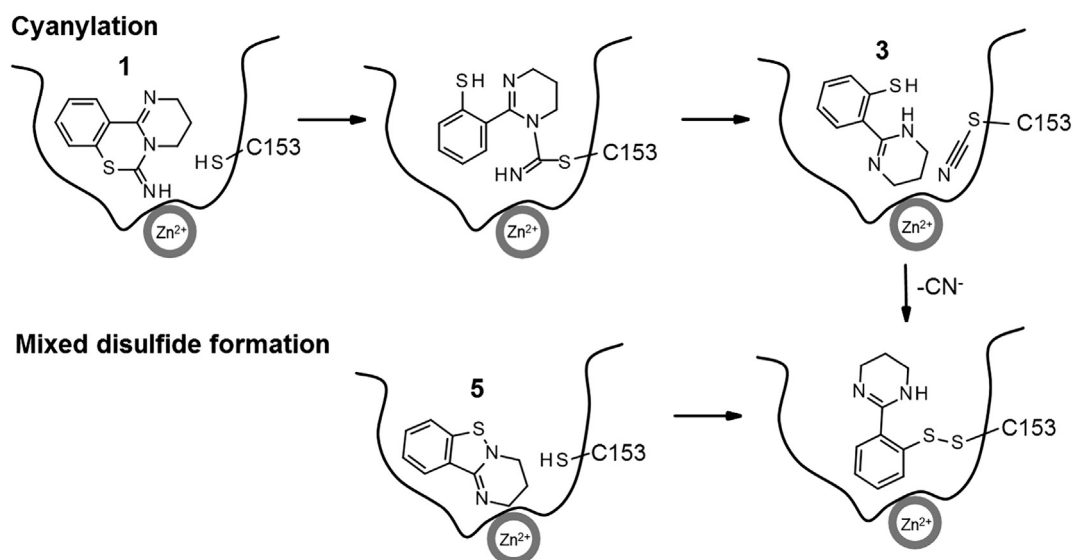


**Fig. 8.** Two pathways of covalent modification at C153 in the active site of HDAC8 by **1** or **5** resulting in thiocyanate or mixed disulfide, respectively.

Iia HDAC4 and class Iib HDAC6. Once **1** is non-covalently bound to HDAC8, it is brought in close proximity to C153 lining the active site pocket (Fig. S10) and is supposed to have an increased probability to cyanylate this cysteine (Fig. 8). The released thiophenol **3** is rapidly oxidized to **5** in free solution. But in principle **3** could also remain transiently bound and stabilized by non-covalent interactions before reacting further with the adjacent C153-thiocyanate (Fig. 8). The sulfur atom of the thiocyanate possesses an electrophilic character due to the cyano moiety acting as a leaving group [20]. The experimentally observed mixed disulfide can be reached by substituting the cyanyl group by thiophenol **3**.

Docking **3** into HDAC8 with cyanylated C153 shows that **3** is well accommodated in the binding pocket and has a short distance of 4.7 Å between the thiol group and the sulfur atom of C153 (Fig. S7). During the first hour of interaction between **1** and GSH the next prominent reactive intermediated during the reaction with thiol agents is the sulfenamide **5** which is rapidly formed by oxidation of **3** and rather stable under assay conditions. In fact, **5** showed similar potency against HDAC8 than **1**. Therefore, non-covalent binding of **5** followed by direct conversion of C153 to the mixed disulfide with **3** could be an alternative pathway to inhibition of HDAC8 according to the model reaction between GSH and **1** (Fig. 8). Docking of **5** to HDAC8 revealed a binding mode, where a partially negatively charged nitrogen of **5** binds closely to the zinc ion (Fig. S8). The non-covalent interaction is enhanced by a hydrogen bond to Y306 and various hydrophobic interactions to C153,

W141, H142, H143, F208, M274, Y306 and G304. The thiol group of C153 and the sulfur atom of **5** are brought in proximity (4.8 Å) allowing for a subsequent modification reaction (Fig. S8, Table S4). Since ESI-MS/MS data prove the cyanylation of C153, we conclude that the interaction between **1** and HDAC8 follows the cyanylation pathway (Fig. 8 upper panel). However, since **1** is not so stable in aqueous solution and **5** is also capable to inhibit HDAC8 with comparable potency, we cannot rule out the second pathway which starts with the interaction between metastable **5** and HDAC8 producing a mixed disulfide that blocks access to the active site (Fig. 8 lower panel).

#### 4. Conclusions

The benzothiazine-imine **1** is a potent and selective inhibitor of HDAC8 with an unprecedented chemical scaffold lacking traditional zinc binding groups. This study provides detailed insight in the reaction mechanism of **1** with GSH on the basis of quantitative and time-resolved ESI-MS/MS data. Compound **1** is chemically not stable in the presence of GSH. The reaction produces thiocyanate and disulfide modifications of GSH, GSSG as well as a mixed disulfide with **3**. Surprisingly, the sulfenamide **5** appears to be relatively stable over the course of 15 h at pH 8.0.

Combined MS, biochemical and crystal structure data of the interaction of HDAC8 with **1** provide clear evidence that 1) **1** is a covalent inhibitor of HDAC8, 2) inhibition is reversible in the presence of

reducing agents, 3) C153 in the active site and adjacent C102 are involved in the inhibition mechanism and 4) **1** modifies various cysteines in HDAC8 forming either thiocyanates or mixed disulfides with **3**.

The reactive nature of **1** is obviously the cause for its moderate inhibitory effects against several other targets. However, the single-digit nanomolar potency and high selectivity of **1** for HDAC8 even against closely related HDAC isoenzymes requires a further important component in the specific recognition of **1** by HDAC8.

On the basis of molecular docking results we propose putative selective non-covalent binding of **1** and **5** to HDAC8 prior to covalent modification. The optimal binding mode of **1** at the bottom of the active site protrudes into the acetate release channel showing distinct amino acid differences to other HDAC isoenzymes. The close proximity of **1** and C153 within the active site pocket is supposed to accelerate the covalent inactivation particularly in HDAC8 and is proposed to be a major determinant for the observed selectivity.

It is quite clear, that the reactive nature of **1** and its analogs render them unsuitable for therapeutic treatment. However, it appears attractive to further examine the specific molecular recognition motif of **1** that utilizes the transition area between the catalytic site and acetate release channel. We are currently pursuing several strategies towards less reactive variants of **1** that exploit the specific non-covalent molecular recognition of this class of compounds by HDAC8.

#### Conflict of interest

The authors declare no competing financial interest.

#### Acknowledgement

NW and MJ thank the Deutsche Forschungsgemeinschaft (DFG, Ju295/14-1) for funding.

#### Appendix A. Supplementary data

Supplementary data to this article can be found online at <https://doi.org/10.1016/j.bbagen.2019.01.001>.

#### References

- [1] M.R. Birck, T.P. Holler, R.W. Woodard, Identification of a slow tight-binding inhibitor of 3-deoxy-d-manno-octulosonic acid 8-phosphate synthase, *J. Am. Chem. Soc.* 122 (2000) 9334–9335.
- [2] Y.T. Ghebremariam, D.A. Erlanson, J.P. Cooke, A novel and potent inhibitor of dimethylarginine dimethylaminohydrolase: a modulator of cardiovascular nitric oxide, *J. Pharmacol. Exp. Ther.* 348 (2014) 69–76.
- [3] A.M. Chamoun, K. Chockalingam, M. Bobardt, R. Simeon, J. Chang, P. Gally, Z. Chen, PD 404,182 is a virocidal small molecule that disrupts hepatitis C virus and human immunodeficiency virus, *Antimicrob. Agents Chemother.* 56 (2012) 672–681.
- [4] National Center for Biotechnology Information, PubChem Compound Database; CID = 6603967, <https://pubchem.ncbi.nlm.nih.gov/compound/6603967>, (2018), Accessed date: 21 April 2018.
- [5] A. Kleinschek, C. Meyners, E. Digiorgio, C. Brancolini, F.J. Meyer-Almes, Potent and selective non-hydroxamate histone deacetylase 8 inhibitors, *ChemMedChem* 11 (2016) 2598–2606.
- [6] A. Chakrabarti, J. Melesina, F.R. Kolbinger, I. Oehme, J. Senger, O. Witt, W. Sippl, M. Jung, Targeting histone deacetylase 8 as a therapeutic approach to cancer and neurodegenerative diseases, *Future Med. Chem.* 8 (2016) 1609–1634.
- [7] S. Okazaki, S. Oishi, T. Mizuhara, K. Shimura, H. Murayama, H. Ohno, M. Matsuoka, N. Fujii, Investigations of possible prodrug structures for 2-(2-mercaptophenyl) tetrahydropyrimidines: reductive conversion from anti-HIV agents with pyrimidobenzothiazine and isothiazolopyrimidine scaffolds, *Org. Biomol. Chem.* 13 (2015) 4706–4713.
- [8] B. Heltweg, J. Trapp, M. Jung, In vitro assays for the determination of histone deacetylase activity, *Methods* 36 (2005) 332–337.
- [9] C. Meyners, A. Kramer, O. Yildiz, F.J. Meyer-Almes, The thermodynamic signature of ligand binding to histone deacetylase-like amidohydrolases is most sensitive to the flexibility in the L2-loop lining the active site pocket, *Biochim. Biophys. Acta* 1861 (2017) 1855–1863.
- [10] C.E. Weston, A. Kramer, F. Colin, O. Yildiz, M.G. Baud, F.J. Meyer-Almes, M.J. Fuchter, Toward photopharmacological antimicrobial chemotherapy using photoswitchable amidohydrolase inhibitors, *ACS Infect. Dis.* 3 (2017) 152–161.
- [11] S. Hoops, S. Sahle, R. Gauges, C. Lee, J. Pahle, N. Simus, M. Singhal, L. Xu, P. Mendes, U. Kummer, COPASI—a COMplex PATHway Simulator, *Bioinformatics* 22 (2006) 3067–3074.
- [12] S. Shen, A.P. Kozikowski, Why hydroxamates may not be the best histone deacetylase inhibitors—what some may have forgotten or would rather forget? *ChemMedChem* 11 (2016) 15–21.
- [13] J.L. Dahlin, K.M. Nelson, J.M. Strasser, D. Barsyte-Lovejoy, M.M. Szewczyk, S. Organ, M. Cuellar, G. Singh, J.H. Shrimp, N. Nguyen, J.L. Meier, C.H. Arrowsmith, P.J. Brown, J.B. Baell, M.A. Walters, Assay interference and off-target liabilities of reported histone acetyltransferase inhibitors, *Nat. Commun.* 8 (2017) 1527.
- [14] J.R. Somoza, R.J. Skene, B.A. Katz, C. Mol, J.D. Ho, A.J. Jennings, C. Luong, A. Arvai, J.J. Buggy, E. Chi, J. Tang, B.C. Sang, E. Verner, R. Wynands, E.M. Leahy, D.R. Dougan, G. Snell, M. Navre, M.W. Knuth, R.V. Swanson, D.E. McRee, L.W. Tari, Structural snapshots of human HDAC8 provide insights into the class I histone deacetylases, *Structure* 12 (2004) 1325–1334.
- [15] M. Brunsteiner, P.A. Petukhov, Insights from comprehensive multiple receptor docking to HDAC8, *J. Mol. Model.* 18 (2012) 3927–3939.
- [16] D.P. Dowling, S.L. Gantt, S.G. Gattis, C.A. Fierke, D.W. Christianson, Structural studies of human histone deacetylase 8 and its site-specific variants complexed with substrate and inhibitors, *Biochemistry* 47 (2008) 13554–13563.
- [17] N. Deschamps, C.A. Simões-Pires, P.-A. Carrupt, A. Nurisso, How the flexibility of human histone deacetylases influences ligand binding: an overview, *Drug Discov. Today* 20 (2015) 736–742.
- [18] L. Whitehead, M.R. Dobler, B. Radetich, Y. Zhu, P.W. Atadja, T. Claiborne, J.E. Grob, A. McRiner, M.R. Pancost, A. Patnaik, W. Shao, M. Shultz, R. Tichkule, R.A. Tommasi, B. Vash, P. Wang, T. Stams, Human HDAC isoform selectivity achieved via exploitation of the acetate release channel with structurally unique small molecule inhibitors, *Bioorg. Med. Chem.* 19 (2011) 4626–4634.
- [19] S. Haider, C.G. Joseph, S. Neidle, C.A. Fierke, M.J. Fuchter, On the function of the internal cavity of histone deacetylase protein 8: R37 is a crucial residue for catalysis, *Bioorg. Med. Chem. Lett.* 21 (2011) 2129–2132.
- [20] T. Castanheiro, J. Suffert, M. Donnard, M. Gulea, Recent advances in the chemistry of organic thiocyanates, *Chem. Soc. Rev.* 45 (2016) 494–505.

---

**Titel:**

Switching the Switch: Ligand Induced Disulfide Formation in HDAC8

**Autoren:**

Niklas Jansch, Wisely Oki Sugiarto, Marius Muth, Aleksandra Kopranovic, Charlotte Desczyk, Matthias Ballweg, Frank Kirschhöfer, Gerald Brenner-Weiss, Franz-Josef Meyer-Almes

**Bibliographische Daten:**

Chemistry – A European Journal (doi.org/10.1002/chem.202001712)

**Zusammenfassung:**

Die humane Histondeacetylase 8 ist ein bekanntes Zielmolekül für die Behandlung von T-Zell-Lymphomen und insbesondere von Neuroblastomen bei Kindern. PD-404,182 hat sich als selektiver kovalenter Inhibitor von HDAC8 erwiesen, welcher gemischte Disulfide mit mehreren Cysteinresten bildet und auch in der Lage ist, Thiolgruppen in Thiocyanate umzuwandeln. Darüber hinaus wurde gezeigt, dass HDAC8 durch einen Redox-Schalter reguliert wird, welcher auf der reversiblen Bildung einer Disulfidbindung zwischen den Cysteinen Cys<sub>102</sub> und Cys<sub>153</sub> beruht. Diese Studie über die unterschiedlichen Auswirkungen von PD-404,182 auf HDAC8 zeigt, dass diese Verbindung die dosisabhängige Formierung intramolekularer Disulfidbrücken induziert. Der Mechanismus der Hemmung von HDAC8 durch PD-404,182 umfasst daher sowohl die kovalente Modifikation von Thiolen als auch die ligandenvermittelte Bildung von Disulfiden. Darüber hinaus bietet diese Studie einen tiefen molekularen Einblick in den Regulierungsmechanismus von HDAC8, bei dem mehrere Cysteine mit abgestufter Tendenz zur Bildung reversibler Disulfidbrücken beteiligt sind.

## Enzymes

## Switching the Switch: Ligand Induced Disulfide Formation in HDAC8

Niklas Jänsch,<sup>[a]</sup> Wisely Oki Sugiarto,<sup>[a]</sup> Marius Muth,<sup>[a, b]</sup> Aleksandra Koprancovic,<sup>[a]</sup> Charlotte Desczyk,<sup>[a]</sup> Matthias Ballweg,<sup>[a]</sup> Frank Kirschhöfer,<sup>[b]</sup> Gerald Brenner-Weiss,<sup>[b]</sup> and Franz-Josef Meyer-Almes<sup>\*[a]</sup>

**Abstract:** Human histone deacetylase 8 is a well-recognized target for T-cell lymphoma and particularly childhood neuroblastoma. PD-404,182 was shown to be a selective covalent inhibitor of HDAC8 that forms mixed disulfides with several cysteine residues and is also able to transform thiol groups to thiocyanates. Moreover, HDAC8 was shown to be regulated by a redox switch based on the reversible formation of a disulfide bond between cysteines Cys<sub>102</sub> and Cys<sub>153</sub>. This study on the distinct effects of PD-404,182 on HDAC8 re-

veals that this compound induces the dose-dependent formation of intramolecular disulfide bridges. Therefore, the inhibition mechanism of HDAC8 by PD-404,182 involves both, covalent modification of thiols as well as ligand mediated disulfide formation. Moreover, this study provides a deep molecular insight into the regulation mechanism of HDAC8 involving several cysteines with graduated capability to form reversible disulfide bridges.

## Introduction

Human histone deacetylase 8 (HDAC8) belongs to the histone deacetylase family containing 11 human isoenzymes that are subdivided into four classes. Contrary to most other isoenzymes, HDAC8 is not a member of multi-protein complexes, but rather interacts with only a handful of established other mostly cytosolic proteins.<sup>[1–11]</sup> HDAC8 is a validated target for several types of cancer including T-cell lymphoma and childhood neuroblastoma.<sup>[12–18]</sup> In the effort to discover new potent and selective non-hydroxamate inhibitors of HDAC8, we identified PD-404,182 in a medium-scaled compound screening campaign.<sup>[19]</sup> Further studies on the mode of protein-inhibitor interaction revealed that PD-404,182 is a covalent modifier of HDAC8, forms mixed disulfides and transforms thiol groups into thiocyanates.<sup>[20]</sup> In a further study we found that HDAC8 is


regulated by a redox switch involving cysteines Cys<sub>102</sub> and Cys<sub>153</sub>.<sup>[21]</sup> H<sub>2</sub>O<sub>2</sub> was shown to oxidize the protein resulting in a disulfide bridge between these cysteines and concomitant reversible loss of enzyme activity.


Considering protein–inhibitor interactions, there are only very few examples of drug-like small molecules that are able to induce disulfide bond formation. Mathieu et al. showed that thiram, a neurotoxic disulfide-containing dithiocarbamate compound inhibits brain glycogen phosphorylase through the formation of an intramolecular disulfide bond between Cys<sub>318</sub> and Cys<sub>326</sub>, known to be a redox-switch that prevents the allosteric activation of the enzyme by AMP.<sup>[22,23]</sup> The proposed mechanism consists of the reaction of thiram with a cysteine thiol leading to a mixed disulfide followed by the formation of an intramolecular disulfide bond with a vicinal cysteine residue. Another example describes the inactivation of an arginine phosphatase by a seleno-compound that induces an intramolecular disulfide bond between two adjacent active site cysteines via an unclear mechanism.<sup>[24]</sup> Moreover, Yang et al. reported an example for the bile salt-induced isomerization from intramolecular to an intermolecular disulfide bridge between two subunits of a transmembrane transcription factor, which directly activates the virulence cascade of *Vibrio cholerae* by a host signal molecule.<sup>[25]</sup>

In this study, we show that PD-404,182 alters the activity of HDAC8 through the formation of an intramolecular disulfide bond between Cys<sub>102</sub> and Cys<sub>153</sub>. Thus, PD-404,182 acts as a molecular trigger that operates this redox switch resulting in the inactive oxidized form of HDAC8. Moreover, PD-404,182, unlike oxidation by H<sub>2</sub>O<sub>2</sub>, induces additional disulfide bridges in HDAC8. The formation of a distinct disulfide bond between Cys<sub>275</sub> and Cys<sub>352</sub> also has strong impact on HDAC8 activity,

[a] N. Jänsch, W. O. Sugiarto, M. Muth, A. Koprancovic, C. Desczyk, M. Ballweg, Prof. Dr. F.-J. Meyer-Almes  
Department of Chemical Engineering and Biotechnology  
University of Applied Sciences Darmstadt, Stephanstraße 7  
64295 Darmstadt (Germany)  
E-mail: franz-josef.meyer-almes@h-da.de

[b] M. Muth, F. Kirschhöfer, Dr. G. Brenner-Weiss  
Institute of Functional Interfaces (IFG)  
Karlsruhe Institute of Technology (KIT), Hermann-von-Helmholtz Platz-1  
76334 Eggenstein-Leopoldshafen (Germany)

 Supporting information and the ORCID identification number(s) for the author(s) of this article can be found under:  
<https://doi.org/10.1002/chem.202001712>.

 © 2020 The Authors. Published by Wiley-VCH GmbH. This is an open access article under the terms of Creative Commons Attribution NonCommercial License, which permits use, distribution and reproduction in any medium, provided the original work is properly cited and is not used for commercial purposes.



thus acting as allosteric regulative residues besides the already known Cys<sub>102</sub>/Cys<sub>153</sub> redox switch at the active site. These results provide strong evidence for a complex and until now unknown redox-based regulation mechanism of HDAC8 involving more than one disulfide bridge.

## Results and Discussion

In a previous study, we identified PD-404,182 as a potent and selective HDAC8 inhibitor.<sup>[19]</sup> By using time resolved HPLC-MS/MS, we also explained the exact mechanism of PD-404,182 decomposition in aqueous solution and subsequent mixed disulfide formation of various cysteines in HDAC8.<sup>[20]</sup> PD-404,182 decomposes quickly into the corresponding sulfenamide, which forms mixed disulfides with cysteine residues for example, in HDAC8. Another adjacent cysteine can react with this intermediate by forming an intramolecular disulfide bridge between the involved cysteine side chains (Figure 1). In the light of our previous study about the redox regulation of HDAC8<sup>[21]</sup> we questioned whether PD-404,182 is able to induce a disulfide bridge between Cys<sub>102</sub> and Cys<sub>153</sub> of HDAC8 through its mixed disulfide and thus acts as a molecular trigger of the corresponding redox switch that regulates the enzyme activity of HDAC8.

### Structural and sequence alignments

HDAC8 contains ten cysteines, eight of them are in proximity to each other and therefore able to form disulfides in general (Figure 2). To clarify if these eight cysteines are conserved through the other HDAC isoenzymes we made a structural alignment of HDACs 1–8 (Figure 3). Additionally, we made sequence alignments including HDAC8 homologues from different species (Figure S1). As discussed in the context of redox regulation of HDAC8,<sup>[21]</sup> Cys<sub>102</sub> is conserved in all class I HDACs and Cys<sub>153</sub> is conserved throughout all other HDACs. Also, both cysteines are conserved in all HDAC8 homologues from different species. This implies a fundamental role for Cys<sub>102</sub> and Cys<sub>153</sub> for HDAC and particularly HDAC8 function.

Taking a glance at the crystal structure of HDAC8 (PDB-ID: 1T69) reveals three additional pairs of cysteines (Cys<sub>125</sub>/Cys<sub>131</sub>, Cys<sub>275</sub>/Cys<sub>352</sub> and Cys<sub>244</sub>/Cys<sub>287</sub>) in proximity (3.6–11.9 Å between the corresponding sulfur atoms) potentially enabling the formation of further disulfide bonds.

Cys<sub>125</sub> and Cys<sub>131</sub> are unique for HDAC8 and not present in other human isoenzymes. Interestingly, these cysteines are conserved in ortholog HDAC8 sequences from other species with a slightly difference for HDAC8 from *Schistosoma mansoni*

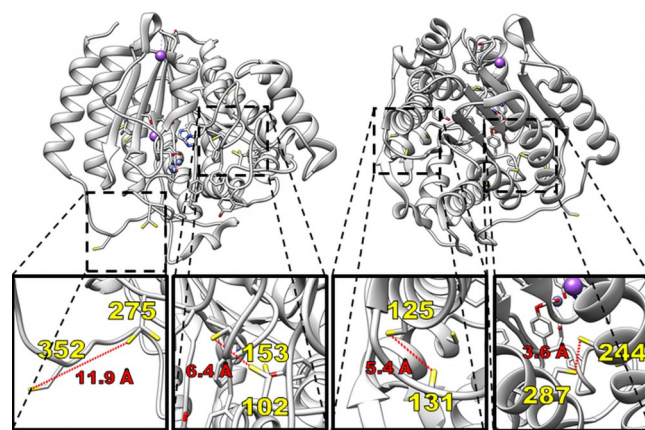


Figure 2. Structural overview of the investigated Cysteine pairs in HDAC8 (PDB-ID: 1T64).

(smHDAC8). The possible disulfide bond between Cys<sub>275</sub> and Cys<sub>352</sub> is interesting because Cys<sub>275</sub> is only conserved in HDACs from class I and Cys<sub>352</sub> is unique to HDAC8. Both cysteines are conserved in HDAC8 homologues except for smHDAC8. The same observation could be made for the last putative disulfide bond. Cys<sub>287</sub> is conserved in class I HDACs and Cys<sub>244</sub> is unique to HDAC8. Both are conserved in HDAC8 homologues and not present in smHDAC8. To rationalize the reactivity of each disulfide pair, we calculated the pK<sub>a</sub> value and the solvent accessible surface area (SASA) of each mentioned cysteine in HDAC8 (Figure S7). A plot of pK<sub>a</sub> values against the logarithmic SASA reveals that Cys<sub>153</sub> has the lowest pK<sub>a</sub> value. Therefore, the disulfide bond between Cys<sub>102</sub> and Cys<sub>153</sub> should be the most reactive one. Cys<sub>275</sub> and Cys<sub>352</sub> are the most accessible cysteines in HDAC8. We conclude that the reactivity of this disulfide bond is mainly driven by accessibility. Cys<sub>125</sub> and Cys<sub>131</sub> range between the two other disulfide bonds in terms of both, reactivity and accessibility. Cys<sub>244</sub> and Cys<sub>287</sub> are the most buried ones with the highest pK<sub>a</sub> value and thus lowest theoretical reactivity. With these characteristic values it seems remarkable that these cysteines can undergo disulfide formation. Nevertheless, there exists a crystal structure where precisely these cysteines are interconnected by a disulfide bridge (PDB: 1VKG). The alignments and the reactivity/accessibility calculations suggest that HDAC8 consists of a unique pattern of cysteines not found in other HDACs and therefore provides an excellent basis for utilizing redox based regulation mechanisms to achieve isoenzyme selectivity through targeted cysteine oxidation or alkylation.

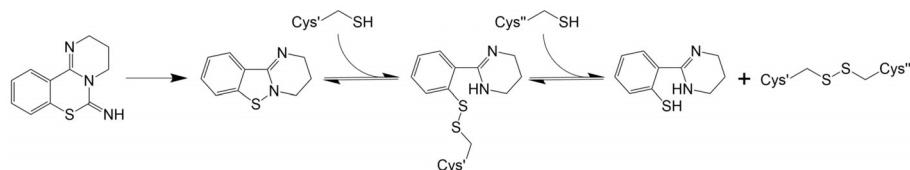
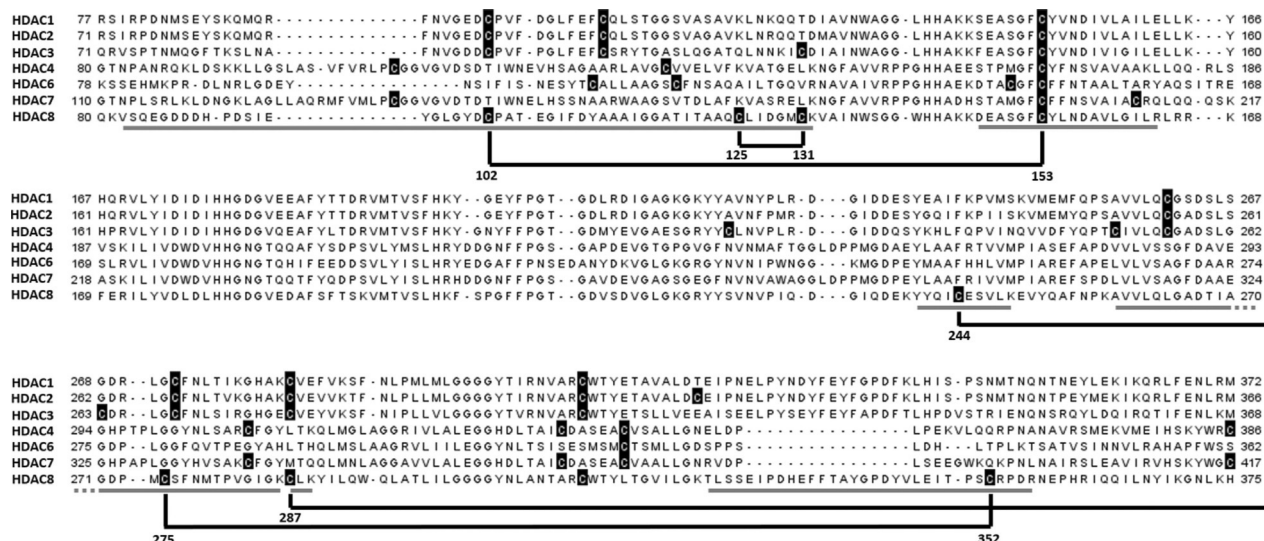


Figure 1. Mechanism of PD-404,182 induced disulfide formation.



**Figure 3.** Structural alignment of HDAC1, 2, 3, 4, 6, 7 and 8. Cysteines are marked in black and disulfides in HDAC8 relate to black lines. Theoretical peptide fragments are indicated with grey bars beneath the alignment. Numbers on the left and right edge indicates the amino acid numbers corresponding to following PDB IDs: HDAC1 (4BKX), HDAC2 (5IWG), HDAC3 (4A69), HDAC4 (2VQJ), HDAC6 (5W5K), HDAC7 (3C0Z), HDAC8 (1T69).

### Electrophoretic mobility shift assays (EMSA)

In our previous study, the  $H_2O_2$  dependent formation of a single disulfide bond between Cys<sub>102</sub> and Cys<sub>153</sub> was demonstrated by using a non-reductive electrophoretic mobility shift assay (EMSA).<sup>[21]</sup> The difference in the mobility shift of the protein on a non-reductive SDS-PAGE depends predominantly on the amino acid distance between the two covalently bound cysteines. Thus, it should be possible to clarify if PD-404,182 is inducing one or more disulfide bonds.

At first, the EMSA was performed with the HDAC8<sub>wt</sub> enzyme (Figure 4A). HDAC8 was incubated with different concentrations of PD-404,182. Afterwards, an aliquot of the reaction mixture was removed and conducted to an enzyme activity assay. The rest of the reaction mixture was precipitated with trichloroacetic acid (TCA), the supernatant was removed, and the protein precipitate was resuspended in non-reducing sample buffer with the addition of 50 mM NEM. The alkylation of the protein is necessary to prevent nascent thiols from artificial oxidation with oxygen whilst the following non-reductive SDS-PAGE. The concentration dependent inhibition of the wild type enzyme shows a dependence between loss in enzyme activity (left bar) and disulfide bond formation (right bar) (Figure 4A). The first band shift is identified as the disulfide bond between Cys<sub>102</sub> and Cys<sub>153</sub> according to our previous study on the redox switch of HDAC8.<sup>[21]</sup> Therefore, PD-404,182 is mainly regulating the enzyme activity of HDAC8 by triggering its redox switch. Interestingly, more disulfides occur at higher concentrations of PD-404,182. The appearance of additional bands in the EMSA experiment enabled the identification of three distinct oxidative species of HDAC8 shifted to apparent lower molecular weights on the gel (Figure 4A). As mentioned before, the amino acid distance is the key feature that determines divergent migration behavior in an EMSA gel. The two additional oxidative species are supposed to be disulfide bonds between

Cys<sub>275</sub>/Cys<sub>244</sub> and Cys<sub>275</sub>/Cys<sub>352</sub>. The distance between Cys<sub>125</sub> and Cys<sub>131</sub> seems too small to expect a visible difference in an EMSA gel without the utilization of special polymer-based alkylation agents like poly (ethylene glycol)-maleimides as electrophiles.

To confirm the hypothesis that the first disulfide bond formed upon the addition of PD-404,182 is between Cys<sub>102</sub> and Cys<sub>153</sub> further EMSA experiments were carried out with the double mutant enzyme HDAC8<sub>C102S/C153S</sub>. In contrast to our expectations, the double mutant enzyme is not fully resistant to PD-404,182. Surprisingly, the enzyme activity drops to about 50% compared with the control (Figure 4B). This behavior led us to the assumption that HDAC8 contains at least one allosteric regulating disulfide bond beyond the redox switch between Cys<sub>102</sub> and Cys<sub>153</sub>. To dissect this unexpected behavior, three constructs were generated on the basis of the HDAC8<sub>C102S/C153S</sub> vector, where in each case one additional pair of cysteines is changed to serine, namely HDAC8<sub>C102S/C153S/C125S/C131S</sub>, HDAC8<sub>C102S/C153S/C244S/C287S</sub> and HDAC8<sub>C102S/C153S/C275S/C352S</sub>. Interestingly, the yield of recombinant protein varies dramatically between the mutant variants. The EMSA experiments with these multiple mutant variants of HDAC8 clearly shows that the HDAC8<sub>C102S/C153S/C275S/C352S</sub> variant retains nearly full enzyme activity in the presence of even the highest used concentrations of PD-404,182 (Figure 4C). Therefore, we conclude that the formation of a disulfide bond between Cys<sub>275</sub> and Cys<sub>352</sub> is regulating the enzyme activity in an allosteric manner. The EMSA results for the HDAC8<sub>C102S/C153S/C125S/C131S</sub> and HDAC8<sub>C102S/C153S/C244S/C287S</sub> mutant variants are shown in Figure S8.

The enzyme activity of both mutant variants drops below 50% residual activity at the highest concentrations of PD-404,182. This underlines the assumption that the disulfide bond between Cys<sub>275</sub> and Cys<sub>352</sub> is regulating the enzyme activity because this disulfide bond is still present in these mutants.

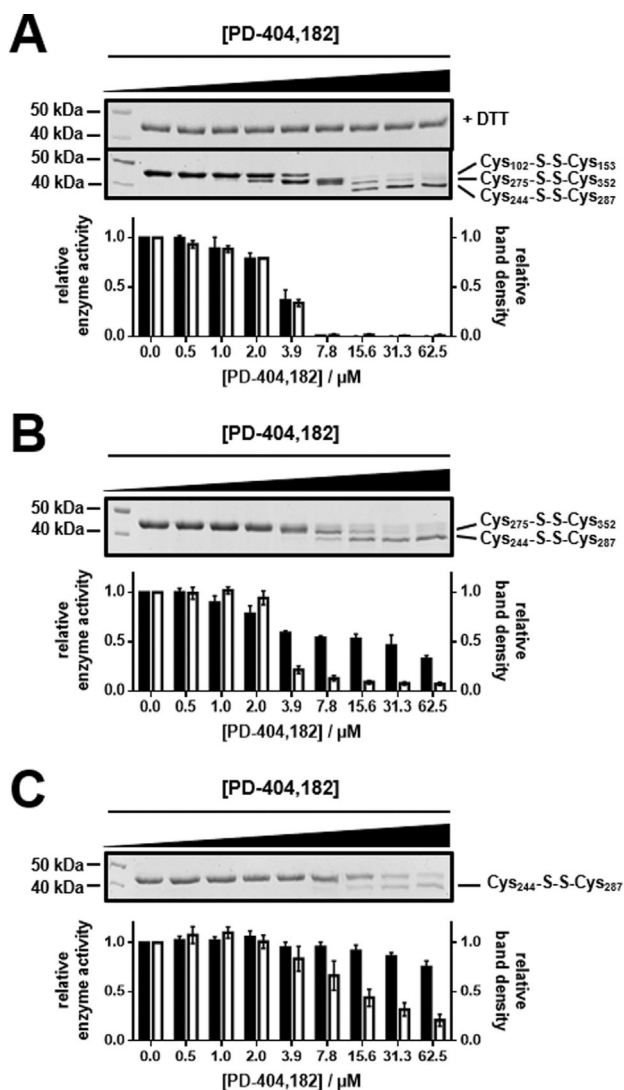


**Figure 4.** Electrophoretic mobility shift assay (EMSA) showing disulfide bond induced loss of enzyme activity. A) EMSA for the HDAC8<sub>wt</sub>, B) HDAC8<sub>C102S/C153S</sub>, C) HDAC8<sub>C102S/C153S/C275S/C352S</sub> enzyme.

Moreover, we were able to show that the disulfide bond between Cys<sub>125</sub> and Cys<sub>131</sub> is not observable in the EMSA, because the HDAC8<sub>C102S/C153S/C125S/C131S</sub> mutant variant behaves similarly to the HDAC8<sub>C102S/C153S</sub> variant and shows two distinct shifts on the EMSA gel, which correspond to the disulfide bonds between Cys<sub>244</sub>/Cys<sub>287</sub> and Cys<sub>275</sub>/Cys<sub>352</sub>.

To test for reversibility of disulfide bond formation and verify that the observed mobility shift on the EMSA gel occurs exclusively throughout disulfide formation, the EMSA was performed with the wild type enzyme and PD-404,182 with subsequent addition of 50 mM β-ME. No band shifts can be observed implying that all changes on EMSA must be due to disulfide formation. In addition, it was shown in our previous study that inhibition of HDAC8 enzyme activity through PD-404,182 is reversible after the addition of TCEP and β-ME.<sup>[20]</sup>

## HPLC-MS/MS confirmation of induced disulfide bridges

To confirm the formation of the proposed regulating disulfide bonds, we performed high-resolution HPLC-MS/MS experiments. Therefore, we primarily induced the disulfide bonds in HDAC8<sub>wt</sub> by the reaction with PD-404,182 under comparable conditions and the same inhibitor/enzyme ratio (25-fold excess of inhibitor) corresponding to the highest concentration in the EMSA (Figure 4). A solvent control without inhibitor was carried out simultaneously to ensure that the generated disulfides are specific for the treatment. After treatment the reaction was immediately stopped by TCA precipitation and guanidine denaturation of HDAC8<sub>wt</sub> followed by iodoacetamide alkylation. Subsequently, samples were cleaved into peptides using trypsin under non-reductive conditions to obtain treatment dependent disulfide bonds. Possible disulfide shuffling during the digestion process was prevented by mild buffer conditions, 10 mM ammonium bicarbonate pH 8.0, and relatively short digestion times of three hours. To ensure the accuracy of the acquired results, two independent replicates were made for the treated and control samples (Figure S2). The chromatographic separation of the digested samples already revealed distinct differences in their composition between treated and non-treated samples (Figure 5A). Beside the decreasing total ion

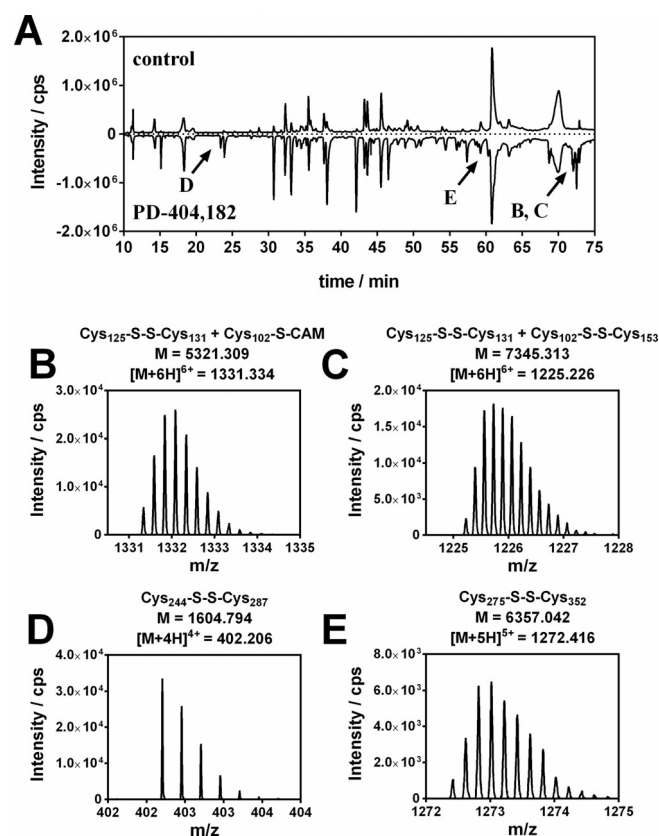


**Figure 5.** HPLC-MS/MS analysis of disulfide linked tryptic HDAC8 fragments. A) HPLC chromatogram of the untreated and PD-404,182 treated HDAC8 samples. B) Mass spectra for the Cys<sub>125</sub>-S-S-Cys<sub>131</sub>-S-CAM, C) Cys<sub>125</sub>-S-S-Cys<sub>131</sub>+Cys<sub>102</sub>-S-S-Cys<sub>153</sub>, D) Cys<sub>244</sub>-S-S-Cys<sub>287</sub>, E) Cys<sub>275</sub>-S-S-Cys<sub>352</sub> peptide fragment.

current (TIC) of peptide fragments with alkylated cysteines and increasing intensity of cyanlated cysteine fragments (not shown,<sup>[20]</sup> for reference), the appearance of four distinct peaks in the treated sample is most noticeable as highlighted in Figure 5A. These new arising signals (5C, 5D and 5E) are not present in the control samples or clearly enriched in the treated samples (5B). For those signals the assigned masses match the theoretical masses of the four proposed disulfide linked peptides with an error below 2 ppm (Figure 5B-E, Table S1). The observed masses and isotopic distributions fit perfectly to the expected masses of the disulfide linked tryptic peptides Cys<sub>125</sub>-Cys<sub>131</sub>, Cys<sub>125</sub>-Cys<sub>132</sub> + Cys<sub>102</sub>-Cys<sub>153</sub>, Cys<sub>244</sub>-Cys<sub>287</sub> and Cys<sub>275</sub>-Cys<sub>352</sub>. To confirm the identity of these interlinked peptides, we acquired high resolution fragmentation spectra (Figures S3–S6). Because of the quadrupole ion selection prior to collision induced fragmentation only one peptide ion is observed and fragmented at a time. Therefore, several situations should be observable: 1) intermolecular linked tryptic peptides should generate N- and C-terminal fragmentation patterns specific for these two peptides, 2) disulfide linked fragment ions should occur due to favored fragmentation of the more fragile peptide bonds or 3) intramolecular linked fragments can be identified by the absence of carbamidomethyl (CAM) groups and a distinct mass difference of two protons as a result of the connected thiols. Also, the large size of such linked peptides, especially Cys<sub>125</sub>-Cys<sub>132</sub> + Cys<sub>102</sub>-Cys<sub>153</sub>, can lead to internal fragmentations. In this work, we were able to clearly identify all four proposed disulfide bonds in HDAC8<sub>wt</sub> induced by PD-404,182 on the basis of all the above-mentioned states (Figures S3–S6, Tables S2–5). The intramolecular and in proximity located disulfide bond between Cys<sub>125</sub>-Cys<sub>131</sub> could be observed in several fragment ions, where the thiols show the absent hydrogens and CAM group. However, Cys<sub>102</sub> was modified by a CAM group in the same precursor ion. This was the only disulfide linked species, which was also observed in the untreated control sample (Figure S3 and S4, Tables S2 and S3). Considering that this disulfide bond is not observable in the EMSA, we hypothesize that this disulfide bond is easily build even in the absence of oxidizing agents. The other three disulfide linked peptides were exclusively observed in the treated samples. The precursor of Cys<sub>102</sub>-Cys<sub>153</sub> shows a similar fragment pattern of the Cys<sub>125</sub>-Cys<sub>131</sub> peptide in addition to the N- and C-terminal (b- and y-ion) fragments of the peptide, where Cys<sub>153</sub> is located. Only few Cys<sub>102</sub>-Cys<sub>153</sub> linked fragments were identified, likely because of the large size of those peptides. Both, the N- and C-terminal fragmentations as well as several disulfide-linked fragment ions were identified in the Cys<sub>244</sub>-Cys<sub>287</sub> and Cys<sub>275</sub>-Cys<sub>352</sub> fragmentation spectra providing clear evidence for their existence. Overall, these data confirm the presence of all four disulfide linked peptides, especially Cys<sub>102</sub>-Cys<sub>153</sub>, Cys<sub>244</sub>-Cys<sub>287</sub> and Cys<sub>275</sub>-Cys<sub>352</sub>, after treatment with a 25-fold excess of PD404,182.

### Thermal shift assay provides insight into disulfide induced enzyme stabilization

As proven by EMSA and HPLC-MS/MS, the interaction between HDAC8 and PD-404,182 leads to several oxidized enzyme species. In general, it would be expected that the formation of disulfide bonds leads to protein stabilization. To elucidate the effect on increasing concentrations of PD-404,182 on the overall stability of HDAC8, thermal shift assays were performed using SYPRO orange dye on a real time PCR thermo cycler (Figure 6). To allow for a meaningful comparison, the concentrations of HDAC8 and PD-404,182 were the same as in the previous EMSA experiment (Figure 4). Considering that the fluorescence of SYPRO orange increases upon binding to exposed hydrophobic domains of the protein, the fluorescence signal can not only be used to detect thermal unfolding, but also changes in hydrophobic surface area due to conformational changes. Interestingly, at low concentrations of PD-404,182, ranging from 1  $\mu\text{M}$  to 7.8  $\mu\text{M}$  the melting temperature increases from 47  $^{\circ}\text{C}$  to about 51  $^{\circ}\text{C}$ . This correlates with the first mobility shift on the EMSA, which is supposed to be the

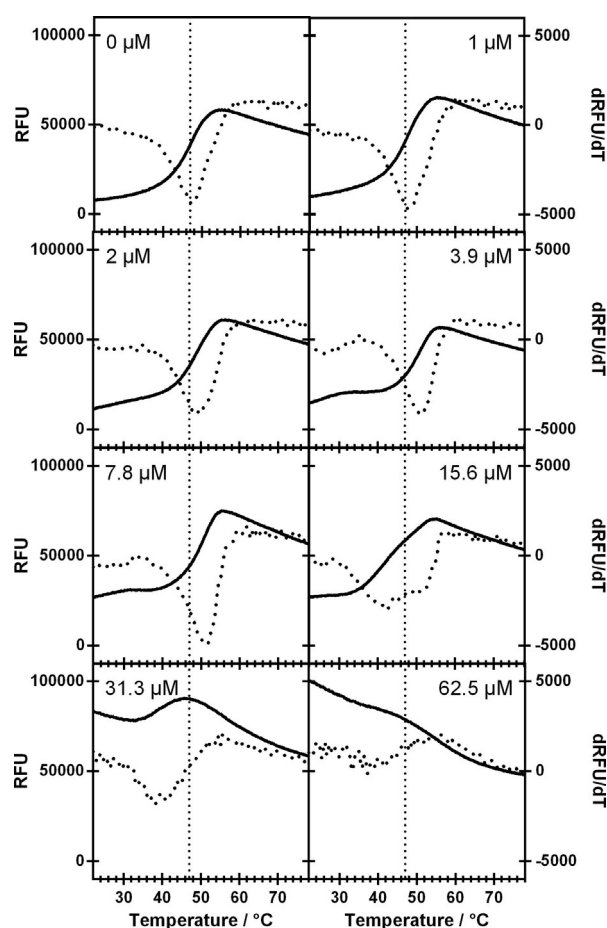


**Figure 6.** Thermal shift assay of HDAC8 incubated with various concentrations of PD-404,182. The black lines show the increase of SYPRO orange fluorescence upon thermal unfolding of HDAC8. The dotted lines represent the first derivatives of thermograms. Vertical dotted lines correspond to the melting point of the untreated control sample.

disulfide bond between Cys<sub>102</sub> and Cys<sub>153</sub>, as well as the allosteric disulfide bond between Cys<sub>275</sub> and Cys<sub>352</sub> (Figure 4). The oxidation of these residues results in a thermodynamically stabilized and therefore favored conformation of the enzyme. At 15.6  $\mu\text{M}$  of PD-404,182 a second inflection point is observed. The melting point of the stabilized protein disappears, and a second melting point occurs at about 40 °C. In the presence of the two highest concentration of PD-404,182 the melting point at elevated temperature disappears completely and only one transition at lower temperature (40 °C) remains visible. We conclude that very high concentrations of PD-404,182 inducing the formation of two additional disulfide bridges destabilize HDAC8 compared to its reduced form. The destabilization of the enzyme in the presence of the highest inhibitor concentrations correlates with a considerably elevated onset in the thermogram, which is indicative for a dramatic change in the hydrophobic surface area and tertiary structure of the peroxidized HDAC8 protein.

## Conclusions

This study provides detailed insight into how PD-404,182 acts as a molecular trigger of intermolecular disulfide bond formation within HDAC8. We identified the disulfide bond between Cys<sub>102</sub> and Cys<sub>153</sub> as a main regulatory switch for enzyme activity after treatment with PD-404,182. Additionally, we were able to identify an allosteric regulating disulfide bond between Cys<sub>275</sub> and Cys<sub>352</sub>, which inhibits HDAC8 activity to about 50% residual enzyme activity. A mutant HDAC8 variant, where those four cysteines are mutated to serine retains enzyme activity at the same concentration of PD-404,182. At higher concentrations of PD-404,182 all proposed four disulfides are formed. The findings were confirmed by tryptic digestion and mass analytics. Additionally, we verified that the oxidation of the disulfide bonds between Cys<sub>102</sub>/Cys<sub>153</sub> and Cys<sub>275</sub>/Cys<sub>352</sub> results in a thermodynamically stabilized protein and further oxidation results in a dramatic destabilization of the enzyme. The impact of oxidation on the overall HDAC8 structure is still unclear and needs further research.

Based on the knowledge gained in this study and the unique pattern of regulative disulfide bonds in HDAC8, we propose to develop covalent isoenzyme selective inhibitors that target the identified pairs of cysteines. Corresponding work is ongoing in our laboratory.

## Experimental Section

### Electrophoretic mobility shift assay (EMSA)

For the determination of ligand induced disulfide bond formation 2.5  $\mu\text{M}$  wild type and mutant HDAC8 was treated with the indicated concentrations of PD-404,182 for 1 h at 30 °C in assay buffer (pH 8.0, 25 mM Tris, 75 mM KCl, 0.001% Pluronic F-68) in 50  $\mu\text{L}$  reaction volume. Afterwards 10  $\mu\text{L}$  were removed and diluted 1:100 in assay buffer and stored on ice until the activity assay was performed as described later. The remaining reaction mixture was treated with 10% TCA and protein precipitation was performed at –20 °C for 20 min with subsequent centrifugation at 18000 g for

10 min at 4 °C. Afterwards, the supernatant was removed and precipitate was dissolved in 30  $\mu\text{L}$  alkylation buffer (pH 7.0) containing 150 mM NaCl, 20 mM NaH<sub>2</sub>PO<sub>4</sub>, 20 mM Na<sub>2</sub>HPO<sub>4</sub>, 5 mM EDTA, 50 mM NEM and 10  $\mu\text{L}$  non-reducing Laemmli sample buffer (4x, pH 6.8) containing 250 mM Tris, 8% SDS, 40% glycerol, 0.02% bromophenol blue for 30 min at 30 °C with subsequent heat denaturation at 95 °C for 5 min. For the determination of the reversibility against reducing agents the precipitate was dissolved in alkylation buffer without NEM and 10  $\mu\text{L}$  4x Laemmli sample buffer with the addition of 200 mM DTT and conducted as listed above. Finally, 15  $\mu\text{L}$  of the sample was subjected to SDS-PAGE and gels were stained with Coomassie brilliant blue solution.

### Enzyme activity assay

For the determination of disulfide bond induced changes in enzyme activity 20 nM of the prior treated HDAC8 dilution was mixed with 20  $\mu\text{M}$  Boc-Lys(trifluoroacetyl)-AMC as substrate in a black 96-well microtiter plate (Greiner) in assay buffer for 15 min at 30 °C. For the HDAC8<sub>C102S/C153S</sub> mutant the substrate reaction was conducted for 1 h. After substrate conversion the reaction was stopped by the addition of 1.7  $\mu\text{M}$  SATFMK and fluorescent AMC was released by the addition 0.4 mg mL<sup>-1</sup> trypsin. Relative fluorescent units were measured in a microplate reader at 450 nm ( $\lambda_{\text{ex}} = 350 \text{ nm}$ ) and normalized to the untreated control.

### Sample preparation for mass spectrometry

HDAC8<sub>wt</sub> in storage buffer containing (pH 8.0, 150 mM KCl, 50 mM Tris, 25% glycerol, 1 mM TCEP) was buffer exchanged to 10 mM NH<sub>4</sub>HCO<sub>3</sub> pH 8.0 with mini GPC column (self-packed Bio Gel-P6, Biorad) at 1020 g for 4 min. Buffer exchanged samples containing 25.5  $\mu\text{M}$  HDAC8 were treated with no inhibitor and 25-fold excess (637  $\mu\text{M}$ ) PD-404,182 (TOCRIS) for 1 h at 30 °C followed by protein precipitation with 10% TCA (see EMSA section). Precipitated protein was resuspended in 10 mM NH<sub>4</sub>HCO<sub>3</sub> containing 5 M guanidine and 10 mM iodoacetamide (Merck). Alkylation was performed at 22 °C for 20 min under exclusion of light followed by desalting with mini GPC columns. Samples were tryptic digested with 5  $\mu\text{g}$  (50 ng  $\mu\text{L}^{-1}$ ) in 10 mM NH<sub>4</sub>HCO<sub>3</sub> activated trypsin sequencing grade (Promega) for 3 h at 37 °C and 550 rpm. Reaction was stopped by addition of 1% FA (VWR) and prior to injection centrifugated at 18000 g for 10 min. 10  $\mu\text{L}$  Supernatant was used for HPLC-MS injection.

## Acknowledgements

This work was supported by a fellowship of the Platform for PhD students of the Technical University of Darmstadt. The excellent technical support of Michael Schröder is gratefully acknowledged. Open access funding enabled and organized by Projekt DEAL.

## Conflict of interest

The authors declare no conflict of interest.

**Keywords:** cysteine • HDAC8 • covalent inhibitors • redox switch • sulfenamides

- [1] N. Alam, L. Zimmerman, N. A. Wolfson, C. G. Joseph, C. A. Fierke, O. Schueler-Furman, *Structure* **2016**, *24*, 458–468.
- [2] F. Beckouët, B. Hu, M. B. Roig, T. Sutani, M. Komata, P. Uluocak, V. L. Katis, K. Shirahige, K. Nasmyth, *Mol. cell* **2010**, *39*, 689–699.
- [3] M. A. Deardorff, M. Bando, R. Nakato, E. Watrin, T. Itoh, M. Minamino, K. Saitoh, M. Komata, Y. Katou, D. Clark, K. E. Cole, E. de Baere, C. Decroos, N. Di Donato, S. Ernst, L. J. Francey, Y. Gyftodimou, K. Hirashima, M. Hullings, Y. Ishikawa, C. Jaulin, M. Kaur, T. Kiyono, P. M. Lombardi, L. Magnaghi-Jaulin, G. R. Mortier, N. Nozaki, M. B. Petersen, H. Seimiya, V. M. Siu, Y. Suzuki, K. Takagaki, J. J. Wilde, P. J. Willems, C. Prigent, G. Gillissen-Kaesbach, D. W. Christianson, F. J. Kaiser, L. G. Jackson, T. Hirota, I. D. Krantz, K. Shirahige, *Nature* **2012**, *489*, 313–317.
- [4] K. L. Durst, B. Lutterbach, T. Kummalu, A. D. Friedman, S. W. Hiebert, *Mol. Cell. Biol.* **2003**, *23*, 607–619.
- [5] J. Gao, B. Siddoway, Q. Huang, H. Xia, *Biochem. Biophys. Res. Commun.* **2009**, *379*, 1–5.
- [6] D. E. Olson, N. D. Udeshi, N. A. Wolfson, C. A. Pitcairn, E. D. Sullivan, J. D. Jaffe, T. Svinkina, T. Natoli, X. Lu, J. Paulk, P. McCarren, F. F. Wagner, D. Barker, E. Howe, F. Lazzaro, J. P. Gale, Y.-L. Zhang, A. Subramanian, C. A. Fierke, S. A. Carr, E. B. Holson, *ACS Chem. Biol.* **2014**, *9*, 2210–2216.
- [7] Y. Qian, J. Zhang, Y.-S. Jung, X. Chen, *PLoS One* **2014**, *9*, e84015.
- [8] C. Schölz, B. T. Weinert, S. A. Wagner, P. Beli, Y. Miyake, J. Qi, L. J. Jensen, W. Streicher, A. R. McCarthy, N. J. Westwood, S. Lain, J. Cox, P. Matthias, M. Mann, J. E. Bradner, C. Choudhary, *Nat. Biotechnol.* **2015**, *33*, 415–423.
- [9] T. B. Toro, T. J. Watt, *Protein Sci.* **2015**, *24*, 2020–2032.
- [10] B. J. Wilson, A. M. Tremblay, G. Deblois, G. Sylvain-Drolet, V. Giguère, *Mol. Endocrinol.* **2010**, *24*, 1349–1358.
- [11] N. A. Wolfson, C. A. Pitcairn, C. A. Fierke, *Biopolymers* **2013**, *99*, 112–126.
- [12] I. Rettig, E. Koeneke, F. Trippel, W. C. Mueller, J. Burhenne, A. Kopp-Schneider, J. Fabian, A. Schober, U. Fernekorn, A. von Deimling, H. E. Deubzer, T. Milde, O. Witt, I. Oehme, *Cell Death Dis.* **2015**, *6*, e1657.
- [13] S. Y. Park, J. A. Jun, K. J. Jeong, H. J. Heo, J. S. Sohn, H. Y. Lee, C. G. Park, J. Kang, *Oncol. Rep.* **2011**, *25*, 1677–1681.
- [14] I. Oehme, H. E. Deubzer, D. Wegener, D. Pickert, J.-P. Linke, B. Hero, A. Kopp-Schneider, F. Westermann, S. M. Ulrich, A. von Deimling, M. Fischer, O. Witt, *Clin. Cancer Res.* **2009**, *15*, 91–99.
- [15] G. Niegisch, J. Knievel, A. Koch, C. Hader, U. Fischer, P. Albers, W. A. Schulz, *Urol. Oncol.* **2013**, *31*, 1770–1779.
- [16] G. Lopez, K. L. J. Bill, H. K. Bid, D. Braggio, D. Constantino, B. Prudner, A. Zewdu, K. Batte, D. Lev, R. E. Pollock, *PLoS One* **2015**, *10*, e0133302.
- [17] A. Chakrabarti, J. Melesina, F. R. Kolbinger, I. Oehme, J. Senger, O. Witt, W. Sippl, M. Jung, *Future Med. Chem.* **2016**, *8*, 1609–1634.
- [18] S. Balasubramanian, J. Ramos, W. Luo, M. Sirisawad, E. Verner, J. J. Buggy, *Leukemia* **2008**, *22*, 1026–1034.
- [19] A. Kleinschek, C. Meyners, E. Digiorgio, C. Brancolini, F.-J. Meyer-Almes, *ChemMedChem* **2016**, *11*, 2598–2606.
- [20] M. Muth, N. Jänsch, A. Koprancovic, A. Krämer, N. Wössner, M. Jung, F. Kirschhöfer, G. Brenner-Weiss, F.-J. Meyer-Almes, *General Subj.* **2019**, *1863*, 577–585.
- [21] N. Jänsch, C. Meyners, M. Muth, A. Koprancovic, O. Witt, I. Oehme, F.-J. Meyer-Almes, *Redox Rep.* **2019**, *20*, 60–67.
- [22] C. Mathieu, R. Duval, A. Cocaign, E. Petit, L.-C. Bui, I. Haddad, J. Vinh, C. Etchebest, J.-M. Dupret, F. Rodrigues-Lima, *J. Biol. Chem.* **2016**, *291*, 23842–23853.
- [23] C. Mathieu, L.-C. Bui, E. Petit, I. Haddad, O. Agbulut, J. Vinh, J.-M. Dupret, F. Rodrigues-Lima, *J. Biol. Chem.* **2017**, *292*, 1603–1612.
- [24] J. Fuhrmann, V. Subramanian, P. R. Thompson, *ACS Chem. Biol.* **2013**, *8*, 2024–2032.
- [25] M. Yang, Z. Liu, C. Hughes, A. M. Stern, H. Wang, Z. Zhong, B. Kan, W. Fenical, J. Zhu, *Proc. Natl. Acad. Sci. USA* **2013**, *110*, 2348–2353.

---

Manuscript received: April 8, 2020

Revised manuscript received: May 11, 2020

Accepted manuscript online: May 19, 2020

Version of record online: September 11, 2020

---

**Titel:**

Assessment of tractable cysteines by covalent fragments screening

**Autoren:**

László Petri, Péter Ábrányi-Balogh, Tímea Imre, Gyula Pálffy, András Perczel, Damijan Knez, Martina Hrast, Martina Gobec, Izidor Sosič, Kinga Nyíri, Beáta G. Vértessy, Niklas Jänsch, Charlotte Desczyk, Franz-Josef Meyer-Almes, Iza Ogris, Simona Golič Grdadolnik, Luca Giacinto Iacovino, Claudia Binda, Stanislav Gobec and György M. Keserű

**Bibliographische Daten:**

ChemBioChem (doi.org/10.1002/cbic.202000700)

**Zusammenfassung:**

Gezielte kovalente Hemmung und die Verwendung irreversibler chemischer Sonden sind wichtige Strategien in der chemischen Biologie und der Arzneimittelentdeckung. Bisher wurde die Verfügbarkeit und Reaktivität von Cysteinresten, die sich für ein kovalentes Targeting eignen, mit Hilfe von Proteomik- und Computertools bewertet. Hier stellen wir eine Toolbox von Fragmenten vor, die einen 3,5-Bis(trifluormethyl)phenyl-Kern enthalten, der mit chemisch vielfältigen elektrophilen funktionellen Gruppen ausgestattet wurde, die eine Reihe von Reaktivitäten aufweisen. Wir charakterisierten die Mitglieder der Bibliothek hinsichtlich ihrer Reaktivität, ihrer Stabilität in Wasser und ihrer Spezifität für nukleophile Aminosäuren. Durch Screening dieser Bibliothek gegen eine Reihe von Enzymen, die sich für eine kovalente Hemmung eignen, konnten wir zeigen, dass dieser Ansatz die Zugänglichkeit und Reaktivität der Ziel-Cysteine experimentell charakterisiert. Für alle untersuchten cysteinhaltigen Enzyme wurden interessante kovalente Fragmente identifiziert.



## Accepted Article

**Title:** Assessment of tractable cysteines by covalent fragments screening

**Authors:** László Petri, Péter Ábrányi-Balogh, Tímea Imre, Gyula Pálffy, András Perczel, Damijan Knez, Martina Hrast, Martina Gobec, Izidor Sosič, Kinga Nyíri, Beáta G. Vértessy, Niklas Jänsch, Charlotte Desczyk, Franz-Josef Meyer-Almes, Iza Ogris, Simona Golič Grdadolnik, Luca Giacinto Iacovino, Claudia Binda, Stanislav Gobec, and György M. Keserű

This manuscript has been accepted after peer review and appears as an Accepted Article online prior to editing, proofing, and formal publication of the final Version of Record (VoR). This work is currently citable by using the Digital Object Identifier (DOI) given below. The VoR will be published online in Early View as soon as possible and may be different to this Accepted Article as a result of editing. Readers should obtain the VoR from the journal website shown below when it is published to ensure accuracy of information. The authors are responsible for the content of this Accepted Article.

**To be cited as:** *ChemBioChem* 10.1002/cbic.202000700

**Link to VoR:** <https://doi.org/10.1002/cbic.202000700>



# Assessment of tractable cysteines by covalent fragments screening

László Petri,<sup>#[a]</sup> Péter Ábrányi-Balogh,<sup>#[a]</sup> Tímea Imre,<sup>[b]</sup> Gyula Pálffy,<sup>[c]</sup> András Perczel,<sup>[c]</sup> Damijan Knez,<sup>[d]</sup> Martina Hrast,<sup>[d]</sup> Martina Gobec,<sup>[d]</sup> Izidor Sosič,<sup>[d]</sup> Kinga Nyíri,<sup>[e]</sup> Beáta G. Vértessy,<sup>[e,f]</sup> Niklas Jänsch,<sup>[g]</sup> Charlotte Desczyk,<sup>[g]</sup> Franz-Josef Meyer-Almes,<sup>[g]</sup> Iza Ogris,<sup>[h]</sup> Simona Golič Grdadolnik,<sup>[h]</sup> Luca Giacinto Iacovino,<sup>[i]</sup> Claudia Binda,<sup>[i]</sup> Stanislav Gobec\*<sup>[d]</sup> and György M. Keserű\*\*<sup>[a]</sup>

- [a] L. Petri, Dr. P. Ábrányi-Balogh and Prof. Dr. G. M. Keserű  
Medicinal Chemistry Research Group  
Research Centre for Natural Sciences  
Magyar tudósok krt 2, H-1117 Budapest, Hungary  
E-mail: keseru.gyorgy@ttk.mta.hu
- [b] Dr. I. Tímea  
MS Metabolomics Research Group  
Research Centre for Natural Sciences  
Magyar tudósok krt 2, H-1117 Budapest, Hungary
- [c] Dr. G. Pálffy and Prof. Dr. A. Perczel  
Laboratory of Structural Chemistry and Biology & MTA-ELTE Protein Modelling Research Group  
Eötvös Lóránd University  
Pázmány Péter sétány 1/A, 1117 Budapest, Hungary
- [d] Dr. D. Knez, Dr. M. Hrast, Dr. M. Gobec, Dr. I. Susic, and Prof. Dr. S. Gobec  
Faculty of Pharmacy  
University of Ljubljana  
Aškerčeva 7, SI-1000 Ljubljana, Slovenia
- [e] Dr. K. Nyíri and Prof. Dr. B. G. Vértessy  
Genome Metabolism Research Group  
Research Centre for Natural Sciences  
Magyar tudósok krt 2, H-1117 Budapest, Hungary
- [f] Prof. Dr. B. G. Vértessy  
Department of Applied Biotechnology  
Budapest University of Technology and Economics  
Szt Gellért tér 4, H-1111 Budapest, Hungary
- [g] N. Jänsch, C. Desczyk, Prof. Dr. F.-J. Meyer-Almes  
Department of Chemical Engineering and Biotechnology  
University of Applied Sciences Darmstadt,  
Schnittspahnstraße 12, 64287 Darmstadt, Germany
- [h] I. Ogris, Dr. S. Golič G  
Laboratory for Molecular Structural Dynamics  
National Institute of Chemistry  
Hajdrihova 19, 1000 Ljubljana, Slovenia
- [i] L. G. Iacovino and Prof. Dr. C. Binda  
Department of Biology and Biotechnology  
University of Pavia  
via Ferrata 1, 27100 Pavia, Italy

# These authors contributed equally

\* Correspondence: stanislav.gobec@ffa.uni-lj.si

\*\* Correspondence: keseru.gyorgy@ttk.mta.hu

Supporting information for this article is given via a link at the end of the document.

**Abstract:** Targeted covalent inhibition and the use of irreversible chemical probes are important strategies in chemical biology and drug discovery. To date, the availability and reactivity of cysteine residues amenable for covalent targeting have been evaluated by proteomic and computational tools. Here, we present a toolbox of fragments containing a 3,5-bis(trifluoromethyl)phenyl core that was equipped with chemically diverse electrophilic warheads showing a range of reactivities. We characterized the library members for their reactivity, aqueous stability and specificity for nucleophilic amino acids. By screening this library against a set of enzymes amenable for covalent inhibition, we showed that this approach experimentally characterized the accessibility and reactivity of targeted cysteines. Interesting covalent fragment hits were obtained for all investigated cysteine-containing enzymes.

## Introduction

Targeted covalent inhibitors (TCIs) are important chemical biology tools and therapeutic agents.<sup>1</sup> TCIs form covalent bonds with nucleophilic residues, most often cysteine, but also others, e.g. lysine, serine, threonine or tyrosine.<sup>2</sup> Advantages of TCIs include increased biochemical efficiency, prolonged duration of action leading to less frequent dosing, and an opportunity to target shallow binding sites, which were previously considered “undruggable”.<sup>3</sup> TCIs initially interact with the target by forming a noncovalent complex, followed by the reaction of the electrophilic functional group (a “warhead”) with the nucleophilic amino acid residue.<sup>4</sup> A closer look at electrophilic natural products reveals the presence of many reactive functionalities with diverse reaction

## FULL PAPER

mechanisms and varying intrinsic reactivities.<sup>5</sup> The most common TCI design strategy, however, pays less attention to the warheads<sup>6</sup> since they are typically attached to optimized noncovalent inhibitors.<sup>7</sup> By neglecting warhead reactivity optimization, this approach fails to enable the parallel optimization of covalent and noncovalent interactions that could contribute to the discovery of specific and safe covalent drugs.<sup>8</sup> Recent proteomic studies have suggested that the reactivity of cysteines is remarkably diverse in distinct proteins;<sup>9</sup> therefore, commonly used warheads should not be considered as the most suitable during the design process without experimental evaluation of their suitability. As mostly only computational approaches were used for the characterisation of reactive cysteines,<sup>6b,10</sup> screening a diverse set of covalent fragments<sup>11</sup> represents an experimental alternative to these methods. Therefore, in contrast to previous studies,<sup>12</sup> our objective was not only to compare warheads reactivity, but to investigate the reactivity and accessibility of targeted cysteines with a set of covalent fragments, covering a suitable range of reactivity. To avoid the influence of noncovalent contributions, we equipped a single scaffold with a variety of warheads, composing a reactivity mapping toolbox. The constructed electrophilic fragment library was first characterized with experimental reactivity descriptors, aqueous stability and amino acid specificity information. These data confirmed their cysteine specificity and the range of reactivity covered. Then, we screened the library against proteins having different levels of functional and structural complexity (MurA, MAO-A, MAO-B, HDAC8, the immunoproteasome, and KRAS<sup>G12C</sup>). Comparative profiling demonstrated that it is possible to pinpoint reactivity- and accessibility-based specificity caveats for the individual target. Furthermore, the study suggested the optimal warheads for the design of covalent inhibitors for a target of interest.

## Results and Discussion

### Mapping library design and characterization

To investigate the reactivity of different warheads in an unbiased way, we equipped the 3,5-bis(trifluoromethyl)phenyl group, a chemically stable and common motif in medicinal chemistry,<sup>13</sup> with different warheads. There are specific advantages of this scaffold. The limited size and complexity of the 3,5-bis(trifluoromethyl)phenyl fragment, which forms minimal noncovalent protein-ligand interactions, allowed screening against structurally diverse targets. Electron withdrawing properties and the orientation of the trifluoromethyl groups enhance the electrophilic character of the warheads. Therefore, functional groups with lower reactivity could also be investigated. After the proper analysis of the most common cysteine-targeting warheads,<sup>6</sup> we selected 28 covalent fragments representing 20 warhead chemotypes (Figure 1), with an average heavy atom count of  $19 \pm 2$  and a molecular weight of  $289 \pm 36$  g/mol. The library was assembled by acquiring compounds or their intermediates either from commercial sources or by synthesis (see Experimental section).

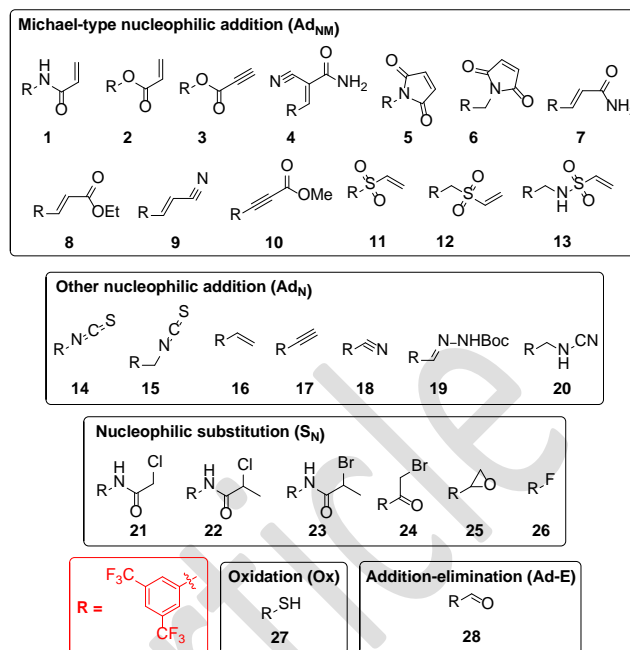


**Figure 1.** Comparative analysis of the reactivity profile for mapping library (1–28) obtained by residual activities (RA%) of MurA and MAO proteins at 500  $\mu$ M, HDAC8 at 250  $\mu$ M and the  $\beta$ 5i subunit of the iCP at 100  $\mu$ M determined by biochemical assay, and free thiol ratio (FTR%) of the KRAS<sup>G12C</sup> at 200  $\mu$ M determined by Ellmann's assay. Heatmap colouring is in line with activity differing from the inactives in red to the actives in green.

To test the reactivity range experimentally, we performed the thiol surrogate glutathione (GSH) reactivity assay (Table S1),<sup>12a,14</sup> which showed that the library includes molecules from highly reactive fragments (2, 5, 6, 11, 12, 14, 15, and 24) to GSH nonreactive compounds (7, 8, 16, 17, 18, 22, and 28). Notably, the known reversible<sup>15</sup> binding of the cyano-acrylamide warhead (4) was confirmed. Next, the labelling efficiency and cysteine selectivity of the library members were evaluated against a nonapeptide model (KGDYHFPIC) containing multiple nucleophilic residues (Cys, His, Tyr, and Lys).<sup>12a</sup> Here, the cysteine selectivity of the fragments was confirmed. Furthermore, one should note that the fragments showed appropriate aqueous stability for biological testing (Table S1).

### Profiling cysteines' reactivity and accessibility

Despite the usefulness of both surrogate model methods to obtain preliminary information on the reactivity and selectivity of warheads, we are well aware that these results do not always reflect events in complex biological systems. In our case, the results from the GSH reactivity assay and nonapeptide model were mostly, but not always, consistent with the results of enzyme assays (Tables 1 and S1).

Single concentration analyses against different protein targets were then performed to obtain preliminary reactivity profiles in a more complex system. Since all library members had an identical scaffold, the reactivity heat map (Figure S1) suggested that the warhead chemotype had a significant impact on the labelling efficiency. Active warheads were identified in all chemical classes, and a trend that different tractable cysteines prefer different warhead chemotypes was also clear. A more detailed confirmation of the reactivity profiles was obtained by enzyme kinetic experiments.

## FULL PAPER

## Profiling on MurA

MurA (UDP-N-acetylglucosamine enolpyruvyl transferase) is a key enzyme in the biosynthesis of bacterial peptidoglycan precursors containing catalytic Cys115.<sup>16</sup> Single concentration screening showed that several fragments caused inhibition with residual activity (RA) between 0% and 50% (Figure S1) and these were subjected to IC<sub>50</sub> measurements (Table 1). Notably, while in most cases the IC<sub>50</sub> values fell in the range of 38–399 μM, we were able to identify compounds with low micromolar inhibitory potencies (IC<sub>50</sub> values 0.5–14 μM for compounds **5**, **6**, **11**, and **27**), indicating that a well-chosen covalent warhead might be able to cause a drastic increase in potency even with a non-optimized scaffold.

The inhibitory potencies for all enzyme inhibitors in this manuscript are expressed as IC<sub>50</sub> values (Table 1), although the compounds are in most cases irreversible. The IC<sub>50</sub> values are therefore dependent on the assay conditions and particularly on the preincubation period. Despite these limitations, the measured IC<sub>50</sub> values still allow relatively simple comparisons of compounds within a series. However, additional methods were used in all cases to provide further information about the enzyme-inhibitor interactions. The covalent binding of the active compounds was confirmed by MS/MS studies, revealing that compounds **11** and **24** form covalent bonds with Cys115 located in the active site of MurA (Figure S2 and Table S2). Furthermore, STD NMR measurements were also performed to confirm the binding of fragments **6**, **7** and **27** to MurA (Figure S3).

**Table 1.** IC<sub>50</sub> values of the electrophilic covalent fragments on MurA, MAO-A, MAO-B, HDAC8, and β5i subunit of the iCP.

Entr y	MurA (μM)	MAO-A (μM)	MAO-B (μM)	HDAC8 (μM)	iCP β5i (μM)
1	164±1	N.A.	N.A.	N.A.	N.A.
2	264±2	N.A.	N.A.	24.42±8.9	18.50±9.19
3	N.A.	N.A.	N.A.	13.22±3.9	N.A.
4	N.A.	61.2±9.0	N.A.	>50	N.A.
5	1.5±0.	0.34±0.01	52.5±10.	0.51±0.05	0.43±0.53
6	11±2.0	4.04±0.24	N.A.	0.03±0.01	N.A.
7	107±1	16.4±2.0	23.6±1.2	4.00±0.76	60.50±3.53
8	N.A.	116.1±22.	58.9±3.9	16.65±6.7	N.A.
10	339±3	N.A.	95.0±9.0	34.96±7.4	N.A.
11	13±2.7	9.65±1.53	N.A.	6.11±1.78	5.90±2.50
12	97±10	13.53±2.4	N.A.	1.95±0.34	25.50±17.6
15	381±2	7.60±1.84	N.A.	4.56±0.40	12.50±12.0
21	76±8	314±74	N.A.	>50	N.A.
24	53±7	N/D	N/D	1.02±0.12	18.00±8.0
27	14±3	113±29	N.A.	N.A.	5.00±2.82

## Profiling on monoamine oxidases

Monoamine oxidases A and B (MAO-A and MAO-B) are isoenzymes that catalyse oxidative deamination of monoamines. Known covalent inhibitors bind to the flavin adenine dinucleotide (FAD) cofactor. Notably, Cys321 and Cys323 in MAO-A and Cys172 in MAO-B, which are located in the active site or in close vicinity, could be targeted by electrophiles.<sup>17</sup> Activity profiling demonstrated that several fragments inhibited both enzymes, whereas some selectively targeted only one isoform (Table 1). We identified low micromolar MAO-A inhibitors (**4**, **6**, **11**, **12**, **15**, **21**, and **27**) with IC<sub>50</sub> values in the range of 4.0–314.0 μM, with no inhibition of MAO-B, and only one selective inhibitor of MAO-B (propiolate **10**). Maleimide **5** was active on both isoforms, favouring MAO-A (IC<sub>50</sub> = 0.3 μM) over MAO-B (IC<sub>50</sub> = 52.5 μM). A detailed kinetic study revealed time-dependent and irreversible inhibition of fragments **6**, **11**, **12**, and **15** (Figures S4 and S5). The covalent binding to MAO-A was confirmed by MS/MS proteomics, where vinyl sulfone **12** formed a covalent bond with Cys321 and Cys323 (Figure 2, more details in Figure S6 and Table S3). To the best of our knowledge, these are the first experimentally confirmed covalent fragments that bind to a specific cysteine and not to the FAD cofactor of MAO-A.

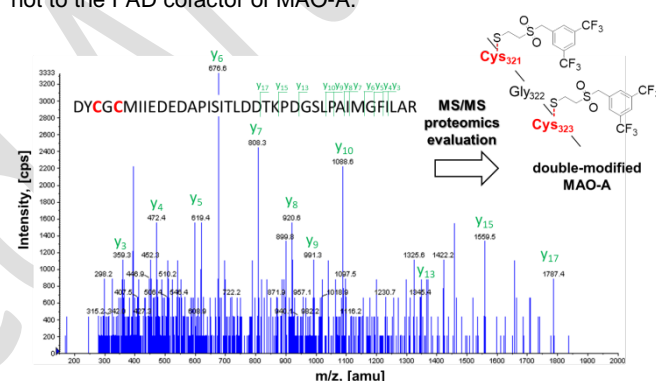


**Figure 2.** The MS/MS spectra of the enzyme-digested MAO-A peptide modified by covalent fragment **11** and the identified adduct.

## Profiling on HDAC8

Histone deacetylase 8 (HDAC8) is an enzyme that plays a critical role in cell cycle progression by catalysing the deacetylation of histones and a number of cytosolic proteins.<sup>18</sup> Considering the effects on cell reproduction, HDAC8 has attracted significant attention in oncology.<sup>19</sup> Numerous active fragments were identified in the HDAC8 inhibition screening (Figure S1). IC<sub>50</sub> values were determined for **11** active hits (Table 1). Notably, the acrylamide was clearly preferred in a more sterically hindered orientation, as **7** (IC<sub>50</sub> = 4.0 μM) outperformed **1**, whereas the other acrylic fragment pair, esters **2** (IC<sub>50</sub> = 24.4 μM) and **8** (IC<sub>50</sub> = 16.7 μM), showed a similar potency. Maleimides were the only fragments active in the sub-micromolar range (IC<sub>50</sub> values of 0.5 μM and 0.03 μM for **5** and **6**, respectively). The potencies of the other nine compounds were in the low-micromolar range (Table 1). In addition, the time-dependency of inhibition was shown for the four most potent fragments (i.e., maleimides **5** and **6**, vinylsulfone **12**, and haloacetophenone **24**; Figure S7). The site of labelling was determined by MS/MS after tryptic digestion of the labelled protein samples with the most active compounds **5**, **6**, and **24**. Maleimides **5** and **6** were anchored to cysteines 244 and 275, while haloacetophenone **24**



## FULL PAPER

parameters (kinetic rate constant, half-life time) a programmed excel (Visual Basic for Applications) was utilized. The data are expressed as means of duplicate determinations, and the standard deviations were within 10% of the given values.

The calculation of the kinetic rate constant for the degradation and corrected GSH-reactivity is the following. Reaction half-life for pseudo-first order reactions is  $t_{1/2} = \ln 2/k$ , where  $k$  is the reaction rate. In the case of competing reactions (reaction with GSH and degradation), the effective rate for the consumption of the starting compound is  $k_{\text{eff}} = k_{\text{deg}} + k_{\text{GSH}}$ . When measuring half-lives experimentally, the  $t_{1/2(\text{eff})} = \ln 2/(k_{\text{eff}}) = \ln 2/(k_{\text{deg}} + k_{\text{GSH}})$ . In our case, the corrected  $k_{\text{deg}}$  and  $k_{\text{eff}}$  (regarding to blank and GSH containing samples, respectively) can be calculated by linear regression of the data points of the kinetic measurements. The corrected  $k_{\text{GSH}}$  is calculated by  $k_{\text{eff}} - k_{\text{deg}}$ , and finally half-life time is determined using the equation  $t_{1/2(\text{GSH})} = \ln 2/k_{\text{GSH}}$ .

### Oligopeptide selectivity assay<sup>[12a]</sup>

For nonapeptide assay 2 mM solution of the fragment (PBS buffer pH 7.4 with 20% acetonitrile) was added to 200  $\mu\text{M}$  nonapeptide solution (PBS buffer pH 7.4) in 1:1 ratio. The final assay mixture contained 1 mM fragment, 100  $\mu\text{M}$  peptide and 10% acetonitrile. The samples were incubated at room temperature overnight. Based on the GSH reactivity the applied incubation time was 16 h or 24 h. Fragments with less than 12 h half-life time against GSH were incubated for 16 h, the others for 24 h. Information Dependent Acquisition (IDA) LC-MS/MS experiment was used to identify, whether the fragment binding was specific to thiol residues or not. Enhanced MS scan was applied as survey scan and enhanced product ion (EPI) was the dependent scan. The collision energy in EPI experiments was set to 30 eV with collision energy spread (CES) of 10 V. The identification of the binding position of the fragments to the nonapeptide was performed by GPMW 4.2. software. Relative quantitation of the nonapeptide – fragment covalent conjugates was calculated from the total ion chromatograms (based on peak area of the selected ion chromatograms).

### MurA biochemical assay<sup>[24]</sup>

MurA protein was recombinant, expressed in *E. coli*. The inhibition of MurA was monitored with the colorimetric malachite green method in which orthophosphate generated during reaction is measured. MurA enzyme (*E. coli*) was pre-incubated with the substrate UDP-*N*-acetylglucosamine (UNAG) and compound for 30 min at 37 °C. The reaction was started by the addition of the second substrate PEP, resulting in a mixture with final volume of 50  $\mu\text{L}$ . The mixtures contained: 50 mM Hepes, pH 7.8, 0.005% Triton X-114, 200  $\mu\text{M}$  UNAG, 100  $\mu\text{M}$  PEP, purified MurA (diluted in 50 mM Hepes, pH 7.8) and 500  $\mu\text{M}$  of each tested compound dissolved in DMSO. All compounds were soluble in the assay mixtures containing 5% DMSO (v/v). After incubation for 15 min at 37 °C, the enzyme reaction was terminated by adding Biomol<sup>®</sup> reagent (100  $\mu\text{L}$ ) and the absorbance was measured at 650 nm after 5 min. Residual activities (RAs) were calculated with respect to similar assays without the tested compounds and with 5% DMSO. The IC<sub>50</sub> values were determined by measuring the residual activities at seven different compound concentrations. The data are expressed as means of duplicate determinations, and the standard deviations were within 10% of the given values.

### STD NMR of MurA

The <sup>1</sup>H STD NMR spectra were recorded on Bruker Avance Neo 600 MHz (NMR Center, National Institute of Chemistry, Slovenia), using cryoprobe, at 25 °C. The pulse sequences provided in the Bruker library of pulse programmes were used. The samples were prepared in 90% D<sub>2</sub>O/10% DMSO-*d*<sub>6</sub> buffer containing 20 mM Tris-*d*<sub>11</sub>, 150 mM NaCl, and 0.049 mM dithiothreitol-*d*<sub>10</sub>; pD 7.4. Substrate UNAG was added at an enzyme:substrate ratio of 1:5. All the spectra were recorded at an enzyme:ligand ratio of 1:100. The enzyme concentration was 0.004 mM, and the ligand concentration was 0.4 mM.

STD experiments were performed with a 6250 Hz spectral width, 16.384 data points, a saturation time of 2 s, a relaxation delay of 2 s, and 480

scans. Selective saturation was achieved by a train of 50 ms long Gauss-shaped pulses separated by a 1 ms delay. Water was suppressed via excitation sculpting. The on-resonance selective saturation of the enzyme was applied at -0.42 ppm. The off-resonance irradiation was applied at 30 ppm for the reference spectrum.

### Protein labeling for MurA MS/MS proteomics<sup>[12a]</sup>

For the MurA labelling experiment the 42  $\mu\text{M}$  stock solution of MurA in 20 mM Hepes at pH 7.2–7.4 with 1 mM DTT was filtered through a G25 column and the medium was changed to 50 mM Tris with 0.005% Triton X-100 at pH 8.0. For the activation of the enzyme 1 mg UDPNAG was added as a solid to reach 40 mM concentration and the mixture was incubated at 37 °C for 30 min. Fragments were added from a 250 mM DMSO stock diluted in the labelling solution to 5 mM. The incubation was continued at 37 °C for additional 30 min. After the labelling, the mixture was purified on a G25 column.

### MAO-A and MAO-B biochemical assay

The effects of the test compounds on MAO-A and MAO-B were investigated using a fluorimetric assay, following a previously described literature method.<sup>[25]</sup> The inhibitory potency of the compounds was evaluated by their effects on the production of hydrogen peroxide (H<sub>2</sub>O<sub>2</sub>) from *p*-tyramine. The production of the H<sub>2</sub>O<sub>2</sub> was detected using Amplex Red reagent in the presence of horseradish peroxidase, where a highly sensitive fluorescent product, resorufin, is produced at stoichiometric amounts. Recombinant human microsomal MAO-A and MAO-B enzymes expressed in baculovirus infected insect cells (BTI-TN-5B1-4), horseradish peroxidase (type II, lyophilized powder), and *p*-tyramine hydrochloride were obtained from Sigma Aldrich. 10-Acetyl-3,7-dihydroxyphenoxazine (Amplex Red reagent) was synthesized as described in the literature.<sup>[26]</sup>

Briefly, 100  $\mu\text{L}$  50 mM sodium phosphate buffer (pH 7.4, 0.05% [v/v] Triton X-114) containing the compounds and MAO-A/B were incubated for 30 min at 37 °C in a flat-bottomed black 96-well microplate. After the pre-incubation (30 min for the screening), the reaction was started by adding the final concentrations of 200  $\mu\text{M}$  Amplex Red reagent, 2 U/mL horseradish peroxidase, and 1 mM *p*-tyramine (final volume, 200  $\mu\text{L}$ ). The production of resorufin was quantified on the basis of the fluorescence generated ( $\lambda_{\text{ex}} = 530 \text{ nm}$ ,  $\lambda_{\text{em}} = 590 \text{ nm}$ ) at 37 °C over a period of 30 min, during which time the fluorescence increase linearly. For control experiments, DMSO was used instead of the appropriate dilutions of the compounds in DMSO. To determine the blank value ( $b$ ), phosphate-buffered solution replaced the enzyme solution. The initial velocities were calculated from the trends obtained, with each measurement carried out in duplicate. The specific fluorescence emission to obtain the final result was calculated after subtraction of the blank activity ( $b$ ). The inhibitory potencies are expressed as the residual activities ( $\text{RA} = (v_t - b) / (v_0 - b)$ ), where  $v_t$  is the velocity in the presence of the test compounds, and  $v_0$  the control velocity in the presence of DMSO. The IC<sub>50</sub> values were calculated using GraphPad Prism v8.0 software. The results are mean  $\pm$  SEM of three independent experiments, each performed in duplicate. For determination of time-dependency, MAO-A was pre-incubated with the fragments for 5 min, 15 min and 30 min and the assay was performed as described above.

For the reversibility assay, MAO-A at 100-fold final concentration was incubated with the fragments at a concentration 10-fold the IC<sub>50</sub> at 37 °C (volume, 50  $\mu\text{L}$ ). After 30 min, the mixture was diluted 100-fold into the reaction buffer containing Amplex Red reagent, horseradish peroxidase, and *p*-tyramine hydrochloride. The final concentrations of all of the reagents and MAO-A were the same as in the assay described above. The reaction was monitored for 30 min. Control experiments were carried out in the same manner, where the inhibitor solution was replaced by DMSO. Clorgyline and harmaline were used as control irreversible and reversible MAO-A inhibitors, respectively. The results are mean  $\pm$  SD of three independent experiments, each performed in quadruplicate.

### Protein labeling for MAO-A MS/MS proteomics

## FULL PAPER

Human recombinant MAO-A (52 mM nominal concentration) in 50 mM sodium phosphate buffer at pH 7.8 together with 300 mM NaCl, 20 mM imidazole, 0.05% FOS-choline-12 and 40% glycerol was used for the labelling. The enzyme was expressed in *Pichia pastoris* and purified following published protocols.<sup>[27]</sup> The MAO-A sample was quickly thawed from  $-78^{\circ}\text{C}$  to  $37^{\circ}\text{C}$ , and centrifuged (5 min at 10000 rpm) in order to remove the aggregated protein. MAO-A was buffer exchanged to 50 mM  $\text{K}_3\text{PO}_4$  at pH 7.5 together with 0.25% Triton X-100<sup>[28]</sup> and stored on ice. The electrophilic fragments were added in 0.5  $\mu\text{L}$  DMSO (100 mM) to a 35–50  $\mu\text{L}$  of the enzyme solution to reach 35–50-fold excess of the fragments. The samples were incubated at  $4^{\circ}\text{C}$  for 24 h.

**HDAC8 biochemical assay**

Enzyme activity assay was executed in assay buffer (25 mM Tris-HCl pH 8.0, 50 mM NaCl and 0.001% (v/v) Pluronic F-68) in black half area 96-well microplates (Greiner Bio-One, Germany). For the initial screening 10 nM HDAC8 was pre-incubated with 250  $\mu\text{M}$  of the indicated compounds for 2 h at  $30^{\circ}\text{C}$ . For  $\text{IC}_{50}$  determination 10 nM HDAC8 was pre-incubated with a serial dilution of the indicated compounds for 1 h and with varying times for the time dependent  $\text{IC}_{50}$  curves. The enzyme reaction was initiated by the addition of 20  $\mu\text{M}$  Boc-Lys(TFA)-AMC (Bachem, Switzerland). After substrate conversion at  $30^{\circ}\text{C}$  for 1 h the reaction was stopped by adding 1.67  $\mu\text{M}$  suberylanilide trifluoromethylketone (SATFMK). For time dependent  $\text{IC}_{50}$  measurements the substrate conversion was stopped after 5 min. The deacetylated substrate was cleaved with 0.42 mg/mL trypsin to release fluorescent 7-amino-4-methylcoumarin (AMC), which was detected with a microplate reader (PHERAstar FS or BMG LABTECH) with fluorescence excitation at 360 nm and emission at 460 nm.  $\text{IC}_{50}$  values were calculated by generating dose-response curves in GraphPad Prism 6 and fitting those to a 4-parameter logistic model.

**Protein labeling for HDAC8 MS/MS proteomics**

For covalent labeling 25  $\mu\text{M}$  HDAC8 was treated with 250  $\mu\text{M}$  of the indicated compound for 1 h at  $30^{\circ}\text{C}$  in assay buffer as described above. After reaction the protein was precipitated by the addition of 10 % TCA and afterwards centrifuged at 18000 g for 15 min. The supernatant was removed, and dry pellet was diluted in buffer (50 mM  $\text{NH}_4\text{HCO}_3$ , pH = 7.8).

**Immunoproteasome ( $\beta 5\text{i}$ ) biochemical assay**

The screening of compounds was performed at 100  $\mu\text{M}$  final concentrations in assay buffer (0.01% SDS, 50 mM Tris-HCl, 0.5 mM EDTA, pH 7.4). To each electrophilic fragment, 0.2 nM human iCP (Boston Biochem, Inc., Cambridge/MA, USA) was added and incubated for 30 min at  $37^{\circ}\text{C}$ . Afterwards, the reaction was initiated by the addition of Suc-LLVY-AMC (a substrate to evaluate the activity of the  $\beta 5\text{i}$  subunit of the immunoproteasome, Bachem, Bubendorf, Switzerland) at 25  $\mu\text{M}$  final concentration. The reaction progress was recorded on the BioTek Synergy HT microplate reader by monitoring fluorescence at 460 nm ( $\lambda_{\text{ex}} = 360$  nm) for 90 min at  $37^{\circ}\text{C}$ . The initial linear ranges were used to calculate the velocity and to determine the residual activity. The results are means from at least three independent measurements. Standard errors for RAs were less than 15% in every cases.

Compounds that showed average residual activity below 50% in the RA determination assay were initially dissolved in DMSO, and then added to black 96-well plates in the assay buffer (0.01% SDS, 50 mM Tris-HCl, 0.5 mM EDTA, pH 7.4) to obtain eight different final concentrations. The inhibitors were pre-incubated with 0.2 nM human iCP (Boston Biochem, Inc., Cambridge/MA, USA) at  $37^{\circ}\text{C}$  30 min, before the reaction was initiated by the Suc-LLVY-AMC substrate (Bachem, Bubendorf, Switzerland). The fluorescence was monitored at 460 nm ( $\lambda_{\text{ex}} = 360$  nm) for 90 min at  $37^{\circ}\text{C}$ . The progress of the reactions was recorded and the initial linear ranges were used to calculate the velocity.  $\text{IC}_{50}$  values were calculated in Prism (GraphPad Software, CA, USA) and are means from at least three independent determinations.

**Protein labeling for immunoproteasome ( $\beta 5\text{i}$ ) MS analysis**

For the immunoproteasome labelling experiments, isolated  $\beta 5\text{i}$  subunit was purchased from ProSpec-Tany TechnoGene Ltd, as 22  $\mu\text{M}$  solution in 20 mM Tris-HCl buffer (pH = 8.0), with 0.4 M urea and 10% glycerol. The peptide solution was filtered through a G25 column and the medium was changed to 50 mM Tris (pH = 7.4) with 0.5 mM EDTA and 0.01% SDS. Fragments were added from a 100 mM DMSO stock diluted in the labelling solution to 1 mM. The samples were kept at  $37^{\circ}\text{C}$  for 5h, then at room temperature for further 12h. Finally, the samples were purified on a G25 column.

**MS analysis of the labelled immunoproteasome ( $\beta 5\text{i}$ )**

The molecular weights of the conjugates of IPS  $\beta 5\text{i}$  were identified using a Triple TOF 5600+ hybrid Quadrupole-TOF LC/MS/MS system (Sciex, Singapore, Woodlands) equipped with a DuoSpray IonSource coupled with a Shimadzu Prominence LC20 UFLC (Shimadzu, Japan) system consisting of binary pump, an autosampler and a thermostated column compartment. Data acquisition and processing were performed using Analyst TF software version 1.7.1 (AB Sciex Instruments, CA, USA). Chromatographic separation was achieved on a Thermo Beta Basic C8 (50 mm  $\times$  2.1mm, 3  $\mu\text{m}$ , 150  $\text{\AA}$ ) HPLC column. Sample was eluted in gradient elution mode using solvent A (0.1% formic acid in water) and solvent B (0.1% formic acid in ACN). The initial condition was 20% B for 1 min, followed by a linear gradient to 90% B by 4 min, from 5 to 6 min 90% B was retained; and from 6 to 6.5 min back to initial condition with 20 % eluent B and retained from 6.5 to 9.0 min. Flow rate was set to 0.4 ml/min. The column temperature was  $40^{\circ}\text{C}$  and the injection volume was 5  $\mu\text{L}$ . Nitrogen was used as the nebulizer gas (GS1), heater gas (GS2), and curtain gas with the optimum values set at 30, 30 and 35 (arbitrary units), respectively. Data were acquired in positive electrospray mode in the mass range of  $m/z=300$  to 2500, with 1 s accumulation time. The source temperature was  $350^{\circ}\text{C}$  and the spray voltage was set to 5500 V. Declustering potential value was set to 80 V. Peak View SoftwareTM V.2.2 (version 2.2, Sciex, Redwood City, CA, USA) was used for deconvoluting the raw electrospray data to obtain the neutral molecular masses.

**Digestion and proteomics MS/MS analysis**<sup>[12a]</sup>

After the labelling 40–50  $\mu\text{L}$  of the sample and 10  $\mu\text{L}$  0.2% (w/v) RapiGest SF (Waters, Milford, USA) solution buffered with 3.3  $\mu\text{L}$  of 45 mM DTT in 100 mM  $\text{NH}_4\text{HCO}_3$  were added and kept at  $37.5^{\circ}\text{C}$  for 30 min. After cooling the sample to room temperature, 4.16  $\mu\text{L}$  of 100 mM iodoacetamide in 100 mM  $\text{NH}_4\text{HCO}_3$  were added and placed in the dark in room temperature for 30 min. The reduced and alkylated protein was then digested by 10  $\mu\text{L}$  (1 mg/mL) trypsin (the enzyme-to-protein ratio was 1:10) (Sigma, St Louis, MO, USA). The sample was incubated at  $37^{\circ}\text{C}$  for overnight. To degrade the surfactant, 7  $\mu\text{L}$  of formic acid (500 mM) solution was added to the digested protein sample to obtain the final 40 mM concentration (pH  $\approx$  2) and was incubated at  $37^{\circ}\text{C}$  for 45 min. For LC-MS analysis, the acid treated sample was centrifuged for 5 min at 13 000 rpm. QTRAP 6500 triple quadrupole – linear ion trap mass spectrometer, equipped with a Turbo V source in electrospray mode (AB Sciex, CA, USA) and a Perkin Elmer Series 200 micro LC system (Massachusetts, USA) was used for LC-MS/MS analysis. Data acquisition and processing were performed using Analyst software version 1.6.2 (AB Sciex Instruments, CA, USA). Chromatographic separation was achieved by using the Vydac 218 TP52 Protein & Peptide C18 column (250 mm  $\times$  2.1 mm, 5  $\mu\text{m}$ ). The sample was eluted with a gradient of solvent A (0.1% formic acid in water) and solvent B (0.1% formic acid in ACN). The flow rate was set to 0.2 mL/min. The initial conditions for separation were 5% B for 7 min, followed by a linear gradient to 90% B by 53 min, from 60 to 63 min 90% B is retained; from 64 to 65 min back to the initial conditions with 5% eluent B retained to 70 min. The injection volume was 10  $\mu\text{L}$  (300 pmol on the column). Information Dependent Acquisition (IDA) LC-MS/MS experiment was used to identify the modified tryptic peptide fragments. Enhanced MS scan (EMS) was applied as survey scan and enhanced product ion (EPI) was the dependent scan. The collision energy in EPI experiments was set to rolling collision energy mode, where the actual value was set on the basis of the mass and charge state of the selected ion. Further IDA criteria:

## FULL PAPER

ions greater than: 400.000 m/z, which exceeds 106 counts, exclude former target ions for 30 seconds after 2 occurrence(s). In EMS and in EPI mode the scan rate was 1000 Da/s as well. Nitrogen was used as the nebulizer gas (GS1), heater gas (GS2), and curtain gas with the optimum values set at 50, 40 and 40 (arbitrary units). The source temperature was 350 °C and the ion spray voltage set at 5000 V. Declustering potential value was set to 150 V. GPMW 4.2 software and ProteinProspector<sup>[29]</sup> was used to analyse the large number of MS-MS spectra and identify the modified tryptic peptides.

**KRASG12C analysis by Ellman's assay**

To measure thiol-reactivity, 2 μM KRAS<sup>G12C</sup> in assay buffer (25 mM NaH<sub>2</sub>PO<sub>4</sub>, 0.1 mM EDTA, 150 mM NaCl, pH 6.6) was treated with 200 μM of fragments, resulting 5% DMSO concentration in the mixture. After 2 hours of incubation on room temperature, 16 μL of the sample was pipetted into a black, 384 well assay plate (Corning, Ref No.: 4514) and 4 μL of thiol detection reagent (Invitrogen, Ref No.: TC012-1EA) was added. After brief shaking, the plate was incubated in dark, room temperature for 30 min, then fluorescence was measured in duplicates in a microplate reader (BioTek Synergy Mx) ( $\lambda_{\text{ex}} = 390 \text{ nm}$  and  $\lambda_{\text{em}} = 510 \text{ nm}$ ). Free thiol ratio (FTR%) labelling ratio (LR%) values were calculated, as follows:

$$\text{FTR}[\%] = 100 \cdot \frac{\text{RFU}_{\text{sample}} - \text{RFU}_{\text{background}}}{\text{RFU}_{\text{DMSO}} - \text{RFU}_{\text{background}}} \quad \text{LR}[\%] = 100 \cdot \frac{\text{RFU}_{\text{DMSO}} - \text{RFU}_{\text{sample}}}{\text{RFU}_{\text{DMSO}} - \text{RFU}_{\text{background}}}$$

**KRASG12C analysis by NMR**

NMR measurements for testing binding BTF compounds to KRAS4BG12C-GDP protein were carried out on a Bruker Avance III 700 MHz spectrometer equipped with a 5-mm Prodigy TCI H&F-C/N-D, z-gradient probehead operating at 700.05 MHz for <sup>1</sup>H and 70.94 MHz for <sup>15</sup>N and 658.71 MHz for <sup>19</sup>F nuclei. Spectra were recorded at 298 K. TFA standard solution contained 0.1% trifluoroacetic acid in H<sub>2</sub>O. For NMR samples BTF compounds were dissolved in DMSO in 12 mM concentration. To obtain reference spectra free BTF molecules (without protein) were measured in PBS buffer (pH 7.4), 5 mM MgCl<sub>2</sub>, 10% D<sub>2</sub>O and 5% BTF-stock solution (in DMSO) and 0.2% TFA standard solution (1 μL in 500 μL NMR sample) and for the protein (without BTF molecules) were measured in <sup>15</sup>N-labeled KRAS4B-G12C<sup>1-169</sup> (catalytic domain) mutant in 0.2 mM concentration, 5 mM GDP, 10 mM EDTA, 15 mM MgCl<sub>2</sub> in PBS buffer (pH 7.4), 10% D<sub>2</sub>O, 5% DMSO and 1% DSS standard. NMR samples for binding tests contained <sup>15</sup>N-labeled KRAS4B-G12C<sup>1-169</sup> in 0.2 mM concentration, 5% BTF-stock solution (in DMSO, the final concentration of the compound is 0.6 mM), 2–3 mM GDP, 3–5 mM EDTA, 8–10 mM MgCl<sub>2</sub> in PBS buffer (pH 7.4), 10% D<sub>2</sub>O and 0.2% TFA standard solution (1 μL in 500 μL NMR sample).

In binding tests 1D <sup>19</sup>F-NMR (NS = 4), 1D <sup>1</sup>H-NMR (NS = 64) and 2D <sup>1</sup>H,<sup>15</sup>N-SOFAST-HMQC (NS = 64) spectra were performed subsequently immediately after mixing (i.e. 0.3–1 h) and after 1 day incubation (22–28 h) at room temperature. In case of those BTF molecules which half lives in PBS + 5% DMSO buffer were shorter than 24 h according to HPLC measurements, the incubation time was a minimum of 10 times longer than the (estimated) half-life if shorter than 1 day. To obtain reference signals for free BTF molecules, <sup>19</sup>F-NMR spectra were performed with the same parameters as in the binding test after a minimum of 3–4 half-life time incubation and for the free protein a 2D <sup>1</sup>H,<sup>15</sup>N-SOFAST-HMQC spectrum were used. Sequence specific assignment of H<sup>N</sup> and N in the bound KRAS4B-G12C spectra were transferred from previous results.<sup>[30]</sup> All <sup>1</sup>H chemical shifts were referenced to the DMSO peaks (which were calibrated to DSS resonance before in free protein measurements) as DSS were not added to avoid any side reactions with the limited amount of small molecules. <sup>15</sup>N chemical shift values were referenced indirectly using the corresponding gyromagnetic ratios according to IUPAC convention. <sup>19</sup>F chemical shifts were referenced to the TFA signal corresponding to its CF<sub>3</sub> group. All spectra were processed with Bruker TOPSPIN. Binding was confirmed in every case by both <sup>19</sup>F- and SOFAST-HMQC spectra: based on the BTF compound evidenced by comparing <sup>19</sup>F-NMR spectra of free BTF compound and BTF + protein and KRAS-G12C demonstrated by comparing SOFAST-HMQC spectra of free KRAS-G12C-GDP and BTF + protein. Based on the assignment of SOFAST-HMQC spectra KRAS-

G12C-GDP, the cysteines modified covalently by BTF molecules were determined as well.

**Synthesis***N*-(3,5-Bis(trifluoromethyl)phenyl)acrylamide (**1**)<sup>[31]</sup>

To a solution of 3,5-bis(trifluoromethyl)aniline (1.56 mL, 10 mmol) in DCM (30 mL) triethylamine (1.40 mL, 10 mmol) was added, and the mixture was allowed to stir under Ar at room temperature (RT) for 10 min. The mixture was cooled with iced water and then acryloyl chloride (0.81 mL, 10 mmol) was added dropwise, and the reaction was left to stir at RT for 2 h. The reaction was concentrated under vacuum. The residue was diluted with H<sub>2</sub>O and extracted with EtOAc. The organic layer was washed with 1 M aq. HCl, dried over Na<sub>2</sub>SO<sub>4</sub>, filtered, and concentrated under vacuum. The product was washed with Et<sub>2</sub>O and then vacuum dried to afford **1** as a white powder (2.06 g, 70%). <sup>1</sup>H NMR (500 MHz, DMSO-*d*<sub>6</sub>) δ 10.76 (s, 1H, NH), 8.32 (s, 2H, ArH), 7.76 (s, 1H, ArH), 6.37 (qd, *J* = 17.0, 5.9 Hz, 2H, =CH–), 5.86 (dd, *J* = 9.7, 2.1 Hz, 1H, =CH–) ppm. <sup>19</sup>F NMR (650 MHz, D<sub>2</sub>O) δ –62.7 ppm.

*3,5-Bis(trifluoromethyl)phenyl acrylate* (**2**)

In 10 mL dichloromethane 3,5-bis(trifluoromethyl)phenol (0.15 mL, 1 mmol) and *N,N*-diisopropylethylamine (0.17 mL, 1 mmol) was dissolved and stirred at RT for 10 min. The reaction mixture was cooled with iced water and then acryloyl chloride (0.08 mL, 1 mmol) was added dropwise. Then the reaction was allowed to stir at RT overnight. The solvent was removed under vacuum and the residue was dissolved in ethyl acetate. The solution was washed with saturated sodium bicarbonate and water. The organic phase was dried over Na<sub>2</sub>SO<sub>4</sub>, filtered, and concentrated under vacuum. The product was purified by flash column chromatography using a mixture of hexane and ethyl acetate as eluent. The compound **2** was obtained as a colourless oil (39 mg, 14%) <sup>1</sup>H NMR (300 MHz, CDCl<sub>3</sub>) δ 7.82 (s, 1H, ArH), 7.70 (s, 2H, ArH), 6.72 (d, *J* = 17.2 Hz, 1H, =CH–), 6.39 (dd, *J* = 17.2, 10.5 Hz, 1H, =CH<sub>2</sub>), 6.16 (d, *J* = 10.4 Hz, 1H, =CH<sub>2</sub>) ppm. <sup>13</sup>C NMR (75 MHz, CDCl<sub>3</sub>) δ 163.75, 151.33, 134.47, 133.21 (q, *J* = 34.1 Hz, 2C), 127.12, 123.01 (d, *J* = 272.9 Hz, 2C), 122.71 (2C), 120.49 – 119.43 (m) ppm. <sup>19</sup>F NMR (650 MHz, D<sub>2</sub>O) δ –64.6 ppm. Anal. calcd. for C<sub>11</sub>H<sub>6</sub>F<sub>6</sub>O<sub>2</sub>: C, 46.47; H, 2.11. found: C, 46.38; H, 2.15.

*3,5-Bis(trifluoromethyl)phenyl propionate* (**3**)

3,5-Bis(trifluoromethyl)phenol (0.15 mL, 1 mmol), dicyclohexylcarbodiimide (0.21 g, 1 mmol), *N,N*-dimethylaminopyridine (1.2 mg, 0.01 mmol) and propionic acid (68 μL, 1.1 mmol) was dissolved in DCM (5 mL) at 0 °C, and stirred for 5 h turning the colourless solution to a yellow suspension. The reaction mixture was quenched with 20 mL of water and separated. The aqueous phase was extracted with dichloromethane (2 × 20 mL). The organic phase was dried over MgSO<sub>4</sub>, filtered, and concentrated under vacuum. The product was purified by flash column chromatography using a mixture of hexane and ethyl acetate as eluent. Compound **3** was obtained as a white solid (40 mg, 14%). <sup>1</sup>H NMR (500 MHz, DMSO-*d*<sub>6</sub>) δ 8.14 (s, 2H, ArH), 8.05 (s, 1H, ArH), 4.92 (s, 1H, ≡CH) ppm. <sup>13</sup>C NMR (125 MHz, DMSO-*d*<sub>6</sub>) δ 150.7, 150.5, 132.1 (q, *J* = 33.7 Hz, 2C), 124.2 (d, *J* = 3.8 Hz, 2C), 123.1 (q, *J* = 271.3 Hz, 2C), 120.8–121.0 (m), 82.9, 74.2 ppm. <sup>19</sup>F NMR (650 MHz, D<sub>2</sub>O) δ –64.7 ppm. Anal. calcd. for C<sub>11</sub>H<sub>4</sub>F<sub>6</sub>O<sub>2</sub>: C, 46.81; H, 1.42. found: C, 46.67; H, 1.49

*3-(3,5-Bis(trifluoromethyl)phenyl)-2-cyanoacrylamide* (**4**)<sup>[31]</sup>

3,5-Bis(trifluoromethyl)benzaldehyde (0.33 mL, 2 mmol) and 2-cyanoacetamide (252 mg, 3 mmol) were dissolved in methanol (15 mL). To this solution catalytic NaOH (1 mg, 1 %) was added, and the reaction was stirred at 45 °C for 4 h. The reaction was concentrated under vacuum, followed by adding 25 mL water and 25 mL ethyl acetate to the residue. After separation, the organic layer was washed with brine, dried over Na<sub>2</sub>SO<sub>4</sub>, filtered, and concentrated under vacuum. The product was obtained as white powder (228 mg, 37%) by column chromatography with a mixture of hexane and ethyl acetate as eluent. <sup>1</sup>H NMR (500 MHz, DMSO-*d*<sub>6</sub>) δ 8.54 (s, 2H, ArH), 8.37 (s, 1H, ArH), 8.31 (s, 1H, =CH–), 7.97

## FULL PAPER

(s, 1H, NH<sub>2</sub>), 7.89 (s, 1H, NH<sub>2</sub>) ppm. <sup>19</sup>F NMR (650 MHz, D<sub>2</sub>O) δ -62.7 ppm.

**1-(3,5-Bis(trifluoromethyl)phenyl)-1H-pyrrole-2,5-dione (5)** <sup>[32]</sup>

To a solution of maleic anhydride (214 mg, 2.18 mmol) in dichloromethane (20 mL) 3,5-bis(trifluoromethyl)aniline (0.34 mL, 2.2 mmol) was added dropwise at 40 °C, and the mixture was allowed to stir for 2 h. The intermediate was obtained as white crystals (705 mg, 98 %) and collected by filtration. The intermediate was dissolved in toluene (30 mL), then catalytical amount of H<sub>2</sub>SO<sub>4</sub> was added (1–2 drops). The reaction flask was equipped with a Dean-Stark apparatus and the mixture was refluxed at 130 °C for 3 h. The solvent was removed under vacuum and the residue was purified by flash column chromatography with a mixture of hexane and ethyl acetate as eluent. The product was obtained as brown solid (272 mg, 40%). <sup>1</sup>H NMR (500 MHz, DMSO-*d*<sub>6</sub>) δ 8.15 (s, 1H, ArH), 8.12 (s, 2H, ArH), 7.27 (s, 2H, =CH-) ppm. <sup>19</sup>F NMR (650 MHz, D<sub>2</sub>O) δ -62.7 ppm.

**1-(3,5-Bis(trifluoromethyl)benzyl)-1H-pyrrole-2,5-dione (6)**

The same procedure as for **5** except using 3,5-bis(trifluoromethyl)benzylamine (535 mg, 2.18 mmol). The product was obtained as brown solid (317 mg, 45 %). <sup>1</sup>H NMR (500 MHz, DMSO-*d*<sub>6</sub>) δ 8.27 (s, 2H, ArH), 8.21 (s, 2H, -CH=), 8.11 (s, 1H, ArH), 4.25 (d, *J* = 5.2 Hz, 2H, CH<sub>2</sub>) ppm. <sup>13</sup>C NMR (125 MHz, DMSO-*d*<sub>6</sub>) δ 172.5 (2C), 137.7 (2C), 130.8 (2C), 130.7 (q, *J* = 32.5 Hz), 130.6 (2C), 124.7, 122.5–122.7 (m, 2C), 41.8 ppm. <sup>19</sup>F NMR (650 MHz, D<sub>2</sub>O) δ -62.5 ppm. HRMS (ESI): (M+H)<sup>+</sup> calcd. for C<sub>13</sub>H<sub>7</sub>F<sub>6</sub>NO<sub>2</sub><sup>+</sup>, 324.0459; found, 324.0447.

**3-(3,5-Bis(trifluoromethyl)phenyl)acrylamide (7)**

In a sealed tube 3,4-bis(trifluoromethyl)bromobenzene (0.35 mL, 2 mmol), acrylamide (171 mg, 2.4 mmol), Pd(OAc)<sub>2</sub> (11 mg, 0.05 mmol), diisopropylethylamine (0.42 mL, 2.4 mmol) and tri(*o*-tolyl)phosphine (30 mg, 0.1 mmol) was added to dimethylformamide (5 mL) under Ar and heated at 130 °C for 1.5 h. The crude mixture was filtered from activated charcoal and water:MeOH 1:1 was added. The forming yellow crystals were filtered (140 mg, 49%). <sup>1</sup>H NMR (500 MHz, CDCl<sub>3</sub>) δ 7.92 (s, 2H, ArH), 7.86 (s, 1H, ArH), 7.70 (d, *J* = 15.7 Hz, 1H, =CH-), 6.60 (d, *J* = 15.7 Hz, 1H, =CH-), 5.71 (s, 2H, NH<sub>2</sub>) ppm. <sup>13</sup>C NMR (125 MHz, CDCl<sub>3</sub>) δ 166.3, 138.3, 136.3 (2C), 131.3 (q, *J* = 33.0 Hz), 128.4, 128.3, 127.1 (2C), 124.7, 122.5–122.8 (m) ppm. <sup>19</sup>F NMR (650 MHz, D<sub>2</sub>O) δ -62.6 ppm. HRMS (ESI): (M+H)<sup>+</sup> calcd. for C<sub>11</sub>H<sub>7</sub>F<sub>6</sub>NO<sup>+</sup>, 284.0510; found, 284.0509.

**Ethyl 3-(3,5-bis(trifluoromethyl)phenyl)acrylate (8)** <sup>[33]</sup>

In a sealed tube 0.35 mL 3,4-bis(trifluoromethyl)bromobenzene (2 mmol), ethylacrylate (0.26 mL, 2.4 mmol), Pd(OAc)<sub>2</sub> (11 mg, 0.05 mmol), diisopropylethylamine (0.42 mL, 2.4 mmol) and tri(*o*-tolyl)phosphine (30 mg, 0.1 mmol) was added to dimethylformamide (5 mL) under Ar and heated at 100 °C for 4 h. The crude mixture was filtered from activated charcoal and water:MeOH 1:1 was added. The forming yellow crystals were filtered (300 mg, 48%). <sup>1</sup>H NMR (500 MHz, DMSO-*d*<sub>6</sub>) δ 8.46 (s, 1H, ArH), 8.08 (s, 2H, ArH), 7.81 (d, *J* = 16.1 Hz, 1H, =CH-), 7.02 (d, *J* = 16.1 Hz, 1H, =CH-), 4.20 (q, *J* = 7.1 Hz, 1H, CH<sub>2</sub>), 1.26 (t, *J* = 7.1 Hz, 2H, CH<sub>3</sub>) ppm. <sup>19</sup>F NMR (650 MHz, D<sub>2</sub>O) δ -64.5 ppm.

**3-(3,5-Bis(trifluoromethyl)phenyl)acrylonitrile (9)**

In a sealed tube 3,4-bis(trifluoromethyl)bromobenzene (0.69 mL, 4 mmol), acrylonitrile (0.32 mL, 4.8 mmol), Pd(OAc)<sub>2</sub> (9 mg, 0.04 mmol), diisopropyl-ethylamine (0.84 mL, 4.8 mmol) and biphenyl-diisopropylphosphine (24 mg, 0.08 mmol) was added to dimethylacetamide (2 mL) under Ar and heated at 130 °C for 4 h. Then 10 mL water and 20 mL methyl-*t*-butylether was added to the reaction mixture and the phases were separated. The organic phase was dried over MgSO<sub>4</sub>, filtered, and evaporated to silica. The residue was purified with flash column chromatography with hexane and ethyl acetate eluent mixture to give the product as a white solid (120 mg, 11%). <sup>1</sup>H NMR (500 MHz, CDCl<sub>3</sub>) δ 7.92 (s, 1H, ArH), 7.88 (s, 2H, ArH), 7.47 (d, *J* = 16.7 Hz, 1H, =CH-), 6.08 (d, *J* = 16.7 Hz, 1H, =CH-) ppm. <sup>13</sup>C NMR (125 MHz, CDCl<sub>3</sub>)

δ 146.9, 135.4, 133.9 (d, *J* = 33.8 Hz), 127.3 (q, *J* = 3.9 Hz), 124.4–124.2 (m), 122.7 (d, *J* = 272.9 Hz), 116.6, 101.01 ppm. <sup>19</sup>F NMR (650 MHz, D<sub>2</sub>O) δ -62.8 ppm. HRMS calcd. for C<sub>11</sub>H<sub>6</sub>F<sub>6</sub>N 266.0404; found 266.0396.

**Methyl 3-(3,5-bis(trifluoromethyl)phenyl)propionate (10)** <sup>[34]</sup>

In a sealed tube 3,5-bis(trifluoromethyl)phenylboronic acid (218 mg, 1 mmol), methyl propionate (0.13 mL, 1.5 mmol), copper(I) iodide (29 mg, 0.15 mmol), silver(I) oxide (462 mg, 2 mmol) and caesium carbonate (652 mg, 2 mmol) was dissolved in dichloroethane (5 mL). The reaction mixture was stirred under Ar at 80 °C overnight. 10 mL water was added to the mixture then the separated organic layer was washed with brine, dried over Na<sub>2</sub>SO<sub>4</sub>, filtered, and concentrated under vacuum. The crude product was purified by flash column chromatography with mixture of hexane and ethyl acetate as eluent. The product was obtained as a light brown oil (115 mg, 39%). <sup>1</sup>H NMR (CDCl<sub>3</sub>) δ 8.06 (2H, s, ArH), 7.94 (s, 1H, ArH), 3.88 (3H, CH<sub>3</sub>) ppm. <sup>19</sup>F NMR (650 MHz, D<sub>2</sub>O) δ -64.9 ppm.

**3,5-Bis(trifluoromethyl)phenyl vinylsulfone (11)** <sup>[35]</sup>

3,5-Bis(trifluoromethyl)thiophenol (505 μL, 3 mmol) and potassium-carbonate (830 mg, 6 mmol) was dissolved in *N,N*-dimethylformamide (25 mL), then 2-chloroethanol (270 μL, 4 mmol) was added and the mixture was stirred at RT. After 4 hours, the solvent was evaporated and the residue was dissolved in 50 mL ethyl acetate, then washed with 50 mL brine. The organic layer was dried and concentrated. The crude product was dissolved in 30 mL dichloromethane and *meta*-chloroperoxybenzoic acid (1.29 g, 7.5 mmol) was added slowly. The mixture was stirred for 3 hours, then it was washed with 1 M aqueous solution of sodium hydroxide. After the extraction the organic phase was dried and concentrated, then the product was dissolved in 20 mL dry dichloromethane. To this solution methanesulfonyl-chloride (230 μL, 3 mmol) was added at 0 °C, then triethylamine (625 μL, 4.5 mmol) was dropped slowly into the mixture. After the addition of the base, the reaction was heated up to RT and stirred for 3 hours. Finally, the solvent was removed and the crude product was purified by column chromatography to give the **11** vinylsulfone product (128 mg, 14%) <sup>1</sup>H NMR (500 MHz, DMSO-*d*<sub>6</sub>) δ 8.34 (s, 2H), 8.13 (s, 1H), 6.74 – 6.61 (m, 2H), 6.24 (d, *J* = 8.7 Hz, 1H) ppm. <sup>19</sup>F NMR (650 MHz, D<sub>2</sub>O) δ -62.8 ppm.

**3,5-Bis(trifluoromethyl)benzyl vinylsulfone (12)**

3,5-Bis(trifluoromethyl)benzyl chloride (1313 mg, 5 mmol) in *N,N*-dimethylformamide (10 mL) was added dropwise to the solution of 2-mercaptoethanol (350 μL, 5 mmol) and potassium carbonate (1037 mg, 7.5 mmol) in *N,N*-dimethylformamide (20 mL), then the mixture was stirred at RT. After 3 hours, the solvent was evaporated and the residue was dissolved in 50 mL ethyl acetate, then washed with 50 mL brine. The organic layer was dried and concentrated. The crude product was dissolved in 50 mL dichloromethane and *meta*-chloroperoxybenzoic acid (2.16 g, 12.5 mmol) was added slowly. The mixture was stirred for 3 hours, and then it was washed with 1 M aqueous solution of sodium hydroxide. After the extraction the organic phase was dried and concentrated, then the product was dissolved in 20 mL dry dichloromethane. To this solution methanesulfonyl-chloride (464 μL, 6 mmol) was added at 0 °C, and triethylamine (1043 μL, 7.5 mmol) was dropped slowly into the mixture. After the addition of the base, the reaction was heated up to RT and stirred for 2 hours. Finally, the solvent was removed and the product was purified by column chromatography to obtain **12** as a white powder (328 mg, 21%). <sup>1</sup>H NMR (500 MHz, DMSO-*d*<sub>6</sub>) δ 8.14 (s, 1H), 8.09 (s, 2H), 7.00 (dd, *J* = 16.6, 10.0 Hz, 1H), 6.26 (d, *J* = 9.9 Hz, 1H), 6.08 (d, *J* = 16.6 Hz, 3H), 4.84 (s, 6H) ppm. <sup>13</sup>C NMR (125 MHz, CDCl<sub>3</sub>) δ 136.4, 132.8, 132.2 (2C), 131.8, 130.7 (q, *J* = 32.5 Hz, 2C), 123.6 (q, *J* = 271.3 Hz, 2C), 122.8 – 122.6 (m), 57.9 ppm. <sup>19</sup>F NMR (650 MHz, D<sub>2</sub>O) δ -62.6 ppm. HRMS (DUI): (M-H)<sup>-</sup> calcd. for C<sub>11</sub>H<sub>7</sub>F<sub>6</sub>O<sub>2</sub>S<sup>-</sup>, 317.0076; found 317.0046.

***N*-(3,5-Bis(trifluoromethyl)benzyl)ethanesulfonamide (13)**

To a stirred solution of 3,5-bis(trifluoromethyl)benzyl amine (1215 mg, 5 mmol) and trimethylamine (2087 μL, 15 mmol) in DCM (40 mL) at 0 °C, 2-chloroethanesulfonylchloride (1045 μL, 10 mmol) was added dropwise.



## FULL PAPER

The resulting mixture was then stirred at 0 °C until the amine was consumed as determined by TLC. The reaction was quenched with water (300 mL) and the mixture was extracted with DCM (3 × 25 mL). The combined organic extracts were washed with brine (10 mL), dried with anhydrous Na<sub>2</sub>SO<sub>4</sub>. The solvent was removed under vacuum and the residue was purified by column chromatography with a mixture of hexane and ethyl acetate as the eluent, to give the product as a white powder (882 mg, 53%). <sup>1</sup>H NMR (500 MHz, DMSO-*d*<sub>6</sub>) δ 8.04 (t, *J* = 6.3 Hz, 1H), 8.03 (s, 2H), 8.00 (s, 1H) 6.74 (dd, *J* = 16.5, 10.0 Hz, 1H), 6.06 (d, *J* = 16.5 Hz, 1H), 5.98 (d, *J* = 10.0 Hz, 1H), 4.28 (d, *J* = 6.3 Hz, 2H) ppm. <sup>13</sup>C NMR (125 MHz, DMSO-*d*<sub>6</sub>) δ 147.3, 142.0, 135.4 (q, *J* = 32.5 Hz, 2C), 133.6 (2C), 131.2, 128.5 (q, *J* = 271.3 Hz, 2C), 126.3 – 126.0 (m), 49.9 ppm. <sup>19</sup>F NMR (650 MHz, D<sub>2</sub>O) δ –62.6 ppm. HRMS (DUIS): (M–H)<sup>–</sup> calcd. for C<sub>11</sub>H<sub>8</sub>F<sub>6</sub>NO<sub>2</sub>S<sup>–</sup>, 332.0185; found 332.0157.

**1-(Isothiocyanatomethyl)-3,5-bis(trifluoromethyl)benzene (15)**

In a round bottom flask 1,1'-thiocarbonylbis(pyridin-2(1*H*)-one) (3 mmol, 0.7 g) was dissolved in DCM (100 mL). 3,5-Bistrifluoromethylbenzylamine (0.24 g, 1 mmol) was dissolved in dichloromethane (50 mL) and added dropwise. The reaction mixture was stirred at RT for 50 min. Then the reaction mixture was washed with brine (2 × 20 mL) and 1 M HCl (20 mL), and the organic phase was dried over MgSO<sub>4</sub>. The solvent was evaporated, and the crude product was purified with flash column chromatography using hexane and ethyl acetate as the eluent (9:1) resulting in the product as a colourless oil (171 mg, 60%). <sup>1</sup>H NMR (500 MHz, CDCl<sub>3</sub>) δ 7.88 (s, 1H, ArH), 7.79 (s, 2H, ArH), 4.89 (s, 2H, CH<sub>2</sub>) ppm. <sup>13</sup>C NMR (125 MHz, CDCl<sub>3</sub>) 185.4 (d, *J* = 338.6 Hz), 140.0, 132.2 (d, *J* = 33.5 Hz), 127.7 – 127.5 (m), 124.1, 122.0 – 121.7 (m), 47.6 ppm. <sup>19</sup>F NMR (650 MHz, D<sub>2</sub>O) δ –64.4 ppm. HRMS (DUIS): (M–H)<sup>–</sup> calcd. for C<sub>10</sub>H<sub>4</sub>F<sub>6</sub>NS<sup>–</sup>, 283.9968; found 283.9967.

**Tert-butyl 2-(3,5-bis(trifluoromethyl)benzylidene)hydrazine carboxylate (19)**

3,5-Bis(trifluoromethyl)benzaldehyde (0.16 mL, 1 mmol) and *tert*-butyl hydrazinecarboxylate (145 mg, 1.1 mmol) were dissolved in 1:1 mixture of tetrahydrofuran and dichloromethane (30 mL). Then catalytic amount of H<sub>2</sub>SO<sub>4</sub> (1–2 drops) was added and the reaction was stirred at RT for 2 h. The solvent was removed under vacuum, then crude product was filtered through a silica pad using dichloromethane-methanol solvent mixture. Then 25 mL water and 25 mL ethyl acetate was added to the residue. After the separation, the organic layer was washed with brine, dried over Na<sub>2</sub>SO<sub>4</sub>, filtered, and concentrated under vacuum. The product was obtained by flash column chromatography with a mixture of hexane and ethyl acetate as the eluent. The product was obtained as a yellow powder (281 mg, 78%). <sup>1</sup>H NMR (500 MHz, DMSO-*d*<sub>6</sub>) δ 11.29 (s, 1H, NH), 8.25 (s, 2H, ArH), 8.15 (s, 1H, ArH), 8.05 (s, 1H, =CH–), 1.46 (s, 9H, CH<sub>3</sub>) ppm. <sup>13</sup>C NMR (125 MHz, DMSO-*d*<sub>6</sub>) δ 152.7, 138.0 (2C), 131.2 (q, *J* = 33.1 Hz, 2C), 126.9–127.1 (m, 3C), 124.7, 122.6, 80.4, 29.4 (3C) ppm. <sup>19</sup>F NMR (650 MHz, D<sub>2</sub>O) δ –62.7 ppm. HRMS (ESI): (M+H)<sup>+</sup> calcd. for C<sub>14</sub>H<sub>14</sub>F<sub>6</sub>N<sub>2</sub>O<sub>2</sub><sup>+</sup>, 357.1037; found, 357.1039.

**N-(3,5-bis(trifluoromethyl)benzyl)cyanamide (20)**

To a cooled solution (0 °C) of 3,5-bis(trifluoromethyl)benzyl amine (486 mg, 2 mmol) in dry diethyl ether (20 mL) cyanogen bromide as 3 M solution in DCM (100 μL, 2 mmol) was added dropwise. The reaction was warmed to RT and stirred for 16 h. The mixture was filtered to remove the residual salt and the filtrate was concentrated. The residue was diluted in 25 mL ethyl acetate, washed with water (30 mL) and brine (30 mL). Organic extracts were dried over Na<sub>2</sub>SO<sub>4</sub>, filtered, and concentrated under vacuum. The product was obtained by flash column chromatography with a mixture of hexane and ethyl acetate as the eluent. Compound **20** was obtained as a white solid (453 mg, 34%). <sup>1</sup>H NMR (500 MHz, DMSO-*d*<sub>6</sub>) δ 8.05 (s, 1H), 7.41 (s, 1H), 4.34 (d, *J* = 4.0 Hz, 1H) ppm. <sup>13</sup>C NMR (125 MHz, CDCl<sub>3</sub>) δ 142.0, 130.9 (q, *J* = 32.8 Hz, 2C), 129.0 (2C), 123.7 (q, *J* = 268.3 Hz, 2C), 122.7 – 121.9 (m), 117.2, 47.6 ppm. <sup>19</sup>F NMR (650 MHz, D<sub>2</sub>O) δ –62.5 ppm. HRMS (DUIS): (M–H)<sup>–</sup> calcd. for C<sub>10</sub>H<sub>8</sub>F<sub>6</sub>N<sub>2</sub>, 267.0362; found 267.0325.

**N-(3,5-bis(trifluoromethyl)phenyl)-2-chloro-acetamide (21)<sup>[36]</sup>**

The same procedure as for **1** except using chloroacetyl chloride (0.80 mL, 10 mmol). Pure **21** was obtained as a white powder (2.31 g, 75%). <sup>1</sup>H NMR (500 MHz, DMSO-*d*<sub>6</sub>) δ 10.90 (s, 1H, NH), 8.24 (s, 2H, ArH), 7.80 (s, 1H, ArH), 4.32 (s, 2H, CH<sub>2</sub>Cl) ppm. <sup>19</sup>F NMR (650 MHz, D<sub>2</sub>O) δ –62.7 ppm.

**N-(3,5-bis(trifluoromethyl)phenyl)-2-chloro-propanamide (22)<sup>[31]</sup>**

The same procedure as for **1** except using 2-chloropropanoyl chloride (0.97 mL, 10 mmol) and the reaction mixture was allowed to stir at RT overnight. Crude product was purified by flash column chromatography with a mixture of hexane and ethyl acetate as an eluent to give the pure product as a white powder (1.35 g, 42%). <sup>1</sup>H NMR (500 MHz, CDCl<sub>3</sub>) δ 10.21 (s, 1H, NH), 8.34 (s, 2H, ArH), 7.68 (s, 1H, ArH), 5.38 (q, *J* = 7.0 Hz, 1H, CHCl), 1.99 (d, *J* = 7.1 Hz, 3H, CH<sub>3</sub>) ppm. <sup>19</sup>F NMR (650 MHz, D<sub>2</sub>O) δ –62.7 ppm.

**N-(3,5-bis(trifluoromethyl)phenyl)-2-bromo-propanamide (23)<sup>[31]</sup>**

The same procedure as for **1** except using 2-bromopropanoyl chloride (1.01 mL, 10 mmol) and the reaction mixture was allowed to stir at RT for 2 days. Crude product was purified by flash column chromatography with a mixture of hexane and ethyl acetate as an eluent to give the pure product as a brown powder (1.38 g, 38%). <sup>1</sup>H NMR (500 MHz, DMSO-*d*<sub>6</sub>) δ 10.95 (s, 1H, NH), 8.25 (s, 1H, ArH), 7.78 (s, 1H, ArH), 4.67 (q, *J* = 6.7 Hz, 1H, CHBr), 1.76 (d, *J* = 6.7 Hz, 1H, CH<sub>3</sub>) ppm. <sup>19</sup>F NMR (650 MHz, D<sub>2</sub>O) δ –62.7 ppm.

**1-(3,5-Bis(trifluoromethyl)phenyl)-2-bromoethanone (24)<sup>[37]</sup>**

To a stirred solution of 3',5'-bis(trifluoromethyl)acetophenone (0.18 mL, 1 mmol) in THF (10 mL) pyridinium tribromide (0.32 mL, 1 mmol) dissolved in THF (10 mL) was added dropwise. The reaction mixture was stirred for 4 h. Water (20 mL) was added, and the phases were separated. The aqueous phase was extracted with ethyl acetate (2 × 20 mL). The organic phase was dried over MgSO<sub>4</sub> and evaporated. Flash column chromatography using hexane and ethyl acetate (95:5) as the eluent afforded the product as a yellow oil that solidified overnight (190 mg, 57%). <sup>1</sup>H NMR (500 MHz, DMSO-*d*<sub>6</sub>) δ 8.55 (s, 2H, ArH), 8.44 (s, 1H, ArH), 5.12 (s, 2H, CH<sub>2</sub>Br) ppm. <sup>19</sup>F NMR (650 MHz, D<sub>2</sub>O) δ –62.7 ppm.

**2-(3,5-Bis(trifluoromethyl)phenyl)oxirane (25)<sup>[38]</sup>**

3,5-Bistrifluoromethylphenyl-styrene (0.36 mL, 2 mmol) was dissolved in chloroform (20 mL), and *meta*-chloroperoxybenzoic acid (1.38 g, 4 mmol) was added at 0 °C. The reaction mixture was stirred overnight, followed by washing with saturated NaHCO<sub>3</sub> (10 mL). The organic phase was dried over MgSO<sub>4</sub> and evaporated. The crude product was purified with flash chromatography using hexane and ethyl acetate (93:7) as the eluent, resulting in the product as a colourless oil (364 mg, 71%). <sup>1</sup>H NMR (500 MHz, CDCl<sub>3</sub>) δ 7.82 (s, 1H, ArH), 7.74 (s, 2H, ArH), 3.99 (dd, *J* = 3.8, 2.6 Hz, 1H, CH<sub>2</sub>O), 3.23 (dd, *J* = 5.3, 4.1 Hz, 1H, CH<sub>2</sub>O), 2.79 (dd, *J* = 5.4, 2.4 Hz, 1H, CH<sub>2</sub>O) ppm. <sup>19</sup>F NMR (650 MHz, D<sub>2</sub>O) δ –62.6 ppm.

**Acknowledgements**

The research was funded by H2020 MSCA Fagnet (project 675899), SNN 125496, OTKA PD124598 and 2018-2.1.11-TÉT SI-2018-00005, NVKP\_16-1-2016-0020 and NKP-2018-1.2.1-NKP-2018-00005 (National Research, Development and Innovation Office of Hungary), the ELTE Thematic Excellence Programme and BME-Biotechnology FIKP grant (BME FIKP-BIO) supported by the Hungarian Ministry for Innovation and Technology, the Slovenian Research Agency (Grants Z1-1859 N1-0068, J3-1745, J1-8145 and P1-0208), and a grant from the Hessian Landes-Offensive zur Entwicklung Wissenschaftlich-ökonomischer Exzellenz (LOEWE TRABITA). The work of A.

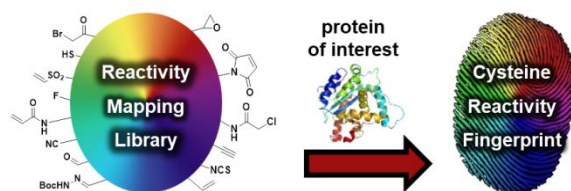
## FULL PAPER

Scarpino, K. Németh, G. Koppány and I. Vida is gratefully acknowledged.

**Keywords:** drug design • electrophilic warheads • KRAS<sup>G12C</sup> • MAO • targeted covalent inhibitors

- [1] a) T. A. Baillie, *Angew. Chemie Int. Ed.* **2016**, *55*, 13408–13421; b) R. A. Bauer, *Drug Discov. Today* **2015**, *20*, 1061–1073. c) A. Vasudevan, M. A. Argiriadi, A. Baranczak, M. Friedman, J. Gavriluyk, A. D. Hobson, J. J. Hulce, S. Osman, N. S. Wilson, *Prog. Med. Chem.* **2019**, *58*, 1–62.
- [2] D. A. Shannon, E. Weerapana, *Curr. Opin. Chem. Biol.* **2015**, *24*, 18–26.
- [3] a) A. J. T. Smith, X. Zhang, A. G. Leach, K. N. Houk, *J. Med. Chem.* **2009**, *52*, 225–233; b) C. González-Bello, *ChemMedChem* **2016**, *11*, 22–30.
- [4] A. Tuley, W. Fast, *Biochemistry* **2018**, *57*, 3326–3337.
- [5] M. Gersch, J. Kreuzer, S. A. Sieber, *Nat. Prod. Rep.* **2012**, *29*, 659–682.
- [6] a) T. Zhang, J. M. Hatcher, M. Teng, N. S. Gray, M. Kostic, *Cell Chem. Biol.* **2019**, *26*, 1486–1500. b) M. Gehringer, S. A. Laufer, *J. Med. Chem.* **2019**, *62*, 5673–5724. c) J. S. Martin-Claire, J. McKenzie, D. F. Ian, H. Gilbert, *Bioorg. Med. Chem.* **2019**, *27*, 2066–2074.
- [7] S. G. Kathman, A. V. Statsyuk, *MedChemComm* **2016**, *7*, 576–585.
- [8] a) A. M. Embaby, S. Schoffelen, C. Kofoed, M. Meldal, F. Diness, *Angew. Chemie Int. Ed.* **2018**, *57*, 8022–8026; b) P. Martín-Gago, C. A. Olsen, *Angew. Chemie Int. Ed.* **2019**, *58*, 957–966.
- [9] E. Weerapana, C. Wang, G. M. Simon, F. Richter, S. Khare, M. B. D. Dillon, D. A. Bachovchin, K. Mowen, D. Baker, B. F. Cravatt, *Nature* **2010**, *468*, 790–795.
- [10] a) W. Zhang, J. Pei, L. Lai, *J. Chem. Inf. Model.* **2017**, *57*, 1453–1460.; b) E. Awoonor-Williams, C. N. Rowley, *J. Chem. Inf. Model.* **2018**, *58*, 1935–1946.; c) R. Liu, Z. Yue, C. C. Tsai, J. Shen, *J. Am. Chem. Soc.* **2019**, *141*, 6553–6560. d) Z. Zhao, Q. Liu, S. Bliven, L. Xie, P. E. Bourne, *J. Med. Chem.* **2017**, *60*, 2879–2889.
- [11] a) E. Resnick, A. Bradley, J. Gan, A. Douangamath, T. Krojer, R. Sethi, P. P. Geurink, A. Aimon, G. Amitai, D. Bellini, J. Bennett, M. Fairhead, O. Fedorov, R. Gabizon, J. Gan, J. Guo, A. Plotnikov, N. Reznik, G. F. Ruda, L. Díaz-Sáez, V. M. Straub, T. Szommer, S. Velupillai, D. Zaidman, Y. Zhang, A. R. Coker, C. G. Dowson, H. M. Barr, C. Wang, K. V. M. Huber, P. E. Brennan, H. Ovaa, F. von Delft N. London, *J. Am. Chem. Soc.* **2019**, *141*, 8951–8968. b) A. Keeley, L. Petri, P. Ábrányi-Balogh, G. M. Keserű, *Drug Discov. Today* **2020**, *25*, 983–996.
- [12] a) P. Ábrányi-Balogh, L. Petri, T. Imre, P. Szijj, A. Scarpino, M. Hrast, A. Mitrović, U. P. Fonovič, K. Németh, H. Barreateau, D. I. Roper, K. Horvát, G. G. Ferenczy, J. Kos, J. Ilaš, S. Gobec, G. M. Keserű, *Eur. J. Med. Chem.* **2018**, *160*, 94–107. b) E. H. Krenske, R. C. Petter, K. N. Houk, *J. Org. Chem.* **2016**, *81*, 11726–11733; c) V. J. Cee, L. P. Volak, Y. Chen, M. D. Bartberger, C. Tegley, T. Arvedson, J. McCarter, A. S. Tasker, C. Fotsch, *J. Med. Chem.* **2015**, *58*, 9171–9178; d) R. Lonsdale, J. Burgess, N. Colclough, N. L. Davies, E. M. Lenz, A. L. Orton, R. A. Ward, *J. Chem. Inf. Model.* **2017**, *57*, 3124–3137; e) A. A. Adhikari, T. C. M. Seegar, S. B. Ficarro, M. D. McCurry, D. Ramachandran, L. Yao, S. N. Chaudhari, S. Ndousse-Fetter, A. S. Banks, J. A. Marto, S. C. Blacklow, A. S. Devlin, *Nat. Chem. Biol.* **2020**, *16*, 318–326.
- [13] a) A. Liu, X. Wang, X. Ou, M. Huang, C. Chen, S. Liu, L. Huang, X. Liu, C. Zhang, Y. Zheng, Y. Ren, L. He, J. Yao, *J. Agric. Food Chem.* **2008**, *56*, 6562–6566; b) B. Lallemand, F. Chaix, M. Bury, C. Bruyère, J. Ghostin, J.-P. Becker, C. Delporte, M. Gelbcke, V. Mathieu, J. Dubois, M. Prévost, I. Jabin, R. Kiss, *J. Med. Chem.* **2011**, *54*, 6501–6513.
- [14] M. E. Flanagan, J. A. Abramite, D. P. Anderson, A. Aulabaugh, U. P. Dahal, A. M. Gilbert, C. Li, J. Montgomery, S. R. Oppenheimer, T. Ryder, B. P. Schuff, D. P. Uccello, G. S. Walker, Y. Wu, M. F. Brown, J. M. Chen, M. M. Hayward, M. C. Noe, R. S. Obach, L. Philippe, V. Shanmugasundaram, M. J. Shapiro, J. Starr, J. Stroh, Y. Che, *J. Med. Chem.* **2014**, *57*, 10072–10079.
- [15] I. M. Serafimova, M. A. Pufall, S. Krishnan, K. Duda, M. S. Cohen, R. L. Maglathlin, J. M. McFarland, R. M. Miller, M. Frödin, J. Taunton, *Nat. Chem. Biol.* **2012**, *8*, 471–476.
- [16] H. Han, Y. Yang, S. H. Olesen, A. Becker, S. Betzi, E. Schönbrunn, *Biochemistry* **2010**, *49*, 4276–4282.
- [17] L. De Colibus, M. Li, C. Binda, A. Lustig, D. E. Edmondson, A. Mattevi, *Proc. Natl. Acad. Sci. USA* **2005**, *102*, 12684–12689.
- [18] A. Chakrabarti, I. Oehme, O. Witt, G. Oliveira, W. Sippl, C. Romier, R. J. Pierce, M. Jung, *Trends Pharmacol. Sci.* **2015**, *36*, 481–492.
- [19] O. Witt, H. E. Deubzer, T. Milde, I. Oehme, *Cancer Lett.* **2009**, *277*, 8–21.
- [20] M. Muth, N. Jänsch, A. Koprancovic, A. Krämer, N. Wössner, M. Jung, F. Kirschhöfer, G. Brenner-Weiβ, F.-J. Meyer-Almes, *Biochim. Biophys. Acta Gen. Subj.* **2019**, *1863*, 577–585.
- [21] T. A. Thibaudeau, D. M. Smith, *Pharmacol. Rev.* **2019**, *71*, 170–197.
- [22] J. M. L. Ostrem, K. M. Shokat, *Nat. Rev. Drug Discov.* **2016**, *15*, 771–785.
- [23] R. J. Simpson, *CSH. Protoc.* **2008**, *pdb.prot4699*.
- [24] K. Rožman, S. Lešnik, B. Brus, M. Hrast, M. Sova, D. Patin, H. Barreateau, J. Konc, D. Janežič, S. Gobec, *Bioorg. Med. Chem. Lett.* **2017**, *27*, 944–949.
- [25] O.-M. Bautista-Aguilera, A. Samadi, M. Chioua, K. Nikolic, S. Filipic, D. Agbaba, E. Soriano, L. de Andrés, M. I. Rodríguez-Franco, S. Alcaro, R. R. Ramsay, F. Ortuso, M. Yañez, J. Marco-Contelles, *J. Med. Chem.* **2014**, *57*, 10455–10463.
- [26] H. von der Eltz, H.-J. Guder, K. Muehlegger, *US4900822* **1990**.
- [27] M. Li, F. Hubálek, P. Newton-Vinson, D. E. Edmondson, *Protein Expr. Purif.* **2002**, *24*, 152–162.
- [28] F. Hubálek, J. Pohl, D. E. Edmondson, *J. Biol. Chem.* **2003**, *278*, 28612–28618.
- [29] <http://prospector.ucsf.edu/prospector/mshome.htm> (retrieved on 10/08/2020)
- [30] G. Pálffy, I. Vida, A. Perczel, *Biomol. NMR Assign.* **2020**, *14*, 1–7.
- [31] B. F. Cravatt, *WO2017210600/A1* **2017**.
- [32] R. Callahan, O. Ramirez, K. Rosmarion, R. Rothchild, K. C. Bynum, *J. Heterocycl. Chem.* **2005**, *42*, 889–898.
- [33] Y.-H. Zhang, B.-F. Shi, J.-Q. Yu, *J. Am. Chem. Soc.* **2009**, *131*, 5072–5074.
- [34] A. W.-H. Cheung, S. B. Ferguson, L. H. Foley, A. J., Lovey, *US6310247/B1* **2001**.
- [35] L. Al-Riyami, M. A. Pineda, J. Rzepecka, J. K. Huggan, A. I. Khalaf, C. J. Suckling, F. J. Scott, D. T. Rodgers, M. M. Harnett, W. Harnett, *J. Med. Chem.* **2013**, *56*, 9982–10002.
- [36] T. R. K. Reddy, C. Li, X. Guo, P. M. Fischer, L. V. Dekker, *Bioorg. Med. Chem.* **2014**, *22*, 5378–5391.
- [37] Z.-W. Chen, D.-N. Ye, M. Ye, Z.-G. Zhou, S.-H. Li, L.-X. Liu, *Tetrahedron Lett.* **2014**, *55*, 1373–1375.
- [38] S. A. Weissman, K. Rossen, P. J. Reider, *Org. Lett.* **2001**, *3*, 2513–2515.

## Entry for the Table of Contents



We present a toolbox of covalent fragments containing chemically diverse electrophilic warheads. By screening this library against a set of enzymes amenable for covalent inhibition, we experimentally characterized the accessibility and reactivity of targeted cysteines. We propose this approach to be used as an experimental method for warhead selection in the development of targeted covalent inhibitors or irreversible probes.

Accepted Article

Accepted Manuscript

---

**Titel:**

3-Chloro-5-Substituted-1,2,4-Thiadiazoles (TDZs) as Selective and Efficient Protein Thiol Modifiers

**Autoren:**

Niklas Jansch, Anton Frühauf, Markus Schweipert, Cécile Debarnot, Miriam Erhardt, Gerald Brenner-Weiss, Frank Kirschhöfer, Thomas Jasionis, Edita Capkauskaitė, Asta Zubriene, Damantas Matulis, Franz-Josef Meyer-Almes

**Bibliographische Daten:**

ChemBioChem (doi.org/10.1002/cbic.202200417)

**Zusammenfassung:**

Der Untersuchung von Cysteinmodifikationen wurde in den letzten Jahren viel Aufmerksamkeit geschenkt. Dazu gehören detaillierte Untersuchungen auf dem Gebiet der Redoxbiologie mit Schwerpunkt auf den zahlreichen Redoxderivaten wie Nitrosothiolen, Sulfensäuren, Sulfinensäuren und Sulfonsäuren, welche durch eine zunehmende Oxidation entstehen, sowie der S-Lipidierung und Perthiolen. Für diese Studien ist eine selektive und schnelle Blockierung von freien Protein Thiolen erforderlich, um Disulfid-Austauschreaktionen zu verhindern. In unserer Suche nach neuen Inhibitoren der humanen Histondeacetylase 8 (HDAC8) entdeckten wir 5-Sulfonyl- und 5-Sulfinyl-substituierte 1,2,4-Thiadiazole (TDZ), die überraschenderweise eine hervorragende Reaktivität gegenüber Thiolen in wässriger Lösung zeigen. Ermutigt durch diese Beobachtungen haben wir den Wirkmechanismus im Detail untersucht und zeigen, dass diese Verbindungen spezifischer und schneller reagieren als das üblicherweise verwendete N-Ethylmaleinimid, was sie zu hervorragenden Alternativen für die effiziente Blockierung freier Thiole in Proteinen macht. Wir zeigen, dass 5-Sulfonyl TDZ ohne weiteres in gängigen Biotin-Switch-Assays eingesetzt werden kann. Am Beispiel von humaner HDAC8 zeigen wir, dass die Cysteinmodifikation durch ein 5-Sulfonyl-TDZ mit quantitativer HPLC/ESI- und QTOF-MS/MS-Methode leicht messbar ist und die gleichzeitige Messung der Modifikationskinetik von sieben lösungsmittelzugänglichen Cysteinen in HDAC8.

# 3-Chloro-5-Substituted-1,2,4-Thiadiazoles (TDZs) as Selective and Efficient Protein Thiol Modifiers

Niklas Jänsch,<sup>[a]</sup> Anton Frühauf,<sup>[a]</sup> Markus Schweipert,<sup>[a]</sup> Cécile Debarnot,<sup>[a]</sup> Miriam Erhardt,<sup>[b]</sup> Gerald Brenner-Weiss,<sup>[b]</sup> Frank Kirschhöfer,<sup>[b]</sup> Tomas Jasionis,<sup>[c]</sup> Edita Čapkauskaitė,<sup>[c]</sup> Asta Zubrienė,<sup>[c]</sup> Daumantas Matulis,<sup>[c]</sup> and Franz-Josef Meyer-Almes<sup>\*[a]</sup>

The study of cysteine modifications has gained much attention in recent years. This includes detailed investigations in the field of redox biology with focus on numerous redox derivatives like nitrosothiols, sulfenic acids, sulfinic acids and sulfonic acids resulting from increasing oxidation, S-lipidation, and perthiols. For these studies selective and rapid blocking of free protein thiols is required to prevent disulfide rearrangement. In our attempt to find new inhibitors of human histone deacetylase 8 (HDAC8) we discovered 5-sulfonyl and 5-sulfinyl substituted 1,2,4-thiadiazoles (TDZ), which surprisingly show an outstanding reactivity against thiols in aqueous solution. Encouraged by

these observations we investigated the mechanism of action in detail and show that these compounds react more specifically and faster than commonly used *N*-ethyl maleimide, making them superior alternatives for efficient blocking of free thiols in proteins. We show that 5-sulfonyl-TDZ can be readily applied in commonly used biotin switch assays. Using the example of human HDAC8, we demonstrate that cysteine modification by a 5-sulfonyl-TDZ is easily measurable using quantitative HPLC/ESI-QTOF-MS/MS, and allows for the simultaneous measurement of the modification kinetics of seven solvent-accessible cysteines in HDAC8.

## Introduction

Cysteines are underrepresented amino acids in proteins, which are very often highly conserved in protein families indicating their structural and functional importance. Cysteines can undergo numerous posttranslational modifications (PTMs), which maintain redox homeostasis inside cells, as well as cell signaling via coupled redox systems.<sup>[1]</sup> There is a range of reversible thiol modifications, such as intramolecular or intermolecular disulfide formation between proteins, but also between a protein and a low molecular weight thiol. Other modifications include nitrosothiols, sulfenic acids, sulfinic acids and sulfonic acids resulting from increasing oxidation, S-lipidation, and perthiols.<sup>[1c,2]</sup> All of these modifications have been shown to be involved in a variety of biological processes.<sup>[3]</sup> Thus, there is a growing

interest in analyzing these PTMs to expand the knowledge about the biological role of a cysteine containing protein in every possible modification state and correlate these results with biological activity. The typical chemical approach to study cysteine modifications on proteins involves selective labeling of reduced cysteine residues by a highly reactive blocking agent, which is compatible with aqueous solutions.<sup>[2a,4]</sup> Effective capture of unmodified cysteines prevents subsequent unspecific oxidation or other thiol-mediated cross-reactions, which can obscure the analysis of cysteine modifications during sample preparation. Chemical modification of cysteines are widely used to facilitate biophysical studies for the elucidation of molecular mechanisms.<sup>[5]</sup>

Furthermore, originally unmodified cysteines can be unambiguously identified by mass spectrometry and the expected mass shift upon thiol blocking. If more than one cysteine is contained in an analyzed peptide fragment, the specific position, where the modification has occurred, can be assigned by using MS/MS fragmentation procedures.<sup>[6]</sup> Most standard operation procedures employ iodoacetamide (IAM) or *N*-ethyl maleimide (NEM) as rather thiol-selective thiol-modifier in the first step of cysteine PTM analysis. Consequently, the efficiency of assays to examine thiol-modifications relies heavily on the reactivity and selectivity of the used thiol modifying reagent. Although widely used, IAM and NEM have been shown to also react with other nucleophilic amino acids, such as lysine or histidine.<sup>[7]</sup> Consequently, thiol blocking reagents with improved reactivity and selectivity are required to optimize the analysis of protein PTMs at cysteine residues, which is particularly true for large scale proteomic studies. Methylsulfonyl benzothiazole (MSBT) has been suggested as effective and selective thiol blocker alternative to commonly used IAM and NEM.<sup>[8]</sup> MSBT contains a methylsulfonyl leaving group,

[a] N. Jänsch, A. Frühauf, M. Schweipert, C. Debarnot, Prof. Dr. F.-J. Meyer-Almes  
Fachbereich Chemie-und Biotechnologie  
Hochschule Darmstadt, Stephanstraße 7, 64295 Darmstadt (Germany)  
E-mail: franz-josef.meyer-almes@h-da.de

[b] M. Erhardt, Dr. G. Brenner-Weiss, F. Kirschhöfer  
Bioproszesstechnik und Biosysteme  
Institut für Funktionelle Grenzflächen  
Karlsruher Institut für Technologie  
Kaiserstraße 12, 76131 Karlsruhe (Germany)

[c] T. Jasionis, Dr. E. Čapkauskaitė, Dr. A. Zubrienė, Prof. Dr. D. Matulis  
Department of Biothermodynamics and Drug Design, Institute of Biotechnology, Life Sciences Center  
Vilnius University, Saulėtekio 7, Vilnius 10257 (Lithuania)

Supporting information for this article is available on the WWW under <https://doi.org/10.1002/cbic.202200417>

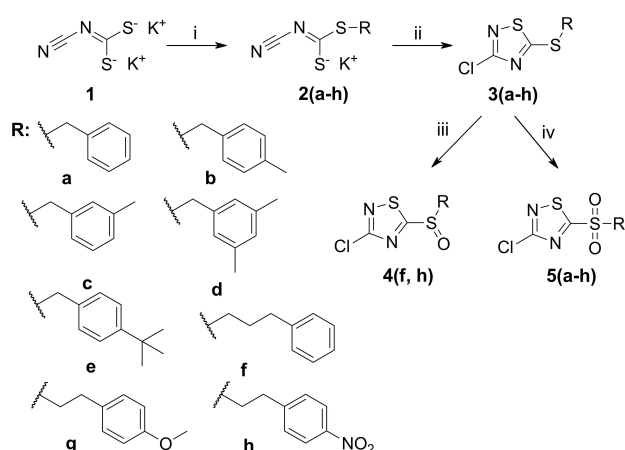
© 2022 The Authors. ChemBioChem published by Wiley-VCH GmbH. This is an open access article under the terms of the Creative Commons Attribution Non-Commercial NoDerivs License, which permits use and distribution in any medium, provided the original work is properly cited, the use is non-commercial and no modifications or adaptations are made.

which is attached to the C-2 position of a 1,3-benzothiazole moiety. Interestingly, we identified very similar compounds as inhibitors of human histone deacetylase 8 (HDAC8), and wondered, whether these compounds unfold their inhibitory effect through modification of C153, which is located in the active site pocket of HDAC8. In this study we elucidate the molecular interaction between thiol groups in HDAC8 and low molecular weight thiol model compounds with 3-chloro-1,2,4-thiadiazole (TDZ) analogues, which carry organo-sulfonyl, -sulfinyl or -sulfanyl substituents at 5-position as potential leaving groups. The observed thiol-modifications are further analyzed by kinetic experiments, quantitative HPLC/ESI-QTOF tandem mass spectrometry and supporting techniques.

## Results and Discussion

In our current research attempts we discovered a variety of 5-sulfonyl-3-chloro-1,2,4-thiadiazoles as potent HDAC8 inhibitors. To explore the structure activity relationship and the mode of action of this class of compounds further, we synthesized a series of analogues. The synthesis of 3-chloro-5-substituted-1,2,4-thiadiazoles was performed according to Wittenbrook (Scheme 1).<sup>[9]</sup> Dipotassium cyanodithioimidocarbonate (**1**) was alkylated with various alkyl bromides (**a–h**) to give the corresponding monoalkyl derivatives **2(a–h)**. 3-chloro-5-alkylsulfanyl-1,2,4-thiadiazoles **3(a–h)** were synthesized by oxidative cyclization of monoalkyl derivatives **2(a–h)** with sulfuryl chloride. The obtained sulfanyl compounds **3(a–h)** were oxidized to sulfinyl compounds **4(f, h)**, and sulfonyl compounds **5(a–h)** using *in situ* generated peracetic acid (Scheme 1):

The IC<sub>50</sub>-values of **5(a–h)** were very similar between 0.1 and 0.3 μM under assay conditions suggesting that the R-group has essentially no influence on the inhibitory activity (Table S4). Corresponding compounds **4f** and **4h** were similarly active. All tested compounds of the 4- and 5-series showed high selectivity (20–160 fold) for class I HDAC HDAC8 compared to



**Scheme 1.** Synthesis of 2-chloro-5-substituted thiadiazole derivatives: i) RBr (**a–h**), H<sub>2</sub>O, acetone, 0 °C, r. t., 24 h, yield 55–88%; ii) SO<sub>2</sub>Cl<sub>2</sub>, CHCl<sub>3</sub>, 0 °C, r. t., 24 h, yield 43–78%; iii) 1.2 eq 30% H<sub>2</sub>O<sub>2</sub> (aq), 0 °C, r. t., 24 h, 25–90%; iv) 3 eq 30% H<sub>2</sub>O<sub>2</sub> (aq), 0 °C, r. t., 24 h, yield 31–87%.

class IIa member HDAC4. This might be explained by the fast modification of cysteines C153 and C275, which are involved in redox-regulation of HDAC8.<sup>[10]</sup> The cysteine redox switch partner of C153 in HDAC8, C102, as well as C275 are not present in HDAC4. In comparison, **3(a–h)** showed significantly lower inhibitory activity against HDAC8. Therefore, the SO<sub>2</sub><sup>-</sup> and SO-functionalities turned out as determining factor for HDAC8 activity.

Based on our knowledge of the special disulfide and cysteine dependent regulation mechanism of this enzyme and the structural similarity to the published cysteine modifier MSBT, we wondered whether compounds from the 4- and 5-series unfold their inhibitory potential through cysteine thiol modification. To test the general reactivity against thiols we used the thiol reactivity assay first described by Resnick et. al.<sup>[11]</sup> For that purpose we followed the time dependent loss in light absorption at 412 nm of 5-thio-2-nitrobenzoic acid (TNB<sup>2-</sup>) generated with TCEP from 5,5'-dithiobis-2-nitrobenzoic acid (DTNB) upon reaction of a cysteine modifier (Figure 1A and B). To our surprise we figured out that the reaction of 5-substituted sulfonyl TDZ (**5h**, 5-SO<sub>2</sub>-TDZ) occurs nearly immediately after mixing TNB<sup>2-</sup> with a stoichiometric amount of cysteine modifier (Figure 1B). The reaction was so fast that we were not able to observe a time dependent decrease in absorption in the time window of our instrumentation.

On the other hand, structurally very similar 5-substituted sulfinyl TDZ (**4f**, 5-SO-TDZ) is less reactive than the sulfonyl analogue. For this compound we observed a decrease in absorption in the first minutes of measurement. Interestingly, the 5-substituted sulfanyl analogue (**3h**, 5-S-TDZ) shows no reactivity towards free thiols. As a control we followed the reaction of *N*-ethylmaleimide (NEM) with TNB<sup>2-</sup> under the same experimental conditions. NEM reacts much slower than the examined **5h** and **4f**. All thiol-reactive compounds react to nearly 100% completion. These first experiments let us conclude, that TDZs are highly thiol reactive compounds with much higher reactivity against TNB<sup>2-</sup> as the frequently employed cysteine modifier NEM. A general reaction scheme for sulfonyl, sulfinyl and sulfanyl TDZ analogues is shown in Figure 2. The next question we asked was, whether TDZs are reacting solely with cysteine or also with other nucleophilic amino acids like serine, histidine and lysine. For that we set up several reactions and analyzed the conversion of the used 5-sulfonyl, sulfinyl and sulfanyl substituted TDZs by thin layer chromatography (TLC), HPLC-MS and HRMS.

The results (Figures S1–S19) show that the probed **5h** is not solely reacting with cysteine. It also consumes all of the histidine after 1 h at 30 °C. In contrast, the slower reacting **4f** basically reacts only with cysteine (Figures S2, S5–S13). We confirmed that **3h** (5-S-TDZ) is unreactive against cysteine and also does not react with histidine, lysine or serine (Figures S15–S17). Therefore, **4f** modifies cysteine selectively with a slightly lower reactivity compared with **5h**. Nevertheless, the reactivity of the probed **4f** is still much higher than that of the commonly used NEM, which makes it in our opinion an excellent agent for selective and rapid thiol blocking in aqueous solutions.

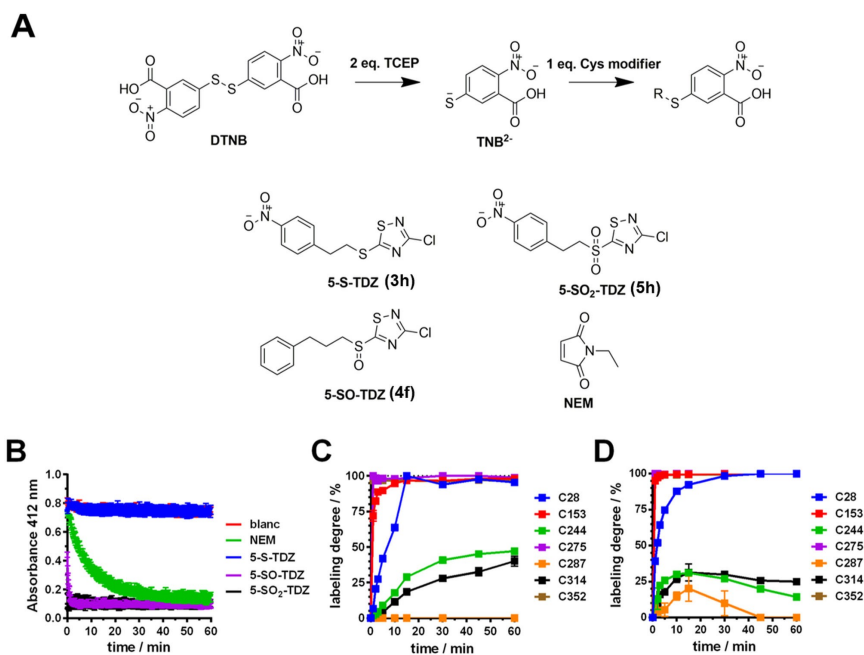


**Figure 1.**  $\text{TNB}^{2-}$  reactivity assay and covalent HDAC8 labelling. A) is showing the general reaction scheme of the used  $\text{TNB}^{2-}$  reactivity assay and the structures of the used compounds as cysteine modifiers. B) Reactivity of the four studied cysteine modifier against  $\text{TNB}^{2-}$  followed by decrease in absorbance at 412 nm. Time dependent increase in labeling degree of HDAC8 bound cysteines for *N*-benzyl maleimide (C) and **5h** (D), as determined from quantitative HPLC/ESI-QTOF measurements

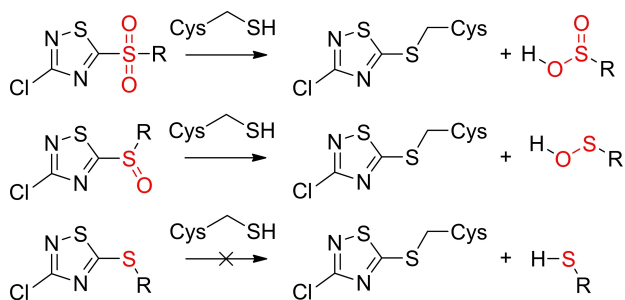


**Figure 2.** Reaction scheme for the reaction of 5- $\text{SO}_2$ -TDZs, 5- $\text{SO}$ -TDZs and 5- $\text{S}$ -TDZs with free cysteine thiols. 5- $\text{SO}_2$ -TDZs are reacting faster than 5- $\text{SO}$ -TDZs, whilst 5- $\text{S}$ -TDZs are showing no reactivity against free thiols.

Encouraged by the fast reactivity and selectivity towards cysteine we tested the potential for labeling of cysteine residues in HDAC8. HDAC8 consists of 10 cysteines showing special redox regulative features.<sup>[10]</sup> We quantified the degree of labeling for seven solvent accessible cysteine residues of HDAC8 by tryptic digestion and high resolution HPLC-MS/MS. With this approach we investigated whether **5h** has a beneficial labeling behavior by means of reactivity compared with *N*-benzyl maleimide. The protein was incubated with a 40-fold molar excess of arylating agent. The reaction was stopped after different indicated reaction times by trichloroacetic acid mediated protein precipitation. After removing cysteine modifiers in the supernatant, remaining free thiol groups of precipitated protein were labelled using NEM to enable the precise quantification of thiol groups not modified by **5h** or *N*-benzyl maleimide during the respective reaction time period.

The amount of *N*-benzyl maleimide and TDZ-modified peptide fragment was normalized to that of NEM modified peptide fragment. The amount of alkylated fragments was calculated by the sum of the areas of all charge states of the respective peptide fragments. The exact theoretical and observed masses of each single alkylated cysteine containing fragment are summarized in the supporting information (Table SI 1–3). The peptide fragment containing cysteines 102, 125 and 131 was not analyzed because all three cysteines are part of one fragment and therefore, we were not able to determine, which cysteine exactly was alkylated at each time point of alkylation. In the case of no reaction with the specific modifier the amount of NEM labelled peptide fragment was 100% and decreased with increasing amount of specific labeled peptide fragment up to 100% labeling degree with increasing modification by *N*-benzyl maleimide or **5h**. Like for our observations for the reaction of **5h** with  $\text{TNB}^{2-}$ , **5h** reacts faster with cysteine thiols in protein context than the control compound *N*-benzyl maleimide. In our opinion this makes **5h** an outstanding protein thiol blocker for several applications in the field of cysteine modifications and cysteine dependent redox biology, where fast blocking of nascent thiols is mandatory to freeze specific redox states and prevent disulfide shuffling. If specificity towards cysteine is needed, we recommend using the slower but still fast, reacting 5- $\text{SO}$ -analogues. To test for a potential biological application we performed a commonly used assay in the field of redox biology, the biotin switch assay, and checked whether our described thiol blocker is capable of blocking free or nascent thiols.<sup>[12]</sup> At first, we labeled HDAC8 with **5h** and NEM. Afterwards, we labeled free thiols with *N*-biotin maleimide

and conducted a western blot and quantified free thiol content with an HRP-Streptavidin conjugate. As expected, the probed **5h** and **4f** analogues show comparable results to NEM as control (Figure 3).

The 5-SO-TDZ and 5-SO<sub>2</sub>-TDZ scaffolds add to the repertoire of already known heteroaryl sulfones reacting by nucleophilic aromatic substitution reactions (S<sub>N</sub>Ar).<sup>[13]</sup>

Retrospective to our first experiments and the observed inhibitory potential against HDAC8, we hypothesize that the new scaffolds may be useful as integral part of enzyme inactivators. However, it is anticipated, that a rational design of such covalent inactivators would be challenging, because specific non-covalent recognition by the target protein has to be optimized by rational design of both, a suitable substitution pattern at the TDZ-ring, and the structure of the leaving group containing the sulfonyl- or sulfinyl-group. Furthermore, it is of utmost importance to reduce the reactivity of optimized inactivators by design in order to prevent undesired off-target effects. For example, changing the substituent in the 2 position of the TDZ ring should allow to tune the cysteine-reactivity of this class of inactivators. Despite these challenges, integral TDZ-groups with suitable leaving groups might offer new opportunities in the design of covalent inactivators apart from known and partly clinically approved covalent inhibitors, which are limited to acrylamide, haloacetamide or maleimide functionalities that are usually later connected to an existing non-covalent inhibitor.

## Conclusion

In summary, this study describes for the first time 5-SO<sub>2</sub>- and 5-SO-TDZs as promising cysteine reactive chemicals with the

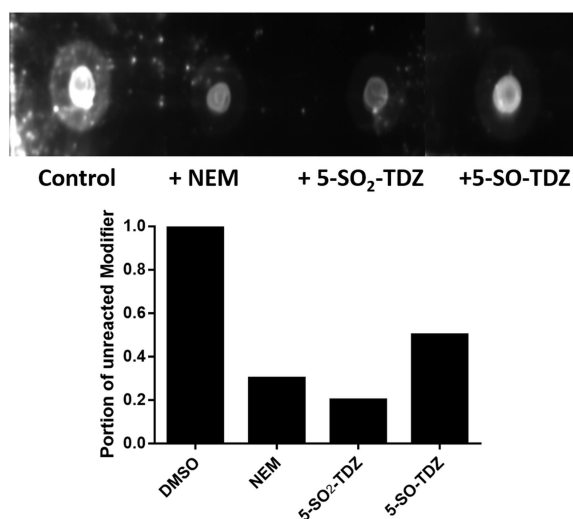


**Figure 3.** Dot Blot for cysteine reactivity of different TDZs with HDAC8. HDAC8 cysteines were blocked with indicated TDZs and *N*-ethylmaleimide (NEM) as a common thiol blocking agent. A DMSO control without thiol blocking agent was also prepared. Unblocked thiols were subsequently blocked with NEM-biotin. Brightness of dots indicate HRP activity of Streptavidin-HRP conjugate bound to biotin labeled thiols.

potential for versatile usage in biorthogonal tagging, classic biotin switch assays, but also in MS-based proteomic studies. 5-SO<sub>2</sub>-TDZ or 5-SO-TDZ analogues are anticipated to serve as beneficial blocking reagents in the field of redox biology because of their fast cysteine modifying reaction kinetics in aqueous environment. Also, TDZ analogues with tunable cysteine reactivity and carefully designed substitution patterns may be useful in the design of specific covalent inactivator compound.

## Experimental Section

### HDAC8 production

HDAC8 was produced and purified as described earlier according to Jänsch et al.<sup>[10b]</sup>

### Synthesis

**General procedure for the synthesis of 2(a–h):** To a stirred solution of dipotassium cyanodithioimidocarbonate (**1**) (500 mg, 2.57 mmol) in water (2 mL) and acetone (2.20 mL) previously cooled to 0 °C is added in three portions over three hours a solution of appropriate arylalkyl bromide (2.57 mmol) in acetone (1.5 mL). The reaction mixture is allowed to stir overnight at room temperature. The vigorous stirring is maintained throughout the reaction time. The reaction is monitored by thin-layer chromatography (the first eluent chloroform was used to determine unreacted arylalkyl bromide, the second eluent ethyl acetate containing 2% ethanol is used to monitor the formation of the product). Solvents are removed under reduced pressure raising the water bath's temperature evenly from 45 °C to 60 °C. A solid residue is slurred in acetone, the inorganic salt is filtered off, the filtrate is concentrated under reduced pressure to furnish a solid residue which is treated with ethyl acetate. The resulting mixture is filtered to remove insoluble impurities. Ethyl acetate is removed under reduced pressure, a solid residue is suspended in chloroform, stirred for one hour, filtered and washed with chloroform.

**General procedure for the synthesis of 3(a–h):** To a stirred suspension of the appropriate compound **2(a–h)** (1.06 mmol) in chloroform (1.6 mL) previously cooled to 0 °C sulfuryl chloride (1.28 mmol) is added in three portions every 30 minutes. The reaction mixture is allowed to stir overnight at room temperature. The progress of reaction is monitored by TLC (first eluent chloroform is used to monitor the formation of the reaction product, then ethyl acetate with 2% ethanol to check that all of the starting compound has reacted). The solvent is evaporated under reduced pressure. The product is purified by vacuum chromatography on a column of silica gel.

**General procedure for the synthesis of 4(f, h):** To a stirred solution of the appropriate compound **3(f, h)** (0.500 mmol) in a mixture of acetic acid (250 μL) and acetic anhydride (250 μL) previously cooled to 0 °C is added 30% H<sub>2</sub>O<sub>2</sub>(aq.) (0.600 mmol, 0.118 mL) in three portions every hour. The reaction mixture is allowed to stir overnight at room temperature. The reaction progress is monitored by TLC (hexane/chloroform 2:1). The solvents are removed under reduced pressure and the product is purified by vacuum chromatography.

**General procedure for the synthesis of 5(a–h):** To a stirred solution of the appropriate compound **3(a–h)** (0.500 mmol) in a mixture of acetic acid (250 μL) and acetic anhydride (250 μL) previously cooled



to 0 °C is added 30% H<sub>2</sub>O<sub>2</sub>(aq.) (1.50 mmol, 0.148 mL) in three portions every hour. The reaction mixture is allowed to stir overnight at room temperature. The reaction progress is monitored by TLC (hexane/chloroform 2:1). The solvents are removed under reduced pressure and the product is purified by vacuum chromatography. The details of the characterization of the new compounds are reported in Supporting information.

### TNB<sup>2-</sup> reactivity assay

To test reactivity of cysteine modification 100 μM 5,5'-dithiobis-2-nitrobenzoic acid (DTNB) was reduced with 200 μM tris(2-carboxyethyl) phosphine (TCEP) to yield 200 μM 5-thio-2-nitrobenzoic acid (TNB<sup>2-</sup>). Reaction was started by adding 200 μM cysteine modifier in sodium phosphate buffer (20 mM, pH 7.4) with 150 mM NaCl and decrease in absorbance at 405 nm was monitored using a Tecan Spark plate reader.

### Thin layer chromatography

Protocols and methods for conducting and quantification of thin layer chromatography data are provided in the supplementary information.

### Protein labelling

HDAC8 was labelled for subsequent digestion and mass analysis by mixing 1 mg/mL protein with 1 mM benzyl-maleimide or 5-SO<sub>2</sub>-TDZ in sodium phosphate buffer (20 mM, pH 7.4) with 150 mM NaCl in a final volume of 100 μL. Reactions were stopped, and protein was precipitated by adding 10 μL trichloroacetic acid (TCA, 100%). Afterwards, samples were centrifuged at 18000 g for 5 mins and supernatant was discarded. The remaining pellet was then dissolved in 100 μL alkylation buffer (6 M Gdn-HCl, 50 mM NEM, 10 mM TCEP, 100 mM sodium phosphate, pH 8.0) and mixed slightly for 30 minutes at 30 °C. After alkylation 900 μL ice-cold ethanol was added to precipitate protein again. HDAC8 immediately precipitates and the turbidity raises. After 30 minutes in the freezer at -20 °C the samples were centrifuged at 18000 g and 4 °C for 15 minutes and again the supernatant was discarded. Finally, the precipitate was dried with an open cap for about 30 minutes at 30 °C.

### Tryptic digestion

HDAC8 precipitates were dissolved in 10 mM NH<sub>4</sub>HCO<sub>3</sub> pH 8 to get a protein solution with a concentration of 1 mg\*mL<sup>-1</sup> HDAC8. Tryptic digestion was performed with 1 μg/mL trypsin over night while shaking at room temperature. The digestion process was stopped by freezing and storing the samples at -20 °C until measurement.

### HPLC-MS/MS

The separation of peptides was performed using the Shimadzu ExionLC AD UHPLC System with a ZORBAX 300SB-C18, 1.8 μm, 2.1 × 100 mm column which was directly coupled to an X500R QTOF mass spectrometer (AB Sciex) equipped with an IonDrive Turbo V ESI-source. After injection of 4 μL sample onto the column, separation was carried out under gradient conditions of the solvents ACN (A) and water (B) with 0.1% FA each at a flow rate of 0.2 mL/min. The separation started with 10% A for 1 min and an increase to 25% A in 3 min. It was followed by a slow linear gradient to 40% A in 11 min, hold for 1 min, and a fast linear

gradient to 90% A in 1 min, which was hold for 2 min. To reach starting conditions again, a linear gradient to 10% A in 2 min was performed and 10% A was hold for 3 min. The parameters used for ESI-QTOF-MS/MS analysis in positive mode were as follows: nebulizer (gas 1), 55 psi; turbo gas (gas 2), 55 psi; curtain gas, 35 arbitrary units; collision gas (CAD gas), 7 arbitrary units; source temperature, 450 °C; ionspray voltage, +5 kV; declustering potential (DP), 20 V; collision energy (CE), 10 V. TOF MS full scan and product ion Data were acquired by information dependent acquisition (IDA) scan mode in the mass range of 300–2000 Da. Dynamic collision energy mode was set active. The software BioPharmaView was used to analyze the mass spectrometric data. The expected mass differences after modification of cysteines with *N*-ethylmaleimide (125,048 Da), 3-chloro-1,2,4-thiadiazole (117,939 Da) and *N*-benzylmaleimide (187,063 Da) were set. The modifications could replace disulfide bridges and the protein was present in reduced form. For *in silico* hydrolysis, trypsin as used enzyme, three maximum modifications per peptide and a maximum of one missed enzyme site was set. The *m/z* tolerance for matching a measured peptide to a theoretical peptide was ±5 ppm and the tolerance for successful assignment of fragment ions was ±0.03 Da. Assigned peptides must achieve a score of at least 3.0 to be included in the calculation of the fraction of modified cysteine-containing peptides. The score is based on the accuracy of the assignment of a precursor ion and the associated fragment ions and can take on values between 0 and 100. The higher the score, the more reliable the assignment of the respective peptide. For the semiquantitative analysis of the fraction of covalently modified cysteines, the peak areas (XIC area) of the cysteine-containing peptides successfully assigned with a score of at least 3.0 were used from the extracted ion chromatogram (XIC). The calculation of the fraction of covalently modified cysteines was performed individually for each cysteine-containing peptide according to Equation 1.

$$\frac{\sum XIC \text{ area (peptide } X \text{ with modification)}}{\sum XIC \text{ area (peptide } X \text{ with and without modifications)}} * 100 \% \quad (1)$$

### Biotin-switch assay

A solution of 23.8 μM HDAC8 and 953 μM modifier was prepared in assay buffer (25 mM Tris-HCl, pH 8.0, 75 mM KCl, 0.001% Pluronic F-127) and was incubated for 1 h at 30 °C and 450 rpm. Subsequently 10% trichloroacetic acid was added to the solution and incubated for 10 min at room temperature under occasionally mixing to precipitate the protein. The solution was then centrifuged for 15 min. The supernatant was discarded and the precipitate resuspended in alkylation buffer (6 M Guanidine Hydrochloride, 1 mM *N*-Ethylmaleimide-Biotin, 10 mM Tris-(2-carboxyethyl)-phosphine, 100 mM Na<sub>3</sub>PO<sub>4</sub>, pH 8.0). The solution was incubated for 1 h at 30 °C and 450 rpm. For precipitation, the solution was diluted in a 1:10 ratio with -80 °C absolute ethanol and stored at -80 °C for 2 h. Afterwards the sample was centrifuged for 15 min and the pellet was washed twice by the addition of fresh absolute ethanol, centrifugation and discarding of the supernatant and left to dry for 1 h. Subsequently, the precipitate was resuspended in alkylation buffer without *N*-Ethylmaleimide-Biotin. 2 μL of sample was directly applied on a nitrocellulose blotting membrane (Nitrocellulose Blotting Membrane, Amersham Protran 0.2 μm NC, GE Healthcare Life Science, Germany) and left to dry for 1 h at room temperature. The membrane was treated with blocking buffer (5% BSA in TBS-T buffer) for 1 h at 4 °C. After discarding the blocking buffer, the membrane was incubated with a 1:10000 diluted horseradish peroxidase-streptavidin conjugate (HRP-Conjugated Streptavidin, Thermo Scientific, Germany) in TBS-T overnight at 4 °C. To remove the HRP-conjugate the membrane was washed with

TBS-T buffer, once for 15 min and twice for 5 min. Finally, the membrane was washed once for 5 min with TBS buffer. For measuring, 300  $\mu\text{L}$  of HRP substrate was prepared (Luminol Enhancer Solution, Amersham ECL Prime and Peroxide Solution; GE Healthcare UK Limited, Little Chalfont Buckinghamshire; 1:1 ratio) and added to the membrane. The chemiluminescent signal was captured with a CCD camera (Celvin S, Biostep GmbH, Burkhardtshof, Germany).

All centrifugation steps were carried out at 18000 g and 4 °C. TBS buffer contained 25 mM Tris-HCl, 150 mM NaCl at pH 7.5. TBS-T buffer was TBS buffer with 0.05% Tween 20 (VWR Chemicals, Radnor, PA, USA).

## Acknowledgements

This research was supported by the LOEWE priority program TRABITA, State of Hesse, Germany (to F. J. M. A.). This research was also supported by Grant S-MIP-22-35 from the Research Council of Lithuania. Open Access funding enabled and organized by Projekt DEAL.

## Conflict of Interest

The authors declare no conflict of interest.

## Data Availability Statement

The data that support the findings of this study are available in the supplementary material of this article.

**Keywords:** biotin switch assay · covalent inactivators · nucleophilic aromatic substitution · proteomic studies · thiol modification

- [1] a) J. M. Held, *Antioxid. Redox Signaling* **2020**, *32*, 659–676; b) Y. M. Go, J. D. Chandler, D. P. Jones, *Free Radical Biol. Med.* **2015**, *84*, 227–245; c) L. B. Poole, *Free Radical Biol. Med.* **2015**, *80*, 148–157.

- [2] a) Y. Shi, K. S. Carroll, *Acc. Chem. Res.* **2020**, *53*, 20–31; b) L. Gu, R. A. Robinson, *Proteomics Clin. Appl.* **2016**, *10*, 1159–1177.  
 [3] a) M. Radzinski, T. Oppenheim, N. Metanis, D. Reichmann, *Biomol. Eng.* **2021**, *11*; b) C. Lennicke, H. M. Cochemé, *Redox Biol.* **2021**, *42*, 101964; c) A. B. Das, A. R. Seddon, K. M. O'Connor, M. B. Hampton, *Free Radical Biol. Med.* **2021**, *170*, 131–149; d) A. Musaogullari, Y. C. Chai, *Int. J. Mol. Sci.* **2020**, *21*.  
 [4] J. A. Reisz, E. Bechtold, S. B. King, L. B. Poole, C. M. Furdul, *FEBS J.* **2013**, *280*, 6150–6161.  
 [5] E. Calce, M. Leone, F. A. Mercurio, L. Monfregola, S. De Luca, *Org. Lett.* **2015**, *17*, 5646–5649.  
 [6] a) F. Meng, A. J. Forbes, L. M. Miller, N. L. Kelleher, *Mass Spectrom. Rev.* **2005**, *24*, 126–134; b) M. S. Goyder, F. Rebeaud, M. E. Pfeifer, F. Kalman, *Expert Rev. Proteomics* **2013**, *10*, 489–501.  
 [7] a) Z. Yang, A. B. Attygalle, *J. Mass Spectrom.* **2007**, *42*, 233–243; b) J. Ying, N. Clavreul, M. Sethuraman, T. Adachi, R. A. Cohen, *Free Radical Biol. Med.* **2007**, *43*, 1099–1108.  
 [8] D. Zhang, N. O. Devarie-Baez, Q. Li, J. R. Lancaster, Jr., M. Xian, *Org. Lett.* **2012**, *14*, 3396–3399.  
 [9] L. S. Wittenbrook, G. L. Smith, R. J. Timmons, *J. Org. Chem.* **1973**, *38*, 465–471.  
 [10] a) N. Jansch, C. Meyners, M. Muth, A. Koprancovic, O. Witt, I. Oehme, F. J. Meyer-Almes, *Redox Biol.* **2019**, *20*, 60–67; b) N. Jansch, W. O. Sugiarto, M. Muth, A. Koprancovic, C. Desczyk, M. Ballweg, F. Kirschhofer, G. Brenner-Weiss, F. J. Meyer-Almes, *Chem. Eur. J.* **2020**, *26*, 13249–13255.  
 [11] E. Resnick, A. Bradley, J. Gan, A. Douangamath, T. Krojer, R. Sethi, P. P. Geurink, A. Aimon, G. Amitai, D. Bellini, J. Bennett, M. Fairhead, O. Fedorov, R. Gabizon, J. Gan, J. Guo, A. Plotnikov, N. Reznik, G. F. Ruda, L. Diaz-Saez, V. M. Straub, T. Szommer, S. Velupillai, D. Zaidman, Y. Zhang, A. R. Coker, C. G. Dowson, H. M. Barr, C. Wang, K. V. M. Huber, P. E. Brennan, H. Ovaas, F. von Delft, N. London, *J. Am. Chem. Soc.* **2019**, *141*, 8951–8968.  
 [12] a) J. R. Burgoyne, P. Eaton, in *Methods Enzymol.*, Vol. 473 (Eds.: E. Cadenas, L. Packer), Academic Press, **2010**, pp. 281–303; b) R. Li, J. Kast, in *Methods Enzymol.*, Vol. 585 (Ed.: A. K. Shukla), Academic Press, **2017**, pp. 269–284.  
 [13] a) N. Toda, S. Asano, C. F. Barbas, 3rd, *Angew. Chem. Int. Ed.* **2013**, *52*, 12592–12596; *Angew. Chem.* **2013**, *125*, 12824–12828; b) C. Zambaldo, E. V. Vinogradova, X. Qi, J. Iaconelli, R. M. Suci, M. Koh, K. Senkane, S. R. Chadwick, B. B. Sanchez, J. S. Chen, A. K. Chatterjee, P. Liu, P. G. Schultz, B. F. Cravatt, M. J. Bollong, *J. Am. Chem. Soc.* **2020**, *142*, 8972–8979; c) M. R. Bauer, A. C. Joerger, A. R. Fersht, *Proc. Natl. Acad. Sci. USA* **2016**, *113*, E5271–E5280.

Manuscript received: July 21, 2022  
 Revised manuscript received: September 5, 2022  
 Accepted manuscript online: September 6, 2022  
 Version of record online: September 27, 2022

---

## 5.2 Wirkstoffe mit Dithiocarbamat Funktionalität als potenzielle HDAC8 Inhibitoren

Ausgehend von den Erkenntnissen über den Wirkmechanismus von PD-404,182 wurden strukturell ähnliche Substanzen bezüglich Ihrer Hemmeigenschaften auf HDAC8 untersucht. Bei diesen Substanzen ist das Imin innerhalb des Benzothiazin Grundgerüsts durch ein Thion ausgetauscht, was in zyklischen Dithiocarbamaten oder genauer Benzothiazinthionen resultiert. Diese Substanzen zeigen ähnlich gute Hemmeigenschaften wie PD-404,182, gegenüber HDAC8. Außerdem weisen sie eine gute Selektivität im Vergleich zu anderen Histondeacetylasen auf.

Die erste Publikation dieses Unterkapitels befasst sich mit der Untersuchung des Wirkmechanismus einer Vielzahl von PD-404,182 abgeleiteten zyklischen Dithiocarbamaten als mögliche HDAC8-selektive Inhibitoren. Anders als bei PD-404,182 wurde herausgefunden, dass durch Austausch von Stickstoff gegen Schwefel diese Substanzen keine Reaktion mit dem freien Thiol von Glutathion eingehen und somit vermutlich weniger, bis nicht mehr, redoxaktiv sind. Dies verhindert die bei Wirkstoffen ungewollte Eigenschaft der unkontrollierten Reaktion mit Thiolen und insbesondere freien Cysteinen auf Proteinen. Somit ist anzunehmen, dass die inhibitorische Aktivität dieser Substanzen auf HDAC8 ausschließlich durch die Bindung an das Zink im Aktivzentrum von HDAC8 hervorgerufen wird, was durch die Verdrängung einer fluoreszierenden Sonde *in vitro* nachgewiesen wurde.

Besonders attraktiv sind Dithiocarbamate als Alternative zu den oft untersuchten Zink-komplexierenden Inhibitoren wie Hydroxamsäuren. Studien zeigen, dass Hydroxamsäuren zu starken Nebenwirkungen führen können, da diese unspezifisch und sehr potent an alle möglichen Zink abhängigen Proteine binden können. Somit ist die Entwicklung von Hydroxamsäure freien HDAC8 Inhibitoren der Hauptantrieb für die Weiterentwicklung von Dithiocarbamaten als Zink-bindende Inhibitoren. Zusätzlich zur hohen Potenz und Selektivität wurde in Kooperation mit dem Deutschen Krebsforschungszentrum in Heidelberg an Neuroblastom-Zellkulturen gezeigt, dass die entwickelten bityklischen Dithiocarbamate, im gleichen Konzentrationsbereich, die Acetylierung von SMC3 erhöhen, wie der zurzeit beste HDAC8 selektive Referenzinhibitor PCI-34051. SMC3 ist das prominenteste proteinogene Substrat von HDAC8 und eine Inhibition von HDAC8 führt zellulär zur Erhöhung der Acetylierung, was mittels Western-Blot nachgewiesen werden kann. Zusätzlich zeigte sich, dass die Acetylierung von Histon 4, welches ein Substrat von HDAC1, 2 und 3 ist und Tubulin als Substrat von HDAC6, nicht beeinflusst wird. Somit konnte gezeigt werden, dass die entwickelten Inhibitoren auch zellulär spezifisch ihre Wirkung durch die Bindung an HDAC8 entfalten.

Die zweite Publikation dieses Unterkapitels befasst sich mit der Weiterentwicklung der Synthese von Dithiocarbamaten und der Testung der daraus resultierenden linearen Inhibitoren gegen HDAC8. Zusammen mit Wissenschaftlern der Shanghai Key Laboratories of Green Chemistry and Green Chemical Processes innerhalb der School of Chemistry and Molecular Sciences an der East China Normal University (ECNU) wurde ein Verfahren entwickelt, um in einer Ein-Topf Synthese strukturell beliebige lineare Dithiocarbamate durch die Zugabe von Kaliumsulfat und Chloroform zu konstruieren. In erster Instanz waren diese Inhibitoren wesentlich weniger potent als die zuerst untersuchten zyklischen Dithiocarbamate, aber es wurde gezeigt, dass sich solche Wirkstoffe einfach, schnell und umweltfreundlichen synthetisieren lassen, wenn es zur Großproduktion käme.

---

**Titel:**

Synthesis and structure activity relationship of 1, 3-benzo-thiazine-2- thiones as selective HDAC8 inhibitors

**Autoren:**

Benjamin Wolff, Niklas Jänsch, Wisely Oki Sugiarto, Stefan Frühschulz, Maraike Lang, Rabia Altintas, Ina Oehme, Franz-Josef Meyer-Almes

**Bibliographische Daten:**

European Journal of Medicinal Chemistry (doi.org/10.1016/j.ejmech.2019.111756)

**Zusammenfassung:**

Die humane Histondeacetylase 8 (HDAC8) ist ein vielversprechendes Ziel für die Behandlung von Neuroblastomen und andere Krebsarten. Mehrere HDAC-Inhibitoren sind für die Behandlung spezieller Krebs-Subtypen zugelassen oder werden in klinischen Studien evaluiert. Die weitaus meisten Arzneimittel oder Arzneimittelkandidaten enthalten eine Hydroxamatgruppe, die das katalytische Zinkion in HDACs chelatisiert. Die meisten Hydroxamat-Inhibitoren sind mehr oder weniger unselektiv, obwohl es zahlreiche Ausnahmen gibt, die zeigen, dass es generell möglich ist, zumindest für HDAC-Isoenzyme selektive Inhibitoren zu entwickeln. Darüber hinaus sind Hydroxamate in letzter Zeit wegen ihres Mutagenitätspotenzials in die Diskussion geraten. Vor kurzem wurde PD-404,182 als selektiver und potenter Nicht-Hydroxamat-Inhibitor von HDAC8 entdeckt. Es stellte sich jedoch heraus, dass dieser Wirkstoff in Gegenwart von Glutathion (GSH) zersetzt wird. Hier beschreiben wir die Synthese von deutlich verbesserten Analoga von PD-404,182, die sowohl eine hohe Selektivität für HDAC8 als auch eine chemische Stabilität in Gegenwart von GSH aufweisen. Die Verbindungen werden im Hinblick auf die Struktur-Aktivitäts-Beziehung, den Bindungsmodus und der zellulären Bindung in Neuroblastomzellen charakterisiert, indem biochemische und biophysikalische Methoden mit Chemoinformatik kombiniert werden.



## Research paper

## Synthesis and structure activity relationship of 1, 3-benzo-thiazine-2-thiones as selective HDAC8 inhibitors

Benjamin Wolff<sup>a</sup>, Niklas Jänsch<sup>a</sup>, Wisely Oki Sugiarto<sup>a</sup>, Stefan Frühschulz<sup>a</sup>,  
Maraike Lang<sup>a</sup>, Rabia Altintas<sup>b, c, d, e</sup>, Ina Oehme<sup>b, c, d</sup>, Franz-Josef Meyer-Almes<sup>a, \*</sup>

<sup>a</sup> Department of Chemical Engineering and Biotechnology, University of Applied Sciences, Haardtring 100, 64295, Darmstadt, Germany

<sup>b</sup> Preclinical Program, Hopp Children's Cancer Center at NCT Heidelberg (KITZ), Germany

<sup>c</sup> Clinical Cooperation Unit Pediatric Oncology, German Cancer Research Center (DKFZ), INF 280, D-69120 Heidelberg, Germany

<sup>d</sup> German Cancer Research Consortium (DKTK), Germany

<sup>e</sup> Medical Faculty of Heidelberg University, Germany

## ARTICLE INFO

## Article history:

Received 10 July 2019

Received in revised form

29 September 2019

Accepted 2 October 2019

Available online 7 October 2019

## Keywords:

Neuroblastoma

Cancer

Drug design

Non-chelating inhibitor

Drug discovery

Histone deacetylase 8

## ABSTRACT

Human histone deacetylase 8 (HDAC8) is a highly promising target for neuroblastoma and other types of cancer. Several HDAC inhibitors are approved for the treatment of special cancer subtypes or are evaluated in clinical trials. By far the most drugs or drug candidates contain a hydroxamate group that chelates the catalytic zinc ion within HDACs. Most hydroxamate inhibitors are more or less unselective, although there are considerable exceptions demonstrating the general feasibility to develop at least HDAC isoenzyme selective inhibitors. In addition, hydroxamates have recently come under discussion regarding their potential for mutagenicity. Recently, PD-404,182 was discovered as a selective and potent non-hydroxamate inhibitor of HDAC8. However, this active compound turned out to be decomposed in the presence of glutathion (GSH).

Here, we describe the synthesis of significantly improved analogs of PD-404,182 that demonstrate both, great selectivity for HDAC8 and also chemical stability in the presence of GSH. The compounds are characterized with respect to structure-activity relationship, binding mode and target engagement in neuroblastoma cells by combining biochemical and biophysical methods with chemoinformatics.

© 2019 Elsevier Masson SAS. All rights reserved.

## 1. Introduction

Histone deacetylases (HDACs) are established and validated cancer targets [1–8]. There are 11 human members of the HDAC super family, which can be functionally divided into the classic HDACs with a catalytic zinc ion at the bottom of the highly conserved binding site and sirtuins that are NAD<sup>+</sup> dependent. By means of multiple sequence alignment, the classic HDACs are subdivided into class I, containing HDACs 1,2,3 and 8, class IIa including HDAC4, 5, 7 and 9, class IIb, which consists of HDAC6 and HDAC10 and class IV with only one member, HDAC11. The sirtuins form class III. HDAC8 is least related to the other class I HDACs. In fact, its functionality in terms of substrate and inhibitor recognition resembles that of class II isoenzymes, so that it can be classified at the interface between class I and class II HDACs. HDAC8 is also

special regarding protein-protein and substrate recognition [9]: Unlike all other HDAC isoenzymes, HDAC8 is not member of a multi-enzyme complex. Furthermore, only a handful of interaction partners and substrates have been unambiguously identified [10–15]. In fact, although histone H3- and H4-derived peptides can be deacetylated *in vitro*, there is no clear evidence that histones are deacetylated by HDAC8 *in vivo* [16]. Intensive efforts to elucidate the physiological role of HDAC8 revealed a pivotal role in several types of cancer [8,17–19]. The most significant results were reported for the participation of HDAC8 in the development and maintenance of childhood neuroblastoma [20,21]. A combination of retinoic acid and a selective HDAC8 inhibitor showed a synergistic and specific effect on the reduction of tumor cells in BE(2)-C xenografted NMRI nude mice [20]. The authors could also demonstrate less side effects with a HDAC8 selective inhibitor compared with vorinostat, a pan-inhibitor that hits various HDAC isoenzymes. Therefore, there is an urgent need for the development of selective HDAC8 inhibitors. Most described HDAC8 selective inhibitors contain a hydroxamate group to increase affinity through chelating

\* Corresponding author.

E-mail address: [franz-josef.meyer-almes@h-da.de](mailto:franz-josef.meyer-almes@h-da.de) (F.-J. Meyer-Almes).

the catalytic zinc ion [21]. However, aside the potential to bind to other free or enzyme-bound zinc ions, hydroxamic acids have raised some concerns about their potential mutagenicity, particular for the treatment of chronic diseases [22]. To avoid hydroxamate groups, several other zinc binding groups (ZBG's) have been explored [23,24]. One of the most promising potent and selective HDAC8 inhibitors lacking the hydroxamate moiety are benzothiazine-imines, which have been recently discovered in our laboratory [25]. Showing extraordinary high potency in the single-digit nanomolar range in an *in vitro* biochemical enzyme activity assay, the compounds were about 1000-fold less active in tumor cell lines. Okazaki et al. showed that the basic benzothiazine-imine (PD-404,182) was converted into the corresponding thiophenol in the presence of GSH [26]. Therefore, it appears plausible that PD-404,182 is captured by intracellular GSH and only a small portion of the compound reaches its cellular target. Most recently, we elucidated the mechanism by which PD-404,182 inhibits HDAC8 in great detail demonstrating that this compound is indeed a covalent modifier of cysteine-residues in HDAC8 [27]. Since the pharmacophore is unprecedented regarding its unusual chemical structure as well as *in vitro* potency and selectivity, we aimed at the development of GSH-resistant analogs of PD-404,182.

In this study, we synthesized two series of 1,3-benzothiazine-2-thione (BTZT) analogs of PD-404,182. The compounds are characterized regarding their chemical stability in the presence of GSH, HDAC8 selectivity as well as target engagement in neuroblastoma tumor cells. The results are complemented by structure activity relationship analysis and molecular docking.

## 2. Results and discussion

### 2.1. Synthesis

The synthetic route towards the pyrimido[1,2-*c*] [1,3]benzothiazin-6-imines ( $n = 1$ ) and imidazo[1,2-*c*] [1,3]benzothiazin-6-imines ( $n = 0$ ) is described in Scheme 1 and essentially follows the procedure of Mizuhara et al. [28].

#### 2.1.1. General synthesis of the 2-aryl-4,5-dihydro-1H-imidazole (2a–v, $n = 0$ ) and 2-aryl-1,4,5,6-tetrahydropyrimidine (3a–u, $n = 1$ )

To a solution of the aldehyde **1a–v** (1 eq.) in *tert*-butanol (9.0 ml/mmol) the diamine (1.1 eq.) was added and the solution was stirred at 70 °C for 30 min  $K_2CO_3$  (4 eq.) and  $I_2$  (1.25 eq.) was added at 70 °C and the mixture was stirred at this temperature for further 3 h. The mixture was cooled down to rt and  $Na_2S_2O_3$  was added until the iodine color almost disappear. The organic layer was separated and the solvent was removed *in vacuo*. The received solid

was dissolved in water (7.5 ml/mmol) and 2 N  $NaOH_{aq}$  was added until  $pH = 12–14$ . The aqueous layer was separated with  $CHCl_3$  ( $3 \times 3.75$  ml/mmol), the combined organic layers were dried ( $Na_2SO_4$ ) and the solvent was removed *in vacuo*. The product can be used without further purification.

#### 2.1.2. General procedure of the cyclization using carbon disulfide

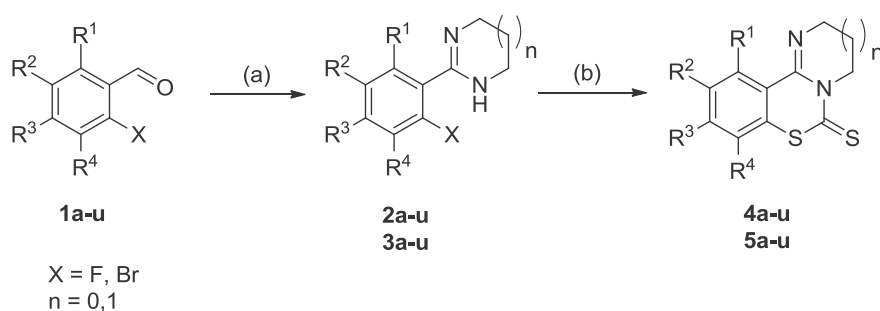
To a mixture of **2a–v** or **3a–u** (1 eq.) and NaH (2 eq.) in DMF (3.3 ml/mmol) was added  $CS_2$  (2 eq.) under nitrogen atmosphere. After stirring at 80 °C for 16 h the mixture was concentrated *in vacuo*. The product was purified via chromatography ( $SiO_2$ , hexane:ethyl acetate = 4:1, v/v).

Detailed synthesis procedures and chemical analytics including NMR-spectra and MS data are provided in the Experimental Section and Supporting Information.

### 2.2. Thiol-reactivity of BTZT derivatives

In a previous study we identified the benzothiazine-imine scaffold as a novel pharmacophore for potent and selective HDAC8 inhibitors [25]. However, compounds from this series were 1000-fold less potent in cells compared with the biochemical assay. This loss in potency was attributed to thiol-reactivity and effective degradation in the presence of e.g. GSH. More recently, we elucidated the details of the reaction mechanism between benzothiazine-imine PD 404,182 and GSH and showed that this compound is a rather unselective cysteine modifier yielding thiocyanates or mixed disulfides with the thiophenol metabolite of PD 404,182 in protein context [27]. The compound is chemically stable in the absence of reducing agents, but is quickly decomposed in the presence of GSH. Despite the unselective nature of this thiol reactivity, inhibitors of the benzothiazine-imine series showed very high isoenzyme selectivity for HDAC8. In this study we also provided arguments that the covalent modification of C153 within the active site pocket is preceded by non-covalent recognition of the benzothiazine motif, which is supposed to be a key element for selectivity.

Based on this hypothesis we aimed at shifting the balance between unselective thiol-reactivity and selective non-covalent molecular recognition towards lower reactivity while preserving isoenzyme-selectivity for HDAC8. At first we determined the time dependence of the decomposition of PD-404,182 analogs, where the imine nitrogen was exchanged by oxygen (**6**) or sulfur (**51**), or where the sulfur atom in the thiazine ring was changed to oxygen (**7**) (Fig. 1). In accordance with our previous study [27], PD-404,182 was completely decomposed after 24 h in the presence of 10 mM GSH at 20 °C (Fig. 1). The chemical stability of **6** and **7** is significantly higher with 62 and 48 % of the initial substance remaining after



(a) ethylene diamine or 1,3-diaminopropane,  $K_2CO_3$ ,  $I_2$ ; (b)  $CS_2$ , NaH

**Scheme 1.** Synthetic route to the 1,3-benzothiazine-2-thiones.

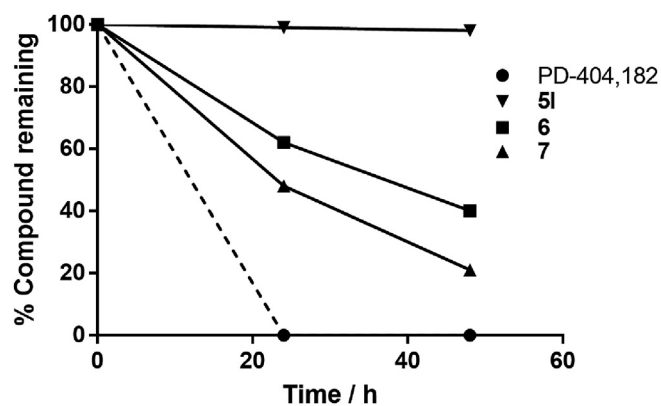


**Fig. 1.** Chemical stability of BTZT analogs (5 mM) with exchanged heteroatoms in the presence of 2eq GSH (10 mM). For comparison purposes: GSH concentrations in animal cells range from 0.5 to 10 mM. The dashed line indicates that the decomposition of PD-404,182 is complete within 24 h and occurs much faster than that of the other analogs.

24 h, respectively (Table 1). Compared with these derivatives, the BTZT **5I** shows extraordinary high chemical resistance against GSH with essentially unaffected compound even after 48 h incubation time under the same conditions as previously (Fig. 1). Based on these results, we synthesized 42 further compounds and determined their chemical stability in the presence of 10 mM GSH concentrations that mimic intracellular conditions. All tested BTZT derivatives are chemically stable under reducing conditions in the presence of GSH (Table 2).

### 2.3. Structure-activity relationship analysis

To evaluate the inhibitory potency and isoenzyme selectivity of BTZT analogs of PD-404,182 for HDAC8, we measured the activity profile of all BTZT analogs against a panel of HDAC isoenzymes (Fig. 2A, Table 2). One of the best BTZT's, **5b**, achieves almost the potency of the standard HDAC8 inhibitor PCI-34051 and is more potent against this enzyme than Trichostatin A (TSA) or suberoylanilide hydroxamic acid (SAHA) (Fig. 2A). Overall, two series of compounds, dihydroimidazoles (DHIs,  $n = 0$ ) and tetrahydropyrimidines (THPs,  $n = 1$ ), with different heteroring sizes were synthesized. The BTZT pharmacophore in both series was modified at

all aromatic positions to deduce a structure-activity relationship (SAR). In addition, THP analogs with dimethylated nitrogen heterocycle and oxygen atoms in place of sulfur atoms were synthesized. Both, DHIs and THPs, show different activities against HDAC8. 5 THPs show  $IC_{50}$ -values less than  $1 \mu\text{M}$ , while only 2 DHIs are below this threshold and the four most potent compounds (**5a**, **5b**, **5c**, **5d**) are from the THP series. This could indicate a slight preference of HDAC8 for the 6-membered heterocycle.

A methyl- and chlorine scan at the aromatic ring reveals a clear up to 35-fold improvement of inhibitory activity at the R1- and R2-position upon substitution of hydrogen by methyl or chlorine for both, the THP- and the DHI-series of the BTZT pharmacophore. The effect of the methyl-substitution in R2 position is stronger than that of chlorine at the same position for both heterocycle sizes ( $n = 0$  and  $n = 1$ ). The effect of methyl-substitution at R3 is significantly lower, but still beneficial for activity. The effect of chlorine substitution at this position is different for  $n = 0$  and  $n = 1$ . Methyl-substitutions at ring position R4 is detrimental for both heterocycle ring sizes, while a chlorine atom at this position shows an increase in activity for the 5-membered and a decrease for the 6-membered heterocycle.

To determine whether the increase in activity would be due to halogen bonding, positions R1 and R2 were also substituted by the fluorine, bromine and iodine. For the DHI series ( $n = 0$ ) the potency of the inhibitors increases from  $F \ll Cl < Br$  at the R1 position. For iodine the potency decreases again, but is still much higher than for the fluorine analog. For the THP-series ( $n = 1$ ) there is a similar but less pronounced dependency on halogen atoms. The activity increases from fluorine to iodine ( $F \ll Cl < I$ ), while the activity of the bromine THP lies between that of the corresponding fluorinated and the chlorinated analog. Together with the gain in activity due to a methyl group at position R1, these findings suggest hydrophobic interactions with a weakly hydrated hydrophobic part of the receptor surface. The slightly reduced or similar effect of iodine with respect to chlorine could also be due to sterical reasons so that a halogen bond at the R1 position cannot be fully excluded at this point.

At the R2-position the strongest effects for both, the DHI- and the THP-series, come from methyl-substitutions and there is no significant gain in activity from fluorine to the heavier halogens. Therefore, a halogen bond at this position is unlikely. However, a DHI with a bromine substitution at R2-position shows similar

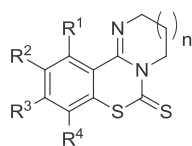
**Table 1**  
Impact of heteroatom exchange on potency and GSH stability.

#	Chemical Structure	$IC_{50}$ ( $\mu\text{M}$ )				GSH-stability (%) <sup>a</sup>
		HDAC1	HDAC4	HDAC6	HDAC8	
PD-404,182		$3.6 \pm 0.8^b$	$8.6 \pm 1.5^b$	$6.7 \pm 0.8^b$	$0.011 \pm 0.001^b$	<5
5I		>50 <sup>b</sup>	>50 <sup>b</sup>	>50 <sup>b</sup>	$2.8 \pm 0.3^b$	>95
6		>50	$5.9 \pm 0.7$	>50	$2.0 \pm 0.2$	62
7			$13 \pm 1.6$		$9.5 \pm 1.1$	48

<sup>a</sup> Percent parent compound remaining uncomposed after 24 h incubation in the presence of 10 mM GSH.

<sup>b</sup> [25].

**Table 2**  
Activity profile of BTZTs against a panel of HDAC isoenzymes and chemical stability (in the presence of GSH).



#	n <sup>a</sup>	R1	R2	R3	R4	IC <sub>50</sub> (μM)								GSH stability (%) <sup>b</sup>
						HDAC1	HDAC2	HDAC3	HDAC4	HDAC5	HDAC6	HDAC7	HDAC8	
4a	0	H	H	CN	H	17.7	>50	>50	6.8	16.1	0.3	6.2	0.17	–
4b	0	H	Br	H	H	>50	>50	>50	17	4	>50	4.5	0.26	>95
4c	0	Br	H	H	H	38	45	>50	5.1	>50	14	–	0.42	–
4d	0	Cl	H	H	H	>50	>50	>50	14	>50	>50	–	0.60	–
4e	0	H	H	Br	H	>50	>50	>50	>50	>50	>50	>50	1.0	>95
4f	0	H	I	H	H	>50	>50	>50	20	>50	>50	–	1.0	>95
4g	0	H	F	H	H	>50	>50	>50	>50	>50	>50	>50	1.2	>95
4h	0	F	H	Br	H	50	50	50	4.1	>50	1.7	–	1.2	–
4i	0	H	CH <sub>3</sub>	H	H	>50	>50	>50	>50	>50	>50	>50	1.3	>95
4j	0	H	H	Cl	H	>50	>50	>50	11	>50	9	–	1.6	>95
4k	0	CH <sub>3</sub>	H	H	H	>50	>50	>50	>50	9.5	>50	>50	1.7	>95
4l	0	I	H	H	H	>50	>50	43	20	>50	>50	10	2.3	–
4m	0	H	H	H	Cl	>50	>50	>50	16	21	>50	–	3.2	>95
4n	0	H	H	H	F	>50	>50	>50	>50	>50	>50	>50	6.7	>95
4°	0	H	H	N(CH <sub>3</sub> ) <sub>2</sub>	H	>50	50	50	32	>50	>50	>50	7.0	–
4p	0	H	OCH <sub>3</sub>	H	H	>50	>50	>50	16	>50	>50	–	7.8	>95
4q	0	H	H	OCH <sub>3</sub>	H	>50	>50	>50	>50	>50	>50	>50	12	>95
4r	0	H	Cl	H	H	>50	>50	>50	>50	>50	>50	>50	13	>95
4s	0	F	H	H	H	>50	>50	>50	>50	>50	>50	>50	13	>95
4t	0	H	H	CH <sub>3</sub>	H	>50	>50	>50	>50	>50	>50	>50	13	>95
4u	0	H	H	H	H	>50	>50	>50	19	>50	>50	>50	21	>95
4v	0	H	H	H	CH <sub>3</sub>	>50	>50	>50	>50	>50	>50	–	31	>95
5a	1	H	CH <sub>3</sub>	H	H	>50	>50	>50	1.9	20	20	–	0.057	–
5b	1	I	H	H	H	12	8.1	20	2.2	8	24	–	0.076	–
5c	1	Cl	H	H	H	24	14	26	1.4	6.8	6.9	–	0.13	>95
5d	1	CH <sub>3</sub>	H	H	H	>50	>50	>50	>50	39	>50	3.4	0.13	–
5e	1	H	H	CN	H	>50	>50	50	3.8	2.7	1.8	3.2	0.37	–
5f	1	H	Cl	H	H	>50	>50	>50	29	18	>50	>50	0.54	>95
5g	1	H	CF <sub>3</sub>	H	H	>50	>50	>50	>50	>50	>50	>50	0.83	>95
5h	1	H	H	CH <sub>3</sub>	H	>50	>50	>50	>50	>50	>50	>50	1.0	>95
5i	1	H	I	H	H	>50	>50	>50	8.1	>50	>50	>50	1.0	–
5j	1	H	H	Br	H	>50	>50	>50	>50	>50	12	>50	1.1	>95
5k	1	H	H	F	H	>50	>50	>50	>50	>50	>50	>50	1.3	>95
5l	1	H	H	H	H	>50	>50	>50	>50	>50	4.7	>50	1.5	>95
5m	1	H	Br	H	H	>50	>50	>50	>50	>50	>50	15	1.6	>95
5n	1	H	F	H	H	>50	>50	>50	>50	>50	>50	>50	1.8	>95
5°	1	F	H	H	H	>50	>50	>50	>50	>50	>50	>50	2.3	>95
5p	1	H	H	N(CH <sub>3</sub> ) <sub>2</sub>	H	>50	>50	>50	>50	>50	4.7	>50	2.7	–
5q	1	Br	H	H	H	>50	>50	>50	>50	>50	>50	>50	0.52	>95
5r	1	H	H	Cl	H	>50	>50	>50	21	34	>50	–	5.4	>95
5s	1	H	H	H	F	>50	>50	>50	>50	>50	>50	>50	21	>95
5t	1	H	H	H	Cl	>50	>50	>50	8.8	>50	>50	–	30	>95
5u	1	H	H	H	CH <sub>3</sub>	>50	>50	>50	>50	>50	>50	–	>50	>95

<sup>a</sup> n = 0: DHI; n = 1: THP.

<sup>b</sup> Percent parent compound remaining uncomposed after 24 h incubation in the presence of 10 mM GSH.

potency than a methyl substitution pointing towards hydrophobic interactions with HDAC8. For THPs halogen substitution at R2-position does not lead to a significant improvement. Chlorine- and bromine substituents at the R3-position increase the inhibitory activity against HDAC8 only for DHIs but not for THPs. The reason behind this divergent behavior could be due to slightly deviating binding poses. Although, chlorine at R3-positions in THPs seems to have an adverse effect on activity, the analog with bromine at this positions shows essentially the same activity than the unsubstituted core compound **5l**. Therefore, we reasoned that the halogen substituents in R3 position seem not to be involved in substantial clashes with the receptor surface and that this position could be further explored with larger substituents for further optimization. Fluorine and chlorine atoms, but not a methyl group

at R4 lead to an increase in potency within the DHI-series.

However, the absolute activities of all DHI-analogs are still less than those for the unsubstituted THP **5l**. Within the THP-series at position R4 the substitution of hydrogen by larger moieties, whether it be a methyl group or a halogen, causes a pronounced more than 10-fold drop in potency.

In a further attempt we explored the impact of larger cyano-dimethylamino- and methoxy-groups at position R3 on potency. Interestingly, the cyano-group leads to a considerable increase of activity in the nanomolar range. In contrast, dimethylamino- and methoxy-substitution in R3 position turned out to be detrimental. Dimethylation at the R5-position in the 6-membered nitrogen heterocycle of THPs also led to a decline in activity. Compared with the original substance PD-404,182, the best BTZT **5a** has 5–6 times



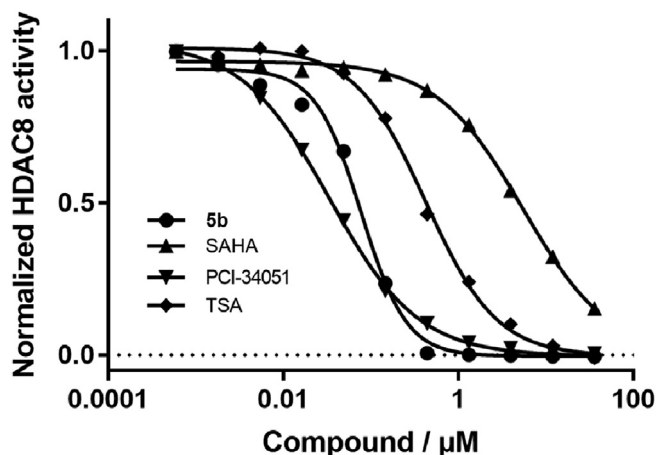


Fig. 2. Dose-response curves of **5b** and reference inhibitors suberoylanilide hydroxamic acid (SAHA), PCI-34051, Trichostatin A (TSA) against HDAC8.

less activity against HDAC8, but shows dramatically enhanced chemical stability against GSH, while the selectivity for HDAC8 is preserved (Table 2). Substitution of the sulfur atom within the thiazine ring of **5l** by oxygen causes a 3–4 fold drop in activity and significant decrease in GSH-stability (Fig. 1, Table 1). The exchange of the thione-sulfur against oxygen leads to similar activities against HDAC8, but concurrently causes clearly less GSH-stability (Fig. 1, Table 1).

The impact of structural variations on the inhibitory activity of BTZT derivatives against HDAC8 is summarized in Fig. 3. Taken together, a tetrahydropyrimidine heterocycle ( $n=1$ ) is more favorable than a dihydroimidazole ring and the substitution of the heterocyclic sulfur atom against oxygen has a detrimental effect. Furthermore, hydrophobic groups are beneficial at positions R1 and R2, whereas methyl groups at R4 or R5 appear to have negative effects on activity. The R4 position in THPs tolerates also no exchange of hydrogen against halogens. At position R3 a cyano group is most beneficial suggesting that a negative partial charge would be required for optimal interaction with HDAC8.

#### 2.4. Selectivity correlates with activity

BTZTs show remarkable potency and selectivity for HDAC8 (Table 2). An increase in potency is easily achieved by introducing e.g. a general metal chelating group (e.g. hydroxamates) or a larger hydrophobic group. In such cases the gain in activity is often at the cost of selectivity, because of the unspecific binding character of such groups. Therefore, it is important to make sure that not only potency, but also selectivity, is increased during drug optimization. The SAR of BTZT derivatives shows that the potency of both, the DHI and the THP, series is highly correlated with selectivity for HDAC8 (Fig. 4). This finding points to a special molecular recognition scheme between BTZTs and HDAC8, which is different to other HDAC isoenzymes. Since the catalytic center of zinc-dependent HDACs is highly conserved, the BTZTs are supposed to exploit specific cavities of HDAC8. HDAC8 is known to be exceptionally malleable around the active site binding tunnel. In addition, some crystal structures show also considerable movement of internal residues that open an additional transient pocket adjacent to the

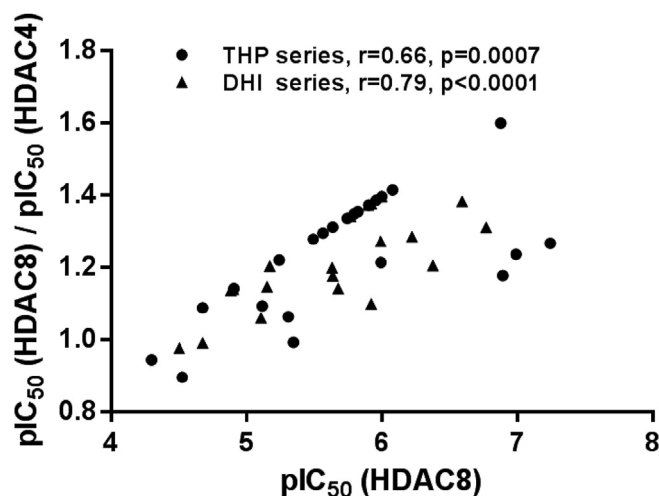


Fig. 4. Selectivity of BTZTs from the DHI- and THP-series. The ratio of logarithmized  $IC_{50}$ -values ( $pIC_{50}$ ) against HDAC4 and HDAC8 is plotted versus the  $pIC_{50}$  of HDAC8 to demonstrate the correlation between activity and selectivity. The spearman correlation coefficient  $r$  and the  $p$ -value are given for each series.

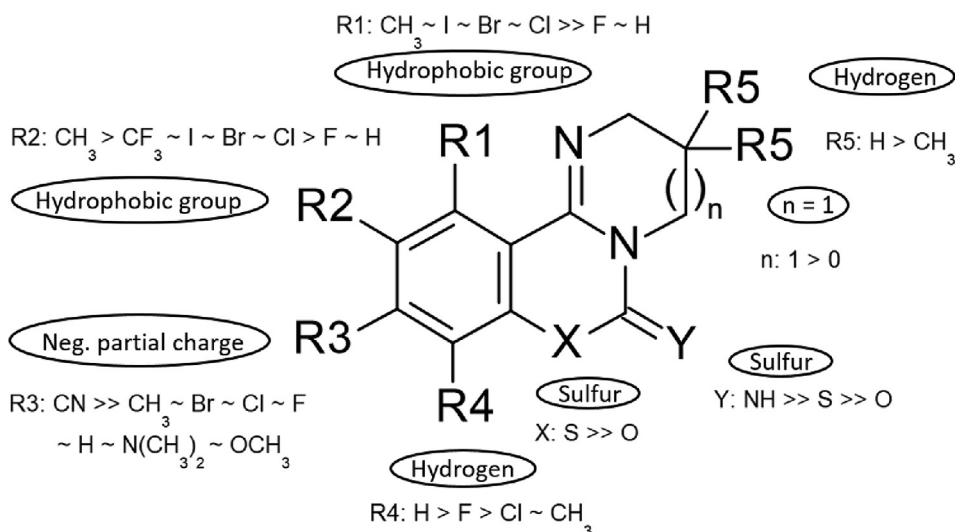


Fig. 3. Summary of the SAR for the benzothiazine pharmacophore.

active site (PDB-ID 1T64) or enable access to the acetate release channel (PDB-ID 3SFF).

### 2.5. BTZTs bind to the active site pocket

Although BTZTs inhibit the enzyme activity of HDAC8, the binding site would not be necessarily identical to the active site of the enzyme, since allosteric inhibition would also be possible. To provide evidence for the site of molecular recognition we exploited a DBD-probe that was developed in our lab for class IIa HDACs, but also works for HDAC8. Noncovalent binding of the fluorescent DBD-probe to HDAC8 leads to increased fluorescence polarization (Fig. 5). After addition of representative BTZTs **5a-c** in 100-fold molar excess, the DBD-probe is displaced from HDAC8 as indicated by a decrease of the fluorescence polarization signal. Thus, the data provide clear evidence that BTZTs target the active site of HDAC8.

### 2.6. Docking studies

HDAC8 is known to contain extraordinary flexible regions around the conservative binding pocket enabling to accommodate a variety of structurally diverse inhibitors [29,30]. This is documented by more than 70 crystal structures of HDAC8 (47 from homo sapiens). The inhibitors are supposed to stabilize the extremely flexible binding site, thereby inducing conformational changes in loops L1 and L2 flanking the active site binding pocket. HDAC8 essentially undergoes a transition between a more compact „open“ (e.g. PDB-ID 1T69), a „sub-open“ (e.g. PDB-ID 1T64) with an additional transient pocket, and a „wide-open“ conformation (e.g. PDB-ID 1VKG). In addition, Whitehead et al. showed a considerable malleability of HDAC8 at the transition between the conserved binding tunnel and the acetate release channel in the interior of the protein (e.g. PDB-ID 3SFF) [31]. To elucidate the binding pose of BTZTs to HDAC8 we docked compounds **5l**, **5c**, **5b**, **5q** and **5d** to above mentioned major conformational representatives of HDAC8 using MOE software. The docking procedure took the flexibility of residues in proximity to the binding site into account. Subsequently, the resulting protein-ligand complex was subjected to an energy-minimizing step that was applied to a larger area within a 10 Å radius around the bound ligand.

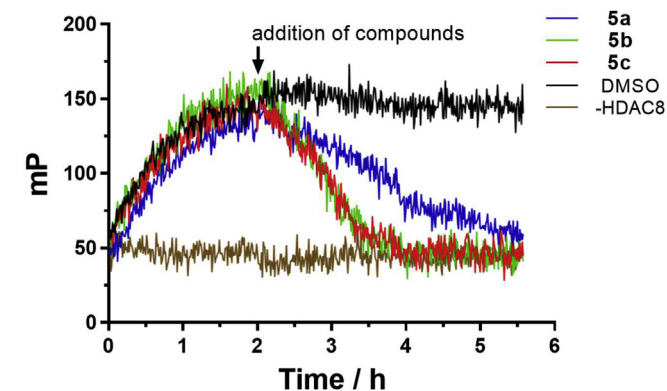


**Fig. 5.** Displacement assay demonstrating competitive binding of **5a-c** to the active site of HDAC8. 500 nM HDAC8 are mixed with 500 nM DBD-probe that leads to an increase in fluorescence polarization (Exc. 420 nm/Em. 520 nm) in assay buffer at 25 °C. Upon addition of 50 μM **5a**, **5b** or **5c**, the probe is displaced from HDAC8. The free DBD-probe in the absence of HDAC8 is used as low control for complete displacement. Addition of DMSO at the same concentration than that of the added compound solutions serves as high control for none displacement. Each kinetic curve represents the average of 6 replicate measurements in order to improve the signal to noise ratio.

The corresponding energy minimized protein-ligand structures were aligned and superposed for each conformational representative of HDAC8 in order to analyze structural deviations (Fig. 6A–D). The various docking poses in Fig. 6A show diverse orientations and are located in the transient secondary binding pocket far away from the catalytic zinc ion, which is only present in the “sub-open”-conformation of PDB-ID 1T64. In contrast, all docking poses in the other three crystal structures of HDAC8 (Fig. 6B–D) coincide and are located at the transition between the conserved binding pocket and the acetate release channel. The biggest structural changes of internal amino acid residues in the crystal structures of 1T69 and 3SFF, which are induced upon binding of **5d**, are found in five narrowly defined regions: L31–R37, W137–A144, S150–D157, D178–D183 and G302–Y306 (Fig. S2). A closer look at the docking poses of **5d**, **5b** and **5q** in PDB-ID 3SFF reveals several types of interactions: Zn<sup>2+</sup>-coordination by the thione sulfur, parallel π–π-stacking with W141, a conventional hydrogen bond with Y306 and amide–π interaction with the peptide backbone of G303 and G304 (Fig. 6E). In addition, there are several hydrophobic interactions, e.g. with the side chains of K33, I34 and F152. Docking of the imine-derivative of **5l** to PDB-ID 1T69 lead to a very similar binding pose via imine–nitrogene coordinating to the catalytic zinc ion [27]. The amino acids R37, G303 and W141 that show significant movements induced by binding of **5d** are considered to be involved in gating the acetate release channel [32]. Moreover, the π-stacking interaction between the aromatic ring of **5d** and W141 is very similar to that of known amino-acid derived class I HDAC inhibitors, which are supposed to achieve isoform selectivity via access to the internal acetate release channel [31]. The hydrophobic interactions between the methyl-substituent in R1-position with K33, I34 and F152 are in agreement with the observed increase in activity of this analog, when compared with that of the unsubstituted **5l**. Moreover, the striking beneficial effect of a cyano group in R3-position can also be explained by the best energy minimized docking pose of **5e** in the binding pocket of HDAC8 indicating an additional hydrogen bond between the nitrogen of the cyano group and the positively charged guanidinium group of R37 (Fig. S3).

### 2.7. Intracellular target engagement

Acetylated SMC3 (ac-SMC3) is a *bona fide* substrate of HDAC8 and generally accepted as a suitable marker for HDAC8 enzyme activity [10]. To analyze the efficacy of BTZTs on intracellular HDAC8 activity, we used the SK-N-BE(2)-C neuroblastoma tumor cell line known to depend on HDAC8 for cell growth and survival [8,20,33]. Increasing concentrations of **4b** lead to a dose-dependent rise of the ac-SMC3 level clearly indicating the inhibition of cellular HDAC8 (Fig. 7A/B). The ac-SMC3 level in the presence of 5 μM **4b** is about 3.2-fold increased compared with untreated cell control (Fig. 7B). This compares well with the effect of the known HDAC8 inhibitor PCI-35051 at a concentration of 6 μM, which increases the ac-SMC3 level by a factor of about 2.9 (Fig. 7A). Thus, BTZTs pass the cell membrane and bind to their target HDAC8 within cells. The intracellular level of acetylated histone 4 (ac-H4), which is a substrate of HDACs 1, 2 and 3, and acetylated tubulin, a specific substrate of HDAC6, does not change upon the treatment with up to 5 μM of **4b** (Fig. 7C/D). Therefore, **4b** is also isoenzyme selective for HDAC8 within cells in agreement with the biochemical profiling (Table 2). Furthermore, **5a** and **4b** reduce clonogenic growth of SK-N-BE(2)-C cells with comparable or greater efficacy than the reference compound PCI-34051 (Fig. 8). The GI<sub>50</sub>-values of the active substances, where 50% of maximal clonogenic growth is inhibited, have been determined by fitting the data in Fig. 8 yielding values of about 21, 6 and 15 μM for **5a**, **4b** and PCI-35051, respectively.

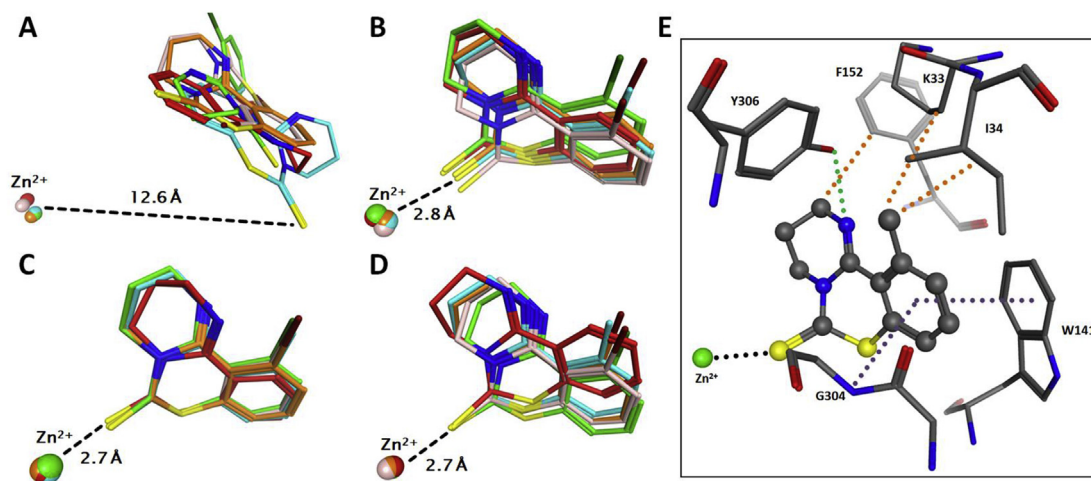


**Fig. 6.** Molecular docking of 5 BTZT derivatives (**5l**: red, **5c**: green, **5b**: orange, **5q**: pink, **5d**: cyan) into four different X-ray structures of HDAC8: A) PDB-ID 1T64, B) PDB-ID 1T69, C) PDB-ID 1VKG, D) PDB-ID 3SFF. E) Docking pose of **5d** in PDB-ID 3SFF. Dotted lines indicate protein-ligand interactions: zinc-sulfur coordination (black), hydrogen-bond (green),  $\pi$ - $\pi$ -stacking and  $\pi$ -amide-interaction (magenta) and hydrophobic interactions (orange).

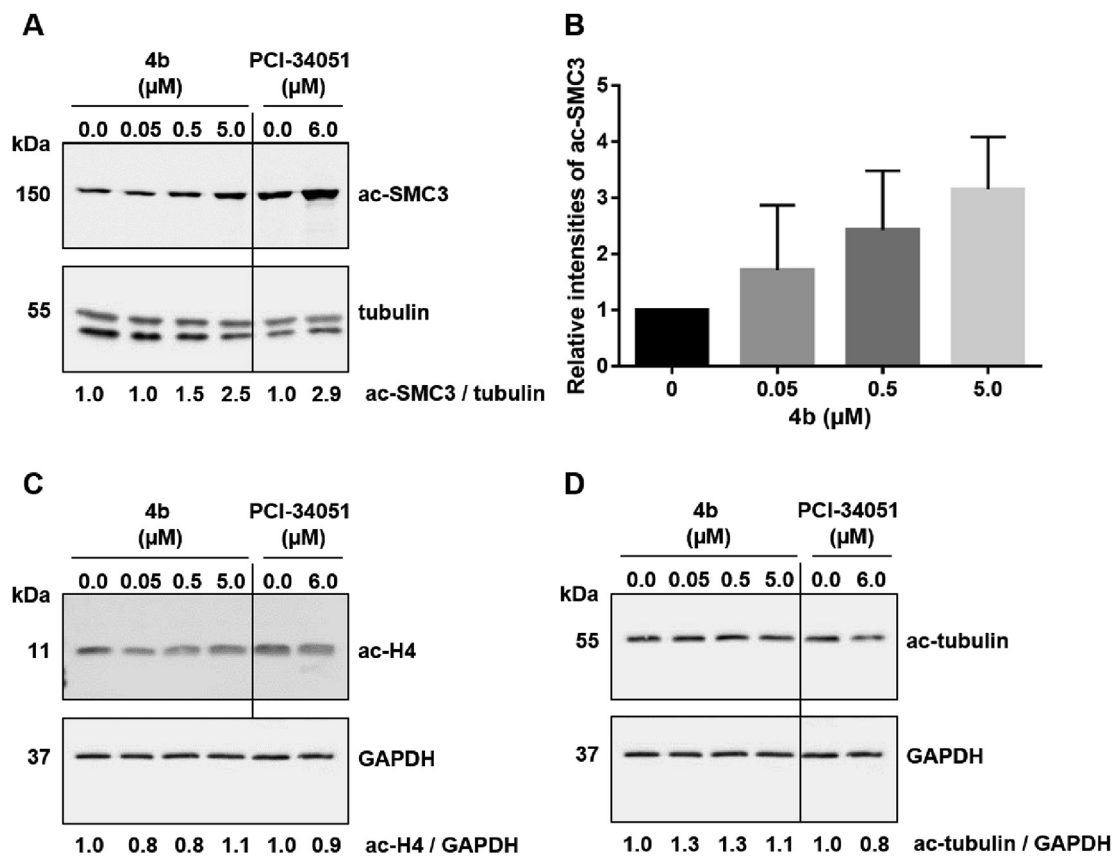


**Fig. 7.** Inhibition of HDAC8 **4b** leads to concentration dependent increased acetylation of SMC3 in SK-N-BE(2)-C neuroblastoma tumor cells. PCI-34051 is a known HDAC8 selective inhibitor and serves as control. Tubulin and GAPDH are used as loading control, respectively. A) Exemplary quantitative Westernblot of cell extracts in the absence or in the presence of different concentrations of **4b**. B) The diagram refers to A) and shows mean band intensities and standard deviations from three independent Westernblots. The y-axis shows relative intensities of ac-SMC3 with respect to an untreated contol. C) **4b** does not interfere with the level of ac-H4 or D) ac-tubulin indicating isoenzyme selectivity of **4b** within tumor cells.

Comparing  $GI_{50}$ -values with  $IC_{50}$ -values, there is only a moderate loss of potency when going from the biochemical to the cell-based assay. For **4b** this loss is only a factor of 23. In contrast, the imine-analogs of the BTZTs appear to be at least 1000-fold less

effective on cells compared with biochemical data [25]. Therefore, our results confirm the initial hypothesis that the dramatic loss in activity of the chemically unstable imine analogs within cells could be prevented by using the GSH resistant BTZT compounds of this

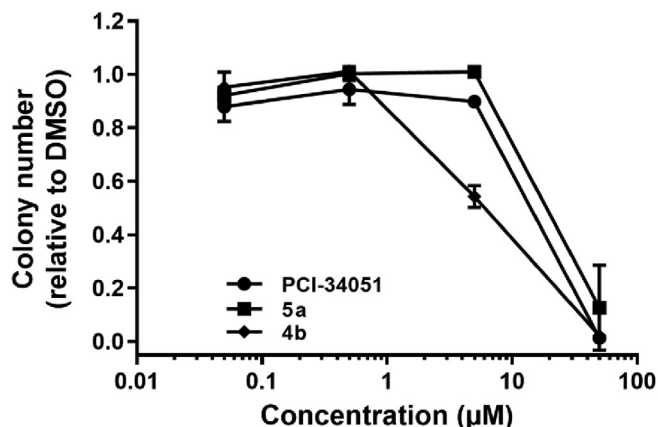


**Fig. 8.** Colony assay using SK-N-BE(2)-C neuroblastoma tumor cells and treating them with different concentrations of indicated compounds. Compounds **5a** and **4b** show comparable and even greater anti-proliferative activity than the known potent HDAC8 inhibitor PCI-34051. Data are means and standard deviations of three independent experiments.

study.

## 2.8. Drug metabolism and pharmacokinetic properties

The BTZT compounds show also promising *in silico* drug metabolism and pharmacokinetic (DMPK) properties (Table S2). All compounds fulfill the Lipinski rule of 5, which speaks for good absorption and permeation. The compounds show a Topological Polar Surface Area (TPSA) [34] between 73 and 97 Å<sup>2</sup> (Table S2). These values are significantly below the threshold of 140 Å<sup>2</sup> indicating that the compounds are supposed to penetrate cell membranes in agreement with the target engagement data within cells [34]. To prioritize compounds towards a specific target usually normalized activity measures such as Ligand Efficiency (LE) [35] or Lipophilic Ligand Efficiency (LLE) [36] are exploited to correct for bias towards lipophilicity and high molecular weight compounds. The great potential of the BTZT compounds is confirmed by beneficial LE-values ranging from 0.37 to 0.62 and LLE-values from 3.1 to 6.4 (Table S2). Lead compounds usually show LLE-values above 3 and clinical candidates above 5.

## 3. Conclusions

In our effort to develop potent and selective HDAC8 inhibitors, we identified a novel class of active substances, BTZTs, that lack classic zinc binding groups, but bind to the active site of the enzyme. The most potent representative of BTZT derivatives shows double digit nanomolar potency and considerable isoenzyme selectivity for HDAC8. In contrast to the starting structure, PD-404,182, all BTZT analogs are extremely robust against millimolar concentration of GSH that occurs in cells and is responsible for the maintenance of the cellular redox state. BTZTs penetrate cell membranes and inhibit the enzyme activity of intracellular HDAC8. Furthermore, compound **4b** reduces colony growth of neuroblastoma tumor cells in the range of the known HDAC8 inhibitor PCI-34051 with hydroxamate zinc binding group. The BTZT pharmacophore bears considerable potential for further optimization, since both, potency and selectivity, are highly correlated. In addition, BTZT compounds avoid intrinsic drawbacks of the hydroxamate zinc binding group of conventional HDAC inhibitors like unselectivity and potential mutagenicity. As potent and selective HDAC8 inhibitors, BTZT analogs are predestined as tools for the investigation of the biological function of HDAC8. Beyond, they are

promising candidates for the development of anti-cancer drugs and particularly neuroblastoma.

## 4. Experimental section

### 4.1. Chemical analytics 4-(4,5-dihydro-1H-imidazol-2-yl)-3-fluorobenzonitrile (**2a**)

3-Fluoro-4-formylbenzonitrile (**1a**) (1.00 g, 6.71 mmol) was subjected to general procedure, using ethane-1,2-diamine (493 µL, 443 mg, 7.38 mmol) K<sub>2</sub>CO<sub>3</sub> (2.81 g, 20.3 mmol) and I<sub>2</sub> (2.13 g, 8.38 mmol). 4-(4,5-Dihydro-1H-imidazole-2-yl)-3-fluorobenzonitrile (**2a**) was received as yellowish solid (1.18 g, 6.26 mmol, 93%).

<sup>1</sup>H NMR (CDCl<sub>3</sub>, 500 MHz): δ = 8.16 (t, J = 7.8 Hz, 1H), 7.45 (dd, J = 8.1, 1.5 Hz, 1H), 7.38 (dd, J = 10.9, 1.5 Hz, 1H), 3.75 (s, 4H).

<sup>13</sup>C NMR (CDCl<sub>3</sub>, 126 MHz): δ = 160.90 (s), 159.34 (d, J = 2.2 Hz), 158.88 (s), 132.17 (d, J = 3.4 Hz), 128.12 (d, J = 3.2 Hz), 122.90 (d, J = 11.1 Hz), 120.26 (s), 120.04 (s), 116.98 (d, J = 2.0 Hz), 115.33 (d, J = 10.3 Hz).

HPLC/MS (t<sub>r</sub> = 10.551 min, 70 eV, EI) m/z (%) = 190.100 (100) [M+H]<sup>+</sup>

### 4.1.1. 2-(2,5-Dibromophenyl)-4,5-dihydro-1H-imidazole (**2b**)

2,5-Dibromobenzaldehyde (**1b**) (2.38, 9.00 mmol) was subjected to general procedure, using ethane-1,2-diamine (661 µL, 595 mg, 9.90 mmol), K<sub>2</sub>CO<sub>3</sub> (3.73 g, 27.0 mmol) and I<sub>2</sub> (2.86 g, 11.25 mmol). 2-(2,5-Dibromophenyl)-4,5-dihydro-1H-imidazole (**2b**) was received as yellowish solid (2.61 g, 8.59 mmol, 95%).

<sup>1</sup>H NMR (CDCl<sub>3</sub>, 500 MHz): δ = 7.77 (d, J = 2.4 Hz, 1H), 7.41 (d, J = 8.5 Hz, 1H), 7.35 (dd, J = 8.5, 2.4 Hz, 1H), 3.76 (s, 5H).

<sup>13</sup>C NMR (CDCl<sub>3</sub>, 126 MHz): δ = 163.25 (s), 134.74 (s), 134.67 (s), 134.14 (s), 134.10 (s), 121.48 (s), 119.56 (s), 50.60 (s).

GC/MS (t<sub>r</sub> = 19.717 min, 70 eV, EI) m/z (%) = 305.9 (20), 303.9 [M<sup>+</sup>] (42), 301.9 (25), 276.9 (49), 274.8 (100), 272.9 (51), 195.9 (18), 193.9 (18), 143.0 (8), 115.0 (18), 88.0 (10) 75.0 (13).

### 4.1.2. 2-(2-Bromo-6-fluorophenyl)-4,5-dihydro-1H-imidazole (**2c**)

2-Bromo-6-fluorobenzaldehyde (**1c**) (500 mg, 2.46 mmol) was subjected to general procedure, using ethane-1,2-diamine (181 µL, 163 mg, 2.71 mmol) K<sub>2</sub>CO<sub>3</sub> (1.03 g, 7.46 mmol) and I<sub>2</sub> (781 mg, 3.08 mmol). 2-(2-Bromo-6-fluorophenyl)-4,5-dihydro-1H-imidazole (**2c**) was received as yellowish solid (529 mg, 2.18 mmol, 88%).

<sup>1</sup>H NMR (CDCl<sub>3</sub>, 500 MHz): δ = 7.36 (d, J = 8.1 Hz, 1H), 7.21 (td, J = 8.2, 5.8 Hz, 1H), 7.07–7.02 (m, 1H), 3.77 (s, 4H).

<sup>13</sup>C NMR (CDCl<sub>3</sub>, 126 MHz): δ = 159.94 (d, J = 407.1 Hz), 159.55 (s), 131.63 (d, J = 9.0 Hz), 128.64 (d, J = 3.2 Hz), 122.87 (d, J = 3.4 Hz), 119.20 (dd, J = 864.2, 20.6 Hz), 114.98 (d, J = 22.0 Hz), 62.27 (s), 50.56 (s).

HPLC/MS (t<sub>r</sub> = 1.269 min, 70 eV, EI) m/z (%) = 245.000/243.100 (100/85) [M+H]<sup>+</sup>

### 4.1.3. 2-(2-Chloro-6-fluorophenyl)-4,5-dihydro-1H-imidazole (**2d**)

2-Chloro-6-fluorobenzaldehyde (**1d**) (1.00 g, 6.31 mmol) was subjected to general procedure, using ethane-1,2-diamine (463 µL, 417 mg, 6.94 mmol) K<sub>2</sub>CO<sub>3</sub> (2.64 g, 19.1 mmol) and I<sub>2</sub> (2.00 g, 7.88 mmol). 2-(2-Chloro-6-fluorophenyl)-4,5-dihydro-1H-imidazole (**2d**) was received as yellowish solid (1.16 g, 5.82 mmol, 92%).

<sup>1</sup>H NMR (CDCl<sub>3</sub>, 500 MHz): δ = 7.31–7.25 (m, 1H), 7.19 (d, J = 8.1 Hz, 1H), 7.03–6.98 (m, 1H), 3.76 (s, 1H).

<sup>13</sup>C NMR (CDCl<sub>3</sub>, 126 MHz): δ = 160.69 (d, J = 252.5 Hz), 157.51 (d, J = 229.7 Hz), 134.13 (s), 131.28 (d, J = 9.4 Hz), 125.55 (d, J = 3.1 Hz), 117.73 (dd, J = 666.6, 20.7 Hz), 114.43 (d, J = 22.0 Hz), 62.42 (s), 50.33 (s).

GC/MS (t<sub>r</sub> = 10.062 min, 70 eV, EI) m/z (%) = 198.0 [M<sup>+</sup>] (30),

171.0 (33), 169.0 (100), 156.0 (6), 134.0 (13), 107.0 (25).

#### 4.1.4. 2-(4-Bromo-2-fluorophenyl)-4,5-dihydro-1H-imidazole (**2e**)

4-Bromo-2-fluorobenzaldehyde (**1e**) (2.03 g, 10.00 mmol) was subjected to general procedure, using ethane-1,2-diamine (735  $\mu$ L, 661 mg, 11.0 mmol),  $K_2CO_3$  (4.15 g, 30.0 mmol) and  $I_2$  (3.17 g, 12.5 mmol). 2-(4-Bromo-2-fluorophenyl)-4,5-dihydro-1H-imidazole (**2e**) was received as yellowish solid (2.36 g, 9.70 mmol, 97%).

$^1H$  NMR ( $CDCl_3$ , 500 MHz):  $\delta$  = 7.91 (t,  $J$  = 8.3 Hz, 1H), 7.31 (dd,  $J$  = 8.3, 1.8 Hz, 1H), 7.27 (dd,  $J$  = 11.2, 1.8 Hz, 1H), 3.73 (s, 4H).

$^{13}C$  NMR ( $CDCl_3$ , 126 MHz):  $\delta$  = 161.34 (s), 160.23 (s), 159.32 (s), 132.04 (d,  $J$  = 3.5 Hz), 128.05 (d,  $J$  = 3.0 Hz), 125.12 (d,  $J$  = 10.2 Hz), 119.80 (d,  $J$  = 26.7 Hz), 117.27 (d,  $J$  = 10.9 Hz), 49.84 (s).

GC/MS ( $t_r$  = 16.687 min, 70 eV, EI)  $m/z$  (%) = 244.0 (37), 242 [ $M^+$ ] (40), 215.0 (97), 213.0 (100), 162.1 (11), 134.0 (23), 107.0 (21), 94.0 (13).

#### 4.1.5. 2-(2-Fluoro-5-iodophenyl)-4,5-dihydro-1H-imidazole (**2f**)

2-Fluoro-5-iodobenzaldehyde (**1f**) (500 mg, 2.00 mmol) was subjected to general procedure, using ethane-1,2-diamine (147  $\mu$ L, 132 mg, 2.20 mmol)  $K_2CO_3$  (838 mg, 6.06 mmol) and  $I_2$  (635 mg, 2.50 mmol). 2-(2-Fluoro-5-iodophenyl)-4,5-dihydro-1H-imidazole (**2f**) was received as yellowish solid (450 mg, 1.55 mmol, 78%).

$^1H$  NMR ( $CDCl_3$ , 500 MHz):  $\delta$  = 8.37 (dd,  $J$  = 7.0, 2.4 Hz, 1H), 7.66 (ddd,  $J$  = 8.7, 4.8, 2.4 Hz, 1H), 6.84 (dd,  $J$  = 11.4, 8.7 Hz, 1H), 3.74 (s, 5H).

$^{13}C$  NMR ( $CDCl_3$ , 126 MHz):  $\delta$  = 161.62 (s), 159.66 (s), 140.94 (d,  $J$  = 8.8 Hz), 139.56 (d,  $J$  = 2.5 Hz), 120.21 (d,  $J$  = 11.7 Hz), 118.44 (s), 118.24 (s), 87.55 (d,  $J$  = 2.9 Hz), 49.90 (s).

HPLC/MS ( $t_r$  = 2.053 min, 70 eV, EI)  $m/z$  (%) = 291.000 (100) [ $M+H$ ] $^+$

#### 4.1.6. 2-(2-Bromo-5-fluorophenyl)-4,5-dihydro-1H-imidazole (**2g**)

2-Bromo-5-fluorobenzaldehyde (**1g**) (2.03 g, 10.00 mmol) was subjected to general procedure, using ethane-1,2-diamine (735  $\mu$ L, 661 mg, 11.0 mmol),  $K_2CO_3$  (4.15 g, 30.0 mmol) and  $I_2$  (3.17 g, 12.5 mmol). 2-(2-Bromo-5-fluorophenyl)-4,5-dihydro-1H-imidazole (**2g**) was received as yellowish solid (2.13 g, 8.76 mmol, 88%).

$^1H$  NMR ( $CDCl_3$ , 500 MHz):  $\delta$  = 7.51 (dd,  $J$  = 8.8, 5.1 Hz, 1H), 7.36 (dd,  $J$  = 8.9, 3.1 Hz, 1H), 6.96 (ddd,  $J$  = 8.8, 7.7, 3.1 Hz, 1H), 3.75 (s, 1H).

$^{13}C$  NMR ( $CDCl_3$ , 126 MHz):  $\delta$  = 163.46 (s), 161.67 (d,  $J$  = 248.5 Hz), 134.79 (d,  $J$  = 7.8 Hz), 134.79–134.58 (m), 118.55 (d,  $J$  = 2.4 Hz), 118.36 (s), 115.10 (d,  $J$  = 3.2 Hz), 50.60 (s).

GC/MS ( $t_r$  = 16.301 min, 70 eV, EI)  $m/z$  (%) = 244.0 (33), 242 [ $M^+$ ] (49), 214.9 (98), 212.9 (100), 162.0 (13), 134.0 (52), 107.0 (45), 94.0 (15).

#### 4.1.7. 2-(2,6-Difluoro-4-bromophenyl)-4,5-dihydro-1H-imidazole (**2h**)

2,6-Difluoro-4-bromobenzaldehyde (**1h**) (500 mg, 2.26 mmol) was subjected to general procedure, using ethane-1,2-diamine (166  $\mu$ L, 150 mg, 2.49 mmol),  $K_2CO_3$  (947 mg, 6.86 mmol) and  $I_2$  (718 mg, 2.83 mmol). 2-(2,6-Difluoro-4-bromophenyl)-4,5-dihydro-1H-imidazole (**2h**) was received as yellowish solid (273 mg, 1.05 mmol, 46%).

$^1H$  NMR ( $CDCl_3$ , 300 MHz):  $\delta$  = 7.18 (s, 1H), 7.15 (s, 1H), 3.80 (s, 4H).

#### 4.1.8. 2-(2-Fluoro-5-methylphenyl)-4,5-dihydro-1H-imidazole (**2i**)

2-Fluoro-5-methylbenzaldehyde (**1i**) (1.38 g, 10.00 mmol) was subjected to general procedure, using ethane-1,2-diamine (734  $\mu$ L, 660 mg, 11.0 mmol),  $K_2CO_3$  (4.18 g, 30.3 mmol) and  $I_2$  (3.17 g, 12.5 mmol). 2-(2-Fluoro-5-methylphenyl)-4,5-dihydro-1H-imidazole (**2i**) was received as yellowish solid (1.71 g, 9.57 mmol, 96%).

$^1H$  NMR ( $CDCl_3$ , 500 MHz):  $\delta$  = 7.82 (dd,  $J$  = 7.2, 2.1 Hz, 1H), 7.17–7.11 (m, 1H), 6.93 (dd,  $J$  = 11.7, 8.4 Hz, 1H), 5.69 (s, 1H), 3.72 (s, 5H), 2.27 (s, 4H).

$^{13}C$  NMR ( $CDCl_3$ , 126 MHz):  $\delta$  = 161.30 (s), 159.03 (d,  $J$  = 247.1 Hz), 134.12 (s), 133.72–130.23 (m), 117.14 (d,  $J$  = 10.8 Hz), 115.80 (d,  $J$  = 23.5 Hz), 49.62 (s), 20.45 (s).

#### 4.1.9. 2-(2-Fluoro-4-chlorophenyl)-4,5-dihydro-1H-imidazole (**2j**)

2-Fluoro-4-chlorobenzaldehyde (**1j**) (500 mg, 3.15 mmol) was subjected to general procedure, using ethane-1,2-diamine (232  $\mu$ L, 208 mg, 3.47 mmol),  $K_2CO_3$  (1.32 g, 9.55 mmol) and  $I_2$  (1.00 g, 3.94 mmol). 2-(2-Fluoro-4-chlorophenyl)-4,5-dihydro-1H-imidazole (**2j**) was received as yellowish solid (590 mg, 2.97 mmol, 92%).

$^1H$  NMR ( $CDCl_3$ , 300 MHz):  $\delta$  = 7.37 (dd,  $J$  = 14.4, 6.7 Hz, 1H), 7.01 (t,  $J$  = 7.9 Hz, 1H), 3.36 (t,  $J$  = 5.7 Hz, 2H), 1.83 (dt,  $J$  = 11.3, 5.7 Hz, 1H).

$^{13}C$  NMR ( $CDCl_3$ , 126 MHz):  $\delta$  = 155.07 (d,  $J$  = 252.6 Hz), 152.64 (s), 132.31 (s), 128.61 (d,  $J$  = 1.5 Hz), 124.74 (d,  $J$  = 4.5 Hz), 123.59 (d,  $J$  = 12.8 Hz), 121.51 (d,  $J$  = 18.3 Hz), 52.96 (d,  $J$  = 98.15 Hz), 40.96 (s), 19.54 (s).

#### 4.1.10. 2-(2-Fluoro-6-methylphenyl)-4,5-dihydro-1H-imidazole (**2k**)

2-Fluoro-6-methylbenzaldehyde (**1k**) (1.08 g, 7.85 mmol) was subjected to general procedure, using ethane-1,2-diamine (531  $\mu$ L, 479 mg, 7.96 mmol),  $K_2CO_3$  (3.00 g, 21.7 mmol) and  $I_2$  (2.30 g, 9.05 mmol). 2-(2-Fluoro-6-methylphenyl)-4,5-dihydro-1H-imidazole (**2k**) was received as yellowish solid (1.24 g, 6.95 mmol, 89%).

GC/MS ( $t_r$  = 14.195 min, 70 eV, EI)  $m/z$  (%) = 178.1 (87), 149.1 (65), 148.1 (100), 122.0 (32), 101.0 (14), 28.0 (40).

#### 4.1.11. 2-(2-Fluoro-6-iodophenyl)-4,5-dihydro-1H-imidazole (**2l**)

2-Fluoro-6-iodobenzaldehyde (**1l**) (500 mg, 2.00 mmol) was subjected to general procedure, using ethane-1,2-diamine (147  $\mu$ L, 132 mg, 2.20 mmol),  $K_2CO_3$  (838 mg, 6.06 mmol) and  $I_2$  (635 mg, 2.50 mmol). 2-(2-Fluoro-6-iodophenyl)-4,5-dihydro-1H-imidazole (**2l**) was received as yellowish solid (575 mg, 1.98 mmol, 99%).

$^1H$  NMR ( $CDCl_3$ , 500 MHz):  $\delta$  = 7.61 (ddd,  $J$  = 6.7, 4.0, 1.0 Hz, 1H), 7.08–7.07 (m, 1H), 7.07–7.04 (m, 1H), 3.78 (s, 4H).

$^{13}C$  NMR ( $CDCl_3$ , 126 MHz):  $\delta$  = 161.18 (d,  $J$  = 121.0 Hz), 159.87 (d,  $J$  = 300.5 Hz), 136.05–134.48 (m), 132.16 (d,  $J$  = 8.6 Hz), 121.44 (dd,  $J$  = 1208.4, 20.2 Hz), 115.77 (d,  $J$  = 21.9 Hz), 96.73 (d,  $J$  = 1.0 Hz), 62.01 (s), 50.59 (s).

HPLC/MS ( $t_r$  = 1.415 min, 70 eV, EI)  $m/z$  (%) = 291.000 (100) [ $M+H$ ] $^+$

#### 4.1.12. 2-(3-Chloro-2-fluorophenyl)-4,5-dihydro-1H-imidazole (**2m**)

2-Fluoro-3-chlorobenzaldehyde (**1m**) (500 mg, 3.15 mmol) was subjected to general procedure, using ethane-1,2-diamine (232  $\mu$ L, 208 mg, 3.47 mmol),  $K_2CO_3$  (1.32 g, 9.55 mmol) and  $I_2$  (1.00 g, 3.94 mmol). 2-(3-Chloro-2-fluorophenyl)-4,5-dihydro-1H-imidazole (**2m**) was received as yellowish solid (510 mg, 2.55 mmol, 81%).

$^1H$  NMR ( $CDCl_3$ , 300 MHz):  $\delta$  = 7.87 (t,  $J$  = 7.2 Hz, 1H), 7.41 (t,  $J$  = 7.5 Hz, 1H), 7.07 (t,  $J$  = 7.9 Hz, 1H), 5.44 (s, 1H), 3.72 (s, 4H).

$^{13}C$  NMR ( $CDCl_3$ , 75 MHz):  $\delta$  = 160.24 (s), 156.10 (d,  $J$  = 252.2 Hz), 132.56 (s), 129.23 (d,  $J$  = 2.3 Hz), 124.75 (d,  $J$  = 4.3 Hz), 121.83 (d,  $J$  = 19.1 Hz), 119.75 (d,  $J$  = 11.0 Hz), 49.85 (s).

HPLC/MS ( $t_r$  = 1.689 min, 70 eV, EI)  $m/z$  (%) = 199.000 (100) [ $M+H$ ] $^+$ , 201.100 (32).

#### 4.1.13. 2-(2,3-Difluorophenyl)-4,5-dihydro-1H-imidazole (**2n**)

2,3-Difluorobenzaldehyde (**1n**) (1.43 g, 10.00 mmol) was subjected to general procedure, using ethane-1,2-diamine (738  $\mu$ L,

664 mg, 11.0 mmol),  $K_2CO_3$  (4.21 g, 30.4 mmol) and  $I_2$  (3.19 g, 12.5 mmol). 2-(2,3-Difluorophenyl)-4,5-dihydro-1H-imidazole (**2n**) was received as yellowish solid (1.55 g, 8.51 mmol, 85%).

$^1H$  NMR ( $CDCl_3$ , 500 MHz):  $\delta$  = 7.75 (ddt,  $J$  = 8.0, 6.3, 1.7 Hz, 1H), 7.20 (dtd,  $J$  = 9.8, 8.0, 1.7 Hz, 1H), 7.08 (tdd,  $J$  = 8.2, 4.8, 1.6 Hz, 1H), 5.15 (s, 1H), 3.74 (d,  $J$  = 7.7 Hz, 4H).

$^{13}C$  NMR ( $CDCl_3$ , 126 MHz):  $\delta$  = 160.13 (s), 151.79 (d,  $J$  = 13.6 Hz), 150.21 (d,  $J$  = 14.3 Hz), 149.82 (d,  $J$  = 13.6 Hz), 148.20 (d,  $J$  = 14.2 Hz), 125.46 (s), 124.33 (dd,  $J$  = 6.3, 4.7 Hz), 120.31 (d,  $J$  = 7.7 Hz), 119.07 (d,  $J$  = 17.1 Hz), 49.91 (s).

GC/MS ( $t_r$  = 13.551 min, 70 eV, EI)  $m/z$  (%) = 182.1 [ $M^+$ ] (38), 153.0 (100), 126.0 (9), 113.0 (9).

#### 4.1.14. 3-Bromo-4-(4,5-dihydro-1H-imidazole-2-yl)-N,N-dimethylaniline (**2o**)

2-Bromo-4-(dimethylamino)benzaldehyde (**1o**) (458 mg, 2.01 mmol) was subjected to general procedure, using ethane-1,2-diamine (147  $\mu$ L, 133 mg, 2.21 mmol),  $K_2CO_3$  (841 mg, 6.08 mmol) and  $I_2$  (637 mg, 2.51 mmol). 3-Bromo-4-(4,5-dihydro-1H-imidazole-2-yl)-N,N-dimethylaniline (**2o**) was received as yellowish solid (520 mg, 1.94 mmol, 97%).

$^1H$  NMR ( $CDCl_3$ , 500 MHz):  $\delta$  =  $^1H$  NMR ( $CDCl_3$ , 500 MHz):  $\delta$  =  $^1H$  NMR ( $CDCl_3$ , 500 MHz):  $\delta$  = 7.60 (d,  $J$  = 8.8 Hz, 1H), 6.78 (d,  $J$  = 2.6 Hz, 1H), 6.58 (dd,  $J$  = 8.8, 2.6 Hz, 1H), 3.71 (s, 4H), 2.94 (d,  $J$  = 2.9 Hz, 7H).

$^{13}C$  NMR ( $CDCl_3$ , 126 MHz):  $\delta$  = 164.68 (s), 151.90 (s), 132.14 (s), 121.72 (s), 118.69 (s), 115.79 (s), 110.76 (s), 50.05 (s), 40.05 (s).

GC/MS ( $t_r$  = 23.206 min, 70 eV, EI)  $m/z$  (%) = 269.1 (80), 267.1 [ $M^+$ ] (85), 240.1 (97), 238.1 (100), 225.1 (18), 187.2 (9), 159.1 (15), 143.1 (13), 119.2 (13).

#### 4.1.15. 2-(2-Fluoro-5-methoxyphenyl)-4,5-dihydro-1H-imidazole (**2p**)

2-Fluoro-5-methoxybenzaldehyde (**1p**) (500 mg, 3.24 mmol) was subjected to general procedure, using ethane-1,2-diamine (238  $\mu$ L, 214 mg, 3.57 mmol),  $K_2CO_3$  (1.36 g, 9.83 mmol) and  $I_2$  (1.03 g, 4.05 mmol). 2-(2-Fluoro-5-methoxyphenyl)-4,5-dihydro-1H-imidazole (**2p**) was received as yellowish solid (876 mg, 3.38 mmol, 84%).

$^1H$  NMR ( $DMSO-d_6$ , 300 MHz):  $\delta$  = 7.85–7.76 (m, 1H), 7.35–7.18 (m, 2H), 4.22–3.86 (m, 8H).

HPLC/MS ( $t_r$  = 1.597 min, 70 eV, EI)  $m/z$  (%) = 195.100 (100) [ $M+H$ ] $^+$

#### 4.1.16. 2-(2-Fluoro-4-methoxyphenyl)-4,5-dihydro-1H-imidazole (**2q**)

2-Fluoro-4-methoxybenzaldehyde (**1x**) (308 mg, 2.00 mmol) was subjected to general procedure, using ethane-1,2-diamine (147  $\mu$ L, 132 mg, 2.20 mmol),  $K_2CO_3$  (828 mg, 5.99 mmol) and  $I_2$  (639 mg, 2.52 mmol). 2-(2-Fluoro-4-methoxyphenyl)-4,5-dihydro-1H-imidazole (**2q**) was received as brown solid (409 mg, 1.97 mmol, 98%).

$^1H$  NMR (300 MHz,  $CDCl_3$ )  $\delta$  7.95 (t,  $J$  = 8.9 Hz, 1H), 6.69 (dd,  $J$  = 8.8, 2.5 Hz, 1H), 6.56 (dd,  $J$  = 13.8, 2.5 Hz, 1H), 3.77 (s, 3H), 3.69 (s, 4H).

$^{13}C$  NMR ( $CDCl_3$ , 75 MHz):  $\delta$  = 163.25 (s), 162.68 (d,  $J$  = 12.1 Hz), 160.89 (s), 159.95 (s), 131.67 (d,  $J$  = 4.9 Hz), 110.61 (s), 101.71 (s), 101.35 (s), 55.66 (s), 49.59 (s).

GC/MS ( $t_r$  = 18.404 min, 70 eV, EI)  $m/z$  (%) = 194.200 (50), 165.100 (100), 150.1 (37), 95.1 (9).

#### 4.1.17. 2-(2-Bromo-5-chlorophenyl)-4,5-dihydro-1H-imidazole (**2r**)

2-Bromo-5-chlorobenzaldehyde (**1r**) (878 mg, 4.00 mmol) was subjected to general procedure, using ethane-1,2-diamine (294  $\mu$ L, 265 mg, 4.40 mmol),  $K_2CO_3$  (1.66 g, 12.0 mmol) and  $I_2$  (1.27 g,

5.00 mmol). 2-(2-Bromo-5-chlorophenyl)-4,5-dihydro-1H-imidazole (**2r**) was received as yellowish solid (876 mg, 3.38 mmol, 84%).

$^1H$  NMR ( $CDCl_3$ , 500 MHz):  $\delta$  = 7.61 (d,  $J$  = 2.6 Hz, 1H), 7.47 (d,  $J$  = 8.6 Hz, 1H), 7.20 (dd,  $J$  = 8.6, 2.6 Hz, 1H), 3.74 (s, 4H).

$^{13}C$  NMR ( $CDCl_3$ , 126 MHz):  $\delta$  = 163.28 (s), 134.39 (s), 133.64 (s), 131.15 (s), 131.07 (s), 118.69 (s), 50.55 (s).

GC/MS ( $t_r$  = 18.778 min, 70 eV, EI)  $m/z$  (%) = 260.000 [ $M^+$ ] (42), 258.0 (33), 231.0 (100), 229.0 (78), 150.1 (23), 123.1 (16) 75.1 (10).

#### 4.1.18. 2-(2,6-Difluorophenyl)-4,5-dihydro-1H-imidazole (**2s**)

2,6-Difluorobenzaldehyde (**1s**) (1.42 g, 10.00 mmol) was subjected to general procedure, using ethane-1,2-diamine (734  $\mu$ L, 660 mg, 11.0 mmol),  $K_2CO_3$  (4.15 g, 30.0 mmol) and  $I_2$  (3.17 g, 12.5 mmol). 2-(2,6-Difluorophenyl)-4,5-dihydro-1H-imidazole (**2s**) was received as yellowish solid (1.54 g, 8.48 mmol, 85%).

$^1H$  NMR ( $CDCl_3$ , 500 MHz):  $\delta$  = 7.30 (tt,  $J$  = 8.4, 6.3 Hz, 1H), 6.93–6.87 (m, 2H), 5.03 (s, 1H), 3.73 (s, 4H).

$^{13}C$  NMR ( $CDCl_3$ , 126 MHz):  $\delta$  = 160.96 (dd,  $J$  = 253.6, 6.5 Hz), 156.37 (s), 131.41 (t,  $J$  = 10.7 Hz), 112.00 (dd,  $J$  = 21.6, 4.1 Hz), 109.57 (t,  $J$  = 17.3 Hz), 50.08 (s).

GC/MS ( $t_r$  = 13.858 min, 70 eV, EI)  $m/z$  (%) = 182.100 [ $M^+$ ] (32), 153.100 (100).

#### 4.1.19. 2-(2-Fluoro-4-methylphenyl)-4,5-dihydro-1H-imidazole (**2t**)

2-Fluoro-4-methylbenzaldehyde (**1t**) (1.38 g, 10.00 mmol) was subjected to general procedure, using ethane-1,2-diamine (734  $\mu$ L, 660 mg, 11.0 mmol),  $K_2CO_3$  (4.18 g, 30.3 mmol) and  $I_2$  (3.17 g, 12.5 mmol). 2-(2-Fluoro-4-methylphenyl)-4,5-dihydro-1H-imidazole (**2t**) was received as yellowish solid (1.68 g, 9.43 mmol, 94%).

$^1H$  NMR ( $CDCl_3$ , 500 MHz):  $\delta$  = 7.89 (t,  $J$  = 8.0 Hz, 1H), 6.96 (d,  $J$  = 8.0 Hz, 1H), 6.87 (d,  $J$  = 12.8 Hz, 1H), 5.80 (s, 1H), 3.73 (s, 4H), 2.33 (s, 3H).

$^{13}C$  NMR ( $CDCl_3$ , 126 MHz):  $\delta$  = 161.21 (s,  $J$  = 1.7 Hz), 160.66 (d,  $J$  = 249.7 Hz), 143.65 (d,  $J$  = 9.0 Hz), 130.63 (d,  $J$  = 3.0 Hz), 125.44 (d,  $J$  = 2.1 Hz), 116.54 (d,  $J$  = 23.1 Hz), 114.66 (d,  $J$  = 10.8 Hz), 49.46 (s), 21.32 (s).

#### 4.1.20. 2-(2-Bromophenyl)-4,5-dihydro-1H-imidazole (**2u**)

2-Bromobenzaldehyde (**1u**) (924 mg, 5.00 mmol) was subjected to general procedure, using ethane-1,2-diamine (367  $\mu$ L, 330 mg, 5.50 mmol),  $K_2CO_3$  (2.09 g, 15.1 mmol) and  $I_2$  (1.58 g, 6.24 mmol). 2-(2-Bromophenyl)-4,5-dihydro-1H-imidazole (**2u**) was received as yellowish solid (926 mg, 4.11 mmol, 82%).

$^1H$  NMR ( $CDCl_3$ , 300 MHz):  $\delta$  = 7.55 (td,  $J$  = 7.9, 1.6 Hz, 2H), 7.25 (tdd,  $J$  = 15.2, 7.5, 1.6 Hz, 2H), 3.72 (s, 4H).

$^{13}C$  NMR ( $CDCl_3$ , 75 MHz):  $\delta$  = 164.50 (s), 133.21 (s), 132.73 (s), 131.09 (d,  $J$  = 3.3 Hz), 127.38 (s), 120.80 (s), 50.30 (s).

GC/MS ( $t_r$  = 16.819 min, 70 eV, EI)  $m/z$  (%) = 224.100 [ $M^+$ ] (48).

#### 4.1.21. 2-(2-Fluoro-3-methylphenyl)-4,5-dihydro-1H-imidazole (**2v**)

2-Fluoro-3-methylbenzaldehyde (**1v**) (500 mg, 3.62 mmol) was subjected to general procedure, using ethane-1,2-diamine (266  $\mu$ L, 239 mg, 3.98 mmol),  $K_2CO_3$  (1.52 g, 10.97 mmol) and  $I_2$  (1.15 g, 4.52 mmol). 2-(2-Fluoro-3-methylphenyl)-4,5-dihydro-1H-imidazole (**2v**) was received as yellowish solid (503 mg, 2.82 mmol, 78%).

$^1H$  NMR (300 MHz,  $DMSO$ )  $\delta$  7.50 (t,  $J$  = 7.2 Hz, 1H), 6.98 (t,  $J$  = 7.3 Hz, 1H), 6.78 (t,  $J$  = 7.6 Hz, 1H), 4.33 (s, 2H), 3.46 (s, 4H).

$^{13}C$  NMR ( $DMSO$ , 75 MHz):  $\delta$  = 160.83 (s), 158.55 (d,  $J$  = 249.6 Hz), 133.09 (d,  $J$  = 5.8 Hz), 134.07–127.87 (m), 127.65 (d,  $J$  = 2.7 Hz), 124.94 (d,  $J$  = 18.7 Hz), 123.30 (d,  $J$  = 3.9 Hz), 49.07 (s), 13.99 (d,  $J$  = 5.2 Hz).

#### 4.1.22. 2-(2-Fluoro-5-methylphenyl)-1,4,5,6-tetrahydropyrimidine (3a)

2-Fluoro-5-methylbenzaldehyde (**1i**) (500 mg, 3.62 mmol) was subjected to general procedure, using propane-1,3-diamine (328  $\mu$ l, 295 mg, 3.98 mmol),  $K_2CO_3$  (1.52 g, 11.0 mmol) and  $I_2$  (1.15 g, 4.52 mmol). 2-(2-Fluoro-5-methylphenyl)-1,4,5,6-tetrahydropyrimidine (**3a**) was received as brown solid (800 mg, 3.11 mmol, 86%).

$^1H$  NMR ( $CDCl_3$ , 500 MHz):  $\delta$  = 7.33 (dd,  $J$  = 6.8, 1.8 Hz, 1H), 7.18–7.12 (m, 1H), 6.89 (dd,  $J$  = 10.5, 8.5 Hz, 1H), 3.34 (t,  $J$  = 5.8 Hz, 4H), 2.23 (s, 3H), 1.84–1.76 (m, 2H).

$^{13}C$  NMR ( $CDCl_3$ , 126 MHz):  $\delta$  = 157.71 (d,  $J$  = 249.4 Hz), 154.52 (s), 134.26 (d,  $J$  = 3.1 Hz), 133.53 (d,  $J$  = 8.3 Hz), 130.39 (s), 119.32 (d,  $J$  = 12.3 Hz), 115.95 (d,  $J$  = 22.0 Hz), 40.26 (s), 20.47 (s), 19.01 (s).

HPLC/MS ( $t_r$  = 1.728 min, 70 eV, EI)  $m/z$  (%) = 193.100 (100)  $[M+H]^+$

#### 4.1.23. 2-(2-Fluoro-6-iodophenyl)-1,4,5,6-tetrahydropyrimidine (3b)

2-Fluoro-6-iodobenzaldehyde (500 mg, 2.00 mmol) (**1i**) was subjected to general procedure, using propane-1,3-diamine (181  $\mu$ l, 163 mg, 2.20 mmol),  $K_2CO_3$  (838 mg, 6.06 mmol) and  $I_2$  (635 mg, 2.50 mmol). 2-(2-Fluoro-6-iodophenyl)-1,4,5,6-tetrahydropyrimidine (**3b**) was received as brown solid (268 mg, 0.88 mmol, 44%).

HPLC/MS ( $t_r$  = 1.400 min, 70 eV, EI)  $m/z$  (%) = 305.000 (100)  $[M+H]^+$

#### 4.1.24. 2-(2-Chloro-6-fluorophenyl)-1,4,5,6-tetrahydropyrimidine (3c)

2-Chloro-6-fluorobenzaldehyde (**1d**) (1.00 g, 6.31 mmol) was subjected to general procedure, using propane-1,3-diamine (584  $\mu$ l, 514 mg, 6.94 mmol),  $K_2CO_3$  (2.64 g, 19.1 mmol) and  $I_2$  (2.00 g, 7.88 mmol). 2-(2-Chloro-6-fluorophenyl)-1,4,5,6-tetrahydropyrimidine (**3c**) was received as brown solid (1.24 g, 5.82 mmol, 92%).

$^1H$  NMR ( $CDCl_3$ , 500 MHz):  $\delta$  = 7.19 (td,  $J$  = 8.3, 6.0 Hz, 1H), 7.00 (d,  $J$  = 8.1 Hz, 1H), 6.83 (td,  $J$  = 8.5, 0.7 Hz, 1H), 3.01 (t,  $J$  = 5.8 Hz, 4H), 1.61–1.54 (m, 2H).

$^{13}C$  NMR ( $CDCl_3$ , 126 MHz):  $\delta$  = 159.19 (d,  $J$  = 253.0 Hz), 151.43 (s), 132.80 (s), 131.73 (d,  $J$  = 9.2 Hz), 124.86 (s), 120.84 (d,  $J$  = 19.6 Hz), 113.94 (d,  $J$  = 21.3 Hz), 18.35 (s).

HPLC/MS ( $t_r$  = 1.164 min, 70 eV, EI)  $m/z$  (%) = 213.100/215.100 (100)  $[M+H]^+$

#### 4.1.25. 2-(2-Fluoro-6-methylphenyl)-1,4,5,6-tetrahydropyrimidine (3d)

2-Fluoro-6-methylbenzaldehyde (**1k**) (1.01 g, 7.30 mmol) was subjected to general procedure, using propane-1,3-diamine (663  $\mu$ l, 590 mg, 7.75 mmol),  $K_2CO_3$  (2.99 g, 21.7 mmol) and  $I_2$  (2.30 g, 9.06 mmol). 2-(2-Fluoro-6-methylphenyl)-1,4,5,6-tetrahydropyrimidine (**3d**) was received as yellowish solid (1.13 mg, 5.87 mmol, 80%).

GC/MS ( $t_r$  = 15.93 min, 70 eV, EI)  $m/z$  (%) = 192  $[M^+]$  (100), 177 (45), 173 (19), 135 (46), 116 (15), 89 (12).

$^1H$  NMR ( $CDCl_3$ , 300 MHz):  $\delta$  = 7.25 (s,  $J$  = 3.7 Hz, 1H), 7.17 (td,  $J$  = 8.0, 5.9 Hz, 1H), 6.90 (d,  $J$  = 7.6 Hz, 1H), 6.82 (t,  $J$  = 8.8 Hz, 1H), 3.12–3.02 (m, 4H), 2.17 (s, 3H), 1.71–1.60 (m, 2H).

$^{13}C$  NMR ( $CDCl_3$ , 75 MHz):  $\delta$  = 159.7 (d,  $J$  = 247.3 Hz), 152.4 (s), 138.7 (d,  $J$  = 2.4 Hz), 130.3 (d,  $J$  = 8.8 Hz), 125.8 (d,  $J$  = 2.8 Hz), 123.9 (d,  $J$  = 16.5 Hz), 112.8 (d,  $J$  = 21.6 Hz), 40.8 (s), 19.9 (s), 18.6 (d,  $J$  = 2.1 Hz).

#### 4.1.26. 4-Fluoro-3-(1,4,5,6-tetrahydropyrimidin-2-yl)benzonitrile (3e)

4-Fluoro-3-formylbenzonitrile (**1a**) (1.00 g, 6.71 mmol) was subjected to general procedure, using propane-1,3-diamine (608  $\mu$ l, 547 mg, 7.38 mmol),  $K_2CO_3$  (2.81 g, 20.3 mmol) and  $I_2$  (2.13 g, 8.38 mmol). 4-Fluoro-3-(1,4,5,6-tetrahydropyrimidin-2-yl)benzonitrile (**3e**) was received as brown solid (879 mg, 4.33 mmol, 65%).

HPLC/MS ( $t_r$  = 11.075 min, 70 eV, EI)  $m/z$  (%) = 204.100 (100)  $[M+H]^+$

#### 4.1.27. 2-(2-Bromo-5-chlorophenyl)-1,4,5,6-tetrahydropyrimidine (3f)

2-Bromo-5-chlorobenzaldehyde (**1r**) (878 g, 4.00 mmol) was subjected to general procedure, using propane-1,3-diamine (367 ml, 327 mg, 4.41 mmol),  $K_2CO_3$  (1.66 g, 12.0 mmol) and  $I_2$  (1.30 g, 5.12 mmol). 2-(2-Bromo-5-chlorophenyl)-1,4,5,6-tetrahydropyrimidine (**3f**) was received as yellow solid (992.7 mg, 3.63 mmol, 91%).

$^1H$  NMR ( $CDCl_3$ , 500 MHz):  $\delta$  = 7.42 (d,  $J$  = 8.5 Hz, 12H), 7.36 (d,  $J$  = 2.6 Hz, 11H), 7.28–7.24 (m, 2H), 7.14 (dd,  $J$  = 8.5, 2.6 Hz, 12H), 4.97 (s, 13H), 3.40–3.33 (m, 50H), 1.84–1.75 (m, 25H).

$^{13}C$  NMR ( $CDCl_3$ , 125 MHz):  $\delta$  = 154.4, 140.4, 134.0, 133.5, 130.4, 130.2, 118.7, 42.2, 20.5.

#### 4.1.28. 2-(2-Bromo-4-(trifluoromethyl)phenyl)-1,4,5,6-tetrahydropyrimidine (3g)

2-Bromo-4-(trifluoromethyl)benzaldehyde (**1v**) (504 mg, 1.99 mmol) was subjected to general procedure, using propane-1,3-diamine (181  $\mu$ l, 163 mg, 2.19 mmol),  $K_2CO_3$  (835 mg, 6.04 mmol) and  $I_2$  (632 mg, 2.49 mmol). 2-(2-Bromo-4-(trifluoromethyl)phenyl)-1,4,5,6-tetrahydropyrimidine (**3g**) was received as brown solid (478 mg, 1.56 mmol, 78%).

$^1H$  NMR ( $CDCl_3$ , 500 MHz):  $\delta$  = 7.64 (t,  $J$  = 5.4 Hz, 2H), 7.43 (dd,  $J$  = 8.3, 2.0 Hz, 1H), 3.42–3.35 (m, 4H), 1.87–1.79 (m, 2H).

$^{13}C$  NMR ( $CDCl_3$ , 126 MHz):  $\delta$  = 154.60 (s), 139.47 (s), 133.71 (s), 130.26 (s), 129.99 (s), 127.35 (d,  $J$  = 3.5 Hz), 126.94 (d,  $J$  = 3.2 Hz), 125.02 (s), 42.15 (s), 30.98 (s), 20.43 (s).

GC/MS ( $t_r$  = 17.461 min, 70 eV, EI)  $m/z$  (%) = 307.000  $[M^+]$  (78).

#### 4.1.29. 2-(2-Fluoro-4-methylphenyl)-1,4,5,6-tetrahydropyrimidine (3h)

2-Fluoro-4-methylbenzaldehyde (**1t**) (1.38 g, 10.0 mmol) was subjected to general procedure, using propane-1,3-diamine (916  $\mu$ l, 815 mg, 11.0 mmol),  $K_2CO_3$  (4.15 g, 30.0 mmol) and  $I_2$  (3.19 g, 12.6 mmol). 2-(2-Fluoro-4-methylphenyl)-1,4,5,6-tetrahydropyrimidine (**3h**) was received as brown viscous oil (1.93 mg, 10.0 mmol, quant.).

GC/MS ( $t_r$  = 16.55 min, 70 eV, EI)  $m/z$  (%) = 192  $[M^+]$  (65), 191  $[(M-H)^+]$  (100), 173 (38), 136 (68), 116 (20), 89 (18).

$^1H$  NMR ( $CDCl_3$ , 500 MHz):  $\delta$  = 7.48 (t,  $J$  = 8.0 Hz, 1H), 6.93–6.87 (m, 1H), 6.81 (d,  $J$  = 12.3 Hz, 1H), 6.36 (s, 1H), 3.38 (dd,  $J$  = 13.1, 7.3 Hz, 4H), 2.31 (s, 3H), 1.85–1.74 (m, 2H).

$^{13}C$  NMR ( $CDCl_3$ , 125 MHz):  $\delta$  = 159.8 (d,  $J$  = 248.8 Hz), 153.0 (s), 142.8 (d,  $J$  = 8.6 Hz), 130.1 (d,  $J$  = 2.6 Hz), 125.2 (d,  $J$  = 2.1 Hz), 119.7 (d,  $J$  = 11.8 Hz), 116.5 (d,  $J$  = 22.7 Hz), 41.4 (s), 21.2 (s), 20.1 (s).

#### 4.1.30. 2-(2-Fluoro-5-iodophenyl)-1,4,5,6-tetrahydropyrimidine (3i)

2-Fluoro-5-iodobenzaldehyde (**1f**) (500 mg, 2.00 mmol) was subjected to general procedure, using propane-1,3-diamine (181  $\mu$ l, 163 mg, 2.20 mmol),  $K_2CO_3$  (838 mg, 6.06 mmol) and  $I_2$  (635 mg, 2.50 mmol). 2-(2-Fluoro-5-iodophenyl)-1,4,5,6-tetrahydropyrimidine (**3i**) was received as brown solid (433 mg, 1.42 mmol, 71%).

$^1H$  NMR ( $CDCl_3$ , 500 MHz):  $\delta$  = 8.02 (dd,  $J$  = 7.0, 2.4 Hz, 1H), 7.60

(ddd,  $J = 8.6, 4.7, 2.4$  Hz, 1H), 6.79 (dd,  $J = 11.1, 8.7$  Hz, 1H), 3.46–3.40 (m, 4H), 1.87–1.79 (m, 2H).

$^{13}\text{C}$  NMR ( $\text{CDCl}_3$ , 126 MHz):  $\delta = 160.00$  (d,  $J = 249.5$  Hz), 150.83 (s), 140.05 (d,  $J = 8.5$  Hz), 139.18 (d,  $J = 2.4$  Hz), 125.88 (d,  $J = 12.7$  Hz), 118.29 (d,  $J = 24.5$  Hz), 87.52 (s), 20.42 (s).

HPLC/MS ( $t_r = 3.402$  min, 70 eV, EI)  $m/z$  (%) = 305.000 (100)  $[\text{M}+\text{H}]^+$

#### 4.1.31. 2-(4-Bromo-2-fluorophenyl)-1,4,5,6-tetrahydropyrimidine (3j)

4-Bromo-2-fluorobenzaldehyde (**1e**) (5.08 g, 25.0 mmol) was subjected to general procedure, using propane-1,3-diamine (2.29 ml, 2.04 g, 27.5 mmol),  $\text{K}_2\text{CO}_3$  (10.4 g, 75.0 mmol) and  $\text{I}_2$  (7.98 g, 31.4 mmol). 2-(4-Bromo-2-fluorophenyl)-1,4,5,6-tetrahydropyrimidine (**3j**) was received as brown solid (800 mg, 3.11 mmol, 12%).

$^1\text{H}$  NMR ( $\text{CDCl}_3$ , 500 MHz):  $\delta = 7.61$  (t,  $J = 8.3$  Hz, 1H), 7.25 (dd,  $J = 8.4, 1.9$  Hz, 1H), 7.20 (dd,  $J = 10.9, 1.8$  Hz, 1H), 5.38 (s, 1H), 3.43 (t,  $J = 5.8$  Hz, 4H), 1.81 (p,  $J = 5.8$  Hz, 2H).

$^{13}\text{C}$  NMR ( $\text{CDCl}_3$ , 125 MHz):  $\delta = 159.78$  (d,  $J = 252.3$  Hz), 151.12 (s), 131.76 (d,  $J = 3.6$  Hz), 127.79 (d,  $J = 3.0$  Hz), 123.76 (d,  $J = 10.0$  Hz), 123.29 (d,  $J = 11.7$  Hz), 119.55 (d,  $J = 26.9$  Hz), 42.13 (s), 20.53 (s).

#### 4.1.32. 2-(2,4-Difluorophenyl)-1,4,5,6-tetrahydropyrimidine (3k)

2,4-Difluorobenzaldehyde (**1w**) (1.43 g, 10.0 mmol) was subjected to general procedure, using propane-1,3-diamine (916  $\mu\text{L}$ , 815 mg, 11.0 mmol),  $\text{K}_2\text{CO}_3$  (4.15 g, 30.0 mmol) and  $\text{I}_2$  (3.18 g, 12.5 mmol). 2-(2,4-Difluorophenyl)-1,4,5,6-tetrahydropyrimidine (**3k**) was received as brown solid (1.73 g, 8.80 mmol, 88%).

GC/MS ( $t_r = 14.63$  min, 70 eV, EI)  $m/z$  (%) = 196 (62)  $[\text{M}^+]$ , 195 (86)  $[\text{M}^+ - \text{H}]$ , 177 (69), 140 (100), 139 (46), 120 (39).

$^1\text{H}$  NMR (500 MHz,  $\text{CDCl}_3$ ):  $\delta = 7.71$  (td,  $J = 8.8, 6.6$  Hz, 1H), 6.87–6.81 (m, 1H), 6.74 (ddd,  $J = 11.3, 8.7, 2.5$  Hz, 1H), 5.74 (s, 1H), 3.49–3.33 (m, 4H), 1.98–1.58 (m, 2H).

$^{13}\text{C}$  NMR (126 MHz,  $\text{CDCl}_3$ ):  $\delta = 163.5$  (dd,  $J = 251.9, 12.3$  Hz), 160.3 (dd,  $J = 250.5, 12.0$  Hz), 151.3 (s), 131.9 (dd,  $J = 9.7, 4.6$  Hz), 120.4 (d,  $J = 11.8$  Hz), 111.8 (dd,  $J = 21.2, 3.1$  Hz), 104.1 (t,  $J = 26.4$  Hz), 42.00 (s), 20.5 (s).

#### 4.1.33. 2-(2-Bromophenyl)-1,4,5,6-tetrahydropyrimidine (3l)

2-Bromobenzaldehyde (**1u**) (1 ml, 8.56 mmol) and 1,3-diaminopropane (0.785 ml, 9.42 mmol) were dissolved in *t*-BuOH (86 ml) and stirred for 30 min at 70 °C, then  $\text{Na}_2\text{CO}_3$  (2.72 g, 25.7 mmol) and  $\text{I}_2$  (2.72 g, 10.7 mmol) were added and the mixture was stirred 3h at the same temperature. Afterwards  $\text{Na}_2\text{SO}_3$  sat. was added until the organic layer turns slightly yellow. The organic layer was separated and concentrated *in vacuo*. The obtained bright yellow solid was dissolved in 100 ml water followed by addition of 1M NaOH till pH 13. The mixture was extracted (2  $\times$  60 ml  $\text{CHCl}_3$ ), the combined organics were dried over  $\text{Na}_2\text{SO}_4$ , filtered and concentrated to obtain a yellow oil. After recrystallization ( $\text{CHCl}_3$ -hexane) the title compound was obtained as a white solid (970 mg, 47%).

$^1\text{H}$  NMR ( $\text{CDCl}_3$ , 300 MHz):  $\delta = 7.53$ –7.47 (m, 1H, Ar), 7.35–7.23 (m, 2H, Ar), 7.23–7.14 (m, 1H, Ar), 5.82 (s, 1H, NH), 3.28 (t, 4H, 2  $\times$   $\text{CH}_2$ ), 1.86–1.64 (m, 2H,  $\text{CH}_2$ ).

$^{13}\text{C}$  NMR ( $\text{CDCl}_3$ , 75 MHz):  $\delta = 155.84, 138.53, 132.88, 130.40, 130.28, 127.51, 120.87, 41.86, 20.37$ .

#### 4.1.34. 2-(2,5-Dibromoophenyl)-1,4,5,6-tetrahydropyrimidine (3m)

2,5-Dibromobenzaldehyde (**1b**) (2.38 g, 9.00 mmol) was subjected to general procedure, using propane-1,3-diamine (825  $\mu\text{L}$ , 734 mg, 9.90 mmol),  $\text{K}_2\text{CO}_3$  (3.73 g, 27.0 mmol) and  $\text{I}_2$  (2.86 g, 11.3 mmol). 2-(2,5-Dibromoophenyl)-1,4,5,6-tetrahydropyrimidine

(**3m**) was received as brown solid (726 mg, 2.28 mmol, 25%).

GC/MS ( $t_r = 20.92$  min, 70 eV, EI)  $m/z$  (%) = 318.9 (52), 316.9 (100), 261.8 (32), 237.0 (60), 158.1 (36), 102.0 (25).

$^1\text{H}$  NMR ( $\text{CDCl}_3$ , 500 MHz):  $\delta = 7.49$  (d,  $J = 2.4$  Hz, 1H), 7.37 (d,  $J = 8.5$  Hz, 1H), 7.31 (dd,  $J = 8.5, 2.4$  Hz, 1H), 3.38–3.31 (m, 1H), 1.84–1.75 (m, 1H).

$^{13}\text{C}$  NMR ( $\text{CDCl}_3$ , 126 MHz):  $\delta = 154.58$  (s), 140.17 (s), 134.38 (s), 133.37 (s), 133.24 (s), 121.37 (s), 119.60 (s), 42.05 (s), 20.41 (s).

#### 4.1.35. 2-(2-Bromo-5-fluorophenyl)-1,4,5,6-tetrahydropyrimidine (3n)

2-Bromo-5-fluorobenzaldehyde (**1s**) (2.03 g, 10.0 mmol) was subjected to general procedure, using propane-1,3-diamine (916  $\mu\text{L}$ , 815 mg, 11.0 mmol),  $\text{K}_2\text{CO}_3$  (4.15 g, 30.0 mmol) and  $\text{I}_2$  (3.17 g, 12.5 mmol).

2-(2-Bromo-5-fluorophenyl)-1,4,5,6-tetrahydropyrimidine (**3n**) was received as brown solid (1.93 g, 7.51 mmol, 75%).

$^1\text{H}$  NMR ( $\text{CDCl}_3$ , 500 MHz):  $\delta = 7.45$  (dd,  $J = 8.8, 5.1$  Hz, 1H), 7.09 (dd,  $J = 8.6, 3.1$  Hz, 1H), 6.90 (ddd,  $J = 8.8, 7.9, 3.1$  Hz, 1H), 4.92 (s, 1H), 3.40–3.33 (m, 4H), 1.84–1.75 (m, 2H).

$^{13}\text{C}$  NMR ( $\text{CDCl}_3$ , 126 MHz):  $\delta = 161.78$  (d,  $J = 248.3$  Hz), 154.55 (s), 140.69 (d,  $J = 7.5$  Hz), 134.28 (d,  $J = 7.9$  Hz), 117.63 (d,  $J = 23.9$  Hz), 117.42 (d,  $J = 22.5$  Hz), 115.07 (d,  $J = 3.0$  Hz), 42.23 (s), 20.56 (s).

GC/MS ( $t_r = 17.662$  min, 70 eV, EI)  $m/z$  (%) = 257 (79)  $[\text{M}^+ (^{81}\text{Br})]$ .

#### 4.1.36. 2-(2,6-Difluorophenyl)-1,4,5,6-tetrahydropyrimidine (3o)

2,6-Difluorobenzaldehyde (**1h**) (1.42 g, 10.0 mmol) was subjected to general procedure, using propane-1,3-diamine (916  $\mu\text{L}$ , 815 mg, 11.0 mmol),  $\text{K}_2\text{CO}_3$  (4.15 g, 30.0 mmol) and  $\text{I}_2$  (3.17 g, 12.5 mmol). 2-(2,6-Difluorophenyl)-1,4,5,6-tetrahydropyrimidine (**3o**) was received as brown solid (892 mg, 4.55 mmol, 46%).

$^1\text{H}$  NMR ( $\text{CDCl}_3$ , 500 MHz):  $\delta = 7.31$ –7.21 (m, 2H), 6.83 (p,  $J = 2.9$  Hz, 2H), 6.51 (s, 1H), 3.34–3.20 (m, 4H), 1.79–1.68 (m, 2H).

$^{13}\text{C}$  NMR ( $\text{CDCl}_3$ , 126 MHz):  $\delta = 160.13$  (dd,  $J = 251.3, 6.7$  Hz), 147.70 (s), 130.90 (t,  $J = 10.0$  Hz), 114.41 (t,  $J = 20.2$  Hz), 111.60 (dd,  $J = 20.6, 4.4$  Hz), 41.54 (s), 20.06 (s).

GC/MS ( $t_r = 15.341$  min, 70 eV, EI)  $m/z$  (%) = 196.100 (36).

#### 4.1.37. 3-Bromo-N,N-dimethyl-4-(1,4,5,6-tetrahydropyrimidin-2-yl)aniline (3p)

2-Bromo-4-(dimethylamino)benzaldehyde (**1o**) (458 mg, 2.01 mmol) was subjected to general procedure, using propane-1,3-diamine (182  $\mu\text{L}$ , 164 mg, 2.21 mmol),  $\text{K}_2\text{CO}_3$  (840 mg, 6.08 mmol) and  $\text{I}_2$  (636 mg, 2.51 mmol). 3-Bromo-N,N-dimethyl-4-(1,4,5,6-tetrahydropyrimidin-2-yl)aniline (**3p**) was received as brown solid (566 mg, 2.01 mmol, 100%).

$^1\text{H}$  NMR ( $\text{CDCl}_3$ , 500 MHz):  $\delta = 7.21$  (d,  $J = 8.6$  Hz, 1H), 6.75 (d,  $J = 2.5$  Hz, 1H), 6.55 (dd,  $J = 8.6, 2.6$  Hz, 1H), 3.39–3.26 (m, 2H), 2.92 (s, 3H), 1.76 (t,  $J = 5.8$  Hz, 3H).

$^{13}\text{C}$  NMR ( $\text{CDCl}_3$ , 126 MHz):  $\delta = 156.11$  (s), 151.49 (s), 130.79 (s), 125.63 (s), 121.42 (s), 115.51 (s), 110.91 (s), 41.81 (s), 40.22 (s), 20.42 (s).

GC/MS ( $t_r = 23.206$  min, 70 eV, EI)  $m/z$  (%) = 282.100 (86).

#### 4.1.38. 2-(2-Bromo-6-fluorophenyl)-1,4,5,6-tetrahydropyrimidine (3q)

2-Bromo-6-fluorobenzaldehyde (**1c**) (2.03 g, 10.0 mmol) was subjected to general procedure, using propane-1,3-diamine (916  $\mu\text{L}$ , 815 mg, 11.0 mmol),  $\text{K}_2\text{CO}_3$  (4.15 g, 30.0 mmol) and  $\text{I}_2$  (3.17 g, 12.5 mmol).

2-(2-Bromo-6-fluorophenyl)-1,4,5,6-tetrahydropyrimidine (**3q**) was received as yellowish solid (2.14 mg, 8.32 mmol, 83%).

GC/MS ( $t_r = 17.93$  min, 70 eV, EI)  $m/z$  (%) = 258 (22)  $[\text{M}^+ (^{81}\text{Br})]$ , 256 (27)  $[\text{M}^+ (^{79}\text{Br})]$ , 239 (26), 237 (27), 201 (20), 200 (30), 177



(100), 121 (29), 18 (27).

$^1\text{H}$  NMR ( $\text{CDCl}_3$ , 500 MHz):  $\delta$  = 7.31 (d,  $J$  = 8.1 Hz, 1H), 7.18 (td,  $J$  = 8.2, 5.8 Hz, 1H), 7.00 (td,  $J$  = 8.5, 0.9 Hz, 1H), 3.36–3.27 (m, 2H), 1.83–1.75 (m, 1H).

$^{13}\text{C}$  NMR ( $\text{CDCl}_3$ , 125 MHz):  $\delta$  = 160.1 (d,  $J$  = 252.3 Hz), 151.1 (s), 131.2 (d,  $J$  = 8.8 Hz), 128.5 (d,  $J$  = 3.1 Hz), 126.7 (d,  $J$  = 20.1 Hz), 122.7 (d,  $J$  = 3.5 Hz), 115.0 (d,  $J$  = 22.0 Hz), 41.8 (s), 20.2 (s).

#### 4.1.39. 2-(4-Chloro-2-fluorophenyl)-1,4,5,6-tetrahydropyrimidine (3r)

4-Chloro-2-fluorobenzaldehyde (**1j**) (500 mg, 3.15 mmol) was subjected to general procedure, using propane-1,3-diamine (286  $\mu\text{l}$ , 257 mg, 3.47 mmol),  $\text{K}_2\text{CO}_3$  (1.32 g, 9.55 mmol) and  $\text{I}_2$  (1.00 g, 3.94 mmol).

2-(4-Chloro-2-fluorophenyl)-1,4,5,6-tetrahydropyrimidine (**3r**) was received as brown solid (340 mg, 1.60 mmol, 51%).

$^1\text{H}$  NMR ( $\text{CDCl}_3$ , 300 MHz):  $\delta$  = 7.60 (t,  $J$  = 8.3 Hz, 1H), 7.06 (ddd,  $J$  = 12.9, 9.7, 2.1 Hz, 2H), 5.64 (s, 1H), 3.43–3.34 (m, 4H), 1.86–1.73 (m, 2H).

HPLC/MS ( $t_r$  = 1.466 min, 70 eV, EI)  $m/z$  (%) = 213.100/215.100 (100)  $[\text{M}+\text{H}]^+$

#### 4.1.40. 2-(2,3-Difluorophenyl)-1,4,5,6-tetrahydropyrimidine (3s)

2,3-Difluorobenzaldehyde (**1n**) (1.43 g, 10.0 mmol) was subjected to general procedure, using propane-1,3-diamine (916  $\mu\text{l}$ , 815 mg, 11.0 mmol),  $\text{K}_2\text{CO}_3$  (4.15 g, 30.0 mmol) and  $\text{I}_2$  (3.16 g, 12.5 mmol). 2-(2,3-Difluorophenyl)-1,4,5,6-tetrahydropyrimidine (**3s**) was received as brown solid (1.35 mg, 6.89 mmol, 69%).

$^1\text{H}$  NMR ( $\text{CDCl}_3$ , 500 MHz):  $\delta$  = 7.36 (ddt,  $J$  = 7.9, 6.3, 1.7 Hz, 1H), 7.13 (dtd,  $J$  = 9.9, 8.3, 1.7 Hz, 1H), 7.02 (tdd,  $J$  = 8.2, 4.8, 1.5 Hz, 1H), 5.95 (s, 1H), 3.40 (t,  $J$  = 5.8 Hz, 4H), 1.80 (p,  $J$  = 5.8 Hz, 2H).

$^{13}\text{C}$  NMR ( $\text{CDCl}_3$ , 125 MHz):  $\delta$  = 151.3 (d,  $J$  = 2.6 Hz), 151.7–149.1 (m), 147.4 (d,  $J$  = 13.9 Hz), 126.2 (d,  $J$  = 8.9 Hz), 125.0 (s), 124.2 (dd,  $J$  = 6.0, 5.0 Hz), 118.2 (d,  $J$  = 17.1 Hz), 41.9 (s), 20.3 (s).

#### 4.1.41. 2-(3-Chloro-2-fluorophenyl)-1,4,5,6-tetrahydropyrimidine (3t)

3-Chloro-2-fluorobenzaldehyde (**1m**) (500 mg, 3.15 mmol) was subjected to general procedure, using propane-1,3-diamine (286  $\mu\text{l}$ , 257 mg, 3.47 mmol),  $\text{K}_2\text{CO}_3$  (1.32 g, 9.55 mmol) and  $\text{I}_2$  (1.00 g, 3.94 mmol).

2-(3-Chloro-2-fluorophenyl)-1,4,5,6-tetrahydropyrimidine (**3t**) was received as brown solid (373 mg, 1.75 mmol, 56%).

$^1\text{H}$  NMR ( $\text{CDCl}_3$ , 300 MHz):  $\delta$  = 7.37 (dd,  $J$  = 14.4, 6.7 Hz, 1H), 7.01 (t,  $J$  = 7.9 Hz, 1H), 3.36 (t,  $J$  = 5.7 Hz, 2H), 1.83 (dt,  $J$  = 11.3, 5.7 Hz, 1H).

$^{13}\text{C}$  NMR ( $\text{CDCl}_3$ , 75 MHz):  $\delta$  = 155.16 (d,  $J$  = 252.6 Hz), 152.73 (s), 132.40 (s), 128.71 (d,  $J$  = 1.5 Hz), 124.83 (d,  $J$  = 4.5 Hz), 123.68 (d,  $J$  = 12.8 Hz), 121.60 (d,  $J$  = 18.3 Hz), 59.55 (s), 46.54 (s), 41.05 (s), 19.63 (s).

#### 4.1.42. 2-(2-Fluoro-3-methylphenyl)-1,4,5,6-tetrahydropyrimidine (3u)

2-Fluoro-3-methylbenzaldehyde (**1u**) (500 mg, 3.62 mmol) was subjected to general procedure, using propane-1,3-diamine (335  $\mu\text{l}$ , 295 mg, 3.98 mmol),  $\text{K}_2\text{CO}_3$  (1.52 g, 11.0 mmol) and  $\text{I}_2$  (1.15 g, 4.52 mmol).

2-(2-Fluoro-3-methylphenyl)-1,4,5,6-tetrahydropyrimidine (**3u**) was received as brown solid (331 mg, 1.72 mmol, 48%).

$^1\text{H}$  NMR (DMSO, 300 MHz):  $\delta$  = 7.02 (t,  $J$  = 7.3 Hz, 1H), 6.85 (t,  $J$  = 7.2 Hz, 1H), 6.65 (t,  $J$  = 7.6 Hz, 1H), 3.04 (t,  $J$  = 5.7 Hz, 2H), 1.91 (s, 2H), 1.54–1.40 (m, 1H).

$^{13}\text{C}$  NMR (DMSO, 75 MHz):  $\delta$  = 157.43 (d,  $J$  = 247.7 Hz), 152.13 (s), 131.80 (d,  $J$  = 5.4 Hz), 127.02 (d,  $J$  = 2.8 Hz), 123.77 (dd,  $J$  = 100.7, 16.0 Hz), 122.92 (d,  $J$  = 4.0 Hz), 77.36 (s), 40.78 (s), 19.45 (s), 13.82 (d,

$J$  = 4.7 Hz).

#### 4.1.43. 5-Thioxo-3,5-dihydro-2H-benzo[e]imidazo [1,2-c] [1,3]thiazine-8-carbonitrile (4a)

4-(4,5-Dihydro-1H-imidazole-2-yl)-3-fluorobenzonitrile (**2a**) (1.22 g, 4.00 mmol) was subjected to general procedure for cyclization using NaH (60%, 321 mg, 8.02 mmol) and carbon disulfide (480  $\mu\text{l}$ , 609 mg, 8.00 mmol). 5-Thioxo-3,5-dihydro-2H-benzo[e]imidazo [1,2-c] [1,3]thiazine-8-carbonitrile (**4a**) was received as yellow solid (3 mg, 12.2  $\mu\text{mol}$ , 1%).

$^1\text{H}$  NMR ( $\text{CDCl}_3$ , 300 MHz):  $\delta$  = 8.28 (d,  $J$  = 8.2 Hz, 1H), 7.57 (dd,  $J$  = 8.2, 1.6 Hz, 1H), 7.44–7.41 (m, 1H), 4.41 (t,  $J$  = 1.1 Hz, 2H), 4.20 (t,  $J$  = 1.4 Hz, 2H).

HPLC/MS ( $t_r$  = 2.832 min, 70 eV, CI)  $m/z$  (%) = 246.000 (100)  $[\text{M}+\text{H}]^+$

#### 4.1.44. 9-Bromo-2H-benzo[e]imidazo [1,2-c] [1,3]thiazine-5(3H)-thione (4b)

2-(2,5-Dibromophenyl)-4,5-dihydro-1H-imidazole (**2b**) (1.22 g, 4.00 mmol) was subjected to general procedure for cyclization using NaH (60%, 321 mg, 8.02 mmol) and carbon disulfide (480  $\mu\text{l}$ , 609 mg, 8.00 mmol). 9-Bromo-2H-benzo[e]imidazo [1,2-c] [1,3]thiazine-5(3H)-thione (**4b**) was received as yellow solid (mg, mmol, %).

$^1\text{H}$  NMR ( $\text{CDCl}_3$ , 500 MHz):  $\delta$  = 8.29 (d,  $J$  = 2.1 Hz, 1H), 7.55 (dd,  $J$  = 8.5, 2.2 Hz, 1H), 6.96 (d,  $J$  = 8.5 Hz, 1H), 4.37 (t,  $J$  = 8.9 Hz, 2H), 4.14 (t,  $J$  = 9.0 Hz, 3H), 3.60 (s, 1H).

$^{13}\text{C}$  NMR ( $\text{CDCl}_3$ , 126 MHz):  $\delta$  = 182.39 (s), 150.62 (s), 135.64 (s), 133.91 (s), 131.88 (s), 123.89 (s), 122.45 (s), 121.35 (s), 52.79 (s), 52.27 (s).

HPLC/MS ( $t_r$  = 15.815 min, 70 eV, EI)  $m/z$  (%) = 298.901/300.900 (100)  $[\text{M}+\text{H}]^+$

#### 4.1.45. 10-Bromo-2H-benzo[e]imidazo [1,2-c] [1,3]thiazine-5(3H)-thione (4c)

2-(2-Bromo-6-fluorophenyl)-4,5-dihydro-1H-imidazole (**2c**) (200 mg, 823  $\mu\text{mol}$ ) was subjected to general procedure for cyclization using NaH (60%, 66.8 mg, 1.67 mmol) and carbon disulfide (99.4  $\mu\text{l}$ , 125 mg, 1.65 mmol). 10-Bromo-2H-benzo[e]imidazo [1,2-c] [1,3]thiazine-5(3H)-thione (**4c**) was received as yellow solid (5 mg, 16.7  $\mu\text{mol}$ , 2%).

HPLC/MS ( $t_r$  = 14.996 min, 70 eV, EI)  $m/z$  (%) = 298.800 (100)  $[\text{M}+\text{H}]^+$

#### 4.1.46. 10-Chloro-2H-benzo[e]imidazo [1,2-c] [1,3]thiazine-5(3H)-thione (4d)

2-(2-Chloro-6-fluorophenyl)-4,5-dihydro-1H-imidazole (**2d**) (500 mg, 2.52 mmol) was subjected to general procedure for cyclization using NaH (60%, 204 mg, 5.11 mmol) and carbon disulfide (304  $\mu\text{l}$ , 383 mg, 5.03 mmol). 10-Chloro-2H-benzo[e]imidazo [1,2-c] [1,3]thiazine-5(3H)-thione (**4d**) was received as yellow solid (10.2 mg, 40  $\mu\text{mol}$ , 2%).

$^1\text{H}$  NMR (DMSO, 300 MHz):  $\delta$  = 7.55–7.45 (m, 1H), 7.36 (dd,  $J$  = 6.3, 2.9 Hz, 1H), 4.27–4.08 (m, 2H).

$^{13}\text{C}$  NMR (DMSO, 75 MHz):  $\delta$  = 180.86 (s), 147.91 (s), 136.49 (s), 134.88 (s), 132.46 (s), 131.63 (s), 122.05 (s), 117.93 (s), 53.19 (s), 51.05 (s).

HPLC/MS ( $t_r$  = 14.777 min, 70 eV, EI)  $m/z$  (%) = 255.000 (100)  $[\text{M}+\text{H}]^+$ , 256.998 (43)  $[\text{M}+\text{H}]^+$

#### 4.1.47. 8-Bromo-2H-benzo[e]imidazo [1,2-c] [1,3]thiazine-5(3H)-thione (4e)

2-(2-Fluoro-4-bromophenyl)-4,5-dihydro-1H-imidazole (**2e**) (973 mg, 4.00 mmol) was subjected to general procedure for cyclization using NaH (60%, 321 mg, 8.02 mmol) and carbon

disulfide (480  $\mu$ l, 609 mg, 8.00 mmol). 8-Bromo-2H-benzo[e]imidazo[1,2-c][1,3]thiazine-5(3H)-thione (**4e**) was received as yellow solid (159 mg, 0.53 mmol, 13%)

GC/MS ( $t_r$  = 25.27 min, 70 eV, EI) m/z (%) = 299.9 (100) [ $M^+$  ( $^{81}\text{Br}$ )], 297.9 (96) [ $M^+$  ( $^{79}\text{Br}$ )],

#### 4.1.48. 9-Iodo-2H-benzo[e]imidazo[1,2-c][1,3]thiazine-5(3H)-thione (**4f**)

2-(2-Fluoro-5-iodophenyl)-4,5-dihydro-1H-imidazole (**2f**) (200 mg, 689  $\mu$ mol) was subjected to general procedure for cyclization using NaH (60%, 56 mg, 1.40 mmol) and carbon disulfide (83.3  $\mu$ l, 105 mg, 1.38 mmol). 9-Iodo-2H-benzo[e]imidazo[1,2-c][1,3]thiazine-5(3H)-thione (**4f**) was received as yellow solid (13.6 mg, 39.3  $\mu$ mol, 6%)

$^1\text{H}$  NMR (DMSO, 300 MHz):  $\delta$  = 8.34 (d,  $J$  = 1.9 Hz, 1H), 7.93 (dd,  $J$  = 8.4, 1.9 Hz, 1H), 7.25 (d,  $J$  = 8.4 Hz, 1H), 4.27 (ddd,  $J$  = 8.6, 6.1, 2.1 Hz, 2H), 4.06 (dd,  $J$  = 9.1, 7.7 Hz, 2H), 1.32–1.18 (m, 4H).

HPLC/MS ( $t_r$  = 17.491 min, 70 eV, EI) m/z (%) = 346.900 (100) [ $M+H$ ] $^+$

#### 4.1.49. 7-Fluoro-2H-benzo[e]imidazo[1,2-c][1,3]thiazine-5(3H)-thione (**4g**)

2-(2-Bromo-5-fluorophenyl)-4,5-dihydro-1H-imidazole (**2g**) (971 mg, 4.00 mmol) was subjected to general procedure for cyclization using NaH (60%, 321 mg, 8.02 mmol) and carbon disulfide (480  $\mu$ l, 609 mg, 8.00 mmol). 7-Fluoro-2H-benzo[e]imidazo[1,2-c][1,3]thiazine-5(3H)-thione (**4g**) was received as yellow solid (841 mg, 3.53 mmol, 88%)

$^1\text{H}$  NMR ( $\text{CDCl}_3$ , 500 MHz):  $\delta$  = 7.89 (dd,  $J$  = 9.0, 2.5 Hz, 1H), 7.21 (td,  $J$  = 8.5, 2.8 Hz, 1H), 7.10 (dd,  $J$  = 8.8, 4.9 Hz, 1H), 4.40 (t,  $J$  = 9.1 Hz, 2H), 4.15 (t,  $J$  = 8.9 Hz, 2H).

$^{13}\text{C}$  NMR ( $\text{CDCl}_3$ , 126 MHz):  $\delta$  = 182.78 (s), 162.76 (s), 160.78 (s), 151.18 (d,  $J$  = 2.6 Hz), 130.50 (d,  $J$  = 2.5 Hz), 124.46 (d,  $J$  = 7.8 Hz), 122.70 (d,  $J$  = 8.6 Hz), 120.83 (d,  $J$  = 23.3 Hz), 115.80 (d,  $J$  = 24.7 Hz), 52.67 (s), 52.33 (s).

HPLC/MS ( $t_r$  = 20.659 min, 70 eV, EI) m/z (%) = 239.000 (100) [ $M+H$ ] $^+$

#### 4.1.50. 8-Bromo-10-fluoro-2H-benzo[e]imidazo[1,2-c][1,3]thiazine-5(3H)-thione (**4h**)

2-(4-Bromo-2,6-difluorophenyl)-4,5-dihydro-1H-imidazole (**2h**) (100 mg, 383  $\mu$ mol) was subjected to general procedure for cyclization using NaH (60%, 31.1 mg, 778  $\mu$ mol) and carbon disulfide (46.3  $\mu$ l, 58.3 mg, 766  $\mu$ mol). 8-Bromo-10-fluoro-2H-benzo[e]imidazo[1,2-c][1,3]thiazine-5(3H)-thione (**4h**) was received as yellow solid (17.2 mg, 54.2  $\mu$ mol, 14%)

$^1\text{H}$  NMR ( $\text{CDCl}_3$ , 500 MHz):  $\delta$  = 6.62 (s, 1H), 6.49 (d,  $J$  = 12.2 Hz, 1H), 3.93 (t,  $J$  = 5.8 Hz, 2H), 3.40 (dd,  $J$  = 10.8, 5.3 Hz, 2H).

#### 4.1.51. 7-Methyl-2H-benzo[e]imidazo[1,2-c][1,3]thiazine-5(3H)-thione (**4i**)

2-(2-Fluoro-5-methylphenyl)-4,5-dihydro-1H-imidazole (**2i**) (713 mg, 4.00 mmol) was subjected to general procedure for cyclization using NaH (60%, 320 mg, 8.00 mmol) and carbon disulfide (483  $\mu$ l, 609 mg, 8.00 mmol). 7-Methyl-2H-benzo[e]imidazo[1,2-c][1,3]thiazine-5(3H)-thione (**4i**) was received as yellow solid (589 mg, 2.51 mmol, 63%)

$^1\text{H}$  NMR ( $\text{CDCl}_3$ , 500 MHz):  $\delta$  = 7.94 (s, 1H), 7.25 (d,  $J$  = 7.2 Hz, 1H), 6.96 (d,  $J$  = 7.9 Hz, 1H), 4.35 (t,  $J$  = 8.6 Hz, 2H), 4.10 (t,  $J$  = 8.4 Hz, 2H), 2.34 (s, 3H).

$^{13}\text{C}$  NMR ( $\text{CDCl}_3$ , 126 MHz):  $\delta$  = 183.44 (s), 151.67 (s), 138.11 (s), 133.75 (s), 131.58 (s), 129.22 (s), 122.29 (s), 120.27 (s), 52.46 (s), 52.12 (s), 21.12 (s).

GC/MS ( $t_r$  = 23.96 min, 70 eV, EI) m/z (%) = 234.0 (100) [ $M^+$ ],

#### 4.1.52. 8-Chloro-2H-benzo[e]imidazo[1,2-c][1,3]thiazine-5(3H)-thione (**4j**)

2-(4-Chloro-2-fluorophenyl)-4,5-dihydro-1H-imidazole (**2j**) (200 mg, 1.01 mmol) was subjected to general procedure for cyclization using NaH (60%, 81.8 mg, 2.04 mmol) and carbon disulfide (122  $\mu$ l, 153 mg, 2.01 mmol). 8-Chloro-2H-benzo[e]imidazo[1,2-c][1,3]thiazine-5(3H)-thione (**4j**) was received as yellow solid (32.1 mg, 126  $\mu$ mol, 13%)

$^1\text{H}$  NMR (DMSO, 300 MHz):  $\delta$  = 8.06 (d,  $J$  = 8.6 Hz, 1H), 7.67 (d,  $J$  = 2.0 Hz, 1H), 7.49 (dd,  $J$  = 8.6, 2.1 Hz, 1H), 4.34–4.19 (m, 2H), 4.12–3.98 (m, 2H).

$^{13}\text{C}$  NMR (DMSO, 75 MHz):  $\delta$  = 181.26 (s), 149.69 (s), 137.51 (s), 135.62 (s), 130.18 (s), 128.18 (s), 122.47 (s), 119.20 (s), 52.36 (s), 52.06 (s).

HPLC/MS ( $t_r$  = 15.046 min, 70 eV, EI) m/z (%) = 257.000/254.800 (100) [ $M+H$ ] $^+$

#### 4.1.53. 8-Methyl-2H-benzo[e]imidazo[1,2-c][1,3]thiazine-5(3H)-thione (**4k**)

2-(2-Fluoro-6-methylphenyl)-4,5-dihydro-1H-imidazole (**2k**) (713 mg, 4.00 mmol) was subjected to general procedure for cyclization using NaH (60%, 320 mg, 8.00 mmol) and carbon disulfide (483  $\mu$ l, 609 mg, 8.00 mmol). 8-Methyl-2H-benzo[e]imidazo[1,2-c][1,3]thiazine-5(3H)-thione (**4k**) was received as yellow solid (527 mg, 2.25 mmol, 56%)

$^1\text{H}$  NMR ( $\text{CDCl}_3$ , 500 MHz):  $\delta$  = 7.27 (dd,  $J$  = 9.9, 5.6 Hz, 1H), 7.16–7.11 (m, 1H), 6.93 (dd,  $J$  = 7.9, 0.6 Hz, 1H), 4.35–4.27 (m, 2H), 4.19–4.11 (m, 2H), 2.72 (s, 3H).

$^{13}\text{C}$  NMR ( $\text{CDCl}_3$ , 126 MHz):  $\delta$  = 183.43 (s), 151.42 (s), 143.02 (s), 135.54 (s), 131.53 (s), 131.17 (s), 120.52 (s), 119.48 (s), 52.91 (s), 51.16 (s), 25.07 (s).

GC/MS ( $t_r$  = 23.79 min, 70 eV, EI) m/z (%) = 234.0 (100) [ $M^+$ ],

#### 4.1.54. 10-Iodo-2H-benzo[e]imidazo[1,2-c][1,3]thiazine-5(3H)-thione (**4l**)

2-(2-Fluoro-6-iodophenyl)-4,5-dihydro-1H-imidazole (**2l**) (200 mg, 689  $\mu$ mol) was subjected to general procedure for cyclization using NaH (60%, 56.0 mg, 1.40 mmol) and carbon disulfide (83.3  $\mu$ l, 105 mg, 1.38 mmol). 10-Iodo-2H-benzo[e]imidazo[1,2-c][1,3]thiazine-5(3H)-thione (**4l**) was received as yellow solid (11.4 mg, 32.9  $\mu$ mol, 5%)

$^1\text{H}$  NMR (DMSO, 300 MHz):  $\delta$  = 8.14 (dd,  $J$  = 7.8, 1.1 Hz, 1H), 7.44 (dd,  $J$  = 7.9, 1.1 Hz, 1H), 7.20 (t,  $J$  = 7.9 Hz, 1H), 4.31–4.19 (m, 2H), 4.18–4.07 (m, 2H).

$^{13}\text{C}$  NMR (DMSO, 75 MHz):  $\delta$  = 180.76 (s), 148.08 (s), 142.98 (s), 135.66 (s), 132.65 (s), 123.17 (s), 120.77 (s), 97.04 (s), 52.65 (s), 51.96 (s).

HPLC/MS ( $t_r$  = 15.702 min, 70 eV, EI) m/z (%) = 346.986 (100) [ $M+H$ ] $^+$

#### 4.1.55. 7-Chloro-2H-benzo[e]imidazo[1,2-c][1,3]thiazine-5(3H)-thione (**4m**)

2-(3-Chloro-2-fluorophenyl)-4,5-dihydro-1H-imidazole (**2m**) (200 mg, 1.01 mmol) was subjected to general procedure for cyclization using NaH (60%, 81.8 mg, 2.04 mmol) and carbon disulfide (122  $\mu$ l, 153 mg, 2.01 mmol). 7-Chloro-2H-benzo[e]imidazo[1,2-c][1,3]thiazine-5(3H)-thione (**4m**) was received as yellow solid (3 mg, 11.8  $\mu$ mol, 1%)

$^1\text{H}$  NMR ( $\text{CDCl}_3$ , 500 MHz):  $\delta$  = 7.45 (dd,  $J$  = 8.5, 2.3 Hz, 1H), 7.36 (t,  $J$  = 2.1 Hz, 1H), 7.13 (dd,  $J$  = 8.6, 2.5 Hz, 1H), 4.41 (t,  $J$  = 8.8 Hz, 2H), 4.16 (t,  $J$  = 9.0 Hz, 2H).

HPLC/MS ( $t_r$  = 14.880 min, 70 eV, EI) m/z (%) = 255.000 (20) [ $M+H$ ] $^+$

4.1.56. 7-Fluoro-2H-benzo[e]imidazo [1,2-c] [1,3]thiazine-5(3H)-thione (**4n**)

2-(2,3-Difluorophenyl)-4,5-dihydro-1H-imidazole (**2n**) (728 mg, 4.00 mmol) was subjected to general procedure for cyclization using NaH (60%, 321 mg, 8.02 mmol) and carbon disulfide (490  $\mu$ l, 617 mg, 8.11 mmol). 7-Fluoro-2H-benzo[e]imidazo [1,2-c] [1,3]thiazine-5(3H)-thione (**4n**) was received as yellow solid (727 mg, 3.05 mmol, 76%).

GC/MS ( $t_r$  = 22.54 min, 70 eV, EI)  $m/z$  (%) = 238 [ $M^+$ ] (100), 205 (30), 179 (30), 153 (20), 86 (48).  $^1H$  NMR ( $CDCl_3$ , 500 MHz):  $\delta$  = 7.94 (d,  $J$  = 7.9 Hz, 1H), 7.35–7.24 (m, 1H), 7.22–7.15 (m, 1H), 4.39–4.33 (m, 2H), 4.16–4.11 (m, 2H).

$^{13}C$  NMR ( $CDCl_3$ , 125 MHz):  $\delta$  = 181.4 (s), 154.4 (d,  $J$  = 246.3 Hz), 150.7 (s), 128.4 (d,  $J$  = 7.6 Hz), 124.7 (d,  $J$  = 3.1 Hz), 123.4 (d,  $J$  = 19.7 Hz), 122.4 (s), 118.5 (d,  $J$  = 19.8 Hz), 52.9 (s), 52.3 (s).

4.1.57. 8-(Dimethylamino)-2H-benzo[e]imidazo [1,2-c] [1,3]thiazine-5(3H)-thione (**4o**)

2-(2-Bromo-4-(dimethylamino)phenyl)-4,5-dihydro-1H-imidazole (**2o**) (266 mg, 992  $\mu$ mol) was subjected to general procedure for cyclization using NaH (60%, 81.9 mg, 2.05 mmol) and carbon disulfide (121  $\mu$ l, 152 mg, 2.00 mmol). 8-(Dimethylamino)-2H-benzo[e]imidazo [1,2-c] [1,3]thiazine-5(3H)-thione (**4o**) was received as yellow solid (206 mg, 783  $\mu$ mol, 79%).

$^1H$  NMR ( $CDCl_3$ , 300 MHz):  $\delta$  = 7.78 (d,  $J$  = 9.1 Hz, 1H), 6.47 (dd,  $J$  = 9.1, 2.5 Hz, 1H), 6.04 (d,  $J$  = 2.5 Hz, 1H), 4.21–4.09 (m, 2H), 3.96–3.83 (m, 3H), 2.86 (s, 7H).

GC/MS ( $t_r$  = 28.923 min, 70 eV, EI)  $m/z$  (%) = 263.1 (100) [ $M^+$ ],

4.1.58. 9-Methoxy-2H-benzo[e]imidazo [1,2-c] [1,3]thiazine-5(3H)-thione (**4p**)

2-(2-Fluoro-5-methoxyphenyl)-4,5-dihydro-1H-imidazole (**2p**) (200 mg, 1.03 mmol) was subjected to general procedure for cyclization using NaH (60%, 83.6 mg, 2.09 mmol) and carbon disulfide (124  $\mu$ l, 157 mg, 2.06 mmol). 9-Methoxy-2H-benzo[e]imidazo [1,2-c] [1,3]thiazine-5(3H)-thione (**4p**) was received as yellow solid (44.7 mg, 179  $\mu$ mol, 17%).

$^1H$  NMR (DMSO, 300 MHz):  $\delta$  = 8.18 (d,  $J$  = 0.7 Hz, 1H), 7.66 (d,  $J$  = 2.6 Hz, 1H), 7.24 (dt,  $J$  = 8.7, 5.7 Hz, 1H), 4.38 (t,  $J$  = 8.7 Hz, 1H), 4.15 (t,  $J$  = 8.8 Hz, 1H), 3.89 (s, 1H).

$^{13}C$  NMR (DMSO, 75 MHz):  $\delta$  = 181.82 (s), 158.52 (s), 150.39 (s), 124.98 (s), 123.82 (s), 121.19 (s), 120.54 (s), 111.34 (s), 55.27 (s), 51.92 (d,  $J$  = 1.9 Hz).

HPLC/MS ( $t_r$  = 13.974 min, 70 eV, EI)  $m/z$  (%) = 251.000 (100) [ $M+H$ ] $^+$

4.1.59. 8-Methoxy-2H-benzo[e]imidazo [1,2-c] [1,3]thiazine-5(3H)-thione (**4q**)

2-(2-Fluoro-4-methoxyphenyl)-4,5-dihydro-1H-imidazole (**2q**) (194 mg, 1.00 mmol) was subjected to general procedure for cyclization using NaH (60%, 85.4 mg, 2.15 mmol) and carbon disulfide (121  $\mu$ l, 152 mg, 2.00 mmol). 8-Methoxy-2H-benzo[e]imidazo [1,2-c] [1,3]thiazine-5(3H)-thione (**4q**) was received as yellow crystals (233 mg, 931  $\mu$ mol, 93%).

$^1H$  NMR ( $CDCl_3$ , 300 MHz):  $\delta$  = 8.06 (d,  $J$  = 8.9 Hz, 1H), 6.87 (dd,  $J$  = 8.9, 2.5 Hz, 1H), 6.56 (d,  $J$  = 2.5 Hz, 1H), 4.36 (dd,  $J$  = 9.6, 8.1 Hz, 2H), 4.11 (dd,  $J$  = 9.4, 7.8 Hz, 2H), 3.85 (s, 3H).

$^{13}C$  NMR ( $CDCl_3$ , 75 MHz):  $\delta$  = 183.20 (s), 162.81 (s), 151.41 (s), 136.55 (s), 130.91 (s), 115.30 (s), 113.39 (s), 106.07 (s), 55.87 (s), 52.54 (s), 52.11 (s).

HPLC/MS ( $t_r$  = 12.841 min, 70 eV, EI)  $m/z$  (%) = 251.000 (100) [ $M+H$ ] $^+$

4.1.60. 9-Chloro-2H-benzo[e]imidazo [1,2-c] [1,3]thiazine-5(3H)-thione (**4r**)

2-(2-Bromo-5-chlorophenyl)-4,5-dihydro-1H-imidazole (**2r**) (520 mg, 2.00 mmol) was subjected to general procedure for cyclization using NaH (60%, 82.1 mg, 2.05 mmol) and carbon disulfide (120  $\mu$ l, 151 mg, 1.99 mmol). 9-Chloro-2H-benzo[e]imidazo [1,2-c] [1,3]thiazine-5(3H)-thione (**4r**) was received as yellow crystals (360 mg, 1.41 mmol, 71%).

GC/MS ( $t_r$  = 24.61 min, 70 eV, EI)  $m/z$  (%) = 254 [ $M^+$ ] (100), 221 (36), 195 (34), 169 (22), 86 (64).  $^1H$  NMR ( $CDCl_3$ , 500 MHz):  $\delta$  = 8.13 (d,  $J$  = 2.3 Hz, 1H), 7.42 (dd,  $J$  = 8.5, 2.3 Hz, 1H), 7.04 (d,  $J$  = 8.5 Hz, 1H), 4.48–4.29 (m, 2H), 4.22–4.07 (m, 2H).

$^{13}C$  NMR ( $CDCl_3$ , 125 MHz):  $\delta$  = 182.4, 150.7, 133.8, 133.2, 132.9, 128.9, 123.8, 122.1, 52.8, 52.3.

4.1.61. 10-Fluoro-3,4-dihydrobenzo[e]pyrimido [1,2-c] [1,3]thiazine-6(2H)-thione (**4s**)

2-(2,6-Difluorophenyl)-4,5-dihydro-1H-imidazole (**2s**) (729 mg, 4.00 mmol) was subjected to general procedure for cyclization using NaH (60%, 160 mg, 4.00 mmol) and carbon disulfide (242  $\mu$ l, 305 mg, 4.00 mmol). 10-Fluoro-3,4-dihydrobenzo[e]pyrimido [1,2-c] [1,3]thiazine-6(2H)-thione (**4s**) was received as yellow solid (310 mg, 1.30 mmol, 33%).

$^1H$  NMR ( $CDCl_3$ , 500 MHz):  $\delta$  = 7.42 (td,  $J$  = 8.1, 4.9 Hz, 1H), 7.06 (ddd,  $J$  = 11.1, 8.3, 1.0 Hz, 1H), 6.92 (d,  $J$  = 8.0 Hz, 1H), 4.36–4.28 (m, 2H), 4.28–4.20 (m, 2H).

$^{13}C$  NMR ( $CDCl_3$ , 126 MHz):  $\delta$  = 182.40 (s), 162.25 (d,  $J$  = 266.9 Hz), 148.28 (d,  $J$  = 10.3 Hz), 136.90 (s), 133.53 (d,  $J$  = 10.2 Hz), 118.41 (d,  $J$  = 4.1 Hz), 116.02 (d,  $J$  = 22.7 Hz), 110.26 (d,  $J$  = 9.8 Hz), 53.50 (s), 50.84 (s).

GC/MS ( $t_r$  = 23.23 min, 70 eV, EI)  $m/z$  (%) = 238 [ $M^+$ ] (100).

4.1.62. 8-Methyl-2H-benzo[e]imidazo [1,2-c] [1,3]thiazine-5(3H)-thione (**4t**)

2-(2-Bromo-4-methylphenyl)-4,5-dihydro-1H-imidazole (**2t**) (956 mg, 4.00 mmol) was subjected to general procedure for cyclization using NaH (60%, 160 mg, 4.00 mmol) and carbon disulfide (242  $\mu$ l, 305 mg, 4.00 mmol). 8-Methyl-2H-benzo[e]imidazo [1,2-c] [1,3]thiazine-5(3H)-thione (**4t**) was received as yellow crystals (899 mg, 3.84 mmol, 96%).

$^1H$  NMR ( $CDCl_3$ , 300 MHz):  $\delta$  = 8.00 (d,  $J$  = 8.2 Hz, 1H), 7.16–7.06 (m, 1H), 6.88 (s, 1H), 4.41–4.28 (m, 2H), 4.17–4.03 (m, 2H), 2.35 (s, 3H).

$^{13}C$  NMR ( $CDCl_3$ , 75 MHz):  $\delta$  = 183.41 (s), 151.55 (s), 143.74 (s), 134.64 (s), 129.00 (d,  $J$  = 3.9 Hz), 122.44 (s), 117.90 (s), 52.43 (s), 52.05 (s), 21.65 (s).

HPLC/MS ( $t_r$  = 14.153 min, 70 eV, EI)  $m/z$  (%) = 235.131 (100) [ $M+H$ ] $^+$

4.1.63. 2H-benzo[e]imidazo [1,2-c] [1,3]thiazine-5(3H)-thione (**4u**)

2-(2-bromophenyl)-4,5-dihydro-1H-imidazole (**2u**) (261 mg, 1.00 mmol) was subjected to general procedure for cyclization using NaH (60%, 80.0 mg, 2.00 mmol) and carbon disulfide (120  $\mu$ l, 151 mg, 1.99 mmol). 2H-benzo[e]imidazo [1,2-c] [1,3]thiazine-5(3H)-thione (**4u**) was received as yellow crystals (156 mg, 612  $\mu$ mol, 61%).

GC/MS ( $t_r$  = 23.03 min, 70 eV, EI)  $m/z$  (%) = 220 [ $M^+$ ] (100), 187 (30), 161 (31), 135 (27), 86 (37).  $^1H$  NMR ( $CDCl_3$ , 500 MHz):  $\delta$  = 8.17 (d,  $J$  = 7.9 Hz, 1H), 7.47 (td,  $J$  = 8.0, 1.2 Hz, 1H), 7.38–7.29 (m, 1H), 7.11 (d,  $J$  = 8.0 Hz, 1H), 4.46–4.33 (m, 2H), 4.21–4.11 (m, 2H).

$^{13}C$  NMR ( $CDCl_3$ , 125 MHz):  $\delta$  = 183.3, 151.6, 134.9, 132.7, 129.2, 127.8, 122.4, 120.6, 52.5, 52.1.

#### 4.1.64. 7-Methyl-2H-benzo[e]imidazo [1,2-c] [1,3]thiazine-5(3H)-thione (**4v**)

2-(2-Fluoro-3-methylphenyl)-4,5-dihydro-1H-imidazole (**2v**) (200 mg, 1.12 mmol) was subjected to general procedure for cyclization using NaH (60%, 91.1 mg, 2.28 mmol) and carbon disulfide (136  $\mu$ l, 171 mg, 2.24 mmol). 7-Methyl-2H-benzo[e]imidazo [1,2-c] [1,3]thiazine-5(3H)-thione (**4v**) was received as yellow crystals (60.4 mg, 258  $\mu$ mol, 23%).

$^1\text{H NMR}$  ( $\text{CDCl}_3$ , 300 MHz):  $\delta$  = 8.04 (dd,  $J$  = 7.8, 0.9 Hz, 1H), 7.32 (d,  $J$  = 6.8 Hz, 1H), 7.24 (t,  $J$  = 7.6 Hz, 2H), 4.46–4.36 (m, 2H), 4.20–4.11 (m, 2H).

HPLC/MS ( $t_r$  = 14.335 min, 70 eV, EI)  $m/z$  (%) = 235.000 (100)  $[\text{M}+\text{H}]^+$

#### 4.1.65. 10-Methyl-3,4-dihydrobenzo[e]pyrimido [1,2-c] [1,3]thiazine-6(2H)-thione (**5a**)

2-(2-Fluoro-5-methylphenyl)-1,4,5,6-tetrahydropyrimidine (**3a**) (200 mg, 1.04 mmol) was subjected to general procedure for cyclization using NaH (60%, 84.5 mg, 2.11 mmol) and carbon disulfide (126  $\mu$ l, 158 mg, 2.08 mmol). 10-Methyl-3,4-dihydrobenzo[e]pyrimido [1,2-c] [1,3]thiazine-6(2H)-thione (**5a**) was received as yellow crystals (7.4 mg, 29.8  $\mu$ mol, 3%).

$^1\text{H NMR}$  ( $\text{CDCl}_3$ , 500 MHz):  $\delta$  = 8.02 (s, 1H), 7.23 (dd,  $J$  = 8.0, 1.1 Hz, 1H), 6.93 (d,  $J$  = 8.0 Hz, 1H), 4.49–4.39 (m, 2H), 3.75 (t,  $J$  = 5.6 Hz, 2H), 2.37 (s, 3H), 2.08–1.99 (m, 2H).

$^{13}\text{C NMR}$  ( $\text{CDCl}_3$ , 126 MHz):  $\delta$  = 190.20 (s), 144.67 (s), 137.87 (s), 132.33 (s), 129.08 (s), 128.84 (s), 126.35 (s), 121.72 (s), 48.85 (s), 45.69 (s), 21.82 (s), 21.36 (s).

HPLC/MS ( $t_r$  = 14.958 min, 70 eV, EI)  $m/z$  (%) = 249.040 (100)  $[\text{M}+\text{H}]^+$

#### 4.1.66. 11-Iodo-3,4-dihydrobenzo[e]pyrimido [1,2-c] [1,3]thiazine-6(2H)-thione (**5b**)

2-(2-Fluoro-6-iodophenyl)-1,4,5,6-tetrahydropyrimidine (**3b**) (150 mg, 493  $\mu$ mol) was subjected to general procedure for cyclization using NaH (60%, 40.1 mg, 1.00 mmol) and carbon disulfide (59.6  $\mu$ l, 75.1 mg, 987  $\mu$ mol). 11-Iodo-3,4-dihydrobenzo[e]pyrimido [1,2-c] [1,3]thiazine-6(2H)-thione (**5b**) was received as yellow crystals (11.3 mg, 31.4  $\mu$ mol, 6%).

HPLC/MS ( $t_r$  = 14.072 min, 70 eV, EI)  $m/z$  (%) = 361.000 (100)  $[\text{M}+\text{H}]^+$

#### 4.1.67. 11-Chloro-3,4-dihydrobenzo[e]pyrimido [1,2-c] [1,3]thiazine-6(2H)-thione (**5c**)

2-(2-Chloro-6-fluorophenyl)-1,4,5,6-tetrahydropyrimidine (**3c**) (200 mg, 941  $\mu$ mol) was subjected to general procedure for cyclization using NaH (60%, 76.4 mg, 1.91 mmol) and carbon disulfide (114  $\mu$ l, 143 mg, 1.88 mmol). 11-Chloro-3,4-dihydrobenzo[e]pyrimido [1,2-c] [1,3]thiazine-6(2H)-thione (**5c**) was received as yellow crystals (6.8 mg, 25.3  $\mu$ mol, 3%).

$^1\text{H NMR}$  ( $\text{CDCl}_3$ , 500 MHz):  $\delta$  = 7.42 (dd,  $J$  = 8.0, 1.1 Hz, 1H), 7.31 (t,  $J$  = 7.9 Hz, 1H), 7.04 (dd,  $J$  = 7.8, 1.1 Hz, 1H), 4.37–4.33 (m, 2H), 3.85 (t,  $J$  = 5.7 Hz, 2H), 2.12 (dt,  $J$  = 11.7, 6.0 Hz, 2H).

HPLC/MS ( $t_r$  = 15.083 min, 70 eV, EI)  $m/z$  (%) = 269.000 (100)  $[\text{M}+\text{H}]^+$

#### 4.1.68. 11-Methyl-3,4-dihydrobenzo[e]pyrimido [1,2-c] [1,3]thiazine-6(2H)-thione (**5d**)

2-(2-Fluoro-6-methylphenyl)-1,4,5,6-tetrahydropyrimidine (**3d**) (716 mg, 3.72 mmol) was subjected to general procedure for cyclization using NaH (60%, 325 mg, 8.13 mmol) and carbon disulfide (480  $\mu$ l, 605 mg, 7.94 mmol). 11-Methyl-3,4-dihydrobenzo[e]pyrimido [1,2-c] [1,3]thiazine-6(2H)-thione (**5d**) was received as yellow solid (528 mg, 2.13 mmol, 57%).

$^1\text{H NMR}$  ( $\text{CDCl}_3$ , 500 MHz):  $\delta$  = 7.28 (dd,  $J$  = 15.1, 7.3 Hz, 1H), 7.19

(d,  $J$  = 7.6 Hz, 1H), 6.95 (d,  $J$  = 7.8 Hz, 1H), 4.38–4.30 (m, 2H), 3.79 (t,  $J$  = 5.7 Hz, 2H), 2.61 (d,  $J$  = 8.5 Hz, 3H), 2.11–2.05 (m, 2H).

$^{13}\text{C NMR}$  ( $\text{CDCl}_3$ , 126 MHz):  $\delta$  = 189.28, 146.14, 139.82, 133.02, 131.44, 130.29, 125.80, 120.37, 48.35, 45.74, 23.38, 22.84.

#### 4.1.69. 6-Thioxo-2,3,4,6-tetrahydrobenzo[e]pyrimido [1,2-c] [1,3]thiazine-9-carbonitrile (**5e**)

3-Fluoro-4-(1,4,5,6-tetrahydropyrimidin-2-yl)benzotrile (**3e**) (200 mg, 984  $\mu$ mol) was subjected to general procedure for cyclization using NaH (60%, 79.9 mg, 2.00 mmol) and carbon disulfide (119  $\mu$ l, 150 mg, 1.97 mmol). 6-Thioxo-2,3,4,6-tetrahydrobenzo[e]pyrimido [1,2-c] [1,3]thiazine-9-carbonitrile (**5e**) was received as yellow crystals (8.6 mg, 33.2  $\mu$ mol, 3%).

$^1\text{H NMR}$  ( $\text{CDCl}_3$ , 500 MHz):  $\delta$  = 8.33 (d,  $J$  = 8.4 Hz, 1H), 7.53 (ddd,  $J$  = 8.4, 1.5, 0.6 Hz, 1H), 7.36–7.30 (m, 1H), 4.43 (dd,  $J$  = 6.5, 5.9 Hz, 2H), 3.79 (t,  $J$  = 5.6 Hz, 2H), 2.08–2.02 (m, 2H).

HPLC/MS ( $t_r$  = 13.235 min, 70 eV, EI)  $m/z$  (%) = 259.967 (100)  $[\text{M}+\text{H}]^+$

#### 4.1.70. 10-Chloro-3,4-dihydrobenzo[e]pyrimido [1,2-c] [1,3]thiazine-6(2H)-thione (**5f**)

2-(2-Bromo-5-chlorophenyl)-1,4,5,6-tetrahydropyrimidine (**3f**) (274 mg, 1.00 mmol) was subjected to general procedure for cyclization using NaH (60%, 80.9 mg, 2.00 mmol) and carbon disulfide (121  $\mu$ l, 152 mg, 2.00 mmol). 10-Chloro-3,4-dihydrobenzo[e]pyrimido [1,2-c] [1,3]thiazine-6(2H)-thione (**5f**) was received as yellow crystals (168 mg, 626  $\mu$ mol, 63%).

GC/MS ( $t_r$  = 25.49 min, 70 eV, EI)  $m/z$  (%) = 268  $[\text{M}^+]$  (100), 235 (14), 210 (62), 169 (22), 133 (16), 100 (28), 72 (65).

$^1\text{H NMR}$  ( $\text{CDCl}_3$ , 500 MHz):  $\delta$  = 8.21 (d,  $J$  = 2.3 Hz, 1H), 7.36 (dd,  $J$  = 8.4, 2.3 Hz, 1H), 6.96 (d,  $J$  = 8.4 Hz, 1H), 4.50–4.31 (m, 2H), 3.75 (t,  $J$  = 5.6 Hz, 2H), 2.03 (ddd,  $J$  = 11.4, 7.8, 6.0 Hz, 2H).

$^{13}\text{C NMR}$  ( $\text{CDCl}_3$ , 125 MHz):  $\delta$  = 189.1, 143.3, 133.6, 131.4, 130.2, 128.8, 127.8, 123.0, 48.7, 45.6, 21.6.

#### 4.1.71. 9-(Trifluoromethyl)-3,4-dihydrobenzo[e]pyrimido [1,2-c] [1,3]thiazine-6(2H)-thione (**5g**)

2-(2-Bromo-4-trifluoromethylphenyl)-1,4,5,6-tetrahydropyrimidine (**3g**) (306 mg, 1.00 mmol) was subjected to general procedure for cyclization using NaH (60%, 80 mg, 2.00 mmol) and carbon disulfide (121  $\mu$ l, 152 mg, 2.00 mmol). 9-(Trifluoromethyl)-3,4-dihydrobenzo[e]pyrimido [1,2-c] [1,3]thiazine-6(2H)-thione (**5g**) was received as yellow crystals (177 mg, 585  $\mu$ mol, 59%).

$^1\text{H NMR}$  ( $\text{CDCl}_3$ , 300 MHz):  $\delta$  = 8.50 (dd,  $J$  = 1.3, 0.6 Hz, 1H), 7.66–7.57 (m, 1H), 7.13 (d,  $J$  = 8.3 Hz, 1H), 4.43 (dd,  $J$  = 6.5, 5.9 Hz, 2H), 3.78 (t,  $J$  = 5.6 Hz, 2H).

GC/MS ( $t_r$  = 22.976 min, 70 eV, EI)  $m/z$  (%) = 302  $[\text{M}^+]$  (100).

#### 4.1.72. 9-Methyl-3,4-dihydrobenzo[e]pyrimido [1,2-c] [1,3]thiazine-6(2H)-thione (**5h**)

2-(2-Fluoro-4-methylphenyl)-1,4,5,6-tetrahydropyrimidine (**3h**) (767 mg, 3.99 mmol) was subjected to general procedure for cyclization using NaH (60%, 322 mg, 8.06 mmol) and carbon disulfide (490  $\mu$ l, 617 mg, 8.11 mmol). 9-Methyl-3,4-dihydrobenzo[e]pyrimido [1,2-c] [1,3]thiazine-6(2H)-thione (**5h**) was received as yellow crystals (323 mg, 1.30 mmol, 33%).

$^1\text{H NMR}$  ( $\text{CDCl}_3$ , 500 MHz):  $\delta$  = 8.14 (d,  $J$  = 8.0 Hz, 1H), 7.12 (d,  $J$  = 8.1 Hz, 1H), 6.83 (s, 1H), 4.49–4.41 (m, 2H), 3.75 (t,  $J$  = 5.6 Hz, 2H), 2.36 (s, 3H), 2.04 (dt,  $J$  = 11.8, 5.9 Hz, 2H).

$^{13}\text{C NMR}$  ( $\text{CDCl}_3$ , 125 MHz):  $\delta$  = 190.1, 144.9, 142.3, 132.0, 129.1, 129.0, 123.6, 121.8, 48.9, 45.4, 21.6, 21.4.

#### 4.1.73. 10-Iodo-3,4-dihydrobenzo[e]pyrimido [1,2-c] [1,3]thiazine-6(2H)-thione (**5i**)

2-(2-Fluoro-5-iodophenyl)-1,4,5,6-tetrahydropyrimidine (**3i**) (200 mg, 658  $\mu$ mol) was subjected to general procedure for cyclization using NaH (60%, 53.4 mg, 1.34 mmol) and carbon disulfide (79.5  $\mu$ l, 100 mg, 1.32 mmol). 10-Iodo-3,4-dihydrobenzo[e]pyrimido [1,2-c] [1,3]thiazine-6(2H)-thione (**5i**) was received as yellow crystals (20.5 mg, 56.9 mmol, 9%).

$^1\text{H}$  NMR (DMSO, 300 MHz):  $\delta$  = 8.44 (d,  $J$  = 1.9 Hz, 1H), 7.86 (dd,  $J$  = 8.3, 1.9 Hz, 1H), 7.13 (d,  $J$  = 8.3 Hz, 1H), 4.36–4.28 (m, 2H), 3.68 (t,  $J$  = 5.6 Hz, 2H), 1.94 (dt,  $J$  = 11.4, 5.9 Hz, 2H).

HPLC/MS ( $t_r$  = 17.725 min, 70 eV, EI)  $m/z$  (%) = 360.900 (100)  $[\text{M}+\text{H}]^+$

#### 4.1.74. 9-Bromo-3,4-dihydrobenzo[e]pyrimido [1,2-c] [1,3]thiazine-6(2H)-thione (**5j**)

2-(4-Bromo-2-fluorophenyl)-1,4,5,6-tetrahydropyrimidine (**3j**) (1.02 g, 3.96 mmol) was subjected to general procedure for cyclization using NaH (60%, 322 mg, 8.05 mmol) and carbon disulfide (480  $\mu$ l, 605 mg, 8.05 mmol). 9-Bromo-3,4-dihydrobenzo[e]pyrimido [1,2-c] [1,3]thiazine-6(2H)-thione (**5j**) was received as yellow crystals (578 mg, 1.84 mmol, 47%).

GC/MS ( $t_r$  = 26.19 min, 70 eV, EI)  $m/z$  (%) = 314 (100)  $[\text{M}^+ (^{81}\text{Br})]$ , 312 (94)  $[\text{M}^+ (^{79}\text{Br})]$ , 256 (67), 254 (76), 113 (26), 72 (80), 41 (32).

$^1\text{H}$  NMR ( $\text{CDCl}_3$ , 500 MHz):  $\delta$  = 8.05 (d,  $J$  = 8.7 Hz, 1H), 7.38 (dd,  $J$  = 8.7, 1.9 Hz, 1H), 7.15 (d,  $J$  = 1.9 Hz, 1H), 4.47–4.35 (m, 2H), 3.72 (t,  $J$  = 5.6 Hz, 2H), 2.02 (dt,  $J$  = 11.6, 5.9 Hz, 2H).

$^{13}\text{C}$  NMR ( $\text{CDCl}_3$ , 125 MHz):  $\delta$  = 188.9, 143.7, 133.8, 130.7, 126.0, 125.4, 124.07, 48.7, 45.7, 21.6.

#### 4.1.75. 9-Fluoro-3,4-dihydrobenzo[e]pyrimido [1,2-c] [1,3]thiazine-6(2H)-thione (**5k**)

2-(2,4-Difluorophenyl)-1,4,5,6-tetrahydropyrimidine (**3k**) (783 mg, 3.99 mmol) was subjected to general procedure for cyclization using NaH (60%, 195 mg, 8.14 mmol) and carbon disulfide (483  $\mu$ l, 609 mg, 8.00 mmol). 9-Fluoro-3,4-dihydrobenzo[e]pyrimido [1,2-c] [1,3]thiazine-6(2H)-thione (**5k**) was received as yellow crystals (656 mg, 2.60 mmol, 65%).

GC/MS ( $t_r$  = 23.17 min, 70 eV, EI)  $m/z$  (%) = 252 (100)  $[\text{M}^+]$ , 194 (50), 192 (17), 166 (16), 99 (18), 72 (52), 41 (22).

$^1\text{H}$  NMR ( $\text{CDCl}_3$ , 500 MHz):  $\delta$  = 8.20 (dd,  $J$  = 9.0, 5.6 Hz, 1H), 6.96 (td,  $J$  = 8.6, 2.5 Hz, 1H), 6.70 (dd,  $J$  = 7.9, 2.5 Hz, 1H), 4.45–4.34 (m, 2H), 3.72 (t,  $J$  = 5.6 Hz, 2H), 2.02 (dt,  $J$  = 11.9, 5.9 Hz, 2H).  $^{13}\text{C}$  NMR ( $\text{CDCl}_3$ , 125 MHz):  $\delta$  = 188.9 (s), 164.0 (d,  $J$  = 255.4 Hz), 143.5 (s), 134.1 (d,  $J$  = 8.7 Hz), 131.8 (d,  $J$  = 8.9 Hz), 122.8 (s), 115.2 (d,  $J$  = 22.0 Hz), 108.1 (d,  $J$  = 24.7 Hz), 48.8 (s), 45.5 (s), 21.6 (s).

#### 4.1.76. 3,4-Dihydrobenzo[e]pyrimido [1,2-c] [1,3]thiazine-6(2H)-thione (**5l**)

2-(2-Bromophenyl)-1,4,5,6-tetrahydropyrimidine (**3l**) (930 mg, 3.89 mmol) was dissolved in 10 ml dry DMF, NaH (311 mg, 7.78 mmol, 60% suspension in oil) and  $\text{CS}_2$  (470  $\mu$ l, 7.78 mmol) were added and the mixture stirred for 15 h at rt. Afterwards 800  $\mu$ l MeOH was added and the solvent was evaporated. Purification via silica column chromatography (hexane:EtOAc 8:2;  $R_f$ : 0.4) gave the product as a bright yellow solid (500 mg, 55%).

$^1\text{H}$  NMR (300 MHz,  $\text{CDCl}_3$ )  $\delta$  8.21 (dd,  $J$  = 8.0, 1.3 Hz, 1H, Ar), 7.44–7.36 (m, 1H, Ar), 7.33–7.26 (m, 1H, Ar), 7.10–6.94 (m, 1H, Ar), 4.56–4.25 (m, 2H,  $\text{CH}_2$ ), 3.75 (t,  $J$  = 5.6 Hz, 2H,  $\text{CH}_2$ ), 2.22–1.86 (m, 2H,  $\text{CH}_2$ ).

$^{13}\text{C}$  NMR (75 MHz,  $\text{CDCl}_3$ )  $\delta$  189.78, 144.43, 131.93, 131.24, 128.95, 127.60, 126.31, 121.66, 48.76, 45.51, 21.62.

#### 4.1.77. 10-Bromo-3,4-dihydrobenzo[e]pyrimido [1,2-c] [1,3]thiazine-6(2H)-thione (**5m**)

2-(2,5-Dibromophenyl)-1,4,5,6-tetrahydropyrimidine (**3m**) (580 mg, 1.82 mmol) was subjected to general procedure for cyclization using NaH (60%, 146 mg, 3.64 mmol) and carbon disulfide (220  $\mu$ l, 277 mg, 3.64 mmol). 10-Bromo-3,4-dihydrobenzo[e]pyrimido [1,2-c] [1,3]thiazine-6(2H)-thione (**5m**) was received as yellow solid (417 mg, 1.33 mmol, 73%).

$^1\text{H}$  NMR ( $\text{CDCl}_3$ , 500 MHz):  $\delta$  = 8.37 (d,  $J$  = 2.1 Hz, 1H), 7.49 (dd,  $J$  = 8.4, 2.2 Hz, 1H), 6.88 (d,  $J$  = 8.4 Hz, 1H), 4.44–4.39 (m, 2H), 3.75 (t,  $J$  = 5.6 Hz, 2H), 2.03 (dq,  $J$  = 7.8, 6.0 Hz, 2H).

$^{13}\text{C}$  NMR ( $\text{CDCl}_3$ , 126 MHz):  $\delta$  = 189.02 (s), 143.16 (s), 134.20 (s), 131.80 (s), 131.01 (s), 128.02 (s), 123.16 (s), 121.28 (s), 48.70 (s), 45.67 (s), 21.65 (s).

GC/MS ( $t_r$  = 26.28 min, 70 eV, EI)  $m/z$  (%) = 313.9 (100)  $[\text{M}^+ (^{81}\text{Br})]$ , 311.9 (95)  $[\text{M}^+ (^{79}\text{Br})]$ ,

#### 4.1.78. 10-Fluoro-3,4-dihydrobenzo[e]pyrimido [1,2-c] [1,3]thiazine-6(2H)-thione (**5n**)

2-(2-Bromo-5-fluorophenyl)-1,4,5,6-tetrahydropyrimidine (**3n**) (1.03 g, 4.00 mmol) was subjected to general procedure for cyclization using NaH (60%, 320 mg, 8.00 mmol) and carbon disulfide (490  $\mu$ l, 617 mg, 8.11 mmol). 10-Fluoro-3,4-dihydrobenzo[e]pyrimido [1,2-c] [1,3]thiazine-6(2H)-thione (**5n**) was received as yellow solid (482 mg, 1.90 mmol, 48%).

GC/MS ( $t_r$  = 23.41 min, 70 eV, EI)  $m/z$  (%) = 252 (100)  $[\text{M}^+]$ , 194 (49), 100 (24), 72 (59).

$^1\text{H}$  NMR ( $\text{CDCl}_3$ , 500 MHz):  $\delta$  = 7.92 (dd,  $J$  = 10.1, 2.8 Hz, 1H), 7.16–7.10 (m, 1H), 6.98 (dd,  $J$  = 8.7, 5.0 Hz, 1H), 4.47–4.39 (m, 2H), 3.74 (t,  $J$  = 5.6 Hz, 2H), 2.03 (dt,  $J$  = 12.2, 5.9 Hz, 2H).

$^{13}\text{C}$  NMR ( $\text{CDCl}_3$ , 125 MHz):  $\delta$  = 189.3 (s), 161.9 (d,  $J$  = 247.1 Hz), 143.4 (s), 128.5 (d,  $J$  = 8.1 Hz), 127.4 (s), 123.6 (d,  $J$  = 7.8 Hz), 119.2 (d,  $J$  = 23.4 Hz), 115.6 (d,  $J$  = 25.2 Hz), 48.6 (s), 45.6 (s), 21.6 (s).

#### 4.1.79. 11-Fluoro-3,4-dihydrobenzo[e]pyrimido [1,2-c] [1,3]thiazine-6(2H)-thione (**5o**)

2-(2,6-Difluorophenyl)-1,4,5,6-tetrahydropyrimidine (**3o**) (785 mg, 4.00 mmol) was subjected to general procedure for cyclization using NaH (60%, 320 mg, 8.00 mmol) and carbon disulfide (483  $\mu$ l, 609 mg, 8.00 mmol). 11-Fluoro-3,4-dihydrobenzo[e]pyrimido [1,2-c] [1,3]thiazine-6(2H)-thione (**5o**) was received as yellow solid (300 mg, 1.20 mmol, 30%).

$^1\text{H}$  NMR ( $\text{CDCl}_3$ , 500 MHz):  $\delta$  = 7.35 (td,  $J$  = 8.1, 4.7 Hz, 1H), 7.02 (ddd,  $J$  = 11.0, 8.3, 1.0 Hz, 1H), 6.85 (d,  $J$  = 7.9 Hz, 1H), 4.38–4.31 (m, 1H), 3.79 (t,  $J$  = 5.6 Hz, 1H), 2.07 (td,  $J$  = 11.7, 5.9 Hz, 1H).

$^{13}\text{C}$  NMR ( $\text{CDCl}_3$ , 126 MHz):  $\delta$  = 188.41 (s), 160.68 (d,  $J$  = 263.1 Hz), 141.92 (d,  $J$  = 9.3 Hz), 134.57 (s), 132.11 (d,  $J$  = 9.8 Hz), 117.97 (d,  $J$  = 4.3 Hz), 116.00 (d,  $J$  = 23.5 Hz), 48.45 (s), 46.23 (s), 22.65 (s).

GC/MS ( $t_r$  = 23.49 min, 70 eV, EI)  $m/z$  (%) = 252 (100)  $[\text{M}^+]$ ,

#### 4.1.80. 9-(Dimethylamino)-3,4-dihydrobenzo[e]pyrimido [1,2-c] [1,3]thiazine-6(2H)-thione (**5p**)

2-(2-Bromo-4-dimethylaminophenyl)-1,4,5,6-tetrahydropyrimidine (**3p**) (283 mg, 1.00 mmol) was subjected to general procedure for cyclization using NaH (60%, 87.0 mg, 2.18 mmol) and carbon disulfide (120  $\mu$ l, 151 mg, 1.99 mmol). 9-(dimethylamino)-3,4-dihydrobenzo[e]pyrimido [1,2-c] [1,3]thiazine-6(2H)-thione (**5p**) was received as yellow crystals (159 mg, 574  $\mu$ mol, 57%).

GC/MS ( $t_r$  = 28.95 min, 70 eV, EI)  $m/z$  (%) = 277  $[\text{M}^+]$  (100), 244 (14), 219 (66), 191 (27), 177 (37).

#### 4.1.81. 11-Bromo-3,4-dihydrobenzo[e]pyrimido [1,2-c] [1,3]thiazine-6(2H)-thione (**5q**)

2-(2-Bromo-6-fluorophenyl)-1,4,5,6-tetrahydropyrimidine (**3q**) (1.03 g, 4.00 mmol) was subjected to general procedure for cyclization using NaH (60%, 320 mg, 8.00 mmol) and carbon disulfide (490  $\mu$ l, 617 mg, 8.11 mmol). 11-Bromo-3,4-dihydrobenzo[e]pyrimido[1,2-c] [1,3]thiazine-6(2H)-thione (**5q**) was received as yellow crystals (210 mg, 670  $\mu$ mol, 17%).

GC/MS ( $t_r$  = 25.54 min, 70 eV, EI)  $m/z$  (%) = 314 (80) [ $M^+$  ( $^{81}\text{Br}$ )], 312 (76) [ $M^+$  ( $^{79}\text{Br}$ )], 255 (64), 253 (73), 133 (30), 100 (37), 72 (100), 41 (42).

$^1\text{H NMR}$  ( $\text{CDCl}_3$ , 500 MHz):  $\delta$  = 7.63 (dd,  $J$  = 8.0, 0.9 Hz, 1H), 7.21 (t,  $J$  = 7.9 Hz, 1H), 7.07 (dd,  $J$  = 7.9, 0.9 Hz, 1H), 4.39–4.28 (m, 2H), 3.84 (t,  $J$  = 5.7 Hz, 2H), 2.16–2.06 (m, 2H).

$^{13}\text{C NMR}$  ( $\text{CDCl}_3$ , 125 MHz):  $\delta$  = 187.9, 144.6, 134.9, 134.3, 131.2, 125.9, 122.8, 121.9, 48.3, 45.9, 23.4.

#### 4.1.82. 9-Chloro-3,4-dihydrobenzo[e]pyrimido [1,2-c] [1,3]thiazine-6(2H)-thione (**5r**)

2-(4-Chloro-2-fluorophenyl)-1,4,5,6-tetrahydropyrimidine (**3r**) (200 mg, 941  $\mu$ mol) was subjected to general procedure for cyclization using NaH (60%, 76.4 mg, 1.91 mmol) and carbon disulfide (114  $\mu$ l, 143 mg, 1.88 mmol). 9-Chloro-3,4-dihydrobenzo[e]pyrimido [1,2-c] [1,3]thiazine-6(2H)-thione (**5r**) was received as yellow crystals (118 mg, 440  $\mu$ mol, 47%).

$^1\text{H NMR}$  ( $\text{CDCl}_3$ , 500 MHz):  $\delta$  = 8.15 (d,  $J$  = 8.7 Hz, 1H), 7.24 (dd,  $J$  = 8.7, 2.0 Hz, 1H), 7.02 (d,  $J$  = 2.0 Hz, 1H), 4.47–4.37 (m, 2H), 3.74 (t,  $J$  = 5.6 Hz, 2H), 2.09–1.97 (m, 2H).

$^{13}\text{C NMR}$  ( $\text{CDCl}_3$ , 126 MHz):  $\delta$  = 189.04 (s), 143.64 (s), 137.77 (s), 133.59 (s), 130.61 (s), 127.89 (s), 124.99 (s), 121.24 (s), 48.79 (s), 45.64 (s), 21.64 (s).

#### 4.1.83. 8-Fluoro-3,4-dihydrobenzo[e]pyrimido [1,2-c] [1,3]thiazine-6(2H)-thione (**5s**)

2-(2,3-Difluorophenyl)-1,4,5,6-tetrahydropyrimidine (**3s**) (788 mg, 4.01 mmol) was subjected to general procedure for cyclization using NaH (60%, 320 mg, 8.00 mmol) and carbon disulfide (490  $\mu$ l, 617 mg, 8.11 mmol). 8-Fluoro-3,4-dihydrobenzo[e]pyrimido[1,2-c] [1,3]thiazine-6(2H)-thione (**5s**) was received as yellow crystals (595 mg, 2.36 mmol, 59%).

GC/MS ( $t_r$  = 23.53 min, 70 eV, EI)  $m/z$  (%) = 252 (100) [ $M^+$ ], 219 (10), 194 (46), 153 (17), 72 (48), 41 (21).

$^1\text{H NMR}$  ( $\text{CDCl}_3$ , 500 MHz):  $\delta$  = 8.00 (d,  $J$  = 8.1 Hz, 1H), 7.25 (ddd,  $J$  = 13.8, 7.9, 5.7 Hz, 1H), 7.16–7.09 (m, 1H), 4.46–4.38 (m, 2H), 3.75 (t,  $J$  = 5.6 Hz, 2H), 2.08–1.99 (m, 2H).

$^{13}\text{C NMR}$  ( $\text{CDCl}_3$ , 125 MHz):  $\delta$  = 188.2 (s), 153.8 (d,  $J$  = 245.2 Hz), 143.3 (d,  $J$  = 3.4 Hz), 128.0 (s,  $J$  = 2.1 Hz), 127.9 (d,  $J$  = 7.6 Hz), 124.4 (d,  $J$  = 2.9 Hz), 120.7 (d,  $J$  = 20.1 Hz), 117.0 (d,  $J$  = 19.5 Hz), 48.8 (s), 45.6 (s), 21.6 (s).

#### 4.1.84. 8-Chloro-3,4-dihydrobenzo[e]pyrimido [1,2-c] [1,3]thiazine-6(2H)-thione (**5t**)

2-(3-Chloro-2-fluorophenyl)-1,4,5,6-tetrahydropyrimidine (**3t**) (200 mg, 941  $\mu$ mol) was subjected to general procedure for cyclization using NaH (60%, 76.4 mg, 1.91 mmol) and carbon disulfide (114  $\mu$ l, 143 mg, 1.88 mmol). 8-Chloro-3,4-dihydrobenzo[e]pyrimido [1,2-c] [1,3]thiazine-6(2H)-thione (**5t**) was received as yellow crystals (101 mg, 375  $\mu$ mol, 40%).

$^1\text{H NMR}$  ( $\text{CDCl}_3$ , 300 MHz):  $\delta$  = 8.12 (d,  $J$  = 8.1 Hz, 1H), 7.41 (d,  $J$  = 7.9 Hz, 1H), 7.22 (t,  $J$  = 8.0 Hz, 1H), 4.41 (t,  $J$  = 6.0 Hz, 2H), 3.74 (t,  $J$  = 5.4 Hz, 2H), 2.15–1.92 (m, 2H).

$^{13}\text{C NMR}$  ( $\text{CDCl}_3$ , 75 MHz):  $\delta$  = 188.86 (s), 143.83 (s), 131.40 (s), 128.23 (s), 127.73 (s), 127.35 (s), 126.26 (s), 48.77 (s), 45.66 (s), 21.46 (s).

#### 4.1.85. 8-Methyl-3,4-dihydrobenzo[e]pyrimido [1,2-c] [1,3]thiazine-6(2H)-thione (**5u**)

2-(2-Fluoro-3-methylphenyl)-1,4,5,6-tetrahydropyrimidine (**3u**) (200 mg, 1.04 mmol) was subjected to general procedure for cyclization using NaH (60%, 84.5 mg, 2.11 mmol) and carbon disulfide (126  $\mu$ l, 158 mg, 2.08 mmol). 8-Methyl-3,4-dihydrobenzo[e]pyrimido [1,2-c] [1,3]thiazine-6(2H)-thione (**5u**) was received as yellow crystals (83.9 mg, 338  $\mu$ mol, 32%).

$^1\text{H NMR}$  (DMSO, 300 MHz):  $\delta$  = 8.00 (dd,  $J$  = 8.0, 0.7 Hz, 1H), 7.40 (dd,  $J$  = 4.3, 3.9 Hz, 1H), 7.29 (t,  $J$  = 7.7 Hz, 1H), 4.37–4.28 (m, 1H), 3.67 (t,  $J$  = 5.6 Hz, 1H), 2.25 (s, 1H).

$^{13}\text{C NMR}$  (DMSO, 75 MHz):  $\delta$  = 187.84 (s), 143.62 (s), 132.79 (s), 130.81 (s), 130.45 (s), 127.74 (s), 126.64 (d,  $J$  = 7.1 Hz), 49.04 (s), 45.44 (s), 21.37 (s), 18.33 (s).

#### 4.2. Method for the determination of chemical stability against GSH

Substrate (5 mM) was treated with 2 eq of glutathione in a bicarbonate-buffer (10 mM) and measured via HPLC/MS. Samples were measured after 0h, 24h and in case of **6**, **5l**, **7** and **8** after 48h.

Mass spectral (MS) data were obtained using an Agilent 6110 Quadrupole LC/MS system with a 0.3 mL/min flow rate using a gradient mobile phase consisting of 0.1% trifluoroacetic acid (TFA) in water and 0.1% TFA in acetonitrile. UV detection was monitored at 254 nm. Mass spectra were acquired either in positive or in negative mode scanning over the mass range of 105–1500. The device used was an Agilent 1200 series HPLC system using a C-18 column (Waters XSelect Peptide C18 3.5  $\mu$ m, 2.1 mm  $\times$  100 mm) at 30  $^\circ\text{C}$ .

#### 4.3. HDAC4 and 8 expression and purification

All recombinant HDACs were purchased at BPS Bioscience except HDAC4 and HDAC8. Recombinant HDAC4 was expressed using a pET14b vector (Novagen, EMD Millipore) containing the codon-optimized catalytic domain of human HDAC4, fused to a N-terminal His6-SUMO tag and a C-terminal SII tag in *E. coli* (BL21) DE3 pLysS in autoinduction media (4.56 g/L glycerol, 3.08 g/L  $\text{KH}_2\text{PO}_4$ , 3.10 g/L  $\text{Na}_2\text{HPO}_4 \times 2\text{H}_2\text{O}$ , 0.44 g/L  $\text{MgSO}_4 \times 7\text{H}_2\text{O}$ , 20 g/L LB, 0.45 g/L glucose, 1.2 g/L lactose) at 30  $^\circ\text{C}$  for about 24 h. Cells were harvested by centrifugation for 10 min at 8000 g and 4  $^\circ\text{C}$  and resuspended in binding buffer (pH 8.0) containing 150 mM KCl, 50 mM Tris with the addition of 5 mM DTT and 5 mM imidazole. The cell suspension was sonicated, and lysates were clarified by centrifugation at 18000g for 30 min at 4  $^\circ\text{C}$  and filtration with a pore size of 0.45  $\mu$ m. The filtrate was then loaded onto a 5 mL cComplete™ His-Tag purification column (Roche) equilibrated with binding buffer using a ÄKTA pure FPLC system (GE Healthcare). After washing, the protein was eluted using a linear gradient of IMAC elution buffer (pH 8.0) containing 150 mM KCl, 50 mM Tris and 500 mM imidazole. Peak fractions were pooled and 10  $\mu$ g/mL His6 tagged SUMO-Protease was added. Cleavage of His6-SUMO tag occurred overnight whilst dialyzing against binding buffer. After dialysis the His6-SUMO free cHDAC4-SII was loaded on a Strep-Trap™ HP 5 mL column (GE Healthcare) and eluted with a step gradient of 2.5 mM d-desthiobiotin (Sigma) in binding buffer. Afterwards the protein containing fractions were concentrated and loaded onto a SEC column HiLoad Superdex 75 (GE Healthcare) equilibrated with binding buffer. Finally, the protein containing fractions were concentrated and 25% glycerol and 1 mM TCEP was added. The protein was flash frozen in liquid nitrogen and stored at –20  $^\circ\text{C}$ . We typically obtained about 10 mg cHDAC4-SII from 1 L culture.

Recombinant HDAC8 was expressed using the same vector system listed above containing the codon-optimized full length

human HDAC8, fused to a N-terminal His6-SUMO tag. Expression and purification were conducted in the same way as for HDAC4 with some minor changes. Cleavage of His6-SUMO tag occurred overnight whilst dialyzing against AIC binding buffer (pH 8.0) 25 mM Tris, 50 mM NaCl supplemented with 5 mM  $\beta$ -ME at 4 °C. At the next day His6-SUMO tag and His6-SUMO-Protease were removed by a second IMAC equilibrated with AIC binding buffer. HDAC8 containing flow-through was pooled and loaded on a strong anion exchanger (MiniChrom Toyopearl SuperQ-650M, 5 mL, Tosoh Bioscience GmbH, Griesheim, Germany) and protein was concentrated using a step elution with AIC elution buffer (pH 8.0) 25 mM Tris, 1 M NaCl. The final purification consists of a SEC and was conducted as for HDAC4. Protein containing fractions were collected, concentrated, 25% glycerol, 1 mM TCEP was added, flash frozen in liquid nitrogen and the protein was stored at -20 °C. We typically obtained about 10 mg HDAC8 from 1 L culture.

#### 4.4. Enzyme activity assay

All HDAC assays were executed in assay buffer (25 mM Tris-HCl pH 8.0, 50 mM NaCl and 0.001% (v/v) pluronic F-68) in black half area 96-well microplates (Greiner Bio-One, Germany). The different HDAC isoenzymes were preincubated with a serial dilution of the indicated compounds for 1 h at 30 °C and the enzyme reaction was initiated by the addition of 20  $\mu$ M Boc-Lys(TFA)-AMC (Bachem, Switzerland) for HDACs 4, 5, 7 and 8. For HDACs 1, 2, 3 and 6 50  $\mu$ M of Boc-Lys(Ac)-AMC (Bachem, Switzerland) was used. After substrate conversion at 30 °C for 1 h the reaction was stopped by adding 1.67  $\mu$ M suberoylanilide trifluoromethylketone (SATFMK) for HDACs 4, 5, 7 and 8 and 4.17  $\mu$ M suberoylanilide hydroxamic acid (SAHA) for HDACs 1, 2, 3, and 6. The deacetylated substrate was cleaved with 0.42 mg/mL trypsin to release fluorescent 7-amino-4-methylcoumarin (AMC), which was detected with a microplate reader (PHERAstar FS or BMG LABTECH) with fluorescence excitation at 360 nm and emission at 460 nm. IC<sub>50</sub> values were calculated by generating dose-response curves in GraphPad Prism 6 and fitting those to a 4-parameter fit model.

#### 4.5. Fluorescence polarization based displacement kinetics

For the measurement of fluorescence polarization based ligand displacement 500 nM of DBD probe and 500 nM HDAC8 were incubated in assay buffer (25 mM Tris-HCl, pH 8.0, 75 mM KCl, 0.001% Pluronic F-127) and measured in black 96-well microtiter plate (Greiner) for 2 h at 30 °C to reach complete binding equilibrium. Subsequently, the displacements were initiated by the addition of 50  $\mu$ M of the indicated inhibitor. The DBD ligands were displaced and the dissociation kinetics was measured for additional 3.5 h in a microplate reader at  $\lambda_{\text{Ex}} = 420$  nm (parallel polarized) and two distinguished emissions at  $\lambda_{\text{Em}} = 520$  nm (parallel and perpendicular polarized).

#### 4.6. Molecular docking and energy minimization

Modeling, preparation and visualization of structural data as well as molecular docking was performed using MOE 2018 software (Chemical Computing Group ULC, Canada). Four crystal structures representing significant conformations of HDAC8 (PDB-ID's 1T64, 1T69, 1VKG, 3SFF) were obtained from RCSB Protein Data Bank. The structure files were loaded into the program and subjected to structure preparation including 3D protonation for subsequent docking. The partial charges of all protein and ligand atoms were calculated using the implemented Amber14 force field. Molecular docking was performed choosing the triangle matcher for placement of the ligand in the binding site and ranked with the London

dG scoring function. The best 30 poses were passed to the refinement and energy minimization in the pocket using the induced fit method and then rescored with the GBVI/WSA dG scoring function. Subsequently, the resulting HDAC8 complex was energy-minimized within a radius of 10 Å around the ligand using the Amber14 force field.

#### 4.7. Western blot analysis

Western blot analysis was performed as described previously [20]. The following antibodies were used for detection: anti-tubulin (#2148, Cell Signaling Technology), anti-acetylated tubulin (#6793, Sigma-Aldrich), anti-acetylated SMC3 (kindly provided by Katsuhiko Shirahige, Institute for Molecular and Cellular Biosciences, University of Tokyo, Japan [37]), anti-acetyl-histone H4 (polyclonal; Upstate, Lake Placid, NY, USA), and anti-GAPDH (JC1682928, Millipore, Darmstadt, Germany).

#### 4.8. Colony assay

SK-N-BE(2)-C were plated on 6-well plates at a density of 800 cells per well and treated as indicated for 96 h. Adherent cells were washed three times with PBS and cultured for 7 additional days before staining of viable cell colonies with crystal violet (1% in 70% ethanol). For quantification, the plates were scanned, and colonies were counted in 16-bit binary pictures with the ITCN plugin for ImageJ software (U. S. National Institutes of Health, Bethesda, MD, USA; <http://imagej.nih.gov/ij/>).

#### Acknowledgements

This work was supported by the University of Applied Sciences Darmstadt. The authors are grateful to Michael Schröder for excellent technical and administrative support. The kind gift of the anti-Ac-SMC3 antibody by Prof. K. Shirahige at the University of Tokyo is gratefully acknowledged.

#### Appendix A. Supplementary data

Supplementary data to this article can be found online at <https://doi.org/10.1016/j.ejmech.2019.111756>.

#### References

- [1] K.J. Falkenberg, R.W. Johnstone, Histone deacetylases and their inhibitors in cancer, neurological diseases and immune disorders, *Nat. Rev. Drug Discov.* 13 (2014) 673–691.
- [2] J. Kollar, V. Frezer, Selective inhibitors of zinc-dependent histone deacetylases. Therapeutic targets relevant to cancer, *Curr. Pharmaceut. Des.* 21 (2015) 1472–1502.
- [3] E. Ceccacci, S. Minucci, Inhibition of histone deacetylases in cancer therapy: lessons from leukaemia, *Br. J. Cancer* 114 (2016) 605–611.
- [4] Y. Li, E. Seto, HDACs, H.D.A.C. Inhibitors, In cancer development and therapy, *Cold Spring Harb. Perspect. Med.* 6 (2016).
- [5] C. Damaskos, N. Garmpis, S. Valsami, M. Kontos, E. Spartalis, T. Kalampokas, E. Kalampokas, A. Athanasiou, D. Moris, A. Daskalopoulou, S. Davakis, G. Tsourouffis, K. Kontzoglou, D. Perrea, N. Nikiteas, D. Dimitroulis, Histone deacetylase inhibitors: an attractive therapeutic strategy against breast cancer, *Anticancer Res.* 37 (2017) 35–46.
- [6] R. Sangwan, R. Rajan, P.K. Mandal, HDAC as onco target: reviewing the synthetic approaches with SAR study of their inhibitors, *Eur. J. Med. Chem.* 158 (2018) 620–706.
- [7] A. Suraweera, K.J. O'Byrne, D.J. Richard, Combination therapy with histone deacetylase inhibitors (HDACi) for the treatment of cancer: achieving the full therapeutic potential of HDACi, *Front. Oncol.* 8 (2018) 92.
- [8] I. Oehme, H.E. Deubzer, D. Wegener, D. Pickert, J.P. Linke, B. Hero, A. Kopp-Schneider, F. Westermann, S.M. Ulrich, A. von Deimling, M. Fischer, O. Witt, Histone deacetylase 8 in neuroblastoma tumorigenesis, *Clin. Cancer Res.* 15 (2009) 91–99.
- [9] T.B. Toro, T.J. Watt, KDAC8 substrate specificity quantified by a biologically relevant, label-free deacetylation assay, *Protein Sci.* 24 (2015) 2020–2032.

- [10] M.A. Dearnorff, M. Bando, R. Nakato, E. Watrin, T. Itoh, M. Minamino, K. Saitoh, M. Komata, Y. Katou, D. Clark, others, HDAC8 mutations in Cornelia de Lange syndrome affect the cohesin acetylation cycle, *Nature* 489 (2012) 313–317.
- [11] B.J. Wilson, A.M. Tremblay, G. Deblois, G. Sylvain-Drolet, V. Giguère, An acetylation switch modulates the transcriptional activity of estrogen-related receptor  $\alpha$ , *Mol. Endocrinol.* 24 (2010) 1349–1358.
- [12] D.E. Olson, N.D. Udeshi, N.A. Wolfson, C.A. Pitcairn, E.D. Sullivan, J.D. Jaffe, T. Svinikina, T. Natoli, X. Lu, J. Paulk, P. McCarren, F.F. Wagner, D. Barker, E. Howe, F. Lazzaro, J.P. Gale, Y.L. Zhang, A. Subramanian, C.A. Fierke, S.A. Carr, E.B. Holson, An unbiased approach to identify endogenous substrates of "Histone" Deacetylase 8, *ACS Chem. Biol.* 9 (2014) 2210–2216.
- [13] J. Gao, B. Siddoway, Q. Huang, H. Xia, Inactivation of CREB mediated gene transcription by HDAC8 bound protein phosphatase, *Biochem. Biophys. Res. Commun.* 379 (2009) 1–5.
- [14] K.L. Durst, B. Lutterbach, T. Kummalau, A.D. Friedman, S.W. Hiebert, The inv (16) fusion protein associates with corepressors via a smooth muscle myosin heavy-chain domain, *Mol. Cell. Biol.* 23 (2003) 607–619.
- [15] Y. Qian, J. Zhang, Y.S. Jung, X. Chen, DEC1 coordinates with HDAC8 to differentially regulate TAp73 and DeltaNp73 expression, *PLoS One* 9 (2014) e84015.
- [16] C. Scholz, B.T. Weinert, S.A. Wagner, P. Beli, Y. Miyake, J. Qi, L.J. Jensen, W. Streicher, A.R. McCarthy, N.J. Westwood, S. Lain, J. Cox, P. Matthias, M. Mann, J.E. Bradner, C. Choudhary, Acetylation site specificities of lysine deacetylase inhibitors in human cells, *Nat. Biotechnol.* 33 (2015) 415–423.
- [17] S. Balasubramanian, J. Ramos, W. Luo, M. Sirisawad, E. Verner, J.J. Buggy, A novel histone deacetylase 8 (HDAC8)-specific inhibitor PCI-34051 induces apoptosis in T-cell lymphomas, *Leukemia* 22 (2008) 1026–1034.
- [18] G. Niegisch, J. Knievel, A. Koch, C. Hader, U. Fischer, P. Albers, W.A. Schulz, Changes in histone deacetylase (HDAC) expression patterns and activity of HDAC inhibitors in urothelial cancers, *Urol. Oncol.* 31 (2013) 1770–1779.
- [19] S.Y. Park, J.A. Jun, K.J. Jeong, H.J. Heo, J.S. Sohn, H.Y. Lee, C.G. Park, J. Kang, Histone deacetylases 1, 6 and 8 are critical for invasion in breast cancer, *Oncol. Rep.* 25 (2011) 1677–1681.
- [20] I. Rettig, E. Koeneke, F. Trippel, W.C. Mueller, J. Burhenne, A. Kopp-Schneider, J. Fabian, A. Schober, U. Fernekorn, A. von Deimling, H.E. Deubzer, T. Milde, O. Witt, I. Oehme, Selective inhibition of HDAC8 decreases neuroblastoma growth in vitro and in vivo and enhances retinoic acid-mediated differentiation, *Cell Death Dis.* 6 (2015) e1657.
- [21] A. Chakrabarti, J. Melesina, F.R. Kolbinger, I. Oehme, J. Senger, O. Witt, W. Sippl, M. Jung, Targeting histone deacetylase 8 as a therapeutic approach to cancer and neurodegenerative diseases, *Future Med. Chem.* 8 (2016) 1609–1634.
- [22] S. Shen, A.P. Kozikowski, Why hydroxamates may not be the best histone deacetylase inhibitors-what some may have forgotten or would rather forget? *ChemMedChem* 11 (2016) 15–21.
- [23] T. Suzuki, N. Miyata, Non-hydroxamate histone deacetylase inhibitors, *Curr. Med. Chem.* 12 (2005) 2867–2880.
- [24] S.A. Amin, N. Adhikari, T. Jha, Structure-activity relationships of HDAC8 inhibitors: non-hydroxamates as anticancer agents, *Pharmacol. Res.* 131 (2018) 128–142.
- [25] A. Kleinschek, C. Meyners, E. Digiorgio, C. Brancolini, F.J. Meyer-Almes, Potent, Selective Non-hydroxamate, Histone deacetylase 8 inhibitors, *ChemMedChem* 11 (2016) 2598–2606.
- [26] S. Okazaki, S. Oishi, T. Mizuhara, K. Shimura, H. Murayama, H. Ohno, M. Matsuoka, N. Fujii, Investigations of possible prodrug structures for 2-(2-mercaptophenyl) tetrahydropyrimidines: reductive conversion from anti-HIV agents with pyrimidobenzothiazine and isothiazolopyrimidine scaffolds, *Org. Biomol. Chem.* 13 (2015) 4706–4713.
- [27] M. Muth, N. Jansch, A. Kopranovic, A. Kramer, N. Wossner, M. Jung, F. Kirschhofer, G. Brenner-Weiss, F.J. Meyer-Almes, Covalent inhibition of histone deacetylase 8 by 3,4-dihydro-2H-pyrimido[1,2-c][1,3]benzothiazin-6-imine, *Biochimica et biophysica acta, Gen. Subj.* 1863 (2019) 577–585.
- [28] T. Mizuhara, S. Oishi, N. Fujii, H. Ohno, Efficient synthesis of pyrimido [1, 2-c] [1, 3] benzothiazin-6-imines and related tricyclic heterocycles by SNA $\alpha$ -type C- S, C- N, or C- O bond formation with heterocumulenes, *J. Org. Chem.* 75 (2009) 265–268.
- [29] D.P. Dowling, S.L. Gantt, S.G. Gattis, C.A. Fierke, D.W. Christianson, Structural studies of human histone deacetylase 8 and its site-specific variants complexed with substrate and inhibitors, *Biochemistry* 47 (2008) 13554–13563.
- [30] C. Decroos, D.J. Clausen, B.E. Haines, O. Wiest, R.M. Williams, D.W. Christianson, Variable active site loop conformations accommodate the binding of macrocyclic largazole analogues to HDAC8, *Biochemistry* 54 (2015) 2126–2135.
- [31] L. Whitehead, M.R. Dobler, B. Radetich, Y. Zhu, P.W. Atadja, T. Claiborne, J.E. Grob, A. McRiner, M.R. Pancost, A. Patnaik, W. Shao, M. Shultz, R. Tichkule, R.A. Tommasi, B. Vash, P. Wang, T. Stams, Human HDAC isoform selectivity achieved via exploitation of the acetate release channel with structurally unique small molecule inhibitors, *Bioorg. Med. Chem.* 19 (2011) 4626–4634.
- [32] S. Haider, C.G. Joseph, S. Neidle, C.A. Fierke, M.J. Fuchter, On the function of the internal cavity of histone deacetylase protein 8: R37 is a crucial residue for catalysis, *Bioorg. Med. Chem. Lett* 21 (2011) 2129–2132.
- [33] J. Shen, S. Najafi, S. Stable, J. Fabian, E. Koeneke, F.R. Kolbinger, J.K. Wrobel, B. Meder, M. Distel, T. Heimburg, W. Sippl, M. Jung, H. Peterziel, D. Kranz, M. Boutros, F. Westermann, O. Witt, I. Oehme, A kinome-wide RNAi screen identifies ALK as a target to sensitize neuroblastoma cells for HDAC8-inhibitor treatment, *Cell Death Differ.* (2018).
- [34] P. Ertl, B. Rohde, P. Selzer, Fast calculation of molecular polar surface area as a sum of fragment-based contributions and its application to the prediction of drug transport properties, *J. Med. Chem.* 43 (2000) 3714–3717.
- [35] A.L. Hopkins, C.R. Groom, A. Alex, Ligand efficiency: a useful metric for lead selection, *Drug Discov. Today* 9 (2004) 430–431.
- [36] M.D. Shultz, The thermodynamic basis for the use of lipophilic efficiency (LipE) in enthalpic optimizations, *Bioorg. Med. Chem. Lett.* 23 (2013) 5992–6000.
- [37] T. Nishiyama, R. Ladurner, J. Schmitz, E. Kreidl, A. Schleiffer, V. Bhaskara, M. Bando, K. Shirahige, A.A. Hyman, K. Mechtler, J.M. Peters, Sororin mediates sister chromatid cohesion by antagonizing Wapl, *Cell* 143 (2010) 737–749.



---

**Titel:**

Thiocarbonyl Surrogate via Combination of Potassium Sulfide and Chloroform for Dithiocarbamate Construction

**Autoren:**

Wie Tan, Niklas Jäsch, Tina Öhlmann, Franz-Josef Meyer-Almes, Xuefeng Jiang

**Bibliographische Daten:**

Organic Letters (doi.org/10.1021/acs.orglett.9b02784)

**Zusammenfassung:**

Eine effiziente und praktische Alternative für die Synthese von Thiocarbamaten wurde mittels Kombination von Kaliumsulfid und Chloroform entwickelt. In einer Ein-Topf-Reaktion, bei der das Thiocarbonyl-Motiv in situ erzeugt wurde, wurden eine Vielzahl von Dithiocarbamaten und vier neue chemische Bindungen hergestellt.

Darüber hinaus zeigten diese leicht zugänglichen Moleküle eine vielversprechende Aktivität gegen HDAC8, was ein potenzielles Tor zur Entdeckung einer neuen Art von nicht-Hydroxamat und isoenzymselektiven HDAC-Inhibitoren eröffnet.

# Thiocarbonyl Surrogate via Combination of Potassium Sulfide and Chloroform for Dithiocarbamate Construction

Wei Tan,<sup>†</sup> Niklas Jansch,<sup>‡</sup> Tina Öhlmann,<sup>‡</sup> Franz-Josef Meyer-Almes,<sup>\*,†,§</sup> and Xuefeng Jiang<sup>\*,†,§</sup>

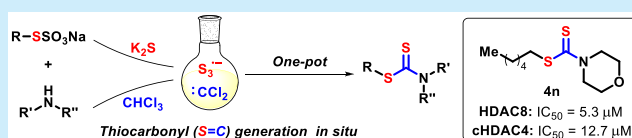
<sup>†</sup>Shanghai Key Laboratory of Green Chemistry and Chemical Process, School of Chemistry and Molecular Engineering, East China Normal University, 3663 North Zhongshan Road, Shanghai 200062, P.R. China

<sup>‡</sup>Department of Chemical Engineering and Biotechnology, University of Applied Sciences Darmstadt, Darmstadt 64295, Germany

<sup>§</sup>State Key Laboratory of Elemento-organic Chemistry, Nankai University, Tianjin 300071, P.R. China

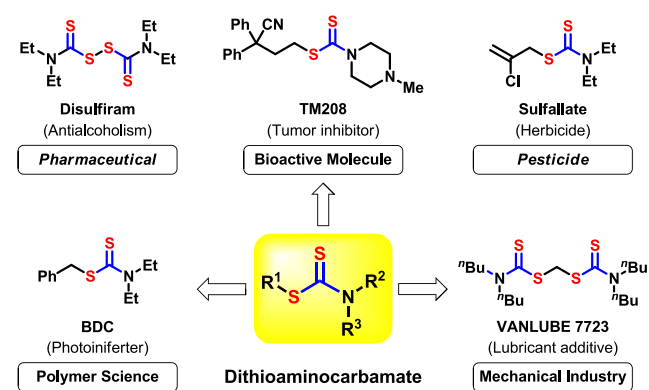
**S** Supporting Information

**ABSTRACT:** An efficient and practical thiocarbonyl surrogate via combination of potassium sulfide and chloroform was established. A variety of dithiocarbamates were afforded along with four new chemical bond formations in a one-pot reaction in which the thiocarbonyl motif was generated in situ. Furthermore, these readily accessed molecules showed promising activity against HDAC8, opening a potential gateway to discover a new type of nonhydroxamate and isoenzyme-selective HDAC inhibitors.



Dithiocarbamate is an important class of molecule with extensive value in pharmaceuticals, agrochemicals, and organic materials (Scheme 1).<sup>1–5</sup> Disulfiram with a dithio-

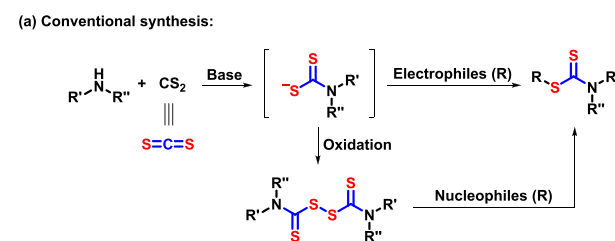
**Scheme 1. Representative Dithiocarbamates**



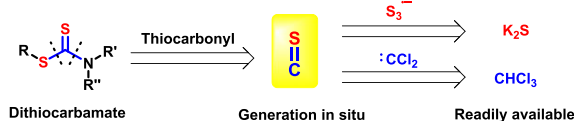
carbamate motif is a famous molecule previously applied for alcoholism treatment<sup>1a</sup> and recently as a drug candidate for its anticancer activity in preclinical models.<sup>1b</sup> Moreover, other dithiocarbamates are attracting more and more attention based on their variety of biological activities<sup>2</sup> such as antitumor,<sup>2a</sup> antibacterial,<sup>2b</sup> cholinesterase inhibition,<sup>2c</sup> etc. Sulfallate is a chlorinated dithiocarbamate derivative that is used as an herbicide.<sup>3</sup> Meanwhile, dithiocarbamate also serves a unique role in material science, such as a radical chain transfer agent BDC in reversible addition–fragmentation chain transfer (RAFT) polymerizations.<sup>4</sup> VANLUBE 7723 is a nonnegligible chemical widely applied as a lubricant additive in the mechanical industry.<sup>5</sup>

Accordingly, numerous procedures have been developed for the synthesis of dithiocarbamate. Most of these strategies revolved around the reactions of volatile and flammable carbon disulfide<sup>6</sup> with electrophiles through a dithiocarbamic acid salt intermediate<sup>7</sup> in which the electrophiles included alkyl halides,<sup>7a</sup> epoxides,<sup>7b</sup> alkynes,<sup>7c</sup> alkyl vinyl ethers,<sup>7d</sup> etc. (Scheme 2). Furthermore, there is an alternative procedure<sup>8</sup> involving the reaction of pre-prepared tetramethylthiuram

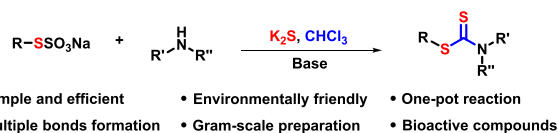
**Scheme 2. Strategies for Dithiocarbamate Construction**



(b) Our strategy:



(c) This work:



Received: August 6, 2019

Published: September 9, 2019

disulfide and organozinc<sup>8a</sup> or organolithium<sup>8b</sup> reagents as nucleophiles that are sensitive to air and moisture. However, the development of a practical and environmentally friendly process for dithiocarbamate construction is still highly desirable. Based on our continuous study on organosulfur chemistry<sup>9</sup> especially in thiocarbonyl chemistry,<sup>10</sup> we envisioned that dithiocarbamate can be assembled from a combination of sulfur, carbon, and amino sources in one pot along with the direct generation of a thiocarbonyl group in situ, avoiding the use thiocarbonyl reagents. Following our concept, potassium sulfide provides trisulfur radical anion ( $S_3^{\bullet-}$ )<sup>11</sup> as an inorganic sulfur source and chloroform<sup>12</sup> provides dichlorocarbene as one carbon source. Herein, we developed a straightforward method for preparation of dithiocarbamate with potassium sulfide and chloroform in the presence of readily available thiosulfate salts<sup>9c,13</sup> and organic amines, in which a library of valuable bioactive molecules was well established.

We commenced our studies with *S*-phenethyl thiosulfate sodium salt **1a** and morpholine **2a** as the model substrate in combination with potassium sulfide and chloroform. The desired product **3a** could be obtained in 56% yield by using lithium hydroxide as a base and *N*-methylpyrrolidone (NMP) as a solvent at 80 °C under nitrogen atmosphere (Table 1, entry 1). When the odorous phenylethyl mercaptan or *S*-phenethylethanethioate was employed in the corresponding conditions, the product **3a** was only formed in 38% or 13% yields, respectively (Table 1, entries 2 and 3). The results

**Table 1. Optimization for the Synthesis of Dithiocarbamate<sup>a</sup>**

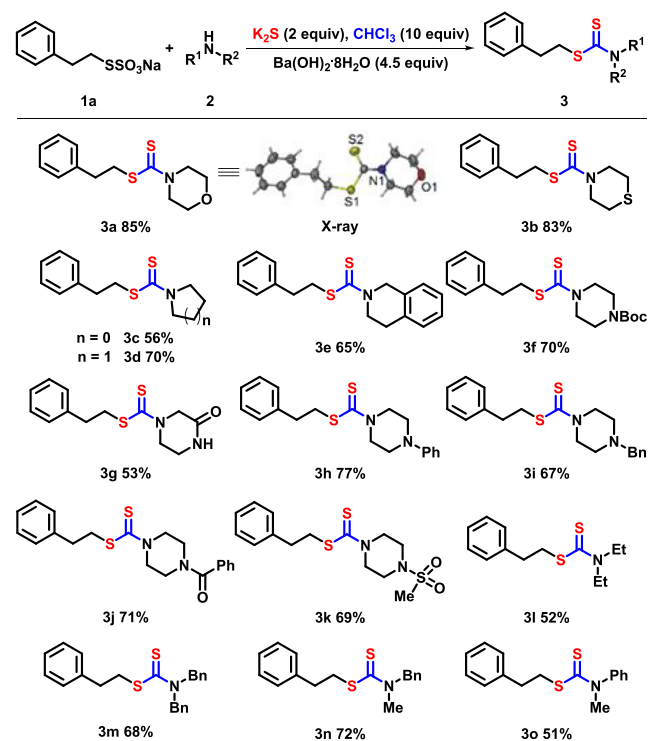
entry	"S"	base	solvent	yield <sup>b</sup> (%)
1	K <sub>2</sub> S	LiOH	NMP	56
2 <sup>c</sup>	K <sub>2</sub> S	LiOH	NMP	38
3 <sup>d</sup>	K <sub>2</sub> S	LiOH	NMP	13
4 <sup>e</sup>	K <sub>2</sub> S	LiOH	NMP	47
5	S <sub>8</sub>	LiOH	NMP	trace
6	Na <sub>2</sub> S <sub>2</sub> O <sub>3</sub>	LiOH	NMP	trace
7	KSAc	LiOH	NMP	47
8	K <sub>2</sub> S	LiOH	DMF	55
9	K <sub>2</sub> S	LiOH	MeCN	trace
10	K <sub>2</sub> S	LiOH	DMSO	19
11	K <sub>2</sub> S	LiOH	1,4-dioxane	nd
12	K <sub>2</sub> S	KOH	NMP	17
13	K <sub>2</sub> S	K <sub>3</sub> PO <sub>4</sub>	NMP	41
14	K <sub>2</sub> S	<sup>t</sup> BuOLi	NMP	53
15	K <sub>2</sub> S	<sup>t</sup> BuOK	NMP	33
16	K <sub>2</sub> S	Ba(OH) <sub>2</sub> ·8H <sub>2</sub> O	NMP	81
17 <sup>f</sup>	K <sub>2</sub> S	Ba(OH) <sub>2</sub> ·8H <sub>2</sub> O	NMP	81
18 <sup>g</sup>	K <sub>2</sub> S	Ba(OH) <sub>2</sub> ·8H <sub>2</sub> O	NMP	76
19 <sup>h</sup>	K <sub>2</sub> S	Ba(OH) <sub>2</sub> ·8H <sub>2</sub> O	NMP	85

<sup>a</sup>Reaction conditions: **1a** (0.2 mmol), **2a** (0.4 mmol), "S" (0.4 mmol), CHCl<sub>3</sub> (2 mmol), and base (1.2 mmol) in solvent (1 mL) was stirred at 80 °C for 12 h under nitrogen atmosphere. <sup>b</sup>Isolated yields. nd = not detected. <sup>c</sup>Phenylethyl mercaptan is instead of **1a**. <sup>d</sup>*S*-Phenethylethanethioate is instead of **1a**. <sup>e</sup>Air is instead of nitrogen atmosphere. <sup>f</sup>Ba(OH)<sub>2</sub>·8H<sub>2</sub>O (0.9 mmol). <sup>g</sup>Ba(OH)<sub>2</sub>·8H<sub>2</sub>O (0.6 mmol). <sup>h</sup>NMP (2 mL).

indicated that odorless *S*-phenethyl thiosulfate salt **1a** had a distinct advantage not only for the ecofriendly procedure but also for the chemical "mask" effect.<sup>9c</sup> When the reaction was carried out under air atmosphere, the yield decreased (Table 1, entry 4 vs entry 1). Meanwhile, other inorganic sulfur sources were examined, and only a trace amount of product could be observed by substituting elemental sulfur or sodium thiosulfate for potassium sulfide while potassium thioacetate afford product in 47% yield (Table 1, entries 5–7). Various polar solvents were explored, in which the target product **3a** could be afforded in 55% yield with *N,N*-dimethylformamide (DMF) (Table 1, entries 8–11). Subsequently, barium hydroxide octahydrate was employed as a base in the reaction, and the compound **3a** was isolated in 81% yield with a significant elevation compared to other base usage (Table 1, entries 12–16). Finally, the product **3a** was obtained in 85% yield with a slight improvement by adjusting the base amount and solvent concentration (Table 1, entries 17–19).

On the basis of the optimized conditions, the scope of amines was examined as shown in Scheme 3. First, various

**Scheme 3. Scope of Amines<sup>a</sup>**



<sup>a</sup>Reaction conditions: **1a** (0.2 mmol), **2** (0.4 mmol),  $K_2S$  (0.4 mmol),  $CHCl_3$  (2 mmol), and  $Ba(OH)_2 \cdot 8H_2O$  (0.9 mmol) in NMP (2 mL) was stirred at 80 °C for 8–12 h under nitrogen atmosphere. Isolated yields.

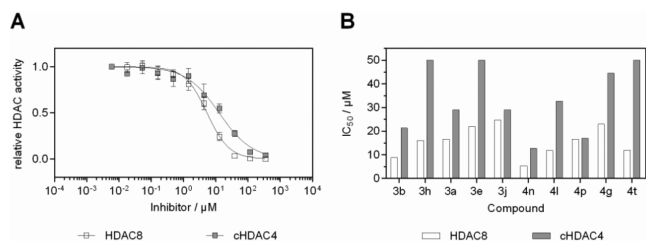
cyclic amines (**3a–3k**) were tested, and the corresponding products were formed in moderate to good yields, in which the hydrolyzable lactam (**3g**), amide (**3j**), and sulfone groups (**3k**) under alkaline conditions were tolerable in the reaction system. Meanwhile, the structure of product **3a** was further confirmed through X-ray crystallographic analysis. Noncyclic amines could also perform as amino sources (**3l–3o**). Diethylamine could give the related product **3l** in 52% yield, while dibenzylamine (**3m**) and *N*-methylbenzylamine (**3n**) afforded their respective products in good yields. Moreover, *N*-



to afford another imine cation **D** via intermediate **C**. Trisulfur radical anion ( $S_3^{\bullet-}$ ) could be formed from potassium sulfide in NMP solvent, which had been demonstrated by detection experiments in our previous work.<sup>10c</sup> Herein, trisulfur radical anion ( $S_3^{\bullet-}$ ) generating from  $K_2S$  in the solvent of NMP interacted with imine cation **D** to produce intermediate **E** along with the establishment of the C–S bond. Next, the  $\alpha$ -aminoalkyl radical **F** was obtained through an intramolecular hydrogen atom transfer (HAT) process of intermediate **E**.<sup>15</sup> Finally, homolysis of the S–S bond in the intermediate **F** provides the target product in the presence of base along with the generation of disulfur radical anion ( $S_2^{\bullet-}$ ).

The pyrimido[1,2-*c*][1,3]benzothiazin-6-imine PD-404,182 was recently shown to be a potent and selective inhibitor of the established cancer target human histone deacetylase 8 (HDAC8).<sup>16</sup> However, this compound class turned out to be unstable in the presence of thiol groups in aqueous solution, and the reaction of PD-404,182 leads to chemical modifications of HDAC8 cysteine residues such as cyanation and the formation of mixed disulfides.<sup>16b</sup> What attracted our attention is that the thiocarbonyl analogues of PD-404,182 still retain their activity against HDAC8.<sup>16a</sup> This inspired us to explore the biological activity of the noncyclic dithiocarbamate compounds of this study against human HDAC8 and the catalytic domain of human HDAC4 (cHDAC4). Most interestingly, some of these compounds exhibited promising bioactivity against HDAC8 with less activity against cHDAC4, in which **4n** showed impressive activity with an  $IC_{50}$  value in the low micromolar range (Scheme 8; see the SI for more

Scheme 8.  $IC_{50}$  Values on HDAC8 and cHDAC4<sup>a</sup>



<sup>a</sup>(A) Representative dose–response curves of **4n** on HDAC8 and cHDAC4. (B) Comparison of the selected compounds with an  $IC_{50} < 25 \mu M$  on HDAC8 with cHDAC4.

details). The results indicated potential for the development of novel nonhydroxamate- and isoenzyme-selective HDAC8 inhibitors with a dithiocarbamate core, which is different from the widely studied HDAC inhibitors with a hydroxamate warhead.

In summary, we have developed an efficient and practical thiocarbonyl surrogate via combination of potassium sulfide and chloroform, in which the thiocarbonyl motif was generated in situ under this novel synthesis strategy. A variety of dithiocarbamates were straightforwardly established along with four new chemical bond formations in a one-pot reaction in which each component was effectively embedded in the target structure. Meanwhile, a preliminary biological study indicated that the dithiocarbamates obtained from this reaction exhibit promising activity against HDAC8, which is a potential gateway to discover a new type of nonhydroxamate and isoenzyme-selective HDAC inhibitors.

## ■ ASSOCIATED CONTENT

### Supporting Information

The Supporting Information is available free of charge on the ACS Publications website at DOI: 10.1021/acs.orglett.9b02784.

Experimental procedures, NMR spectral, X-ray, and analytical data for all new compounds (PDF)

### Accession Codes

CCDC 1935361 contains the supplementary crystallographic data for this paper. These data can be obtained free of charge via [www.ccdc.cam.ac.uk/data\\_request/cif](http://www.ccdc.cam.ac.uk/data_request/cif), or by emailing [data\\_request@ccdc.cam.ac.uk](mailto:data_request@ccdc.cam.ac.uk), or by contacting The Cambridge Crystallographic Data Centre, 12 Union Road, Cambridge CB2 1EZ, UK; fax: +44 1223 336033.

## ■ AUTHOR INFORMATION

### Corresponding Authors

\*E-mail: [franz-josef.meyer-almes@h-da.de](mailto:franz-josef.meyer-almes@h-da.de).

\*E-mail: [xfjiang@chem.ecnu.edu.cn](mailto:xfjiang@chem.ecnu.edu.cn).

### ORCID

Franz-Josef Meyer-Almes: 0000-0002-1001-3249

Xuefeng Jiang: 0000-0002-1849-6572

### Notes

The authors declare no competing financial interest.

## ■ ACKNOWLEDGMENTS

We are grateful for financial support provided by the National Key Research and Development Program of China (2017YFD0200500), NSFC (21971065, 21722202, 21672069), the S&TCSM of Shanghai (Grant 18JC1415600), Professor of Special Appointment (Eastern Scholar) at Shanghai Institutions of Higher Learning, and the National Program for Support of Top-notch Young Professionals.

## ■ REFERENCES

- (1) (a) Iljin, K.; Ketola, K.; Vainio, P.; Halonen, P.; Kohonen, P.; Fey, V.; Grafström, R. C.; Perälä, M.; Kallioniemi, O. *Clin. Cancer Res.* **2009**, *15*, 6070. (b) Skrott, Z.; Mistrik, M.; Andersen, K. K.; Friis, S.; Majera, D.; Gursky, J.; Ozdian, T.; Bartkova, J.; Turi, Z.; Moudry, P.; Kraus, M.; Michalova, M.; Vaclavkova, J.; Dzubak, P.; Vrobel, I.; Pouckova, P.; Sedlacek, J.; Miklovicova, A.; Kutt, A.; Li, J.; Mattova, J.; Driessen, C.; Dou, Q. P.; Olsen, J.; Hajduch, M.; Cvek, B.; Deshaies, R. J.; Bartek, J. *Nature* **2017**, *552*, 194.
- (2) (a) Zhang, N.; Guo, W.; Wang, L.; Huang, W.; Xu, B.; Ge, Z.; Li, M.; Li, R. T.; Cui, J. R. *Anti-Cancer Drugs* **2008**, *19*, 593. (b) Bala, V.; Jangir, S.; Mandalapu, D.; Gupta, S.; Chhonker, Y. S.; Lal, N.; Kushwaha, B.; Chandasana, H.; Krishna, S.; Rawat, K.; Maikhuri, J. P.; Bhatta, R. S.; Siddiqi, M. I.; Tripathi, R.; Gupta, G.; Sharma, V. L. *Bioorg. Med. Chem. Lett.* **2015**, *25*, 881. (c) Altintop, M. D.; Gurkan-Alp, A. S.; Özkay, Y.; Kaplancikli, Z. A. *Arch. Pharm.* **2013**, *346*, 571.
- (3) Rosen, J. D.; Schuphan, I.; Segall, Y.; Casida, J. E. *J. Agric. Food Chem.* **1980**, *28*, 880.
- (4) (a) Otsu, T.; Matsunaga, T.; Kuriyama, A.; Yoshioka, M. *Eur. Polym. J.* **1989**, *25*, 643. (b) Mayadunne, R. T. A.; Rizzardo, E.; Chiefari, J.; Chong, Y. K.; Moad, G.; Thang, S. H. *Macromolecules* **1999**, *32*, 6977.
- (5) Nakazato, M.; Magarifuchi, J.; Mochizuki, A.; Tanabe, H. US 6531428 B2, 2003.
- (6) (a) Davidson, M.; Feinleib, M. *Am. Heart J.* **1972**, *83*, 100. (b) Gelbke, H.; Göen, T.; Mäurer, M.; Sulsky, S. I. *Crit. Rev. Toxicol.* **2009**, *39*, 1.

(7) (a) Azizi, N.; Aryanasab, F.; Saidi, M. R. *Org. Lett.* **2006**, *8*, 5275. (b) De Sousa, R.; Thurier, C.; Len, C.; Pouilloux, Y.; Barrault, J.; Jérôme, F. *Green Chem.* **2011**, *13*, 1129. (c) Ziyaei Halimehjani, A.; Breit, B. *Chem. Commun.* **2019**, *55*, 1253. (d) Halimehjani, A. Z.; Marjani, K.; Ashouri, A. *Green Chem.* **2010**, *12*, 1306. (e) Azizi, N.; Gholibeglo, E. *RSC Adv.* **2012**, *2*, 7413. (f) Saha, A.; Nasir Baig, R. B.; Leazer, J.; Varma, R. S. *Chem. Commun.* **2012**, *48*, 8889. (g) Sha, Q.; Wei, Y. *Org. Biomol. Chem.* **2013**, *11*, 5615.

(8) (a) Krasovskiy, A.; Gavryushin, A.; Knochel, P. *Synlett* **2006**, *5*, 792. (b) Gronowitz, S.; Hörnfeldt, A. B.; Temciuc, M. *Synthesis* **1993**, 483. (c) Zeng, M.; Xu, W.; Liu, X.; Chang, C.; Zhu, H.; Dong, Z. *Eur. J. Org. Chem.* **2017**, *2017*, 6060. (d) Dong, Z.; Liu, X.; Bolm, C. *Org. Lett.* **2017**, *19*, 5916. (e) Xu, W.; Gao, F.; Dong, Z. *Eur. J. Org. Chem.* **2018**, *2018*, 821.

(9) Reviews: (a) Liu, H.; Jiang, X. *Chem. - Asian J.* **2013**, *8*, 2546. (b) Feng, M.; Tang, B.; Liang, S.; Jiang, X. *Curr. Top. Med. Chem.* **2016**, *16*, 1200. (c) Qiao, Z.; Jiang, X. *Org. Biomol. Chem.* **2017**, *15*, 1942. (d) Wang, M.; Jiang, X. *Top. Curr. Chem.* **2018**, *376*, 14. (e) Wang, N.; Saidhareddy, P.; Jiang, X. *Nat. Prod. Rep.* **2019**, DOI: [10.1039/C8NP00093J](https://doi.org/10.1039/C8NP00093J). For representative examples, see: (f) Qiao, Z.; Liu, H.; Xiao, X.; Fu, Y.; Wei, J.; Li, Y.; Jiang, X. *Org. Lett.* **2013**, *15*, 2594. (g) Qiao, Z.; Wei, J.; Jiang, X. *Org. Lett.* **2014**, *16*, 1212. (h) Qiao, Z.; Ge, N.; Jiang, X. *Chem. Commun.* **2015**, *51*, 10295. (i) Xiao, X.; Feng, M.; Jiang, X. *Angew. Chem., Int. Ed.* **2016**, *55*, 14121. (j) Wang, M.; Wei, J.; Fan, Q.; Jiang, X. *Chem. Commun.* **2017**, *53*, 2918. (k) Li, Y.; Wang, M.; Jiang, X. *ACS Catal.* **2017**, *7*, 7587. (l) Xiao, X.; Xue, J.; Jiang, X. *Nat. Commun.* **2018**, *9*, 2191. (m) Wang, M.; Fan, Q.; Jiang, X. *Green Chem.* **2018**, *20*, 5469. (n) Wang, M.; Qiao, Z.; Zhao, J.; Jiang, X. *Org. Lett.* **2018**, *20*, 6193. (o) Wang, M.; Zhao, J.; Jiang, X. *ChemSusChem* **2019**, *12*, 3064. (p) Wang, M.; Dai, Z.; Jiang, X. *Nat. Commun.* **2019**, *10*, 2661. (q) Li, Y.; Rizvi, S. A.; Hu, D.; Sun, D.; Gao, A.; Zhou, Y.; Li, J.; Jiang, X. *Angew. Chem., Int. Ed.* **2019**, DOI: [10.1002/anie.201906080](https://doi.org/10.1002/anie.201906080).

(10) (a) Wei, J.; Li, Y.; Jiang, X. *Org. Lett.* **2016**, *18*, 340. (b) Tan, W.; Wei, J.; Jiang, X. *Org. Lett.* **2017**, *19*, 2166. (c) Tan, W.; Wang, C.; Jiang, X. *Org. Chem. Front.* **2018**, *5*, 2390.

(11) Reviews: (a) Chivers, T.; Elder, P. J. W. *Chem. Soc. Rev.* **2013**, *42*, 5996. (b) Steudel, R.; Chivers, T. *Chem. Soc. Rev.* **2019**, *48*, 3279. For selected examples, see: (c) Zhang, G.; Yi, H.; Chen, H.; Bian, C.; Liu, C.; Lei, A. *Org. Lett.* **2014**, *16*, 6156. (d) Gu, Z. Y.; Cao, J. J.; Wang, S. Y.; Ji, S. J. *Chem. Sci.* **2016**, *7*, 4067. (e) Li, J. H.; Huang, Q.; Wang, S. Y.; Ji, S. J. *Org. Lett.* **2018**, *20*, 4704.

(12) (a) Fedoryński, M. *Chem. Rev.* **2003**, *103*, 1099. (b) Gockel, S. N.; Hull, K. L. *Org. Lett.* **2015**, *17*, 3236. (c) Zhao, H.; Du, H.; Yuan, X.; Wang, T.; Han, W. *Green Chem.* **2016**, *18*, 5782.

(13) For selected examples, see: (a) Reeves, J. T.; Camara, K.; Han, Z. S.; Xu, Y.; Lee, H.; Busacca, C. A.; Senanayake, C. H. *Org. Lett.* **2014**, *16*, 1196. (b) Liu, F.; Jiang, L.; Qiu, H.; Yi, W. *Org. Lett.* **2018**, *20*, 6270.

(14) Halimehjani, A. Z.; Pourshojaei, Y.; Saidi, M. R. *Tetrahedron Lett.* **2009**, *50*, 32.

(15) (a) Roberts, B. P. *Chem. Soc. Rev.* **1999**, *28*, 25. (b) Qvortrup, K.; Rankic, D. A.; MacMillan, D. W. C. *J. Am. Chem. Soc.* **2014**, *136*, 626.

(16) (a) Kleinschek, A.; Meyners, C.; Digiorio, E.; Brancolini, C.; Meyer-Almes, F. *ChemMedChem* **2016**, *11*, 2598. (b) Muth, M.; Jänsch, N.; Kopranovic, A.; Krämer, A.; Wössner, N.; Jung, M.; Kirschhöfer, F.; Brenner-Weiß, G.; Meyer-Almes, F. *Biochim. Biophys. Acta, Gen. Subj.* **2019**, *1863*, 577.

---

### 5.3 Umnutzung von Thiazolidindionen als HDAC8 Inhibitoren

Thiazolidindione, auch Glitazone genannt, sind schon seit mehreren Jahrzehnten in der Forschung, vor allem als Wirkstoffe gegen Diabetes. Jedoch zeigten sich einige dramatische Nebenwirkungen, welche dazu führten, dass diese Wirkstoffe für die weitere Entwicklung nicht mehr in Betracht gezogen wurden. Im Rahmen der praktischen Arbeiten dieser Dissertation wurde festgestellt, dass sich eine Reihe von Substanzen dieser Wirkstoffklasse als potenzielle HDAC8 Inhibitoren eignen. Viele der bekannten Nebenwirkungen der Thiazolidindione stellen Probleme bei der Langzeitbehandlung von Patienten dar. Das mögliche Einsatzfeld der Krebstherapie wirft solche Fragen nur bedingt auf, da es sich meistens um Therapien im höheren Alter handelt und Langzeiteffekte eine untergeordnete Rolle spielen. Die Umnutzung bereits untersuchter Wirkstoffe hat den Vorteil, dass schon eine breite Studienlage vorliegt, was in einer schnelleren Entwicklung und Verfügbarkeit am Patienten resultieren kann. In einer internationalen Kooperation wurde eine Fülle an bereits synthetisierten Thiazolidindionen auf HDAC8 getestet und potente strukturelle Untergruppen identifiziert. Die folgenden beiden Publikationen befassen sich mit der Untersuchung des genauen Wirkmechanismus, der Wirkung auf Zellkulturen und dem molekularen Docking zur annähernden Identifizierung des Bindungsmodus.

Zusammengefasst könnten sich Thiazolidindione als neue Strukturen für die Weiterentwicklung von HDAC8 spezifischen Wirkstoffen als Alternative zu den gängigen Hydroxamsäuren eignen, jedoch bedarf es dazu noch weitergehender Studien.

---

**Titel:**

Discovery of 5-naphthylidene-2,4-thiazolidinedione derivatives as selective HDAC8 inhibitors and evaluation of their cytotoxic effects in leukemic cell lines

**Autoren:**

Kalpana Tilekar, Neha Upadhyay, Niklas Jäsch, Markus Schweipert, Piotr Mrowka, Franz-Josef Meyer-Almes, C.S. Ramaa

**Bibliographische Daten:**

Bioorganic Chemistry (doi.org/10.1016/j.bioorg.2019.103522)

**Zusammenfassung:**

Histondeacetylasen (HDACs) werden als therapeutisches Ziel für Interventionen bei verschiedenen Krebsarten erforscht. HDAC8 ist eine HDAC der Klasse I, die als therapeutisches Ziel in verschiedenen Indikationsbereichen, einschließlich verschiedener Krebsarten und insbesondere des kindlichen Neuroblastoms, in Betracht gezogen wird. Die meisten bisher beschriebenen HDAC8-selektiven Inhibitoren enthalten eine Hydroxamatfunktion als Zinkbindungsgruppe (ZBG), um ihre Wirksamkeit zu erhöhen. Die HDAC-Inhibitoren der Hydroxamatklasse haben jedoch zunehmend Bedenken hinsichtlich ihres mutagenen Charakters aufgeworfen. Daher könnten sich Inhibitoren, die nicht auf Hydroxamaten basieren, als sicherer erweisen als Hydroxamate. In der vorliegenden Arbeit wurde eine Reihe neuartiger 5-Naphthyliden-2,4-Thiazolidindione entwickelt und als potenzielle antiproliferative Wirkstoffe bewertet, die selektiv das Enzym HDAC8 hemmen. Elf neue Derivate wurden synthetisiert, gereinigt und durch spektroskopische Techniken charakterisiert. Die Verbindungen 3k und 3h erwiesen sich als die stärksten selektiven Inhibitoren von HDAC8 mit IC<sub>50</sub>-Werten von 2,7  $\mu$ M bzw. 6,3  $\mu$ M. 3a bis 3i erwiesen sich in leukämischen Zelllinien als am zytotoxischsten. Sowohl 3a als auch 3h induzierten Apoptose und bewirkten einen Stillstand des Zellzyklus in der G2/M-Phase.





# Discovery of 5-naphthylidene-2,4-thiazolidinedione derivatives as selective HDAC8 inhibitors and evaluation of their cytotoxic effects in leukemic cell lines

Kalpana Tilekar<sup>a</sup>, Neha Upadhyay<sup>a</sup>, Niklas Jänsch<sup>c</sup>, Markus Schweipert<sup>c</sup>, Piotr Mrowka<sup>b</sup>, F.J. Meyer-Almes<sup>c,\*</sup>, C.S. Ramaa<sup>a,\*</sup>

<sup>a</sup> Department of Pharmaceutical Chemistry, Bharati Vidyapeeth's College of Pharmacy, Navi Mumbai, Maharashtra, India

<sup>b</sup> Department of Biophysics and Human Physiology, Medical University of Warsaw, Chalubinskiego, Warsaw, Poland

<sup>c</sup> Department of Chemical Engineering and Biotechnology, University of Applied Sciences, Darmstadt, Germany

## ARTICLE INFO

### Keywords:

HDAC8  
Antiproliferative  
Thiazolidinedione (TZD)  
Naphthalene  
Leukemia  
Cytotoxicity

## ABSTRACT

Histone deacetylases (HDACs) are being explored as a therapeutic target for interventions in different types of cancer. HDAC8 is a class I HDAC that is implicated as a therapeutic target in various indication areas, including different types of cancer and particularly childhood neuroblastoma. Most previously described HDAC8-selective inhibitors contain a hydroxamate function as zinc binding group (ZBG) to confer potency. However, hydroxamate class HDAC inhibitors have raised increasing concerns about their mutagenic character. Therefore, non-hydroxamate based inhibitors could prove to be safer than hydroxamates. In the present work, a series of novel 5-naphthylidene-2,4-thiazolidinedione was designed and evaluated as potential antiproliferative agents targeting selectively HDAC8 enzyme. Eleven novel derivatives were synthesized, purified and characterized by spectroscopic techniques. Compounds **3k** and **3h** was found to be most potent selective inhibitors of HDAC8 with IC<sub>50</sub> values of 2.7 μM and 6.3 μM respectively. **3a** to **3i** was found to be most cytotoxic in leukemic cell lines. **3a** and **3h** both were found to induce apoptosis and cause cell cycle arrest in G2/M phase.

## 1. Introduction

Epigenetic abnormalities are hallmarks of carcinogenesis and cancer progression [1]. Histone deacetylases (HDACs) are major regulators for chromatin remodeling and epigenetics via deacetylation of acetylated lysine residues of histone and non-histone proteins. Therefore, HDACs have been considered to be relevant targets for therapeutic intervention in different types of cancer. Meanwhile, HDACs have become established targets, predominantly for cutaneous T-cell lymphoma and multiple myeloma [2,3]. At this time five HDAC inhibitors have been approved world wide (vorinostat, romidepsin, panobinostat, belinostat, and chidamide), which are more or less nonselective.

HDACs belong to the major enzyme family of lysine deacetylases, which are divided into 4 classes: Classes I, II, subdivided into IIa and IIb, and IV contain a catalytic zinc ion within the active site and are referred to as HDACs in the narrower sense. Class III deacetylases are

named sirtuins and their activity depends on NAD<sup>+</sup>. In human cells 11 HDACs and 7 sirtuins are expressed.

Class I member HDAC8 has been considered as promising target for childhood neuroblastoma, T-cell lymphoma [4,5] and connected to several other types of cancer [6,7]. The structure activity relationship analysis of HDAC8 inhibitors containing the widely used hydroxamate group as ZBG revealed a fish-like structural arrangement for HDAC inhibitors with hydrophobic aromatic cap function as head to recognize surface regions and a tail comprising the ZBG [8]. Cap group and ZBG are connected by a mostly hydrophobic linker. The characteristic malleability of the binding pocket of HDAC8 enabled the development of isoenzyme selective hydroxamate inhibitors containing hydroxamate group as zinc binding group (ZBG) such as PCI-34051 [5].

In order to analyze the molecular determinants for selective inhibition of HDAC8 diverse classes of HDAC8 inhibitors with different ZBGs were analyzed by using structure activity relationships and

*Abbreviations:* TZD, thiazolidinedione; HDAC, histone deacetylase; DMF, dimethyl Formamide; DCM, dichloromethane; NMR, nuclear magnetic resonance spectroscopy; IR, infrared spectroscopy; DMEM, Dulbecco's Modified Eagle Medium; MTT, 3-(4,5-dimethylthiazol-2-yl)-2,5-diphenyltetrazolium bromide; FBS, fetal calf serum; RT, room temperature

\* Corresponding authors.

E-mail addresses: [franz-josef.meyer-almes@h-da.de](mailto:franz-josef.meyer-almes@h-da.de) (F.J. Meyer-Almes), [sinharamaa@yahoo.in](mailto:sinharamaa@yahoo.in) (C.S. Ramaa).

<https://doi.org/10.1016/j.bioorg.2019.103522>

Received 2 October 2019; Received in revised form 14 December 2019; Accepted 17 December 2019

Available online 18 December 2019

0045-2068/ © 2019 Elsevier Inc. All rights reserved.

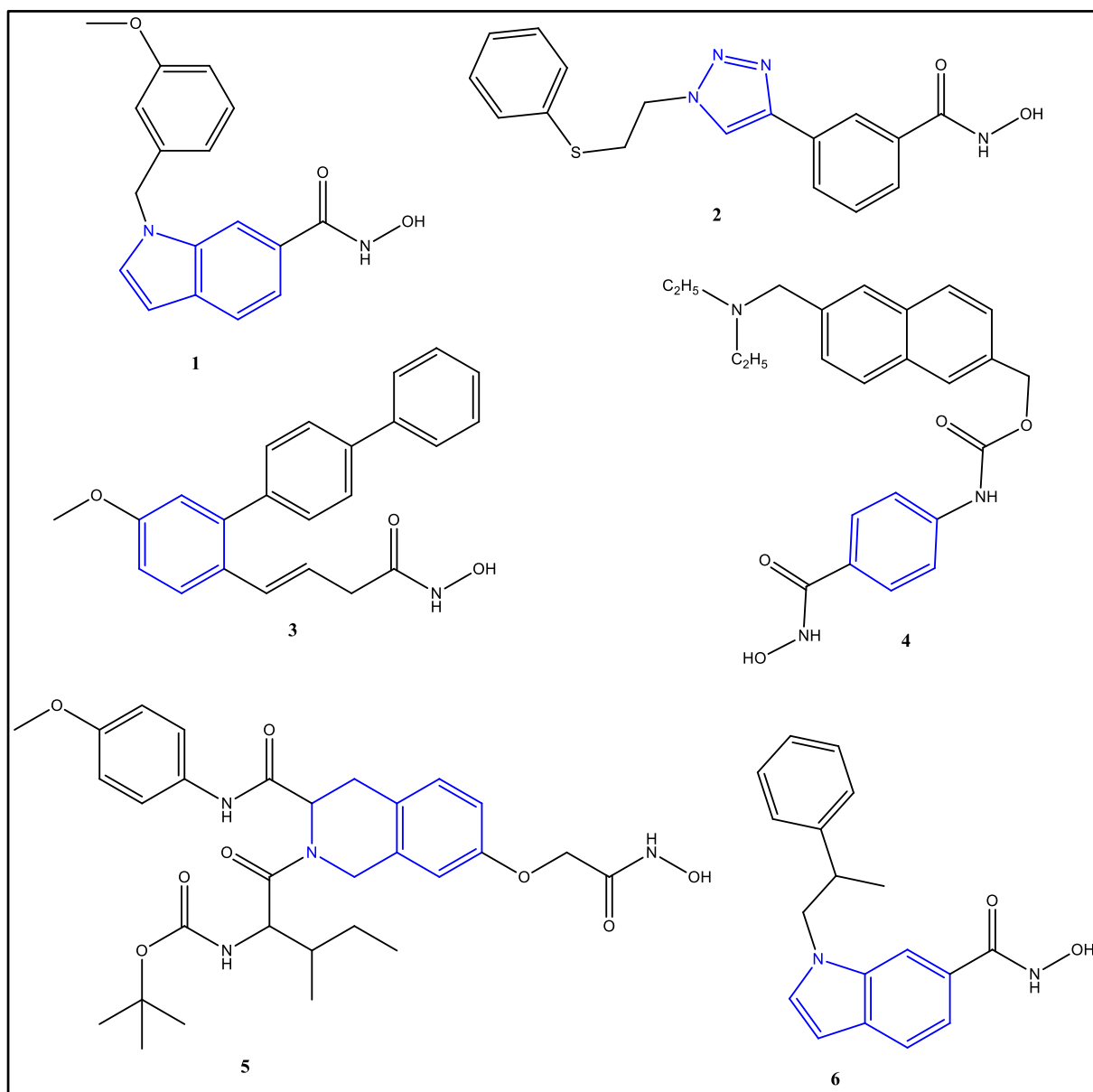


Fig. 1. Reported HDAC8 inhibitors with hydroxamic acid as ZBG.

Bayesian classification approaches [9]. Benzamides show selectivity for class I HDACs 1, 2 and 3 but are dramatically less active on HDAC8 that is also a member of class I, whereas electrophilic ketones have been developed which inhibit preferably class IIa HDACs and HDAC8 demonstrating that the binding pocket of HDAC8 shares features of class II as well as class I HDACs. These analyses revealed that hydroxamates or carboxylates would be the most beneficial ZBGs. Moreover, so called linkerless compounds with bulky head groups also show selectivity for HDAC8. Many analogs with cyclic linkers attached to hydroxamate group found to exhibit HDAC8 selectivity (Fig. 1).

However, hydroxamate groups are inherently unselective and could potentially interfere with other enzymes containing divalent cations or metal homeostasis. Moreover, some suspicion about the potentially mutagenic character of compounds with hydroxamate groups has been raised, which is particularly critical for long term treatments [10]. Therefore, HDAC inhibitors without hydroxamate as ZBG promise to be more beneficial in terms of selectivity and toxicity. A wide number of non-hydroxamate structures with carboxylates, electrophilic ketones,

benzamides, and cyclic peptides as zinc binding groups (ZBGs) have been reported earlier and shown to inhibit the activity of different subtypes of HDACs [11–14]. But only a few non-hydroxamate compounds have been described as isozyme selective inhibitor of HDAC8, such as amino acid derivatives that demonstrate isoform selectivity via access to the internal acetate release channel of the enzyme [15], azetidione ( $\beta$  lactams) with *N*-thiomethyl group [16], metabolites of organoselenium compounds such as methylselenocysteine (MSC) and selenomethionine (SM) [17], a dihydro-imidazole-thiones [18] or most recently pyrimido[1,3]benzothiazin-derivatives [19,20].

In the light of the drawbacks of the hydroxamate ZBG regarding potential mutagenicity, poor pharmacokinetics and bioavailability, a broad variety of alternative ZBGs were explored and the structure-activity relationship of corresponding classes of inhibitors analyzed [9]. However without any doubts, there is still urgent need for new pharmacophores that do not contain hydroxamate groups and can be developed to selective and potent HDAC8 inhibitors.

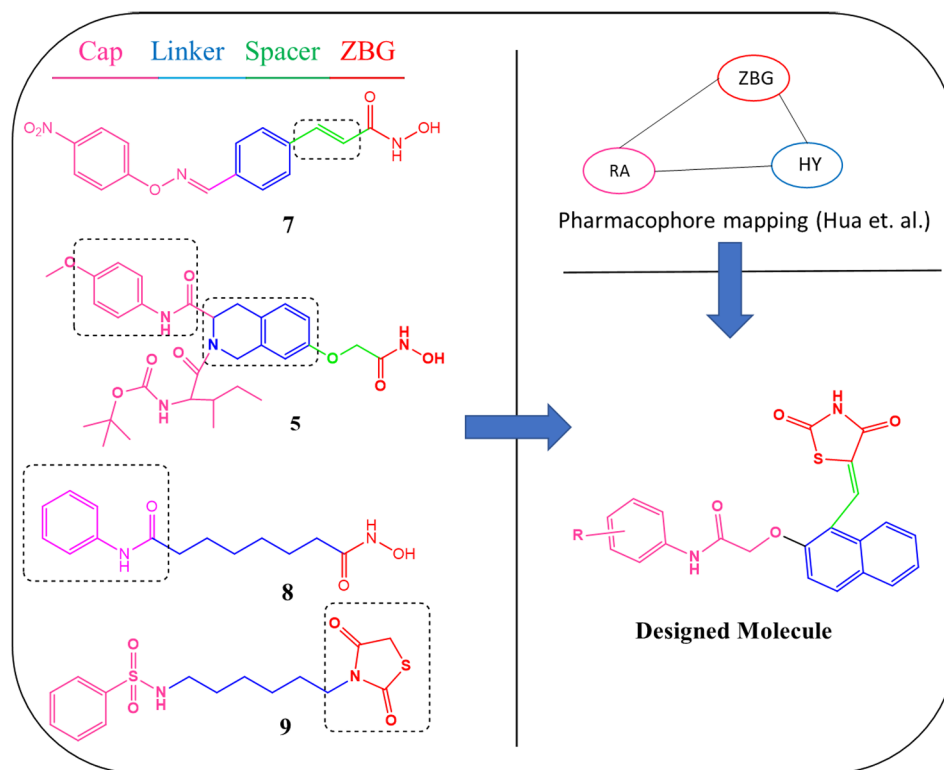


Fig. 2. Designing considerations of novel series targeting HDAC8.

## 2. Results and discussion

### 2.1. Designing of the molecules

We designed our novel series of naphthylidene TZDs based on proposed structural backbone of HDAC8 inhibitors (Fig. 2), with the following considerations:

**LINKER**-Attempts towards the discovery of hydroxamic acid derivatives with HDAC8 selectivity, that fit into the unique sub-pocket of HDAC8, have been found to contain cyclic linkers such as indole-1,6 [21,22], benzo-triazole- 2 [23–25], benzyl-3,4 [26], tetrahydro-isoquinoline-5 [27–29] (Fig. 1). It has been proven that naphthalene hydroxamate analogs, 6 possess higher HDAC-8 selectivity over HDAC1 and HDAC6 [30,31] (Fig. 1), which gave us impetus to develop HDAC inhibitors with cyclic linker, naphthalene.

**SPACER**- We introduced  $-\text{CH}=\text{CH}-$  as a spacer between linker and ZBG, as it was hypothesized that selective inhibition of HDAC8 may be implicated by a beneficial balance between the chemical structure and conformational flexibility of those inhibitors. Compound 7 (Fig. 2) and similar molecules with  $-\text{CH}=\text{CH}-$ , unsaturated spacer have been reported to show promising HDAC8 inhibitory activities and some of them are currently under clinical investigations [32]. Moreover, naphthalene hydroxamate analogs with unsaturated linker spacer showed higher HDAC-8 selectivity over HDAC-1 and -6 [30].

**CAP**- Our molecules contain phenyl acetamide in cap portion, as in SAHA and  $\alpha$ -cetomide. HDAC8 inhibitors with phenyl acetamide group in cap, have also been reported, however selectivity has not been related to this particular functionality [16].

**ZBG**- In search of non-hydroxamate HDAC inhibitors, we have earlier reported 2,4-thiazolidinedione [33] as ZBG, compound 9, (Fig. 2), which we have retained in this series of compounds.

Further structural analyses revealed that HDAC8-selective inhibitors show an L-shaped structure, to enable interactions with residues of an HDAC8-specific side pocket [34]. Hou et al. [35] virtually screened some HDAC8 inhibitors and validated ZBG-based pharmacophore

models (Fig. 2). Finally, we arranged all the fractions with the naphthalene linker being ortho substituted with the purpose of deriving an L-shaped structure, conforming to Hou's pharmacophoric model (Fig. 2).

### 2.2. Chemistry

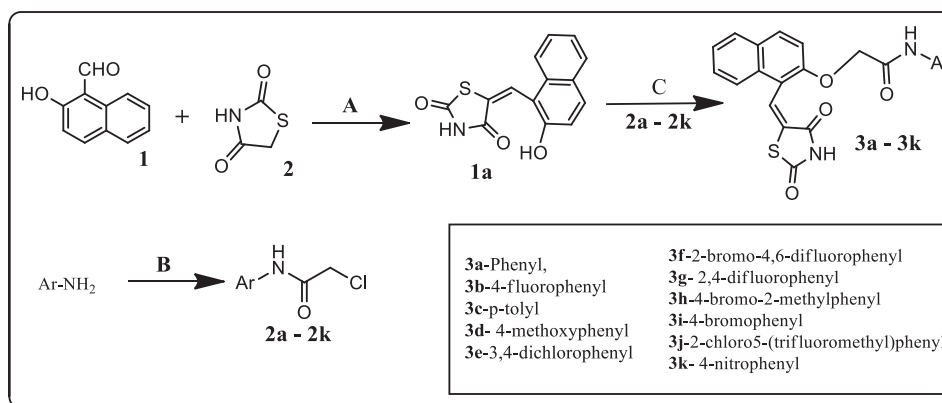
The synthetic route of the compounds is outlined in Scheme 1. A new class of 5-Naphthylidene-2,4-thiazolidinedione derivatives, 3a-3k (Scheme 1), were synthesized from the condensation of synthetic intermediates 1a with 2a-2k. 1a was synthesized from 1 and 2 (Scheme 1) by Knoevenagel condensation as described previously [36], with slight modifications, in which the product formed was removed intermediately. The product was obtained in good yield of 85% and was yellow crystalline needles. The  $^1\text{H}$  NMR spectra of 1a displayed 3 singlets at 12.59, 10.21 and 8.04 ppm representing the protons of  $-\text{NH}$  (broad singlet),  $-\text{OH}$  and benzylidene double bond ( $\text{Ph}-\text{CH}=\text{C}$ ) respectively, confirming the formation of 1a. Discussion about the chemistry 2a-2k has been described in our previously published work [36,37].

In the IR spectra of 3a-3k the band for  $\text{CO}-\text{NH}-\text{CO}$  and  $\text{C}=\text{O}$  were seen in the region  $3400-3300\text{ cm}^{-1}$  and  $1700-1650\text{ cm}^{-1}$  respectively. In the  $^1\text{H}$  NMR spectra, presence of singlet between 4.1 and 4.5 ppm, provides evidence for formation of  $-\text{CH}_2-\text{O}-$  linkage in final compounds, 3a-3k. The singlet at 7.9–8.1 ppm is characteristic of benzylidene proton which confirms that the molecules are in Z-configuration, as described by Momose et al. [38]. Additional spectral characteristics were confirmed by  $^{13}\text{C}$  NMR and Mass spectroscopy and are presented in experimental section.

### 2.3. In vitro HDAC screening

#### 2.3.1. HDAC enzyme inhibition assay

To assess selectivity, the synthesized derivatives were screened against a panel of human HDAC isoenzymes using procedures described in method section. Interestingly 6 out of 11 compounds displayed



**Scheme 1.** Reagents and conditions. A: Toluene, Piperidinium acetate- Reflux 2–3 h. B: Chloroacetyl Chloride, DCM,  $K_2CO_3$ , stirring at RT. overnight, C: DMF,  $K_2CO_3$ - stirring at RT. overnight.

**Table 1**

SAR table of naphthylidene-2,4-TZD derivatives for selectivity between HDAC1, HDAC4, HDAC6 and HDAC8.

$IC_{50}$ / $\mu M$												
#	$R_1$	$R_2$	$R_3$	$R_4$	$R_5$	HDAC1	HDAC2	HDAC3	HDAC4	HDAC5	HDAC6	HDAC8
3a	H	H	H	H	H	> 50	> 50	> 50	> 50	> 50	> 50	44
3b	H	H	F	H	H	> 50	> 50	> 50	> 50	> 50	> 50	> 50
3c	H	H	CH <sub>3</sub>	H	H	> 50	> 50	> 50	> 50	> 50	> 50	> 50
3d	H	H	OCH <sub>3</sub>	H	H	> 50	> 50	> 50	> 50	> 50	> 50	> 50
3e	H	Cl	Cl	H	H	> 50	> 50	> 50	> 50	> 50	> 50	> 50
3f	Br	H	F	H	F	> 50	> 50	> 50	> 50	> 50	> 50	12
3g	F	H	F	H	H	> 50	> 50	> 50	> 50	> 50	> 50	> 50
3h	CH <sub>3</sub>	H	Br	H	H	> 50	> 50	> 50	> 50	> 50	> 50	6.3
3i	H	H	Br	H	H	> 50	> 50	> 50	> 50	> 50	> 50	8.8
3j	H	H	H	CF <sub>3</sub>	H	> 50	> 50	> 50	> 50	> 50	> 50	12
3k	H	H	NO <sub>2</sub>	H	H	23	35	> 50	15	> 50	44	2.7
PCI-34051						3.0*	45*	38*	10*	> 50*	18*	0.024*

\* Kleinschek, A., et al. (2016). "Potent and Selective Non-hydroxamate Histone Deacetylase 8 Inhibitors." *ChemMedChem* 11(23): 2598–2606.

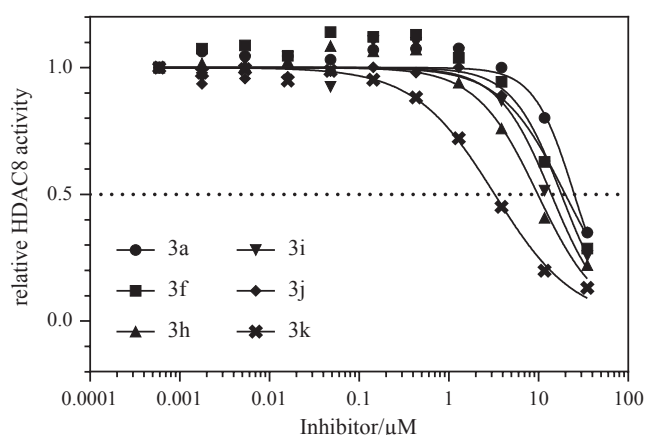


**Fig. 3.** Dose response curves of indicated compounds against HDAC8. The relative enzyme activity is plotted versus increasing compound concentrations.

potent inhibition of HDAC8 compared to the other HDAC isoenzymes (Table 1, Fig. 3). The derivatives that exhibited maximum selectivity with  $IC_{50}$  values less than 15  $\mu M$  were, 4-nitro(3k), 4-bromo (3i), 3-

trifluoromethyl (3j), 2-fluoro-4-bromo (3h) and 2-bromo-6-methyl (3f). 3k exhibited most potent HDAC8 inhibition with  $IC_{50}$  value of 2.7  $\mu M$  with 6- to 16-fold selectivity for HDAC8 over HDAC1, HDAC4 and HDAC6 and even higher selectivity over HDAC3 and HDAC5. This data is not enough to discuss the structure activity relationships, but some primary conclusions can be made. The presence of halogen Br (3i, 3h) and nitro group (3k) at para position may lead to enhanced HDAC8 inhibition. Amongst halogens only F containing compounds (3b, 3g) were found to be ineffective against all four subtypes of HDACs, but if it is present along with Br on the same ring (3f), it leads to HDAC8 inhibition. Electron withdrawing groups such as  $NO_2$  was found to have HDAC inhibitory potential as compared to electron donating groups (3c, 3d). Amongst brominated derivatives, 3h and 3i potency was found to be slightly enhanced if methyl group is present along with Bromine.

### 2.3.2. Thermal shift assay

Several promising lead compounds have failed in advanced clinical trials [39–41] and subsequently it has been shown that they do not act in predicted or in vitro observed way [42]. Hence target engagement (TE) i.e. extend to which the drug binds to its target protein of enzyme in situ, should be studied from the drug development and primary

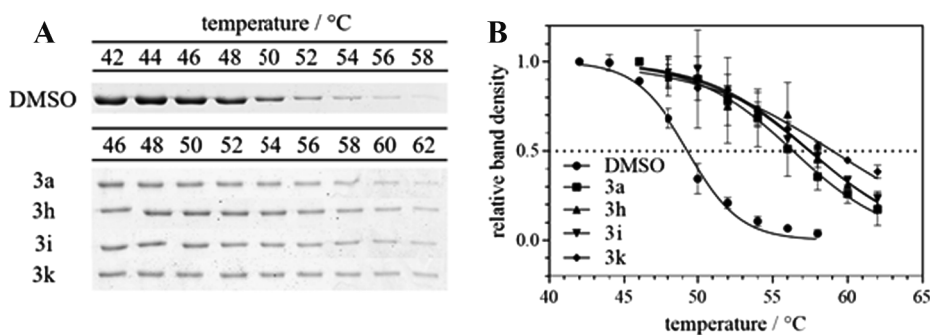


Fig. 4. Thermal stabilization of 2.5  $\mu$ M HDAC8 upon binding of 100  $\mu$ M of 3a (square), 3h (up-triangle), 3i (down-triangle) and 3k (diamond). Dots denote the control of HDAC8 in the absence of compounds but with matching DMSO concentration. The data points represent means and standard deviations of 3 independent experiments. Compound binding to HDAC8 leads to strong stabilization of the protein-ligand complex with thermal shifts of 7  $^{\circ}$ C and more.

preclinical stage. Thermal shift assay (TSA) is the means by which TE can be established in vitro using isolated enzyme to ascertain enzyme-ligand stability with increasing temperature or in cells and tissues to confirm binding. TSA provide characteristic sigmoidal melting curves for a protein. It has been observed that, when ligand binds to protein, melting temperature ( $T_m$ ) of protein shift to a higher temperature producing thermal shift ( $\Delta T_m$ ), and lead to stabilization of the protein (Fig. 4).

To assess the target engagement of synthesised derivatives, we undertook TSA for derivatives 3a, 3h, 3i and 3k by incubating with recombinant HDAC8 for 1 h and then exposed to different temperatures ranging from 46  $^{\circ}$ C to 62  $^{\circ}$ C. We observed the characteristic sigmoidal curve. Thus, binding of compounds to HDAC8 leads to strong stabilization of the protein-ligand complex with thermal shifts ( $\Delta T_m$ ) of 7  $^{\circ}$ C and more. We did in vitro thermal shift experiments and did not analyze the cell lysates of living cells that were treated with the compounds. However, at stage we can say that the enzyme-ligand complexes are highly stable and, are more likely to bind a desired target, HDAC8 when in whole cells or tissue, making them suitable agents for preclinical developments.

## 2.4. In vitro anticancer screening

### 2.4.1. MTT assay and cell viability

The effects of newly synthesized TZD derivatives 3a-3k, on the viability of normal Human WBCs and cancerous K562 and CEM cells, were assessed by the MTT assay, which has been described as one of the most reliable indicators of metabolic activity of cells and widely used to ascertain cell viability [43,44]. It relies on the ability of dehydrogenase enzymes to reduce MTT dye to its water insoluble purple coloured formazan salt in the mitochondria of cells. formazan crystals can be finally solubilized and quantified using a spectrophotometer. Since reduction of MTT can only occur in metabolically active cells the level of activity is a measure of the viability of the cells. In this study, Paclitaxel was used as references.

We determined the  $IC_{50}$  values corresponding to the concentrations of drug attaining 50% inhibition of cell viability. Paclitaxel was used as standard reference compound whereas untreated cells were used as negative control and the results are presented in Table 2. Compounds 3a, 3b, 3c, 3d and 3e were found to exhibit anti-proliferative effects at sub-micromolar concentrations on K562 cell line. CEM cell lines are less sensitive, though the observed activity of the compounds is lesser as compared to K562.  $IC_{50}$  values for CEM cells are around 30  $\mu$ M and compound 3a and 3h have exhibited  $IC_{50}$  values less or equal to that of standard drug Paclitaxel. This difference in activity on K562, which is chronic myeloid leukemia cell line and CEM, which is lymphoblastic leukemia cell line, may be due to subtypes of leukemia.

After considering the results of HDAC inhibition and MTT assay, Compounds 3a and 3h was chosen for further evaluation as both exhibited excellent HDAC8 inhibiting activity, 3a exerted high cytotoxicity in both leukemic cell lines with being most cytotoxic compound against K562 cells and compound 3h most cytotoxic compound against

Table 2

$IC_{50}$  values for compounds 3a-3k on K562 and CEM cell line viability.

Compound	$IC_{50}^a$ in $\mu$ M	
	K562	CEM
3a	0.42	13.94
3b	0.46	29.40
3c	0.73	38.60
3d	0.52	32.79
3e	0.81	nd <sup>b</sup>
3f	0.97	29.29
3g	0.96	nd <sup>b</sup>
3h	2.05	15.71
3i	1.94	21.22
3j	1.62	nd <sup>b</sup>
3k	nd <sup>b</sup>	nd <sup>b</sup>
Std. Paclitaxel	0.29	15.5

<sup>a</sup> Data shown is the means of 3 independent experiments.

<sup>b</sup> Not determined.

CEM cells.

### 2.4.2. Apoptosis by flowcytometry

HDAC8 inhibitors have induced necrosis and apoptosis via various mechanisms in different types of solid and hematological cancer cells. PCI-34051, a HDAC8 inhibitor have been found to induce apoptosis in T-cell lymphoma cells by caspase activation [5]. HDAC8 inhibition in gastric carcinoma cells, have reported to induce apoptosis mediated by Bcl-2-modifying factor (BMF) and STAT3 [45]. A selective HDAC8 inhibitor induces Dose-dependent selective apoptosis of CD34 + leukemic stem cells and progenitor cells [7]. The up-regulation of histone deacetylase 8 promotes proliferation and inhibits apoptosis in hepatocellular carcinoma [46].

To examine whether the cytotoxicity induced by 3a and 3h was associated with apoptosis, we used annexin V-FITC/ propidium iodide (PI) double staining of K562 and CEM cells treated with indicated compounds and determined rate of apoptosis by flow cytometry. K562 cells are very sensitive to the chosen compounds and treatment of the cells with 3a and 3h at  $IC_{50}$  concentration was leading to rapid cell death. In that circumstances getting accurate results were difficult, thus we choose CEM cell line for apoptosis experiments in order to obtain reproducible results. CEM cells exposed to 3a and 3h at their  $IC_{50}$  concentrations caused increase of apoptotic cells apoptotic (Fig. 5). For 3a the percentage of apoptotic cells in late and early apoptosis was 41.88% and 2.80% respectively. In case of 3h similar results were observed: 42.78% of cells were in the late apoptosis and 1.63% in early phase of apoptosis. was 1.63%. This result indicates that compound 3a and 3h both have the ability to induce apoptotic death in CEM cell line. As apoptosis is a type of cellular death that seems to be safer to patients because of non-inflammatory character and HDAC inhibitors considered for anticancer use all induce apoptosis we conclude studied compounds can proceed to further testing as potential anti-leukemic drug candidate [47] However, further molecular level studies are

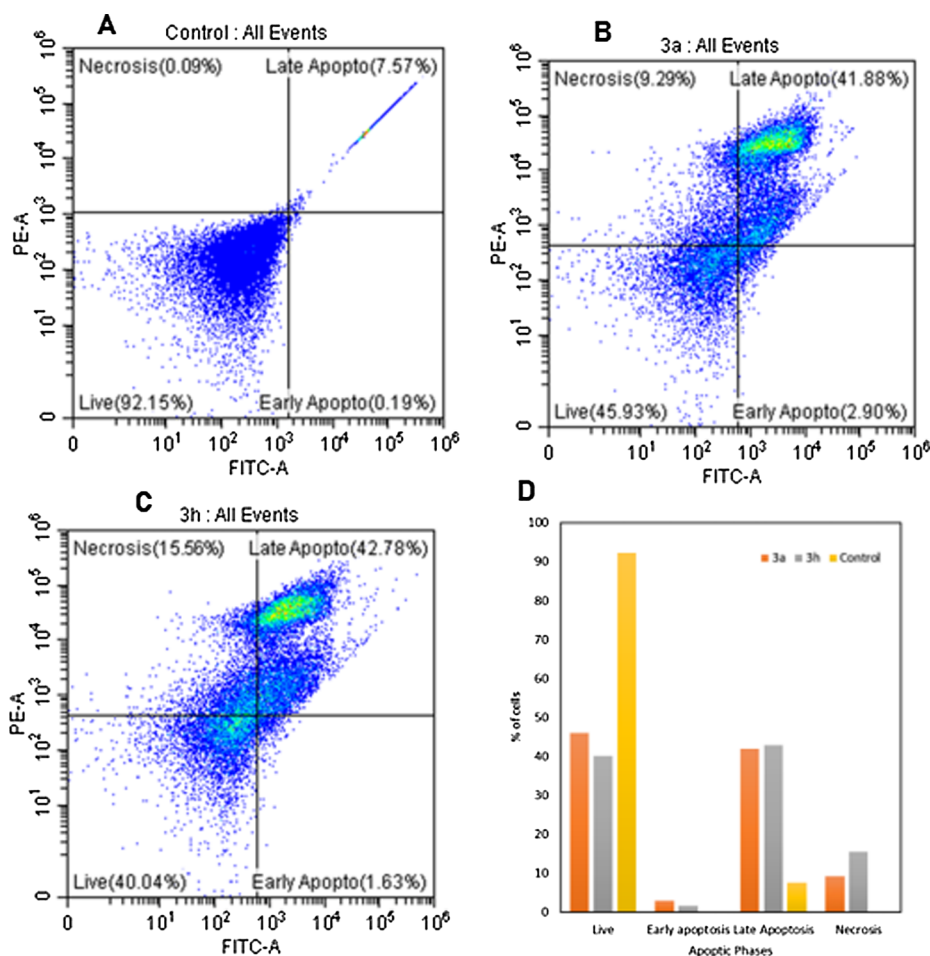


**Fig. 5.** Annexin V-FITC/PI flow cytometry analysis. CEM cells were treated with 3a and 3h at  $IC_{50}$  concentration. After 24 h cells were stained with annexin V-FITC/PI to distinguish live cells from apoptotic and necrotic cells. Cells considered alive are both Propidium Iodide (PI) & AnnexinV negative, cells in early apoptotic stage are Annexin V positive and PI negative and cells in late apoptotic phase are both PI & Annexin V positive. Dead/necrotic cells are PI positive & Annexin V negative. (A) Cytograms of untreated control CEM cells. (B) Cytograms of 3a treated CEM cells. (C) Cytograms of 3h treated CEM cells. (D) Graphical representation of apoptotic events of untreated, 3a and 3h treated CEM cells.

indicted to unearth the exact mechanism of induction of apoptosis by these compounds.

#### 2.4.3. Cell cycle analysis

Most of pan HDAC inhibitors produce G0/G1 cell cycle arrest and apoptosis through the increased accumulation of acetylated histones, resulting in decreased availability of nuclear DNA to bind to transcription factors and thus decreased transcription that leads to decreases intracellular protein levels the trigger for cell cycle arrest. However, G2/M have been also shown as an outcome of HDAC inhibition. PAC-320, a polyoxometalates compound, is a broad-spectrum HDAC inhibitor have shown potent prostate cancer inhibitory activity mediated by G2/M cell cycle arrest and apoptosis [48]. Not much literature is available about exact behavior of HDAC8 inhibitors in various phases of cell growth and arrest, knockdown of HDAC8 in gastric cancer cells, have been reported to promote G0/G1 arrest and apoptosis[45], whereas knockdown of HDAC8 in lung cancer cell line, A549, Found to promote growth arrest in mitotic G2-M phase[49]. Thus, cell growth arrest has been observed in HDAC8 knockdown cells as well as HDAC8 inhibitor treated cells, but in different phases of growth.

We investigated the effects of 3a and 3h on cell cycle using flow cytometric analysis, to find out if it's antiproliferative effects can be attributed to arrest of cells in particular phase (Fig. 6). Treatment of CEM cells with 3a and 3h at their  $IC_{50}$  concentrations, resulted in marked increase in the number of cells in G2/M phase and a concomitant decrease in the number of cells in G0/G1 phase as compared to control. For 3a, the percentage of cells in G2-M phase was found to increase from 3.58% to 35.4%, while the percentage of cells in G0-G1 phase was found to decrease from 73.4% to 37.3% and the percentage of cells in S phase found to be change very slightly as compared to

control. For 3h the percentage of cells in G2-M phase was found to increase from 3.58% to 27.0%, while the percentage of cells in G0-G1 phase was found to decrease from 73.4% to 50.0% and the percentage of cells in S phase found to be remain almost similar as compared to control. Thus, our results may suggest that the reductions in cell growth may be due to direct or indirect interference of 3a and 3h with DNA replication resulting block at G2/M cell cycle check point.

#### 2.4.4. Assessment of cell viability on non-transformed cells

In leukemia treatment we are looking for medicines that will be lethal to cancer cells and at the same time relatively safe for patient and his normal cells. Since 3a was most cytotoxic in both K562 and CEM cells, we compared cytotoxicity of the compound against leukemic cells and normal WBCs. The cells were exposed to 2.5, 10, 25, 75 and 100  $\mu$ M concentrations of 3a and 3h for 48h. to normal WBCs and  $IC_{50}$  values, were established. For 3a the  $IC_{50}$  value was found to be 67.24  $\mu$ M, which is 5 times that of  $IC_{50}$  for CEM cells ( $IC_{50} = 13.39 \mu$ M) and for 3 h it was 152.2  $\mu$ M, which is 15 times that of  $IC_{50}$  for CEM lines, (Fig. 7), which indicates that 3a and 3h could be safer to normal cells.

#### 2.5. In-silico studies

##### 2.5.1. Docking of 3k into HDAC8 (PDB-ID: 3SFF)

HDAC8 is known as an enzyme with extraordinary malleable binding site suitable to accommodate inhibitors with widely different structures [50,51]. To study the putative molecular determinants of TZD binding to HDAC8, we performed docking studies using three solved crystal structures of HDAC8 (PDB-ID's 1T69, 1VKG and 3SFF), which represent different major conformers of this enzyme [52]. PDB-ID 1T69 shows a complex between HDAC8 and SAHA with one narrow

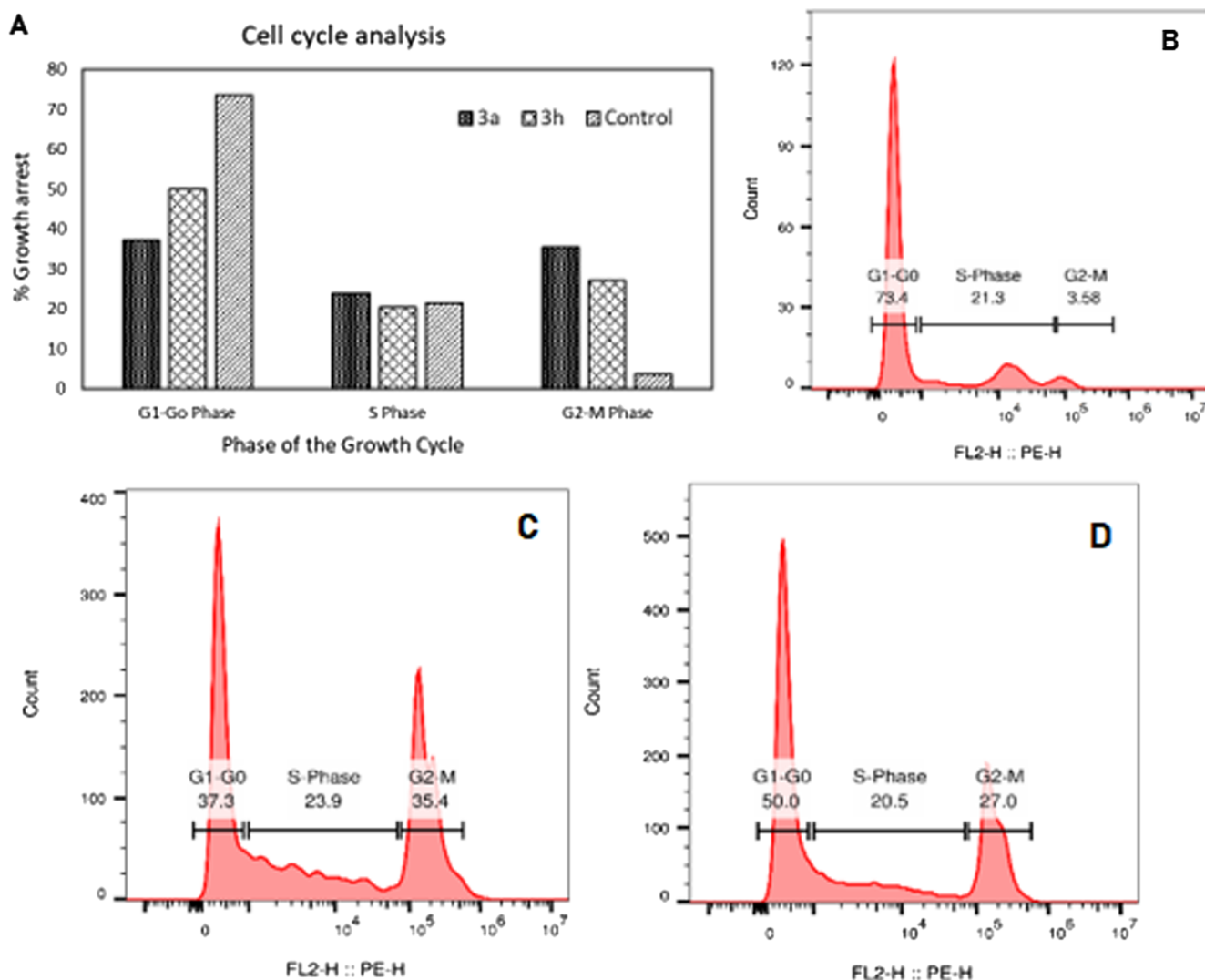


Fig. 6. Effect of 3a and 3 h on cell cycle. Cells were treated with compounds for 24 h, stained with PI, and analysed by flow cytometry. (A) Graphical representation of CEM cells population of in G0/G1, S and G2/M phases of the cell cycle shown as % of all cells. (B) Representative histogram of untreated control cells (C) Representative histogram of 3a treated cells. (D) Representative histogram of 3 h showing treated cells.

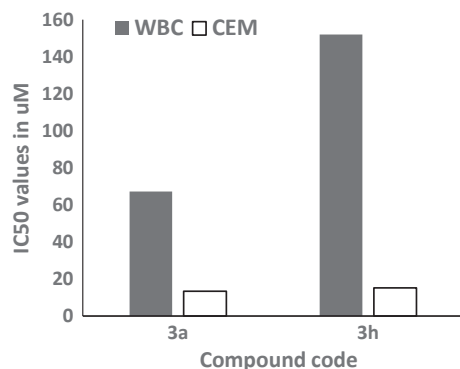


Fig. 7. 3a and 3h inhibits cell proliferation in the human Leukemic cell line, CEM, significantly more than it does in normal WBCs after 48 h treatment.

binding channel, 1VKG shows the wide-open conformation of HDAC8 and 3SFF shows a HDAC8 conformation with an open cavity connecting the conventional catalytic site with the entry of the acetate release channel. The far best docking score was obtained with PDB-ID 3SFF (Table 3). Surprisingly, not the thiazolidinedione group, but the oxygen of the carboxamide group chelates the zinc cation at the bottom of the

Table 3

Docking scores for 3k within different crystal structures and conformations of HDAC8 using MOE software and AMBER 14 forcefield.

PDB-ID	Score
3SFF	-9.5
1T69	-7.3
1VKG	-7.4

catalytic binding pocket. In addition, an oxygen of the nitro group forms a hydrogen bond to a nitrogen of R37 (Fig. 8). The naphthalene moiety of the TZDs appears to be rather movable and to enable pi-pi-interactions with neighbouring F208 and F152 residues lining the binding pocket.

The general binding pose of 3k was confirmed by very similar docking results with analogs, where the para-nitro group was omitted (3a) or exchanged against methyl (3c), methoxy (3d) or bromine (3i). The TZDs without nitro-group are no longer able to form a hydrogen bond with R37 resulting in rather weak docking scores (Table 4). In contrast, the most potent compound 3k shows the best docking score based on the hypothesized hydrogen bond between the nitro group and

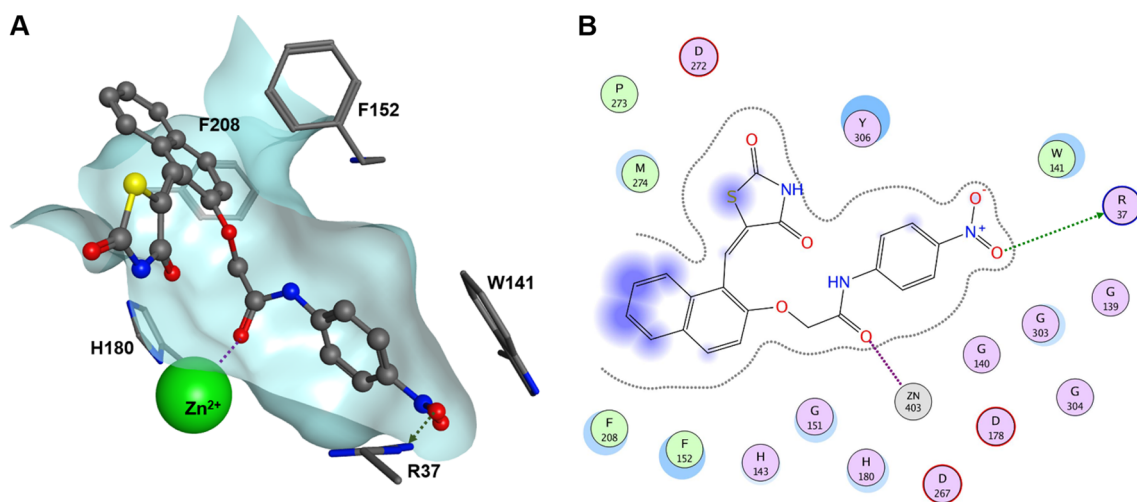


**Fig. 8.** Best docking pose of **3k** within the binding pocket of HDAC8 (PDB-ID: 3SFF). (A) 3D view of binding pocket. (B) 2D ligand interactions. Magenta dotted lines indicate metal ion contacts and green arrows hydrogen bonds. The violet or light blue shades denote ligand or receptor exposure, respectively.

R37. Thus, the docking scores are consistent with the experimental activity of the compounds in terms of  $IC_{50}$ -values providing further evidence for the correctness of the putative binding pose of the TZDs within HDAC8.

### 2.5.2. SwissADME predictions

Calculation of ADME profile is essential part of drug development, but determination of ADME parameters by laboratory experimentations for large number of compounds would be difficult and very time-consuming task. In these circumstances, simulated computer-models provides realistic replacements to experiments [53]. The SwissADME web tool is freely available which gives access to the fast and robust models for appropriate prediction of physicochemical properties, pharmacokinetic behaviour and drug-likeness. We used SwissADME tool to predict properties of our synthetic derivatives. All the compounds were observed to follow the Lipinski's rule of five (Table 5) with 2 violations of molecular weight. All molecules demonstrated  $\log P$  in the acceptable range of 2.00 to 5.00. Topological polar surface area (TPSA), the surface sum over all polar atoms, primarily oxygen and nitrogen, also including their attached hydrogen atoms, has been shown to be a very good descriptor characterizing drug absorption, including intestinal absorption, bioavailability. Literature implies that  $TPSA < 140$  is essential for good absorption. The naphthylidene derivatives exemplified TPSA in the range 109–135 Å<sup>2</sup>. The solubility class predicted indicates that compounds are moderately or poorly soluble, which could be problematic in formulation stage and can be overcome by solubility enhancement techniques such as salt formation. Judging the data, the molecules seem to be drug like and may have good passive oral absorption.

## 3. Materials and methods

### 3.1. Chemistry

Commercial reagents were from either S D Fine, Research Lab or Sigma Aldrich and were procured from suppliers in India. Thin layer

chromatography was performed on Merck pre-coated Silica Gel 60 F254. Melting points were determined by open capillary method on a VEEGO melting point apparatus and are uncorrected. Infrared spectra were recorded on Shimadzu FT/IR-8400S by direct sampling technique. <sup>1</sup>H and <sup>13</sup>C NMR spectra were recorded at 400 MHz on a Bruker instrument using TMS as internal standard and chemical shifts ( $\delta$ ) are reported in ppm. Mass spectra were recorded using LC-MS Agilent Technologies 1260 Infinity instrument.

#### 3.1.1. Procedure for synthesis of 5-((2-hydroxynaphthalen-1-yl)methylene)thiazolidine-2,4-dione (**1a**)

Compound **1a** was synthesized as per the procedure that we have reported earlier [36]. In short 0.01 mol of 2-hydroxy naphthaldehyde **1** and 0.01 mol of 2,4-thiazolidinedione **2** with catalytic quantity of piperidinium benzoate was refluxed in toluene for 4–5 h. The reaction mixture was cooled to room temperature and solid separated was collected by filtration, washed with cold toluene, dried and recrystallised from hydroalcoholic mixture.

Yellow crystals; yield 79.5%; m.p, 253 °C; <sup>1</sup>H NMR (400 MHz, DMSO-d<sub>6</sub>) -  $\delta$  12.59 (s, 1H),  $\delta$  10.21 (s, 1H),  $\delta$  8.04 (s, 1H),  $\delta$  7.89 (m, 2H),  $\delta$  7.79 (d,  $J = 8.82$  Hz, 1H),  $\delta$  7.57–7.55 (m, 1H), 7.17–7.19 (m, 2H); IR (neat) 3115.14, 1674.27, 1508, 1340 and 1211 cm<sup>-1</sup>; anal. calc. for C<sub>14</sub>H<sub>9</sub>NO<sub>3</sub>S, C, 61.98; H, 3.34; N, 5.16; O, 17.69; S, 11.82.

#### 3.1.2. General procedure for synthesis of **2a–2k**

We have previously reported preparation, purification and characterization of **2a–2k** in our research papers [36,37]. Briefly, Chloroacetyl chloride (0.1 mol) was added drop wise to a mixture of appropriate amines (0.05 mol) and anhydrous potassium carbonate (K<sub>2</sub>CO<sub>3</sub>) (0.075 mol) in dichloromethane or chloroform in an ice-cold condition. The reaction mixture was then stirred at room temperature. After completion of reaction, solvent was evaporated under reduced pressure, ice cold water was added to the obtained dry mass and the insoluble product was filtered and dried and purified by recrystallization with appropriate solvents.

**Table 4**

Docking scores and  $IC_{50}$ -values for different **3k** analogs using MOE software and AMBER 14 forcefield.

Cpd.	p-substituent	$IC_{50}$ (HDAC8) / $\mu$ M	Score	Cpd.	p-substituent	$IC_{50}$ (HDAC8) / $\mu$ M	Score
3k	-NO <sub>2</sub>	2.7	-9.5	3a	-H	44	-8.5
3h	-Br + CH <sub>3</sub> in ortho	6.3	-8.6	3c	-CH <sub>3</sub>	> 50	-8.8
3i	-Br	8.8	-8.6	3d	-OCH <sub>3</sub>	> 50	-7.9



**Table 5**  
SwissADME prediction data.

Code	TPSA <sup>a</sup>	Log P <sup>b</sup>	Log S <sup>c</sup>	ESOL <sup>d</sup> Class	GI <sup>e</sup> absorption	Lipinski #violations	Bioavailability Score
3a	109.8	2.21	-5.08	Moderately soluble	High	0	0.55
3b	109.8	2.59	-5.24	Moderately soluble	High	0	0.55
3c	109.8	2.42	-5.38	Moderately soluble	High	0	0.55
3d	119.03	1.89	-5.16	Moderately soluble	High	0	0.55
3e	109.8	3.17	-6.28	Poorly soluble	High	0	0.55
3f	109.8	3.54	-6.32	Poorly soluble	Low	1	0.55
3g	109.8	2.96	-5.4	Moderately soluble	High	0	0.55
3h	109.8	3.01	-6.3	Poorly soluble	High	0	0.55
3i	109.8	2.8	-5.99	Moderately soluble	High	0	0.55
3j	109.8	3.48	-6.54	Poorly soluble	Low	1	0.55
3k	135.62	2.14	-5.15	Moderately soluble	Low	0	0.55

<sup>a</sup> Topological polar surface area.

<sup>b</sup> Log of partition coefficient (P).

<sup>c</sup> Log solubility.

<sup>d</sup> estimated aqueous solubility in mg/mL.

<sup>e</sup> Gastrointestinal.

### 3.1.3. General procedure for synthesis of 3a-3k by condensation of 1a with 2a-2k.

The final compounds 3a-3k were synthesized by stirring compound 0.1 mol of (1a) with 0.1 mol of (2a-2k) for 24 h, in presence of K<sub>2</sub>CO<sub>3</sub> in dimethyl formamide (DMF). The reaction was monitored by TLC. On completion of the reaction, the reaction mixture was poured on crushed ice. The precipitated crude product was filtered, washed with water and purified by column chromatography using ethyl acetate and hexane in appropriate ratio.

**3.1.3.1. 2-((1-((2,4-dioxothiazolidin-5-ylidene) methyl) naphthalen-2-yl)oxy)-N-phenylacetamide (3a).** Yellow powder; yield 35.8%; m.p, 234 °C(charred); <sup>1</sup>H NMR (400 MHz, DMSO-d<sub>6</sub>): δ 10.51 (s,1H), δ 8.68 (s,1H), δ 8.48-8.46 (d, J = 8.0 Hz, 1H), δ 8.04-8.06 (d, J = 8.0 Hz, 1H), 7.98-8.00 (d, J = 8.0 Hz, 1H), δ 7.71-7.73 (m, 1H), δ 7.65-7.67 (m, 2H), δ 7.57-7.61 (m, 1H), δ 7.49-7.51 (d, J = 8.0 Hz, 1H), δ 7.32-7.36 (t, J = 8.0 Hz, 2H), δ 7.06-7.10 (t, J = 8.0 Hz, 1H), δ 4.15 (s, 2H); <sup>13</sup>C NMR (400 MHz, DMSO-d<sub>6</sub>): δ 158.24, 150.38, 113.23, 138.67, 116.28, 129.95, 131.33, 123.66, 127.67, 122.08, 131.59, 166.38, 40.06, 128.83, 122.08, 128.66, 127.93, 126.03, 119.18; IR (neat) 3340.82, 1693.56, 1672.34, 1494.88, 1325.14 and 1213.72 cm<sup>-1</sup>; Theoretical mass: 404.08, LC-MS (m/z, I %): 403.1 [(M-H)<sup>+</sup>, 100]; anal. calc. for C<sub>14</sub>H<sub>9</sub>NO<sub>3</sub>S: C, 65.33; H, 3.99; N, 6.93; O, 15.82; S, 7.93.

**3.1.3.2. 2-((1-((2,4-dioxothiazolidin-5-ylidene) methyl) naphthalen-2-yl)oxy)-N-(4-fluorophenyl) acetamide (3b).** Yellow powder; yield 30.3%; m.p, 259 °C (charred); <sup>1</sup>H NMR (400 MHz, DMSO-d<sub>6</sub>): δ 10.48 (s,1H), δ 8.77 (s,1H), δ 8.53-8.55 (d, J = 8.0 Hz, 1H), δ 8.13-8.15 (d, J = 8.0 Hz, 1H), 8.06-8.07 (d, J = 4.0 Hz, 1H), δ 7.74-7.77 (t, J = 6.0 Hz, 1H), δ 7.65-7.60 (m, 4H), δ 7.13-7.16 (t, J = 6.0 Hz, 2H), δ 4.12 (s, 2H); <sup>13</sup>C NMR (400 MHz, DMSO-d<sub>6</sub>): δ 159.49, 158.27, 111.45, 131.68, 125.74, 126.10, 127.74, 127.99, 128.73, 129.66, 109.04, 150.46, 166.40, 54.93, 122.17, 113.30, 131.46, 130.02; IR (neat) 1689, 1284, 1213, 3335, 1618 and 1099 cm<sup>-1</sup>; Theoretical mass: 422.07, LC-MS (m/z, I %): 421.1 [(M-H)<sup>+</sup>, 100]; anal. calc. for C<sub>22</sub>H<sub>13</sub>FN<sub>2</sub>O<sub>4</sub>S: C, 62.55; H, 3.58; F, 4.50; N, 6.63; O, 15.15; S, 7.59.

**3.1.3.3. 2-((1-((2,4-dioxothiazolidin-5-ylidene)methyl)naphthalen-2-yl)oxy)-N-(p-tolyl) acetamide (3c).** Yellow powder; yield 25.97%; m.p, 220.2 °C (charred); <sup>1</sup>H NMR (400 MHz, DMSO-d<sub>6</sub>): δ 10.38 (s,1H), δ 8.74 (s,1H), δ 8.53-8.51 (d, J = 8.0 Hz, 1H), δ 8.10-8.12 (d, J = 8.0 Hz, 1H), 8.03-8.05 (d, J = 4.0 Hz, 1H), δ 7.72-7.76 (m, 1H), δ 7.57-7.64 (m, 2H), δ 7.48-7.50 (m, 3H), δ 7.10-7.12 (m, 1H), δ 4.11 (s, 2H), 2.23 (s, 3H); <sup>13</sup>C NMR (400 MHz, DMSO-d<sub>6</sub>): δ 158.29, 150.49, 113.34, 131.44, 127.79, 128.05, 126.15, 128.78, 129.18,

130.06, 119.17, 136.15, 166.07, 40.07, 131.70, 122.21, 129.18, 132.61; IR (neat) 1695, 1246, 1213, 3342, 1555 and 1170 cm<sup>-1</sup>; Theoretical mass: 418.1, LC-MS (m/z, I %): 416.8[(M-H)<sup>+</sup>, 100]; anal. calc. for C<sub>23</sub>H<sub>18</sub>N<sub>2</sub>O<sub>4</sub>S: C, 66.01; H, 4.34; N, 6.69; O, 15.29; S, 7.66.

**3.1.3.4. 2-((1-((2,4-dioxothiazolidin-5-ylidene)methyl)naphthalen-2-yl)oxy)-N-(4-methoxyphenyl) acetamide (3d).** Buff Yellow powder; yield 30%; m.p, 231.9 °C; <sup>1</sup>H NMR (400 MHz, DMSO-d<sub>6</sub>): δ 10.36 (s,1H), δ 8.69 (s,1H), δ 8.47-8.49 (d, J = 8.0 Hz, 1H), δ 8.05-8.07 (d, J = 8.0 Hz, 1H), 8.01-7.99 (d, J = 8.0 Hz, 1H), δ 7.70-7.74 (m, 1H), δ 7.51-7.62 (m, 4H), δ 6.89-6.91(m, 2H), δ 4.11 (s, 2H), δ 3.71 (s, 3H); <sup>13</sup>C NMR (400 MHz, DMSO-d<sub>6</sub>): δ 157.40, 154.59, 113.06, 130.94, 119.90, 127.85, 127.11, 125.21, 126.86, 125.02, 129.14, 164.98, 54.25, 130.42, 121.26, 115.47, 149.54; IR (neat) 1691, 1240, 1213, 3336, 1545 and 1168 cm<sup>-1</sup>; Theoretical mass: 434.09, LC-MS (m/z, I %): 433 [(M-H)<sup>+</sup>, 100]; anal. calc. for C<sub>23</sub>H<sub>18</sub>N<sub>2</sub>O<sub>5</sub>S: C, 63.58; H, 4.18; N, 6.45; O, 18.41; S, 7.38.

**3.1.3.5. N-(3,4-dichlorophenyl)-2-((1-((2,4-dioxothiazolidin-5-ylidene) methyl) naphthalen-2-yl)oxy) acetamide (3e).** Yellow powder; yield 30%; m.p, 293.6 °C(charred); <sup>1</sup>H NMR (400 MHz, DMSO-d<sub>6</sub>): δ 10.73 (s,1H), δ 8.75 (s,1H), δ 8.52-8.54 (d, J = 8.0 Hz, 1H), δ 8.13-8.15 (d, J = 8.0 Hz, 1H), 8.05-8.07 (d, J = 8.0 Hz, 1H), δ 7.96-7.97 (m, 1H), δ 7.73-7.77 (m, 1H), δ 7.63-7.65(m, 1H), δ 7.56-7.61(m, 2H), δ 7.48-7.51(m, 1H), δ 4.14 (s, 2H); <sup>13</sup>C NMR (400 MHz, DMSO-d<sub>6</sub>): δ 158.31, 150.69, 113.32, 138.70, 119.24, 130.07, 128.81, 127.83, 125.10, 126.18, 122.23, 130.79, 166.95, 40.07, 131.90, 131.04, 128.09, 120.35, 125.31; IR (neat) 1587, 1319, 1213, 3338, 1531 and 736 cm<sup>-1</sup>; Theoretical mass: 472.01, LC-MS (m/z, I %): 471[(M-H)<sup>+</sup>, 100]; anal. calc. for C<sub>22</sub>H<sub>14</sub>Cl<sub>2</sub>N<sub>2</sub>O<sub>4</sub>S: C, 55.82; H, 2.98; Cl, 14.98; N, 5.92; O, 13.52; S, 6.77.

**3.1.3.6. N-(2-bromo-4,6-difluorophenyl)-2-((1-((2,4-dioxothiazolidin-5-ylidene)methyl) naphthalen-2-yl)oxy) acetamide (3f).** Yellow powder; yield 31.2%; m.p, 268.5 °C (charred); <sup>1</sup>H NMR (400 MHz, DMSO-d<sub>6</sub>): δ 10.15 (s,1H), δ 8.73 (s,1H), δ 8.53 (s,1H), δ 8.05-8.12 (m, 2H), δ 7.43-7.74 (m, 5H), δ 4.19 (s, 2H); <sup>13</sup>C NMR (400 MHz, DMSO-d<sub>6</sub>): δ 158.40, 150.67, 113.22, 138.20, 119.20, 130.17, 127.81, 124.20, 126.18, 122.23, 130.79, 166.95, 41.07, 132.90, 131.14, 128.19, 120.32, 125.33; IR (neat) 1587, 1319, 1213, 3338, 1531 and 736 cm<sup>-1</sup>; Theoretical mass: 517.97, LC-MS (m/z, I %): 518.9 [(M + H)<sup>+</sup>, 100]; anal. calc. for C<sub>22</sub>H<sub>13</sub>BrF<sub>2</sub>N<sub>2</sub>O<sub>4</sub>SC, 50.88; H, 2.52; Br, 15.39; F, 7.32; N, 5.39; O, 12.32; S, 6.17.(13C NMR and IR is not available, data entered is approximate)

**3.1.3.7. N-(2,4-difluorophenyl)-2-((1-((2,4-dioxothiazolidin-5-ylidene)**

*methyl naphthalen-2-yl oxy) acetamide (3 g)*. Yellow powder; yield 24.69%; m.p, 231.6 °C (charred); <sup>1</sup>H NMR (400 MHz, DMSO<sub>d</sub><sub>6</sub>): δ 10.26 (s, 1H), δ 8.73 (s, 1H), δ 8.51–8.53 (m, 1H), δ 8.11–8.13 (d, J = 8.0 Hz, 1H), δ 8.04–8.06 (d, J = 8.0 Hz, 1H), δ 7.80–7.86 (m, 1H), δ 7.73–7.76 (m, 1H), δ 7.58–7.65 (m, 2H), δ 7.56–7.61 (m, 2H), δ 7.31–7.36 (t, J = 10.0 Hz, 1H), δ 7.03–7.07 (m, 1H), δ 4.21 (s, 2H); <sup>13</sup>C NMR (400 MHz, DMSO<sub>d</sub><sub>6</sub>): δ 158.30, 150.54, 104.23, 130.06, 111.30, 127.80, 126.15, 125.64, 116.41, 125.44, 113.33, 128.03, 166.92, 40.07, 111.11, 131.76, 104.24, 131.62, 111.11, 122.18; IR (neat) 1666, 1317, 1213, 3338, 1593 and 1006 cm<sup>-1</sup>; Theoretical mass: 440.06, LC-MS (*m/z*, I %): 439 [(M-H)<sup>+</sup>, 100]; anal. calc. for C<sub>22</sub>H<sub>14</sub>F<sub>2</sub>N<sub>2</sub>O<sub>4</sub>S: C, 60.00; H, 3.20; F, 8.63; N, 6.36; O, 14.53; S, 7.28.

**3.1.3.8. N-(4-bromo-2-methylphenyl)-2-((1-(2,4-dioxothiazolidin-5-ylidene) methyl naphthalen-2-yl oxy) acetamide (3 h)**. Deep yellow powder; yield 35%; m.p, 253 °C(charred); <sup>1</sup>H NMR (400 MHz, DMSO<sub>d</sub><sub>6</sub>): δ 10.49 (s, 1H), δ 8.71 (s, 1H), δ 8.50–8.52 (d, J = 8.0 Hz, 1H), δ 8.07–8.10 (d, J = 8.0 Hz, 1H), δ 8.01–8.03 (d, J = 8.0 Hz, 1H), δ 7.71–7.74 (t, J = 6.0 Hz, 1H), δ 7.53–7.63 (m, 2H), δ 7.17–7.25 (m, 2H), δ 6.65–6.67 (d, J = 6.0 Hz, 1H), δ 4.14 (s, 2H), δ 2.52 (s, 2H); <sup>13</sup>C NMR (400 MHz, DMSO<sub>d</sub><sub>6</sub>): δ 158.27, 150.46, 113.30, 139.82, 128.73, 127.74, 126.10, 122.17, 125.74, 116.36, 166.40, 54.93, 131.68; IR (neat) 1672, 1251, 1201, 3390, 1604, 1450 and 1072 cm<sup>-1</sup>; Theoretical mass: 496.01, LC-MS (*m/z*, I %): 496.9 [(M + H)<sup>+</sup>, 100]; anal. calc. for C<sub>23</sub>H<sub>17</sub>BrN<sub>2</sub>O<sub>4</sub>S: C, 58.79; H, 3.36; N, 9.35; O, 21.36; S, 55.54; Br, 16.07; N, 5.63; O, 12.87; S, 6.45, 7.13

**3.1.3.9. N-(4-bromophenyl)-2-((1-(2,4-dioxothiazolidin-5-ylidene) methyl naphthalen-2-yl oxy) acetamide (3i)**. Dark yellow powder; yield 26%; m.p, 262.6 °C(charred); <sup>1</sup>H NMR (400 MHz, DMSO<sub>d</sub><sub>6</sub>): δ 10.59 (s, 1H), δ 8.75 (s, 1H), δ 8.51–8.53 (d, J = 8.0 Hz, 1H), δ 8.12–8.14 (d, J = 8.0 Hz, 1H), δ 8.04–8.06 (d, J = 8.0 Hz, 1H), δ 8.03–8.05 (d, J = 8.0 Hz, 1H), δ 7.73–7.77 (t, J = 8.0 Hz, 1H), δ 7.57–7.65 (m, 5H), δ 7.48–7.50 (m, 2H), δ 4.13 (s, 2H); <sup>13</sup>C NMR (400 MHz, DMSO<sub>d</sub><sub>6</sub>): δ 158.30, 150.59, 113.33, 138.01, 115.25, 128.09, 127.81, 126.17, 122.21, 125.60, 121.09, 128.81, 166.57, 40.07, 131.66, 121.09, 130.07, 116.43; IR (neat) 1672, 1319, 1213, 3346, 1589 and 536 cm<sup>-1</sup>; Theoretical mass: 481.99, LC-MS (*m/z*, I %): 482.9 [(M + H)<sup>+</sup>, 100]; anal. calc. for C<sub>22</sub>H<sub>15</sub>BrN<sub>2</sub>O<sub>4</sub>S: C, 54.67; H, 3.13; Br, 16.53; N, 5.80; O, 13.24; S, 6.63.

**3.1.3.10. N-(2-chloro-5-(trifluoromethyl) phenyl)-2-((1-(2,4-dioxothiazolidin-5-ylidene) methyl naphthalen-2-yl oxy) acetamide (3j)**. Dark yellow powder; yield 28.57%; m.p, 238.6 °C(charred); <sup>1</sup>H NMR (400 MHz, DMSO<sub>d</sub><sub>6</sub>): δ 10.23 (s, 1H), δ 8.76 (s, 1H), δ 8.55–8.57 (d, J = 8.0 Hz, 1H), δ 8.17 (m, 1H), δ 8.12–8.14 (d, J = 8.0 Hz, 1H), δ 8.04–8.06 (m, 1H), δ 7.72–7.76 (m, 2H), δ 7.53–7.65 (m, 3H), δ 4.29 (s, 2H); <sup>13</sup>C NMR (400 MHz, DMSO<sub>d</sub><sub>6</sub>): δ 158.34, 150.71, 113.32, 135.40, 122.27, 130.05, 128.77, 128.19, 127.81, 128.01, 126.15, 130.80, 167.51, 40.07, 131.91, 127.86, 129.99, 125.20, 116.40; IR (neat) 1678, 1359, 1213, 3473, 1587, 1327 and 804 cm<sup>-1</sup>; Theoretical mass: 506.03, LC-MS (*m/z*, I %): 505 [(M-H)<sup>+</sup>, 100]; anal. calc. for C<sub>23</sub>H<sub>14</sub>ClF<sub>3</sub>N<sub>2</sub>O<sub>4</sub>S: C, 54.50; H, 2.78; Cl, 6.99; F, 11.24; N, 5.53; O, 12.63; S, 6.33.

**3.1.3.11. 2-((1-(2,4-dioxothiazolidin-5-ylidene) methyl naphthalen-2-yl oxy)-N-(4-nitrophenyl) acetamide (3k)**. Deep yellow powder; yield 25%; m.p, 264 °C(charred); <sup>1</sup>H NMR (400 MHz, DMSO<sub>d</sub><sub>6</sub>): δ 11.05 (s, 1H), δ 8.75 (s, 1H), δ 8.51–8.53 (d, J = 8.0 Hz, 1H), δ 8.20–8.23 (m, 2H), δ 8.10–8.12 (d, J = 8.0 Hz, 1H), δ 8.03–8.05 (d, J = 8.0 Hz, 1H), δ 7.84–7.87 (d, J = 12.0 Hz, 2H), δ 7.73–7.77 (t, J = 8.0 Hz, 1H), δ 7.62–7.64 (m, 1H), δ 7.56–7.60 (m, 1H), δ 4.21 (s, 2H); <sup>13</sup>C NMR (400 MHz, DMSO<sub>d</sub><sub>6</sub>): δ 158.28, 150.66, 113.27, 142.40, 128.07, 127.79, 126.13, 122.17, 125.18, 118.89, 128.75, 167.43, 40.07, 132.23, 116.38, 125.02, 131.87; IR (neat) 1680, 1257, 1211, 3433, 1597, 1550 and 1006 cm<sup>-1</sup>; Theoretical mass: 449.07, LC-MS (*m/z*, I %): 448 [(M-H)<sup>+</sup>, 100]; anal. calc. for C<sub>22</sub>H<sub>15</sub>N<sub>3</sub>O<sub>6</sub>S: C, 58.79; H,

3.36; N, 9.35; O, 21.36; S, 7.13.

## 3.2. In vitro HDAC screening

### 3.2.1. HDAC enzyme inhibition assay

Recombinant HDACs 1, 2, 3, 5 and 6 were purchased at BPS Bioscience. Recombinant HDAC8 was produced as described recently [54]. HDAC8 was produced in E. coli (BL21) DE3 pLysS cells using a pET14b vector containing codon-optimized human HDAC8. Recombinant cHDAC4 was expressed using a pET14b vector (Novagen, EMD Millipore) containing the codon-optimized catalytic domain of human HDAC4.

A serial dilution of inhibitor in assay buffer (25 mM Tris-HCl, pH 8.0, 75 mM KCl, 0.001% Pluronic F-127) was incubated with HDAC in a black 96-well microtiter half-area plate (Greiner) for 60 min at 30 °C. Afterwards the reaction was initiated by the addition of 20 μM Boc-Lys (trifluoroacetyl)-AMC (Bachem) as substrate for HDAC4, 5 and 8 and 50 μM Boc-Lys(acetyl)-AMC as substrate for HDAC1, 2, 3 and 6. After incubation for 60 min at 30 °C, the reaction was stopped by the addition of 1.7 μM SATFMK for HDAC4, 5 and 8 and 4.2 μM suberoylanilide hydroxamic acid (SAHA, Cayman Chemical Company) for HDACs 1,2,3 and 6. The deacetylated substrate was converted into a fluorescent product by the addition of 0.4 mg/ml trypsin (Applichem). The release of AMC was followed in a microplate reader (PheraStar Plus, BMG Labtech) at 450 nm (λ<sub>Ex</sub> = 350 nm) and correlated to enzyme activity. Dose-response curves were generated by using GraphPad Prism and fitted to a four parameters logistic function to obtain IC<sub>50</sub> values [55]:

$$EA = E_0 + \frac{(E_{max} - E_0)}{1 + 10^{(\log(IC_{50}) - x) \cdot h}}$$

in which EA is the enzyme activity at a given inhibitor concentration *x*, E<sub>max</sub> and E<sub>0</sub> are the enzyme activities determined at zero and complete inhibition, respectively. IC<sub>50</sub> denotes the inhibitor concentration at which half the enzyme is inhibited and *h* is the slope of the curve.

### 3.2.2. Thermal shift assay

The thermal shift assay was performed as described recently [56]. In short, 2.5 μM recombinant HDAC8 was incubated with 100 μM of the indicated inhibitor for 1 h at 30 °C and afterwards aliquoted in PCR-Tubes. Each tube was tempered for 10 min at the indicated temperature and subsequent centrifuged. The soluble protein phase was then conducted to SDS-PAGE and band densities were quantified using Image Studio Lite (LiCor) and plotted against the temperature.

## 3.3. In vitro anticancer screening

### 3.3.1. Cell cultures

K562 cell line (chronic myeloid leukaemia) was purchased from National Centre for Cell Sciences (NCCS), Pune. CEM (acute T-cell lymphoblastic leukemia) was obtained from the Department of Biochemistry Indian Institute of Science, Bangalore. K562 and CEM cells were maintained as suspension in RPMI 1640 medium (Thermo fisher scientific) supplemented with 10% fetal bovine serum (Gibco, Invitrogen) and 1% antibiotic-antimycotic 100X solution (100 units/mL of penicillin, 100 μg/mL of streptomycin, and 0.25 μg/mL of Gibco Amphotericin B). Cells were maintained in a humidified 5% CO<sub>2</sub> atmosphere at 37 °C.

### 3.3.2. Cytotoxicity assay

MTT assay was used to determine cytotoxic potential of **3a** to **3k** on leukemic cell lines, K562 and CEM. The assay was performed as described earlier [57]. Briefly, the cells were seeded at a density of approximately 5 × 10<sup>3</sup> cells/well in a 96-well flat-bottom micro-plate and maintained at 37 °C in 95% humidity and 5% CO<sub>2</sub> overnight. Different concentrations of compounds were diluted in DMSO and were added to

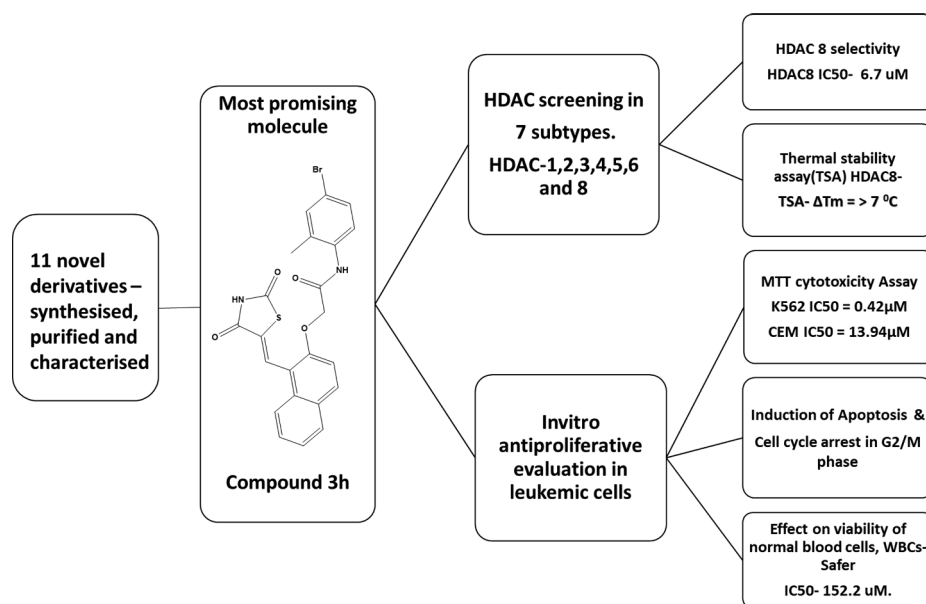


Fig. 9. Schematic representation of results.

the cells. The final concentration of DMSO in the experiments was less than 1.5% and showed no cell toxicity. The cells were incubated with the compounds for 48 h. Next, 96-well plates were centrifuged at 300g, 4 °C for 5 min and cells in well were washed with phosphate buffer solution twice., 20 μL of the MTT staining solution (5 mg/ml in phosphate buffer solution) was added to each well and the plate was incubated at 37 °C. After 4 h, 100 μL of dimethyl sulfoxide (DMSO) was added to each well to dissolve the formazan crystals, and absorbance was recorded with a 570 nm using micro plate reader.

### 3.3.3. Apoptosis by flow cytometry

The induction of apoptosis produced by compound **3a** and **3h** was studied by flow cytometry as described earlier [58]. Cells were seeded in a 24-well flat bottom micro plate and incubated at 37 °C in 5% CO<sub>2</sub> atmosphere for 24 h. The media was replaced with fresh media and then for 24 h, the cells were treated with IC<sub>50</sub> concentration of **3a** and **3h**. Untreated cells were used as negative control. Post incubation, cells were washed with PBS, Centrifuge for 5 min at 300g at 4 °C, and supernatant was discarded. Cell pellets were re-suspended in ice-cold 1X Binding Buffer, 1 μL of annexin V-FITC solution and 5 μL PI (propidium iodide) were added and mixed. Tubes were kept on ice and incubated for 15 min in the dark. 400 μL of ice-cold 1X binding buffer was added and cell preparations were analyzed using flow cytometer (BD Accuri™ C5 flow cytometer, BD Biosciences, CA, USA). FlowJo software was used for data analysis (version 10.1, Ashland, OR, USA).

### 3.3.4. Flow cytometry analysis of cell cycle

Cells were seeded in a 24-well flat bottom micro plate and incubated overnight at 37 °C in CO<sub>2</sub> incubator for 24 h. The media was replaced with fresh media and then for 24 h, the cells were treated with IC<sub>50</sub> concentration of **3a** and **3h**. Untreated cells were used as negative control. Post incubation, cells were washed with PBS, Centrifuge for 5 min at 300g at 4 °C, and supernatant was discarded. Cell were re-suspended in 0.5 ml PBS. The cells were fixed on ice in 4.5 ml of ice cold 70% ethanol for 2 h, centrifuged for 5 min at 200g at 4 °C and ethanol was decanted. Then the cell pellets were Suspended in 5 ml PBS for 1 min, centrifuged for 5 min at 200g at 4 °C and treated with 1 ml propidium iodide staining solution for 15 mins at 37 °C. Cell were analyzed within 30 min. (BD Accuri™ C5 flow cytometer, BD Biosciences, CA, USA). Obtained data was analyzed using FlowJo software (version 10.1, Ashland, OR, USA).

### 3.3.5. Assessment of cell viability on non-transformed cells

Normal human WBCs were isolated from the peripheral blood of healthy blood donor. The study was approved by appropriate Institutional Review Board. Blood was drawn during routine diagnostic procedures after written informed consent was obtained from patient. The blood samples were spun in a centrifuge and WBCs were isolated from the “buffy coat” fraction. Cells were maintained in a humidified 5% CO<sub>2</sub> atmosphere at 37°C.

Effect of the treatment of compounds **3a** and **3h** on the viability of normal human WBCs, were determined by using MTT assay as described above in cytotoxicity assay. Wherein normal WBCs were treated with increasing concentrations of **3a** and **3h** from 2.5 to 100 μM for 48 h to determine the difference in the cell viabilities of normal cells and finally to calculate IC<sub>50</sub> value.

## 3.4. In silico studies

### 3.4.1. Molecular docking and energy minimization

Modeling, preparation and visualization of structural data as well as molecular docking was performed using MOE 2019 software (Chemical Computing Group ULC, Canada). Three crystal structures representing significant conformations of HDAC8 (PDB-ID's 1T69, 1VKG, 3SFF) were obtained from RCSB Protein Data Bank. The structure files were loaded into the program and subjected to structure preparation including 3D protonation for subsequent docking. The partial charges of all protein and ligand atoms were calculated using the implemented Amber14 force field. Molecular docking was performed choosing the triangle matcher for placement of the ligand in the binding site and ranked with the London dG scoring function. The best 30 poses were passed to the refinement and energy minimization in the pocket using the induced fit method and then rescored with the GBVI/WSA dG scoring function.

### 3.4.2. SwissADME predictions

SwissADME is freely available but reliable online tool which can be used to predict physicochemical, pharmacokinetic and bioavailability of the synthetic molecules, simply by providing structural inputs. The web address of the tool is <http://www.swissadme.ch/index.php#>.

## 4. Conclusion

We have successfully synthesized and characterised a series of 5-

naphthylidene-2,4-thiazolidinedione derivatives as selective non-hydroxamate HDAC8 inhibitors. Among the synthesized derivatives, compounds **3a**, **3f** and **3h-3j** were found to be selective for HDAC8 in HDAC screening of HDAC1,2,3, 4, 5, 6 and 8. In TSA, all the screened derivatives showed shift in  $\Delta T_m$  of 7 °C and more. In cytotoxicity assays in K562 and CEM cell lines, **3a** exhibited most potent cytotoxic effects and was found to be safer in normal WBCs. **3a** and **3h** both lead to cell cycle arrest in G2/M phase and was able to induce apoptosis in CEM cells (Fig. 9). Docking studies correlated well with the HDAC inhibitory concentrations and carboxylate group was found to interact with zinc at zinc binding site. Crystallographic studies need to be performed to determine actual interactions at active site of HDAC8. Given that Compound **3h** exhibits HDAC8 selectivity and potent antitumor effects in vitro, further in-depth studies on these molecules are expected to give rise to potent leads.

### Declaration of Competing Interest

The authors declare that they have no known competing financial interests or personal relationships that could have appeared to influence the work reported in this paper.

### Acknowledgement

This study was supported by Indo-Poland joint research programme grant from Department of Science and Technology (DST) with reference number DST/INT/Pol/P-27/2016. We also acknowledge financial support of the University of Applied Sciences Darmstadt.

### Appendix A. Supplementary material

Supplementary data to this article can be found online at <https://doi.org/10.1016/j.bioorg.2019.103522>.

### References

- [1] S. Sharma, T.K. Kelly, P.A. Jones, Epigenetics in cancer, *Carcinogenesis* 31 (2010) 27–36, <https://doi.org/10.1093/carcin/bgp220>.
- [2] B.S. Mann, J.R. Johnson, M.H. Cohen, R. Justice, R. Pazdur, FDA approval summary: vorinostat for treatment of advanced primary cutaneous T-Cell Lymphoma, *Oncologist* 12 (2007) 1247–1252, <https://doi.org/10.1634/theoncologist.12-10-1247>.
- [3] J.P. Laubach, P. Moreau, J.F. San-Miguel, P.G. Richardson, Panobinostat for the treatment of multiple myeloma, *Clin. Cancer Res.* 21 (2015) 4767–4773, <https://doi.org/10.1158/1078-0432.CCR-15-0530>.
- [4] I. Oehme, H.E. Deubzer, M. Lodrini, T. Milde, O. Witt, Targeting of HDAC8 and investigational inhibitors in neuroblastoma, *Exp. Opin. Invest. Drugs* 18 (2009) 1605–1617, <https://doi.org/10.1517/14728220903241658>.
- [5] S. Balasubramanian, J. Ramos, W. Luo, M. Sirisawad, E. Verner, J.J. Buggy, A novel histone deacetylase 8 (HDAC8)-specific inhibitor PCI-34051 induces apoptosis in T-cell lymphomas, *Leukemia* 22 (2008) 1026–1034, <https://doi.org/10.1038/leu.2008.9>.
- [6] A. Chakrabarti, I. Oehme, O. Witt, G. Oliveira, W. Sippl, C. Romier, R.J. Pierce, M. Jung, HDAC8: a multifaceted target for therapeutic interventions, *Trends Pharmacol. Sci.* 36 (2015) 481–492, <https://doi.org/10.1016/j.tips.2015.04.013>.
- [7] A. Chakrabarti, J. Melesina, F.R. Kolbinger, I. Oehme, J. Senger, O. Witt, W. Sippl, M. Jung, Targeting histone deacetylase 8 as a therapeutic approach to cancer and neurodegenerative diseases, *Future Med. Chem.* 8 (2016) 1609–1634, <https://doi.org/10.4155/fmc-2016-0117>.
- [8] S.A. Amin, N. Adhikari, T. Jha, Structure–activity relationships of hydroxamate-based histone deacetylase-8 inhibitors: reality behind anticancer drug discovery, *Future Med. Chem.* 9 (2017) 2211–2237, <https://doi.org/10.4155/fmc-2017-0130>.
- [9] S.K.A. Amin, N. Adhikari, T. Jha, Structure-activity relationships of HDAC8 inhibitors: non-hydroxamates as anticancer agents, *Pharmacol. Res.* 131 (2018) 128–142, <https://doi.org/10.1016/j.phrs.2018.03.001>.
- [10] S. Shen, A.P. Kozikowski, Why hydroxamates may not be the best histone deacetylase inhibitors—what some may have forgotten or would rather forget? *ChemMedChem* 11 (2016) 15–21, <https://doi.org/10.1002/cmdc.201500486>.
- [11] R.W. Johnstone, Histone-deacetylase inhibitors: novel drugs for the treatment of cancer, *Nat Rev Drug Discov* 1 (2002) 287–299, <https://doi.org/10.1038/nrd772>.
- [12] P.A. Marks, R.A. Rifkind, V.M. Richon, R. Breslow, T. Miller, W.K. Kelly, Histone deacetylases and cancer: causes and therapies, *Nat. Rev. Cancer* 1 (2001) 194–202, <https://doi.org/10.1038/35106079>.
- [13] A. Mai, S. Massa, D. Rotili, I. Cerbara, S. Valente, R. Pezzi, S. Simeoni, R. Ragno, Histone deacetylation in epigenetics: an attractive target for anticancer therapy, *Med. Res. Rev.* 25 (2005) 261–309, <https://doi.org/10.1002/med.20024>.
- [14] T.A. Miller, D.J. Witter, S. Belvedere, Histone deacetylase inhibitors, *J. Med. Chem.* 46 (2003) 5097–5116, <https://doi.org/10.1021/jm0303094>.
- [15] L. Whitehead, M.R. Dobler, B. Radetich, Y. Zhu, P.W. Atadja, T. Claiborne, J.E. Grob, A. McRiner, M.R. Pancost, A. Patnaik, W. Shao, M. Shultz, R. Tichkule, R.A. Tommasi, B. Vash, P. Wang, T. Stams, Human HDAC isoform selectivity achieved via exploitation of the acetate release channel with structurally unique small molecule inhibitors, *Bioorg. Med. Chem.* 19 (2011) 4626–4634, <https://doi.org/10.1016/j.bmc.2011.06.030>.
- [16] P. Galletti, A. Quintavalla, C. Ventrici, G. Giannini, W. Cabri, S. Penco, G. Gallo, S. Vincenti, D. Giacomini, Azetidiones as zinc-binding groups to design selective HDAC8 Inhibitors, *ChemMedChem* 4 (2009) 1991–2001, <https://doi.org/10.1002/cmdc.200900309>.
- [17] H. Nian, W.H. Bisson, W.-M. Dashwood, J.T. Pinto, R.H. Dashwood, Keto acid metabolites of organoselenium compounds inhibit histone deacetylase activity in human colon cancer cells, *Carcinogenesis* 30 (2009) 1416–1423, <https://doi.org/10.1093/carcin/bgp147>.
- [18] E. Hu, E. Dul, C.-M. Sung, Z. Chen, R. Kirkpatrick, G.-F. Zhang, K. Johanson, R. Liu, A. Lago, G. Hofmann, R. Macarron, M. De Los Frailes, P. Perez, J. Krawiec, J. Winkler, M. Jaye, Identification of novel isoform-selective inhibitors within class I Histone Deacetylases, *J. Pharmacol. Exp. Ther.* 307 (2003) 720–728, <https://doi.org/10.1124/jpet.103.055541>.
- [19] A. Kleinschek, C. Meyners, E. Digiorio, C. Brancolini, F.-J. Meyer-Almes, Potent and selective non-hydroxamate histone deacetylase 8 inhibitors, *ChemMedChem* 11 (2016) 2598–2606, <https://doi.org/10.1002/cmdc.201600528>.
- [20] B. Wolff, N. Jänsch, W.O. Sugiarto, S. Frühschulz, M. Lang, R. Altintas, I. Oehme, F.-J. Meyer-Almes, Synthesis and structure activity relationship of 1, 3-benzo-thiazine-2-thiones as selective HDAC8 inhibitors, *Eur. J. Med. Chem.* 184 (2019) 111756, <https://doi.org/10.1016/j.ejmech.2019.111756>.
- [21] J.J. Buggy, B. Sriram, M.S. Susanne, inventors; Pharmacyclics Inc., assignee; 2015. Uses of selective inhibitors of HDAC8 and treatment of inflammatory conditions. US20150038542.
- [22] T. Suzuki, Y. Ota, M. Ri, M. Bando, A. Gotoh, Y. Itoh, H. Tsumoto, P.R. Tatum, T. Mizukami, H. Nakagawa, S. Iida, R. Ueda, K. Shirahige, N. Miyata, Rapid discovery of highly potent and selective inhibitors of histone deacetylase 8 Using click chemistry to generate candidate libraries, *J. Med. Chem.* 55 (2012) 9562–9575, <https://doi.org/10.1021/jm300837y>.
- [23] Aaron Beaty Beeler, John A. Porco, Jr., Oscar J. Ingham, James E. Bradner, inventors; Trustees of Boston University, assignee; 2015. Selective histone deacetylase 8 inhibitors. US20150352079.
- [24] A. Oyelere, G. Berkley, inventors; 2013. Histone deacetylase (HDAC) inhibitors targeting prostate tumors and method of making and using thereof. US20130289085.
- [25] W.-J. Huang, Y.-C. Wang, S.-W. Chao, C.-Y. Yang, L.-C. Chen, M.-H. Lin, W.-C. Hou, M.-Y. Chen, T.-L. Lee, P. Yang, C.-I. Chang, Synthesis and biological evaluation of ortho -aryl N -hydroxycinnamides as potent histone deacetylase (HDAC) 8 Isoform-Selective Inhibitors, *ChemMedChem* 7 (2012) 1815–1824, <https://doi.org/10.1002/cmdc.201200300>.
- [26] W. Xu, Y. Zhang, W. Song, inventors; Shouguang Fukang Pharmaceuticals Ltd., assignee; 2012. Preparative method and use of ZYJ-D08A and its epimers as histone deacetylase inhibitors. WO20121274730.
- [27] W. Xu, Y. Zhang, H. Fang, inventors; Shandong University, assignee; 2010. Tyrosine derivatives as histone deacetylase inhibitors and using thereof. CN101723896.
- [28] Y. Zhang, J. Feng, C. Liu, L. Zhang, J. Jiao, H. Fang, L. Su, X. Zhang, J. Zhang, M. Li, B. Wang, W. Xu, Design, synthesis and preliminary activity assay of 1,2,3,4-tetrahydroisoquinoline-3-carboxylic acid derivatives as novel Histone deacetylases (HDACs) inhibitors, *Bioorg. Med. Chem.* 18 (2010) 1761–1772, <https://doi.org/10.1016/j.bmc.2010.01.060>.
- [29] Y. Zhang, J. Feng, Y. Jia, X. Wang, L. Zhang, C. Liu, H. Fang, W. Xu, Development of tetrahydroisoquinoline-based hydroxamic acid derivatives: potent histone deacetylase inhibitors with marked in vitro and in vivo antitumor activities, *J. Med. Chem.* 54 (2011) 2823–2838, <https://doi.org/10.1021/jm101605z>.
- [30] K. KrennHrubeck, B.L. Marshall, M. Hedglin, E. Verdin, S.M. Ulrich, Design and evaluation of 'Linkerless' hydroxamic acids as selective HDAC8 inhibitors, *Bioorg. Med. Chem. Lett.* 17 (2007) 2874–2878, <https://doi.org/10.1016/j.bmcl.2007.02.064>.
- [31] H.-T. Qin, H.-Q. Li, F. Liu, Selective histone deacetylase small molecule inhibitors: recent progress and perspectives, *Expert Opin. Ther. Pat.* 27 (2017) 621–636, <https://doi.org/10.1080/13543776.2017.1276565>.
- [32] J.C. Bressi, R. de Jong, Y. Wu, A.J. Jennings, J.W. Brown, S. O'Connell, L.W. Tari, R.J. Skene, P. Vu, M. Navre, X. Cao, A.R. Gangloff, Benzimidazole and imidazole inhibitors of histone deacetylases: synthesis and biological activity, *Bioorg. Med. Chem. Lett.* 20 (2010) 3138–3141, <https://doi.org/10.1016/j.bmcl.2010.03.092>.
- [33] R. Mohan, A.K. Sharma, S. Gupta, C.S. Ramaa, Design, synthesis, and biological evaluation of novel 2,4-thiazolidinedione derivatives as histone deacetylase inhibitors targeting liver cancer cell line, *Med. Chem. Res.* 21 (2012) 1156–1165, <https://doi.org/10.1007/s00044-011-9623-3>.
- [34] M. Marek, T.B. Shaik, T. Heimburg, A. Chakrabarti, J. Lancelot, E. Ramos-Morales, C. Da Veiga, D. Kalinin, J. Melesina, D. Robaa, K. SchmidtKunz, T. Suzuki, R. Holl, E. Ennifar, R.J. Pierce, M. Jung, W. Sippl, C. Romier, Characterization of Histone Deacetylase 8 (HDAC8) selective inhibition reveals specific active site structural and functional determinants, *J. Med. Chem.* 61 (2018) 10000–10016, <https://doi.org/10.1021/acs.jmedchem.8b01087>.
- [35] X. Hou, J. Du, R. Liu, Y. Zhou, M. Li, W. Xu, H. Fang, Enhancing the sensitivity of pharmacophore-based virtual screening by incorporating customized ZBG features: a case study using histone deacetylase 8, *J. Chem. Inf. Model.* 55 (2015) 861–871,

- <https://doi.org/10.1021/ci500762z>.
- [36] V. Patil, K. Tilekar, S. Mehendale-Munj, R. Mohan, C.S. Ramaa, Synthesis and primary cytotoxicity evaluation of new 5-benzylidene-2,4-thiazolidinedione derivatives, *Eur. J. Med. Chem.* 45 (2010) 4539–4544, <https://doi.org/10.1016/j.ejmech.2010.07.014>.
- [37] A. Kabir, K. Tilekar, N. Upadhyay, C.S. Ramaa, Novel anthraquinone derivatives as dual inhibitors of topoisomerase 2 and casein kinase 2. In silico studies, synthesis and biological evaluation on leukemic cell lines, *ACAMC* 18 (2019) 1551–1562, <https://doi.org/10.2174/1871520618666180423111309>.
- [38] Y. Momose, K. Meguro, H. Ikeda, C. Hatanaka, S. Oi, T. Sohda, Studies on anti-diabetic agents. X. Synthesis and biological activities of pioglitazone and related compounds, *Chem. Pharm. Bull.* 39 (1991) 1440–1445, <https://doi.org/10.1248/cpb.39.1440>.
- [39] D.S. Auld, N. Thorne, W.F. Maguire, J. Inglese, Mechanism of PTC124 activity in cell-based luciferase assays of nonsense codon suppression, *Proc. Natl. Acad. Sci.* 106 (2009) 3585–3590, <https://doi.org/10.1073/pnas.0813345106>.
- [40] C. Schmidt, GSK/Sirtis compounds dogged by assay artifacts, *Nat. Biotechnol.* 28 (2010) 185–186, <https://doi.org/10.1038/nbt0310-185>.
- [41] M. Guha, PARP inhibitors stumble in breast cancer, *Nat. Biotechnol.* 29 (2011) 373–374, <https://doi.org/10.1038/nbt0511-373>.
- [42] X. Liu, Y. Shi, D.X. Maag, J.P. Palma, M.J. Patterson, P.A. Ellis, B.W. Surber, D.B. Ready, N.B. Soni, U.S. Lador, A.J. Xu, R. Iyer, J.E. Harlan, L.R. Solomon, C.K. Donawho, T.D. Penning, E.F. Johnson, A.R. Shoemaker, Iniparib Nonselectively modifies cysteine-containing proteins in tumor cells and is not a bona fide PARP Inhibitor, *Clin. Cancer Res.* 18 (2012) 510–523, <https://doi.org/10.1158/1078-0432.CCR-11-1973>.
- [43] M. Florio, V. Borrell, W.B. Huttner, Human-specific genomic signatures of neocortical expansion, *Curr. Opin. Neurobiol.* 42 (2017) 33–44, <https://doi.org/10.1016/j.conb.2016.11.004>.
- [44] M. Florio, M. Heide, A. Pinson, H. Brandl, M. Albert, S. Winkler, P. Wimberger, W.B. Huttner, M. Hiller, Evolution and cell-type specificity of human-specific genes preferentially expressed in progenitors of fetal neocortex, *eLife*, 7 (2018) e32332. <https://doi.org/10.7554/eLife.32332>.
- [45] S. Song, Y. Wang, P. Xu, R. Yang, Z. Ma, S. Liang, G. Zhang, The inhibition of histone deacetylase 8 suppresses proliferation and inhibits apoptosis in gastric adenocarcinoma, *Int. J. Oncol.* 47 (2015) 1819–1828, <https://doi.org/10.3892/ijo.2015.3182>.
- [46] J. Wu, C. Du, Z. Lv, C. Ding, J. Cheng, H. Xie, L. Zhou, S. Zheng, The up-regulation of histone deacetylase 8 promotes proliferation and inhibits apoptosis in hepatocellular carcinoma, *Dig. Dis. Sci.* 58 (2013) 3545–3553, <https://doi.org/10.1007/s10620-013-2867-7>.
- [47] M. Paris, M. Porcelloni, M. Binaschi, D. Fattori, Histone deacetylase inhibitors: from bench to clinic, *J. Med. Chem.* 51 (2008) 1505–1529, <https://doi.org/10.1021/jm7011408>.
- [48] Z. Dong, Y. Yang, S. Liu, J. Lu, B. Huang, Y. Zhang, HDAC inhibitor PAC-320 induces G2/M cell cycle arrest and apoptosis in human prostate cancer, *Oncotarget* 9 (2018), <https://doi.org/10.18632/oncotarget.23070>.
- [49] A. Vannini, C. Volpari, G. Filocamo, E.C. Casavola, M. Brunetti, D. Renzoni, P. Chakravarty, C. Paolini, R. De Francesco, P. Gallinari, C. Steinkuhler, S. Di Marco, Crystal structure of a eukaryotic zinc-dependent histone deacetylase, human HDAC8, complexed with a hydroxamic acid inhibitor, *Proc. Natl. Acad. Sci.* 101 (2004) 15064–15069, <https://doi.org/10.1073/pnas.0404603101>.
- [50] C. Decroos, D.J. Clausen, B.E. Haines, O. Wiest, R.M. Williams, D.W. Christianson, Variable active site loop conformations accommodate the binding of macrocyclic largazole analogues to HDAC8, *Biochemistry* 54 (2015) 2126–2135, <https://doi.org/10.1021/acs.biochem.5b00010>.
- [51] J.R. Somoza, R.J. Skene, B.A. Katz, C. Mol, J.D. Ho, A.J. Jennings, C. Luong, A. Arvai, J.J. Buggy, E. Chi, J. Tang, B.-C. Sang, E. Verner, R. Wynands, E.M. Leahy, D.R. Dougan, G. Snell, M. Navre, M.W. Knuth, R.V. Swanson, D.E. McRee, L.W. Tari, Structural snapshots of human HDAC8 Provide Insights into the Class I histone deacetylases, *Structure* 12 (2004) 1325–1334, <https://doi.org/10.1016/j.str.2004.04.012>.
- [52] N. Deschamps, C.A. Simões-Pires, P.-A. Carrupt, A. Nurisso, How the flexibility of human histone deacetylases influences ligand binding: an overview, *Drug Discov. Today* 20 (2015) 736–742, <https://doi.org/10.1016/j.drudis.2015.01.004>.
- [53] A. Daina, O. Michielin, V. Zoete, SwissADME: a free web tool to evaluate pharmacokinetics, drug-likeness and medicinal chemistry friendliness of small molecules, *Sci. Rep.* 7 (2017) 42717, <https://doi.org/10.1038/srep42717>.
- [54] N. Jänsch, C. Meyners, M. Muth, A. Kopranovic, O. Witt, I. Oehme, F.-J. Meyer-Almes, The enzyme activity of histone deacetylase 8 is modulated by a redox-switch, *Redox Biol.* 20 (2019) 60–67, <https://doi.org/10.1016/j.redox.2018.09.013>.
- [55] A. Volund, Application of the four-parameter logistic model to bioassay: comparison with slope ratio and parallel line models, *Biometrics* 34 (1978) 357, <https://doi.org/10.2307/2530598>.
- [56] M. Schweipert, N. Jänsch, W.O. Sugiarto, F.-J. Meyer-Almes, Kinetically selective and potent inhibitors of HDAC8, *Biol. Chem.* 400 (2019) 733–743, <https://doi.org/10.1515/hsz-2018-0363>.
- [57] S.S. Bhat, V.K. Revankar, V. Kumbar, K. Bhat, V.A. Kawade, Synthesis, crystal structure and biological properties of a cis -dichloridobis(diimine)copper(II) complex, *Acta Crystallogr. C Struct. Chem.* 74 (2018) 146–151, <https://doi.org/10.1107/S2053229617018551>.
- [58] M.R. Peram, S. Jalalpure, V. Kumbar, S. Patil, S. Joshi, K. Bhat, P. Diwan, Factorial design based curcumin ethosomal nanocarriers for the skin cancer delivery: in vitro evaluation, *J. Liposome Res.* 29 (2019) 291–311, <https://doi.org/10.1080/08982104.2018.1556292>.

---

**Titel:**

Discovery of novel N-substituted thiazolidinediones (TZDs) as HDAC8 inhibitors: in-silico studies, synthesis, and biological evaluation

**Autoren:**

Neha Upadhyay, Kalpana Tilekar, Niklas Jäsch, Markus Schweipert, Jessica D. Hess, Luca Henze Macias, Piotr Mrowka, Renato J. Aguilera, Jun-Yong Choe, Franz-Josef Meyer-Almes, C S Ramaa

**Bibliographische Daten:**

Bioorganic Chemistry (doi.org/10.1016/j.bioorg.2020.103934)

**Zusammenfassung:**

Epigenetik spielt eine grundlegende Rolle bei der Krebsentstehung, und die Entwicklung von Wirkstoffen, welche auf diese Mechanismen Einfluss nehmen, ist für die Krebsbehandlung von entscheidender Bedeutung. Unter den Klasse-I- und Klasse-II-HDACs ist HDAC8 eine der essenziellen epigenetischen Akteure bei der Krebsentstehung. Daher haben wir neue Verbindungen mit N-substituiertem TZD (P1-P25) entwickelt, synthetisiert, gereinigt und strukturell charakterisiert. Die Prüfung der Lebensfähigkeit von Zellen aller Verbindungen an leukämischen Zelllinien (CEM, K-562 und KCL22) zeigte das zytotoxische Potenzial von P8, P9, P10, P12, P19 und P25. Das In-vitro-Screening der verschiedenen HDAC-Isoformen ergab, dass P19 der stärkste und selektivste Inhibitor für HDAC8 war (IC<sub>50</sub> - 9,3 µM). Mittels thermischer Denaturierung (thermal shift assay, TSA) bestätigte sich die Bindung von P19 an HDAC8. Das In-vitro-Screening aller Verbindungen auf die Transportaktivität von GLUT1, GLUT4 und GLUT5 zeigte, dass P19 GLUT1 hemmte (IC<sub>50</sub> - 28,2 µM). P10 und P19 induzierten den apoptotischen Zelltod in CEM-Zellen (55,19% bzw. 60,97%) und P19 zeigte weniger Zytotoxizität auf normale WBKs (CC<sub>50</sub> - 104,2 µM) und humane Fibroblasten (HS27) (CC<sub>50</sub> - 105,0 µM). Unter dieser neuen Reihe von TZD-Derivaten war die Verbindung P19 somit der vielversprechendste HDAC8-Inhibitor, der gleichzeitig zytotoxisch auf leukämische Zellen wirkt. Somit könnte P19 als Leitstruktur für die weitere Entwicklung optimierter Moleküle mit erhöhter Selektivität und Wirksamkeit dienen.



# HHS Public Access

Author manuscript

*Bioorg Chem.* Author manuscript; available in PMC 2020 July 01.

Published in final edited form as:

*Bioorg Chem.* 2020 July ; 100: 103934. doi:10.1016/j.bioorg.2020.103934.

## Discovery of novel N-substituted thiazolidinediones (TZDs) as HDAC8 inhibitors: *in-silico* studies, synthesis, and biological evaluation

Neha Upadhyay<sup>1</sup>, Kalpana Tilekar<sup>1</sup>, Niklas Jänsch<sup>2</sup>, Markus Schweipert<sup>2</sup>, Jessica D. Hess<sup>3</sup>, Luca Henze Macias<sup>3</sup>, Piotr Mrowka<sup>4,5</sup>, Renato J. Aguilera<sup>3</sup>, Jun-yong Choe<sup>6,7</sup>, Franz-Josef Meyer-Almes<sup>\*,2</sup>, C S Ramaa<sup>\*,1</sup>

<sup>1</sup>Department of Pharmaceutical Chemistry, Bharati Vidyapeeth's College of Pharmacy, Navi Mumbai, India. <sup>2</sup>Department of Chemical Engineering and Biotechnology, University of Applied Science, Darmstadt, Germany. <sup>3</sup>The Cellular Characterization and Biorepository Core Facility & Border Biomedical research Centre & Department of Biological Sciences, The University of Texas at El Paso, El Paso, Texas, USA. <sup>4</sup>Department of Biophysics and Human Physiology, Medical University of Warsaw, Chalubinskiego, Warsaw, Poland. <sup>5</sup>Institute of Hematology and Blood Transfusion, Indira Gandhi St., Warsaw, Poland. <sup>6</sup>East Carolina Diabetes and Obesity Institute, East Carolina University, Greenville, NC 27834, USA. <sup>7</sup>Department of Biochemistry and Molecular Biology, The Chicago Medical School, Rosalind Franklin University of Medicine and Science, North Chicago, Illinois, USA.

### Abstract

Epigenetics plays a fundamental role in cancer progression, and developing agents that regulate epigenetics is crucial for cancer management. Among Class I and Class II HDACs, HDAC8 is one of the essential epigenetic players in cancer progression. Therefore, we designed, synthesized, purified, and structurally characterized novel compounds containing N-substituted TZD (**P1-P25**). Cell viability assay of all compounds on leukemic cell lines (CEM, K-562, and KCL22) showed the cytotoxic potential of **P8**, **P9**, **P10**, **P12**, **P19**, and **P25**. *In-vitro* screening of different HDACs isoforms revealed that **P19** was the most potent and selective inhibitor for HDAC8 (IC<sub>50</sub> - 9.3 μM). Thermal shift analysis (TSA) confirmed the binding of **P19** to HDAC8. *In-vitro* screening of all compounds on the transport activity of GLUT1, GLUT4, and GLUT5 indicated that **P19** inhibited GLUT1 (IC<sub>50</sub> - 28.2 μM). **P10** and **P19** induced apoptotic cell death in CEM cells (55.19% and 60.97% respectively) and **P19** was less cytotoxic on normal WBCs (CC<sub>50</sub> - 104.2 μM) and human fibroblasts (HS27) (CC<sub>50</sub> - 105.0 μM). Thus, among this novel series of TZD

\*Corresponding authors: 1. C S Ramaa; sinharamaa@yahoo.in; Tel.: +91 22 27572131/1122; Fax: +91 22 27574515. 2. Franz-Josef Meyer-Almes; franz-josef.meyer-almes@h-da.de; Phone: +49 6151168406; Fax: +49 6151168404.

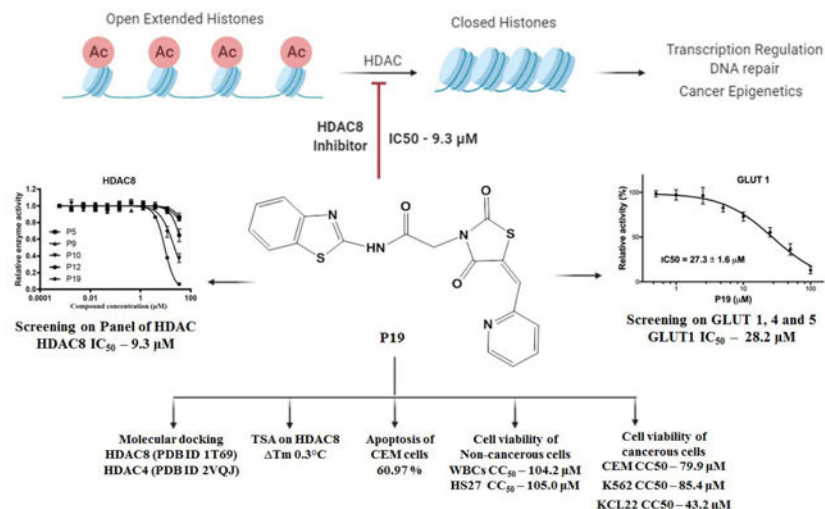
**Publisher's Disclaimer:** This is a PDF file of an unedited manuscript that has been accepted for publication. As a service to our customers we are providing this early version of the manuscript. The manuscript will undergo copyediting, typesetting, and review of the resulting proof before it is published in its final form. Please note that during the production process errors may be discovered which could affect the content, and all legal disclaimers that apply to the journal pertain.

Declaration of interests

The authors declare that they have no known competing financial interests or personal relationships that could have appeared to influence the work reported in this paper.

derivatives, compound **P19** was most promising HDAC8 inhibitor and cytotoxic on leukemic cells. Thus, **P19** could serve as a lead for further development of optimized molecules with enhanced selectivity and potency.

## Graphical Abstract



## Keywords

N-substituted thiazolidinediones; HDAC; GLUT; Leukemia; Docking

## 1. Introduction

Epigenetics is the major contributor to cancer initiation, progression, and metastasis [1]. Histone modifications, a central epigenetics mechanism, include acetylation, methylation, phosphorylation, and many others. Histone acetylation unlocks chromatin and promotes gene transcription. Two enzymes control the acetylation of histones: histone acetyltransferases (HATs) and histone deacetylases (HDACs). Acetylation of lysine residues by HATs on histone tails leaves the chromatin structure intact and accessible and is responsible for transcription activation. In contrast, HDAC removes acetyl groups, leading to a more condensed chromatin structure, and, thus, repressing gene transcription [2]. HDACs are also involved in the regulation of cell differentiation, apoptosis, and cell cycle. Malignant cells have higher levels of HDACs compared with healthy cells, which leads to an abnormal histone acetylation pattern.

There are 18 human HDACs classified into four groups based on their structural homology: Class I comprised of HDAC 1–3 and 8, found in the nucleus; Class II comprised of HDAC 4–7, and 10, which are in the nucleus and cytoplasm; Class III comprised of Sirtuins (SIRT) 1–7, found in the nucleus, cytoplasm and/or mitochondria; and Class IV including the newly discovered HDAC 11. HDAC inhibitors approved by FDA for different types of cancer include: Vorinostat, Belinostat, Panobinostat, Romidepsin, and many others are in clinical studies [3–5]. Currently, FDA-approved HDAC inhibitors are generally pan-inhibitors that



target more than one HDAC isoform and are associated with severe side effects [6–8]. Hence, isoform-selective HDAC inhibitors with fewer side effects and enhanced potency efforts have become a significant research focus.

HDAC8 is one of the essential epigenetic player in cancer progression and overexpresses in different cancer types, including cancers of the colon, breast, lung, gastric, and pancreas, acute myeloid leukemia (AML), and acute lymphocytic leukemia (ALL). Upregulation of HDAC8 inhibited apoptosis and induced cancer cell proliferation [9–12]. Therefore, targeting HDAC8 could counteract cancer and combat the adverse effects associated with paninhibitors.

There is a big challenge to develop HDAC8-selective inhibitors, since the active site is largely conserved among HDACs in general and class I HDACs including HDAC8 in particular. Therefore, linear hydroxamate inhibitors like SAHA are rather unselective on HDAC isoenzymes. However, HDAC8 contains several structural characteristics that allowed the development of different types of inhibitors with selectivity for this enzyme. First of all, HDAC8 shows significantly higher structural flexibility around the binding pocket, particularly at the outer rim between L1-, L2- and L6-loops as well as at the bottom of the catalytic site at the transition to the acetate release channel. Furthermore, crystal structures of three distinct major conformations of HDAC8-ligand complexes demonstrate the extraordinary malleability of HDAC8 around the active site pocket. There is a transition between the closed (PDB-ID 1T69), a sub-open conformation with a second transient binding pocket (PDB-ID 1T64) and a wide-open protein structure (PDB-ID 1VKG) of HDAC8. These structural features have been exploited by a variety of HDAC-inhibitors with selectivity for HDAC8. Most reported isoenzyme selective HDAC8 inhibitors contain a hydroxamate group as zinc chelating warhead. The selectivity of hydroxamate inhibitors was recently attributed to their L-shape and binding to a subpocket between L1- and L6-loop at the outer rim of the active site pocket that is unique for HDAC8 [14]. The selectivity of other non-hydroxamate inhibitors was explained by the occupation of the transition area between the active site and the acetate release channel at the bottom of the conserved binding pocket [17]. This binding mode is also proposed for recently discovered non-hydroxamate inhibitors with benzothiazine scaffold [18,19]. So called linkerless HDAC8 inhibitors (Fig. 1, compound 2) have been shown to induce the formation of a unique subpocket in HDAC8 by splitting F152 and M274 [20]. Additionally, the transient side pocket, which is observed in crystal structure of PDB-ID 1T64 (trichostatin A) would also be a good candidate for the design of selective HDAC8 inhibitors [21,22]. We have previously reported N-substituted-2,4-thiazolidinedione (TZD) derivative SRR2 as HDAC inhibitor (Fig. 2), wherein, TZD was at the tail portion of the compound, and docking revealed its interaction with zinc [11]. In our recent attempt to develop specific HDAC8 inhibitors, we designed naphthylidene TZD derivatives, with naphthalene as the linker, wherein compound 3h (Fig. 2) inhibited HDAC8 potently ( $IC_{50}$  - 6.7  $\mu$ M), though it was hypothesized that the TZD moiety would act as zinc binding group (ZBG), the docking analysis shown that the carboxylate group interacted with zinc, and TZD occupied the hydrophobic pocket [23]. Thus, based on our previously reported HDAC inhibitors, we designed novel HDAC8-selective inhibitors. The nature of CAP plays significant role to enhance the potency of compounds, there are variety of functionalities reported which could serve the purpose [24]

and thus, we placed variously substituted aryl/heteroaryl/fused heterocyclic aromatic rings at the CAP portion. The next essential moiety is the hydrophobic linker which could be linear or cyclic [25,26], hence, similar to our previous HDAC inhibitor SRR2, we retained linear linker but reduced the length to actually see the difference in the activity (Fig. 2). The next part is ZBG, which is the essential game changer and could exert significant effects on the inhibitory activity of the compounds [27]. Thus, we retained N-substituted TZD moiety in the compound to gain HDAC inhibitory potential and attached it to the linker. Moreover, -CH=CH- functionality attached to ZBG were reported to show promising HDAC8 inhibitory activities, and some of them are currently under clinical investigations [24,28,29]. Therefore, similar to compound 3h, we attached TZD ring to pyridine ring with -CH=CH- which led to a completely novel ZBG, pyridin-2-ylmethylene TZD. Interestingly, the designing located the TZD ring at the end of the linker, which will help us to determine the effects of TZD on the activity. Also, this unique structural design of novel HDAC8 inhibitors with pyridin-2-ylmethylene TZD provided L-shape to the compounds and hence we expect them to show HDAC8 inhibitory potential.

Docking studies of the compounds at the active site of HDAC8 showed zinc binding interactions with the carbonyl group of the TZD ring or the nitrogen atom of the pyridine ring or both (supplementary file). Hence by placing the TZD ring centrally, we expected that these newly designed pyridin-2-ylmethylene TZD derivatives might exhibit potential HDAC8 inhibitory activity. Based on these considerations, in the present work, we designed and synthesized 25 novel compounds (**P1-P25**) and studied their *in-vitro* antiproliferative activity.

HDACs are overexpressed in different leukemia subtypes such as acute promyelocytic leukemia (APL) [9,30,31], neuroblastoma [32], and T-cell lymphoma [33]. HDACs overexpression leads to the deacetylation of histones. Increased histone deacetylation causes an increase in the rate of cell cycle and a decrease in the differentiation and apoptosis of leukemic cells. These processes could be important in the identification and treatment of leukemias. Moreover, as our selective HDAC8 inhibitors (naphthylidene TZDs) have proved their *in-vitro* antiproliferative potential in leukemic cells, we decided to evaluate these newly designed HDAC8 inhibitors in leukemic cell lines.

## 2. Results and Discussion

### 2.1. Chemistry

Scheme I illustrates the synthesis of compounds. Synthesis of final compounds **P1-P25** proceeded via four steps. The first step in the synthesis of variously substituted amides was as previously reported [23,34–37]. Substituted amines **1a-1y** were stirred overnight with chloroacetyl chloride in the presence of potassium carbonate ( $K_2CO_3$ ) and dichloromethane (DCM) as a solvent to produce **2a-2y**. The second step included Knoevenagel condensation of pyridine-2-carboxaldehyde **3** and 2,4-thiazolidinedione **4** in the presence of acetic acid and sodium acetate to yield intermediate **5**. By refluxing **5** with **2a-2y** in the presence of methanol did not produce **P1-P25**, so salt of **5** was synthesized in the third step by refluxing **5** with potassium hydroxide in the presence of ethanol to yield Knoevenagel salt i.e. **6**. In the final step, refluxing vigorously **6** and **2a-2y** led to the compounds of interest **P1-P25**.

Knoevenagel salt **6** was common for the synthesis of all the final compounds; therefore, it was synthesized in bulk. The purity of the final compounds **P1-P25** was >95% by HPLC. All the synthesized compounds were confirmed structurally by different methods viz. <sup>1</sup>H-NMR, <sup>13</sup>C-NMR, FTIR, UV Spectroscopy, and Mass Spectrometry (Supplementary file). The detailed synthesis procedure and other spectral observations are in the experimental section.

## 2.2. Biological evaluation

**2.2.1. *In-vitro* cytotoxicity assay**—To evaluate the cytotoxic potential of this series of compounds, we performed the Differential Nuclear Staining (DNS) assay after exposing human cancer cell lines to each compound for 48 h. The DNS assay is typically the first experiment for novel compounds because it provides simple and reliable measure of viability that is quicker/easier to obtain yet robust and comparable to what would be seen if the viability were assessed by flow cytometry. It uses two fluorescent nuclear stains, Hoechst 33342 and Propidium iodide (PI), to selectively label living and dead cells [38]. An initial screening of all 25 compounds, at 50  $\mu$ M concentration, was conducted on K-562, KCL-22, and CEM leukemia cells. Solutions of each compound were prepared in DMSO, and the desired concentration of each compound was added to cell-containing wells at a final concentration of 1% (v/v) DMSO. Six compounds demonstrated activity in previous biological analysis and considerable cell death in one or more cancer cell lines. These six compounds were selected and assessed with a concentration gradient of 100–0.5  $\mu$ M via secondary DNS assays on CEM, K-562, and KCL-22 to estimate their CC<sub>50</sub> values. Cytotoxicity is reported as CC<sub>50</sub> (cytotoxic concentration 50%, concentration of compound needed to kill 50% of the cell population) because in the DNS assay, living and dead cells are differentiated based on their membrane integrity, not on metabolic activity like the popular MTT assay. The CC<sub>50</sub> values were estimated by linear interpolation of the two concentrations nearest 50% cell death. Compounds **P8**, **P9**, **P10**, **P19**, and **P25** displayed CC<sub>50</sub> values in the mid-micromolar range (Table 1). Out of these six compounds, **P12** was the least cytotoxic and did not approach 50% cell death on any cell line at the concentrations used.

### 2.2.2. *In-vitro* HDAC enzyme inhibition assay

**2.2.2.1. Primary screening on HDAC4 and HDAC8:** To determine the HDAC inhibitory potential of the target compounds, we assessed all of them on two isoforms of HDAC viz. HDAC4 and HDAC8. These two isoforms were selected because they possess high deacetylation activity, and belong to two diverse classes of deacetylase: class I (HDAC 8) and class II (HDAC4). The potency and selectivity of the target compounds for the two HDAC isoforms were examined and compared.

The primary screening was done with 50  $\mu$ M concentration of **P1-P25** on HDAC4 and HDAC8. Percent relative activities for all compounds on both HDAC isoforms were determined (Fig. 3A, 3B, and Table 2). Only two compounds, **P5** and **P12**, showed HDAC4 inhibition, with IC<sub>50</sub> of 50  $\mu$ M (Fig. 3C). Interestingly, compounds **P10**, **P12**, and **P19** displayed moderate to good HDAC8 inhibition, with IC<sub>50</sub> values of 23  $\mu$ M, 47  $\mu$ M, and 9.3  $\mu$ M, respectively (Fig. 3D). Among all compounds, **P19** and **P10** were more selective on

HDAC8 over HDAC4, with HDAC8-IC<sub>50</sub> in the sub-micromolar range. The presence of the benzothiazole ring may be responsible for the more potent activity of **P19** on HDAC8; it was suggested that compounds incorporating the benzothiazole ring had good HDAC8 inhibition [39–43]. Thus, we assume that the benzothiazole ring contributed to the selectivity and activity of **P19** against HDAC8. The thermal shift assay (TSA) was performed to examine the effects of **P5**, **P9**, **P10**, **P12**, and **P19** binding to HDAC8 (Supplementary file - Fig. S5). Thermal shift data (T) suggested that the tested compounds did not confer significant stability to the protein; only compound **P19** had a weak stabilizing effect of about 0.3 °C.

**2.2.2.2. HDAC-profiling on a panel of HDACs (HDAC1–8):** In the primary screening on HDAC4 and HDAC8, compounds **P10**, **P12**, and **P19** were HDAC8 inhibitors (Table 2). **P10** and **P19**, the best HDAC8 inhibitors, were screened on a panel of HDACs (HDAC1–8) to establish if they were selective for HDAC8 (Table 3, Fig. 4). Testing **P10** and **P19** on a panel of HDACs revealed that **P10** inhibited multiple HDAC isoforms such as HDAC2, HDAC5, HDAC6, and HDAC8 in mid-micromolar range. In contrast, **P19** displayed HDAC8 inhibition with IC<sub>50</sub> in single-digit micromolar range as compared to other HDACs.

**2.2.3. GLUT 1, 4, and 5 inhibition assay—**The therapeutic effects of HDAC inhibitors stem from their capacity to alter gene expression and acetylation status of histones. Lately, substantial attention has focused on the ability of HDAC inhibitors to modify cellular metabolism; they inhibit glucose transporter 1 (GLUT1)-mediated glucose transport by downregulating GLUT1 expression [44,45]. This downregulation has been linked to a time-dependent decrease in glucose uptake in multiple myeloma cell lines (H929).

Compounds containing N-substituted TZD have been reported as GLUT1 inhibitors [46,47]. Our designed HDAC inhibitors (**P1-P25**) also hold N-substituted TZD and have exhibited HDAC8 inhibitory activity. Considering that HDAC inhibitors also interfere with GLUT1 expression and to assess their inhibitory potential on GLUTs, we screened all target compounds (**P1-P25**) for their effect on the transport activity of GLUT 1, 4, and 5 at 50 μM concentration (Fig. 5). For the transport assay, we used the GLUT-specific systems provided by the hexose transport null (*hxt<sup>0</sup>*) yeast strains engineered to express a particular human GLUT [48,49]; the only glucose or fructose uptake in these cells is through the recombinant human GLUTs.

Among all tested compounds, **P19** showed significant inhibition of GLUT1 (IC<sub>50</sub> = 28.2 ± 1.8 μM) and remained ineffective on the other two GLUT isoforms (Fig. 5). The rest of the compounds exhibited >50% relative activity at 50 μM concentration on all three GLUT members. Thus, **P19** was selective for HDAC8, among other HDAC isoforms, and was also specific for GLUT1, compared with GLUT1 and GLUT4. Moreover, our studies also suggest that cancers depending on GLUT1 for the production of energy and glycolysis might be tackled with HDAC inhibitors.

**2.2.4. Apoptosis studies by flow cytometry—**HDAC8 inhibitors have been found to induce apoptosis in solid and hematological cancer cells through various mechanisms. PCI-34051, a HDAC8 inhibitor have caused apoptosis in T-cell lymphoma cells by caspase

activation [7]. In gastric carcinoma cells, HDAC8 inhibition induced apoptosis facilitated by Bcl-2-modifying factor (BMF) and STAT3 [50]. Selective HDAC8 inhibitors have been found to cause dose-dependent selective apoptosis of CD34<sup>+</sup> leukemic stem cells and progenitor cells [7]. Our recently reported selective HDAC8 inhibitor has found to induce apoptosis in CEM, lymphoid leukemia CEM cell line [23]. Also, the up-regulation of HDAC8 have been found to inhibit apoptosis in hepatocellular carcinoma, indicating a role of HDAC8 inhibitors in induction of apoptosis [51]. Thus HDAC8 inhibitors have ability to cause apoptotic cell death, and hence to determine if the cytotoxicity was induced by **P10** and **P19** was apoptosis-related, we stained CEM cells with annexin V-FITC/PI and determined by flow cytometry the percent of cell apoptosis. Incubation of the CEM cells with **P10** and **P19** at their CC<sub>50</sub> concentrations caused an increase in the cell population in the apoptotic region compared with the control. In **P10**-treated cells, the percent of apoptotic cells was 55.19%, and live cells were only 29.89% when compared with that of control (Fig. 6A, 6C), which was 92.15% (Supplementary file - Fig. S6). **P19**-treated cells had 60.97% apoptotic cells; the living cells were only 30.86% compared with the control (Fig. 6B, 6C). Thus, as seen with reported HDAC8 inhibitors, compounds **P10** and **P19** can induce apoptotic death in the CEM cell line.

#### 2.2.5. Cell viability of P19-treated non-cancerous cells by MTT and DNS assays

—To ascertain the cytotoxicity of **P19** on normal and cancerous cells, we performed both MTT and DNS assays to compare their cytotoxicity concentration 50% by two different assays. We determined the cell viability of CEM cell lines and normal white blood cells (WBCs) with the MTT assay and that of CEM cell lines and normal human fibroblast (HS27) with the DNS assay (Supplementary file - Fig. S7). By MTT assay CC<sub>50</sub> of **P19** in normal WBCs was 104.2 μM, whereas, in CEM cells it was 11.91 μM (Table 4). DNS assay of HS27 showed that CC<sub>50</sub> of **P19** was 105.0 μM, and of CEM cells was 79.9 μM. Thus, compound **P19** could be safe for non-cancerous cells.

### 2.3. In-silico studies

**2.3.1. Molecular docking**—Flexible docking was performed with MOE software, using the crystal structures of HDAC8 (PDB ID 1T69) and HDAC4 (PDB ID 2VQJ). To validate the docking protocol, we determined the Root Mean Square Deviation (RMSD) between the crystal pose vs. the docked pose. The corresponding alkyl chains with zinc-chelating hydroxamate warhead of SAHA bound to HDAC8 superpose excellently within the binding pocket of HDAC8 with an RMSD value of 0.9 Å. Similarly, the buried thiophene linker and trifluoromethyl warhead of the redocked ligand in PDB ID 2VQJ showed an excellent RMSD value of 0.6 Å with respect to the crystal structure. The aromatic head groups of SAHA in complex with HDAC8 and the trifluoromethylketone ligand in HDAC4 reach out of the binding pocket were freely rotatable and therefore not considered for the calculation of RMSD. **P19** showed the highest experimental activity and the best docking score against HDAC8 (Tables 5). The 2D and 3D ligand-enzyme interaction diagrams illustrating the major interactions of the representative compound **P19** with amino acid residue at the active site of HDAC8 are shown in Fig. 7 (Other images in supplementary file). **P19** fitted well in the binding pocket of HDAC8 forming hydrogen bonds with the backbone oxygen of G151 and to the side chain of Y306 at the bottom of the active site. Interestingly, **P19** interacted

with the catalytic zinc ion through carboxamide carbonyl oxygen and not with our hypothesized TZD carbonyl oxygen. The relatively bulky benzothiazole moiety of **P19** was inserted between A37 and W141 and protruded into the acetate release channel. The amino acids of the canonical binding tunnel were highly conserved among all classes of zinc dependent HDACs with one major exception: Y306 in class I HDAC8, which was pivotal for the enzyme mechanism, was exchanged against a histidine that was swung away from the catalytic site. However, the amino acids flanking the acetate release channel differed widely, e.g. W141 is unique for HDAC8. Since the bulky benzothiazole group of **P19** fitted perfectly into the specific acetate release channel of HDAC8, we hypothesized that this feature together with the hydrogen bond between **P19** and Y306, which was not present in HDAC4, could be the reason for the observed inhibitory activity and selectivity towards HDAC8 (Table 2). To visualize the structural differences between HDAC4 and HDAC8, we superposed the best-scoring docking poses of **P19** within the crystal structures of both enzymes (Fig. 7C). At first glance, the corresponding conserved amino acids of the binding pockets in HDAC8 and HDAC4 (F208/F227, F152/F168, H142/H158, H143/H159, respectively) showed no perfect overlap but rather significant shifts. Also it was seen that H332, which corresponds to Y306 in HDAC8, was flipped away from the catalytic site opening a selectivity side pocket that is characteristic to all class IIa HDACs. Therefore, H332, unlike Y306 in HDAC8, was not able to form interactions with **P19**. Most strikingly, HDAC4 did not show an open subpocket at the transition area to the acetate release channel like HDAC8. Consequently, the benzothiazole moiety of **P19**, which protruded into the acetate release channel of HDAC8, would clash with the surface of HDAC4 in a similar docking pose. The unbeneficial docking pose of **P19** at the upper surface of the binding pocket of HDAC4 was in agreement with the observed absent activity against this enzyme (Fig. 7C).

**2.3.2. SwissADME predictions**—The therapeutic action of a compound depends on it reaching the desired target site in the body at sufficient concentration described by its ADME (absorption, distribution, metabolism, and excretion) properties. Lipinski's rule-of-five outlines the probability of a drug to be orally active (i.e., the drug-likeness) and the correlation between the pharmacokinetic and physicochemical parameters. SwissADME has computational models that give fast yet robust predictive data about the physicochemical properties, pharmacokinetics, and drug-likeness along with user-friendly submission and straightforward result interpretation [52]. We used it to predict the physicochemical properties and bioavailability of synthesized compounds **P1-P25**. All 25 compounds obey Lipinski's rule of five (Table 6) with no violations, indicating their drug-likeness. All compounds have an acceptable range of clogP value of 2.00–5.00. Topological polar surface area (TPSA) is a physicochemical descriptor of the surface sum of all the polar atoms in the molecules, and the acceptable region for suitable absorption is between 20 and 130 Å<sup>2</sup>. Four compounds exhibited higher TPSA than 130 Å<sup>2</sup>, and the rest fell in the acceptable zone. Compounds solubility ranged from soluble to moderately soluble. The bioavailability score for all compounds was 0.55. In summary, the compounds had drug-likeness and were good candidates for passive oral absorption.

BOILED-Egg is an intrinsic model in SwissADME for predicting brain access or passage of the brain blood barriers (BBB) and passive gastrointestinal absorption (HIA). It is a proficient method that depends on two descriptors WLOGP (lipophilicity) and TPSA (apparent polarity). The white region of BOILED-Egg represents a high probability of passive absorption by the gastrointestinal tract, and the yellow region represents a strong possibility of reaching the brain. Whether the candidate is (PGP+) or not (PGP-) a substrate for P-gp, a multidrug resistance efflux pump responsible for drug clearing, is indicated by points colored red or blue, respectively [53].

BOILED-Egg was plotted for all the 25 compounds (Supplementary file - Fig. S1). None of them were in the yellow region, implying that they may not penetrate the brain. Twenty-one compounds containing the substituted phenyl rings were in the white region, indicating proper absorption. Four compounds (**P16**, **P18**, **P20**, and **P21**) were outside the egg, suggesting that they neither absorb nor cross the BBB and may have poor bioavailability. These four compounds are substituted five/six-membered aromatic/ heteroaromatic or fused ring viz. nitrophenyl (**P16**), methylisoxazole (**P18**), thiazole (**P20**), or 5-methylthiazole (**P21**). Accordingly, the biological screening of the compounds showed that these four compounds were inactive or nearly inactive at the receptor site.

**2.3.3. Computation of toxic hazards**—Checking the alerts for Cramer rules and cytotoxicity by P450-mediated drug metabolism for the compound **P19** resulted in high Class III and four sites of metabolism (Supplementary file - Fig. S2 and Fig. S3). Verbose explanation stated that, “Compound has heterocyclic ring with complex substituents (Q7 & 11)”, which could be the reason for being under Class III, and that there are four sites of CYP450-mediated metabolism viz. S-oxidation, N-oxidation, and aromatic hydroxylation. Even though **P19** is under Class III and predicted to display toxicity, the possible sites of metabolism by CYP450 could reduce the toxicity by enhancing the compound metabolism.

### 3. Materials and methods

#### 3.1. *In-silico* studies

**3.1.1. Molecular docking**—Molecular docking of the target compounds in the HDAC8 crystal structure was performed with MOE 2019 software (Chemical Computing Group ULC, Canada). The crystal structures of HDAC8 (PDB-ID: 1T69) and HDAC4 (PDB-ID: 2VQJ) were obtained from RCSB Protein Data Bank. The PDB-files were subjected to structure preparation including 3D-protonation for subsequent docking. The partial charges of all protein and ligand atoms were calculated using the implemented Amber14 force field. Molecular docking was performed choosing the triangle matcher for placement of the ligand in the binding site and ranked with the London dG scoring function. The best 30 poses were passed to the refinement and energy minimization in the pocket using the induced fit method and then rescored with the GBVI/WSA dG scoring function.

**3.1.2. SwissADME predictions tool**—SwissADME is a reliable free online tool [52] that predicts the physicochemical properties of the compounds. The bioavailability and pharmacokinetic parameters of any synthetic compound is obtained by inputting its structure on the website <http://www.swissadme.ch/index.php#>.

**3.1.3. Computation of toxic hazards**—Toxtree is a free, user-friendly, and flexible open-source application tool, developed by IDEA Consult Ltd. (Sofia, Bulgaria). It assesses the toxic hazards of a compound by applying a decision tree approach. Toxtree decision tree can be used for applying the Cramer rules, Cramer rules with extensions, Verhaar scheme, Skin irritation and corrosion prediction, eye irritation, and corrosion prediction, Benigni/Bossa rule base (for mutagenicity and carcinogenicity), Michael Acceptors, Skin sensitization alerts, START biodegradability, cytochrome P450-mediated drug metabolism, DNA binding alerts, protein binding alerts etc. It can evaluate the Threshold of Toxicological Concern (TTC) of the material or their potential toxicity. Cramer rules predict toxicological dangers of the molecules when administered orally. In this, molecules are grouped into three classes based on a decision tree. This involves 33 structural rules, and places the assessed molecules into one of three classes: Class I (Low) molecules with low oral toxicity (simple chemical structures with efficient modes of metabolism); Class II (Intermediate) molecules with intermediate toxicity; and Class III (High) molecules that have reactive functional groups and possible significant toxicity. SMARTCyp is a reactivity model that estimates the molecule site(s) labile to metabolism by Cytochromes P450 isoform 3A4 [54,55].

### 3.2. Chemistry

All reagents, solvents, and chemicals were purchased from commercial sources viz. Sigma Aldrich, S.D. Fine Chem. Ltd., Himedia, and VWR. Reactions were monitored by Thin Layer Chromatography (TLC) using Merck precoated silica gel 60 F-254 plates under short wavelength UV-light (254nm) to detect the UV absorbing spots to ensure the completion of the reaction and also the purity of compounds at each step. All intermediates were purified by recrystallization with suitable solvents such as chloroform, methanol, ethanol, etc. The final compounds were purified by either recrystallization or column chromatography. Column chromatography was performed on silica gel 60 (60 to 120 mesh) with combinations of suitable solvents. The purity of all final products (95%) was determined using an Agilent 1200 high-performance liquid chromatography (HPLC) system; software-EZ chrome Elite. The chromatographic column was HemochromIntsil A31 C18 5U 150 mm × 4.6 mm Sn-B180127, with detection at 300 nm. UV-visible detector was used with the flow rate of 1 mL/min. The oven temperature was 30°C; gradient elution with a run time of 10 min using Methanol: Formic Acid (1%) (Formic acid: in 1000 mL double distilled water 1mL formic acid was added) in 80:20 ratio. The melting points of all the intermediates and final compounds were determined with VEEGO, MODEL: VMP-DS Melting Point apparatus.

Structural characterization of the intermediates was done by FTIR and <sup>1</sup>H-NMR, and of the final step products by FTIR, <sup>1</sup>H-NMR, <sup>13</sup>C-NMR, and mass spectrometry. IR was recorded with JASCO FT/IR- 4100 typeA spectrometer using direct sampling technique. <sup>1</sup>H-NMR spectra were recorded on Bruker Avance 400 MHz Spectrometer using DMSO-d<sub>6</sub> as solvent. <sup>13</sup>C-NMR was recorded on a Bruker Avance Spectrometer at 100 MHz using DMSO-d<sub>6</sub> as solvent. All shifts of <sup>1</sup>H NMR are in δ (ppm) units relative to the signals for the solvent DMSO (δ- 2.50 ppm). All coupling constants (J values) are in hertz (Hz). NMR abbreviations are: s, singlet; d, doublet; t, triplet; q, quartet; m, multiplet; and dd, doublet of doublets. The mass spectrum was recorded on LC-MS Agilent Technologies 1260 Infinity



instrument. To determine the absorption of synthesized compounds at different wavelengths, we performed UV Spectroscopy (Supplementary file).

The 25 new derivatives of pyridyl containing N-substituted TZDs were synthesized as shown in Scheme 1. Various substituted chloroacetylated amides (**2a-2y**) were prepared as previously reported [34–37,56,57]. All chloroacetylated amides were purified by recrystallization with suitable solvents and then used for the next reaction steps. The compound 5-(pyridin-2-ylmethylene)thiazolidine-2,4-dione (**5**) was synthesized by following the Knoevenagel condensation. Synthesis of potassium salt of (**5**) was done by refluxing potassium hydroxide in ethanol to produce potassium-2,4-dioxo-5-(pyridin-2-ylmethylene)thiazolidin-3-ide (**6**). The substituted chloroacetylated amides (**2a-2y**) and **6** were added to methanol (10 ml) in round-bottom flask. This solution was then refluxed and after completion the reaction was stopped and the mixture was cooled. The solid precipitated out was collected and purified to produce the final products.

**3.2.1. Synthesis of 5-(pyridine-2-ylmethylene)thiazolidine-2,4-dione (5):** 2-Pyridinecarboxaldehyde **3** (5 ml, 0.046 mol), thiazolidine-2,4-dione (**4**) (5 g, 0.0427 mol) and sodium acetate (3 g, 0.036 mol) were added to acetic acid (5 ml) and refluxed for 5 h. The reaction mixture was then cooled to RT and the precipitated solid was collected by filtering under vacuum, washed several times with water, and dried under RT. Crude solid was purified by recrystallization from an appropriate solvent to obtain brown shiny crystals (**5**). Yield 9 g (90%); Brown shiny crystal; M.P. 232 °C (Charred); IR (cm<sup>-1</sup>): 3136, 1737, 1614. <sup>1</sup>H-NMR (400 MHz, DMSO-d<sub>6</sub>, δ ppm) 7.41–7.42 (m, 1H), 7.80–7.84 (m, 2H), 7.90–7.94 (m, 1H), 8.73–8.74 (m, 1H), 12.40 (s, 1H).

**3.2.2. Synthesis of potassium-2,4-dioxo-5-(pyridine-2-ylmethylene)thiazolidin-3-ide (6):** To the solution of potassium hydroxide (5 g, 0.089 mol) in ethanol (25 ml), (**5**) (10 g, 0.048 mol) was added with stirring, and the reaction mixture was refluxed for 3 h. The fine solid obtained after cooling the reaction mixture was collected by filtering and washed with cold ethanol to obtain potassium salt **6**. Yield 10 g (66%); Light brown color solid; M.P. 292.4 °C (Charred); IR (cm<sup>-1</sup>): 3037, 1626, 1662. <sup>1</sup>H-NMR (400 MHz, DMSO-d<sub>6</sub>, δ ppm). 7.18–7.21 (m, 1H), 7.26 (s, 1H), 7.52 (d, J=8Hz, 1H), 7.74–7.78 (m, 1H), 8.61–8.62 (m, 1H).

**3.2.3. Synthesis of N-(substitutedaryl/heteroaryl)-2-(2,4-dioxo-5-(pyridin-2-ylmethylene)thiazolidin-3-yl)acetamide (P1-P25):** Intermediate **6** (1 g, 0.004 mol) and variously substituted amides (**2a-2y**) (0.004 mol) were dispensed together in a round-bottom flask along with 10 mL methanol. This mixture was refluxed and the reaction was monitored for completion by TLC using appropriate mobile phase of Hexane: Ethyl acetate (1:1). After 5–6 h the reaction was stopped and the mixture was cooled. The precipitated solid was collected by filtering under vacuum and purified by recrystallization (chloroform: methanol, 2:1) or column chromatography (hexane: ethyl acetate, 1.5: 0.5) with an appropriate solvent to give the corresponding final products (**P1-P25**).

**3.2.3.1. 2-(2,4-dioxo-5-(pyridin-2-ylmethylene)thiazolidin-3-yl)-N-phenylacetamide (P1):** Yield 0.9 g (56%); M.P. 282.8 °C (Charred); buff white color solid; IR (cm<sup>-1</sup>): 3267,

1739, 1656, 1683, 1620, 1599, 1388.  $^1\text{H-NMR}$  (400 MHz,  $\text{DMSO-d}_6$ ,  $\delta$  ppm) 4.50 (s, 2H), 7.08 (s, 1H), 7.32 (s, 2H), 7.46 (s, 1H), 7.55 (s, 2H), 7.91–8.00 (m, 3H), 8.79 (s, 1H), 10.39 (s, 1H).  $^{13}\text{C-NMR}$  (400 MHz,  $\text{DMSO-d}_6$ ): 43.355, 119.175, 123.714, 124.264, 125.266, 128.002, 128.854, 129.461, 137.635, 138.320, 149.342, 151.035, 163.880, 165.544, 170.979. UV- Spectrum (10 ppm,  $\lambda_{\text{max}}$  - 331.8 nm). Theoretical mass: 339, LC-MS (m/z, I %): 338 [(M-H)<sup>+</sup>, 100%]. HPLC Purity: % Area 98.32, RT 2.99 mins.

**3.2.3.2. 2-(2,4-dioxo-5-(pyridin-2-ylmethylene)thiazolidin-3-yl)-N-(2-**

**fluorophenyl)acetamide (P2):** Yield 1 g (60%); M.P. 293.9 °C (Charred); buff white color solid; IR ( $\text{cm}^{-1}$ ): 3263, 1737, 1666, 1686, 1616, 1546, 1386, 1298.  $^1\text{H-NMR}$  (400 MHz,  $\text{DMSO-d}_6$ ,  $\delta$  ppm) 4.58 (s, 2H), 7.16–7.18 (m, 2H), 7.25–7.30 (m, 1H), 7.46 (t, J= 5.8 Hz, 1H), 7.85–7.91 (m, 2H), 7.94–8.00 (m, 2H), 8.78 (d, J= 4 Hz, 1H), 10.26 (s, 1H).  $^{13}\text{C-NMR}$  (400 MHz,  $\text{DMSO-d}_6$ ): 43.192, 115.476, 115.669, 123.862, 124.274, 124.476, 125.250, 128.007, 129.472, 137.645, 149.347, 151.028, 164.503, 165.510, 170.955. UV- Spectrum (10 ppm,  $\lambda_{\text{max}}$  - 331.7 nm). Theoretical mass: 357, LC-MS (m/z, I %): 355.9 [(M-2H)<sup>+</sup>, 100%]. HPLC Purity: % Area 97.54, RT 2.97 mins.

**3.2.3.3. 2-(2,4-dioxo-5-(pyridin-2-ylmethylene)thiazolidin-3-yl)-N-(3-**

**fluorophenyl)acetamide (P3):** Yield 0.85 g (75%); M.P. 250.4 °C (Charred); buff color solid; IR ( $\text{cm}^{-1}$ ): 3306, 1739, 1685, 1666, 1602, 1543, 1388, 1325.  $^1\text{H-NMR}$  (400 MHz,  $\text{DMSO-d}_6$ ,  $\delta$  ppm) 4.52 (s, 2H), 6.916 (t, J= 7.6 Hz, 1H), 7.27–7.29 (m, 1H), 7.35 (q, J= 13 Hz, 1H), 7.44–7.53 (m, 2H), 7.89–7.98 (m, 2H), 8.00 (s, 1H), 8.78 (d, J= 3.2 Hz, 1H), 10.63 (s, 1H).  $^{13}\text{C-NMR}$  (400 MHz,  $\text{DMSO-d}_6$ ): 43.372, 105.891, 106.153, 110.118, 110.326, 114.943, 124.283, 125.186, 128.019, 129.542, 130.519, 130.612, 137.638, 139.928, 140.039, 149.341, 151.006, 160.897, 163.298, 164.251, 164.334, 165.500, 170.962. UV- Spectrum (10 ppm,  $\lambda_{\text{max}}$  - 331.8 nm). Theoretical mass: 357, LC-MS (m/z, I %): 356.1 [(M-H)<sup>+</sup>, 100%]. HPLC Purity: % Area 97.28, RT 3.34 mins.

**3.2.3.4. N-(4-bromo-2-fluorophenyl)-2-(2,4-dioxo-5-(pyridin-2-**

**ylmethylene)thiazolidin-3-yl)acetamide (P4):** Yield 0.6 g (52%); M.P. charred above 300 °C; light gray color solid; IR ( $\text{cm}^{-1}$ ): 3306, 1737, 1672, 1597, 1602, 1543, 1386, 1213, 686.  $^1\text{H-NMR}$  (400 MHz,  $\text{DMSO-d}_6$ ,  $\delta$  ppm) 4.58 (s, 2H), 7.38 (d, J= 8.4 Hz, 1H), 7.46 (q, J= 6.6 Hz, 1H), 7.60–7.63 (dd, J= 10.6 Hz, 1H), 7.83–7.86 (m, 1H), 7.87–7.91 (m, 1H), 7.94–7.96 (m, 1H), 7.98 (s, 1H), 8.78 (d, J= 4.4 Hz, 1H), 10.33 (s, 1H).  $^{13}\text{C-NMR}$  (400 MHz,  $\text{DMSO-d}_6$ ): 43.214, 118.813, 119.041, 124.287, 125.034, 125.204, 127.583, 128.014, 129.517, 137.649, 149.344, 151.009, 164.661, 165.478, 170.938. UV- Spectrum (10 ppm,  $\lambda_{\text{max}}$  - 331.8 nm). Theoretical mass: 434, LC-MS (m/z, I %): 433.9 [(M-H)<sup>+</sup>, 100%], 435.9 [(M-H)<sup>+</sup>, 90%]. HPLC Purity: % Area 97.72, RT 4.4 mins.

**3.2.3.5. N-(2,4-difluorophenyl)-2-(2,4-dioxo-5-(pyridin-2-ylmethylene)thiazolidin-3-**

**yl)acetamide (P5):** Yield 0.95 g (77%); M.P. 284.9 °C (Charred); white color solid; IR ( $\text{cm}^{-1}$ ): 3273, 1737, 1672, 1552, 1614, 1505, 1384, 1222.  $^1\text{H-NMR}$  (400 MHz,  $\text{DMSO-d}_6$ ,  $\delta$  ppm) 4.55 (s, 2H), 7.06 (t, J= 7.8 Hz, 1H), 7.31 (t, J= 8.8 Hz, 1H), 7.45 (t, J= 5.8 Hz, 1H), 7.77–7.80 (q, J= 11 Hz, 1H), 7.87–7.89 (m, 1H), 7.93–7.95 (m, 1H), 7.98 (s, 1H), 8.77 (d, J= 3.6 Hz, 1H), 10.27 (s, 1H).  $^{13}\text{C-NMR}$  (400 MHz,  $\text{DMSO-d}_6$ ): 43.056, 104.201, 111.350,

124.296, 125.223, 127.983, 129.481, 137.648, 149.334, 150.968, 164.590, 165.493, 170.981. UV- Spectrum (10 ppm,  $\lambda_{\max}$  - 331.8 nm). Theoretical mass: 375, LC-MS (m/z, I %): 374 [(M-H)<sup>+</sup>, 100%]. HPLC Purity: % Area 95.82, RT 3.31 mins.

**3.2.3.6. 2-(2,4-dioxo-5-(pyridin-2-ylmethylene)thiazolidin-3-yl)-N-(3-(trifluoromethyl)phenyl)acetamide (P6):** Yield 1.2 g (80%); M.P. 244.5 °C (Charred); buff white color solid; IR (cm<sup>-1</sup>): 3273, 1741, 1685, 1666, 1616, 1545, 1390, 1214. <sup>1</sup>H-NMR (400 MHz, DMSO-d<sub>6</sub>,  $\delta$  ppm) 4.54 (s, 2H), 7.44 (t, J= 8.8 Hz, 2H), 7.58 (t, J= 8 Hz, 1H), 7.72–7.74 (m, 1H), 7.88–7.90 (m, 1H), 7.94–7.96 (m, 1H), 7.99 (s, 1H), 8.03 (s, 1H), 8.78 (d, J= 4 Hz, 1H), 10.76 (s, 1H). <sup>13</sup>C-NMR (400 MHz, DMSO-d<sub>6</sub>): 43.365, 115.260, 120.123, 122.800, 124.305, 125.176, 128.004, 129.560, 130.177, 137.649, 138.993, 149.338, 150.967, 164.631, 165.506, 170.997. UV- Spectrum (10 ppm,  $\lambda_{\max}$  - 332.4 nm). Theoretical mass: 407, LC-MS (m/z, I %): 407 [(M+)<sup>+</sup>, 100%]. HPLC Purity: % Area 97.59, RT 2.98 mins.

**3.2.3.7. N-(4-chloro-2-(trifluoromethyl)phenyl)-2-(2,4-dioxo-5-(pyridin-2-ylmethylene)thiazolidin-3-yl)acetamide (P7):** Yield 0.8 g (64%); M.P. charred above 300 °C; cream color solid; IR (cm<sup>-1</sup>): 3217, 1743, 1620, 1668, 1608, 1537, 1309, 1282, 779. <sup>1</sup>H-NMR (400 MHz, DMSO-d<sub>6</sub>,  $\delta$  ppm) 4.52 (s, 2H), 7.45 (t, J= 5.8 Hz, 1H), 7.49–7.51 (m, 1H), 7.76–7.78 (m, 1H), 7.82 (s, 1H), 7.87–7.89 (m, 1H), 7.93–7.95 (m, 1H), 7.98 (s, 1H), 8.77 (d, J= 3.6 Hz, 1H), 10.18 (s, 1H). <sup>13</sup>C-NMR (400 MHz, DMSO-d<sub>6</sub>): 43.416, 113.673, 117.503, 119.575, 119.948, 121.114, 123.837, 126.396, 131.352, 131.797, 133.114, 133.448, 147.955, 149.093, 164.934, 165.442, 167.703. UV- Spectrum (10 ppm,  $\lambda_{\max}$  - 332 nm). Theoretical mass: 441, LC-MS (m/z, I %): 439.9 [(M-H)<sup>+</sup>, 100%]. HPLC Purity: % Area 97.99, RT 3.99 mins.

**3.2.3.8. N-(3,4-dichlorophenyl)-2-(2,4-dioxo-5-(pyridin-2-ylmethylene)thiazolidin-3-yl)acetamide (P8):** Yield 1.1 g (84%); M.P. 269.4 °C (Charred); white color solid; IR (cm<sup>-1</sup>): 3336, 1737, 1668, 1620, 1585, 1531, 1325, 779. <sup>1</sup>H-NMR (400 MHz, DMSO-d<sub>6</sub>,  $\delta$  ppm) 4.51 (s, 2H), 7.45 (d, J= 6.4 Hz, 2H), 7.55–7.58 (m, 1H), 7.87–7.89 (m, 2H), 7.93–7.97 (m, 2H), 8.77 (s, 1H), 10.72 (s, 1H). <sup>13</sup>C-NMR (400 MHz, DMSO-d<sub>6</sub>): 43.349, 119.285, 120.487, 124.294, 125.143, 125.316, 127.996, 129.569, 130.791, 131.124, 137.629, 138.280, 149.320, 150.946, 164.534, 165.475, 170.982. UV- Spectrum (10 ppm,  $\lambda_{\max}$  - 332.2 nm). Theoretical mass: 406, LC-MS (m/z, I %): 405.9 [(M-H)<sup>+</sup>, 100%]. HPLC Purity: % Area 98.68, RT 3.44 mins.

**3.2.3.9. N-(2-chloro-5-(trifluoromethyl)phenyl)-2-(2,4-dioxo-5-(pyridin-2-ylmethylene)thiazolidin-3-yl)acetamide (P9):** Yield 0.5 g (45%); M.P. 282.6 °C (Charred); white color solid; IR (cm<sup>-1</sup>): 3306, 1741, 1676, 1618, 1583, 1548, 1327, 1130, 781. <sup>1</sup>H-NMR (400 MHz, DMSO-d<sub>6</sub>,  $\delta$  ppm) 4.65 (s, 2H), 7.46 (t, J= 6 Hz, 1H), 7.57 (d, J= 8.4 Hz, 1H), 7.77 (d, J= 8.4 Hz, 1H), 7.88–7.90 (m, 1H), 7.94–7.98 (m, 1H), 7.99 (s, 1H), 8.14 (s, 1H), 8.77 (d, J= 4 Hz, 1H), 10.35 (s, 1H). <sup>13</sup>C-NMR (400 MHz, DMSO-d<sub>6</sub>): 43.222, 121.459, 122.823, 124.317, 125.155, 128.009, 129.566, 130.908, 135.101, 137.658, 149.345, 150.957, 165.307, 165.477, 170.974. UV- Spectrum (10 ppm,  $\lambda_{\max}$  - 331.8 nm).

Theoretical mass: 441, LC-MS (m/z, I %): 439.9 [(M-H)<sup>+</sup>, 100%]. HPLC Purity: % Area 98.70, RT 4.48 mins.

**3.2.3.10. N-(1,5-dimethyl-3-oxo-2-phenyl-2,3-dihydro-1H-pyrazol-4-yl)-2-(2,4-dioxo-5-(pyridin-2-ylmethylene)thiazolidin-3-yl)acetamide (P10):** Yield 0.93 g (73%); M.P. 254.6 °C (Charred); light yellow color solid; IR (cm<sup>-1</sup>): 3304, 3052, 1743, 1658, 1618, 1585, 1550, 1300. <sup>1</sup>H-NMR (400 MHz, DMSO-d<sub>6</sub>, δ ppm) 2.10 (s, 3H), 3.04 (s, 3H), 4.46 (s, 2H), 7.33 (d, J= 7.2 Hz, 3H), 7.34–7.51 (m, 3H), 7.86–7.88 (m, 1H), 7.93–7.84 (m, 1H), 7.97 (s, 1H), 8.76 (d, J= 3.2 Hz, 1H), 9.57 (s, 1H). <sup>13</sup>C-NMR (400 MHz, DMSO-d<sub>6</sub>): 11.024, 35.725, 42.835, 106.286, 123.804, 124.246, 125.357, 126.512, 127.948, 129.107, 129.331, 134.759, 137.625, 149.327, 151.012, 152.074, 161.452, 164.916, 165.520, 170.971. UV- Spectrum (10 ppm, λ<sub>max</sub> - 331.5 nm). Theoretical mass: 449, LC-MS (m/z, I %): 448.1 [(M-H)<sup>+</sup>, 100%]. HPLC Purity: % Area 97.32, RT 3.01 mins.

**3.2.3.11. 2-(2,4-dioxo-5-(pyridin-2-ylmethylene)thiazolidin-3-yl)-N-(4-fluorophenyl)acetamide (P11):** Yield 1 g (80%); M.P. 274.5 °C (Charred); buff white color solid; IR (cm<sup>-1</sup>): 3265, 1737, 1681, 16758, 1616, 1548, 1330, 1298. <sup>1</sup>H-NMR (400 MHz, DMSO-d<sub>6</sub>, δ ppm) 4.49 (s, 2H), 7.15 (t, J= 7.8 Hz, 2H), 7.45 (s, 1H), 7.56 (s, 2H), 7.88 (d, J= 7.2 Hz, 1H), 7.94 (d, J= 7.2 Hz, 1H), 7.98 (s, 1H), 8.78 (s, 1H), 10.46 (s, 1H). <sup>13</sup>C-NMR (400 MHz, DMSO-d<sub>6</sub>): 43.249, 115.319, 115.542, 121.033, 121.110, 124.276, 125.230, 127.981, 129.476, 134.648, 137.630, 149.326, 150.981, 157.026, 159.413, 163.871, 165.530, 171.008. UV- Spectrum (10 ppm, λ<sub>max</sub> - 332 nm). Theoretical mass: 357, LC-MS (m/z, I %): 356 [(M-H)<sup>+</sup>, 100%]. HPLC Purity: % Area 95.74, RT 3.14 mins.

**3.2.3.12. 2-(2,4-dioxo-5-(pyridin-2-ylmethylene)thiazolidin-3-yl)-N-(p-tolyl)acetamide (P12):** Yield 1.3 g (90%); M.P. 287.3 °C (Charred); white color solid; IR (cm<sup>-1</sup>): 3250, 3047, 1737, 1681, 1651, 1614, 1548, 1323. <sup>1</sup>H-NMR (400 MHz, DMSO-d<sub>6</sub>, δ ppm) 2.25 (s, 3H), 4.48 (s, 2H), 7.13 (d, J= 8.32 Hz, 2H), 7.42–7.48 (m, 3H), 7.91–7.93 (m, 1H), 7.95–7.99 (m, 1H), 8.01 (s, 1H), 8.79 (d, J= 4.96 Hz, 1H), 10.28 (s, 1H). <sup>13</sup>C-NMR (400 MHz, DMSO-d<sub>6</sub>): 43.803, 113.675, 117.543, 119.165, 119.565, 119.927, 129.214, 132.680, 135.822, 147.948, 149.116, 163.547, 165.083, 167.854. UV- Spectrum (10 ppm, λ<sub>max</sub> - 332.3 nm). Theoretical mass: 353, LC-MS (m/z, I %): 351.8 [(M-2H)<sup>+</sup>, 100%]. HPLC Purity: % Area 98.56, RT 4.48 mins.

**3.2.3.13. 2-(2,4-dioxo-5-(pyridin-2-ylmethylene)thiazolidin-3-yl)-N-(2-phenoxyphenyl)acetamide (P13):** Yield 0.75 g (80%); M.P. 212.3 °C (Charred); gray color solid; IR (cm<sup>-1</sup>): 3265, 1739, 1688, 1668, 1620, 1585, 1107, 1230, 1327. <sup>1</sup>H-NMR (400 MHz, DMSO-d<sub>6</sub>, δ ppm) 4.53 (s, 2H), 6.68 (s, 1H), 7.03 (d, J= 7.2 Hz, 2H), 7.10–7.18 (m, 3H), 7.39–7.97 (m, 3H), 7.87 (d, J= 6.8 Hz, 1H), 7.97 (s, 3H), 8.77 (s, 1H), 10.05 (s, 1H). <sup>13</sup>C-NMR (400 MHz, DMSO-d<sub>6</sub>): 43.255, 118.463, 118.660, 123.269, 123.561, 123.638, 124.268, 125.224, 125.288, 127.978, 128.952, 129.442, 129.950, 137.629, 147.401, 149.331, 150.989, 156.428, 164.419, 165.515, 170.963. UV- Spectrum (10 ppm, λ<sub>max</sub> - 331.7 nm). Theoretical mass: 431, LC-MS (m/z, I %): 430.1 [(M-H)<sup>+</sup>, 100%]. HPLC Purity: % Area 97.97, RT 3.34 mins.

**3.2.3.14. 2-(2,4-dioxo-5-(pyridin-2-ylmethylene)thiazolidin-3-yl)-N-(4-methoxyphenyl)acetamide (P14):** Yield 1.2 g (89%); M.P. 284.8 °C (Charred); buff white color solid; IR (cm<sup>-1</sup>): 3252, 1739, 1685, 1658, 1618, 1583, 1107, 1257, 1327. <sup>1</sup>H-NMR (400 MHz, DMSO-d<sub>6</sub>, δ ppm) 3.06 (s, 3H), 4.57 (s, 2H), 7.38 (d, J=8 Hz, 2H), 7.44 (d, J=5.6 Hz, 1H), 7.60 (d, J=10 Hz, 1H), 7.81–7.89 (m, 2H), 7.93–7.98 (m, 2H), 8.77 (d, J=3.2 Hz, 1H), 10.39 (s, 1H). <sup>13</sup>C-NMR (400 MHz, DMSO-d<sub>6</sub>): 43.179, 118.811, 119.033, 124.309, 125.023, 125.163, 127.550, 128.010, 129.531, 137.657, 149.341, 150.955, 151.978, 164.664, 165.482, 170.982. UV- Spectrum (10 ppm, λ<sub>max</sub> - 331.8 nm). Theoretical mass: 369, LC-MS (m/z, I %): 368.2 [(M-H)<sup>+</sup>, 100%]. HPLC Purity: % Area 97.11, RT 2.9 mins.

**3.2.3.15. N-(4-bromo-2,6-difluorophenyl)-2-(2,4-dioxo-5-(pyridin-2-ylmethylene)thiazolidin-3-yl)acetamide (P15):** Yield 0.8 g (70%); M.P. charred above 300 °C; buff white color solid; IR (cm<sup>-1</sup>): 3250, 1749, 1541, 1678, 1610, 1583, 1384, 1234, 779. <sup>1</sup>H-NMR (400 MHz, DMSO-d<sub>6</sub>, δ ppm) 4.52 (s, 2H), 7.44 (s, 2H), 7.57 (d, J= 5.6 Hz, 1H), 7.87–7.98 (m, 3H), 8.77 (s, 1H), 10.22 (s, 1H). <sup>13</sup>C-NMR (400 MHz, DMSO-d<sub>6</sub>): 42.668, 116.086, 124.295, 125.343, 127.979, 129.432, 137.665, 149.346, 151.612, 164.704, 165.383, 170.850. UV- Spectrum (10 ppm, λ<sub>max</sub> - 331.8 nm). Theoretical mass: 452, LC-MS (m/z, I %): 453.8 [(M-H)<sup>+</sup>, 100%], 452 [(M-H)<sup>+</sup>, 90%]. HPLC Purity: % Area 99.03, RT 2.94 mins.

**3.2.3.16. 2-(2,4-dioxo-5-(pyridin-2-ylmethylene)thiazolidin-3-yl)-N-(4-nitrophenyl)acetamide (P16):** Yield 0.55 g (40%); M.P. 289.4 °C (Charred); cream color solid; IR (cm<sup>-1</sup>): 3259, 1741, 1564, 1678, 1614, 1593, 1379, 1317. <sup>1</sup>H-NMR (400 MHz, DMSO-d<sub>6</sub>, δ ppm) 4.57 (s, 2H), 7.46 (t, J= 6 Hz, 1H), 7.79 (d, J= 8.8 Hz, 2H), 7.88–7.90 (m, 1H), 7.95 (m, 1H), 7.99 (s, 1H), 8.23 (d, J= 8.8 Hz, 2H), 8.78 (d, J= 4 Hz, 1H), 11.04 (s, 1H). <sup>13</sup>C-NMR (400 MHz, DMSO-d<sub>6</sub>): 43.500, 119.039, 124.344, 125.040, 125.086, 128.040, 129.649, 137.670, 142.604, 144.318, 149.346, 150.933, 165.019, 165.467, 170.983. UV- Spectrum (10 ppm, λ<sub>max</sub> - 332.5 nm). Theoretical mass: 384, LC-MS (m/z, I %): 383.1 [(M-H)<sup>+</sup>, 100%]. HPLC Purity: % Area 99.16, RT 3.81 mins.

**3.2.3.17. N-(3-chloro-4-methylphenyl)-2-(2,4-dioxo-5-(pyridin-2-ylmethylene)thiazolidin-3-yl)acetamide (P17):** Yield 1 g (83%); M.P. 273.5 °C (Charred); buff white color solid; IR (cm<sup>-1</sup>): 3246, 2949, 1737, 1581, 1656, 1614, 1579, 1388, 779. <sup>1</sup>H-NMR (400 MHz, DMSO-d<sub>6</sub>, δ ppm) 2.26 (s, 3H), 4.49 (s, 2H), 7.27–7.34 (q, J= 16.8 Hz, 2H), 7.45 (t, J= 6 Hz, 1H), 7.71 (s, 1H), 7.87–7.89 (m, 1H), 7.93–7.95 (m, 1H), 7.98 (s, 1H), 8.77 (d, J= 4 Hz, 1H), 10.52 (s, 1H). <sup>13</sup>C-NMR (400 MHz, DMSO-d<sub>6</sub>): 18.863, 43.303, 117.835, 119.192, 124.303, 125.186, 128.004, 129.513, 130.508, 131.320, 133.067, 137.330, 137.651, 149.341, 150.966, 164.114, 165.515, 171.005. UV- Spectrum (10 ppm, λ<sub>max</sub> - 332 nm). Theoretical mass: 387, LC-MS (m/z, I %): 386 [(M-H)<sup>+</sup>, 100%]. HPLC Purity: % Area 96.36, RT 4.68 mins.

**3.2.3.18. 2-(2,4-dioxo-5-(pyridin-2-ylmethylene)thiazolidin-3-yl)-N-(4-methylisoxazol-3-yl)acetamide (P18):** Yield 0.68 g (50%); M.P. 272.6 °C (Charred); buff white color solid; IR (cm<sup>-1</sup>): 3219, 2982, 1743, 1529, 1687, 1616, 1568, 1325. <sup>1</sup>H-NMR

(400 MHz, DMSO- $d_6$ ,  $\delta$  ppm) 2.36 (s, 3H), 4.51 (s, 2H), 6.55 (s, 1H), 7.45 (t,  $J$ = 6 Hz, 1H), 7.87–7.88 (m, 1H), 7.93–7.95 (m, 1H), 7.97 (s, 1H), 8.77 (d,  $J$ = 4.6 Hz, 1H), 11.40 (s, 1H).  $^{13}\text{C}$ -NMR (400 MHz, DMSO- $d_6$ ): 12.034, 43.053, 96.126, 124.300, 125.180, 127.993, 129.537, 137.641, 149.325, 150.944, 157.537, 164.506, 165.431, 169.985, 170.963. UV-Spectrum (10 ppm,  $\lambda_{\text{max}}$  - 332 nm). Theoretical mass: 344, LC-MS ( $m/z$ , I %): 343 [(M-H) $^+$ , 100%]. HPLC Purity: % Area 98.69, RT 2.67 mins.

**3.2.3.19. N-(benzo[d]thiazol-2-yl)-2-(2,4-dioxo-5-(pyridin-2-**

**ylmethylene)thiazolidin-3-yl)acetamide (P19):** Yield 1.3 g (89%); M.P. 263.9 °C (Charred); white color solid; IR ( $\text{cm}^{-1}$ ): 3227, 1735, 1602, 1666, 1614, 1583, 1383.  $^1\text{H}$ -NMR (400 MHz, DMSO- $d_6$ ,  $\delta$  ppm) 4.68 (s, 2H), 7.32 (t,  $J$ = 7.4 Hz, 1H), 7.44–7.48 (m, 2H), 7.77 (d,  $J$ = 8 Hz, 1H), 7.89–7.90 (m, 1H), 7.93–7.98 (m, 2H), 8.00 (s, 1H), 8.78 (d,  $J$ = 4.4 Hz, 1H), 11.40 (s, 1H).  $^{13}\text{C}$ -NMR (400 MHz, DMSO- $d_6$ ): 30.782, 35.806, 42.934, 120.655, 121.781, 123.893, 124.358, 125.134, 126.309, 128.048, 129.693, 131.336, 137.683, 149.357, 150.933, 162.465, 165.420, 165.666, 170.996. UV- Spectrum (10 ppm,  $\lambda_{\text{max}}$  - 331.7 nm). Theoretical mass: 396, LC-MS ( $m/z$ , I %): 394.9 [(M-2H) $^+$ , 100%]. HPLC Purity: % Area 97.45, RT 4.5 mins.

**3.2.3.20. 2-(2,4-dioxo-5-(pyridin-2-ylmethylene)thiazolidin-3-yl)-N-(thiazol-2-**

**yl)acetamide (P20):** Yield 0.85 g (68%); M.P. charred above 300 °C; buff white color solid; IR ( $\text{cm}^{-1}$ ): 3246, 1726, 1602, 1678, 1579, 1473, 1386.  $^1\text{H}$ -NMR (400 MHz, DMSO- $d_6$ ,  $\delta$  ppm) 4.61 (s, 2H), 7.23 (d,  $J$ = 3.6 Hz, 1H), 7.45–7.49 (m, 2H), 7.88–7.90 (m, 1H), 7.94–7.98 (m, 1H), 7.99 (s, 1H), 8.78 (d,  $J$ = 4.4 Hz, 1H), 12.59 (s, 1H).  $^{13}\text{C}$ -NMR (400 MHz, DMSO- $d_6$ ): 42.691, 114.045, 124.346, 125.162, 128.034, 129.617, 137.684, 149.362, 150.946, 165.435, 170.984. UV- Spectrum (10 ppm,  $\lambda_{\text{max}}$  - 332.3 nm). Theoretical mass: 346, LC-MS ( $m/z$ , I %): 344.9 [(M-2H) $^+$ , 100%]. HPLC Purity: % Area 98.34, RT 2.78 mins.

**3.2.3.21. 2-(2,4-dioxo-5-(pyridin-2-ylmethylene)thiazolidin-3-yl)-N-(5-**

**methylthiazol-2-yl)acetamide (P21):** Yield 0.67 g (60%); M.P. charred above 300 °C; buff white color solid; IR ( $\text{cm}^{-1}$ ): 3338, 2841, 1735, 1500, 1678, 1579, 1465, 1381.  $^1\text{H}$ -NMR (400 MHz, DMSO- $d_6$ ,  $\delta$  ppm) 2.32 (s, 3H), 4.58 (s, 2H), 7.15 (s, 1H), 7.45 (t,  $J$ = 6 Hz, 1H), 7.87–7.89 (m, 1H), 7.93–7.95 (m, 1H), 7.98 (s, 1H), 8.77 (d,  $J$ = 4.4 Hz, 1H), 12.38 (s, 1H).  $^{13}\text{C}$ -NMR (400 MHz, DMSO- $d_6$ ): 11.027, 42.659, 124.322, 125.175, 126.887, 128.013, 129.584, 137.660, 149.341, 150.945, 165.427, 170.975. UV- Spectrum (10 ppm,  $\lambda_{\text{max}}$  - 332 nm). Theoretical mass: 360, LC-MS ( $m/z$ , I %): 358.9 [(M-2H) $^+$ , 100%]. HPLC Purity: % Area 97.49, RT 3.73 mins.

**3.2.3.22. N-(4-bromophenyl)-2-(2,4-dioxo-5-(pyridin-2-yl methylene)thiazolidin-3-**

**yl)acetamide (P22):** Yield 0.9 g (88%); M.P. 279.3 °C (Charred); buff color solid; IR ( $\text{cm}^{-1}$ ): 3254, 1734, 1548, 1676, 1581, 1410, 1386, 727.  $^1\text{H}$ -NMR (400 MHz, DMSO- $d_6$ ,  $\delta$  ppm) 4.50 (s, 2H), 7.43–7.53 (m, 5H), 7.86–7.88 (m, 1H), 7.92–7.94 (m, 1H), 7.97 (s, 1H), 8.76 (d,  $J$ = 3.6 Hz, 1H), 10.55 (s, 1H).  $^{13}\text{C}$ -NMR (400 MHz, DMSO- $d_6$ ): 43.337, 115.394, 121.171, 124.280, 125.178, 127.988, 129.518, 131.668, 137.616, 149.319, 150.952, 164.123, 165.507, 171.007. UV- Spectrum (10 ppm,  $\lambda_{\text{max}}$  - 332.7 nm). Theoretical mass:

416, LC-MS (m/z, I %): 418 [(M+2H)<sup>+</sup>, 100%], 416 [(M+)<sup>+</sup>, 75%]. HPLC Purity: % Area 97.69, RT 4.28 mins.

**3.2.3.23. 2-(2,4-dioxo-5-(pyridin-2-ylmethylene)thiazolidin-3-yl)-N-(pyridin-2-yl)acetamide (P23):** Yield 1.1 g (66%); M.P. 256.3 °C (Charred); buff white color solid; IR (cm<sup>-1</sup>): 3265, 1739, 1543, 1678, 1620, 1577, 1386. <sup>1</sup>H-NMR (400 MHz, DMSO-d<sub>6</sub>, δ ppm) 4.57 (s, 2H), 7.13 (s, 1H), 7.45 (s, 1H), 7.78 (s, 1H), 7.87–7.98 (m, 4H), 8.34 (s, 1H), 8.78 (s, 1H), 10.94 (s, 1H). <sup>13</sup>C-NMR (400 MHz, DMSO-d<sub>6</sub>): 43.329, 113.530, 119.898, 124.303, 125.205, 128.002, 129.509, 137.653, 138.417, 148.083, 149.342, 150.972, 151.244, 164.796, 165.519, 171.012. UV- Spectrum (10 ppm, λ<sub>max</sub> - 331.4 nm). Theoretical mass: 340, LC-MS (m/z, I %): 339 [(M-H)<sup>+</sup>, 100%]. HPLC Purity: % Area 97.76, RT 2.77 mins.

**3.2.3.24. 2-(2,4-dioxo-5-(pyridin-2-ylmethylene)thiazolidin-3-yl)-N-(3-methoxyphenyl)acetamide (P24):** Yield 0.92 g (85%); M.P. 249.3 °C (Charred); buff white color solid; IR (cm<sup>-1</sup>): 3252, 1741, 1556, 1681, 1604, 1581, 1386. <sup>1</sup>H-NMR (400 MHz, DMSO-d<sub>6</sub>, δ ppm) 3.71 (s, 3H), 4.49 (s, 2H), 6.65 (d, J= 7.2 Hz, 1H), 7.07 (d, J= 6.8 Hz, 1H), 7.20–7.24 (m, 2H), 7.44 (s, 1H), 7.86–7.97 (m, 3H), 8.77 (s, 1H), 10.42 (s, 1H). <sup>13</sup>C-NMR (400 MHz, DMSO-d<sub>6</sub>): 43.331, 54.953, 104.867, 109.289, 111.396, 124.271, 125.202, 127.980, 129.492, 129.711, 137.617, 139.449, 149.322, 150.965, 159.528, 163.947, 165.532, 171.024. UV- Spectrum (10 ppm, λ<sub>max</sub> - 332 nm). Theoretical mass: 369, LC-MS (m/z, I %): 368 [(M-H)<sup>+</sup>, 100%]. HPLC Purity: % Area 97.25, RT 3.09 mins.

**3.2.3.25. N-(3,4-dibromophenyl)-2-(2,4-dioxo-5-(pyridin-2-ylmethylene)thiazolidin-3-yl)acetamide (P25):** Yield 1 g (78%); M.P. 272 °C (Charred); buff white color solid; IR (cm<sup>-1</sup>): 3340, 1737, 1531, 1666, 1618, 1583, 1381. <sup>1</sup>H-NMR (400 MHz, DMSO-d<sub>6</sub>, δ ppm) 4.51 (s, 2H), 7.44–7.46 (m, 2H), 7.56–7.58 (m, 1H), 7.87–7.90 (m, 2H), 7.93–7.95 (m, 1H), 7.98 (s, 1H), 8.77 (s, 1H), 10.73 (s, 1H). <sup>13</sup>C-NMR (400 MHz, DMSO-d<sub>6</sub>): 43.344, 119.277, 120.466, 124.313, 125.123, 125.308, 128.012, 129.578, 130.806, 131.120, 137.646, 138.275, 149.332, 150.937, 164.543, 165.477, 170.991. UV- Spectrum (10 ppm, λ<sub>max</sub> - 331.9 nm). Theoretical mass: 494, LC-MS (m/z, I %): 496.9 [(M+2H)<sup>+</sup>, 100%], 496 [(M+2H)<sup>+</sup>, 70%]. HPLC Purity: % Area 95.73, RT 5.61 mins.

### 3.3. Biological Evaluation

**3.3.1. *In-vitro* cytotoxicity assays**—The Differential Nuclear Staining (DNS) assay is a live cell imaging-based assay, which utilizes two nuclear dyes to easily label living and dead cells [38]. An initial assessment of cytotoxicity on this series of 25 compounds was conducted via the DNS assay upon exposure of CEM, K-562 and KCL-22 human cancer cell lines to 50 μM of compounds for 48 h. Compounds were dissolved and diluted in Dimethyl sulfoxide (DMSO) to reach the desired concentration. DMSO, Hydrogen peroxide, and untreated cells were utilized as vehicle, positive, and negative controls, respectively, in all experiments. Cells were seeded in a 96-well plate at a density of 10,000 cells/well in 100 μL of complete culture media. Images of stained cells were collected with the GE Healthcare Life Sciences IN Cell Analyzer 2000. Two h prior to imaging, Hoechst and Propidium iodide (PI) stains were added to each well to distinguish between living and dead/dying

cells. Hoechst is a dye able to permeate the membranes of all cells within a sample, whereas PI only penetrates into cells with compromised membranes. Colocalization of Hoechst (blue) and PI (red) signals indicate the dead cell population. In this initial screening, experimental samples were assessed singularly, and control samples in quadruplicate. Subsequent DNS assays on the CEM, K-562, KCL-22 cell lines, were then performed to determine the  $CC_{50}$  values of the compounds that showed cytotoxicity in the initial screening and activity in other biological analyses. Cells were seeded in an identical manner but were treated with a concentration gradient of compound (**P8**, **P9**, **P10**, **P12**, **P19**, and **P25**) ranging from 0.5  $\mu$ M to 100  $\mu$ M. Experimental samples and controls were evaluated for cytotoxicity in triplicate after 48 h of incubation.

**3.3.1.1. Statistical analysis:** For each sample group, the average of replicates and their corresponding standard deviations are displayed. Statistical significance was determined by two-tailed Student's *t*-test comparing experimental treatments to vehicle controls (DMSO). *P* values < 0.05 were deemed significant and graphically displayed using asterisks (\*=*P*<0.05, \*\*=*P*<0.01, \*\*\*=*P*<0.001).

**3.3.2. HDAC enzyme activity assay—**Recombinant HDAC4 and 8 were produced as in [58]. The other HDAC isoenzymes were purchased from BPS Bioscience. Serial dilutions of the inhibitor in the assay buffer (25 mM Tris-HCl, pH 8.0, 75 mM KCl, 0.001 % Pluronic F-127) were incubated with HDAC in a black 96-well microtiter half-area plate (Greiner) for 60 min at 30 °C. Subsequently the reaction was started by the addition of 20  $\mu$ M Boc-Lys(trifluoroacetyl)-AMC (Bachem) as a substrate for HDAC4, 5 and 8, and 50  $\mu$ M Boc-Lys(acetyl)-AMC as substrate for HDAC1, 2, 3, and 6. After incubation for 60 min at 30 °C, the reaction was stopped by the addition of 1.7  $\mu$ M SATFMK for HDAC4, 5, and 8, and 4.17  $\mu$ M suberoylanilide hydroxamic acid (SAHA, Cayman Chemical Company) for HDAC1, 2, 3, and 6. The deacetylated substrate was transformed into a fluorescent product by the addition of 0.4 mg/ml trypsin (Applichem). The release of AMC was followed in a microplate reader (PheraStar Plus, BMG Labtech) at 450 nm ( $\lambda_{Ex}$  = 350 nm) and correlated to enzyme activity. Dose-response curves were produced with GraphPad Prism and fitted to a four parameters logistic function to obtain  $IC_{50}$  values [59]

$$EA = E_0 + \frac{(E_{max} - E_0)}{1 + 10^{(\log(IC_{50}) - x) * h}}$$

Where,

EA is the enzyme activity at a given inhibitor concentration *x*;  $E_{max}$  and  $E_0$  are the enzyme activities determined at zero and complete inhibition, respectively;  $IC_{50}$  represents the inhibitor concentration at which half the enzyme molecules are inhibited; *h* is the slope of the curve.

**3.3.3. GLUT 1, 4 and 5 transport inhibition assay—**Synthesized compounds were examined for their effect on the transport activity of GLUT1 [48], GLUT4 [48], and GLUT5 [49] expressed in hexose transporter null yeast cells (*hxt<sup>0</sup>*). Yeast cell culturing was done at



30 °C with shaking (180 rpm). VW4000*fgy1* yeast cells expressing GLUT1 [48] were cultured for 2–3 days in the synthetic complete media without uracil (SC-uracil) with 2% (w/v) maltose. Cells were washed once in SC-uracil, 2% (w/v) glucose media, transferred in the same media so that  $OD_{600nm} \sim 0.5$ , and grown further for 1–2 days. VW4000*fgy1erg4* yeast cells expressing GLUT4 [48] were cultured like GLUT1, but in media with lower concentrations of maltose and glucose: SC-uracil, 1% (w/v) maltose media for the initial cell culture, and SC-uracil, 0.2% (w/v) glucose media for the final cell culture. VW4000 yeast cells expressing GLUT5 [49] were cultured for one day in YEP [1% (w/v) yeast extract and 2% (w/v) peptone], 2% (w/v) maltose media, 100 µg/ml geneticin G418. Cells were washed once in YEP, 2% (w/v) fructose media transferred in the same media so that initial  $OD_{600nm} \sim 0.5$ , and grown further for 1–2 days. For transport assay, cells in the hexose media were centrifuged ( $1000 \times g$ , 5 minutes), washed once in PBS buffer (10 mM  $Na_2HPO_4$ , 1.8 mM  $KH_2PO_4$ , 2.7 mM KCl, 137 mM NaCl, pH 7.4), then resuspended in PBS buffer at an  $OD_{600nm} \sim 10$ ; each assay contained 100 µl of this cell solution.

The transport assay was started by the addition of  $C^{14}$ -hexose to a final concentration of 5 mM glucose for GLUT1 or GLUT4, and 10 mM fructose for GLUT5. Transport assay was stopped after 10 minutes by the addition of 3-ml ice-chilled Quench buffer (0.1 M KPi, 0.1 M LiCl, pH 5.5) to the assay, followed by filtration under vacuum on a glass fiber filter (GC50; Advantec, Tokyo, Japan), another wash with 3-ml Quench buffer, and one more filtration. The filtration membranes containing the cells were transferred to scintillation vials, combined with 10 ml of Scintillation buffer (BioSafeII; Research Products International, Mount Prospect, IL, USA), and, after brief vortexing, radioactivity was measured with a scintillation counter (Tri-carb 2900TR, Perkin Elmer, USA). As all synthesized compounds were solubilized in DMSO, controls for calculating the relative activity included 1% (v/v) DMSO -to account for DMSO concentration in the transport assay due to inhibitor addition- and saturating concentrations of known inhibitors for GLUTs [200 µM phloretin for GLUT1 and GLUT4 [60], and 100 µM N-[4-(methylsulfonyl)-2-nitrophenyl]-1,3-benzodioxol-5-amine (MSNBA) for GLUT5 [61]. Initial inhibition screening was done at 100 µM concentration; for the compounds that decreased the relative activity by 50% or more, inhibitor concentration was varied in the transport assay from 0.1 to 100 µM to determine inhibitor  $IC_{50}$ . Data were analyzed with GraphPad Prism (San Diego, CA, USA).

**3.3.4. Apoptosis studies by flowcytometry**—The initiation of apoptosis by compounds **P10** and **P19** was studied by flow cytometry. Cells were seeded in a 24-well flat-bottom micro-plate and incubated overnight at 37 °C in a  $CO_2$  incubator for 24 h. The media was replaced with fresh media, and the cells were incubated with  $IC_{50}$  concentration of **P10** and **P19** for 24 h. Untreated cells were the negative control. Post incubation, cells were washed with PBS, centrifuged for 5 min at  $500 \times g$  at 4 °C, and the supernatant was discarded. Cell pellets were re-suspended in ice-cold 1X Binding Buffer, to which 1 µL of annexin V-FITC solution and 5 µL PI (propidium iodide). Tubes were kept in ice and incubated for 15 min in the dark, 400 µL of ice-cold 1X binding buffer was added. Cell preparations were analyzed by flow cytometry (BD Accuri™ C5 flow cytometer, BD

Biosciences, CA, USA). Cytometry data were analyzed by FlowJo software (version 10.1, Ashland, OR, USA) [62].

### 3.3.5. Cell viability on CEM cell line and normal WBCs by MTT assay

**3.3.6.1. WBCs isolation procedure:** A volume of 2.5 mL HiSep was transferred to a 15 mL clean centrifuge tube and overlaid with 7.5 ml diluted blood, followed by centrifugation at  $400 \times g$  at room temperature for 30 minutes. The supernatant containing most of the plasma and platelet was discarded by aspiration. The mononuclear cells were transferred to a clean centrifuge tube to which 10 ml of isotonic phosphate buffered saline was added and mixed by gentle aspiration. This was followed by centrifugation at  $200 \times g$ , at room temperature for 10 minutes. The cells were washed again with isotonic phosphate buffered saline and re-suspended in an RBC lysis for 5 mins. The tube was then centrifuged at  $300 \times g$  for 5 mins, and the supernatant was discarded. Cells were washed with PBS twice and again centrifuged at  $300 \times g$  for 5 mins. The cells were re-suspended in RPMI 1640 medium, and maintained in a  $CO_2$  incubator at  $37^\circ C$  (95% humidity and 5%  $CO_2$ ) until completion of MTT assay experiments.

**3.3.6.2. Cytotoxicity determination by MTT assay:** The effect of compound **P19** on the viability of CEM cell lines and normal human WBCs were determined by the MTT assay. MTT is a colorimetric assay that measures the reduction of yellow 3-(4,5-dimethylthiazol-2-yl)-2,5-diphenyl tetrazolium bromide (MTT) by mitochondrial succinate dehydrogenase. The reduction of MTT can only occur in metabolically active cells. The level of **P19** activity was determined by measuring cell viability. The cells were seeded at a density of approximately  $5 \times 10^3$  cells/well in a 96-well flat-bottom micro plate, and maintained at  $37^\circ C$  in 95% humidity and 5%  $CO_2$  overnight. The cells were incubated with different concentrations of **P19** (100, 75, 50, 25, 10, and 2.5  $\mu M$ ) for another 48 h. The cells in each well were washed twice with phosphate buffer solution, and 20  $\mu L$  of the MTT staining solution (5 mg/ml in phosphate buffer solution) was added to each well, and the plate was incubated at  $37^\circ C$ . After 4 h, 100  $\mu L$  of dimethyl sulfoxide (DMSO) was added to each well to dissolve the formazan crystals, and the absorbance at 570 nm was recorded with a micro-plate reader [63]. Graph Pad Prism Version 5.1 was used to calculate the  $CC_{50}$ . The DMSO concentration used for the experiments was less 1.5%. All the concentrations were used in duplicates.

The formula used for determining the cell viability:

$$\text{Surviving cells (\%)} = [\text{Mean OD of cells treated with the test compound} / \text{Mean OD of Negative control}] \times 100$$

## 4. Conclusion

We synthesized, purified, and characterized the structures of all 25 compounds through various methods (FTIR,  $^1H$ -NMR,  $^{13}C$ -NMR, and mass spectrometry). Notably, these compounds do not contain a hydroxamate or trifluoromethylketone zinc-binding group typical for canonical HDAC inhibitors used in clinical therapy, trials or academic research. Two compounds, **P10** and **P19** showed moderate activity against HDAC8 and a remarkable

selectivity against other HDAC isoenzymes. Docking analysis of **P19** with best activity ( $IC_{50}$  of 9.3  $\mu$ M) and docking score against HDAC8 revealed significant binding interactions with the catalytic zinc ion and amino acid residues such as Y306, and G151 in the active site pocket of HDAC8 as well as partial occupation of the specific acetate release channel of HDAC8. This finding is in agreement with the observed experimental isoenzyme selectivity. However, the proposed binding mode has to be confirmed by detailed crystallographic studies. Most interestingly, six compounds (**P8**, **P9**, **P10**, **P12**, **P19**, and **P25**) showed cytotoxicity against leukemic cell lines (K562, CEM, and KCL22) in mid-micromolar range. Moreover, the best active compound **P19** was less cytotoxic for non-cancerous cells (WBCs  $IC_{50}$  - 104.2  $\mu$ M and HS27  $IC_{50}$  - 105.0  $\mu$ M). **P10** and **P19** exhibited apoptotic death in CEM cells. As HDAC inhibitors can affect the expression of GLUT1, we also checked the effect of the compounds on GLUT1, and two other GLUT isoforms GLUT4, and GLUT5. We found that among all 25 compounds only **P19** significantly inhibited GLUT1 ( $IC_{50}$  28.2  $\mu$ M), and it did so without affecting GLUT4 or GLUT5. Thus, **P19** is a promising anti-cancer agent, with selectivity and potency against two cancer targets - HDAC8 and GLUT1, offering a starting point for the development of novel non-hydroxamate compounds with enhanced HDAC8 inhibitory potency.

## Supplementary Material

Refer to Web version on PubMed Central for supplementary material.

## Acknowledgments.

This research work was supported by the grant, "Indo-Poland Joint Research Programme" from the Department of Science and Technology (DST), Government of India. Project Reference Number **DST/INT/Pol/P-27/2016**. In addition, the cytotoxicity work was supported by NIMHD grant **SU54MD007592** to the Border Biomedical Research Center (BBRC) at UTEP.

## Abbreviations.

<b>TZDs</b>	Thiazolidinediones
<b>HDAC</b>	Histone Deacetylase
<b>GLUT</b>	Glucose Transporter
<b>HATs</b>	Histone acetylases
<b>AML</b>	Acute myeloid leukemia
<b>ALL</b>	acute lymphocytic leukemia
<b>APL</b>	Acute promyelocytic leukaemia
<b>ZBG</b>	Zinc Binding Group
<b>RMSD</b>	Root Mean Square Deviation
<b>TPSA</b>	Topological Polar Surface Area
<b>AcOH</b>	Acetic acid

<b>EtOH</b>	Ethanol
<b>DCM</b>	Dichloromethane
<b>K<sub>2</sub>CO<sub>3</sub></b>	Potassium carbonate
<b><sup>1</sup>H-NMR</b>	Proton Nuclear Magnetic Resonance
<b>Hz</b>	Hertz
<b>J</b>	Coupling Constant
<b><sup>13</sup>C-NMR</b>	Carbon Nuclear Magnetic Resonance
<b>FTIR</b>	Fourier-transform infrared spectroscopy
<b>UV</b>	Ultraviolet Spectroscopy
<b>HPLC</b>	High Performance Liquid Chromatography
<b>M.P.</b>	Melting Point
<b>DNS</b>	Differential Nuclear Staining
<b>DMSO</b>	Dimethyl sulfoxide
<b>TSA</b>	Thermal Shift Assay
<b>MTT</b>	3-(4,5-dimethylthiazol-2-yl)-2,5-diphenyl tetrazolium bromide

## REFERENCES

- [1]. Mottamal M, Zheng S, Huang TL, Wang G, Histone deacetylase inhibitors in clinical studies as templates for new anticancer agents, *Molecules*. 20 (2015) 3898–3941. [PubMed: 25738536]
- [2]. Min C, Moore N, Shearstone JR, Quayle SN, Huang P, van Duzer JH, Jarpe MB, Jones SS, Yang M, Selective Inhibitors of Histone Deacetylases 1 and 2 Synergize with Azacitidine in Acute Myeloid Leukemia, *PLoS ONE*. 12 (2017) e0169128 10.1371/journal.pone.0169128. [PubMed: 28060870]
- [3]. Benedetti R, Conte M, Altucci L, Targeting Histone Deacetylases in Diseases: Where Are We?, *Antioxid Redox Signal*. 23 (2015) 99–126. 10.1089/ars.2013.5776. [PubMed: 24382114]
- [4]. Gryder BE, Sodji QH, Oyelere AK, Targeted cancer therapy: giving histone deacetylase inhibitors all they need to succeed, *Future Med Chem*. 4 (2012) 505–524. 10.4155/fmc.12.3. [PubMed: 22416777]
- [5]. Suraweera A, O’Byrne KJ, Richard DJ, Combination Therapy With Histone Deacetylase Inhibitors (HDACi) for the Treatment of Cancer: Achieving the Full Therapeutic Potential of HDACi, *Front. Oncol* 8 (2018) 92 10.3389/fonc.2018.00092. [PubMed: 29651407]
- [6]. Amin SA, Adhikari N, Jha T, Structure-activity relationships of hydroxamate-based histone deacetylase-8 inhibitors: reality behind anticancer drug discovery, *Future Medicinal Chemistry*. 9 (2017) 2211–2237. 10.4155/fmc-2017-0130. [PubMed: 29182018]
- [7]. Balasubramanian S, Ramos J, Luo W, Sirisawad M, Verner E, Buggy JJ, A novel histone deacetylase 8 (HDAC8)-specific inhibitor PCI-34051 induces apoptosis in T-cell lymphomas, *Leukemia*. 22 (2008) 1026–1034. 10.1038/leu.2008.9. [PubMed: 18256683]
- [8]. Chakrabarti A, Melesina J, Kolbinger FR, Oehme I, Senger J, Witt O, Sippl W, Jung M, Targeting histone deacetylase 8 as a therapeutic approach to cancer and neurodegenerative diseases, *Future Medicinal Chemistry*. 8 (2016) 1609–1634. [PubMed: 27572818]

- [9]. Ceccacci E, Minucci S, Inhibition of histone deacetylases in cancer therapy: lessons from leukaemia, *Br J Cancer*. 114 (2016) 605–611. 10.1038/bjc.2016.36. [PubMed: 26908329]
- [10]. Chakrabarti A, Oehme I, Witt O, Oliveira G, Sippl W, Romier C, Pierce RJ, Jung M, HDAC8: a multifaceted target for therapeutic interventions, *Trends in Pharmacological Sciences*. 36 (2015) 481–492. 10.1016/j.tips.2015.04.013. [PubMed: 26013035]
- [11]. Mohan R, Sharma AK, Gupta S, Ramaa CS, Design, synthesis, and biological evaluation of novel 2, 4-thiazolidinedione derivatives as histone deacetylase inhibitors targeting liver cancer cell line, *Medicinal Chemistry Research*. 21 (2012) 1156–1165.
- [12]. Yang F, Zhao N, Ge D, Chen Y, Next-generation of selective histone deacetylase inhibitors, *RSC Adv*. 9 (2019) 19571–19583. 10.1039/C9RA02985K.
- [13]. Hou X, Du J, Liu R, Zhou Y, Li M, Xu W, Fang H, Enhancing the Sensitivity of Pharmacophore-Based Virtual Screening by Incorporating Customized ZBG Features: A Case Study Using Histone Deacetylase 8, *J. Chem. Inf. Model* 55 (2015) 861–871. 10.1021/ci500762z. [PubMed: 25757142]
- [14]. Marek M, Shaik TB, Heimburg T, Chakrabarti A, Lancelot J, Ramos-Morales E, Da Veiga C, Kalinin D, Melesina J, Robaa D, Schmidtkunz K, Suzuki T, Holl R, Ennifar E, Pierce RJ, Jung M, Sippl W, Romier C, Characterization of Histone Deacetylase 8 (HDAC8) Selective Inhibition Reveals Specific Active Site Structural and Functional Determinants, *J. Med. Chem* 61 (2018) 10000–10016. 10.1021/acs.jmedchem.8b01087. [PubMed: 30347148]
- [15]. Schweipert M, Jänsch N, Sugiarto WO, Meyer-Almes F-J, Kinetically selective and potent inhibitors of HDAC8, *Biological Chemistry*. 400 (2019) 733–743. 10.1515/hsz-2018-0363. [PubMed: 30521473]
- [16]. Suzuki T, Muto N, Bando M, Itoh Y, Masaki A, Ri M, Ota Y, Nakagawa H, Iida S, Shirahige K, Miyata N, Design, Synthesis, and Biological Activity of NCC149 Derivatives as Histone Deacetylase 8-Selective Inhibitors, *ChemMedChem*. 9 (2014) 657–664. 10.1002/cmcd.201300414. [PubMed: 24403121]
- [17]. Whitehead L, Dobler MR, Radetich B, Zhu Y, Atadja PW, Claiborne T, Grob JE, McRiner A, Pancost MR, Patnaik A, Shao W, Shultz M, Tichkule R, Tommasi RA, Vash B, Wang P, Stams T, Human HDAC isoform selectivity achieved via exploitation of the acetate release channel with structurally unique small molecule inhibitors, *Bioorganic & Medicinal Chemistry*. 19 (2011) 4626–4634. 10.1016/j.bmc.2011.06.030.
- [18]. Muth M, Jänsch N, Kopranovic A, Krämer A, Wössner N, Jung M, Kirschhöfer F, Brenner-Weiß G, Meyer-Almes FJ, Covalent inhibition of histone deacetylase 8 by 3,4-dihydro-2H-pyrimido[1,2-c][1,3]benzothiazin-6-imine, *Biochimica et Biophysica Acta (BBA) - General Subjects*. 1863 (2019) 577–585. 10.1016/j.bbagen.2019.01.001. [PubMed: 30611847]
- [19]. Wolff B, Jänsch N, Sugiarto WO, Frühschulz S, Lang M, Altintas R, Oehme I, Meyer-Almes F-J, Synthesis and structure activity relationship of 1, 3-benzo-thiazine-2-thiones as selective HDAC8 inhibitors, *European Journal of Medicinal Chemistry*. 184 (2019) 111756 10.1016/j.ejmech.2019.111756. [PubMed: 31630054]
- [20]. Tabackman AA, Frankson R, Marsan ES, Perry K, Cole KE, Structure of ‘linkerless’ hydroxamic acid inhibitor-HDAC8 complex confirms the formation of an isoform-specific subpocket, *Journal of Structural Biology*. 195 (2016) 373–378. 10.1016/j.jsb.2016.06.023. [PubMed: 27374062]
- [21]. Uba AI, Weako J, Keskin Ö, Gürsoy A, Yelekçi K, Examining the stability of binding modes of the cocrystallized inhibitors of human HDAC8 by molecular dynamics simulation, *Journal of Biomolecular Structure and Dynamics*. (2019) 1–10. 10.1080/07391102.2019.1615989.
- [22]. Schweipert M, Jänsch N, Sugiarto WO, Meyer-Almes F-J, Kinetically selective and potent inhibitors of HDAC8, *Biological Chemistry*. 400 (2019) 733–743. 10.1515/hsz-2018-0363. [PubMed: 30521473]
- [23]. Tilekar K, Upadhyay N, Jänsch N, Schweipert M, Mrowka P, Meyer-Almes FJ, Ramaa CS, Discovery of 5-naphthylidene-2,4-thiazolidinedione derivatives as selective HDAC8 inhibitors and evaluation of their cytotoxic effects in leukemic cell lines, *Bioorganic Chemistry*. 95 (2020) 103522 10.1016/j.bioorg.2019.103522. [PubMed: 31901516]
- [24]. Banerjee S, Adhikari N, Amin SA, Jha T, Histone deacetylase 8 (HDAC8) and its inhibitors with selectivity to other isoforms: An overview, *European Journal of Medicinal Chemistry*. 164 (2019) 214–240. 10.1016/j.ejmech.2018.12.039. [PubMed: 30594678]

- [25]. Qin H-T, Li H-Q, Liu F, Selective histone deacetylase small molecule inhibitors: recent progress and perspectives, *Expert Opinion on Therapeutic Patents*. 27 (2017) 621–636. 10.1080/13543776.2017.1276565. [PubMed: 28033734]
- [26]. Miller TA, Witter DJ, Belvedere S, Histone Deacetylase Inhibitors, *J. Med. Chem* 46 (2003) 5097–5116. 10.1021/jm0303094. [PubMed: 14613312]
- [27]. Zhang L, Zhang J, Jiang Q, Zhang L, Song W, Zinc binding groups for histone deacetylase inhibitors, *Journal of Enzyme Inhibition and Medicinal Chemistry*. 33 (2018) 714–721. 10.1080/14756366.2017.1417274. [PubMed: 29616828]
- [28]. Bressi JC, de Jong R, Wu Y, Jennings AJ, Brown JW, O'Connell S, Tari LW, Skene RJ, Vu P, Navre M, Cao X, Gangloff AR, Benzimidazole and imidazole inhibitors of histone deacetylases: Synthesis and biological activity, *Bioorganic & Medicinal Chemistry Letters*. 20 (2010) 3138–3141. 10.1016/j.bmcl.2010.03.092.
- [29]. Adhikari N, Amin SA, Jha T, Selective and nonselective HDAC8 inhibitors: a therapeutic patent review, *Pharmaceutical Patent Analyst*. 7 (2018) 259–276. 10.4155/ppa-2018-0019. [PubMed: 30632447]
- [30]. Mummery A, Narendran A, Lee K-Y, Targeting epigenetics through histone deacetylase inhibitors in acute lymphoblastic leukemia, *Current Cancer Drug Targets*. 11 (2011) 882–893. [PubMed: 21762078]
- [31]. Quintás-Cardama A, Santos FPS, Garcia-Manero G, Histone deacetylase inhibitors for the treatment of myelodysplastic syndrome and acute myeloid leukemia, *Leukemia*. 25 (2011) 226–235. 10.1038/leu.2010.276. [PubMed: 21116282]
- [32]. Oehme I, Deubzer HE, Lodrini M, Milde T, Witt O, Targeting of HDAC8 and investigational inhibitors in neuroblastoma, *Expert Opinion on Investigational Drugs*. 18 (2009) 1605–1617. 10.1517/14728220903241658. [PubMed: 19780707]
- [33]. Monga V, Swami U, Tanas M, Bossler A, Mott SL, Smith BJ, Milhem M, A Phase I/II Study Targeting Angiogenesis Using Bevacizumab Combined with Chemotherapy and a Histone Deacetylase Inhibitor (Valproic Acid) in Advanced Sarcomas, *Cancers*. 10 (2018) 53 10.3390/cancers10020053.
- [34]. Bhanushali U, Rajendran S, Sarma K, Kulkarni P, Chatti K, Chatterjee S, Ramaa CS, 5-Benzylidene-2, 4-thiazolidenedione derivatives: Design, synthesis and evaluation as inhibitors of angiogenesis targeting VEGFR-2, *Bioorganic Chemistry*. 67 (2016) 139–147. [PubMed: 27388635]
- [35]. Joshi H, Marulkar K, Gota V, S Ramaa C, Hydroxy Cinnamic Acid Derivatives as Partial PPAR  $\gamma$  Agonists: In silico Studies, Synthesis and Biological Characterization Against Chronic Myeloid Leukemia Cell Line (K562), *Anti-Cancer Agents in Medicinal Chemistry (Formerly Current Medicinal Chemistry-Anti-Cancer Agents)*. 17 (2017) 524–541.
- [36]. Kabir A, Tilekar K, Upadhyay N, Ramaa CS, Novel Anthraquinone Derivatives as Dual Inhibitors of Topoisomerase 2 and Casein Kinase 2: In Silico Studies, Synthesis and Biological Evaluation on Leukemic Cell Lines, *Anti-Cancer Agents in Medicinal Chemistry (Formerly Current Medicinal Chemistry-Anti-Cancer Agents)*. 18 (2018) 1551–1562.
- [37]. Patil V, Tilekar K, Mehendale-Munj S, Mohan R, Ramaa CS, Synthesis and primary cytotoxicity evaluation of new 5-benzylidene-2, 4-thiazolidenedione derivatives, *European Journal of Medicinal Chemistry*. 45 (2010) 4539–4544. [PubMed: 20667627]
- [38]. Lema C, Varela-Ramirez A, Aguilera RJ, Differential nuclear staining assay for high-throughput screening to identify cytotoxic compounds, *Curr Cell Biochem*. 1 (2011) 1–14. [PubMed: 27042697]
- [39]. Choi MA, Park SY, Chae HY, Song Y, Sharma C, Seo YH, Design, synthesis and biological evaluation of a series of CNS penetrant HDAC inhibitors structurally derived from amyloid- $\beta$  probes, *Sci Rep*. 9 (2019) 1–12. 10.1038/s41598-019-49784-9. [PubMed: 30626917]
- [40]. Huang Y, Zhao J, Song Q, Zheng L, Fan C, Liu T, Bao Y, Sun L, Zhang L, Li Y, Virtual screening and experimental validation of novel histone deacetylase inhibitors, *BMC Pharmacol Toxicol*. 17 (2016) 32 10.1186/s40360-016-0075-8. [PubMed: 27443303]

- [41]. Mehta V, Athar M, Jha PC, Panchal M, Modi K, Jain VK, Efficiently functionalized oxalix [4] arenes: Synthesis, characterization and exploration of their biological profile as novel HDAC inhibitors, *Bioorganic & Medicinal Chemistry Letters*. 26 (2016) 1005–1010.
- [42]. Oanh DTK, Van Hai H, Park SH, Kim H-J, Han B-W, Kim H-S, Hong J-T, Han S-B, Nam N-H, Benzothiazole-containing hydroxamic acids as histone deacetylase inhibitors and antitumor agents, *Bioorganic & Medicinal Chemistry Letters*. 21 (2011) 7509–7512.
- [43]. Thanh Tung T, Thi Kim Oanh D, Thi Phuong Dung P, Van Hue TM, Ho Park S, Woo Han B, Kim Y, Hong J-T, Han S-B, Nam N-H, New benzothiazole/thiazole-containing hydroxamic acids as potent histone deacetylase inhibitors and antitumor agents, *Medicinal Chemistry*. 9 (2013) 1051–1057. [PubMed: 23521008]
- [44]. Adekola K, Rosen ST, Shanmugam M, Glucose transporters in cancer metabolism, *Curr Opin Oncol*. 24 (2012) 650–654. 10.1097/CCO.0b013e328356da72. [PubMed: 22913968]
- [45]. Wardell SE, Ilkayeva OR, Wieman HL, Frigo DE, Rathmell JC, Newgard CB, McDonnell DP, Glucose metabolism as a target of histone deacetylase inhibitors, *Molecular Endocrinology*. 23 (2009) 388–401. [PubMed: 19106193]
- [46]. Chen Ching-Shih, Wang Dasheng, GLUCOSE TRANSPORTER INHIBITORS, US 9,174,951 B2, 2015.
- [47]. Wei S, Kulp SK, Chen C-S, Energy Restriction as an Antitumor Target of Thiazolidinediones, *J. Biol. Chem* 285 (2010) 9780–9791. 10.1074/jbc.M109.065466. [PubMed: 20093366]
- [48]. Wieczorke R, Dlugai S, Krampe S, Boles E, Characterisation of mammalian GLUT glucose transporters in a heterologous yeast expression system, *Cell. Physiol. Biochem* 13 (2003) 123–134. 10.1159/000071863. [PubMed: 12876383]
- [49]. Tripp J, Essl C, Iancu CV, Boles E, Choe J-Y, Oreb M, Establishing a yeast-based screening system for discovery of human GLUT5 inhibitors and activators, *Sci Rep*. 7 (2017) 6197 10.1038/s41598-017-06262-4. [PubMed: 28740135]
- [50]. Florio M, Heide M, Pinson A, Brandl H, Albert M, Winkler S, Wimberger P, Huttner WB, Hiller M, Evolution and cell-type specificity of human-specific genes preferentially expressed in progenitors of fetal neocortex, *ELife*. 7 (2018) e32332 10.7554/eLife.32332. [PubMed: 29561261]
- [51]. Song S, Wang Y, Xu P, Yang R, Ma Z, Liang S, Zhang G, The inhibition of histone deacetylase 8 suppresses proliferation and inhibits apoptosis in gastric adenocarcinoma, *International Journal of Oncology*. 47 (2015) 1819–1828. 10.3892/ijo.2015.3182. [PubMed: 26412386]
- [52]. Daina A, Michielin O, Zoete V, SwissADME: a free web tool to evaluate pharmacokinetics, drug-likeness and medicinal chemistry friendliness of small molecules, *Sci Rep*. 7 (2017) 1–13. 10.1038/srep42717. [PubMed: 28127051]
- [53]. Daina A, Zoete V, A boiled-egg to predict gastrointestinal absorption and brain penetration of small molecules, *ChemMedChem*. 11 (2016) 1117–1121. [PubMed: 27218427]
- [54]. Bhatia S, Schultz T, Roberts D, Shen J, Kromidas L, Marie Api A, Comparison of Cramer classification between Toxtree, the OECD QSAR Toolbox and expert judgment, *Regulatory Toxicology and Pharmacology*. 71 (2015) 52–62. 10.1016/j.yrtph.2014.11.005. [PubMed: 25460032]
- [55]. Patlewicz G, Jeliakova N, Safford RJ, Worth AP, Aleksiev B, An evaluation of the implementation of the Cramer classification scheme in the Toxtree software, SAR and QSAR in Environmental Research. 19 (2008) 495–524. 10.1080/10629360802083871. [PubMed: 18853299]
- [56]. Bhanushali U, Kalekar-Joshi S, Kulkarni-Munshi R, Yellanki S, Medishetty R, Kulkarni P, Subramanian Chelakara R, Design, Synthesis and Evaluation of 5-pyridin-4-yl-2-thioxo-[1, 3, 4] oxadiazol-3-yl Derivatives as Anti-angiogenic Agents Targeting VEGFR-2, Anti-Cancer Agents in Medicinal Chemistry (Formerly Current Medicinal Chemistry-Anti-Cancer Agents). 17 (2017) 67–74.
- [57]. Pal T, Joshi H, Ramaa CS, Design and development of oxazol-5-ones as potential partial PPAR- $\gamma$  agonist against cancer cell lines, *Anti-Cancer Agents in Medicinal Chemistry (Formerly Current Medicinal Chemistry-Anti-Cancer Agents)*. 14 (2014) 872–883.

- [58]. Jänsch N, Meyners C, Muth M, Kopranovic A, Witt O, Oehme I, Meyer-Almes F-J, The enzyme activity of histone deacetylase 8 is modulated by a redox-switch, *Redox Biology*. 20 (2019) 60–67. 10.1016/j.redox.2018.09.013. [PubMed: 30292946]
- [59]. Volund A, Application of the Four-Parameter Logistic Model to Bioassay: Comparison with Slope Ratio and Parallel Line Models, *Biometrics*. 34 (1978) 357 10.2307/2530598. [PubMed: 719119]
- [60]. Kasahara T, Kasahara M, Characterization of rat Glut4 glucose transporter expressed in the yeast *Saccharomyces cerevisiae*: comparison with Glut1 glucose transporter, *Biochim. Biophys. Acta* 1324 (1997) 111–119. 10.1016/s0005-2736(96)00217-9. [PubMed: 9059504]
- [61]. George Thompson AM, Ursu O, Babkin P, Iancu CV, Whang A, Oprea TI, Choe J, Discovery of a specific inhibitor of human GLUT5 by virtual screening and in vitro transport evaluation, *Sci Rep*. 6 (2016) 24240 10.1038/srep24240. [PubMed: 27074918]
- [62]. Peram MR, Jalalpure S, Kumbar V, Patil S, Joshi S, Bhat K, Diwan P, Factorial design based curcumin ethosomal nanocarriers for the skin cancer delivery: in vitro evaluation, *Journal of Liposome Research*. (2019) 1–21.
- [63]. Bhat SS, Revankar VK, Kumbar V, Bhat K, Kawade VA, Synthesis, crystal structure and biological properties of a cis-dichloridobis (diimine) copper (II) complex, *Acta Crystallographica Section C: Structural Chemistry*. 74 (2018) 146–151. [PubMed: 29400328]



**HIGHLIGHTS**

- N-substituted TZDs, **P1-P25** were designed, synthesized & structurally characterized.
- Compound **P19** was most active against HDAC8 and produced thermal stabilization.
- It showed apoptotic cell death and cytotoxicity in leukemic cell lines.
- **P19** also interfered with glucose transporter 1 - GLUT1.
- It was also found less cytotoxic on non-cancerous cells (WBCs and HS27).

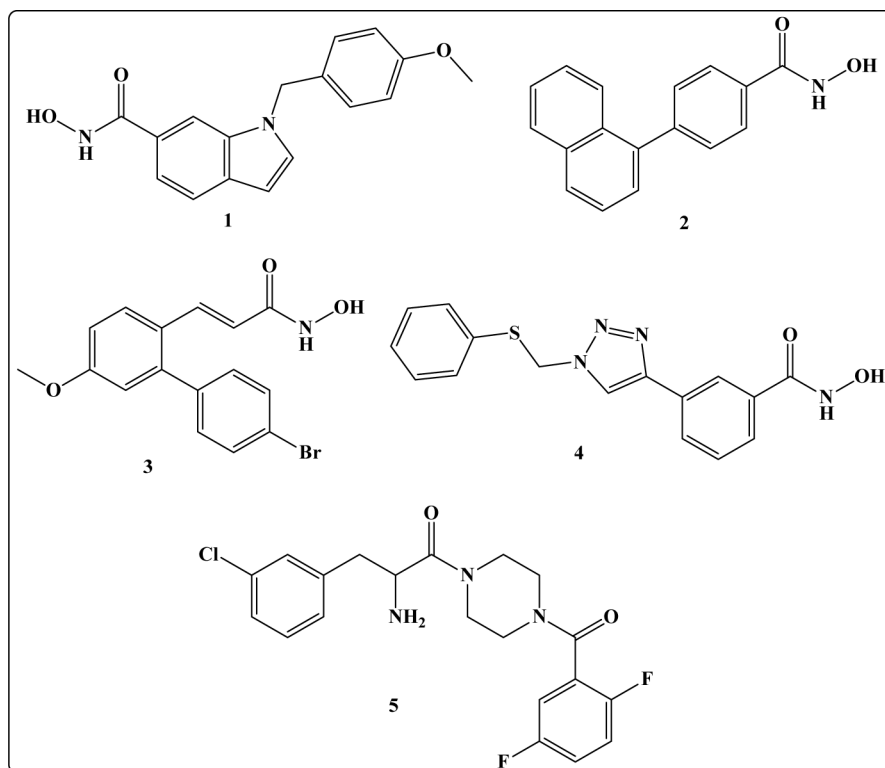


**Figure 1.** Reported selective HDAC8 inhibitors: PCI34051 (1), linkerless hydroxamic acid (2), ortho-aryl N-hydroxycinnamide (3), NCC149 (4), azetidinone (5) [13–16].

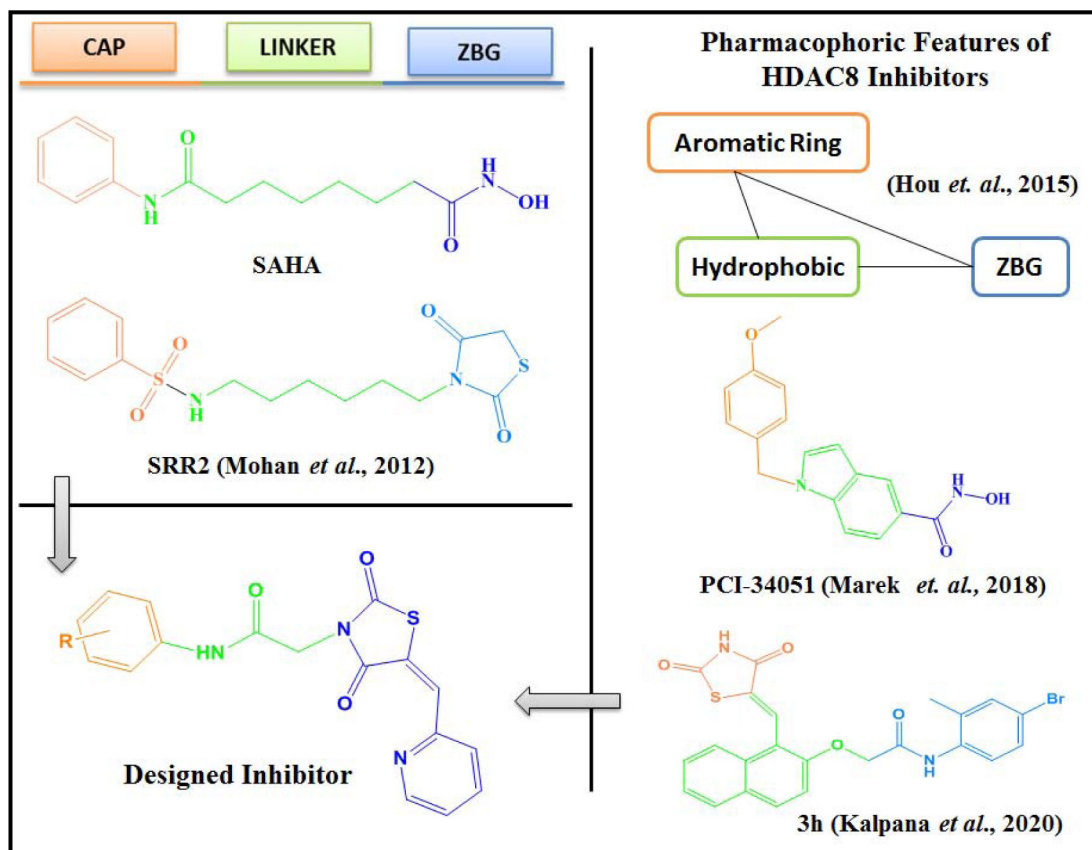


**Figure 2.**  
Designing aspects of novel HDAC8 inhibitors [11,13,14,23].

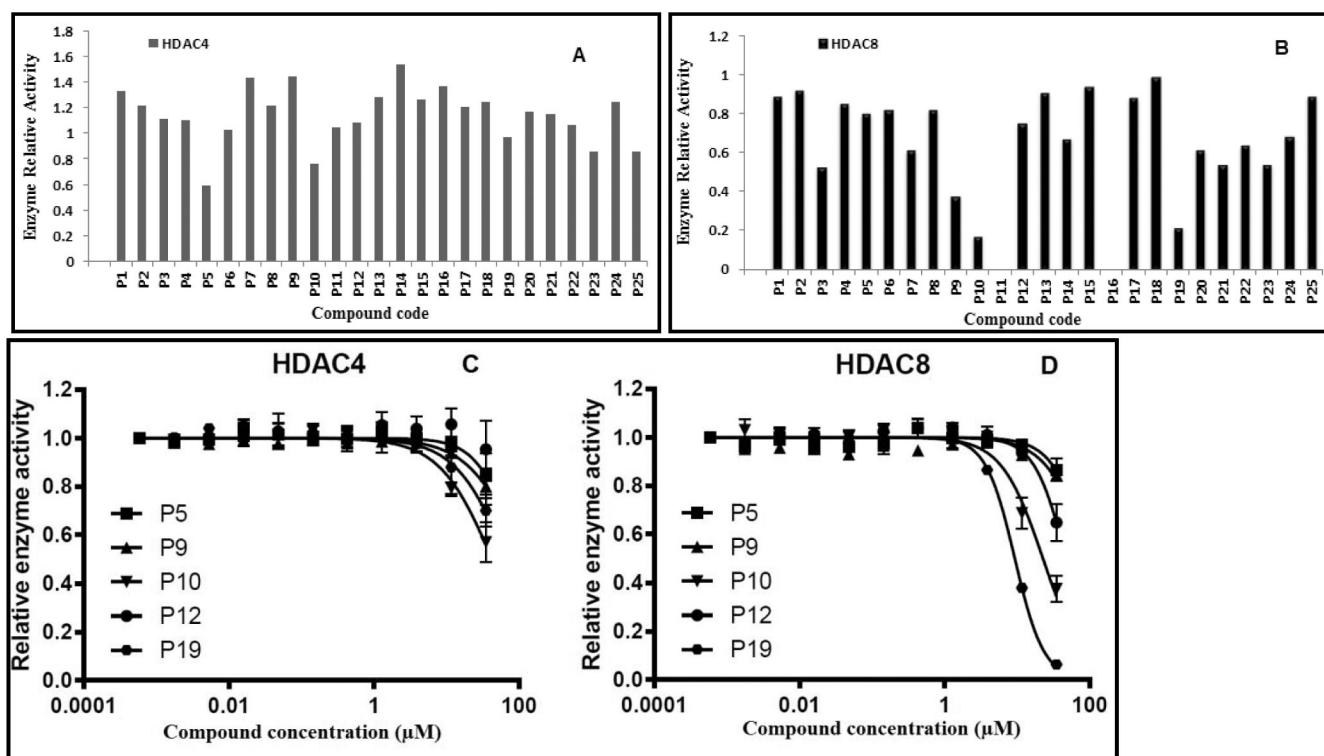


**Figure 3.** Screening of P1-P25 on two different classes of HDAC isoforms, HDAC4 and HDAC8. Primary screening of all target compounds at 50  $\mu\text{M}$  against HDAC4 (A) and HDAC8 (B). (C) Dose response curves of P5, P9, P10, P12, and P19 on HDAC4. (D) Dose response curves of P5, P9, P10, P12, and P19 on HDAC8.

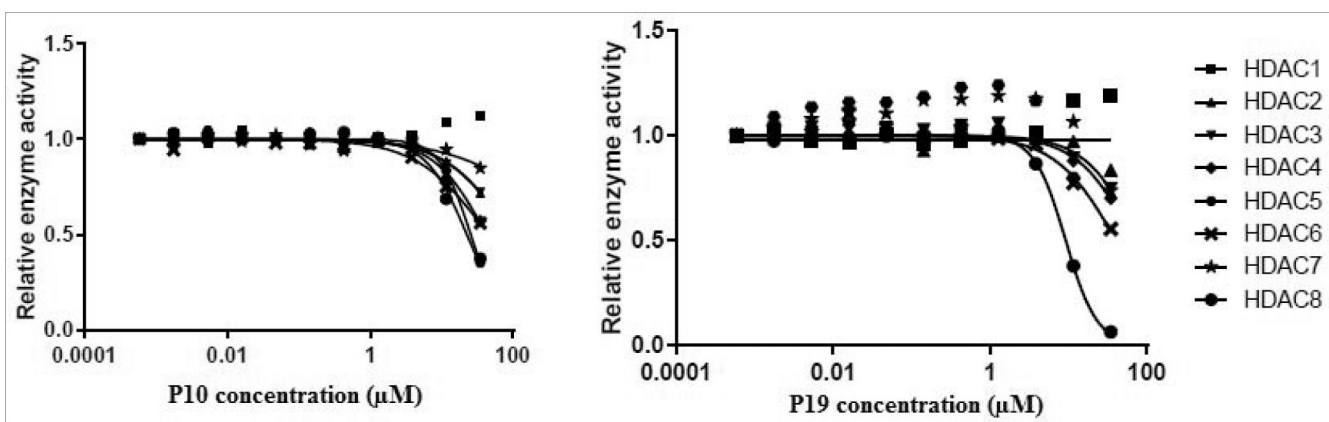


**Figure 4.**  
Dose response curve of P10 and P19 on different HDAC isoforms.

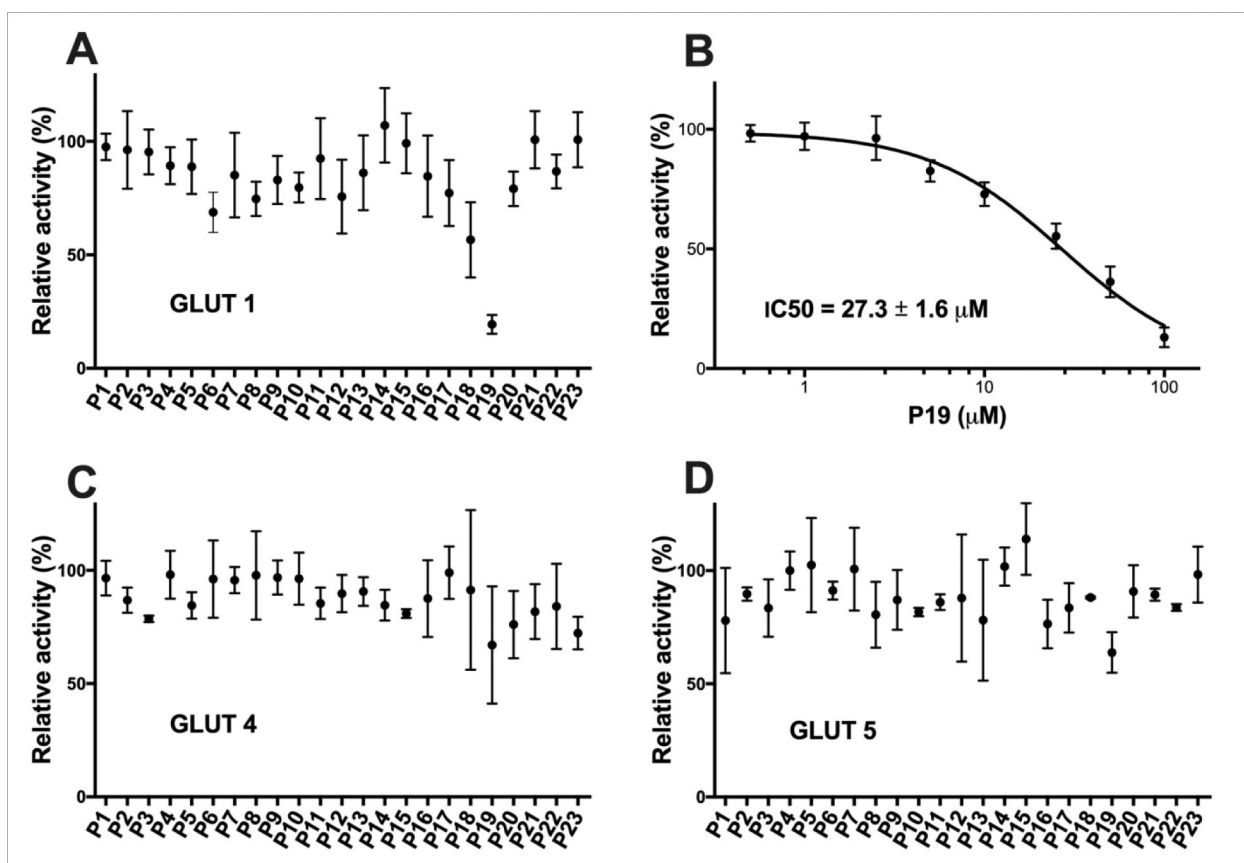


**Figure 5. Effect of the test compounds on the relative transport activity of GLUT 1, 4, and 5.** Percent relative activity of GLUT1 (A), GLUT4 (C), and GLUT5 (D) in the presence of 50 μM concentration of test compound. (B) Dose response curve of **P19** in GLUT1. Transport assay was initiated by the addition of 5 mM C<sup>14</sup>-glucose (for GLUT1 and GLUT4) or 10 mM C<sup>14</sup>- fructose (GLUT5) to *hxt<sup>0</sup>* yeast cells expressing GLUT1, GLUT4, or GLUT5 (see Material and Methods for details). The transport activity was measured in triplicates and means with S.D. are shown.

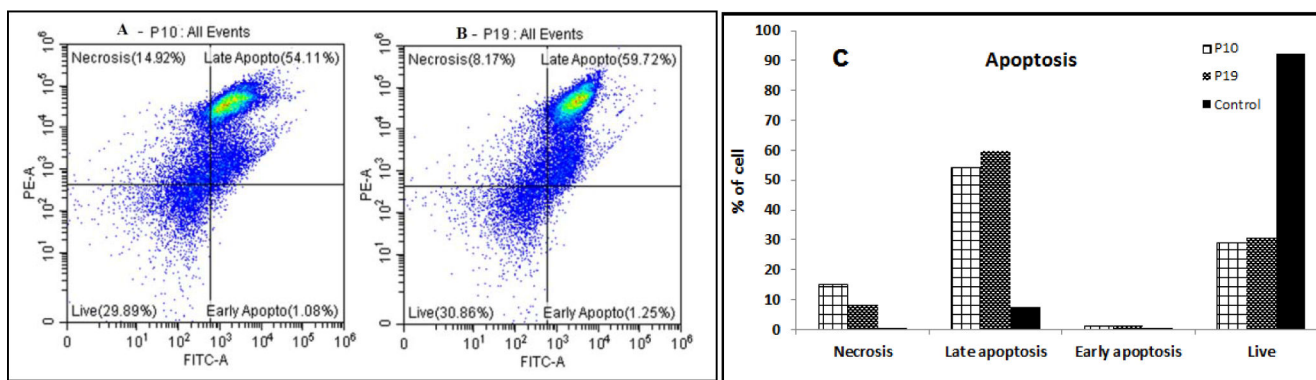


**Figure 6. Analysis of apoptosis induced by compounds P10 and P19 on CEM cells.** (A-B) Cytoplots of test compounds **P10** and **P19**, respectively. CEM cells were treated with  $IC_{50}$  concentration of compounds P10 (A) and compound P19 (B) for 24 h. (C) Graphical representation of apoptotic events of control (1% DMSO), **P10**-treated and **P19**-treated cells.

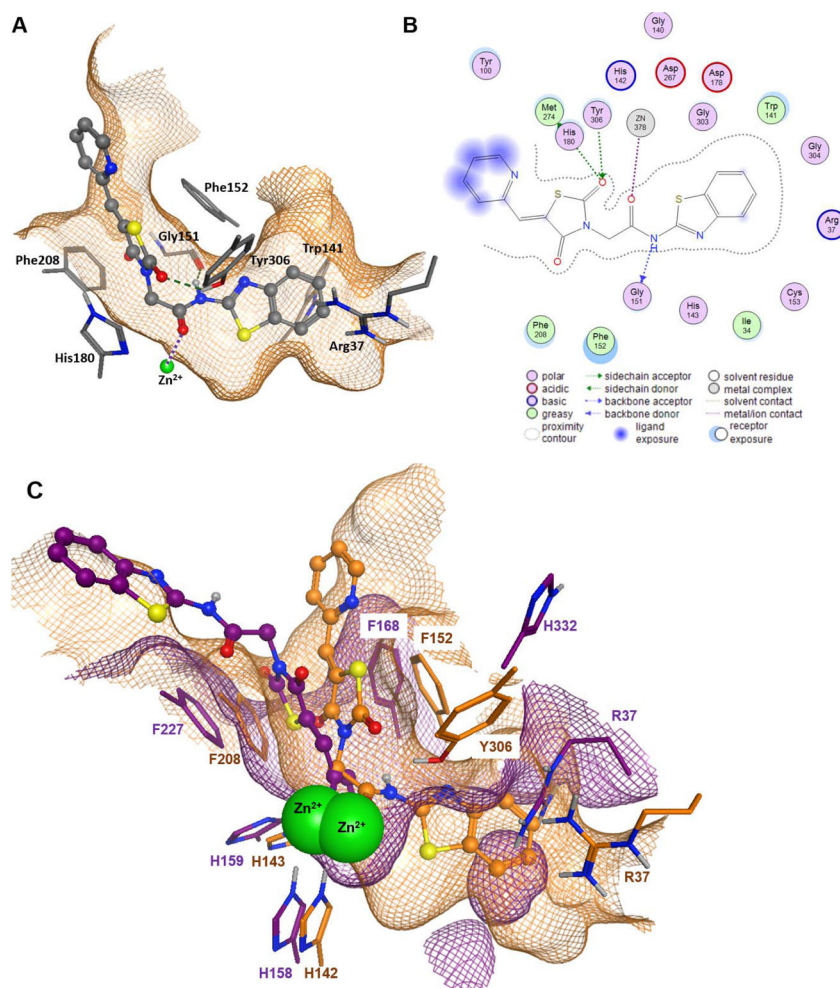
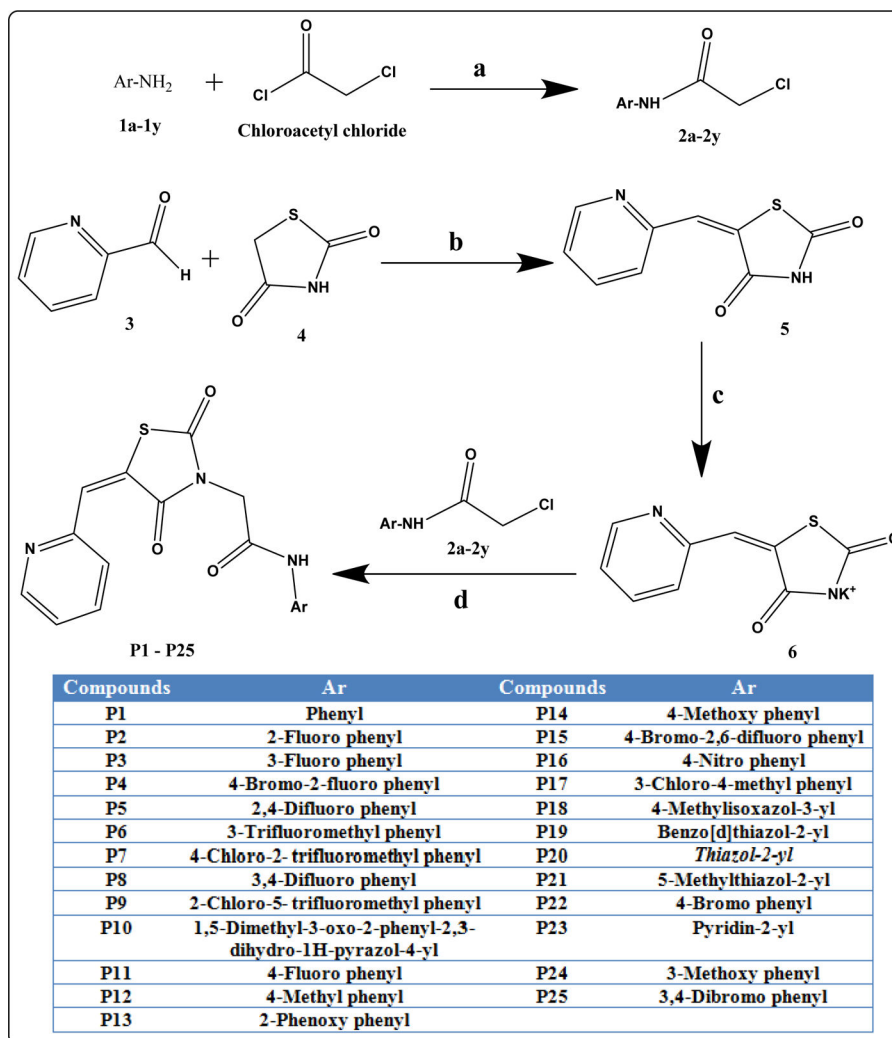


**Figure 7.** Docking analysis of compound **P19** on HDAC8 (PDB ID 1T69) and HDAC4 (PDB ID 2VQJ). A) 3D binding pose of **P19** (stick-and-ball model) within the binding pocket of HDAC8. B) 2D ligand interactions between **P19** and HDAC8. Hydrogen bonds are indicated by dashed green lines (A) or dotted green or blue arrows (B) and metal ion contacts are shown as dotted magenta lines. C) Superposition of docking poses of **P19** in the binding pocket of HDAC8 (PDB ID 1T69, orange) and HDAC4 (PDB ID 2VQJ, magenta). Green spheres represent the catalytic zinc ion of both structures. The amino acids are annotated according to the respective PDB file. The meshed surfaces indicate the respective binding pocket surfaces of HDAC8 (orange) and HDAC4 (magenta).





**Scheme 1. Synthetic route of P1-P25.**

Reaction conditions: a) DCM,  $K_2CO_3$ , 0  $^{\circ}C$ , stirring; b) AcOH, Sodium acetate, reflux 5 h; c) EtOH, KOH, reflux 3 h; d) Methanol, reflux 6 h.

**Table 1.**  
**Cytotoxic concentration 50% (CC<sub>50</sub>) of compounds P8, P9, P10, P12, P19, and P25 in**  
**leukemic cell lines (CEM, K562 and KCL22).**

Cells were exposed to different concentrations of compounds for 48 h.

Compound	Cell Line	CC50 (μM)
<b>P8</b>	CEM	36.9±1.11
	K562	40.28% cell death at 100 μM
	KCL22	29.22% cell death at 100 μM
<b>P9</b>	CEM	4.80% cell death at 100 μM
	K562	101.8±2.45
	KCL22	6.54% cell death at 100 μM
<b>P10</b>	CEM	2.39% cell death at 100 μM
	K562	27.06% cell death at 100 μM
	KCL22	17.4±2.4
<b>P12</b>	CEM	38.67% cell death at 100 μM
	K562	39.42% cell death at 100 μM
	KCL22	24.81% cell death at 100 μM
<b>P19</b>	CEM	79.9±3.74
	K562	85.4±3.25
	KCL22	43.2±0.23
<b>P25</b>	CEM	39±1.69
	K562	65.6±1.13
	KCL22	82.2±0.32

**Table 2.**

Primary screening of P1-P25 on two different classes of HDAC isoforms, HDAC4 and HDAC8.

Code	HDAC4 IC <sub>50</sub> (μM)	HDAC8 IC <sub>50</sub> (μM)	Residual HDAC4 activity at 50 μM	Residual HDAC8 activity at 50 μM
P1	>50	>50	100 %	89 %
P2	>50	>50	100 %	92 %
P3	>50	>50	100 %	53 %
P4	>50	>50	100 %	85 %
P5	50	>50	59 %	80 %
P6	>50	>50	100 %	82 %
P7	>50	>50	100 %	61 %
P8	>50	>50	100 %	82 %
P9	>50	>50	100 %	38 %
P10	>50	23±1.1	76 %	17 %
P11	>50	>50	100 %	n.d.
P12	50	47±1.1	100 %	75 %
P13	>50	>50	100 %	91 %
P14	>50	>50	100 %	67 %
P15	>50	>50	100 %	94 %
P16	>50	>50	100 %	n.d.
P17	>50	>50	100 %	88 %
P18	>50	>50	100 %	99 %
P19	>50	9.3±1.0	97 %	22 %
P20	>50	>50	100 %	92 %
P21	>50	>50	100 %	54 %
P22	>50	>50	100 %	64 %
P23	>50	>50	85 %	54 %
P24	>50	>50	100 %	68 %
P25	>50	>50	86 %	89 %

IC<sub>50</sub>-values were determined in triplicates, N=3. Means and standard deviations are provided. n.d. - not determined.

**Table 3.**IC<sub>50</sub> of P10 and P19 on a panel of HDAC.

Compounds	HDAC1	HDAC2	HDAC3	HDAC4	HDAC5	HDAC6	HDAC7	HDAC8
P10	>50	45	>50	>50	43	26	>50	23
P19	>50	41	>50	>50	>50	17	>50	9.3
PCI-34051 <sup>*</sup>	3.0	45	38	10	>50	18	-	0.024

<sup>\*</sup>Kleinschek, A., *et al.* (2016). "Potent and Selective Non-hydroxamate Histone Deacetylase 8 Inhibitors." *ChemMedChem* 11 (23): 2598–2606.

**Table 4.**

Viability of P19-treated cells by MTT and DNS assays.

<b>P19</b>	<b>MTT assay (CC<sub>50</sub> in <math>\mu</math>M)</b>	<b>DNS assay (CC<sub>50</sub> in <math>\mu</math>M)</b>
CEM	11.91	79.9
Non-cancerous cells	104.2 (WBCs)	105.0 (HS27)

Author Manuscript

Author Manuscript

Author Manuscript

Author Manuscript

**Table 5.**

Docking scores target compounds docking to the HDAC8 crystal structure.

Compound Code	GBVI/WSA dG score	Compound Code	GBVI/WSA dG score
SAHA (redocked)	-11.2	P13	-8.0
P1	-8.0	P14	-7.8
P2	-8.0	P15	-7.9
P3	-7.9	P16	-7.3
P4	-8.2	P17	-8.4
P5	-7.8	P18	-8.4
P6	-8.0	P19	-8.6
P7	-8.4	P20	-7.4
P8	-7.9	P21	-7.9
P9	-7.9	P22	-7.5
P10	-8.4	P23	-7.8
P11	-7.5	P24	-8.4
P12	-8.0	P25	-8.1

**Table 6.**

SwissADME prediction of physicochemical properties and bioavailability of compounds P1-P25.

Code	TPSA <sup>a</sup>	Log P <sup>b</sup>	Log S <sup>c</sup>	ESOL <sup>d</sup> Class	GI <sup>e</sup> absorption	Lipinski #violations	Bioavailability Score
P1	104.67	2.08	-3.4	Soluble	High	0	0.55
P2	104.67	2.64	-3.56	Soluble	High	0	0.55
P3	104.67	2.64	-3.56	Soluble	High	0	0.55
P4	104.67	3.4	-4.47	Moderately soluble	High	0	0.55
P5	104.67	3.19	-3.72	Soluble	High	0	0.55
P6	104.67	4.25	-4.26	Moderately soluble	High	0	0.55
P5	104.67	4.9	-4.86	Moderately soluble	High	0	0.55
P8	104.67	3.38	-4.59	Moderately soluble	High	0	0.55
P9	104.67	4.9	-4.86	Moderately soluble	High	0	0.55
P10	131.6	1.87	-4.21	Moderately soluble	High	0	0.55
P11	104.67	2.64	-3.56	Soluble	High	0	0.55
P12	104.67	2.38	-3.7	Soluble	High	0	0.55
P13	113.9	3.87	-4.86	Moderately soluble	High	0	0.55
P14	113.9	2.08	-3.47	Soluble	High	0	0.55
P15	104.67	3.96	-4.63	Moderately soluble	High	0	0.55
P16	150.49	1.98	-3.47	Soluble	Low	0	0.55
P17	104.67	3.04	-4.3	Moderately soluble	High	0	0.55
P18	145.8	2.69	-4.29	Moderately soluble	Low	0	0.55
P19	130.7	1.37	-2.86	Soluble	High	0	0.55
P20	145.8	1.53	-3.03	Soluble	Low	0	0.55
P21	145.8	1.84	-3.35	Soluble	Low	0	0.55
P22	104.67	2.84	-4.31	Moderately soluble	High	0	0.55
P23	117.56	1.47	-2.94	Soluble	High	0	0.55
P24	113.9	2.08	-3.47	Soluble	High	0	0.55
P25	104.67	3.6	-5.22	Moderately soluble	High	0	0.55

<sup>a</sup>Topological polar surface area;<sup>b</sup>Log of the partition coefficient (P);<sup>c</sup>Log solubility;<sup>d</sup>Estimated aqueous solubility in mg/mL;<sup>e</sup>Gastrointestinal.

---

## 5.4 Publikationen zu anderen Themen während der Doktorarbeit

Das letzte Unterkapitel des kumulativen Teiles der vorliegenden Doktorarbeit fasst sämtliche Publikationen zusammen, welche über die zuvor beschriebenen Themenbereiche hinausgehen und abseits vom Hauptthema auf anderen, aber ähnlichen Gebieten entstanden sind. Die erste Publikation beschreibt detailliert den Wirkmechanismus von Thiazolidindionen auf die katalytische Domäne von HDAC4. Histondeacetylasen teilen sich ein hoch konserviertes Aktivzentrum mit nur geringen Unterschieden untereinander. Darauf aufbauend wurde aus der im vorherigen Unterkapitel beschriebenen Wirkstofffindungs-Kampagne von Thiazolidindionen gegen HDAC8 vielversprechende Treffer gegen HDAC4 gefunden. Diese strukturell unterschiedlichen Thiazolidindione weisen eine bis zu 10-fach höhere Potenz gegen HDAC4 auf und es konnten Inhibitoren bis knapp unter 1  $\mu\text{M}$   $\text{IC}_{50}$  gefunden werden.

Im Rahmen der ersten Publikation wurden durch zielgerichtete Mutagenese ausgewählte Aminosäuren innerhalb des Aktivzentrum mutiert und der Einfluss der Mutation auf die Bindung der Inhibitoren untersucht. Somit konnte klar gezeigt werden, dass diese Gruppe an Inhibitoren im Aktivzentrum der geschlossenen Konformation der HDAC4 bindet und welche Aminosäuren für die Inhibition essenziell sind.

Die zweite Publikation befasst sich mit der Entdeckung eines kinetisch selektiven Inhibitors gegen HDAC8. Der eigentlich als Fluoreszenzsonde verwendende Ligand mm255 weist in erster Betrachtung keine herausragende Selektivität gegenüber anderen Histondeacetylasen auf, jedoch wurde durch kinetische Messungen herausgefunden, dass dieser Ligand eine herausragende Verweilzeit von mehreren Stunden an HDAC8 besitzt, was für andere HDACs nicht der Fall ist. Diese lange Verweilzeit ist abhängig von der Länge des Linkers, was sich mit der Bindung der Kopfgruppe an eine zweite, distale Bindungstasche erklären lässt. Bei Einkürzung des Linkers um eine Methyleneinheit ist der Effekt der langen Verweilzeit nicht mehr zu beobachten, da die Kopfgruppe nicht mehr in die zweite Bindetasche hereinragt. Zusätzlich wurden diese Ergebnisse durch die Messung der thermischen Stabilisierung von HDAC8 durch den Liganden bestätigt, bei welcher sich der gleiche Effekt des Einflusses der Länge des Linkers zeigt.

Die dritte Publikation dieses Unterkapitels widmet sich der Nutzung von statistischer Versuchsplanung für die Optimierung von Enzymaktivitätsassays zur Findung von Inhibitoren. Die Publikation erörtert theoretische Hintergründe der Michaelis-Menten Theorie und kompetitiven Hemmung und wie sich dies mittels Methoden der statistischen Versuchsplanung im Rahmen eines Studentenpraktikums vermitteln lässt. Die Methodik wurde in einem Fachjournal für chemische Hochschullehre von Springer publiziert.

Die letzte und vierte Publikation untersucht den Einfluss der Aminosäure Methionin innerhalb des Aktivzentrums von HDAC8 auf die Bindung Isoenzym-selektiver Inhibitoren. Ausgang der Untersuchung war eine publizierte *in silico* Studie, welche zum Ergebnis hatte, dass Methionin 274 entscheidend für die Bindung L-förmiger Inhibitoren an HDAC8 ist. L-förmige HDAC-Inhibitoren wie PCI-34051 sind allesamt HDAC8 selektiv. Innerhalb dieser Doktorarbeit wurden die *in silico* Ergebnisse herangezogen und durch Mutation von Methionin und *in vitro* Experimente genauer untersucht, um den Grund für die Isoenzym-Selektivität besser zu verstehen. Ergebnis dieser Untersuchung war, dass Met<sub>274</sub> nicht der bestimmende Faktor für die selektive Bindung L-förmiger HDAC8 Inhibitoren an HDAC8 ist.



---

**Titel:**

Mechanistic Insights into Binding of Ligands with Thiazolidinedione Warhead to Human Histone Deacetylase 4

**Autoren:**

Markus Schweipert, Niklas Jansch, Neha Upadhyay, Kalpana Tilekar, Ewelina Wozny, Sidra Basheer, Eva Wurster, Marlene Müller, Ramaa C S and Franz-Josef Meyer-Almes

**Bibliographische Daten:**

Pharmaceuticals (doi.org/10.3390/ph14101032)

**Zusammenfassung:**

Kürzlich haben wir berichtet, dass Nicht-Hydroxamat-Thiazolidindion-Analoga (TZD) in der Lage sind, die humane Histondeacetylase 4 (HDAC4) zu hemmen. Diese Studie zielt darauf ab, die molekularen Determinanten und die Kinetik der molekularen Erkennung von TZD-Liganden durch HDAC4 zu entschlüsseln. Zu diesem Zweck wurde eine Analyse der Struktur-Aktivitäts-Beziehung von 225 Analoga mit einer umfassenden Untersuchung des Enzyms und der Bindungskinetik einer Reihe von HDAC4-Mutanten kombiniert. Die experimentellen Daten wurden durch Docking an die beiden Hauptkonformationen von HDAC4 rationalisiert. Die TZD-Liganden sind kompetitive Inhibitoren und binden über einen zweistufigen Mechanismus, der eine molekulare Haupterkennung und eine induzierte Anpassung umfasst. Die Verweildauer von 24 g beträgt  $(34 \pm 3)$  Minuten und ist damit wesentlich länger als die des kanonischen pan-HDAC-Inhibitors SAHA ( $(5 \pm 2)$  Minuten). Wichtig ist, dass die Bindungskinetik durch Variation der Struktur der CAP-Gruppe eingestellt werden kann.



## Article

# Mechanistic Insights into Binding of Ligands with Thiazolidinedione Warhead to Human Histone Deacetylase 4

Markus Schweipert<sup>1,†</sup>, Niklas Jänsch<sup>1,†</sup>, Neha Upadhyay<sup>2</sup>, Kalpana Tilekar<sup>2</sup>, Ewelina Wozny<sup>1</sup>, Sidra Basheer<sup>1</sup>, Eva Wurster<sup>1</sup>, Marlene Müller<sup>1</sup>, Ramaa C S<sup>2,\*</sup> and Franz-Josef Meyer-Almes<sup>1,\*</sup>

<sup>1</sup> Department of Chemical Engineering and Biotechnology, University of Applied Sciences, 64295 Darmstadt, Germany; markus.schweipert@h-da.de (M.S.); niklas.jaensch@h-da.de (N.J.); ewelina.wozny@stud.h-da.de (E.W.); sidra.basheer@stud.h-da.de (S.B.); eva.wurster@stud.h-da.de (E.W.); marlene.mueller@stud.h-da.de (M.M.)

<sup>2</sup> Department of Pharmaceutical Chemistry, Bharati Vidyapeeth's College of Pharmacy, Navi Mumbai 400614, India; upadhyayneha16@gmail.com (N.U.); kalpana.tilekar@gmail.com (K.T.)

\* Correspondence: sinharamaa@yahoo.in (R.C.S.); franz-josef.meyer-almes@h-da.de (F.-J.M.-A.)

† These authors contributed equally to this work.

**Abstract:** Recently, we have reported that non-hydroxamate thiazolidinedione (TZD) analogs are capable of inhibiting human deacetylase 4 (HDAC4). This study aims at the dissection of the molecular determinants and kinetics of the molecular recognition of TZD ligands by HDAC4. For this purpose, a structure activity relationship analysis of 225 analogs was combined with a comprehensive study of the enzyme and binding kinetics of a variety of HDAC4 mutant variants. The experimental data were rationalized by docking to the two major conformations of HDAC4. TZD ligands are competitive inhibitors and bind via a two-step mechanism involving principal molecular recognition and induced fit. The residence time of 24 g is  $(34 \pm 3)$  min and thus much larger than that of the canonical pan-HDAC inhibitor SAHA ( $(5 \pm 2)$  min). Importantly, the binding kinetics can be tuned by varying the structure of the CAP group.

**Keywords:** Human Histone Deacetylase 4 (HDAC4); thiazolidinediones; binding mechanism; mutational study



**Citation:** Schweipert, M.; Jänsch, N.; Upadhyay, N.; Tilekar, K.; Wozny, E.; Basheer, S.; Wurster, E.; Müller, M.; C S, R.; Meyer-Almes, F.-J. Mechanistic Insights into Binding of Ligands with Thiazolidinedione Warhead to Human Histone Deacetylase 4. *Pharmaceuticals* **2021**, *14*, 1032. <https://doi.org/10.3390/ph14101032>

Academic Editor: Carlos Alberto Manssour Fraga

Received: 6 September 2021

Accepted: 29 September 2021

Published: 11 October 2021

**Publisher's Note:** MDPI stays neutral with regard to jurisdictional claims in published maps and institutional affiliations.



**Copyright:** © 2021 by the authors. Licensee MDPI, Basel, Switzerland. This article is an open access article distributed under the terms and conditions of the Creative Commons Attribution (CC BY) license (<https://creativecommons.org/licenses/by/4.0/>).

## 1. Introduction

HDAC4 is a class IIa zinc-dependent histone deacetylase (HDAC) which is highly expressed in the brain, heart, and skeletal muscle and plays a major role in tissue growth and physiological development [1]. With a length of 972 to 1084 amino acids and a molecular weight of ca. 120 kDa, it is one of the biggest HDACs across all four HDAC classes [2]. For this study, the catalytic domain of HDAC4 (cdHDAC4) was used, which consists of 410 amino acids (human HDAC4 T648-T1057) and has a molecular weight of 44.2 kDa. In vivo as well as in vitro HDAC4 shows an exceptionally low to nonexistent deacetylation activity towards natural acetylated substrates due to tyrosine to histidine mutation located in the active site. Therefore, enzymatic activity is not the primary biological function of HDAC4. Like all members of class IIa HDACs, HDAC4 has a highly flexible structural zinc binding domain (sZBD) with a second zinc atom in addition to the catalytic zinc in the enzyme's active site. Because of the sZBD HDAC4 can adopt two distinct conformations with different types of inhibitors (open and closed) in x-ray crystal structures [3,4]. In the open conformation the sZBD is flipped out of the globular protein structure and therefore far away from HDAC4's catalytic site. For the closed conformation, this is not the case [3]. HDAC4 can shuttle between nucleus and cytoplasm, which is its primary biological function [5]. With the help of nuclear receptor co-repressor (NCoR) as well as silencing mediator for retinoid or thyroid-hormone receptors (SMRT) HDAC4 can shuttle HDAC3 between nucleus and cytoplasm and therefore plays a key role in the distribution

of enzymatically active HDAC3 in mammal cells. For this process, the sZBD serves as a scaffold to bind the SMRT/NCoR protein complex, which subsequently binds HDAC3. The sZBD is essential for the recognition of the SMRT/NCoR protein complex and can only bind in its closed conformation, which is believed to be the biologically relevant conformation [6]. Several nephrological and neurodegenerative diseases, [7,8] as well as cancer types like breast cancer are related to HDAC4 making the protein an attractive drug target [1,2,8,9]. Furthermore, studies showed that inhibition of HDAC4 activity in animal models can reduce symptoms of Huntington's disease, which may be a potential treatment for this yet incurable disease [10,11]. Most of present HDAC inhibitors contain a hydroxamic acid as zinc binding group and are more or less unselective inhibitors of all zinc-dependent HDACs. This applies also to HDAC inhibitory drugs like Vorinostat [12], Belinostat [13], and Panobinostat [14], which are approved for the treatment of cutaneous T-cell lymphoma. Nowadays, hydroxamic acids are not only considered as a source of unselectivity but also under suspicion for their mutagenic potential [15]. Therefore, alternative zinc binding groups are highly desired. 1,3-Thiazolidine-2,4-dione (TZD) containing compounds, also known as glitazones, were originally developed by Takeda Pharmaceutical in Japan as drugs for the treatment of type 2 diabetes mellitus. TZD ligands act via activation of the gamma type of peroxisome proliferator-activated receptors (PPAR $\gamma$ ) in the nucleus [16,17]. Furthermore, some TZD ligands are capable to inhibit aldose reductase (ALR2), protein tyrosine phosphatase 1B (PTP1B) and  $\alpha$ -glucosidase [18]. Very recently, we reported on TZD-containing ligands, which are capable to inhibit HDAC4 [18,19]. Enzyme activity assays of the HDAC family demonstrated activity of TZD ligands against HDAC4 or HDAC8 depending on the substitution pattern. Furthermore, some TZD containing compounds exhibited also activity towards other protein families such as the glucose transporters GLUT1, GLUT4 and GLUT5 [20,21]. Importantly, some of the dual targeting TZD ligands show in vivo effects by drastically lowering the viability of K562 chronic myeloid leukaemia cell lines resulting in rapid cell death as well as anti-tumor effects in tumor xenograft models [18]. Although the activity of TZD ligands towards HDAC4 has been described very recently, their mode of action is still uncharted [18]. This study focuses on the elucidation of the detailed mechanism of interaction between TZD ligands and HDAC4. An extensive structure activity relationship (SAR) analysis was carried out to dissect the structural elements, which are important for the potent and selective inhibition of HDAC4 by TZD ligands. The binding mode was analyzed by Michaelis Menten kinetics [22]. Combined with a comprehensive mutational study we were able to assess the impact of particular amino acids on substrate affinity and binding constant of TZD ligands. The binding kinetics of selected TZD analogs were measured to determine the binding mechanism and important kinetic constants like the residence time of the compounds on the HDAC4 target. Finally, docking was applied to rationalize the experimental binding data and predict binding poses of TZD ligands.

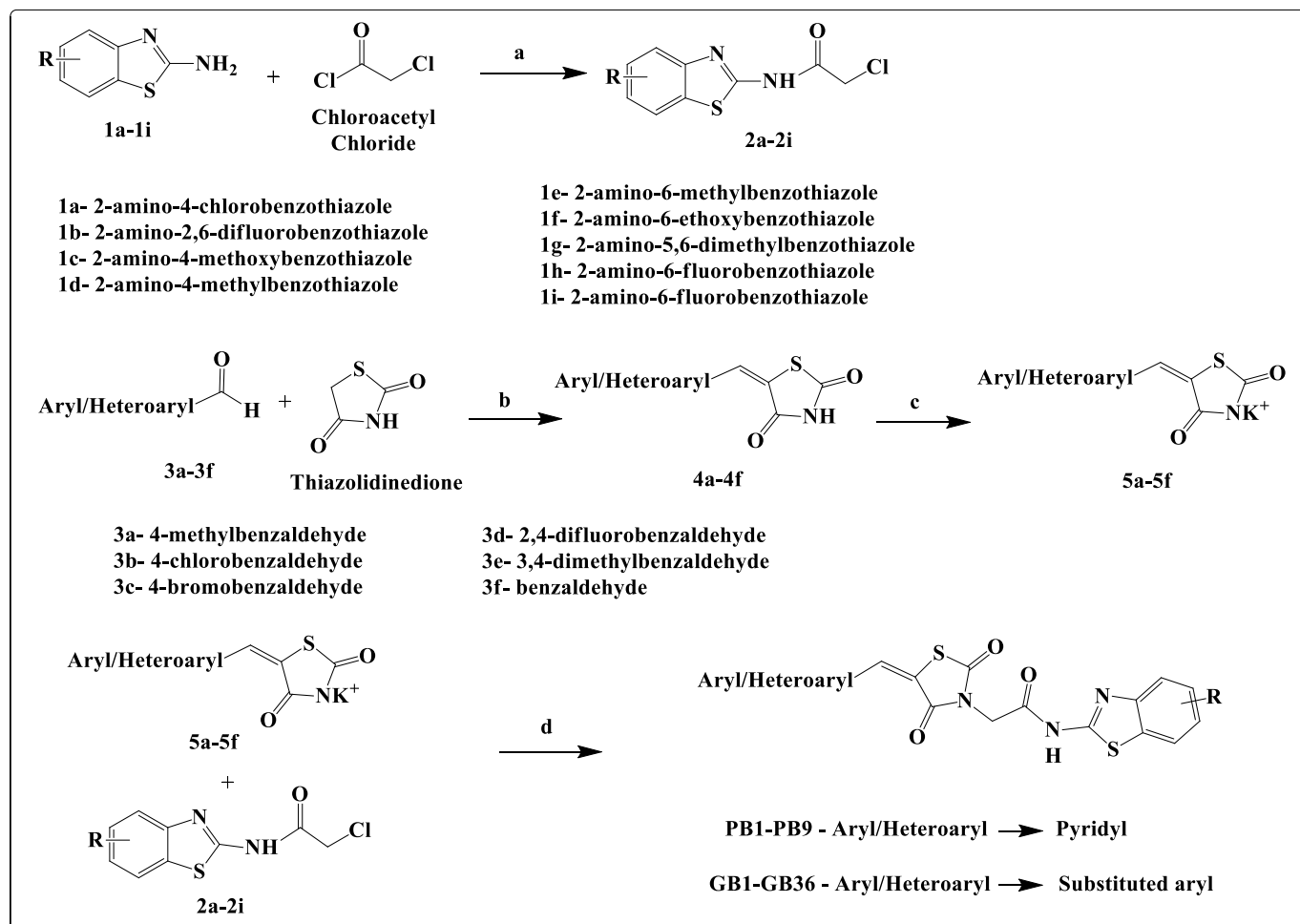
## 2. Results and Discussion

### 2.1. Chemistry

#### Synthesis of Compounds PB1–PB9 and GB1–GB36

The chloroacetylated amide (**2a–2i**) intermediates were synthesized by condensing differently substituted benzothiazoleamines (**1a–1i**) with chloroacetylchloride by procedure previously reported elsewhere (Scheme 1) [23,24]. To brief, chloroacetyl chloride was dropwise added to a chilled solution of substituted amines (**1a–1i**) and potassium carbonate in dichloromethane (DCM) solvent, and allowed to stir overnight. The crude was collected by evaporating the solvent under vacuum and recrystallized with ethanol. This chloroacetylated intermediate was common for the synthesis of both sets of compounds. All the Knoevenagel intermediates (**4a–4f**) were obtained by procedure previously reported [23,24]. Thiazolidine-2,4-dione (5 gm, 0.04 moles) was refluxed for 3–6 h by intermittent stirring with pyridine-2-carboxaldehyde (5 gm, 0.07 moles) (for PB set) in the presence of sodium acetate (3 gm, 0.003 moles), and acetic acid (10 mL). The reaction

mixture was allowed to cool and crystalline crude obtained was collected by vacuum filter and washed with water and air dried to obtain the respective pyridyl Knoevenagel intermediate (4). This intermediate was used for the synthesis of PB set of compounds.



**Scheme 1.** Synthesis of compounds (PB1–PB9 and GB1–GB36). Reagents and conditions: (a)  $K_2CO_3$ , DCM, Stir at RT for 24 h. (b) Acetic acid, Sodium acetate, reflux 3–6 h; (c) EtOH, KOH, reflux 1–2 h. (d) Acetone, reflux 6–10 h.

Potassium hydroxide (2.5 gm, 0.044 moles) in ethanol was added to the pyridyl Knoevenagel intermediate (4) (5.0 gm, 0.025 moles) in a flat bottom flask and this mixture was refluxed with stirring for 3–4 h. After cooling the reaction mixture, crude salt was obtained by filtering under vacuum pump, washed with cold ethanol, and air dried to obtain intermediate 5. Final compounds (**PB1–PB9**) were obtained by refluxing the two intermediates in equimolar ratio, **2a–2i** (0.044 moles) and **5** (0.044 moles) in acetone for 6–8 h. The reaction was monitored for completion by TLC using hexane: ethylacetate mobile phase. The reaction mixture was poured into crushed ice and precipitated solid was filtered under vacuum and this residue was purified by column chromatography by using ethyl acetate: hexane mobile phase in the ratio of 10:90 to 40:60.

For the synthesis of GB set of compounds, thiazolidine-2,4-dione (5 gm, 0.04 moles) was refluxed for 3–6 h with intermittent stirring with differently substituted aldehydes (**3a–3f**, Scheme 1) (5 gm, 0.07 moles) in the presence of sodium acetate (3 gm, 0.003 moles), and acetic acid (10 mL). Upon cooling, a crystalline crude was obtained which was collected by vacuum filter and washed with water, and air dried to obtain the respective Knoevenagel intermediates (**4a–4f**). The potassium salts were prepared as per previously reported procedure [23,24]. Potassium hydroxide (2.5 gm, 0.044 moles) in ethanol was added to Knoevenagel intermediates (**4a–4f**) (5.0 gm, 0.025 moles) in a flat bottom flask and this

mixture was refluxed with stirring for 3–4 h. After cooling, the crude salts were obtained by filtering under vacuum pump, washed with cold ethanol, and air dried to obtain **5a–5f**. Final compounds (**GB1–GB36**) were obtained by refluxing the two intermediates in equimolar ratio, **2a–2i** (0.044 moles) and **5a–5f** (0.044 moles) in acetone for 6–8 h. The reaction was monitored for completion by TLC using hexane: ethylacetate mobile phase. The reaction mixture was poured into crushed ice and precipitated solid was filtered under vacuum and this residue was purified by column chromatography by using ethyl acetate: hexane mobile phase in the ration of 10:90 to 40:60.

## 2.2. Elucidation of the Mechanism of Action of TZD Ligands

### 2.2.1. An Elongated Ligand Structure with Terminal TZD Group Is Crucial for HDAC4 Activity

This study evaluated 223 TZD ligand analogs including newly synthesized compounds PB1–PB9 and GB1–GB36 with different substitution patterns (Table S1). Many of the TZD ligands have been published very recently to be HDAC4 or HDAC8 inhibitors [18,19,25]. This large ensemble of TZD ligands was utilized to derive a SAR and identify ligand moieties crucial for binding to the catalytic domain of human wild type histone deacetylase 4 (cdHDAC4<sub>wt</sub>). To gain a thorough understanding of the binding the enzymatic activity of cdHDAC4<sub>wt</sub> was tested in the presence of TZD ligands with different types of linkers between the TZD moiety and the CAP group and different CAP groups with varying substitution patterns. The linkers have different attachment points that determine the overall elongated or kinked structure of the ligands. 97 out of 223 TZD ligands exhibited IC<sub>50</sub>-values under 50 µM against cdHDAC4<sub>wt</sub>. This data was used for SAR analysis. By utilizing the DataWarrior program ([www.openmolecules.org](http://www.openmolecules.org), accessed on 8 March 2021) and its integrated similarity analysis algorithm, a similarity map of all tested TZD ligands was created that produced ten clusters of structurally similar compounds (Figure 1). Clusters 1–4 included the most potent TZD ligands with IC<sub>50</sub>-values below 2 µM. The members of these clusters differed in CAP group and linker type that connected CAP group and TZD moiety. CAP groups of potent TZD ligands consisted of dihydropyrazole that was decorated either by two differently substituted phenyl rings, furan or thiophene (cluster 1 and 3), single differently substituted phenyl or pyridine rings (cluster 2) or benzothiazoles (cluster 4). Different substitutions at those CAP groups as well as different linker types (e.g., naphthalene, phenyl, pyridine), further tuned individual TZD ligand affinity towards cdHDAC4<sub>wt</sub> within the clusters. TZD ligand **8b** in cluster 1 showed the lowest IC<sub>50</sub>-value of 330 nM (Table 1). The common feature of all potent clusters was a terminal TZD moiety in an elongated overall structure. Cluster 5 contained TZD ligands with moderate activities, which were similar to the compounds in cluster 4. The benzothiazole moiety in cluster 5 compounds was replaced with differently substituted phenyl moieties in cluster 4 analogs. Essentially inactive inhibitors in cluster 6 demonstrated the importance of linker arrangement. The only difference between cluster 6 and cluster 2 was a 1,2- versus 2,6-connection of the naphthyl linker, respectively. Nearly all non-potent TZD ligands contained a TZD moiety in the molecule's center indicating that a central sterically hindered TZD moiety was not able to bind to cdHDAC4<sub>wt</sub> (Cluster 7–10) (Figure 1). In these analogs, the TZD moiety served as a linker between different moieties such as benzothiazoles, differently substituted phenyls, and pyridines. The most active TZD ligands in clusters 1–4 were all elongated compounds with terminal sterically unhindered TZD group and selected to elucidate the binding mode and mechanism to cdHDAC4<sub>wt</sub>.

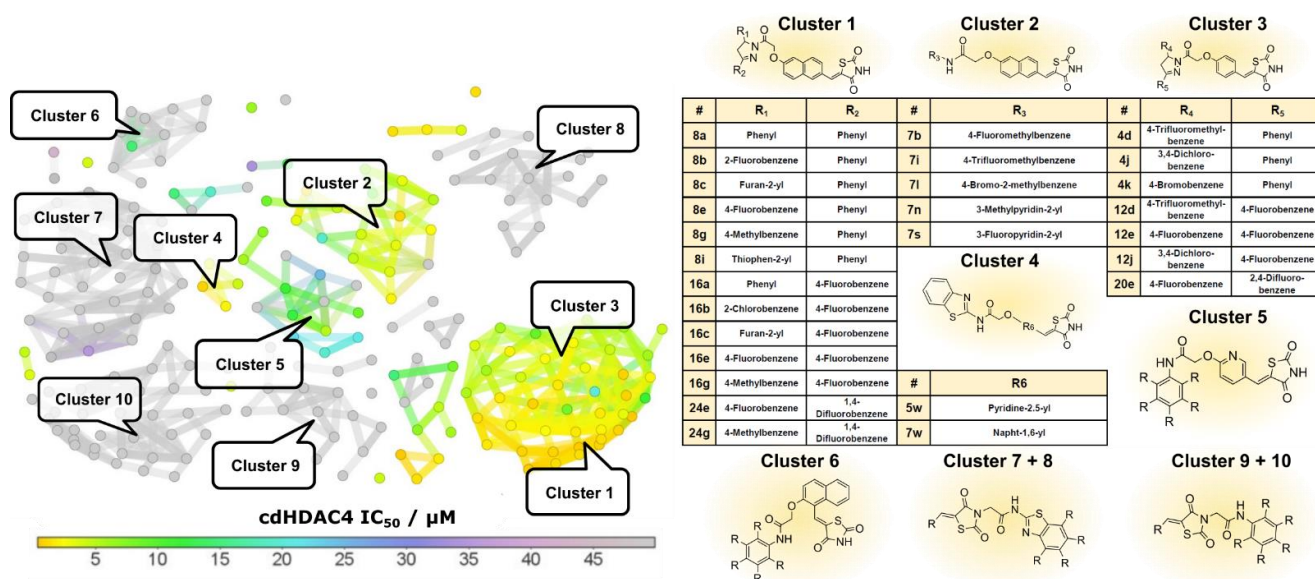


**Figure 1.** Similarity map for structural activity relationship analysis for 225 TZD containing compounds. The similarity map revealed ten clusters with varying inhibitory potencies towards cdHDAC<sub>4wt</sub>. Marker color and connecting lines highlight inhibitory activity and similarity pairs, respectively. Filled gray circles represent inactive TZD ligands with IC<sub>50</sub>-values > 50 μM.

### 2.2.2. TZD Ligands Are Competitive Inhibitors

Encouraged by promising cdHDAC<sub>4wt</sub> activity of the TZD ligands despite the absence of a canonical zinc binding group the mode of action was analyzed by applying Michaelis Menten kinetics to determine, whether TZD ligands are competitive inhibitors and thus bind at the active site, or otherwise bind at an allosteric site of the enzyme. 9,9,9-Trifluoro-8-oxo-N-phenyl-nonanamide (SATFMK), a trifluoromethylketone analog of SAHA (Vorinostat) and known reversible and competitive inhibitor, was used as control. Higher concentrations of both, SATFMK and the representative TZD ligand 5w, produced increasing  $K_m$  values but showed essentially unchanged maximum enzyme velocity,  $v_{max}$  (Figure 2). Therefore, TZD ligand 5w binds as a competitive inhibitor within the active site of cdHDAC<sub>4wt</sub>. The complete set of Michaelis Menten data is available in the supplementary information (Figure S1).

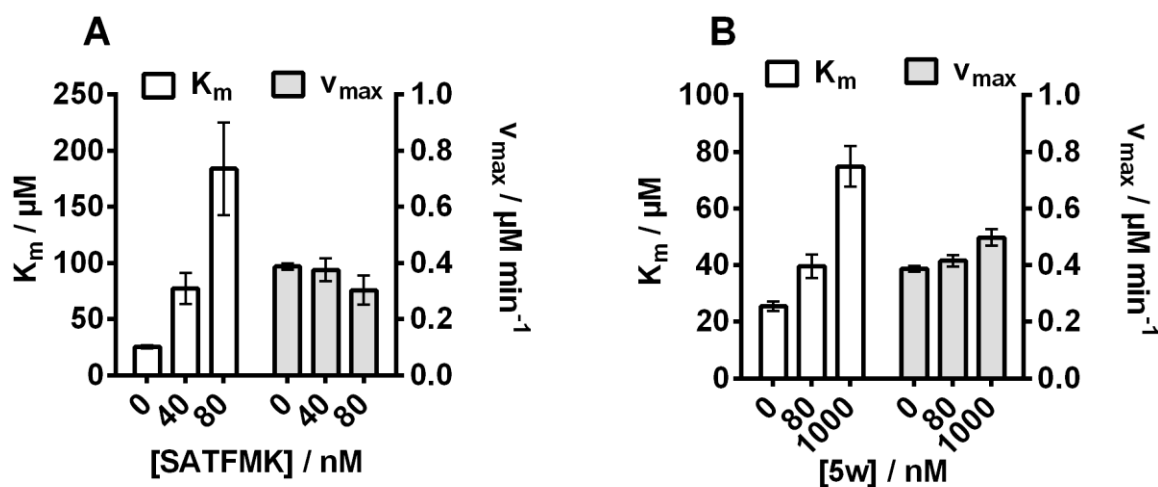


**Figure 2.** Michaelis Menten parameters for the determination of the mode of action with increasing compound concentration.  $K_m$ - and  $V_{max}$ -values of (A) SATFMK and (B) TZD ligand 5w showed increasing and stagnating values, respectively, as expected for a competitive inhibitor. Shown data represent means and standard deviations,  $N = 3$ .

### 2.2.3. Binding Kinetics and Mechanism of TZD Ligands Depend on the CAP-Group

Binding kinetics of potential drugs are crucial for in vivo activity [26]. Therefore association kinetic measurements based on Michaelis Menten enzyme kinetics (Figure 3) were performed for selected compounds including 15 representative TZD ligands (**4d**, **5w**, **7i**, **7s**, **7w**, **8a**, **8b**, **8c**, **8g**, **8i**, **12j**, **16b**, **16c**, **16g**, and **24g**) from structural clusters 1–4 having  $IC_{50}$ -values under 2  $\mu$ M towards cdHDAC4<sub>wt</sub>. The kinetic progression curves revealed a slow association behavior of all tested compounds (Table 1 and Figure 4A,C,E). The association kinetics did not reveal significant differences between clusters 1 and 3 (**4d**, **8a**, **8b**, **8c**, **8g**, **8i**, **12j**, **16b**, **16c**, **16g**, and **24g**). The data were analyzed by plotting the rate,  $k_{obs}$ , by which the enzyme velocity is slowed down, versus inhibitor concentration [27]. All compounds from clusters 1 and 3 showed a saturating behavior of  $k_{obs}$  with increasing ligand concentrations (Figures 4B and S2). The saturating curve progression of the fitted rate values indicated a two-step mechanism, in which the first step was significantly faster than the second step. Although the tested TZD ligands of clusters 1 and 3 exhibited a certain degree of structural diversity, all compounds display similar plateaus of rate constants, suggesting that the rate was limited by conformational changes of the initially formed protein-ligand complex. Consequently, the rate constants were fitted to an induced fit kinetic model, which considers the formation of an initial encounter complex of compound and enzyme under rapid equilibrium conditions followed by a slower rate-limiting subsequent isomerization of the enzyme (Figure 3) [27]. The details about the application of the fitting equations for the association as well as dissociation rate calculations are described in the methods section.

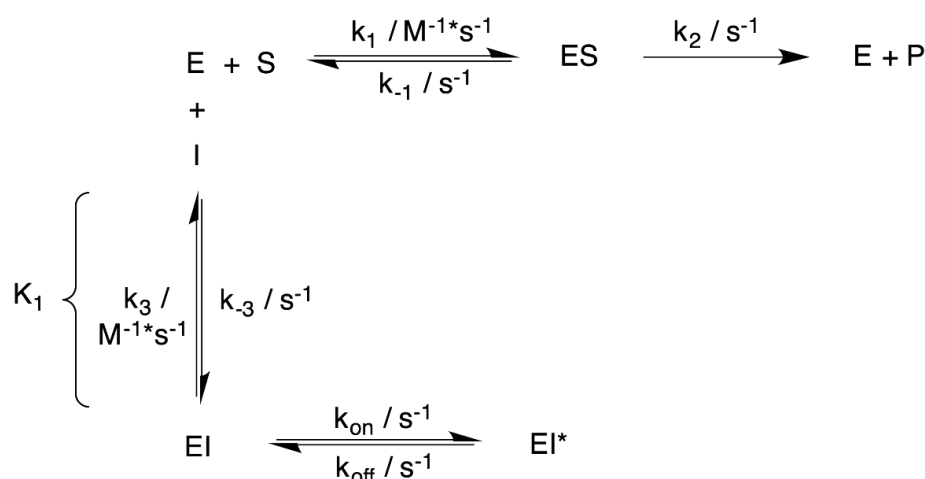


**Figure 3.** Induced fit binding model based on Michaelis Menten enzyme kinetics. Enzyme (E) and Substrate (S) are forming an enzyme-substrate complex (ES) in a reversible manner. Subsequently the substrate is irreversibly converted into the product (P), releasing free enzyme in the process. During an induced fit binding mode the inhibitor (I) and the enzyme form an initial enzyme-inhibitor complex (EI) under rapid equilibrium conditions, followed by an enzyme isomerization resulting in a tight binding enzyme-inhibitor complex (EI\*). Note that  $k_2$  as well as the isomerization rates ( $k_{on}$  and  $k_{off}$ ) are not dose dependent.

The equilibrium constant,  $K_1$ , for the initial encounter complex were determined for TZD ligands **8b**, **8i**, **24g**, **8g**, **8a**, **4d** and ranged from 0.65  $\mu$ M (**8b**) to 3  $\mu$ M (**8g**) (Table 1). However, because of the rapid equilibrium condition and comparably low temporal resolution of the applied manual semi continuous kinetic assay,  $K_1$ -values for TZD ligands **8c**, **16b**, **16c**, **16g** and **12j** could not be determined due to large error values. For these compounds, a faster automated kinetic assay (e.g., stopped flow) may be more useful for resolving the initial association step. Furthermore,  $k_{on}$  rate constants were determined for all TZD ligands in cluster 1 and 3. Said compounds exhibited similar  $k_{on}$ -values between  $(2.1 \pm 0.9) \times 10^{-3} s^{-1}$  (**8c**) and  $(5.4 \pm 0.5) \times 10^{-3} s^{-1}$  (**8i**) (Table 1). Only TZD ligand **4d** showed a moderately deviating  $k_{on}$ -value of  $(8 \pm 1) \times 10^{-3} s^{-1}$ . Within clusters 1 and

3 differently substituted CAP groups did not show a significant influence on  $k_{on}$ -values. However, larger variations of the CAP group had a strong influence on the binding behavior of TZD ligands. By plotting the gained  $k_{obs}$ -values versus the respective TZD ligand concentration, one could clearly distinguish between clusters 1/3 and clusters 2 or cluster 4 (Figures 4 and S2). The already mentioned saturating behavior of plotted  $k_{obs}$ -values was only found with clusters 1 and 3, which contained TZD ligands with dihydropyrazole that was substituted by two phenyl rings, differently substituted phenyl rings, furan or thiophene as CAP group. By plotting  $k_{obs}$ -values against the corresponding ligand concentration the  $y$ -axis intercept marked the dissociation rate ( $k_{off}$ ). Here, the tested TZD ligands had values between  $5.4 \times 10^{-4} \text{ s}^{-1}$  and  $1.8 \times 10^{-3} \text{ s}^{-1}$  resulting in residence times (residence time =  $1/k_{off}$ ) between  $(9 \pm 3) \text{ min}$  (**12j**) and  $(31 \pm 17) \text{ min}$  (**24g**) (Table 1). Unfortunately, the residence times of TZD ligands **16g** and **16c** could not be determined with this method due to large error values. The uncertainty in the determination of the  $y$ -axis intercept was attributed to errors at low TZD ligand concentration. The reciprocal transformation of  $k_{off}$ -values to residence times further enhanced these errors. Therefore, additional reversibility tests were carried out via rapid dilution providing residual  $cdHDAC4_{wt}$  activities between 36% (**24g**) and 88% (**16b**) 15 min after rapid dilution of fully inhibited enzyme-inhibitor complexes (Figure 4H). Under the assumption of first order dissociation behavior, the corresponding residence times were calculated to be between 7 min and 34 min. With this method, the residence times of TZD ligands **16g** and **16c** were determined to be  $(15 \pm 2) \text{ min}$  and  $(21 \pm 7) \text{ min}$ , respectively (Table 1). Within the margin of error, the long residence times calculated by association kinetic measurements were in good agreement with the data obtained from rapid dilution experiments (Table 1). The TZD ligands of cluster 1 and 3 showed a significantly different kinetic behavior compared to reference compound SAHA and TZD ligands of clusters 2 and 4. Members of the latter clusters did not show a saturating behavior of  $k_{obs}$  plotted versus the respective TZD ligand concentration and, therefore, the rate constants were not fitted to the equation considering enzyme isomerization (Figures 4D,F and S2). Linear regression of plotted  $k_{obs}$ -values of TZD ligands **7i** and **7s** of cluster 2 calculated  $k_3$ -values from slopes of  $(100 \pm 30) \text{ M}^{-1} \text{ s}^{-1}$  and  $(210 \pm 40) \text{ M}^{-1} \text{ s}^{-1}$  and  $y$ -intercepts of  $(1.8 \times 10^{-3}) \text{ s}^{-1}$  and  $(1.6 \times 10^{-3}) \text{ s}^{-1}$ . Residence times of  $(9.3 \pm 0.5) \text{ min}$  and  $(10 \pm 1) \text{ min}$  were calculated from the corresponding  $k_{-3}$  rates equal to the  $y$ -axis intercept, respectively.

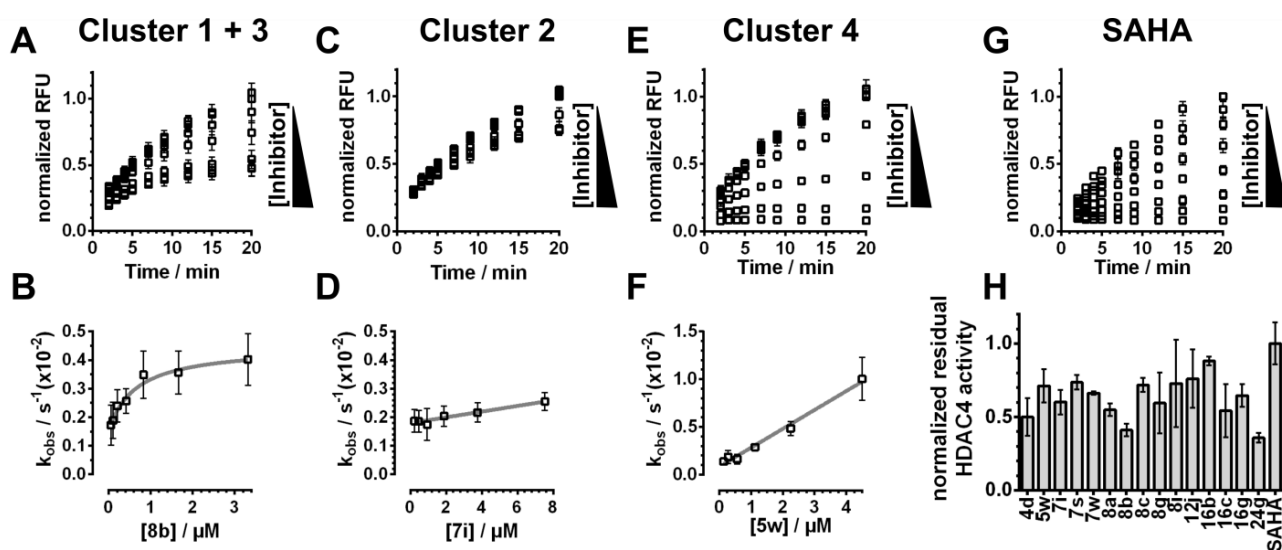


**Figure 4.** Association kinetics of HDAC4 and TZD ligands from different structural clusters. The association kinetics correlates with the chemical structure of TZD ligands and is substantially different between compound clusters 1–4. (A–F) Cluster 1 + 3, cluster 2 and cluster 4 are represented by TZD ligands **8b**, **7i** and **5w**, respectively. (G) Association kinetics of reference compound SAHA. (H) Residual  $cdHDAC4_{wt}$  activity 15 min after rapid dilution of all 15 tested TZD ligands and SAHA. Shown data represent means and standard deviations,  $N = 3$ .



The small slope of  $k_{\text{obs}}$  for cluster 2 TZD ligands indicated slow binding behavior, which was confirmed by the association progress curves and did not reach plateaus within the assay's 20 min timeframe even at 10-fold  $\text{IC}_{50}$  concentration (Figures 4C,D and S2). Cluster 1 and 3 as well as cluster 4 did not show such slow binding behavior. In rapid dilution reversibility experiments TZD ligands **7i** and **7s** of cluster 2 revealed residence times of  $(17 \pm 3)$  min and  $(11 \pm 1)$  min, respectively. In the case of TZD ligand **7s** the residence times calculated from association kinetics and reversibility experiments were in agreement (Table 1). For TZD ligand **7i** the confidence intervals of residence times obtained from both methods did not overlap, but, with values of  $(9.3 \pm 0.5)$  min and  $(17 \pm 3)$  min, was in the same order of magnitude. TZD ligands **5w** and **7w** of cluster 4 exhibited also linear behavior of  $k_{\text{obs}}$  vs. ligand concentration with a slope ( $k_3$ ) of  $(1900 \pm 100) \text{ M}^{-1}\text{s}^{-1}$  and  $(180 \pm 30) \text{ M}^{-1}\text{s}^{-1}$  and y-intercepts of  $(8 \pm 3) \times 10^{-4} \text{ s}^{-1}$  and  $(2.0 \pm 0.2) \times 10^{-3} \text{ s}^{-1}$ , resulting in residence times of  $(19 \pm 7)$  min and  $(8.4 \pm 0.8)$  min, respectively (Figures 4F and S2).

**Table 1.** Kinetic parameters of TZD ligand binding to  $\text{cdHDAC4}_{\text{wt}}$ .

TZD Ligand	Cluster No.	$\text{IC}_{50}/\mu\text{M}$	$K_1/\mu\text{M}$	$k_{\text{on}}/\text{s}$ ( $\times 10^{-2}$ )	$k_{\text{off}}/\text{s}$ ( $\times 10^{-2}$ )	$k_3/\text{M}^{-1}$ $\text{s}^{-1}$	$k_{-3}/\text{s}^{-1}$ ( $\times 10^{-2}$ )	RT (KF)/min	RT (RD)/min
<b>8b</b>	1	$0.33 \pm 0.02$	$0.65 \pm 0.47$	$0.30 \pm 0.06$	$0.15 \pm 0.04$	-	-	$11 \pm 3$	$29 \pm 3$
<b>8i</b>	1	$0.34 \pm 0.04$	$0.65 \pm 0.31$	$0.54 \pm 0.05$	$0.12 \pm 0.03$	-	-	$14 \pm 4$	$13 \pm 8$
<b>16b</b>	1	$0.42 \pm 0.02$	n.d. *	$0.24 \pm 0.11$	$0.17 \pm 0.03$	-	-	$9.8 \pm 1.7$	$7 \pm 1$
<b>16g</b>	1	$0.46 \pm 0.06$	n.d. *	$0.51 \pm 0.11$	n.d. *	-	-	n.d. *	$15 \pm 2$
<b>24g</b>	1	$0.71 \pm 0.04$	$1.3 \pm 0.7$	$0.47 \pm 0.06$	$0.05 \pm 0.03$	-	-	$31 \pm 17$	$34 \pm 3$
<b>8g</b>	1	$0.76 \pm 0.08$	$3 \pm 2$	$0.38 \pm 0.07$	$0.16 \pm 0.03$	-	-	$10 \pm 2$	$18 \pm 7$
<b>8a</b>	1	$0.77 \pm 0.09$	$2.4 \pm 1.8$	$0.49 \pm 0.14$	$0.15 \pm 0.06$	-	-	$11 \pm 4$	$19 \pm 2$
<b>7s</b>	2	$0.78 \pm 0.08$	n.d. *	-	-	$210 \pm 40$	$0.16 \pm 0.02$	$10 \pm 1$	$11 \pm 1$
<b>4d</b>	3	$0.79 \pm 0.04$	$1.7 \pm 0.7$	$0.8 \pm 0.1$	$0.06 \pm 0.03$	-	-	$26 \pm 11$	$23 \pm 6$
<b>12j</b>	3	$0.83 \pm 0.02$	n.d. *	$0.31 \pm 0.07$	$0.18 \pm 0.05$	-	-	$9 \pm 3$	$11 \pm 5$
<b>5w</b>	4	$0.90 \pm 0.08$	n.d. *	-	-	$1900 \pm 100$	$0.08 \pm 0.03$	$19 \pm 7$	$12 \pm 3$
<b>8c</b>	1	$1.2 \pm 0.1$	n.d. *	$0.21 \pm 0.09$	$0.14 \pm 0.07$	-	-	$12 \pm 6$	$12 \pm 1$
<b>7i</b>	2	$1.3 \pm 0.1$	n.d. *	-	-	$100 \pm 30$	$0.18 \pm 0.01$	$9.3 \pm 0.5$	$17 \pm 3$
<b>16c</b>	1	$1.4 \pm 0.2$	n.d. *	$0.35 \pm 0.18$	n.d. *	-	-	n.d. *	$21 \pm 7$
<b>7w</b>	4	$1.6 \pm 0.2$	n.d. *	-	-	$180 \pm 30$	$0.20 \pm 0.02$	$8.4 \pm 0.8$	$13.9 \pm 0.3$
<b>SAHA</b>	-	$40 \pm 2$	n.d. *	n.d. *	n.d. *	n.d. *	n.d. *	n.d. *	$5 \pm 2$

Equilibrium and rate constants refer to the reaction scheme in Figure 3. RD = rapid dilution, RT = residence time, KF = kinetic fit of one step ( $k_{-3}^{-1}$ ) and two step ( $k_{\text{off}}^{-1}$ ) model. Shown data represent means and standard deviations,  $N = 3$ .

Compared with cluster 2 TZD ligands of cluster 4 showed slightly faster association rates, and equilibrium was reached within the assay's timeframe. In rapid dilution experiments said TZD ligands had very similar residence times of  $(12 \pm 3)$  min and  $(13.9 \pm 0.3)$  min for TZD ligand **5w** and **7w**, respectively. These values were essentially in agreement with residence times calculated from association kinetics (Table 1). TZD ligands of clusters 2 and 4 (i.e., benzothiazoles and different substituted phenyl and pyridine rings as CAP groups) like SAHA exhibited linear dependency of  $k_{\text{obs}}$  from ligand concentration, consistent with a single binding step mechanism lacking the second rate limiting step (e.g., enzyme isomerization). The presence of bulkier dihydropyrazole CAP groups (i.e., CAP groups of cluster pair 1 and 3) seemed to be responsible for the observed saturation of  $k_{\text{obs}}$  at high ligand concentration. It should be noted that a saturation of  $k_{\text{obs}}$ -values may also have occurred at drastically higher concentrations of TZD ligands in clusters 2 and 4, which could not be tested in experiment due to limited solubility of the compounds. Altogether, the binding mechanism of TZD ligands was clearly dependent on the CAP group, but not so much on the linker structure, whether it was a bulky naphthyl, or a smaller phenyl or pyrimidyl group. This become particularly obvious, when comparing the association kinetics of TZD-ligands from cluster 1 and cluster 2, both with the same naphthyl linker, but different CAP groups. A similar observation could be made by comparing cluster 3

and cluster 4 members also with the same linkers, but different CAP groups. In conclusion, TZD ligands with branched dihydropyrazole CAP-group that were substituted by two aromatic rings showed a more complex 2-step binding mechanism involving induced conformational changes of the protein, while less bulky CAP groups correlated with one-step binding. Moreover, association kinetics was strikingly slow, which was associated with prolonged residence times in the order of 10–30 min. The four compounds with the slowest dissociation behavior and residence times > 20 min all contained a branched dihydropyrazole CAP group. A long residence time is potentially beneficial for a drug candidate because it can act longer on its target and is not so quickly washed out of cells.

#### 2.2.4. Site Directed Mutagenesis Uncovers Hotspots of TZD Ligand-HDAC4 Interaction

To gain an thorough knowledge of the most involved amino acids necessary for molecular recognition of TZD ligands to cdHDAC4<sub>wt</sub>, a comprehensive mutational study was designed. Amino acids flanking the active site binding pocket in the *closed* (Figure 5A) and *open* (Figure 5B) conformation of the enzyme were systematically exchanged and IC<sub>50</sub>-values of a subset of 25 TZDs were determined against every mutant variant. Because IC<sub>50</sub>-values depends on the substrate concentration and the K<sub>m</sub> of the substrate, the Michaelis Menten parameters were determined first using substrate tert-butyl N-[(2S)-1-[(4-methyl-2-oxochromen-7-yl)amino]-1-oxo-6-[(2,2,2-trifluoroacetyl)amino]hexan-2-yl]carbamate (Boc-Lys{TFA}-AMC) in a semi continuous enzyme activity assay (Figures 5C and S1). IC<sub>50</sub>-values were transformed into binding constant K<sub>i</sub> using the Cheng-Prusoff equation to enable a fair comparison of ligand affinities to the respective HDAC4 variant [28]:

$$IC_{50} = \left( 1 + \frac{[S]}{K_m} \right) \times K_i \quad (1)$$

The application of the classic Cheng-Prusoff equation was justified, as TZD ligands were shown to be competitive inhibitors (see above). K<sub>m</sub> values correlate with substrate affinity to the corresponding enzyme. Consequently, the exchange of amino acids that are important for substrate recognition should have an effect on the K<sub>m</sub> value. The exchange of amino acids, which were far away from the active site (K644, S758, N763, E764, T808, M810) to alanine, had no notable effect on K<sub>m</sub>.

In contrast, amino acids E677, D759, R798, F812, C813, R864, L943 and H976Y showed a high impact on substrate binding, which is sound because these amino acids flank the surface of the active site. The biggest impact was shown for F871, which is a highly conserved amino acid and essential component of the hydrophobic tunnel that accommodates and interacts with the alkyl chain of the acetylated lysine side chain of a substrate, when bound to the enzyme. Our results were in full agreement with previous knowledge about the molecular recognition of substrates by HDACs and, therefore, provided a good basis for the following analysis of the impact of amino acid exchanges on the binding affinity of TZD ligands to cdHDAC4<sub>wt</sub>. Figure 5D shows the log<sub>10</sub> values for K<sub>i</sub> of the mutant enzyme divided by the wildtype's K<sub>i</sub> for the main TZD ligand clusters 1, 2 and 3. This log<sub>10</sub>K<sub>i</sub>-ratio allowed for a precise examination of differences in binding upon amino acid substitution. A value of 0 implies that there is no change, a value between 0 and 1 implies a medium decrease of activity, whilst a value near 2 corresponds to a nearly complete loss of inhibition. Contrarily, a negative value corresponds to enhanced binding of the ligand to the mutant variant with respect to cdHDAC4<sub>wt</sub>. Most amino acid exchanges produced a medium to strong loss of affinity with similar effects for TZD ligands from different structural clusters (1–4) (Figure 5D). Comparing averaged log<sub>10</sub>K<sub>i</sub> ratios of clusters 1–3 and the well-known pan-inhibitor Trichostatin A (TSA), revealed different patterns for the impact of mutations on the recognition of TZD ligands (Figure 5E). The main determinants for TSA binding were amino acids S758, D759, E764, T808, F812, F871 and L943 with a log<sub>10</sub>K<sub>i</sub> ratio above 1. In contrast, the exchange of H976 to Y resulted in pronounced stronger binding of the inhibitor to the mutant variant cdHDAC4<sub>H976Y</sub>, which was in line with previous publications showing that hydroxamic acid inhibitors bind better to the

gain-of-function mutant of HDAC4 [3]. In general, the TZD ligands showed more overall impact of amino acid substitution, which coincided with the generally higher isoenzyme selectivity of TZD ligands compared with pan-inhibitor TSA. Looking closer at the three main TZD ligand cluster revealed only minor differences between the three clusters. There were some subtle differences in the molecular recognition of clusters 2 and 3, particularly for E677A, N763A, C813S, R864A and H976Y, while no significant differences could be observed between clusters 1 and 2 (Figure 5D,E). Looking at the structural differences between cluster 1/2 and 3 compounds, TZD ligands in cluster 3 contained a phenyl linker, while TZD ligands in clusters 1 and 2 had a naphthyl linker. The greatest difference in binding affinity loss between cluster 1/2 and 3 was observed for the H976Y mutant variant of cdHDAC4 (Figure 5D,E) with highest impact on the recognition of cluster 1/2 compounds. Therefore, H976 was more important for the recognition of TZD ligands from clusters 1 and 2 than for members of cluster 3. Taken together, in contrast to TSA nearly each exchanged amino acid had a notable influence on the binding of TZD ligands to cdHDAC4. Most of the amino acid substitutions showed a similar effect on binding of all TZD ligands, but there were some interesting subtle differences between TZD ligand clusters, which suggested preferred molecular recognition of TZD ligands containing naphthyl linker over analog compounds with phenyl linker. The fact that so many amino acids had an impact on TZD ligand binding verified the high inhibitory activity and suggested a sound reason for the observed good isoenzyme selectivity of the investigated TZD ligands. All determined  $IC_{50}$ -values of TZD ligands towards  $cdHDAC4_{wt}$  and mutants are summarized in the Supporting Information (Table S2).

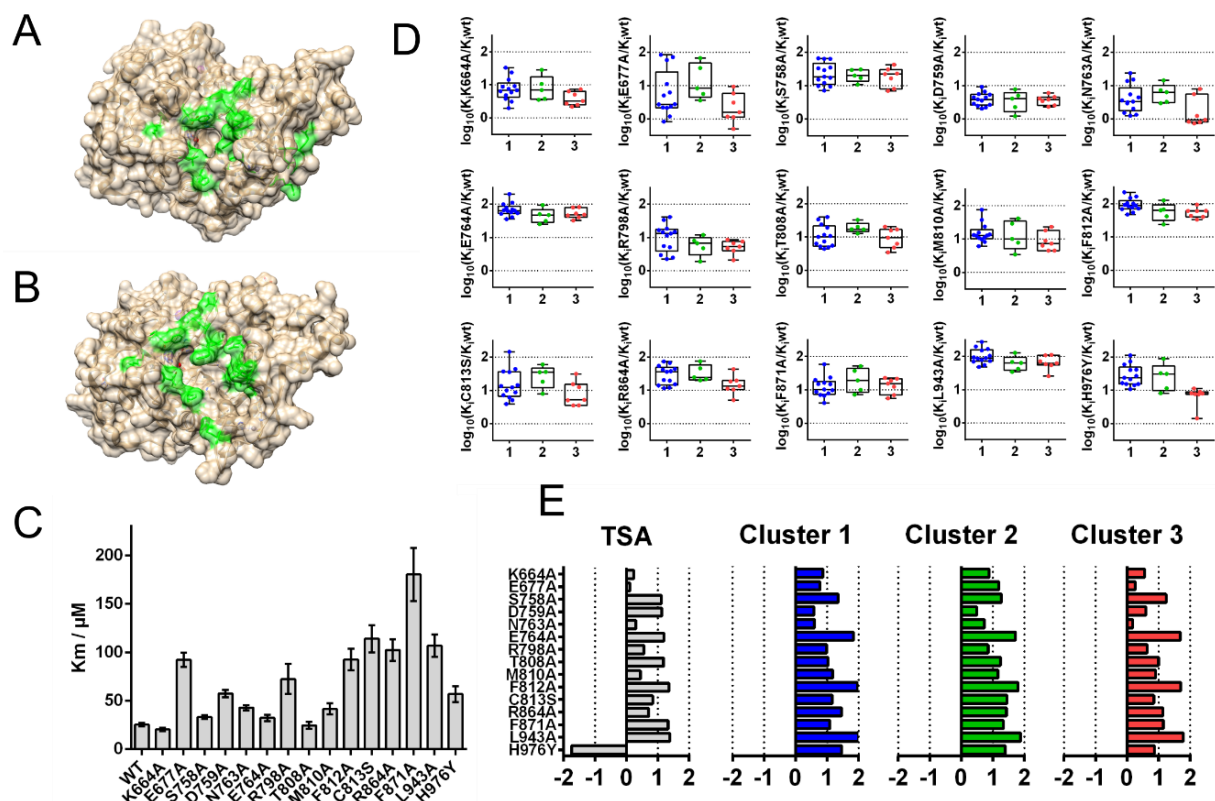


**Figure 5.** Overview of the mutational study. (A,B) are showing the substituted amino acid residues in green for the open (A) and closed (B) conformation. (C)  $K_m$  values for the artificial substrate Boc-Lys{TFA}-AMC. (D) Box-Whisker-Plot showing the impact of amino acid substitution on the binding of TZD-ligands on  $cdHDAC4_{wt}$ . (E) Average impact of amino acid substitution for the three main TZD cluster in comparison to Trichostatin A (TSA).

### 2.2.5. Docking and Mutational Analysis Predicts Binding to the Closed Conformation of HDAC4

The mutational analysis revealed characteristic influences of mutating selected amino acids surrounding the binding pockets of the *open* and *closed* conformation of cdHDAC4<sub>wt</sub> on binding of TZD ligands. To rationalize these effects and gain more insight into key molecular determinants of molecular recognition, a set of TZD ligands was docked into the crystal structures of HDAC4<sub>c</sub> (*closed*, PDB-ID:4CBY) and HDAC4<sub>o</sub> (*open*, PDB-ID:2VQJ). The docking procedure was validated by redocking of the co-crystallized ligands into the respective crystal structure using AMBER 14 forcefield and London dG and GBVI/WSA dG scores implemented in MOE software, and allowing for induced fit around the binding pocket. The docked and crystallized poses of the ligand within the binding pocket of HDAC4<sub>c</sub> (PDB-ID:4CBY) showed excellent overlap for the phenyl-cyclopropylhydroxamate moiety buried in the binding pocket with an RMSD-value of 0.267 Å and an acceptable overall RMSD-value 0.744 Å (Figure S3A). The trifluoromethyl warhead, which coordinates to the catalytic zinc ion, and thiophene linker of the redocked ligand in HDAC4<sub>o</sub> (PDB ID:2VQJ) showed a very good RMSD value of 0.4 Å with respect to the ligand in the crystal structure (Figure S3B). Since the aromatic head group of the trifluoromethyl ketone ligand protrudes into free solution, this part of the molecules is intrinsically flexible and thus not considered for the calculation of RMSD. The largest structural movements during the transition from the *closed* to the *open* conformation of the catalytic domain of cdHDAC4<sub>wt</sub> occur in two regions within the N-terminus of the catalytic domain. The first region between T660 and R681 forms the structural zinc binding domain (ZBD)-loop in the crystal structure of HDAC4<sub>o</sub> (PDB-ID:2VQJ), and the second region between N726 and S767 defines the ZBD-helix of the zinc binding domain (Figure S4). The dramatic outward shift of ZBD-loop and ZBD-helix by about 15–20 Å, and additional minor conformational changes such as turn of the aromatic ring of F812 and some movement of H976 open the sidewall of the canonical binding pocket in the *closed* conformation to form the enlarged binding groove of HDAC4<sub>o</sub> (Figures 6 and S5).

A key amino acid in the ZBD-helix is E764, which forms a salt bridge with R730. The transition from HDAC4<sub>c</sub> to HDAC4<sub>o</sub> involves disruption of this salt bridge and a 8.3 Å shift of the C<sub>β</sub>-atom of E764 (Figures S5 and S6). The effects of an exchange of this amino acid against alanine on the molecular recognition of the TZD ligands are discussed below. Clustering of most active 28 TZD analogs using compound similarity analysis revealed three clearly separated main cluster, a small cluster consisting of **5w** and **7w** carrying a characteristic benzothiazole moiety as head group, and the singleton **14d** with pyrimidine linker (Figure S7). Three representative TZD-analogs were docked for each of the three main clusters in order to identify contacts with surface amino acids and dissect differences between these clusters. Remarkably, docking results provided consistently better binding scores for the docking poses within HDAC4<sub>o</sub> (PDB-ID: 2VQJ) compared with HDAC4<sub>c</sub> (Table 2). Clusters 1 and 3 contained TZD-analogs have a dihydropyrazole CAP group with a stereo center at the heterocycle. Since the absolute configuration was not known, both enantiomers were docked into the respective crystal structures of HDAC4<sub>c</sub> and HDAC4<sub>o</sub>. In all cases, docking scores for HDAC4<sub>o</sub> were consistently more favorable than for HDAC4<sub>c</sub>. Therefore, TZD-analogs were suggested to bind tighter to the enlarged groove in the *open* conformation of HDAC4<sub>o</sub>, which offered more opportunities to interact with the surface than the *closed* conformation. Also, docking results suggested, that the TZD-enantiomers with the same absolute configuration as (S)-**16b** bind stronger or equal to both, HDAC4<sub>c</sub> or HDAC4<sub>o</sub>. In general, the docking poses showed excellent overlap in the lower part of the binding pocket, where the TZD group coordinated to the catalytic zinc ion of both, *open* and *closed* conformation of cdHDAC4<sub>wt</sub>, through a carbonyl oxygen (Figure 6). There was also considerable structural overlap of the aromatic linker moieties among the compounds of a particular cluster docked to HDAC4<sub>o</sub> or HDAC4<sub>c</sub> (Figures 6 and S8).

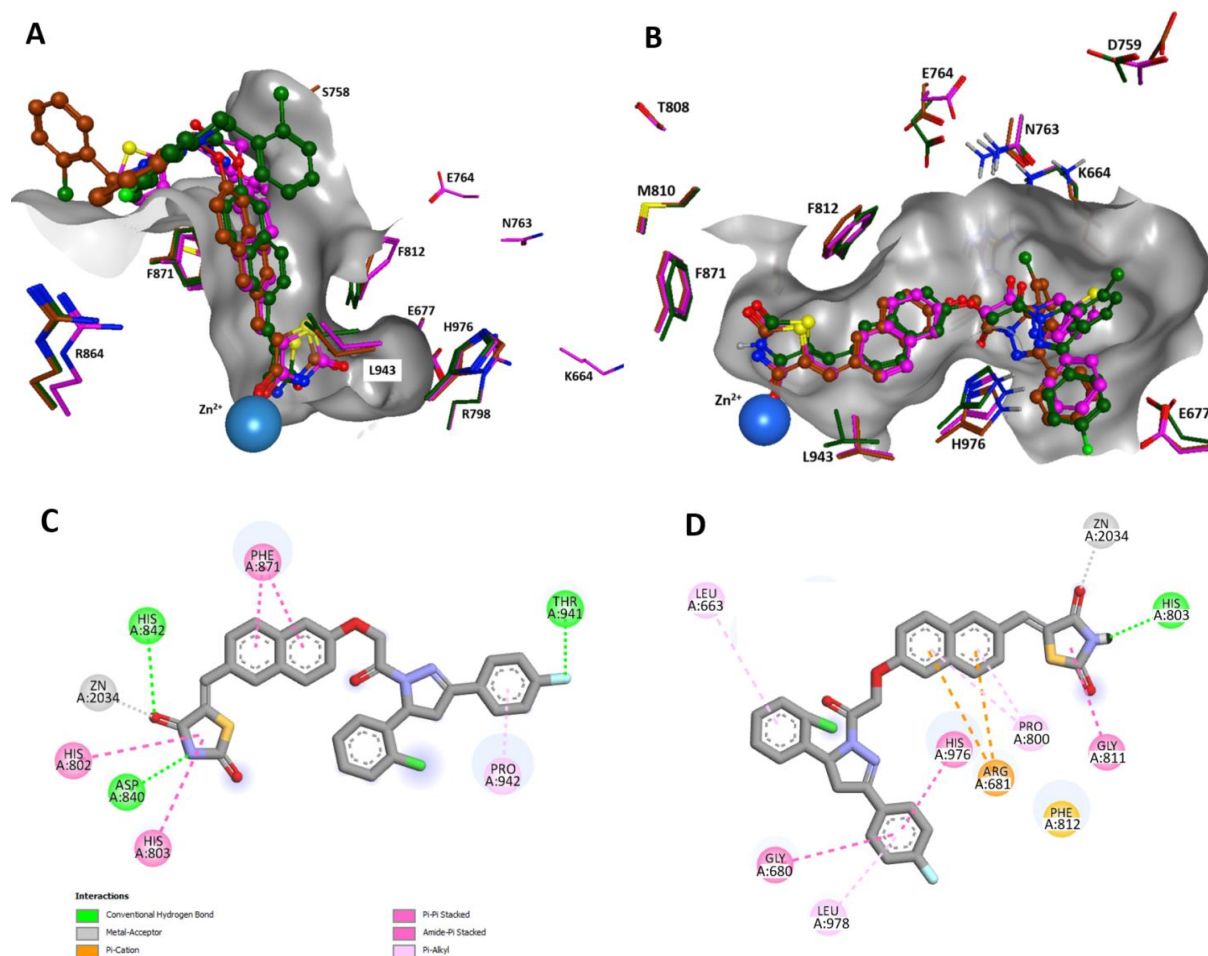


**Figure 6.** Docking poses of (S)-16b (dark green), (S)-8i (magenta) and (S)-8b (brown) within the binding pockets of (A) HDAC4<sub>c</sub> (PDB-ID:4CBY) and (B) HDAC4<sub>o</sub> (PDB-ID:2VQJ). The surface of the binding sites is colored in gray and clipped in the z-plane. The mutated amino acid residues are colored according to the corresponding docked ligand. The two lower panels show 2D ligand interactions of representative compound (S)-16b docked to (C) HDAC4<sub>c</sub> and (D) HDAC4<sub>o</sub>.

**Table 2.** Docking scores of indicated compounds into HDAC4<sub>c</sub> (PDB-ID 4CBY) and HDAC4<sub>o</sub> (PDB-ID 2VQJ).

Cluster #	Title	?	GBVI/WSA dG	
			4CBY (Closed)	2VQJ (Open)
1	(S)-16b *		-9.2	-11.8
	(R)-16b		-8.8	-10.0
	(S)-8i *		-9.3	-10.2
	(R)-8i		-8.7	-10.0
	(S)-8b *		-9.1	-11.4
	(R)-8b		-8.6	-10.2
2	7l		-7.7	-9.4
	7n		-8.5	-9.5
	7s		-7.7	-8.3
3	(S)-12j		-8.8	-9.6
	(R)-12j *		-8.8	-9.9
	(S)-4d		-8.6	-9.6
	(R)-4d *		-9.1	-9.7
	(S)-4j		-8.5	-10.0
	(R)-4j *		-8.5	-10.0

The absolute configuration of compounds in cluster 1 and 3, which are highlighted by \*, is identical.

However, the location of the CAP group in HDAC4<sub>c</sub> was less defined due to the widened upper region of the binding pocket and alternative interactions with the enzyme surface (Figures 6A and S8A–C). In contrast, the binding poses of TZD analogs docked into HDAC4<sub>o</sub> showed much better overlap for all ligand structures (Figures 6B and S8D–F). The binding groove of the *open* conformation, HDAC4<sub>o</sub>, revealed an additional subpocket away from the catalytic zinc ion, which was occupied by an aromatic substituent of the dihydropyrazole CAP group of compounds in clusters 1 and 3 or the aromatic carboxamide CAP group of cluster 2 compounds (Figures 6B and S10D–F).

To gain more insight into the binding mode of TZD ligands, affinity changes upon the mutation of selected amino acids and the contacts between ligands and HDAC4 in corresponding docking poses were analyzed and correlated. Looking at the effects of the exchange of single amino acids on binding affinity of TZD ligands in terms of  $K_i$ -ratio revealed similarities, but also differences between the three TZD ligand clusters (Figure 7). The binding profiles of clusters 1 and 2, which contained a naphthalene linker, showed very similar impacts of amino acid exchanges on binding affinity with a Spearman correlation coefficient of 0.927 (Figure 7). The  $K_i$ -ratios of TZD ligand clusters 2 and 3 were clearly less correlated (Spearman correlation coefficient = 0.818), which corresponded to a different linker and CAP group. Moreover, the binding profiles of cluster 3 and cluster 1 showed intermediate similarity, which corresponded to similar head groups but different linker (Spearman correlation coefficient = 0.851). Overall, these data suggested pronounced similarities in the molecular recognition of TZD ligands by cdHDAC4<sub>wt</sub> with some differences between clusters. This finding was confirmed by docking, which predicted the TZD-group as zinc chelating warhead and additional hydrophobic interactions between the aromatic linker and surface amino acids of the canonical binding pocket in HDAC4<sub>c</sub> or the wide open binding groove in HDAC4<sub>o</sub> as common feature of TZD ligand binding. However, there were also distinct differences in the  $K_i$ -ratio profiles between the TZD ligand clusters, which correlated mainly with the linker structure but also, to a minor extent, with the CAP group.

The specific effect of exchanging amino acids at the expected interaction surfaces on the binding affinity of ligands was supposed to be a mixture of direct effects on specific interactions with the ligand and indirect effects on the conformation of the receptor protein, which vice versa affect binding in a more general way. The exchange of one of the three amino acids, E764, F812 and L943 produced drastic losses in affinity for all three TZD ligand clusters. E764 is a special case, because this amino acid is far away from the binding sites of HDAC4<sub>c</sub>, as well as HDAC4<sub>o</sub>, making a direct protein-ligand interaction unlikely.

The same observation occurred with binding of TSA to cdHDAC4<sub>wt</sub>. There is also a pronounced drop in affinity upon E764A exchange, although there is a very large distance (>20 Å) between TSA and the glutamate in the crystal structure of TSA in complex with HDAC7 that corresponds to E764. Therefore, the loss in affinity upon E764A exchange was essentially independent of the bound ligand and must be a secondary structural effect, which coincides with the disruption of a salt bridge to R730 and a considerable shift of this amino acid upon transition from the *closed* to the *open* conformation of HDAC4. This let us hypothesize, that the salt bridge between E764 and R730 stabilizes the *closed* conformation. If the salt bridge cannot be formed, the conformational equilibrium would be shifted from the *closed* to the *open* or other conformations and, as a general effect, weaken binding to the *closed* conformation. Exchanging amino acids K664, N763 and R798 by alanine produced only minor changes in the binding of TZD ligand in all three clusters. This was in agreement with docking poses in the binding pocket of the *closed* conformation HDAC4<sub>c</sub>, where these amino acids were more than 12 Å away from any docked TZD ligand. Moreover, the experimental binding results were in contrast to the observed close proximity between K664, N763 and R798 and TZD ligands docked into HDAC4<sub>o</sub>. TSA binding was also not impacted by the mutation of K664, N763 or R798. And a crystal structure of the complex between TSA and HDAC7 (PDB-ID:3C10) shows that TSA binds to the *closed* conformation of HDAC7. Since the binding pockets of HDAC4 and HDAC7 consist of identical amino

acids and are structurally highly conserved, TSA was supposed to bind to HDAC4 in the same manner. These findings strongly suggested that the TZD ligands like TSA bind to the *closed* conformation of HDAC4. Docking poses of TZD ligands also indicated pi-pi-stacking between the aromatic naphthyl-linker and F812 for clusters 1 and 2 and aromatic/aliphatic interactions between the phenyl-linker of cluster 3 members and F812, when docked into HDAC4<sub>c</sub> (Figures 6A and S8A–C). Since there was no considerable shift of F812 upon transition from the *closed* to the *open* conformation of HDAC4, these interactions would also be possible in HDAC4<sub>o</sub>. L943 formed hydrophobic interactions with cluster 1 ligands that were docked into the *closed* conformation of HDAC4, but was not in proximity to members of cluster 1, when docked into HDAC4<sub>o</sub>. For cluster 2 and 3, docking results were consistent with both conformations of HDAC4. When F871 is exchanged against alanine, the binding affinity decreased only moderately by about 15–25 fold. Looking at the docking poses of TZD ligands revealed that the ligands form favorable pi-pi-stacking interactions between the aromatic linker and F871, when docked into HDAC4<sub>c</sub>, which was not the case for HDAC4<sub>o</sub> (Figures 6 and S8). This was also an argument for binding of TZD ligands to the *closed* rather than the *open* conformation of cdHDAC4<sub>wt</sub>. The gain-of-function mutant HDAC4<sub>H976Y</sub> was a very interesting case, since Y976 is flipped-inward (PDB-ID:2VQW) and increased enzyme activity, because this residue is involved in the enzyme mechanism [3]. In HDAC4<sub>wt</sub> the corresponding H976 is turned outward and opens a lower selectivity pocket, which was already exploited to develop selective inhibitors against class IIa HDACs [29]. Bottomley et al. showed, that the hydroxamic acid analog of a thiophen inhibitor is about 30-fold more active against HDAC4<sub>H976Y</sub> compared to HDAC4<sub>wt</sub>, while the same inhibitor with a trifluoromethylketone warhead has similar activity against both variants of HDAC4. The crystal structure of the hydroxamate inhibitor with HDAC4<sub>H976Y</sub> (PDB-ID:2VQV) reveals a hydrogen bond between Y976 and the carbonyl oxygen of the hydroxamate group as the most probable cause for the observed increased affinity. For TSA, an increase in affinity was observed upon H976Y exchange, in line with the results from Bottomley et al. In contrast, TZD ligands showed lower affinity to cdHDAC4<sub>H976Y</sub> compared to cdHDAC4<sub>wt</sub>. A possible explanation for this experimental finding is that the flipped-in tyrosine residue may cause sterical hindrance and require conformational rearrangement of the binding pocket to recognize TZD ligands. Combining all binding data from the mutational analysis and molecular docking provided convincing evidence, that TZD ligands share common features of molecular recognition, but still can be grouped in three clusters with slightly different recognition patterns to specific amino acids of cdHDAC4<sub>wt</sub>. Docking suggested the TZD-group as alternative warhead to commonly used hydroxamate or trifluoromethylketone groups. Although docking scores for TZD ligand/HDAC4 complexes were consistently better for HDAC4<sub>o</sub>, the correlation of experimental affinity data and docking poses within HDAC4<sub>c</sub> and HDAC4<sub>o</sub> provided strong evidence that the TZD ligands bind preferentially to the *closed* form of HDAC4. How can the discrepancy between beneficial docking scores for HDAC4<sub>o</sub>, but good agreement between experimental binding data from the mutational study and docking poses within HDAC4<sub>c</sub> be resolved? First of all, it must be considered that proteins in solution are highly flexible and usually exist in a chemical equilibrium between one, two or more major conformational states. Crystal structures reveal only snapshots of possible protein conformations, there is no guarantee that the crystallized conformation would be the dominant one in aqueous solution. Therefore, one has to consider both, the conformational equilibrium between the *open* and *closed* conformation of the catalytic domain of HDAC4, as well as the binding equilibrium of TZD ligands to both protein conformations (Figure 8A). If we assume that a ligand binds much tighter to HDAC4<sub>o</sub> than to HDAC4<sub>c</sub> as suggested by docking, this would predominantly lead to TZD ligand/HDAC4<sub>o</sub> complexes, if similar concentrations of both conformations are present. However, if the equilibrium between HDAC4<sub>o</sub> and HDAC4<sub>c</sub> is shifted towards the *closed* conformation, this has also consequences for the ratio of TZD ligands bound to HDAC4<sub>o</sub> or HDAC4<sub>c</sub>. The energy diagram in Figure 8A demonstrates, that a strong shift

of unbound HDAC<sub>4o</sub> towards HDAC<sub>4c</sub> can produce a higher proportion of the complex of the ligand with HDAC<sub>4c</sub>, HDAC<sub>4c</sub>-I, although the ligand binds with much higher affinity to HDAC<sub>4o</sub>. This effect was simulated under the assumption of 5-fold or 10-fold lower  $K_d$ -values for HDAC<sub>4o</sub> than for HDAC<sub>4c</sub> (Figure 8B). The percentage of HDAC<sub>4c</sub>-I in chemical equilibrium was calculated for different ratios of HDAC<sub>4c</sub> and HDAC<sub>4o</sub> in terms of the ratio of rate constants of the corresponding conformational equilibrium,  $k_1/k_{-1}$ . As expected, the complex of HDAC<sub>4o</sub>-I dominated, if the ratio of HDAC<sub>4c</sub>/HDAC<sub>4o</sub> was 1 or less (Figure 8B). However, conformational equilibria with 50-fold or higher ratios of HDAC<sub>4c</sub> to HDAC<sub>4o</sub> produced more than 80% HDAC<sub>4c</sub>-I in chemical equilibrium.

This implies that the dominant presence of a complex between TZD ligands and HDAC<sub>4c</sub> in chemical equilibrium in solution requires a strong shift of the conformational equilibrium towards HDAC<sub>4c</sub>, e.g., >50:1 HDAC<sub>4c</sub>:HDAC<sub>4o</sub>. This conclusion is in agreement with the fact, that most crystal structures of the catalytic domain of HDAC4 and closely related HDAC7 in apo-form as well as in complex with ligands adopt the *closed* conformation. Only a few crystal structures, all of them protein-ligand complexes, show the *open* conformation. Moreover, the *closed* conformation of HDAC4 is thought to be physiologically relevant, because only the *closed* conformation is able to associate with the N-CoR-HDAC3 repressor complex [3].

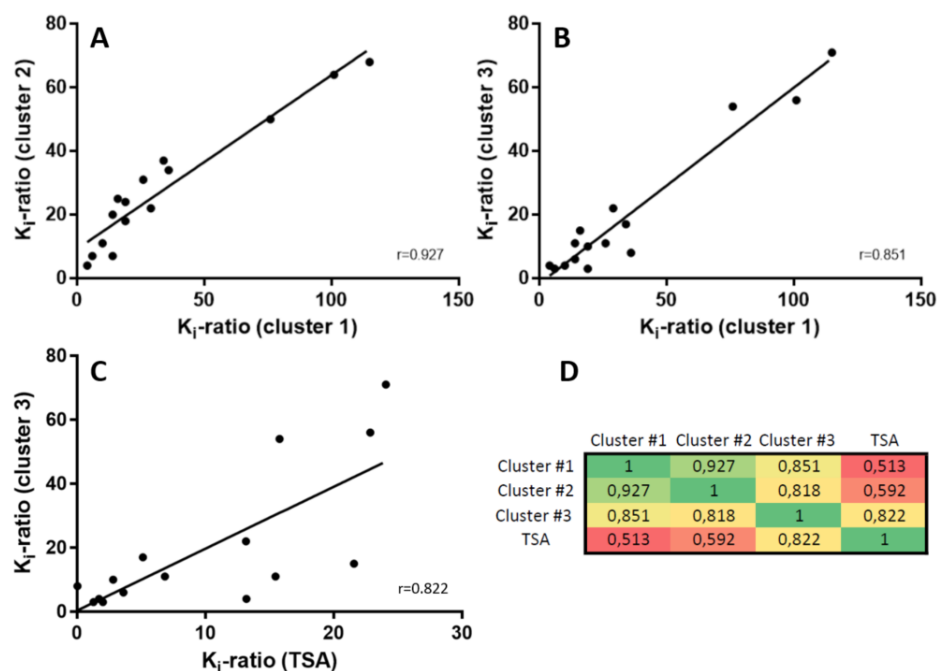


**Figure 7.** Binding profiles of TZD ligand clusters and TSA to HDAC4. Each data point represents a HDAC4-mutant, where one of the amino acids K664, E677, S758, D759, N763, E764, R798, T808, M810, F812, C813, R864, F871 or L943 is exchanged against alanine. The ratio of  $K_i$ -values for binding to a mutant variant and cdHDAC<sub>4wt</sub> indicates the impact of this specific mutation on the molecular recognition of a particular ligand. (A) Averaged  $K_i$ -ratios for binding of TZD ligand cluster 2 and (B) TZD ligand cluster 3 are plotted versus the averaged  $K_i$ -ratios of TZD ligand cluster 1. (C) The averaged  $K_i$ -ratios of TZD ligand cluster 3 is plotted versus the  $K_i$ -ratio of reference compound TSA. (D) Heat map of Spearman correlation coefficients for  $K_i$ -ratios of indicated clusters and TSA.



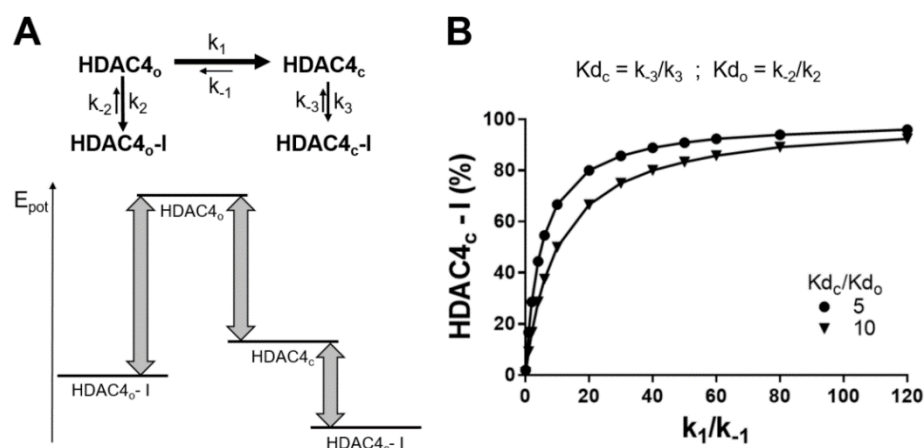


**Figure 8.** Energy diagram and simplified binding mechanism of *open* and *closed* form of cdHDAC4<sub>wt</sub>. (A) The upper panel shows a simplified binding mechanism of a ligand, I, to the *open* (HDAC4<sub>o</sub>) and *closed* (HDAC4<sub>c</sub>) conformation of HDAC4 yielding the corresponding reversible complexes HDAC4<sub>o</sub>-I and HDAC4<sub>c</sub>-I. The binding equilibria are coupled to the conformational equilibrium between HDAC4<sub>o</sub> and HDAC4<sub>c</sub>. The *k*-parameters denote the respective reaction rate. The lower panel shows the corresponding energy diagram, which is consistent with the conformational equilibrium shifted toward HDAC4<sub>c</sub> and larger binding energy for the HDAC4<sub>o</sub>-I complex than for HDAC4<sub>c</sub>-I. (B) Simulation of percentage HDAC4<sub>c</sub>-I as a function of the ratio of HDAC4<sub>c</sub> to HDAC4<sub>o</sub> in terms of  $k_1/k_{-1}$ . Two cases are simulated: Ligand I has 5-times (filled circle) or 10-times (down-triangle) higher affinity for HDAC4<sub>o</sub> than for HDAC4<sub>c</sub>.

### 3. Materials and Methods

#### 3.1. General Procedures

Chemical reagents and solvents were procured from S D Fine or Sigma Aldrich suppliers in India. Thin layer chromatography (TLC) was used to monitor the reaction at each step and TLC was carried out on Merck pre-coated Silica Gel 60 F254 by using mixture of suitable mobile phase. Melting point of the intermediates and final compounds were obtained from VEEGO, MODEL: VMP-DS Melting Point apparatus by open capillary method and are uncorrected. Purity of all the final products were confirmed by Agilent 1200 high-performance liquid chromatography (HPLC) system; software—EZ chrome Elite; chromatographic column—HemochromIntsil A31 C18 5U 150 mm × 4.6 mm Sn-B180127; detection at 300 nm; detector—UV-visible; flow rate—1 mL/min; oven temperature—30 °C; gradient elution run time—10 min; mobile phase—methanol: formic Acid (1%) (formic acid: in 1000 mL double distilled water 1 mL formic acid was added) in 80:20/90:10 ratio. The structures of intermediates were confirmed by FTIR and <sup>1</sup>H-NMR and that of the final compounds by FTIR, <sup>1</sup>H-NMR, <sup>13</sup>C-NMR and Mass spectrometry. FTIR was recorded on Shimadzu FT/IR-8400S by direct sampling technique. <sup>1</sup>H-NMR spectra were recorded by Bruker Avance 400 MHz spectrometer with DMSO-*d*<sub>6</sub>. All shifts are reported in  $\delta$  (ppm) units relative to the signals for solvent DMSO ( $\delta$ - 2.50 ppm). All coupling constants (*J* values) are reported in hertz (Hz). NMR abbreviations are: bs, broad singlet; s, singlet; d, doublet; t, triplet; q, quartet; m, multiplet; and dd, doublet of doublets. <sup>13</sup>C-NMR was recorded on Bruker Avance spectrometer at 100 MHz with DMSO-*d*<sub>6</sub>. Mass spectrum was determined on LC-MS Agilent Technologies 1260 Infinity instrument.

**2-(2,4-dioxo-5-(pyridin-2-ylmethylene)thiazolidin-3-yl)-N-(6-nitrobenzo[d]thiazol-2-yl) acetamide (PB1).** Yield 0.6 g (53%). M.P. 250 °C (charred). White color solid. IR (cm<sup>-1</sup>) 3340 (NH str.), 1739 (C=O str. of cyclic amide), 1658, 1612, 1573, 1548 (C=C str<sup>1</sup>H NMR (400 MHz, DMSO-*d*<sub>6</sub>,  $\delta$  ppm): 4.68 (s, 2H), 7.31–7.35 (m, 1H), 7.46–7.49 (m, 1H), 7.55–7.57 (m, 1H), 7.92–8.00 (m, 3H), 8.04 (s, 1H), 8.81 (d, *J* = 4.4 Hz, 1H), 13.27 (s, 1H). <sup>13</sup>C NMR (400 MHz, DMSO-*d*<sub>6</sub>): 171.41, 166.40, 165.89, 162.76, 159.00, 151.56, 149.86, 145.84, 138.17, 133.56, 130.17, 128.57, 126.82, 125.70, 125.18, 125.05, 124.80, 121.48, 43.34, 36.25. Theoretical mass:

441.44; LCMS ( $m/z$ , I%): 440.0 [(M-H)<sup>+</sup>, 100%]. HPLC Purity: % Area 97.55, Retention Time 6.32 min.

**2-(2,4-dioxo-5-(pyridin-2-ylmethylene)thiazolidin-3-yl)-N-(4-methylbenzo[d]thiazol-2-yl)acetamide (PB2).** Yield 0.5 g (46%). M.P. 260 °C (charred). White color solid. IR (cm<sup>-1</sup>) 3323 (NH str.), 1737 (C=O str. of cyclic amide), 1656, 1614, 1595, 1554 (C=C str.). <sup>1</sup>H NMR (400 MHz, DMSO-d<sub>6</sub>, δ ppm): 2.59 (s, 3H), 4.68 (s, 2H), 7.20–7.28 (m, 2H), 7.46–7.49 (m, 1H), 7.80 (d,  $J = 7.6$  Hz, 1H), 7.92–8.00 (m, 2H), 8.04 (s, 1H), 8.80 (d,  $J = 4.4$  Hz, 1H), 12.95 (s, 1H). <sup>13</sup>C NMR (400 MHz, DMSO-d<sub>6</sub>): 171.41, 165.95, 156.96, 151.55, 149.86, 148.03, 138.16, 131.63, 130.55, 130.15, 128.57, 127.21, 125.72, 124.79, 124.26, 119.67, 43.41, 18.38. Theoretical mass: 410.47; LCMS ( $m/z$ , I%): 409.1 [(M-H)<sup>+</sup>, 100%]. HPLC Purity: % Area 97.11, Retention Time 5.96 min.

**2-(2,4-dioxo-5-(pyridin-2-ylmethylene)thiazolidin-3-yl)-N-(6-methylbenzo[d]thiazol-2-yl)acetamide (PB3).** Yield 0.7 g (67%). M.P. charred at 300 °C. White color solid. IR (cm<sup>-1</sup>) 3323 (NH str.), 1730 (C=O str. of cyclic amide), 1693, 1664, 1616, 1546 (C=C str.). <sup>1</sup>H NMR (400 MHz, DMSO-d<sub>6</sub>, δ ppm): 2.40 (s, 3H), 4.68 (s, 2H), 7.24–7.27 (m, 1H), 7.44–7.47 (m, 1H), 7.65 (d,  $J = 8.4$  Hz, 1H), 7.75 (s, 1H), 7.91 (d,  $J = 7.6$  Hz, 1H), 7.94–8.02 (m, 1H), 8.03 (s, 1H), 8.79 (d,  $J = 4.4$  Hz, 1H), 12.78 (s, 1H). <sup>13</sup>C NMR (400 MHz, DMSO-d<sub>6</sub>): 171.42, 165.91, 156.96, 151.54, 149.84, 146.93, 138.12, 133.80, 132.09, 130.51, 130.13, 128.54, 128.04, 125.71, 124.76, 121.86, 120.86, 43.45, 21.44. Theoretical mass: 410.47; LCMS ( $m/z$ , I%): 409.0 [(M-H)<sup>+</sup>, 100%]. HPLC Purity: % Area 95.25, Retention Time 5.56 min.

**N-(4-chlorobenzo[d]thiazol-2-yl)-2-(2,4-dioxo-5-(pyridin-2-ylmethylene)thiazolidin-3-yl)acetamide (PB4).** Yield 0.75 g (72%). M.P. 273 °C (charred). White color solid. IR (cm<sup>-1</sup>) 3342 (NH str.), 1745 (C=O str. of cyclic amide), 1680, 1631, 1604, 1573, 1548 (C=C str.) 705 (C-Cl str.). <sup>1</sup>H NMR (400 MHz, DMSO-d<sub>6</sub>, δ ppm): 4.69 (s, 2H), 7.31–7.35 (m, 1H), 7.46–7.49 (m, 1H), 7.55–7.57 (m, 1H), 7.92–8.00 (m, 3H), 8.04 (s, 1H), 8.80 (d,  $J = 4.4$  Hz, 1H), 13.26 (s, 1H). <sup>13</sup>C NMR (400 MHz, DMSO-d<sub>6</sub>): 171.41, 166.40, 165.89, 162.77, 159.00, 151.54, 149.86, 145.84, 138.17, 133.56, 130.17, 128.57, 126.82, 125.70, 125.18, 125.05, 124.80, 121.48, 43.44, 36.25, 31.24. Theoretical mass: 430.89; LCMS ( $m/z$ , I%): 428.9 [(M-H)<sup>+</sup>, 100%]. HPLC Purity: % Area 97.60, Retention Time 4.99 min.

**N-(4,6-difluorobenzo[d]thiazol-2-yl)-2-(2,4-dioxo-5-(pyridin-2-ylmethylene)thiazolidin-3-yl)acetamide (PB5).** Yield 0.8 g (85%). M.P. 294 °C (charred). White color solid. IR (cm<sup>-1</sup>) 3360 (NH str.), 1728 (C=O str. of cyclic amide), 1672, 1614, 1577, 1552 (C=C str.), 1383, 1145 (C-F str.). <sup>1</sup>H NMR (400 MHz, DMSO-d<sub>6</sub>, δ ppm): 4.69 (s, 2H), 7.37–7.42 (m, 1H), 7.46–7.49 (m, 1H), 7.81–7.83 (m, 1H), 7.92–8.00 (m, 2H), 8.04 (s, 1H), 8.80 (d,  $J = 4.0$  Hz, 1H), 13.14 (s, 1H). <sup>13</sup>C NMR (400 MHz, DMSO-d<sub>6</sub>): 171.42, 166.43, 165.89, 158.36, 157.51, 157.41, 151.53, 149.86, 138.17, 135.23, 130.17, 128.57, 125.71, 124.81, 105.22, 104.99, 102.86, 102.64, 102.57, 102.35, 43.42. Theoretical mass: 432.42; LCMS ( $m/z$ , I%): 431.0 [(M-H)<sup>+</sup>, 100%]. HPLC Purity: % Area 96.23, Retention Time 5.96 min.

**N-(5,6-dimethylbenzo[d]thiazol-2-yl)-2-(2,4-dioxo-5-(pyridin-2-ylmethylene)thiazolidin-3-yl)acetamide (PB6).** Yield 0.52 g (58%). M.P. 295 °C (charred). White color solid. IR (cm<sup>-1</sup>) 3259 (NH str.), 1741 (C=O str. of cyclic amide), 1668, 1614, 1577, 1552 (C=C str.). <sup>1</sup>H NMR (400 MHz, DMSO-d<sub>6</sub>, δ ppm): 2.32 (d,  $J = 4.4$  Hz, 6H), 4.66 (s, 2H), 7.48–7.57 (m, 2H), 7.72 (s, 1H), 7.94–7.98 (m, 2H), 8.04 (s, 1H), 8.80 (s, 1H), 12.75 (s, 1H). <sup>13</sup>C NMR (400 MHz, DMSO-d<sub>6</sub>): 171.42, 165.92, 165.78, 156.88, 151.56, 149.87, 147.54, 138.17, 135.45, 133.22, 130.13, 129.32, 128.57, 125.72, 124.80, 122.02, 121.56, 43.44, 20.16, 20.02. Theoretical mass: 424.50; LCMS ( $m/z$ , I%): 422.8 [(M-2H)<sup>+</sup>, 100%]. HPLC Purity: % Area 98.58, Retention Time 6.92 min.

**2-(2,4-dioxo-5-(pyridin-2-ylmethylene)thiazolidin-3-yl)-N-(4-methoxybenzo[d]thiazol-2-yl)acetamide (PB7).** Yield 0.4 g (53%). M.P. 220–222 °C. White color solid. IR (cm<sup>-1</sup>) 3296 (NH str.), 1737 (C=O str. of cyclic amide), 1680, 1597, 1562 (C=C str.). <sup>1</sup>H NMR (400 MHz, DMSO-d<sub>6</sub>, δ ppm): 2.91 (s, 3H), 4.66 (s, 2H), 7.02 (d,  $J = 8.0$  Hz, 1H), 7.28 (t,  $J = 8.0$  Hz, 1H), 7.48 (t,  $J = 6.0$  Hz, 1H), 7.54 (d,  $J = 8.0$  Hz, 1H), 7.93–8.01 (m, 2H), 8.04 (s, 1H), 8.80 (d,  $J = 4.8$  Hz, 1H), 12.96 (s, 1H). <sup>13</sup>C NMR (400 MHz, DMSO-d<sub>6</sub>): 171.45, 165.94, 165.88, 151.58, 149.88, 138.18, 130.09, 128.57, 125.80, 125.31, 124.80, 114.06, 108.28, 56.31,

43.45, 29.49. Theoretical mass: 426.47; LCMS ( $m/z$ , I%): 425.1 [(M-H)<sup>+</sup>, 100%]. HPLC Purity: % Area 98.67, Retention Time 5.52 min.

**2-(2,4-dioxo-5-(pyridin-2-ylmethylene)thiazolidin-3-yl)-N-(6-ethoxybenzo[d]thiazol-2-yl)acetamide (PB8).** Yield 0.57 g (55%). M.P. 230 °C (charred). White color solid. IR (cm<sup>-1</sup>) 3259 (NH str.), 1737 (C=O str. of cyclic amide), 1666, 1599, 1552, 1535 (C=C str.). <sup>1</sup>H NMR (400 MHz, DMSO-d<sub>6</sub>, δ ppm): 1.32–1.36 (m, 3H), 4.03–4.08 (m, 2H), 4.67 (s, 2H), 7.01–7.04 (m, 1H), 7.45–7.48 (m, 1H), 7.55 (s, 1H), 7.65 (d, *J* = 8.8 Hz, 1H), 7.91–7.99 (m, 2H), 8.03 (s, 1H), 8.79 (d, *J* = 4.4 Hz, 1H), 12.71 (s, 1H). <sup>13</sup>C NMR (400 MHz, DMSO-d<sub>6</sub>): 171.43, 165.92, 165.75, 156.02, 155.73, 151.54, 149.84, 142.92, 138.13, 133.26, 130.13, 128.55, 125.71, 124.77, 121.81, 115.94, 105.83, 64.08, 43.40, 15.15. Theoretical mass: 440.50; LCMS ( $m/z$ , I%): 438.8 [(M-2H)<sup>+</sup>, 100%]. HPLC Purity: % Area 98.57, Retention Time 4.37 min.

**2-(2,4-dioxo-5-(pyridin-2-ylmethylene)thiazolidin-3-yl)-N-(6-fluorobenzo[d]thiazol-2-yl)acetamide (PB9).** Yield 0.64 g (60%). M.P. 265 °C (charred). White color solid. IR (cm<sup>-1</sup>) 3246 (NH str.), 1732 (C=O str. of cyclic amide), 1689, 1651, 1612, 1566, 1554 (C=C str.), 1390 (C-F str.). <sup>1</sup>H NMR (400 MHz, DMSO-d<sub>6</sub>, δ ppm): 4.70 (s, 2H), 7.26–7.31 (m, 1H), 7.43–7.46 (m, 1H), 7.75–7.79 (m, 1H), 7.87–7.90 (m, 2H), 7.93–7.97 (m, 1H), 8.01 (s, 1H), 8.78 (d, *J* = 4.4 Hz, 1H), 12.88 (s, 1H). <sup>13</sup>C NMR (400 MHz, DMSO-d<sub>6</sub>): 171.43, 166.18, 165.89, 160.43, 158.05, 157.86, 151.51, 149.81, 145.65, 138.09, 133.26, 133.15, 130.16, 128.53, 125.68, 124.74, 122.37, 122.29, 114.96, 114.71, 108.86, 108.60, 43.41. Theoretical mass: 414.43; LCMS ( $m/z$ , I%): 413.0 [(M-H)<sup>+</sup>, 100%]. HPLC Purity: % Area 95.13, Retention Time 4.89 min.

**2-(5-benzylidene-2,4-dioxo thiazolidine-3-yl)-N-(4-chlorobenzo[d]thiazol-2-yl)acetamide (GB1)** Yield 0.53 g (55%); M.P. 279–295 °C. White color solid. IR (cm<sup>-1</sup>) 3340 (NH str.), 1745 (C=O str. of cyclic amide), 1691, 1666, 1595, 1556 (C=C str.), 761 (C-Cl str.); <sup>1</sup>H NMR (400 MHz, DMSO-d<sub>6</sub>, δ ppm): 4.69 (s, 2H), 7.26–7.28 (m, 1H), 7.63–7.67 (m, 3H), 7.69–7.78 (m, 3H), 7.78 (s, 1H), 8.01 (s, 1H), 12.78 (s, 1H). <sup>13</sup>C NMR (100 MHz, DMSO-d<sub>6</sub>): 40.13, 43.54, 120.89, 120.96, 124.54, 124.68, 126.31, 129.40, 130.17, 130.83, 132.78, 133.04, 133.79, 145.31, 158.45, 165.09, 165.74, 167.04. Theoretical mass: 429.90; LCMS ( $m/z$ , I%): 428.0 [(M-H)<sup>+</sup>, 100%]. HPLC Purity: % Area 96.63, RT 8.57 min.

**N-(4-chlorobenzo[d]thiazol-2-yl)-2-(5-(4-methylbenzylidene)-2,4-dioxothiazolidin-3-yl)acetamide (GB2)** Yield 0.6 g (58%); M.P. 292–294 °C. White color solid. IR (cm<sup>-1</sup>) 3340 (NH str.), 1739 (C=O str. of cyclic amide), 1691, 1664, 1595, 1562 (C=C str.), 771 (C-Cl str.); <sup>1</sup>H NMR (400 MHz, DMSO-d<sub>6</sub>, δ ppm): 2.39 (s, 3H), 4.70 (s, 2H), 7.32–7.36 (m, 1H), 7.39–7.41 (m, 1H), 7.56–7.59 (m, 2H), 7.96 (s, 2H), 7.98–7.99 (m, 1H), 8.31 (s, 1H), 13.27 (s, 1H). <sup>13</sup>C NMR (100 MHz, DMSO-d<sub>6</sub>): 21.10, 30.75, 35.76, 79.12, 130.06, 130.29, 162.31; Theoretical mass: 443.93; LCMS ( $m/z$ , I%): 441.9 [(M-2H)<sup>+</sup>, 100%]. HPLC Purity: % Area 98.9, RT 11.41 min.

**N-(4-chlorobenzo[d]thiazol-2-yl)-2-(5-(4-chlorobenzylidene)-2,4-dioxothiazolidin-3-yl)acetamide (GB3)** Yield 0.5 g (55%); M.P. charred above 300 °C. White color solid. IR (cm<sup>-1</sup>) 3346 (NH str.), 1741 (C=O str. of cyclic amide), 1683, 1666, 1597, 1554 (C=C str.), 817, 771 (C-Cl str.); <sup>1</sup>H NMR (400 MHz, DMSO-d<sub>6</sub>, δ ppm): 4.71 (s, 2H), 7.34 (t, *J* = 8.0 Hz, 1H), 7.57 (d, *J* = 8.0 Hz, 1H), 7.63 (d, *J* = 8.4 Hz, 2H), 7.78 (d, *J* = 8.4 Hz, 2H), 7.99–8.00 (m, 2H), 13.26 (s, 1H). <sup>13</sup>C NMR (100 MHz, DMSO-d<sub>6</sub>): 145.17, 133.21, 132.60, 132.43, 131.96, 126.35, 124.75, 124.31, 121.76, 120.98. UV Spectrum (10 ppm, λ<sub>max</sub>—330 nm, absorbance—0.723). Theoretical mass: 464.34; LCMS ( $m/z$ , I%): 463.9 [(M-H)<sup>+</sup>, 100%]. HPLC Purity: % Area 98.7, RT 4.4 min.

**2-(5-(4-bromobenzylidene)-2,4-dioxothiazolidin-3-yl)-N-(4-chlorobenzo[d]thiazol-2-yl)acetamide (GB4)** Yield 0.6 g (62%); M.P. charred above 300 °C. White color solid. IR (cm<sup>-1</sup>) 3335 (NH str.), 1737 (C=O str. of cyclic amide), 1697, 1651, 1595, 1554 (C=C str.), 765 (C-Cl str.), 609 (C-Br str.); <sup>1</sup>H NMR (400 MHz, DMSO-d<sub>6</sub>, δ ppm): 4.71 (s, 2H), 7.32–7.36 (m, 1H), 7.56–7.58 (m, 1H), 7.62–7.64 (m, 2H), 7.77–7.79 (m, 2H), 7.99–8.0 (m, 2H), 13.26 (s, 1H). <sup>13</sup>C NMR (100 MHz, DMSO-d<sub>6</sub>): 120.98, 121.76, 124.31, 124.75, 126.35, 131.96, 132.43, 132.60, 133.21, 145.17; Theoretical mass: 508.80; LCMS ( $m/z$ , I%): 507.8 [(M-H)<sup>+</sup>, 100%]. HPLC Purity: % Area 98.14, RT 9.1 min.

***N*-(4-chlorobenzo[d]thiazol-2-yl)-2-(5-(2,4-difluorobenzylidene)-2,4-dioxothiazolidin-3-yl)acetamide (GB5)** Yield 0.45 g (51%). M.P. 288–289 °C. White color solid. IR (cm<sup>-1</sup>) 3392 (NH str.), 1745 (C=O str. of cyclic amide), 1691, 1681, 1612, 1604, 1589, 1562 (C=C str.), 817 (C-Cl str.), 1276, 1143 (C-F str.). <sup>1</sup>H NMR (400 MHz, DMSO-d<sub>6</sub>, δ ppm): 4.70 (s, 2H), 7.31–7.33 (m, 1H), 7.40 (d, *J* = 8.0 Hz, 1H), 7.43 (s, 1H), 7.56 (d, *J* = 8.0 Hz, 1H), 7.94 (d, *J* = 12.4 Hz, 2H), 7.99 (d, *J* = 8.0 Hz, 1H), 13.27 (s, 1H). <sup>13</sup>C NMR (100 MHz, DMSO-d<sub>6</sub>): 167.15, 165.19, 162.31, 145.32, 140.25, 137.57, 134.00, 133.04, 131.37, 130.51, 130.38, 127.68, 126.34, 124.72, 124.57, 120.98, 119.41, 79.12, 43.47, 19.46, 19.35. UV Spectrum (10 ppm, λ<sub>max</sub>—328 nm, absorbance—0.442). Theoretical mass: 465.88; LCMS (*m/z*, I%): 463.9 [(M-H)<sup>+</sup>, 100%]. HPLC Purity: % Area 97.02, RT 4.01 min.

***N*-(4-chlorobenzo[d]thiazol-2-yl)-2-(5-(3,4-dimethylbenzylidene)-2,4-dioxothiazolidin-3-yl)acetamide (GB6)** Yield 0.61 g (65%); M.P. 214–216 °C. White color solid. IR (cm<sup>-1</sup>) 3342 (NH str.), 1743 (C=O str. of cyclic amide), 1687, 1668, 1597, 1564 (C=C str.), 773 (C-Cl str.); <sup>1</sup>H NMR (400 MHz, DMSO-d<sub>6</sub>, δ ppm): 2.30 (s, 6H), 4.70 (s, 2H), 7.39–7.41 (m, 1H), 7.43 (m, 1H), 7.5–7.57 (m, 1H), 7.92–7.96 (m, 3H), 7.98–8.0 (m, 1H), 13.27 (s, 1H). <sup>13</sup>C NMR (100 MHz, DMSO-d<sub>6</sub>): 19.46, 30.75, 35.76, 43.47, 79.12, 119.41, 120.98, 124.57, 124.72, 126.34, 127.68, 130.38, 130.51, 131.37, 133.04, 134.0, 137.57, 140.25, 145.32, 162.31, 165.19, 167.15. Theoretical mass: 457.95; LCMS (*m/z*, I%): 456.1 [(M-H)<sup>+</sup>, 100%]. HPLC Purity: % Area 95.05, RT 5.77 min.

**2-(5-(4-bromobenzylidene)-2,4-dioxothiazolidin-3-yl)-*N*-(4,6-difluorobenzo[d]thiazol-2-yl)acetamide (GB7)** Yield 0.63 g (59%); M.P. charred above 300 °C. White color solid. IR (cm<sup>-1</sup>) 3275 (NH str.), 1743 (C=O str. of cyclic amide), 1691, 1660, 1608, 1573 (C=C str.), 1288, 1153 (C-F str.), 596 (C-Br str.). <sup>1</sup>H NMR (400 MHz, DMSO-d<sub>6</sub>, δ ppm): 4.71 (s, 2H), 7.37–7.42 (m, 1H), 7.62 (d, *J* = 8.4 Hz, 2H), 7.78 (d, *J* = 8.4 Hz, 2H), 7.80–7.83 (m, 1H), 7.99 (s, 1H), 13.15 (s, 1H). <sup>13</sup>C NMR (100 MHz, DMSO-d<sub>6</sub>): 166.83, 165.68, 165.03, 132.6, 132.42, 132.0, 131.95, 124.42, 121.74, 104.43, 79.12, 43.56. UV Spectrum (10 ppm, λ<sub>max</sub>—326 nm, absorbance—1.817). Theoretical mass: 510.33; LCMS (*m/z*, I%): 509.9 [(M-H)<sup>+</sup>, 100%]. HPLC Purity: % Area 97.20, RT 4.78 min.

**2-(5-benzylidene-2,4-dioxothiazolidin-3-yl)-*N*-(4-methoxybenzo[d]thiazol-2-yl)acetamide (GB8)** Yield 0.54 g (60%); M.P. 157–159 °C. White color solid. IR (cm<sup>-1</sup>) 3342 (NH str.), 1741 (C=O str. of cyclic amide), 1681, 1602, 1568 (C=C str.); <sup>1</sup>H NMR (400 MHz, DMSO-d<sub>6</sub>, δ ppm): 2.93 (s, 3H), 4.68 (s, 2H), 7.01–7.03 (m, 1H), 7.27–7.31 (m, 1H), 7.52–7.60 (m, 4H), 7.67–7.69 (m, 2H), 8.02 (s, 1H), 12.97 (s, 1H). <sup>13</sup>C NMR (100 MHz, DMSO-d<sub>6</sub>): 55.81, 107.79, 113.56, 120.98, 124.87, 129.43, 130.19, 130.85, 132.81, 133.74, 165.17, 167.13; Theoretical mass: 425.48; LCMS (*m/z*, I%): 424.0 [(M-H)<sup>+</sup>, 100%]. HPLC Purity: % Area 97.59, RT 2.98 min.

**2-(5-benzylidene-2,4-dioxothiazolidin-3-yl)-*N*-(4-methylbenzo[d]thiazol-2-yl)acetamide (GB9)** Yield 0.59 g (55%). M.P. 272–273 °C. White color solid. IR (cm<sup>-1</sup>) 3323 (NH str.), 1743, 1712 (C=O str. of cyclic amide), 1672, 1608, 1537 (C=C str.). <sup>1</sup>H NMR (400 MHz, DMSO-d<sub>6</sub>, δ ppm): 2.59 (s, 3H), 4.70 (s, 2H), 7.21–7.29 (m, 2H), 7.53–7.60 (m, 3H), 7.67 (d, *J* = 7.2 Hz, 2H), 7.80 (d, *J* = 7.6 Hz, 1H), 8.01 (s, 1H), 12.96 (s, 1H). <sup>13</sup>C NMR (100 MHz, DMSO-d<sub>6</sub>): 167.09, 165.14, 156.28, 147.53, 133.79, 132.79, 131.12, 130.85, 130.19, 130.09, 129.42, 126.73, 123.80, 120.90, 119.17, 43.49, 17.87. UV Spectrum (10 ppm, λ<sub>max</sub>—326 nm, absorbance—0.929). Theoretical mass: 409.48; LCMS (*m/z*, I%): 408.0 [(M-H)<sup>+</sup>, 100%]. HPLC Purity: % Area 97.73, RT 3.67 min.

**2-(5-(4-fluorobenzylidene)-2,4-dioxothiazolidin-3-yl)-*N*-(4-methylbenzo[d]thiazol-2-yl)acetamide (GB10)** Yield 0.6 g (64%); M.P. 225–227 °C. White color solid. IR (cm<sup>-1</sup>) 3344 (NH str.), 1741 (C=O str. of cyclic amide), 1687, 1633, 1595, 1510 (C=C str.), 1149 (C-F str.), 771 (C-Cl str.); <sup>1</sup>H NMR (400 MHz, DMSO-d<sub>6</sub>, δ ppm): 2.74 (s, 3H), 4.69 (s, 2H), 7.21–7.29 (m, 2H), 7.40–7.45 (m, 2H), 7.74–7.81 (m, 2H), 7.96 (s, 1H), 8.03 (s, 1H), 12.96 (s, 1H). <sup>13</sup>C NMR (100 MHz, DMSO-d<sub>6</sub>): 17.86, 30.75, 35.76, 43.52, 116.50, 116.72, 119.17, 120.60, 123.81, 126.73, 129.50, 130.09, 131.12, 132.68, 132.73, 132.77, 147.52, 161.85, 162.312, 165.10, 165.20, 165.31, 166.98; Theoretical mass: 427.47; LCMS (*m/z*, I%): 426.0 [(M-H)<sup>+</sup>, 100%]. HPLC Purity: % Area 97.97, RT 3.34 min.

**2-(5-(4-chlorobenzylidene)-2,4-dioxothiazolidin-3-yl)-N-(4,6-difluorobenzo[d]thiazol-2-yl)acetamide (GB11)** Yield 0.52 g (55%); M.P. charred above 300 °C. White color solid. IR (cm<sup>-1</sup>) 3267 (NH str.), 1743 (C=O str. of cyclic amide), 1693, 1662, 1608, 1573 (C=C str.), 1153, 1101 (C-F str.), 729 (C-Cl str.); <sup>1</sup>H NMR (400 MHz, DMSO-d<sub>6</sub>, δ ppm): 4.71 (s, 2H), 7.36–7.42 (m, 1H), 7.62–7.64 (m, 2H), 7.68–7.71 (m, 2H), 7.80–7.83 (s, 1H), 8.01 (s, 1H), 13.15 (s, 1H). <sup>13</sup>C NMR (100 MHz, DMSO-d<sub>6</sub>): 43.55, 102.15, 104.47, 104.74, 121.64, 129.48, 131.68, 131.82, 132.50, 135.48, 152.11, 157.78, 165.02, 165.67, 166.84; Theoretical mass: 465.88; LCMS (*m/z*, I%): 463.9 [(M-2H)<sup>+</sup>, 100%]. HPLC Purity: % Area 97.72, RT 4.40 min.

**2-(5-benzylidene-2,4-dioxothiazolidin-3-yl)-N-(4,6-difluorobenzo[d]thiazol-2-yl)acetamide (GB12)** Yield 0.57 g (60%); M.P. 280–282 °C. White color solid. IR (cm<sup>-1</sup>) 3335 (NH str.), 1751 (C=O str. of cyclic amide), 1685, 1626, 1595, 1579 (C=C str.), 1149, 1107 (C-F str.); <sup>1</sup>H NMR (400 MHz, DMSO-d<sub>6</sub>, δ ppm): 4.71 (s, 2H), 7.40–7.42 (m, 1H), 7.53–7.60 (m, 2H), 7.67–7.69 (m, 3H), 7.81–7.83 (s, 1H), 7.95 (s, 1H), 13.15 (s, 1H). <sup>13</sup>C NMR (100 MHz, DMSO-d<sub>6</sub>): 30.75, 35.75, 43.52, 120.89, 129.42, 130.19, 130.87, 132.78, 133.83, 162.31, 165.13, 165.68, 167.09; Theoretical mass: 431.44; LCMS (*m/z*, I%): 429.9 [(M-2H)<sup>+</sup>, 100%]. HPLC Purity: % Area 95.82, RT 3.31 min.

**2-(5-(2,4-difluorobenzylidene)-2,4-dioxothiazolidin-3-yl)-N-(6-methylbenzo[d]thiazol-2-yl)acetamide (GB13)** Yield 0.65 g (68%); M.P. 266–268 °C. White color solid. IR (cm<sup>-1</sup>) 3342 (NH str.), 1745 (C=O str. of cyclic amide), 1685, 1604, 1585, 1548 (C=C str.), 1143, 1107 (C-F str.); <sup>1</sup>H NMR (400 MHz, DMSO-d<sub>6</sub>, δ ppm): 2.42 (s, 3H), 4.70 (s, 2H), 7.27–7.29 (m, 1H), 7.31–7.36 (m, 1H), 7.49–7.55 (m, 1H), 7.66–7.74 (m, 2H), 7.78 (s, 1H), 7.93 (s, 1H), 12.78 (s, 1H). <sup>13</sup>C NMR (100 MHz, DMSO-d<sub>6</sub>): 20.94, 79.12, 105.17, 112.99, 120.41, 121.38, 123.50, 124.24, 127.60, 130.77, 133.39, 164.84, 166.70; Theoretical mass: 445.46; LCMS (*m/z*, I%): 444.0 [(M-H)<sup>+</sup>, 100%]. HPLC Purity: % Area 97.33, RT 3.7 min.

**N-(6-methylbenzo[d]thiazol-2-yl)-2-(5-(4-methylbenzylidene)-2,4-dioxothiazolidin-3-yl)acetamide (GB14)** Yield 0.49 g (56%). M.P. 268–269 °C. White color solid. IR (cm<sup>-1</sup>) 3342 (NH str.), 1739, 1701 (C=O str. of cyclic amide), 1660, 1593, 1546, 1512 (C=C str.). <sup>1</sup>H NMR (400 MHz, DMSO-d<sub>6</sub>, δ ppm): 2.39 (s, 3H), 2.41 (s, 3H), 4.69 (s, 2H), 7.28 (d, *J* = 8.0 Hz, 2H), 7.39 (d, *J* = 8.0 Hz, 2H), 7.57 (d, *J* = 8.0 Hz, 2H), 7.67 (d, *J* = 8.0 Hz, 1H), 7.78 (s, 1H), 12.78 (s, 1H). <sup>13</sup>C NMR (100 MHz, DMSO-d<sub>6</sub>): 167.11, 165.21, 146.41, 141.28, 133.87, 133.37, 131.59, 130.28, 130.05, 127.58, 121.37, 120.40, 119.64, 43.50, 21.10, 20.94. UV Spectrum (10 ppm, λ<sub>max</sub>—331 nm, absorbance—0.543). Theoretical mass: 423.51; LCMS (*m/z*, I%): 422.0 [(M-H)<sup>+</sup>, 100%]. HPLC Purity: % Area 95.87, RT 4.31 min.

**2-(5-(3,4-dimethylbenzylidene)-2,4-dioxothiazolidin-3-yl)-N-(6-methylbenzo[d]thiazol-2-yl)acetamide (GB15)** Yield 0.62 g (65%). M.P. 285–286 °C. White color solid. IR (cm<sup>-1</sup>) 3342 (NH str.), 1739, 1701 (C=O str. of cyclic amide), 1658, 1593, 1548, 1502 (C=C str.). <sup>1</sup>H NMR (400 MHz, DMSO-d<sub>6</sub>, δ ppm): 2.30 (s, 6H), 2.41 (s, 3H), 4.68 (s, 2H), 7.28 (d, *J* = 8.0 Hz, 1H), 7.34 (d, *J* = 7.6 Hz, 1H), 7.40 (d, *J* = 8.0 Hz, 1H), 7.44 (s, 2H), 7.66 (d, *J* = 8.0 Hz, 1H), 7.78 (s, 1H), 12.78 (s, 1H). <sup>13</sup>C NMR (100 MHz, DMSO-d<sub>6</sub>): 167.16, 165.22, 146.41, 140.25, 137.58, 133.98, 133.37, 131.59, 131.37, 130.52, 130.40, 127.68, 127.59, 121.38, 120.40, 119.42, 43.48, 20.94, 19.47, 19.35. UV Spectrum (10 ppm, λ<sub>max</sub>—334 nm, absorbance—1.079). Theoretical mass: 437.53; LCMS (*m/z*, I%): 436.0 [(M-H)<sup>+</sup>, 100%]. HPLC Purity: % Area 96.08, RT 5.36 min.

**2-(5-(4-chlorobenzylidene)-2,4-dioxothiazolidin-3-yl)-N-(6-methylbenzo[d]thiazol-2-yl)acetamide (GB16)** Yield: 0.39 g (48%). M.P. 283–284 °C. White color solid. IR (cm<sup>-1</sup>) 3304 (NH str.), 1739, 1703 (C=O str. of cyclic amide), 1662, 1602, 1585 (C=C str.), 858 (C-Cl str.). <sup>1</sup>H NMR (400 MHz, DMSO-d<sub>6</sub>, δ ppm): 2.39 (s, 3H), 4.70 (s, 2H), 7.34 (t, *J* = 8.0 Hz, 1H), 7.40 (d, *J* = 8.0 Hz, 1H), 7.56–7.59 (m, 2H), 7.96 (s, 1H), 7.98–7.99 (m, 1H), 8.31 (s, 1H), 13.27 (s, 1H). <sup>13</sup>C NMR (100 MHz, DMSO-d<sub>6</sub>): 162.31, 130.29, 130.06, 79.12, 35.76, 30.75, 21.10. UV Spectrum (10 ppm, λ<sub>max</sub>—330 nm, absorbance—1.196). Theoretical mass: 443.93; LCMS (*m/z*, I%): 441.9 [(M-H)<sup>+</sup>, 100%]. HPLC Purity: % Area 96.02, RT 5.45 min.

**2-(5-(4-chlorobenzylidene)-2,4-dioxothiazolidin-3-yl)-N-(6-ethoxybenzo[d]thiazol-2-yl)acetamide (GB17)** Yield 0.47 g (49%). M.P. 260.5–261.5 °C. White color solid. IR (cm<sup>-1</sup>) 3304 (NH str.), 1741 (C=O str. of cyclic amide), 1666, 1604, 1587, 1566, 1548 (C=C

str.), 815 (C-Cl str.).  $^1\text{H}$  NMR (400 MHz, DMSO- $d_6$ ,  $\delta$  ppm): 1.33–1.37 (m, 3H), 4.05–4.08 (m, 2H), 4.69 (s, 2H), 7.04 (dd,  $J = 2.8, 8.8$  Hz, 1H), 7.57 (d,  $J = 2.4$  Hz, 1H), 7.63–7.72 (m, 5H), 8.02 (s, 1H), 12.71 (s, 1H).  $^{13}\text{C}$  NMR (100 MHz, DMSO- $d_6$ ): 166.84, 165.06, 155.54, 135.47, 132.47, 131.83, 131.71, 129.50, 121.67, 121.37, 115.50, 105.37, 79.12, 63.60, 43.52, 14.65. UV Spectrum (10 ppm,  $\lambda_{\text{max}}$ —329 nm, absorbance—0.622). Theoretical mass: 473.95; LCMS ( $m/z$ , I%): 472.0 [(M-H) $^+$ , 100%]. HPLC Purity: % Area 95.63, RT 4.30 min.

**N-(4,6-difluorobenzo[d]thiazol-2-yl)-2-(5-(4-fluorobenzylidene)-2,4-dioxothiazolidin-3-yl)acetamide (GB18)** Yield 0.53 g (57%); M.P. charred above 300 °C. White color solid. IR ( $\text{cm}^{-1}$ ) 3398 (NH str.), 1741 (C=O str. of cyclic amide), 1695, 1662, 1622, 1599 (C=C str.), 1286, 1149, 1101 (C-F str.);  $^1\text{H}$  NMR (400 MHz, DMSO- $d_6$ ,  $\delta$  ppm): 4.71 (s, 2H), 7.37–7.45 (m, 3H), 7.74–7.77 (m, 2H), 7.80–7.83 (m, 1H), 8.31 (s, 1H), 13.15 (s, 1H).  $^{13}\text{C}$  NMR (100 MHz, DMSO- $d_6$ ): 30.75, 35.75, 43.52, 79.12, 102.09, 102.37, 104.49, 104.73, 116.50, 116.72, 120.60, 129.47, 132.68, 132.77, 157.69, 161.86, 162.30, 164.36, 165.09, 166.98; Theoretical mass: 449.43; LCMS ( $m/z$ , I%): 447.9 [(M-2H) $^+$ , 100%]. HPLC Purity: % Area 95.31, RT 3.34 min.

**N-(4,6-difluorobenzo[d]thiazol-2-yl)-2-(5-(4-methylbenzylidene)-2,4-dioxothiazolidin-3-yl)acetamide (GB19)** Yield 0.53 g (58%); M.P. 295–297 °C. White color solid. IR ( $\text{cm}^{-1}$ ) 3348 (NH str.), 1741 (C=O str. of cyclic amide), 1664, 1624, 1575 (C=C str.), 1147, 1103 (C-F str.);  $^1\text{H}$  NMR (400 MHz, DMSO- $d_6$ ,  $\delta$  ppm): 2.38 (s, 3H), 4.70 (s, 2H), 7.37–7.41 (m, 1H), 7.55–7.57 (m, 2H), 7.80–7.82 (m, 1H), 7.97 (m, 1H), 8.31 (s, 1H), 13.15 (s, 1H);  $^{13}\text{C}$  NMR (100 MHz, DMSO- $d_6$ ): 21.09, 30.74, 35.75, 43.46, 79.12, 101.85, 102.08, 102.36, 104.43, 104.70, 133.89, 134.64, 134.72, 141.28, 152.11, 154.50, 154.64, 156.92, 157.03, 157.67, 162.30, 165.18, 167.11; Theoretical mass: 445.46; LCMS ( $m/z$ , I%): 444.0 [(M-H) $^+$ , 100%]. HPLC Purity: % Area 95.99, RT 4.19 min.

**N-(4,6-difluorobenzo[d]thiazol-2-yl)-2-(5-(3,4-dimethylbenzylidene)-2,4-dioxothiazolidin-3-yl)acetamide (GB20)** Yield 0.63 g (65%); M.P. 271–273 °C. White color solid. IR ( $\text{cm}^{-1}$ ) 3398 (NH str.), 1741 (C=O str. of cyclic amide), 1697, 1664, 1641, 1622 (C=C str.), 1284, 1147 (C-F str.);  $^1\text{H}$  NMR (400 MHz, DMSO- $d_6$ ,  $\delta$  ppm): 2.30 (s, 6H), 4.70 (s, 2H), 7.34–7.36 (m, 1H), 7.37–7.44 (m, 2H), 7.81–7.83 (m, 1H), 7.93–7.96 (m, 2H), 13.14 (s, 1H);  $^{13}\text{C}$  NMR (100 MHz, DMSO- $d_6$ ): 19.84, 31.25, 36.26, 43.97, 79.62, 119.93, 128.18, 130.89, 131.03, 131.87, 134.51, 138.09, 140.77, 162.82, 165.70, 167.67; Theoretical mass: 459.49; LCMS ( $m/z$ , I%): 458.0 [(M-H) $^+$ , 100%]. HPLC Purity: % Area 97.49, RT 5.21 min.

**N-(5,6-dimethylbenzo[d]thiazol-2-yl)-2-(5-(4-methylbenzylidene)-2,4-dioxothiazolidin-3-yl)acetamide (GB21)** Yield 0.52 g (53%). M.P. 283–285 °C. White color solid. IR ( $\text{cm}^{-1}$ ) 3246 (NH str.), 1741 (C=O str. of cyclic amide), 1697, 1664, 1593, 1550 (C=C str.).  $^1\text{H}$  NMR (400 MHz, DMSO- $d_6$ ,  $\delta$  ppm): 2.32 (d,  $J = 6.4$  Hz, 6H), 2.39 (s, 3H), 4.67 (s, 2H), 7.39 (d,  $J = 8.0$  Hz, 2H), 7.57 (d,  $J = 8.0$  Hz, 3H), 7.73 (s, 1H), 7.97 (s, 1H), 12.75 (s, 1H).  $^{13}\text{C}$  NMR (100 MHz, DMSO- $d_6$ ): 167.12, 165.21, 146.95, 141.27, 133.85, 132.77, 130.28, 130.06, 121.51, 119.65, 21.10, 19.65, 19.51. UV Spectrum (10 ppm,  $\lambda_{\text{max}}$ —332 nm, absorbance—0.388). Theoretical mass: 437.53; LCMS ( $m/z$ , I%): 435.8 [(M-H) $^+$ , 100%]. HPLC Purity: % Area 95.85, RT 5.47 min.

**2-(5-benzylidene-2,4-dioxothiazolidin-3-yl)-N-(5,6-dimethylbenzo[d]thiazol-2-yl)acetamide (GB22)** Yield 0.57 g (60%); M.P. 276–278 °C. White color solid. IR ( $\text{cm}^{-1}$ ) 3398 (NH str.), 1743 (C=O str. of cyclic amide), 1666, 1597, 1548 (C=C str.);  $^1\text{H}$  NMR (400 MHz, DMSO- $d_6$ ,  $\delta$  ppm): 2.32 (d,  $J = 6.4$  Hz, 3H), 2.39 (s, 3H), 4.67 (s, 2H), 7.39 (d,  $J = 8.0$  Hz, 2H), 7.57 (d,  $J = 8.0$  Hz, 3H), 7.73 (s, 2H), 7.97 (s, 1H), 12.75 (s, 1H).  $^{13}\text{C}$  NMR (100 MHz, DMSO- $d_6$ ): 167.12, 165.21, 146.95, 141.27, 133.85, 132.77, 130.28, 130.06, 121.51, 119.65, 21.10, 19.65, 19.51. Theoretical mass: 423.51; LCMS ( $m/z$ , I%): 421.9 [(M-2H) $^+$ , 100%]. HPLC Purity: % Area 97.41, RT 4.62 min.

**2-(5-(4-bromobenzylidene)-2,4-dioxothiazolidin-3-yl)-N-(5,6-dimethylbenzo[d]thiazol-2-yl)acetamide (GB23)** Yield 0.59 g (60%); M.P. charred above 300 °C. White color solid. IR ( $\text{cm}^{-1}$ ) 3398 (NH str.), 1747 (C=O str. of cyclic amide), 1697, 1655, 1604, 1546 (C=C str.), 650 (C-Br str.);  $^1\text{H}$ -NMR (400 MHz, DMSO- $d_6$ ,  $\delta$  ppm): 2.42 (s, 6H, CH<sub>3</sub>), 4.70 (s, 2H, CH<sub>2</sub>), 7.27–7.36 (m, 2H, ArH), 7.49–7.55 (m, 1H, ArH), 7.66–7.78 (m, 3H, ArH and benzylidene proton), 7.93 (s, 1H, ArH), 12.78 (bs, 1H, NH).  $^{13}\text{C}$ -NMR (100 MHz, DMSO- $d_6$ ): 166.8, 165.0,

135.4, 133.3, 132.4, 131.8, 131.6, 129.4, 127.6, 121.6, 121.3, 120.3, 43.9, 19.9, 19.8. Theoretical mass: 502.40; LCMS ( $m/z$ , I%): 501.7 [(M-H)<sup>+</sup>, 100%]. HPLC Purity: % Area 96.22, RT 5.93 min.

**2-(5-(4-chlorobenzylidene)-2,4-dioxothiazolidin-3-yl)-N-(5,6-dimethylbenzo[d]thiazol-2-yl) acetamide (GB24)** Yield 0.63 g (68%). M.P. charred above 300 °C. White color solid. IR (cm<sup>-1</sup>) 3398 (NH str.), 1745, 1701 (C=O str. of cyclic amide), 1666, 1604, 1587, 1546 (C=C str.), 854 (C-Cl str.). <sup>1</sup>H NMR (400 MHz, DMSO-d<sub>6</sub>, δ ppm): 2.32 (d,  $J = 6.0$  Hz, 6H), 4.69 (s, 2H), 7.57 (s, 1H), 7.63–7.65 (m, 2H), 7.69–7.73 (m, 3H), 8.01 (s, 1H), 12.76 (s, 1H). <sup>13</sup>C NMR (100 MHz, DMSO-d<sub>6</sub>): 166.84, 165.05, 135.46, 135.00, 132.78, 132.46, 131.83, 131.71, 129.50, 121.67, 121.52, 19.65, 19.52. UV Spectrum (10 ppm, λ<sub>max</sub>—329 nm, absorbance—0.219). Theoretical mass: 457.95; LCMS ( $m/z$ , I%): 455.7 [(M-H)<sup>+</sup>, 90%]. HPLC Purity: % Area 95.52, RT 5.04 min.

**N-(5,6-dimethylbenzo[d]thiazol-2-yl)-2-(5-(4-fluorobenzylidene)-2,4-dioxothiazolidin-3-yl)acetamide (GB25)** Yield 0.54 g (59%); M.P. 298–299 °C. White color solid. IR (cm<sup>-1</sup>) 3398 (NH str.), 1745 (C=O str. of cyclic amide), 1699, 1662, 1597 (C=C str.), 1141 (C-F str.); <sup>1</sup>H-NMR (400 MHz, DMSO-d<sub>6</sub>, δ ppm): 2.32–2.33 (d,  $J = 2$  Hz, 6H, CH<sub>3</sub>), 4.69 (s, 2H, CH<sub>2</sub>), 7.57 (s, 1H, benzylidene proton), 7.63–7.73 (m, 5H, ArH), 8.01 (s, 1H, ArH), 12.76 (bs, 1H, NH). <sup>13</sup>C-NMR (100 MHz, DMSO-d<sub>6</sub>): 167.3, 167.2, 155.9, 138.4, 138.3, 130.9, 130.6, 126.8, 126.1, 125.1, 121.0, 120.7, 119.6, 119.5, 111.5, 67.3, 16.0, 13.4. Theoretical mass: 441.50; LCMS ( $m/z$ , I%): 440.0 [(M-H)<sup>+</sup>, 100%]. HPLC Purity: % Area 97.31, RT 4.0 min.

**N-(5,6-dimethylbenzo[d]thiazol-2-yl)-2-(5-(3,4-dimethylbenzylidene)-2,4-dioxothiazolidin-3-yl)acetamide (GB26)** Yield 0.59 g (60%); M.P. 284–286 °C. White color solid. IR (cm<sup>-1</sup>) 3335 (NH str.), 1741 (C=O str. of cyclic amide), 1697, 1658, 1593, 1546 (C=C str.); <sup>1</sup>H-NMR (400 MHz, DMSO-d<sub>6</sub>, δ ppm): 2.74 (m, 6H, CH<sub>3</sub>), 2.90 (m, 6H, CH<sub>3</sub>), 4.70 (s, 2H, CH<sub>2</sub>), 7.34–7.38 (m, 1H, ArH), 7.39–7.44 (m, 2H, ArH), 7.81–7.83 (m, 1H), 7.93–7.96 (d,  $J = 10.8$  Hz, 2H, ArH), 13.14 (bs, 1H, NH). <sup>13</sup>C-NMR (100 MHz, DMSO-d<sub>6</sub>): 165.7, 165.6, 162.8, 140.7, 138.0, 134.5, 131.8, 131.0, 130.8, 128.1, 119.9, 79.6, 43.9, 19.9, 19.8. Theoretical mass: 451.56; LCMS ( $m/z$ , I%): 450.0 [(M-H)<sup>+</sup>, 100%]. HPLC Purity: % Area 98.14, RT 6.48 min.

**N-(4-methoxybenzo[d]thiazol-2-yl)-2-(5-(4-methylbenzylidene)-2,4-dioxothiazolidin-3-yl) acetamide (GB27)** Yield 0.59 g (63%). M.P. 249–251 °C. White color solid. IR (cm<sup>-1</sup>) 3342 (NH str.), 1745, 1708 (C=O str. of cyclic amide), 1687, 1631, 1599, 1566, 1514 (C=C str.). <sup>1</sup>H NMR (400 MHz, DMSO-d<sub>6</sub>, δ ppm): 2.59 (s, 3H), 3.92 (s, 3H), 4.68 (s, 2H), 7.01 (d,  $J = 7.6$  Hz, 1H), 7.28 (t,  $J = 8.0$  Hz, 1H), 7.42 (t,  $J = 8.8$  Hz, 2H), 7.54 (d,  $J = 8.0$  Hz, 1H), 7.73–7.77 (m, 2H), 8.02 (s, 1H), 12.97 (s, 1H). <sup>13</sup>C NMR (100 MHz, DMSO-d<sub>6</sub>): 167.01, 165.12, 164.34, 161.85, 156.11, 151.93, 138.26, 132.82, 132.75, 132.67, 129.50, 129.46, 124.86, 120.68, 116.72, 116.50, 113.54, 107.79, 43.57. UV Spectrum (10 ppm, λ<sub>max</sub>—322 nm, absorbance—0.473). Theoretical mass: 439.51; LCMS ( $m/z$ , I%): 438.0 [(M-H)<sup>+</sup>, 100%]. HPLC Purity: % Area 95.65, RT 3.05 min.

**2-(5-benzylidene-2,4-dioxothiazolidin-3-yl)-N-(4-methylbenzo[d]thiazol-2-yl)acetamide (GB28)** Yield 0.60 g (62%); M.P. 278–280 °C. White color solid. IR (cm<sup>-1</sup>) 3321 (NH str.), 1741 (C=O str. of cyclic amide), 1693, 1666, 1599, 1548 (C=C str.); <sup>1</sup>H NMR (400 MHz, DMSO-d<sub>6</sub>, δ ppm): 2.59 (s, 3H), 4.70 (s, 2H), 7.21–7.29 (m, 2H), 7.53–7.60 (m, 3H), 7.67 (d,  $J = 7.2$  Hz, 2H), 7.80 (d,  $J = 7.6$  Hz, 1H), 8.01 (s, 1H), 12.96 (s, 1H). <sup>13</sup>C NMR (100 MHz, DMSO-d<sub>6</sub>): 167.09, 165.14, 156.28, 147.53, 133.79, 132.79, 131.12, 130.85, 130.19, 130.09, 129.42, 126.73, 123.80, 120.90, 119.17, 43.49, 17.87. Theoretical mass: 409.48; LCMS ( $m/z$ , I%): 408.0 [(M-H)<sup>+</sup>, 100%]. HPLC Purity: % Area 95.09, RT 3.46 min.

**N-(4,6-difluorobenzo[d]thiazol-2-yl)-2-(5-(2,4-difluorobenzylidene)-2,4-dioxothiazolidin-3-yl)acetamide (GB29)** Yield 0.62 g (70%); M.P. 274–276 °C. White color solid. IR (cm<sup>-1</sup>) 3392 (NH str.), 1743 (C=O str. of cyclic amide), 1693, 1666, 1612, 1573 (C=C str.), 1244, 1192, 1145, 1199 (C-F str.); <sup>1</sup>H-NMR (400 MHz, DMSO-d<sub>6</sub>, δ ppm): 4.69 (s, 2H, CH<sub>2</sub>), 7.02 (dd,  $J = 2.8$  Hz, 2.4 Hz, 1H, ArH), 7.57–7.72 (m, 4H, ArH and benzylidene proton), 8.02 (s, 1H, ArH), 12.71 (bs, 1H, NH). <sup>13</sup>C-NMR (100 MHz, DMSO-d<sub>6</sub>): 167.1, 165.2, 146.9, 141.2,

133.8, 132.7, 130.2, 130.0, 121.5, 119.6, 43.9. Theoretical mass: 467.42; LCMS ( $m/z$ , I%): 466.0 [(M-H)<sup>+</sup>, 100%]. HPLC Purity: % Area 97.63, RT 3.62 min.

**2-(5-benzylidene-2,4-dioxothiazolidin-3-yl)-N-(4-fluorobenzo[d]thiazol-2-yl)acetamide (GB30)** Yield 0.63 g (68%); M.P. 272–274 °C. White color solid. IR (cm<sup>-1</sup>) 3398 (NH str.), 1753 (C=O str. of cyclic amide), 1705, 1668, 1604, 1554 (C=C str.), 1147 (C-F str.); <sup>1</sup>H-NMR (400 MHz, DMSO-d<sub>6</sub>, δ ppm): 4.69 (s, 2H, CH<sub>2</sub>), 7.21–7.29 (m, 2H, ArH), 7.40–7.45 (t, 2H, ArH), 7.74–7.81 (m, 3H, ArH and benzylidene proton), 7.96 (s, 1H, ArH), 12.96 (bs, 1H, NH). <sup>13</sup>C-NMR (100 MHz, DMSO-d<sub>6</sub>): 166.9, 165.3, 165.2, 165.1, 162.3, 161.8, 147.5, 132.7, 132.6, 131.1, 130.0, 129.5, 126.7, 123.8, 120.6, 119.1, 116.7, 116.5, 43.5, 17.8. Theoretical mass: 413.45; LCMS ( $m/z$ , I%): 412.0 [(M-H)<sup>+</sup>, 100%]. HPLC Purity: % Area 95.28, RT 3.05 min.

**2-(5-(4-bromobenzylidene)-2,4-dioxothiazolidin-3-yl)-N-(6-methylbenzo[d]thiazol-2-yl)acetamide (GB31)** Yield 0.62 g (65%); M.P. 292–294 °C. White color solid. IR (cm<sup>-1</sup>) 3265 (NH str.), 1753 (C=O str. of cyclic amide), 1703, 1693, 1666, 1602 (C=C str.), 688 (C-Br str.); <sup>1</sup>H-NMR (400 MHz, DMSO-d<sub>6</sub>, δ ppm): 2.41 (s, 3H, CH<sub>3</sub>), 4.69 (s, 2H, CH<sub>2</sub>), 7.26–7.28 (m, 1H, ArH), 7.63–7.78 (m, 6H, ArH and benzylidene proton), 8.01 (s, 1H, ArH), 12.78 (bs, 1H, NH). <sup>13</sup>C-NMR (100 MHz, DMSO-d<sub>6</sub>): 166.8, 165.6, 165.0, 132.6, 132.4, 132.0, 131.9, 124.4, 121.7, 104.4, 79.1, 43.5, 21.7. Theoretical mass: 488.38; LCMS ( $m/z$ , I%): 487.9 [(M-H)<sup>+</sup>, 100%]. HPLC Purity: % Area 95.35, RT 4.85 min.

**N-(6-fluorobenzo[d]thiazol-2-yl)-2-(5-(4-methylbenzylidene)-2,4-dioxothiazolidin-3-yl)acetamide (GB32)** Yield 0.52 g (58%). M.P. 274–275 °C. White color solid. IR (cm<sup>-1</sup>) 3259 (NH str.), 1737, 1703 (C=O str. of cyclic amide), 1658, 1591, 1552 (C=C str.), 1139 (C-F str.). <sup>1</sup>H NMR (400 MHz, DMSO-d<sub>6</sub>, δ ppm): 2.74 (s, 3H), 4.69 (s, 2H), 7.21–7.29 (m, 2H), 7.43 (t,  $J = 8.8$  Hz, 2H), 7.74–7.81 (m, 2H), 7.96 (s, 1H), 8.03 (s, 1H), 12.96 (s, 1H). <sup>13</sup>C NMR (100 MHz, DMSO-d<sub>6</sub>): 166.98, 165.31, 165.20, 165.10, 162.31, 161.85, 147.52, 132.77, 132.73, 132.68, 131.12, 130.09, 129.50, 126.73, 123.81, 120.60, 119.17, 116.72, 116.50, 43.52, 35.76, 30.75, 17.86. UV Spectrum (10 ppm, λ<sub>max</sub>—329 nm, absorbance—0.843). Theoretical mass: 427.47; LCMS ( $m/z$ , I%): 425.9 [(M-H)<sup>+</sup>, 100%]. HPLC Purity: % Area 95.94, RT 3.98 min.

**2-(5-(4-chlorobenzylidene)-2,4-dioxothiazolidin-3-yl)-N-(6-fluorobenzo[d]thiazol-2-yl)acetamide (GB33)** Yield 0.63 g (65%); M.P. 290–292 °C. White color solid. IR (cm<sup>-1</sup>) 3387 (NH str.), 1739 (C=O str. of cyclic amide), 1704, 1664, 1600, 1585 (C=C str.), 1139 (C-F str.), 705 (C-Cl str.); <sup>1</sup>H-NMR (400 MHz, DMSO-d<sub>6</sub>, δ ppm): 4.71 (s, 2H, CH<sub>2</sub>), 7.36–7.42 (m, 1H, ArH), 7.62–7.71 (dd,  $J=8.4$  Hz, 8.8 Hz, 2H, ArH), 7.80–7.83 (m, 4H, ArH and benzylidene proton), 8.01 (s, 1H, ArH), 12.97 (bs, 1H, NH). <sup>13</sup>C-NMR (100 MHz, DMSO-d<sub>6</sub>): 167.1, 165.2, 146.4, 141.2, 133.8, 133.3, 131.5, 130.2, 130.0, 127.5, 121.3, 120.4, 119.6, 43.5. Theoretical mass: 447.89; LCMS ( $m/z$ , I%): 445.9 [(M-2H)<sup>+</sup>, 100%]. HPLC Purity: % Area 95.97, RT 3.98 min.

**N-(6-fluorobenzo[d]thiazol-2-yl)-2-(5-(4-fluorobenzylidene)-2,4-dioxothiazolidin-3-yl)acetamide (GB34)** Yield 0.64 g (68%); M.P. 260–262 °C. White color solid. IR (cm<sup>-1</sup>) 3398 (NH str.), 1741 (C=O str. of cyclic amide), 1712, 1674, 1589, 1545 (C=C str.), 1195, 1138 (C-F str.); <sup>1</sup>H-NMR (400 MHz, DMSO-d<sub>6</sub>, δ ppm): 4.68 (s, 2H, CH<sub>2</sub>), 7.37–7.42 (m, 1H, ArH), 7.61–7.63 (d,  $J=8.4$  Hz, 2H, ArH), 7.77–7.83 (m, 4H, ArH and benzylidene proton), 7.99 (s, 1H, ArH), 13.14 (bs, 1H, NH). <sup>13</sup>C-NMR (100 MHz, DMSO-d<sub>6</sub>): 167.1, 165.2, 146.4, 140.2, 137.5, 133.9, 133.3, 131.5, 131.3, 130.5, 130.4, 127.6, 127.5, 121.3, 120.4, 119.4, 43.4. Theoretical mass: 431.44; LCMS ( $m/z$ , I%): 430.0 [(M-H)<sup>+</sup>, 100%]. HPLC Purity: % Area 97.87, RT 3.04 min.

**2-(5-(4-fluorobenzylidene)-2,4-dioxothiazolidin-3-yl)-N-(4-methoxybenzo[d]thiazol-2-yl)acetamide (GB35)** Yield 0.58 g (60%); M.P. 172–172 °C. White color solid. IR (cm<sup>-1</sup>) 3279 (NH str.), 1743 (C=O str. of cyclic amide), 1687, 1597, 1566, 1554 (C=C str.), 1147 (C-F str.); <sup>1</sup>H NMR (400 MHz, DMSO-d<sub>6</sub>, δ ppm): 3.92 (s, 3H), 4.68 (s, 2H), 7.01–7.02 (m, 1H), 7.26–7.30 (m, 1H), 7.40–7.44 (m, 2H), 7.53–7.55 (m, 1H), 7.73–7.77 (m, 2H), 8.02 (s, 1H), 12.97 (s, 1H); <sup>13</sup>C NMR (100 MHz, DMSO-d<sub>6</sub>): 43.57, 55.80, 79.12, 107.79, 113.54, 116.50, 116.72, 120.68, 124.86, 129.46, 129.50, 132.67, 132.75, 132.82, 138.26, 151.93, 156.11, 161.85, 164.34, 165.12, 167.01; Theoretical mass: 443.47; LCMS ( $m/z$ , I%): 441.9 [(M-2H)<sup>+</sup>, 100%]. HPLC Purity: % Area 96.52, RT 3.05 min.



**2-(5-benzylidene-2,4-dioxothiazolidin-3-yl)-N-(6-ethoxybenzo[d]thiazol-2-yl)acetamide (GB36)** Yield 0.55 g (59%); M.P. charred above 300 °C. White color solid. IR (cm<sup>-1</sup>) 3265 (NH str.), 1739 (C=O str. of cyclic amide), 1695, 1666, 1599, 1550 (C=C str.); <sup>1</sup>H NMR (400 MHz, DMSO-d<sub>6</sub>, δ ppm): 1.33–1.37 (m, 3H), 4.05–4.08 (m, 2H), 4.69 (s, 2H), 7.04 (dd, *J* = 2.8, 8.8 Hz, 1H), 7.57 (d, *J* = 2.4 Hz, 2H), 7.63–7.72 (m, 5H), 8.02 (s, 1H), 12.71 (s, 1H). <sup>13</sup>C NMR (100 MHz, DMSO-d<sub>6</sub>): 166.84, 165.06, 155.54, 135.47, 132.47, 131.83, 131.71, 129.50, 121.67, 121.37, 115.50, 105.37, 79.12, 63.60, 43.52, 14.65. Theoretical mass: 439.51; LCMS (*m/z*, I%): 438.0 [(M-H)<sup>+</sup>, 100%]. HPLC Purity: % Area 96.27, RT 2.94 min.

### 3.2. Mutagenesis, Recombinant Production and Purification of cdHDAC4

The catalytic domain of HDAC4 (cdHDAC4, T648–T1057; construct available in Supporting Information Table S3) was produced in *E. coli* (BL21) DE3 pLysS cells using a pET14b vector containing the cdHDAC4 gene fused with His6-SUMO tag. The respective mutants were generated by splicing by overlap extension polymerase chain reaction (SOE-PCR) [30] with the mutagenesis primers as listed in Table S4. An overnight culture of cells was incubated at 37 °C and 180 rpm in sterile Lennox LB media (20 g/L) containing 100 µg/mL ampicillin and 34 µg/mL chloramphenicol. Subsequently ca. 90 mL of overnight culture was equally transferred to three separate flasks containing a sterile solution of 26.6 g/L auto induction media (containing 3.08 g/L KH<sub>2</sub>PO<sub>4</sub>, 3.10 g/L Na<sub>2</sub>HPO<sub>4</sub>, 0.44 g/L MgSO<sub>4</sub> and 20 g/L Lennox LB media), 4.6 g/L glycerol, 0.45 g/L glucose, 1.2 g/L lactose, 100 µg/mL ampicillin and 34 µg/mL chloramphenicol. The flasks were incubated at 30 °C and 225 rpm overnight. Cell harvest was performed at 8000 g for 10 min at 4 °C (6–16K centrifuge, Sigma, Osterode am Harz, Germany), the supernatant was discarded, cells were resuspended in IMAC-Buffer A (150 mM KCl, 50 mM TRIS-HCl, pH 8.0) and 3 µg/mL DNase I (AppliChem) as well as 5 mM dithiothreitol was added. Cell lysis was performed on ice via ultrasound (Digital Sonofier C25, Branson, MO, USA) with a maximum amplitude of 25% for three minutes and three subsequent repetitions. Cell debris were separated from cdHDAC4 containing lysate via centrifugation at 18,000 × *g* for 30 min at 4 °C (6–16K centrifuge, Sigma). The lysate was filtrated with a 0.45 µm filter (Filtropur, Sarstedt, Nümbrecht, Germany), pooled, diluted to 100 mL with IMAC-Buffer A and 5 mM imidazole was added. First purification step was an IMAC chromatography. After equilibration of the IMAC column (5 mL cOmplete His-Tag Purification Resin, Roche, Basel, Switzerland) with IMAC-Buffer A containing 5 mM imidazole for a duration of 5 column volumes (CV) the lysate was loaded onto the IMAC column. Column wash was performed with IMAC-Buffer A containing 5 mM imidazole for a duration of 10 CV. The His6-tagged cdHDAC4 was eluted with IMAC-Buffer B containing 75 mM imidazole via step elution. The peak fractions were pooled, 6 µg/mL SUMO protease, as well as 5 mM dithiothreitol was added followed by an incubation overnight at 4 °C for cleaving of the SUMO-tag. The next day, the protein solution was diluted with an equally volume of 2 × HIC buffer (4 M NaCl, 50 mM TRIS-HCl, pH 7.0). After equilibration of the HIC column (5 mL Toyopearl Butyl-650M, Tosoh Bioscience, Griesheim, Germany) with HIC Puffer containing 2 M NaCl, 50 mM TRIS-HCl, pH 7.0 for 5 CV the proteins solution was loaded onto the column. Column wash was performed with HIC Buffer for a duration of 10 CV. Elution was performed with HIC elution buffer containing 50 mM NaCl, 50 mM TRIS-HCl and pH 7.0 for a duration of 20 CV via step elution. The protein containing fractions were concentrated via ultrafiltration (Vivaspin 2, MWCO 3.5 kDa, Sartorius, Goettingen, Germany) at 8000 g and 4 °C (3–30KS centrifuge, Sigma, Osterode am Harz, Germany) to ca. 1.5 mL and 5 mM dithiothreitol was added. Last purification step was a size exclusion chromatography (SEC) using a (HiLoad<sup>®</sup> Superdex<sup>®</sup> 16/600 75 pg, Cytiva, Freiburg, Germany) with SEC-Buffer (150 mM KCl, 50 mM TRIS-HCl, pH 8.0. All chromatography steps were performed using a ÄKTA pure chromatography device (GE Healthcare Life Sciences, Freiburg, Germany). All flow rates were 5 mL/min, except for SEC which was 1 mL/min. To the purified cdHDAC4 25% glycerol and 1 mM TCEP tris(2-carboxyethyl)phosphine was added, flash frozen in liquid nitrogen and stored at –20 °C.

### 3.3. Determination of Michaelis Menten Parameters

For the determination of Michaelis Menten parameters a series of different substrate (Boc-Lys(TFA)-7-Amino-4-methylcoumarin) concentrations (200, 160, 120, 80, 60, 40, 20 and 10  $\mu\text{M}$ ) was mixed with 0.5 nM cdHDAC<sub>4wt</sub> or 1 nM mutant variant protein in reaction Buffer (50 mM Tris, 137 mM NaCl, 2.7 mM KCl, 1 mM MgCl<sub>2</sub>, 1 mg/mL BSA, pH 8.0) at room temperature. For E677A, F812A, C813S, F871A and H976Y (GoF) 5 nM enzyme were used. Aliquots of 50  $\mu\text{L}$  were removed at 0, 5, 10, 15, 20 and 30 min and transferred into 50  $\mu\text{L}$  developer solution consisting of reaction buffer with the addition of 100  $\mu\text{M}$  SATFMK and 20 mg/mL trypsin into the cavity of a black 96 well half area plate (Greiner, Kremsmuenster, Austria). Signal was developed for 30 min at room temperature and the fluorescence was measured at 450 nm ( $\lambda_{\text{Ex}} = 350 \text{ nm}$ ) in a PherStar Plus (BMG Labtech, Ortenberg, Germany) fluorescence plate reader. HDAC activity tracking throughout all applied enzyme activity assay was based on the work by Wegener et al. [31]. For the calculation of  $K_m$  the measured fluorescence at each time point and substrate concentration were corrected with the blank (0 min). Afterwards the resulting fluorescence units were calculated to the product concentration using an external AMC calibration with a slope of 5221 rfu/ $\mu\text{M}$  and corrected for the dilution by multiply the product concentration by two. Afterwards, the product concentration was plotted against the time and  $v_0$  ( $\mu\text{M}/\text{min}$ ) was calculated from the resulting slopes. Now the initial velocity was plotted against the substrate concentration and  $K_m$  was calculated using a Michaelis Menten-Fit in GraphPad Prism. The value of  $v_{\text{max}}$  is neglected because enzyme concentration and purity are too inconsistent between the mutant variant to calculate this value appropriate.

### 3.4. Association Kinetics

A serial dilution of inhibitor beginning at 10-fold of respective IC<sub>50</sub>-value in assay buffer (25 mM Tris-HCl, pH 8.0, 75 mM KCl, 0.001% Pluronic F-127) was made in a black 96-well microtiter half-area plate (Greiner, Kremsmuenster, Austria). The dilutions were added to 3 nM cdHDAC<sub>4wt</sub>. Shortly after, the reaction was initiated by adding 20  $\mu\text{M}$  Boc-Lys(TFA)-7-Amino-4-methylcoumarin (Bachem, Bubendorf, Switzerland) as substrate. The reaction was stopped after different incubation times: 2, 3, 4, 5, 7, 9, 12, 15 and 20 min with 500  $\mu\text{M}$  SAHA. Finally 0.4 mg/mL trypsin was added to split the deacetylated substrate in the fluorescent product which was measured at 450 nm ( $\lambda_{\text{Ex}} = 350 \text{ nm}$ ) (PherStar Plus, BMG Labtech, Ortenberg, Germany). 15 compounds with highly structural diversity and IC<sub>50</sub>-values below 2  $\mu\text{M}$  were tested. The standardized RFUs were plotted against the incubation time. The courses suggest the TZD ligands being slow binding inhibitors. Due to this knowledge the data were fitted via non linear regression with GraphPad Prism program to the following equation by Copeland [27]:

$$Y = v_s \cdot t + \frac{v_i - v_s}{k_{\text{obs}}} \cdot (1 - e^{(-k_{\text{obs}} \cdot t)}) + d \quad (2)$$

where  $v_i$  is the initial slope,  $v_s$  is the second lower slope,  $k_{\text{obs}}$  is the respective rate constant,  $t$  is time and  $d$  the correction for possible data offset.

Afterwards  $k_{\text{obs}}$  values were plotted against their respective inhibitor concentration. Because all plots showed a saturation behavior as well as similar plateaus, the data was fitted via non linear regression with GraphPad Prism program to a two step model with the following equation by Copeland [27]:

$$k_{\text{obs}} = k_{\text{off}} + \left( \frac{k_{\text{on}}}{1 + (K_1/I)} \right) \quad (3)$$

where  $K_1$  is the rapid equilibrium constant of an initial enzyme and inhibitor encounter complex  $k_{\text{on}}$  and  $k_{\text{off}}$  are the respective isomerization constants and  $I$  is the inhibitor concentration.

### 3.5. Reversibility Assay

The reversibility of all inhibitors was tested in 96-well microtiter half-area plate (Greiner) via rapid dilution using a modified enzyme activity assay according to Copeland [27]. 100 nM cdHDAC<sub>4wt</sub> was incubated with respective TZD ligand (10-fold IC<sub>50</sub>-value) in assay buffer (25 mM Tris-HCl, pH 8.0, 75 mM KCl, 0.001% Pluronic F-127). Rapid dilution was performed by diluting the incubated mixture 100-fold with substrate (Boc-Lys{TFA}-7-Amino-4-methylcoumarin (Bachem, Bubendorf, Switzerland)) with the final substrate concentration being 20 µM. This caused the protein and the TZD ligand to be diluted down to 1 nM and 10% IC<sub>50</sub>-value, respectively. A positive control without TZD ligand and a blank without enzyme and TZD ligand were also carried out. A binding control was also determined: 10 nM cdHDAC<sub>4wt</sub> and 100-fold IC<sub>50</sub>-value of respective TZD ligand was incubated and diluted 10 fold with substrate, resulting in a final enzyme and TZD ligand concentration of 1 nM and 10-fold IC<sub>50</sub>-value, respectively. Once again the final substrate concentration was 20 µM. The reactions were stopped after 15 min by the addition of 500 µM suberanolhydroxamic acid (Cayman Chemical Company, Ann Arbor, MI, USA). The deacetylated substrate was converted into a fluorescent product by the addition of 0.4 mg/mL trypsin (AppliChem, Darmstadt, Germany). The release of fluorogenic substrate was followed in a microplate reader (PherStar Plus, BMG Labtech, Ortenberg, Germany) at 450 nm (λ<sub>Ex</sub> = 350 nm) and correlated the positive control. The data was analyzed with GraphPad Prism Version 6.01. All incubations steps were performed for 60 min at 30 °C and 450 rpm. The substrate was preheated to 30 °C before the rapid dilution step.

### 3.6. Calculations of Residence Time Based on Reversibility Data

Under the assumption of an exponential decay of the complex formed by cdHDAC<sub>4wt</sub> and TZD ligand after rapid dilution the following equation for exponential decay was utilized [32]:

$$A_t = A_0 \cdot e^{(-k \cdot t)} \quad (4)$$

where  $A_t$  in the concentration of the complex at a specific time,  $A_0$  is the initial complex concentration,  $k$  is the decay constant and  $t$  is time. The reciprocal values for  $k$  equals the residence time of the respective TZD ligand (residence time =  $k_{\text{off}}^{-1}$ ), which can be compared with the residence times gained from association data.

### 3.7. IC<sub>50</sub> Determination

A serial dilution of TZD in assay buffer (25 mM TRIS-HCl, 75 mM KCl, 0.001% Pluronic F-127, pH 8.0) was incubated with 1 nM cdHDAC<sub>4wt</sub> in a black 96-well microtiter plate (Greiner). Afterwards the enzymatic reaction was initiated by the addition of 20 µM Boc-Lys{TFA}-7-Amino-4-methylcoumarin (Bachem, Bubendorf, Switzerland) as substrate. After incubation the enzymatic reaction was terminated by the addition of 1.7 µM SATFMK. The deacetylated substrate was converted into a fluorescent product by the addition of 0.4 mg/mL trypsin (AppliChem, Darmstadt, Germany). The release of fluorogenic substrate was followed in a microplate reader (PherStar Plus, BMG Labtech, Ortenberg, Germany) at 450 nm (λ<sub>Ex</sub> = 350 nm) and correlated to enzyme activity. GraphPad Prism program was used to generate dose response curves and were fitted to a four parameter logistic function to obtain IC<sub>50</sub>-values [33]:

$$EA = E_0 + \frac{(E_{\text{max}} - E_0)}{1 + 10^{\log(\text{IC}_{50}) - x \cdot h}} \quad (5)$$

in which  $EA$  is the enzyme activity for a given inhibitor concentration  $x$ ,  $E_{\text{max}}$  and  $E_0$  are the enzyme activities in the absence of inhibitor and at complete inhibition, respectively.  $h$  is the slope of the curve and  $\text{IC}_{50}$  is the inhibitor concentration at which half of the enzyme activity is inhibited. All incubations steps were performed for 60 min at 30 °C and 450 rpm.

### 3.8. Docking

Modeling, preparation and visualization of structural data as well as molecular docking was performed using MOE 2019 software (Chemical Computing Group ULC, Montreal, QC, Canada). Crystal structures of the closed and open conformation of the catalytic domain of HDAC4, PDB-ID's 4CBY and 2VQJ, were obtained from RCSB Protein Data Bank and subjected to the Quickprep procedure of MOE 2019 including 3D-protonation for subsequent docking. The partial charges of all protein and ligand atoms were calculated using the implemented Amber14 force field. The docking site was defined by the ligand within the binding pocket of the respective crystal structure for HDAC4c (PDB-ID: 4CBY). This approach was not permissible for the open conformation of HDAC4 (PDB-ID:2VQJ), since the ligand covered only part of the significantly enlarged binding groove. In this special case, the binding site was analyzed using the Computed Atlas of Surface Topography of proteins (CASTp) (<http://sts.bioe.uic.edu/castp/>, accessed on 21 August 2021) [34]. The largest identified pocket with an estimated volume of 1019.7 Å<sup>3</sup> was identical with the widely opened binding groove of HDAC4<sub>o</sub>. The flanking amino acids of this pocket (G36, R37, G331, G330, H198, H158, H159, F227, P156, P155, F168, S123, R154) were used to define the binding site of HDAC4<sub>o</sub> for the subsequent docking procedure. Molecular docking was performed choosing the triangle matcher for placement of the ligand in the binding site and ranked with the London dG scoring function. The best 50 poses were passed to the refinement and energy minimization in the pocket using the induced fit method and the 10 best poses rescored using the GBVI/WSA dG scoring function.

## 4. Conclusions

Very recently, we reported TZD ligands as inhibitors of HDAC4 lacking the problematic zinc binding group hydroxamic acid. However, the structural determinants of molecular recognition between TZD analogs and cdHDAC4<sub>wt</sub> as well as the binding mechanism have not been elucidated until now. This study combines a large-scale SAR analysis of TZD ligands, extensive mutagenesis of HDAC4, Michaelis Menten, and binding kinetics as well as molecular docking to dissect the molecular interaction between TZD ligands and cdHDAC4<sub>wt</sub> in molecular detail and advance the knowledge about HDAC inhibitors lacking the canonical hydroxamate zinc binding group. Potent TZD ligands are characterized by a terminal TZD moiety, a bulky hydrophobic linker such as naphthalene, and a hydrophobic CAP group. The mutational study and binding kinetics suggest that TZD compounds bind to the active site of cdHDAC4<sub>wt</sub>, and are competitive and reversible inhibitors, which bind via a two-step or one-step binding mechanism depending on the CAP group. The residence time of **24g** is (34 ± 3) min and therefore 6 times larger than for the clinically approved pan-HDAC inhibitor SAHA (5 ± 2) min. Docking of TZD compounds into the catalytic domain of HDAC4 predicts the TZD group function as a warhead that coordinates to the catalytic zinc ion. Moreover, a comparison of binding constants from the mutational study with docking poses provides evidence that TZD inhibitors bind predominantly to the *closed* conformation of HDAC4 in solution. This is consistent with a conformational equilibrium of HDAC4, which is largely shifted to the *closed* form in the absence of an inhibitor. The predicted zinc binding property of the TZD group offers an alternative to the widely used hydroxamate group, which is found in by far the most known HDAC inhibitors and is suspected to have mutagenic effects. This is particularly relevant for drug application in chronic diseases. The slow two-step binding kinetics of TZD ligands to HDAC4 is consistent with an induced fit binding mechanism, which prolongs the residence time and is an important key parameter for the selection and development of safer active substances with long-lasting biological effects, particularly in indication areas such as cancer or anti-infective applications.

In summary, TZD ligands with a suitable combination of linker and CAP group are selective inhibitors of HDAC4 and show slow two-step binding with prolonged residence time involving a conformational change. These beneficial features make the TZD ligands

promising chemical starting points for the further development of drug candidates against cancer or Huntington's Disease.

**Supplementary Materials:** The following are available online at <https://www.mdpi.com/article/10.3390/ph14101032/s1>, Figure S1: Determination of Michaelis-Menten Parameters; Figure S2: Kinetic data plots of TZD ligands; Figure S3: Overlay of crystallized and redocked ligands; Figure S4: Regions of largest structural shifts for the transition from closed to open conformation of HDAC4; Figure S5: Overlay of HDAC4c and HDAC4o showing the amino acids that are mutated; Figure S6: The distance between C $\beta$ -atoms is plotted versus the number of the mutated amino acids; Figure S7: Cluster analysis of most active TZD analogs; Figure S8: Overlap of docking poses of TZD analogs to (A–C) HDAC4c and (D–F) HDAC4o; Table S1: SMILES Strings and IC<sub>50</sub>-values of all tested TZD ligands; Table S2: IC<sub>50</sub>-values in  $\mu$ M for indicated TZD ligands towards cdHDAC4wt and corresponding mutants; Table S3: Open reading frame of cdHDAC4wt in pET14b for recombinant protein expression; Table S4: Mutant to cdHDAC4wt (WT) IC<sub>50</sub> ratios.

**Author Contributions:** Conceptualization, F.-J.M.-A.; methodology, M.S., N.J., N.U., K.T., E.W. (Ewelina Wozny), S.B., E.W. (Eva Wurster) and M.M.; biophysical studies, M.S., N.J., E.W. (Ewelina Wozny), S.B., E.W. (Ewelina Wozny) and M.M.; data analysis, M.S., N.J. and F.-J.M.-A.; biochemical and biomolecular investigations, M.S., N.J., E.W. (Ewelina Wozny), S.B., E.W. (Ewelina Wozny), M.M.; chemical synthesis and analysis, N.U. and K.T.; writing, M.S., N.J., F.-J.M.-A. and R.C.S.; review and editing, F.-J.M.-A. and R.C.S.; supervision, F.-J.M.-A. and R.C.S.; project administration, F.-J.M.-A. and R.C.S.; funding acquisition, F.-J.M.-A. and R.C.S. All authors have read and agreed to the published version of the manuscript.

**Funding:** This study was funded by the LOEWE priority program TRABITA, State of Hessen, Germany (to FJ), "Indo-ASEAN Collaborative Research Project Grant" from ASEAN-India S&T Development Fund (AISTDF), Department of Science and Technology (DST), Government of India, Project Reference Number IMRC/AISTDF/CRD/2018/000001 (to CSR), and "Indo-Poland Joint Research Program" from the Department of Science and Technology (DST), Government of India. Project Reference Number DST/INT/Pol/P-27/2016 (to CSR). The publication was funded by the Open Access fund for publication of the University of Applied Sciences in Darmstadt.

**Institutional Review Board Statement:** Not applicable.

**Informed Consent Statement:** Not applicable.

**Data Availability Statement:** Data is contained within the article and Supplementary Material.

**Acknowledgments:** This study was supported by the LOEWE priority program TRABITA, State of Hessen, Germany (to FJ), "Indo-ASEAN Collaborative Research Project Grant" from ASEAN-India S&T Development Fund (AISTDF), Department of Science and Technology (DST), Government of India, Project Reference Number IMRC/AISTDF/CRD/2018/000001 (to CSR), and "Indo-Poland Joint Research Program" from the Department of Science and Technology (DST), Government of India. Project Reference Number DST/INT/Pol/P-27/2016 (to CSR). The publication was funded by the Open Access fund for publication of the University of Applied Sciences in Darmstadt.

**Conflicts of Interest:** The authors declare no conflict of interest.

## Abbreviations

AMC	7-amino-4-methylcoumarin
Boc	butoxycarbonyl
Cd	catalytic domain
HDAC4	human histone deacetylase 4
IC <sub>50</sub>	inhibitor concentration at 50% residual enzyme activity
Lys	lysine
NCoR	nuclear receptor co-repressor
RMSD	root mean square deviation

SAHA	suberoylanilide hydroxamic acid
SMRT	silencing mediator for retinoid or thyroid-hormone receptor
sZBD	structural zinc binding domain
TFA	trifluoroacetyl
TZD	1,3-thiazolidine-2,4-dione
Wt	wild type
ZBG	zinc binding group

## References

- Witt, O.; Deubzer, H.E.; Milde, T.; Oehme, I. HDAC family: What are the cancer relevant targets? *Cancer Lett.* **2009**, *277*, 8–21. [[CrossRef](#)] [[PubMed](#)]
- Wang, Z.; Qin, G.; Zhao, T.C. HDAC4: Mechanism of regulation and biological functions. *Epigenomics* **2014**, *6*, 139–150. [[CrossRef](#)] [[PubMed](#)]
- Bottomley, M.J.; Lo Surdo, P.; Di Giovine, P.; Cirillo, A.; Scarpelli, R.; Ferrigno, F.; Jones, P.; Neddermann, P.; de Francesco, R.; Steinkühler, C.; et al. Structural and functional analysis of the human HDAC4 catalytic domain reveals a regulatory structural zinc-binding domain. *J. Biol. Chem.* **2008**, *283*, 26694–26704. [[CrossRef](#)]
- Bürli, R.W.; Luckhurst, C.A.; Aziz, O.; Matthews, K.L.; Yates, D.; Lyons, K.A.; Beconi, M.; McAllister, G.; Breccia, P.; Stott, A.J.; et al. Design, synthesis, and biological evaluation of potent and selective class IIa histone deacetylase (HDAC) inhibitors as a potential therapy for Huntington's disease. *J. Med. Chem.* **2013**, *56*, 9934–9954. [[CrossRef](#)]
- Fischle, W.; Kiermer, V.; Dequiedt, F.; Verdin, E. The emerging role of class II histone deacetylases. *Biochem. Cell Biol.* **2001**, *79*, 337–348. [[CrossRef](#)]
- Park, S.-Y.; Kim, G.S.; Hwang, H.-J.; Nam, T.-H.; Park, H.-S.; Song, J.; Jang, T.-H.; Lee, Y.C.; Kim, J.-S. Structural basis of the specific interaction of SMRT corepressor with histone deacetylase 4. *Nucleic Acids Res.* **2018**, *46*, 11776–11788. [[CrossRef](#)]
- Wang, X.; Liu, J.; Zhen, J.; Zhang, C.; Wan, Q.; Liu, G.; Wei, X.; Zhang, Y.; Wang, Z.; Han, H.; et al. Histone deacetylase 4 selectively contributes to podocyte injury in diabetic nephropathy. *Kidney Int.* **2014**, *86*, 712–725. [[CrossRef](#)]
- Mielcarek, M.; Zielonka, D.; Carnemolla, A.; Marcinkowski, J.T.; Guidez, F. HDAC4 as a potential therapeutic target in neurodegenerative diseases: A summary of recent achievements. *Front. Cell. Neurosci.* **2015**, *9*, 42. [[CrossRef](#)]
- Clocchiatti, A.; Florean, C.; Brancolini, C. Class IIa HDACs: From important roles in differentiation to possible implications in tumorigenesis. *J. Cell. Mol. Med.* **2011**, *15*, 1833–1846. [[CrossRef](#)]
- Mielcarek, M.; Landles, C.; Weiss, A.; Bradaia, A.; Seredenina, T.; Inuabasi, L.; Osborne, G.F.; Wadel, K.; Touller, C.; Butler, R.; et al. HDAC4 reduction: A novel therapeutic strategy to target cytoplasmic huntingtin and ameliorate neurodegeneration. *PLoS Biol.* **2013**, *11*, e1001717. [[CrossRef](#)] [[PubMed](#)]
- Federspiel, J.D.; Greco, T.M.; Lum, K.K.; Cristea, I.M. Hdac4 Interactions in Huntington's Disease Viewed Through the Prism of Multiomics. *Mol. Cell. Proteom.* **2019**, *18*, S92–S113. [[CrossRef](#)] [[PubMed](#)]
- Duvic, M.; Talpur, R.; Ni, X.; Zhang, C.; Hazarika, P.; Kelly, C.; Chiao, J.H.; Reilly, J.F.; Ricker, J.L.; Richon, V.M.; et al. Phase 2 trial of oral vorinostat (suberoylanilide hydroxamic acid, SAHA) for refractory cutaneous T-cell lymphoma (CTCL). *Blood* **2007**, *109*, 31–39. [[CrossRef](#)] [[PubMed](#)]
- Ropero, S.; Esteller, M. The role of histone deacetylases (HDACs) in human cancer. *Mol. Oncol.* **2007**, *1*, 19–25. [[CrossRef](#)] [[PubMed](#)]
- Eckschlager, T.; Plch, J.; Stiborova, M.; Hrabeta, J. Histone Deacetylase Inhibitors as Anticancer Drugs. *Int. J. Mol. Sci.* **2017**, *18*, 1414. [[CrossRef](#)] [[PubMed](#)]
- Shen, S.; Kozikowski, A.P. Why Hydroxamates May Not Be the Best Histone Deacetylase Inhibitors—What Some May Have Forgotten or Would Rather Forget? *ChemMedChem* **2016**, *11*, 15–21. [[CrossRef](#)] [[PubMed](#)]
- Lehmann, J.M.; Moore, L.B.; Smith-Oliver, T.A.; Wilkison, W.O.; Willson, T.M.; Kliewer, S.A. An antidiabetic thiazolidinedione is a high affinity ligand for peroxisome proliferator-activated receptor gamma (PPAR gamma). *J. Biol. Chem.* **1995**, *270*, 12953–12956. [[CrossRef](#)]
- Lalloyer, F.; Staels, B. Fibrates, glitazones, and peroxisome proliferator-activated receptors. *Arterioscler. Thromb. Vasc. Biol.* **2010**, *30*, 894–899. [[CrossRef](#)]
- Tilekar, K.; Hess, J.D.; Upadhyay, N.; Lo Bianco, A.; Schweipert, M.; Laghezza, A.; Loiodice, F.; Meyer-Almes, F.-J.; Aguilera, R.J.; Lavecchia, A.; et al. Thiazolidinedione “Magic Bullets” Simultaneously Targeting PPAR $\gamma$  and HDACs: Design, Synthesis, and Investigations of their In Vitro and In Vivo Antitumor Effects. *J. Med. Chem.* **2021**, *64*, 6949–6971. [[CrossRef](#)]
- Tilekar, K.; Hess, J.D.; Schweipert, M.; Flath, F.; Gutierrez, D.A.; Loiodice, F.; Lavecchia, A.; Meyer-Almes, F.-J.; Aguilera, R.J.; Ramaa, C.S. HDAC4 Inhibitors with Cyclic Linker and Non-hydroxamate Zinc Binding Group: Design, Synthesis, HDAC Screening and in vitro Cytotoxicity evaluation. *Chem. Sel.* **2021**, *6*, 6748–6763. [[CrossRef](#)]
- Chen, C.-S.; Wang, D.; Kulp, S.K. Glucose Transporter Inhibitors. U.S. Patent US9174951B2, 28 March 2013.
- Meng, Y.; Xu, X.; Luan, H.; Li, L.; Dai, W.; Li, Z.; Bian, J. The progress and development of GLUT1 inhibitors targeting cancer energy metabolism. *Future Med. Chem.* **2019**, *11*, 2333–2352. [[CrossRef](#)]
- Michaelis, L.; Menten, M. Die kinetik der invertinwirkung. *Biochem. Z.* **1913**, *49*, 352.

23. Patil, V.; Tilekar, K.; Mehendale-Munj, S.; Mohan, R.; Ramaa, C.S. Synthesis and primary cytotoxicity evaluation of new 5-benzylidene-2,4-thiazolidinedione derivatives. *Eur. J. Med. Chem.* **2010**, *45*, 4539–4544. [[CrossRef](#)] [[PubMed](#)]
24. Kabir, A.; Tilekar, K.; Upadhyay, N.; Ramaa, C.S. Novel Anthraquinone Derivatives as Dual Inhibitors of Topoisomerase 2 and Casein Kinase 2: In Silico Studies, Synthesis and Biological Evaluation on Leukemic Cell Lines. *Anticancer. Agents Med. Chem.* **2018**, *18*, 1551–1562. [[CrossRef](#)] [[PubMed](#)]
25. Tilekar, K.; Upadhyay, N.; Jänsch, N.; Schweipert, M.; Mrowka, P.; Meyer-Almes, F.J.; Ramaa, C.S. Discovery of 5-naphthylidene-2,4-thiazolidinedione derivatives as selective HDAC8 inhibitors and evaluation of their cytotoxic effects in leukemic cell lines. *Bioorg. Chem.* **2020**, *95*, 103522. [[CrossRef](#)] [[PubMed](#)]
26. Swinney, D.C. The role of binding kinetics in therapeutically useful drug action. *Curr. Opin. Drug Discov. Dev.* **2009**, *12*, 31–39.
27. Copeland, R.A. *Evaluation of Enzyme Inhibitors in Drug Discovery: A Guide for Medicinal Chemists and Pharmacologists*; John Wiley & Sons: Hoboken, NJ, USA, 2005; ISBN 978-1-118-48813-3.
28. Yung-Chi, C.; Prusoff, W.H. Relationship between the inhibition constant (KI) and the concentration of inhibitor which causes 50 per cent inhibition (I50) of an enzymatic reaction. *Biochem. Pharmacol.* **1973**, *22*, 3099–3108. [[CrossRef](#)]
29. Luckhurst, C.A.; Breccia, P.; Stott, A.J.; Aziz, O.; Birch, H.L.; Bürli, R.W.; Hughes, S.J.; Jarvis, R.E.; Lamers, M.; Leonard, P.M.; et al. Potent, Selective, and CNS-Penetrant Tetrasubstituted Cyclopropane Class IIa Histone Deacetylase (HDAC) Inhibitors. *ACS Med. Chem. Lett.* **2016**, *7*, 34–39. [[CrossRef](#)]
30. Higuchi, R.; Krummel, B.; Saiki, R.K. A general method of in vitro preparation and specific mutagenesis of DNA fragments: Study of protein and DNA interactions. *Nucleic Acids Res.* **1988**, *16*, 7351–7367. [[CrossRef](#)]
31. Wegener, D.; Wirsching, F.; Riestler, D.; Schwienhorst, A. A Fluorogenic Histone Deacetylase Assay Well Suited for High-Throughput Activity Screening. *Chem. Biol.* **2003**, *10*, 61–68. [[CrossRef](#)]
32. Atkins, P.W.; de Paula, J. *Physikalische Chemie, 5. Auflage*; Wiley-VCH: Weinheim, Germany, 2013; ISBN 978-3-527-33247-2.
33. Vølund, A. Application of the four-parameter logistic model to bioassay: Comparison with slope ratio and parallel line models. *Biometrics* **1978**, *34*, 357–365. [[CrossRef](#)]
34. Tian, W.; Chen, C.; Lei, X.; Zhao, J.; Liang, J. CASTp 3.0: Computed atlas of surface topography of proteins. *Nucleic Acids Res.* **2018**, *46*, W363–W367. [[CrossRef](#)] [[PubMed](#)]

---

**Titel:**

Kinetically selective and potent inhibitors of HDAC8

**Autoren:**

Markus Schweipert, Niklas Jänsch, Wisely Oki Sugiarto and Franz-Josef Meyer-Almes

**Bibliographische Daten:**

Biological Chemistry (doi.org/10.1515/hsz-2018-0363)

**Zusammenfassung:**

HDAC8 ist ein etabliertes und validiertes Zielmolekül für T-Zell-Lymphome und kindliche Neuroblastome. Die Bindungstasche im aktiven Zentrum von HDAC8 ist bei allen zinkhaltigen Vertretern der Histon-Deacetylase-Familie stark konserviert. Dies erklärt, dass die meisten HDACs von ähnlichen Inhibitoren mit einer zinkbindenden Gruppe (ZBG), einem hydrophoben Linker und einer Kopfgruppe unselektiv erkannt werden. Angesichts dieser Schwierigkeit ist die Schaffung einer Isoenzym-Selektivität eine der größten Herausforderungen bei der Entwicklung von HDAC-Inhibitoren. In einer Reihe von Trifluormethylketon-Inhibitoren von HDAC8 zeigt Verbindung 10 einen auffälligen Bindungsmechanismus und eine dramatisch verlängerte Verweilzeit, was zu einer kinetischen Selektivität gegenüber HDAC4 führt. Die Kombination der Ergebnisse der Bindungskinetik mit computergestütztem Docking und der Analyse der Flexibilität der Bindungsstelle legt nahe, dass 10 die konservierte katalytische Stelle sowie eine angrenzende transiente Subtasche von HDAC8 besetzt.



# Biological Chemistry ‘Just Accepted’ Papers

**Biological Chemistry ‘Just Accepted’ Papers** are papers published online, in advance of appearing in the print journal. They have been peer-reviewed, accepted and are online published in manuscript form, but have not been copy edited, typeset, or proofread. Copy editing may lead to small differences between the Just Accepted version and the final version. There may also be differences in the quality of the graphics. When papers do appear in print, they will be removed from this feature and grouped with other papers in an issue.

**Biol Chem ‘Just Accepted’ Papers** are citable; the online publication date is indicated on the Table of Contents page, and the article’s Digital Object Identifier (DOI), a unique identifier for intellectual property in the digital environment (e.g., 10.1515/hsz-2011-xxxx), is shown at the top margin of the title page. Once an article is published as **Biol Chem ‘Just Accepted’ Paper** (and before it is published in its final form), it should be cited in other articles by indicating author list, title and DOI.

After a paper is published in **Biol Chem ‘Just Accepted’ Paper** form, it proceeds through the normal production process, which includes copy editing, typesetting and proofreading. The edited paper is then published in its final form in a regular print and online issue of **Biol Chem**. At this time, the **Biol Chem ‘Just Accepted’ Paper** version is replaced on the journal Web site by the final version of the paper with the same DOI as the **Biol Chem ‘Just Accepted’ Paper version**.

## Disclaimer

**Biol Chem ‘Just Accepted’ Papers** have undergone the complete peer-review process. However, none of the additional editorial preparation, which includes copy editing, typesetting and proofreading, has been performed. Therefore, there may be errors in articles published as **Biol Chem ‘Just Accepted’ Papers** that will be corrected in the final print and online version of the Journal. Any use of these articles is subject to the explicit understanding that the papers have not yet gone through the full quality control process prior to advanced publication.

**Research Article**

**Kinetically selective and potent inhibitors of HDAC8**

Markus Schweipert<sup>1</sup>, Niklas Jänsch<sup>1</sup>, Wisely Oki Sugiarto<sup>1</sup> and Franz-Josef Meyer-Almes<sup>1,\*</sup>

<sup>1</sup>Department of Chemical Engineering and Biotechnology, University of Applied Sciences  
Darmstadt, 64295 Darmstadt, Germany

\*Corresponding author

e-mail: [franz-josef.meyer-almes@h-da.de](mailto:franz-josef.meyer-almes@h-da.de)

### Abstract

HDAC8 is an established and validated target for T-cell lymphoma and childhood neuroblastoma. The active site binding pocket of HDAC8 is highly conserved among all zinc-containing representatives of the histone deacetylase family. This explains that most HDACs are unselectively recognized by similar inhibitors featuring a zinc binding group (ZBG), a hydrophobic linker and a head group. In the light of this difficulty, the creation of isoenzyme-selectivity is one of the major challenges in the development of HDAC inhibitors. In a series of trifluoromethylketone inhibitors of HDAC8 compound **10** shows a distinct binding mechanism and a dramatically increased residence time providing kinetic selectivity against HDAC4. Combining the binding kinetics results with computational docking and binding site flexibility analysis suggests that **10** occupies the conserved catalytic site as well as an adjacent transient sub-pocket of HDAC8.

**Keywords:** histone deacetylase; residence time; transient binding pocket.

## Introduction

HDAC8 is an actual and established prominent target in the indication area cancer, T-cell lymphoma and particularly neuroblastoma. HDAC8 is overexpressed in urothelial and breast cancer (Niegisch *et al.*, 2013, Park *et al.*, 2011). Moreover the level of HDAC8 is significantly increased in advanced tumor stages of neuroblastoma and could therefore be used as an additional marker for poor prognosis (Oehme *et al.*, 2009). The active site binding pocket of HDAC8 with the catalytic zinc ion in its lower section is highly conserved among the representatives of the histone deacetylase family which explains that most HDACs are recognized by similar ligands featuring a zinc binding group (ZBG), a hydrophobic linker and a head group that can interact with the outer rim of the binding pocket. Examples for these unselective inhibitors are vorinostat (Mann *et al.*, 2007), belinostat (Lee *et al.*, 2015) and panobinostat (Fenichel, 2015) which were approved by the FDA for the treatment of cutaneous T-cell lymphoma or multiple myeloma. Meanwhile, several crystal structures of HDAC8/ligand complexes give detailed insight into isoenzyme specific features enabling the design of more selective inhibitors. One of these characteristics is the transiently formed foot pocket that is observed in class I HDACs only (Finnin *et al.*, 1999). The extraordinary flexibility of active site loops is a specific feature of HDAC8. Different ligands induce alternative conformational changes in the L1- and L2-loop flanking the active site (Decroos *et al.*, 2015, Somoza *et al.*, 2004). The active site binding pocket of HDAC8 in complexes with inhibitors can change from a narrow channel (PDB-ID 1T69) to a sub-open conformation with a second transient pocket adjacent to the active site (PDB-ID 1T64) to a structure with a wide-open single pocket (PDB-ID 1VKG). The L1- and L2-loops of HDAC8 are mainly involved in these conformational changes. Furthermore, a molecular dynamics study suggests that the interaction and dynamics between these loops tunes the configuration of functionally important residues and thus the enzyme activity of HDAC8 (Kunze *et al.*, 2013). A variety of HDAC8 inhibitors has already been synthesized and some of them have been claimed to be more or less selective usually on the base of equilibrium  $IC_{50}$ -values (Scheme 1, Tab. 1).

Most described isoenzyme selective HDAC8 inhibitors contain a hydroxamate group as ZBG or are derivatives of amino acids. Recently, our group discovered a new non-hydroxamate class of compounds, pyrimido[1,2-c][1,3]benzothiazin-6-imines, as potent and selective HDAC8 inhibitors (Kleinschek *et al.*, 2016).  $IC_{50}$ -values or better equilibrium dissociation constants are often used as parameter of choice to optimize the potency of compounds.

However, it is well recognized that the interaction between inhibitor and target protein is by far not governed by equilibrium conditions but rather by pharmacokinetics and pharmacodynamics which are linked by binding kinetics and the underlying mechanism of interaction which may also include, for example, conformational changes, multimerization, protein-protein interaction with regulators. It is generally believed, that long residence times (RT) of a drug molecule on its target are particularly beneficial in the context of cancer or infectious diseases and correlate with *in vivo* drug efficacy in these indication areas (Copeland *et al.*, 2006, Tummino and Copeland, 2008, Lu and Tonge, 2010). This is for example reflected in the development of protein kinase inhibitors with extraordinary long residence times up to many hours (Wentsch *et al.*, 2017) or in the increasing number of covalent inhibitors with ultimate RT (Bradshaw *et al.*, 2015, Singh *et al.*, 2011). Very few rare examples of kinetically selective HDAC inhibitors were described (Wagner *et al.*, 2015). They showed that two compounds were kinetically selective for HDAC2 vs. HDAC1, although the achieved maximum ratio of RT's was only about 7. In a previous mechanistic study we demonstrated, that a simple trifluoromethylketone derivative of suberoyl hydroxamic acid (SATFMK) bound to human HDACs via a two-step induced-fit mechanism and showed a strong kinetic preference for HDAC8 vs. HDAC1 and HDAC6 with RT ratios of 30 and 7, respectively. Very recently, we introduced [1,3]dioxolo[4,5-*f*]benzodioxole (DBD) based ligands with trifluoromethylketone (TFMK) war head as fluorescent probe in a competitive binding assay for class IIa HDACs (Meyners *et al.*, 2017). Interestingly, the DBD-ligands turned out to be also inhibitors of HDAC8. However, based on equilibrium IC<sub>50</sub>-values, the compounds appeared to be unselective with respect to class IIa HDACs. Here, we report a comprehensive study to elucidate the binding kinetics and mechanism of DBD-ester ligands with TFMK head group and different alkyl-spacer to HDAC8 (Fig. 1). The deduced binding mechanism and the observed long RT's of the DBD-ligands on HDAC8 are discussed on the basis of accompanying docking results and a computational analysis of the binding site flexibility using TRAPP (Stank *et al.*, 2017). Interestingly, the extraordinary long RT of **10** enables kinetic discrimination against class IIa representative HDAC4. Potential applications as lead compound for kinetically selective HDAC8 inhibitors or as tool compound for intra-cellular localization and mode-of-action studies are suggested.

## Results and discussion

### DBD-ligands are potent inhibitors of HDAC8

The potency of the DBD-ligands **8**, **9** and **10** was determined using a classical enzyme activity assay (Fig. 1). The calculated  $IC_{50}$ -values are summarized and compared with reference compounds in Tab. 1. **10** shows similar potency than one of the best reported selective HDAC8 inhibitors PCI-34051. Compound **10** has a 50-fold higher  $IC_{50}$ -value against HDAC1 ( $1.0 \pm 0.1 \mu\text{M}$ ) within the same HDAC class I and class IIb HDAC6 ( $1.0 \pm 0.1 \mu\text{M}$ ), but is totally unselective against class II HDAC4 (Tab. 1).

The DBD-ligands show beneficial fluorescence with a large stokes-shift (Exc.: 414 nm Em: 518 nm) (Wawrzinek *et al.*, 2013). Moreover, its fluorescence remains essentially unchanged upon binding to HDAC8. Therefore, it is conceivable, to develop a generic fluorescence polarization binding assay for HDAC4 and HDAC8 using DBD-ligands. However, a potential drug candidate should be as selective as possible for one particular HDAC isoenzyme to reduce potential unwanted side effects.

### Dissociation kinetics of DBD-ligands

Two types of DBD-dyes have been developed by Wessig *et al.* : Acyl- and Ester-DBD -dyes (Wawrzinek *et al.*, 2013). The Acyl-DBD-ligands have been used to develop fluorescence lifetime based binding assays for bacterial acetyl polyamine amidohydrolases (Meyners *et al.*, 2014) and class IIa HDACs (Meyners *et al.*, 2017). However, the Acyl-DBD dyes show rather low quantum yields in aqueous solution. In contrast, ester-DBD conjugates show much higher extinction coefficients and quantum yields (Wawrzinek *et al.*, 2013). This predestined the ester-DBD-compounds **8**, **9** and **10** as fluorescent ligands in a fluorescence polarization based assay to measure binding kinetics with high time resolution.

The polarization increases from 50 mP of the free DBD-ligand to about 150 mP upon binding to HDAC8. A titration of 200 nM **10** shows a linear increase of binding degree depending on the concentration of added HDAC8 indicating an equilibrium dissociation constant ( $K_d$ ) much below the ligand concentration of 200 nM in agreement with the previously determined  $IC_{50}$ -value of 20 nM (Fig. S1, Tab. 1). As such, the experiment can be regarded as active site titration. Binding is saturated at about 200 nM HDAC8 indicating stoichiometric 1:1 binding and completely binding active enzyme (Fig. S1). To determine the RT of the DBD-ligands,

they were complexed with HDAC8 and subsequently displaced by the addition of an excess concentration of SATFMK (Fig. 2A). The RT's were calculated from a fit of a one-exponential decay function to the dissociation data and are listed in Tab. 2. The RT's of the DBD-probes depend strongly from the length of the alkyl spacer adjacent to the TFMK war head. The RT's of the shorter DBD-ligands **8** and **9** – ( $1.9 \pm 0.1$ ) and ( $3.3 \pm 0.5$ ) h – are similar whereas there is a large gap between the RT's of the shorter DBD-ligands and that of **10**. The complex between **10** and HDAC8 dissociates to less than 30 % after 15 h giving a conservative estimate of its RT of over 40 h. Most interestingly, the same compound dissociated relatively fast from HDAC4 with a RT of ( $29 \pm 3$ ) min (Fig. 2B) and from HDAC3 with an estimated RT of much less than 30 min (Fig. S5). This means, that compound **10** has essentially no preference for HDAC8 over HDAC4 or HDAC3 in equilibrium, but shows high kinetic selectivity for HDAC8 under non-equilibrium conditions where a continuous flow constantly removes small molecules from the system, e.g. cellular compartment. Dialysis experiments were conducted to confirm the dissociation kinetics of DBD-ligands by an independent method (Fig. 2C). Binding was indirectly determined from the enzyme activity of unbound HDAC8. HDAC8 was mixed with all three DBD-ligands and reference compound SAHA to yield almost complete inhibition of the enzyme. Subsequently, these mixtures were dialyzed for 3 h against a large excess volume of assay buffer. After 3 h dialysis SAHA is completely dissociated in agreement with a previously determined RT of 0.9 min (Meyners *et al.*, 2014). Compound **10** still inhibits HDAC8 after 3 h in accordance with the competitive displacement assay (Fig. 2A). While **9** still inhibits HDAC8 partially, the mixtures of **8** and SAHA with HDAC8 show an increased enzyme activity with respect to free HDAC8 after 3 h dialysis. It has been described, that ligand binding can stabilize proteins and protect them from degradation. This may explain a reproducible apparent increase in HDAC8 activity after several hours of incubation. Therefore, the dialysis experiment can only provide indirect and qualitative information about the underlying dissociation kinetics. However, faster dissociating compounds can clearly be differentiated against compounds with very slow dissociation behavior. The dialysis data essentially confirm the extraordinary long RT of **10** and the shorter RT's of **9** and **8**.

### Association kinetics and binding mechanism

The pronounced gap between the RT's of the shorter DBD-ligands and **10** raised the question whether this would reflect a different binding mechanism. Most widespread protein-ligand

recognition mechanisms comprise simple one-step binding, induced fit (IF) or conformational selection (CS) (Meyer-Almes, 2016, Ma *et al.*, 1999, Koshland Jr, 1958). Both latter binding mechanisms consist of two steps where one step represents physical protein-ligand binding. In case of the IF-model, the binding step is followed by a conformational change of the initially formed complex. In contrast, ligand binding occurs after the conformational conversion of unbound protein according to the CS-mechanism (Fig. 3).

To elucidate the binding mechanism of the DBD-ligands with different spacer lengths, series of association time courses with varying concentrations of HDAC8 were measured for each ligand taking advantage of the change in fluorescence polarization upon complex formation (Fig. 4). The association time courses show essentially mono-exponential behavior and the apparent rate constants increase linearly with increasing concentrations of HDAC8 for all three DBD-ligands (Fig. 4 B/D/E). The overall association kinetics becomes faster from the shorter **8** to **10** with the longest spacer (Fig. 4 A/C/E). For each DBD-ligand, all binding models specified in Fig. 3 were globally fitted to data sets consisting of 4-5 time courses of binding kinetics with different concentrations of HDAC8 (Fig. 4 A/C/E). For DBD-ligands **8** and **9** the global fit analyses applying the more complex IF- and CS-models yielded no improvement in terms of error sums of square compared with the simple one-step-binding model. In addition, the reversed dissociation rate of this mechanism is consistent with the RT's determined from competitive displacement kinetics and dialysis data for **8** and **9**.

Moreover, for these compounds the slope,  $k_{on\_app}$ , of the graphs in Fig. 4B and 4D is in agreement with the corresponding  $k_1$ -values from the global fit analysis considering a somewhat underestimated error of fit parameters (Tab.2, Tab. S1). Thus all orthogonal experimental data is consistent with a one-step-binding mechanism for the shorter DBD-ligands **8** and **9**. In contrast, fitting the CS-model to the family of binding time courses for **10** yields a significantly lower error sum of square compared with both, a one-step- and an IF-model. A statistical analysis according to Akaike's information criterion and F test clearly favors the CS-model (Akaike, 1974) (Tab. S2). Both, the association and the dissociation rate calculated for a one-step-mechanism, are clearly inconsistent with  $k_{on\_app}$  and experimentally determined RT's (Tab.2). Although, the dissociation rate,  $k_{-1}$ , fitted using the CS-model is associated with very high error, the corresponding RT can be roughly estimated from the reversed rate constant to be >40 h and in agreement with RT's determined from competitive displacement and dialysis experiments (Tab. 2). Taken together, binding of **8** and **9** can be described by a simple one-step model and shows medium RT's (1.9 and 3.3 h), while physical



binding of **10** takes place after conformational changes of HDAC8 and is associated with dramatically increased RT of >40 h.

### **Thermal stabilization of HDAC8 by ligand binding**

Thermal shift assays have emerged as a simple and reliable method to demonstrate label-free binding of a small-molecule ligand or inhibitor to its target protein. The method is robust against optical artifacts and also enables the demonstration of intra-cellular target engagement. PCI-34051 causes the largest thermal shift ( $\Delta T = 4\text{ }^{\circ}\text{C}$ ) of established HDAC8 reference inhibitors (Fig. 5A). In comparison, all three DBD-probes cause significantly bigger thermal shifts. **8** and **9** increase the thermal stability of HDAC8 by about  $6\text{ }^{\circ}\text{C}$ . In striking contrast to all other inhibitors, DBD-probe **10** shows an unprecedented large stabilizing effect on HDAC8 by about  $12\text{ }^{\circ}\text{C}$  (Fig. 5C). This correlates with the lowest concentration required to occupy 50% of HDAC8,  $OC_{50}$ , of all tested inhibitors (Fig. 5D). Moreover, the  $OC_{50}$ -values of **8** and **9** are comparable to each other but considerably greater than that of **10** similar to the corresponding  $IC_{50}$ -values of these inhibitors (Fig. 1 and 5D). The thermal shift data are in agreement with all collected  $IC_{50}$ -data, residence times and the observed switch of the binding mechanism when going from the shorter DBD-probes **8** and **9** to the longer analog **10**. Together, all results indicate a clear break in the mode of action between HDAC8 and inhibitors **8**, **9** with medium activity on the one side and the extraordinarily potent **10** on the other side.

### **Docking study suggests occupation of allosteric binding site by 10**

To elucidate the potential binding modes of the DBD-probes, several docking experiments were performed using crystal structures of the closed (PDB-ID: 1T69), sub-open (PDB-ID: 1T64) and wide-open (PDB-ID: 1VKG). The sub-open structure of HDAC8 shows a second allosteric pocket next to the classical binding site with a zinc ion at the bottom. Both pockets are filled with trichostatin A (TSA) in different orientations. The zinc-chelating hydroxamate group in TSA chelates the catalytic zinc-ion at the bottom of the classical binding pocket, but points outward, when bound in the allosteric pocket. Interestingly, the best docking score (GBVI/WSA  $dG = -25$ ) is found for the sub-open conformation, where **10** chelates the catalytic zinc ion in the active site binding pocket via the geminal diol of the hydrated trifluoromethylketone group and the prolonged linker enables the simultaneous occupation of the adjacent allosteric pockets (Fig. S2, Table S3). The binding is stabilized by additional 3

hydrogen bonds to Y100 and K33 and several hydrophobic alkyl- $\pi$  and alkyl-alkyl interactions with Y100, F152, Y306, W141, I34 and P35 in the allosteric pocket (see Fig. 6). These additional interactions are in agreement with the observed significantly enhanced binding affinity, thermal stabilization and enzyme occupancy compared to the shorter analogs **8** and **9** (Tab. 1, Fig. S2).

In addition, the observed dissociation rate is dramatically reduced for **10**. The inverse dissociation rate, also called residence time (RT), of **10** is estimated to be > 25 h, while the derivatives with shorter linker, **9** and **8**, have RT's of only 1.9 and 3.3 h, respectively (Tab. 2).

Combining the dramatic increase in RT and thermal stability of HDAC8 as well as the change in binding mechanism from **8** and **9** to **10** with the docking result, we hypothesize that there is an equilibrium of several meta-stable HDAC8 conformers and **10**, in contrast to **8** and **9**, recognizes and selects mainly the sub-open HDAC8 conformation with both pockets, catalytic and allosteric, open.

### **Analysis of binding site flexibility**

The global fit analysis yielded only an inaccurate but very low dissociation rate of the complex:  $k_{-1} = (0.01 \pm 0.11) \cdot 10^{-4} \text{ s}^{-1}$ . Fitting more complex binding models with additional steps to the data provides no more insight, because the determined kinetic rate constants become more inaccurate with increasing number of fit parameters. However, it seems likely and is consistent with the data, that the initial protein-ligand complex undergoes further conformational adaptation and stabilization due to the known extraordinary malleability of the binding site of HDAC8 (Decroos *et al.*, 2015, Somoza *et al.*, 2004, Deschamps *et al.*, 2015). Consequently, the dynamics of conformational changes within HDAC8 would enable additional contacts to the ligand in an energetically favored state and contribute to the extraordinary retarded dissociation of **10**. At least one of the conformational transitions from the final complex structure to free protein is presumed to be associated with a very high activation barrier. To get more insight into the dynamic processes of HDAC8 during ligand binding, the flexibility of its binding pockets was investigated further by using TRAPP, a tool for the analysis of binding site flexibility and transient binding pockets (Stank *et al.*, 2017). The analysis provides evidence for 5 regions of enhanced flexibility around both binding pockets in HDAC8 (PDB-ID: 1T64) (Fig. S A-C). The predicted increased flexibility of loop 1 (aa 29-36) and loop 2 (aa 99-103) at the upper rim of the binding pocket agrees well with

elevated B-factors in the crystal structure (Fig. S3D). These loops have already been identified before as a major factor responsible for the malleability at the entrance of the binding pocket (Somoza *et al.*, 2004, Dowling *et al.*, 2008). Similarly, the predicted flexibility of F152 in loop 3, which is involved in the inter-conversion between wide-open, sub-open or closed states of HDAC8, correlates with higher B-factors. In summary, the computational analysis of binding site flexibility in solution shows a high level of consistency with X-ray crystallography and provides structural details about 5 regions of elevated malleability surrounding the active site pocket and the adjacent transient sub-pocket (Fig. S3 D/F). These findings support the hypothesis that the high potency of **10** along with its ultra-long RT is enhanced by conformational adaptation of the initial complex between **10** and the sub-open state of HDAC8.

## Conclusions

The creation of isoenzyme-selectivity is one of the major challenges in the development of HDAC inhibitors. DBD-ligands with TFMK war head were originally developed as fluorescent tracer for a fluorescence lifetime-based generic binding assay for class IIa-HDACs that works also with HDAC8. A comprehensive analysis of the binding kinetics and mechanism of DBD-ligands with different spacer lengths to HDAC8 reveals a sharp change of the residence time and the binding mechanism from a one-step model for compounds **8/9** to a CS-model for **10**. Although apparently unselective regarding equilibrium IC<sub>50</sub>-values, **10** shows pronounced kinetic selectivity for HDAC8 against HDAC4. Combining the binding kinetics results with computational docking and binding site flexibility analysis, the most likely binding mechanism of **10** consists of conformational selection of the HDAC8 variant with open transient sub-pocket next to the catalytic site followed by conformational adaptation of the initial complex to enhance residence time as well as potency. The high potency of **10** combined with kinetic selectivity and conformational selection of a particular conformation of HDAC8 makes **10** an interesting tool for selective non-covalent fluorescence-labeling of HDAC8 and suggests the prolonged structure of **10** as promising chemical starting point for the development of selective HDAC8 inhibitors with beneficial features.

## Materials and methods

### *HDAC8 expression and purification*

HDAC8 was produced as described recently (Jänsch *et al.*, 2019). In short, HDAC8 was produced in *E. coli* (BL21) DE3 pLysS cells using a pET14b vector containing codon-optimized human HDAC8 that is fused to a His6 SUMO-tag. Purification included IMAC chromatography, cleavage of the SUMO-tag, anion-exchange chromatography and a final gel permeation chromatography step. Typically 3-5 mg HDAC8 were obtained from 1 L culture.

### *Fluorescence polarization based displacement kinetics*

200 nM of DBD probe and 300 nM HDAC8 were incubated in assay buffer (25 mM Tris-HCl, pH 8.0, 75 mM KCl, 0.001 % Pluronic F-127) and measured in black 96-well microtiter plate (Greiner) for 60 min at 30 °C to allow for complete binding equilibrium. Subsequently the displacement kinetics were initiated by the addition of a high excess of SATFMK (15 μM), the DBD ligands were displaced and the dissociation kinetics were measured in a microplate reader at  $\lambda_{\text{Ex}} = 420$  nm (parallel polarized) and two distinguished emissions at  $\lambda_{\text{Em}} = 520$  nm (parallel and perpendicular polarized) exploiting the decreasing fluorescence polarization of the system. The dissociation curves were generated by using GraphPad Prism and fitted to the following one-exponential decay function to obtain the dissociation constant  $k_{\text{off}}$ :

$$P = P_0 \exp(-k_{\text{off}} t) + p$$

in which  $P$  is the fluorescence polarization,  $P_0$  is the fluorescence polarization before the addition of 15 μM SATFMK,  $p$  is the lower plateau,  $k$  and  $t$  are the dissociation constant and the time, respectively. The reciprocal value of the dissociation constant is the residence time (RT) of the respective DBD probe.

$$RT = \frac{1}{k_{\text{off}}}$$

### *Global fit analysis of binding mechanism*

The global fit of the association data was performed using the program Copasi 4.20, which can be obtained at the following URL: <http://ww.copasi.org> (Hoops *et al.*, 2006). The total

ligand concentration was chosen to be 200 nM and the starting concentration of HDAC8 was varied as indicated. Reaction kinetics with different parameter combinations were fitted to one-step binding, IF- and CS-models. Complete data sets including time courses with different HDAC8 concentrations were analyzed over the entire time range by applying a global fit analysis to the respective binding models. The Copasi function “Parameter Estimation” was used, in which a random number generator is used to obtain promising start values. The start values were the starting point for further fit optimization by minimizing its total error as well as the error of each parameter. Two algorithms, “Evolutionary Programming” and “Levenberg-Marquardt” were applied consecutively using the following parameter setup: Number of Generations = 200, Population = 20, Random Generator = 1, Seed = 0 and Max. Iterations = 2000, Tolerance =  $10^{-6}$ . The global fit procedure yielded rate constants that were optimized to explain the complete data set, rather than single time courses, thereby dramatically increasing the diagnostic power of the method.

### ***HDAC enzyme activity assay***

A serial dilution of DBD probe or inhibitor in assay buffer (25 mM Tris-HCl, pH 8.0, 75 mM KCl, 0.001 % Pluronic F-127) was incubated with 10 nM HDAC8 in a black 96-well microtiter plate (Greiner) for 60 min at 30 °C. Afterwards the reaction was initiated by the addition of 20 μM Boc-Lys(trifluoroacetyl)-AMC as substrate. After incubation for 60 min at 30 °C, the reaction was stopped by the addition of 1.7 μM SATFMK and the deacetylated substrate was converted into a fluorescent product by the addition of 0.4 mg/ml trypsin. The release of AMC was followed in a microplate reader at 450 nm ( $\lambda_{\text{Ex}} = 350 \text{ nm}$ ) and correlated to enzyme activity. Dose-response curves were generated by using GraphPad Prism and fitted to a four parameters logistic function to obtain  $IC_{50}$  values (Volund, 1978):

$$EA = E_0 + \frac{(E_{\text{max}} - E_0)}{1 + 10^{(\log(E_{50}) - x) \cdot h}}$$

in which  $EA$  is the enzyme activity at a given inhibitor concentration  $x$ ,  $E_{\text{max}}$  and  $E_0$  are the enzyme activities determined at zero and complete inhibition, respectively.  $IC_{50}$  denotes the inhibitor concentration at which half the enzyme is inhibited and  $h$  is the slope of the curve.

***Thermal shift assay:***

For the determination of inhibitor induced increase of protein stability 3  $\mu\text{M}$  HDAC8 was incubated with 100  $\mu\text{M}$  of the respective inhibitor for 1 h at 30 °C in assay buffer following a protocol with stepwise increase in temperature (always 2 °C) from 42 °C to 58 °C and 10 min incubation period at each temperature level. For compound **10** the temperature gradient was set from 52 °C to 68 °C. Every 2 °C an aliquot was removed and stored on ice. After protein denaturation the samples were centrifuged for 15 min at 18000 g and 4 °C. The supernatant was subjected to SDS-PAGE. Band densities were analyzed by image studio lite software from LiCor and plotted against the temperature. Melting points were determined using four parameter logistic fit. For the determination of the protein occupancy a serial twofold dilution of the indicated inhibitor was incubated with 3  $\mu\text{M}$  HDAC8 in assay buffer for 1 h at 30 °C following the same temperature protocol as in the prior experiment. All aliquots were removed at 50 °C for all inhibitors except for **10** where the samples were removed at 54 °C. Following heat denaturation, these samples were processed as described above and relative band densities were plotted against the logarithmic inhibitor concentration. The concentration required to occupy 50% of the enzyme ( $\text{OC}_{50}$ ) was determined by four parameter logistic fit.

***Docking:***

Crystal structures were prepared for docking using MOE 2016 from Chemical Computing Group (Montreal, Canada). These steps included correction of missing atoms, missing residues and 3D protonation and calculation of partial charges using the Amber12:EHT force field. The ligands were prepared as hydrated ketones using the Builder functionality in MOE 2016 and hydrogen atoms were adjusted leaving the two hydrate oxygens deprotonated. Then charges were calculated and the molecule energy minimized using the Amber12:EHT force field. After molecule preparation, the induced fit docking protocol was applied using placement by the triangle matcher, London dG as primary scoring function and the forcefield-based scoring function GBVI/WSA dG for rescoring and refinement (Wright *et al.*, 2013, Corbeil *et al.*, 2012). The MOE default scoring function, London dG, estimates the free Gibbs energy of binding from a given pose and is composed of an averaged entropy term, an energy term due to the loss of flexibility of the ligand, hydrogen bond energy, metal ligation energy and desolvation energy. The GBVI/WSA dG scoring function is more accurate and estimates the free Gibbs energy of binding on the basis of MMFF94x and AMBER99 forcefields. The function contains terms for average gain/loss of entropy, coulomb electrostatics, solvation

electrostatics calculated using the GB/VI solvation model, van-der-Waals contribution, and exposed surface area. The obtained binding poses were ranked according to the GBVI/WSA dG score.

### ***Flexibility analysis of binding pockets:***

The flexibility of the HDAC8 binding site was analyzed using the TRAnsient Pockets in Proteins (TRAPP) webserver located at the Institute for Theoretical Studies (HITS) in Heidelberg, Germany (Stank *et al.*, 2017). Ensembles of protein structures were generated starting from crystal structures by applying three different methods: tCONCOORD, L-RIP and RIPlig (Seeliger *et al.*, 2007, Kokh *et al.*, 2016).

## References

- Akaike, H. (1974). A New Look at the Statistical Model Identification. *IEEE Transactions on Automatic Control* *19*, 716-723.
- Balasubramanian, S., Ramos, J., Luo, W., Sirisawad, M., Verner, E. and Buggy, J. J. (2008). A novel histone deacetylase 8 (HDAC8)-specific inhibitor PCI-34051 induces apoptosis in T-cell lymphomas. *Leukemia* *22*, 1026 – 1034.
- Bradshaw, J. M., McFarland, J. M., Paavilainen, V. O., Bisconte, A., Tam, D., Phan, V. T., Romanov, S., Finkle, D., Shu, J., Patel, V., Ton, T., Li, X., Loughhead, D. G., Nunn, P. A., Karr, D. E., Gerritsen, M. E., Funk, J. O., Owens, T. D., Verner, E., Brameld, K. A., Hill, R. J., Goldstein, D. M. and Taunton, J. (2015). Prolonged and tunable residence time using reversible covalent kinase inhibitors. *Nat. Chem. Biol.* *11*, 525-531.
- Copeland, R. A., Pompliano, D. L. and Meek, T. D. (2006). Drug–target residence time and its implications for lead optimization. *Nature reviews Drug discovery* *5*, 730-739.
- Corbeil, C. R., Williams, C. I. and Labute, P. (2012). Variability in docking success rates due to dataset preparation. *J Comput Aided Mol Des* *26*, 775-786.
- Decroos, C., Clausen, D. J., Haines, B. E., Wiest, O., Williams, R. M. and Christianson, D. W. (2015). Variable active site loop conformations accommodate the binding of macrocyclic largazole analogues to HDAC8. *Biochemistry* *54*, 2126-2135.
- Deschamps, N., Simões-Pires, C. A., Carrupt, P.-A. and Nurisso, A. (2015). How the flexibility of human histone deacetylases influences ligand binding: an overview. *Drug Discov. Today* *20*, 736-742.
- Dowling, D. P., Gantt, S. L., Gattis, S. G., Fierke, C. A. and Christianson, D. W. (2008). Structural Studies of Human Histone Deacetylase 8 and Its Site-Specific Variants Complexed with Substrate and Inhibitors. *Biochemistry* *47*, 13554 – 13563.
- Fenichel, M. P. (2015). FDA approves new agent for multiple myeloma. *J. Natl. Cancer Inst.* *107*, djv165.
- Finnin, M. S., Donigian, J. R., Cohen, A., Richon, V. M., Rifkind, R. A., Marks, P. A., Breslow, R. and Pavletich, N. P. (1999). Structures of a histone deacetylase homologue bound to the TSA and SAHA inhibitors. *Nature* *401*, 188-193.
- Hoops, S., Sahle, S., Gauges, R., Lee, C., Pahle, J., Simus, N., Singhal, M., Xu, L., Mendes, P. and Kummer, U. (2006). COPASI--a COMplex PATHway SIMulator. *Bioinformatics* *22*, 3067-3074.
- Huang, W. J., Wang, Y. C., Chao, S. W., Yang, C. Y., Chen, L. C., Lin, M. H., Hou, W. C., Chen, M. Y., Lee, T. L., Yang, P. and Chang, C. I. (2012). Synthesis and biological evaluation of ortho-aryl N-hydroxycinnamides as potent histone deacetylase (HDAC) 8 isoform-selective inhibitors. *ChemMedChem* *7*, 1815-1824.
- Jansch, N., Meyners, C., Muth, M., Koprancovic, A., Witt, O., Oehme, I. and Meyer-Almes, F.-J. (2019). The enzyme activity of histone deacetylase 8 is modulated by a redox-switch. *Redox biology* *20*, 60-67.
- Kleinschek, A., Meyners, C., Digiorgio, E., Brancolini, C. and Meyer-Almes, F. J. (2016). Potent and Selective Non-hydroxamate Histone Deacetylase 8 Inhibitors. *ChemMedChem* *11*, 2598-2606.



- Kokh, D. B., Czodrowski, P., Rippmann, F. and Wade, R. C. (2016). Perturbation Approaches for Exploring Protein Binding Site Flexibility to Predict Transient Binding Pockets. *Journal of chemical theory and computation* *12*, 4100-4113.
- Koshland Jr, D. (1958). Application of a theory of enzyme specificity to protein synthesis. *Proceedings of the National Academy of Sciences of the United States of America* *44*, 98.
- KrennHrubic, K., Marshall, B. L., Hedglin, M., Verdin, E. and Ulrich, S. M. (2007). Design and evaluation of 'Linkerless' hydroxamic acids as selective HDAC8 inhibitors. *Bioorg. Med. Chem. Lett.* *17*, 2874-2878.
- Kunze, M. B., Wright, D. W., Werbeck, N. D., Kirkpatrick, J., Coveney, P. V. and Hansen, D. F. (2013). Loop interactions and dynamics tune the enzymatic activity of the human histone deacetylase 8. *J. Am. Chem. Soc.* *135*, 17862-17868.
- Lee, H. Z., Kwitkowski, V. E., Del Valle, P. L., Ricci, M. S., Saber, H., Habtemariam, B. A., Bullock, J., Bloomquist, E., Li Shen, Y., Chen, X. H., Brown, J., Mehrotra, N., Dorff, S., Charlab, R., Kane, R. C., Kaminskas, E., Justice, R., Farrell, A. T. and Pazdur, R. (2015). FDA Approval: Belinostat for the Treatment of Patients with Relapsed or Refractory Peripheral T-cell Lymphoma. *Clin. Cancer. Res.* *21*, 2666-2670.
- Lu, H. and Tonge, P. J. (2010). Drug-target residence time: critical information for lead optimization. *Curr. Opin. Chem. Biol.* *14*, 467-474.
- Ma, B., Kumar, S., Tsai, C.-J. and Nussinov, R. (1999). Folding funnels and binding mechanisms. *Protein Engineering* *12*, 713-720.
- Mann, B. S., Johnson, J. R., Cohen, M. H., Justice, R. and Pazdur, R. (2007). FDA approval summary: vorinostat for treatment of advanced primary cutaneous T-cell lymphoma. *Oncologist* *12*, 1247-1252.
- Meyer-Almes, F. J. (2016). Discrimination between conformational selection and induced fit protein-ligand binding using Integrated Global Fit analysis. *Eur. Biophys. J.* *45*, 245-257.
- Meyners, C., Baud, M. G., Fuchter, M. J. and Meyer-Almes, F. J. (2014). Kinetic method for the large-scale analysis of the binding mechanism of histone deacetylase inhibitors. *Anal. Biochem.* *460*, 39-46.
- Meyners, C., Mertens, M., Wessig, P. and Meyer-Almes, F. J. (2017). A Fluorescence-Lifetime-Based Binding Assay for Class IIa Histone Deacetylases. *Chemistry* *23*, 3107-3116.
- Meyners, C., Wawrzinek, R., Kramer, A., Hinz, S., Wessig, P. and Meyer-Almes, F. J. (2014). A fluorescence lifetime-based binding assay for acetylpolyamine amidohydrolases from *Pseudomonas aeruginosa* using a [1,3]dioxolo[4,5-f][1,3]benzodioxole (DBD) ligand probe. *Anal. Bioanal. Chem.* *406*, 4889-4897.
- Niegisch, G., Knievel, J., Koch, A., Hader, C., Fischer, U., Albers, P. and Schulz, W. A. (2013). Changes in histone deacetylase (HDAC) expression patterns and activity of HDAC inhibitors in urothelial cancers. *Urol Oncol* *31*, 1770-1779.
- Oehme, I., Deubzer, H. E., Wegener, D., Pickert, D., Linke, J. P., Hero, B., Kopp-Schneider, A., Westermann, F., Ulrich, S. M., von Deimling, A., Fischer, M. and Witt, O. (2009). Histone deacetylase 8 in neuroblastoma tumorigenesis. *Clin. Cancer. Res.* *15*, 91-99.

- Park, S. Y., Jun, J. A., Jeong, K. J., Heo, H. J., Sohn, J. S., Lee, H. Y., Park, C. G. and Kang, J. (2011). Histone deacetylases 1, 6 and 8 are critical for invasion in breast cancer. *Oncol. Rep.* *25*, 1677-1681.
- Seeliger, D., Haas, J. and de Groot, B. L. (2007). Geometry-based sampling of conformational transitions in proteins. *Structure* *15*, 1482-1492.
- Singh, J., Petter, R. C., Baillie, T. A. and Whitty, A. (2011). The resurgence of covalent drugs. *Nat. Rev. Drug Discov.* *10*, 307-317.
- Somoza, J. R., Skene, R. J., Katz, B. A., Mol, C., Ho, J. D., Jennings, A. J., Luong, C., Arvai, A., Buggy, J. J., Chi, E., Tang, J., Sang, B. C., Verner, E., Wynands, R., Leahy, E. M., Dougan, D. R., Snell, G., Navre, M., Knuth, M. W., Swanson, R. V., McRee, D. E. and Tari, L. W. (2004). Structural snapshots of human HDAC8 provide insights into the class I histone deacetylases. *Structure* *12*, 1325-1334.
- Stank, A., Kokh, D. B., Horn, M., Sizikova, E., Neil, R., Panecka, J., Richter, S. and Wade, R. C. (2017). TRAPP webserver: predicting protein binding site flexibility and detecting transient binding pockets. *Nucleic Acids Res.* *45*, W325-W330.
- Suzuki, T., Ota, Y., Ri, M., Bando, M., Gotoh, A., Itoh, Y., Tsumoto, H., Tatum, P. R., Mizukami, T., Nakagawa, H., Iida, S., Ueda, R., Shirahige, K. and Miyata, N. (2012). Rapid discovery of highly potent and selective inhibitors of histone deacetylase 8 using click chemistry to generate candidate libraries. *J. Med. Chem.* *55*, 9562-9575.
- Tummino, P. J. and Copeland, R. A. (2008). Residence Time of Receptor- Ligand Complexes and Its Effect on Biological Function. *Biochemistry* *47*, 5481 – 5492.
- Volund, A. (1978). Application of the four-parameter logistic model to bioassay: comparison with slope ratio and parallel line models. *Biometrics* *34*, 357-365.
- Wagner, F., Zhang, Y.-L., Fass, D., Joseph, N., Gale, J., Weirwer, M., McCarren, P., Fisher, S., Kaya, T. and Zhao, W.-N. (2015). Kinetically selective inhibitors of histone deacetylase 2 (HDAC2) as cognition enhancers. *Chemical Science* *6*, 804-815.
- Wawrzinek, R., Ziolkowska, J., Heuveling, J., Mertens, M., Herrmann, A., Schneider, E. and Wessig, P. (2013). DBD Dyes as Fluorescence Lifetime Probes to Study Conformational Changes in Proteins. *Chemistry* *19*, 17349-17357.
- Wentsch, H. K., Walter, N. M., Buhrmann, M., Mayer-Wrangowski, S., Rauh, D., Zaman, G. J. R., Willemsen-Seegers, N., Buijsman, R. C., Henning, M., Dauch, D., Zender, L. and Laufer, S. (2017). Optimized Target Residence Time: Type I1/2 Inhibitors for p38alpha MAP Kinase with Improved Binding Kinetics through Direct Interaction with the R-Spine. *Angewandte Chemie* *56*, 5363-5367.
- Whitehead, L., Dobler, M. R., Radetich, B., Zhu, Y., Atadja, P. W., Claiborne, T., Grob, J. E., McRiner, A., Pancost, M. R., Patnaik, A., Shao, W., Shultz, M., Tichkule, R., Tommasi, R. A., Vash, B., Wang, P. and Stams, T. (2011). Human HDAC isoform selectivity achieved via exploitation of the acetate release channel with structurally unique small molecule inhibitors. *Bioorg. Med. Chem.* *19*, 4626-4634.
- Wright, J. S., Anderson, J. M., Shadnia, H., Durst, T. and Katzenellenbogen, J. A. (2013). Experimental versus predicted affinities for ligand binding to estrogen receptor: iterative selection and rescoring of docked poses systematically improves the correlation. *J Comput Aided Mol Des* *27*, 707-721.

## Tables and figures

**Table 1** Selectivity profile of DBD-ligands and reference compounds on human HDACs.

Inhibitor	IC <sub>50</sub> / $\mu$ M					
	HDAC1	HDAC2	HDAC3	HDAC4	HDAC6	HDAC8
<b>8</b>	>50 <sup>a</sup>	40 $\pm$ 3	0.30 $\pm$ 0.01	2.20 $\pm$ 0.16	>50 <sup>a</sup>	0.210 $\pm$ 0.015
<b>9</b>	2.5 $\pm$ 0.1 <sup>a</sup>	11 $\pm$ 1	0.30 $\pm$ 0.01	1.7 $\pm$ 0.5	2.9 $\pm$ 0.5 <sup>a</sup>	0.155 $\pm$ 0.004
<b>10</b>	1.0 $\pm$ 0.1 <sup>a</sup>	4.5 $\pm$ 0.2	0.068 $\pm$ 0.002	0.029 $\pm$ 0.006	1.0 $\pm$ 0.1 <sup>a</sup>	0.020 $\pm$ 0.001
SAHA	0.006 $\pm$ 0.004 <sup>b</sup>	0.25 $\pm$ 0.01	0.071 $\pm$ 0.001	27 $\pm$ 4 <sup>b</sup>	0.089 $\pm$ 0.007 <sup>b</sup>	5.8 $\pm$ 0.4
PCI-34051	4.0 <sup>c</sup>	>50	26 $\pm$ 1	>100 <sup>b</sup>	2.9 <sup>c</sup>	0.027 $\pm$ 0.002
<b>2</b>	>100 <sup>d</sup>	-	-	-	55 <sup>d</sup>	0.3 <sup>d</sup>
<b>3</b>	4.5 <sup>c</sup>	>20 <sup>e</sup>	4.8 <sup>c</sup>	>20 <sup>e</sup>	>20 <sup>e</sup>	0.0057 <sup>e</sup>
<b>4</b>	38 <sup>f</sup>	>100 <sup>f</sup>	-	44 <sup>f</sup>	2.4 <sup>f</sup>	0.07 <sup>f</sup>
<b>5</b>	>30 <sup>g</sup>	>30 <sup>g</sup>	-	-	>30 <sup>g</sup>	0.2 <sup>g</sup>
<b>6</b>	1.7 <sup>g</sup>	3.9 <sup>g</sup>	-	-	>30 <sup>g</sup>	0.09 <sup>g</sup>
<b>7</b>	1.7 <sup>b</sup>	>50 <sup>b</sup>	6.7 <sup>b</sup>	2.0 <sup>b</sup>	2.8 <sup>b</sup>	0.0029 <sup>b</sup>

<sup>a</sup>(Meyners *et al.*, 2017)<sup>b</sup>(Kleinschek *et al.*, 2016)<sup>c</sup>(Balasubramanian *et al.*, 2008)<sup>d</sup>(KrennHrubec *et al.*, 2007)<sup>e</sup>(Huang *et al.*, 2012)<sup>f</sup>(Suzuki *et al.*, 2012)<sup>g</sup>(Whitehead *et al.*, 2011).

**Table 2** Kinetic parameter of DBD-ligands binding to HDAC8.

Ligand	$k_1/(M^{-1}s^{-1})$	$k_{-1}/(10^{-4} s^{-1})$	$k_r/(10^{-4} s^{-1})$	$k_{-r}/(10^{-4} s^{-1})$	$k_{on\_app}^e / (M^{-1}s^{-1})$	RT / h
<b>8</b>	458±4	0.64±0.06	-	-	374±4	1.9±0.1 <sup>a</sup> < 3 <sup>b</sup> 4.3±0.5 <sup>c</sup>
<b>9</b>	1930±40	0.53±0.96	-	-	1690±20	3.3±0.5 <sup>a</sup> ca. 3 <sup>b</sup> 5±9 <sup>c</sup>
<b>10</b>	35400±210 0	0.01±0.11	3.4±0.2	14±1	7040±530	>40 <sup>a</sup> >15 <sup>b</sup> >25 <sup>c</sup>
<b>SAHA</b>	-	-	-	-	-	0.0148±0.0007 <sup>d</sup>
<b>TSA</b>	-	-	-	-	-	0.0150±0.0003 <sup>d</sup>
<b>PCI-34051</b>	-	-	-	-	-	0.0011±0.0001 <sup>c</sup>

$k_1$ ,  $k_{-1}$ ,  $k_r$ ,  $k_{-r}$  are rate constant corresponding to model A) for **8** and **9** and model C) for **10** in scheme 1, RT: residence time

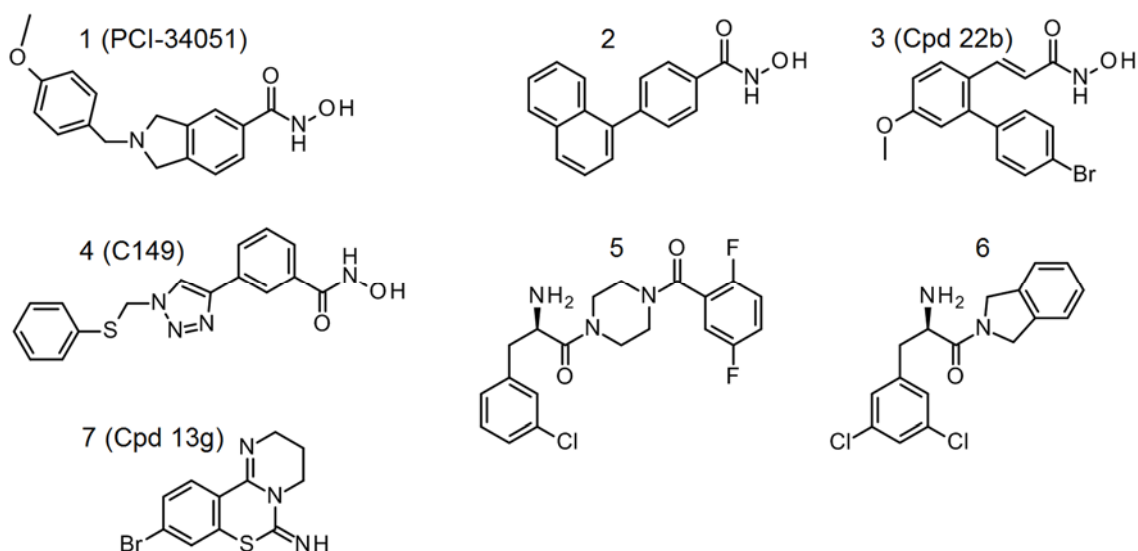
<sup>a</sup>dissociation kinetics

<sup>b</sup>dialysis

<sup>c</sup>global fit analysis

<sup>d</sup>(Meyners et al., 2014)

<sup>e</sup>slope of plot  $k_{app}$  vs.  $c(HDAC8)$  in Fig. 4B/D/F, nd: not determinable due to very large error;

**Scheme 1** Isoenzyme selective HDAC8 inhibitors.

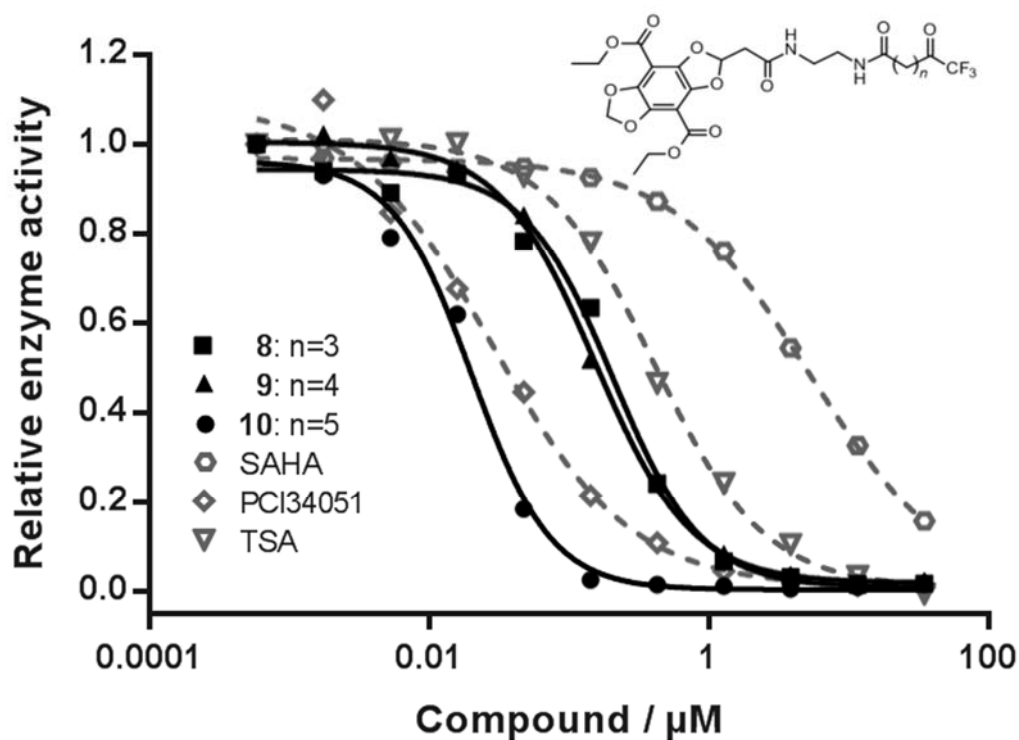


**Figure 1** Dose-Response curves of DBD-ligands (in black) and reference compounds (in grey) on HDAC8. The inset shows the chemical structure of compounds **8**, **9** and **10** with different alkyl spacer lengths. The relative enzyme activity is plotted versus compound concentration. The smooth lines represent non-linear fits to a 4-parameter logistic function (Volund, 1978). The parameters include upper and lower plateau,  $IC_{50}$ -value and steepness of the curve.

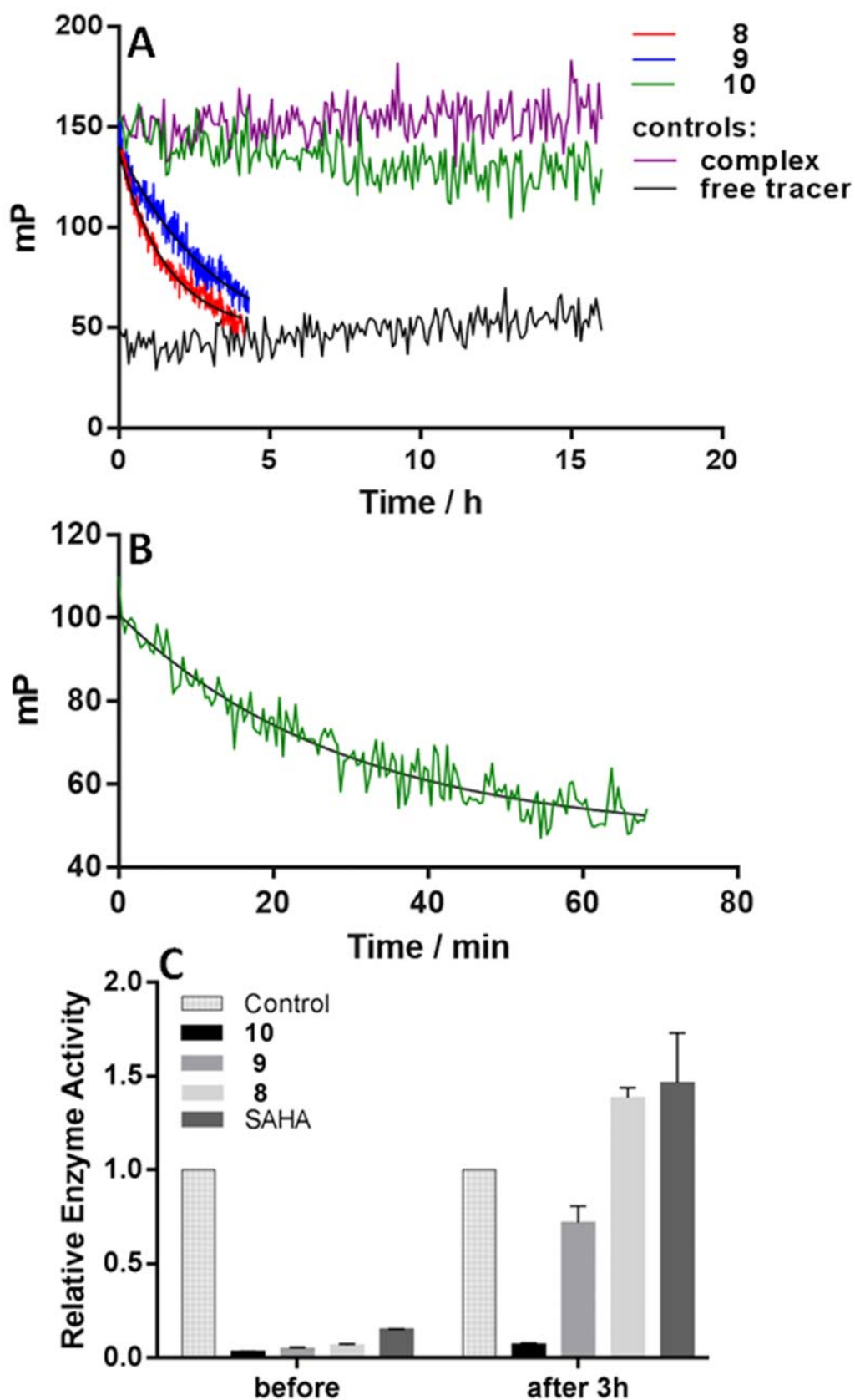


**Figure 2** Dissociation kinetics of A) indicated DBD-ligands from HDAC8 and B) **10** from HDAC4. The time course of fluorescence polarization is shown after the addition of

excess concentrations of SATFMK to a preformed complex between DBD-ligand and HDAC8 or HDAC4, respectively. The fluorescence polarization of unbound **10** (free tracer) and the complex between **10** and HDAC8 (complex) in panel A) remain essentially unchanged over the period of 15 h. C) Relative enzyme activity of preformed complexes between HDAC8 and indicated compounds before and after 3h dialysis against assay buffer at 4<sup>0</sup>C. The control, free HDAC8, was used to normalize the measured enzyme activity. Shown are means and standard errors, n=3.

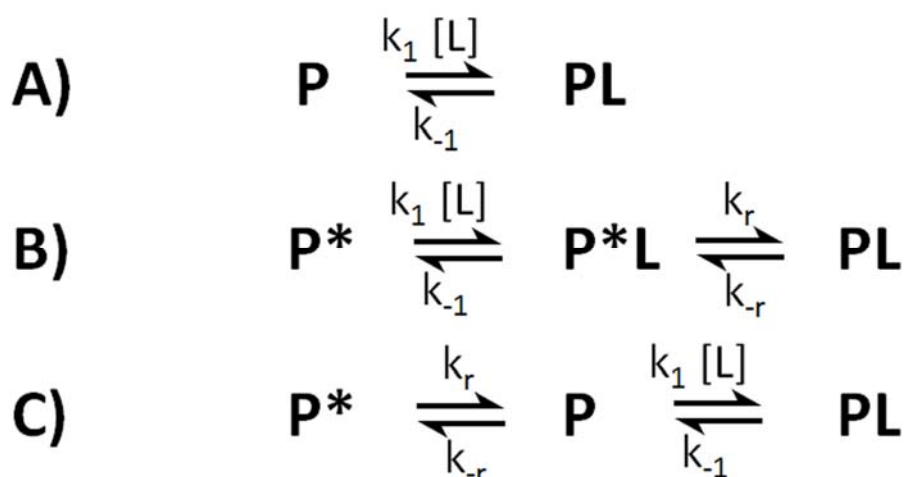


**Figure 3** (A) Simple one-step-binding mechanism, (B) IF-model and (C) CS-mechanism. P\* and P denote the protein before and after the conformational change, respectively. The conformational change occurs after binding of the ligand L (IF-mechanism) or before (CS-mechanism).

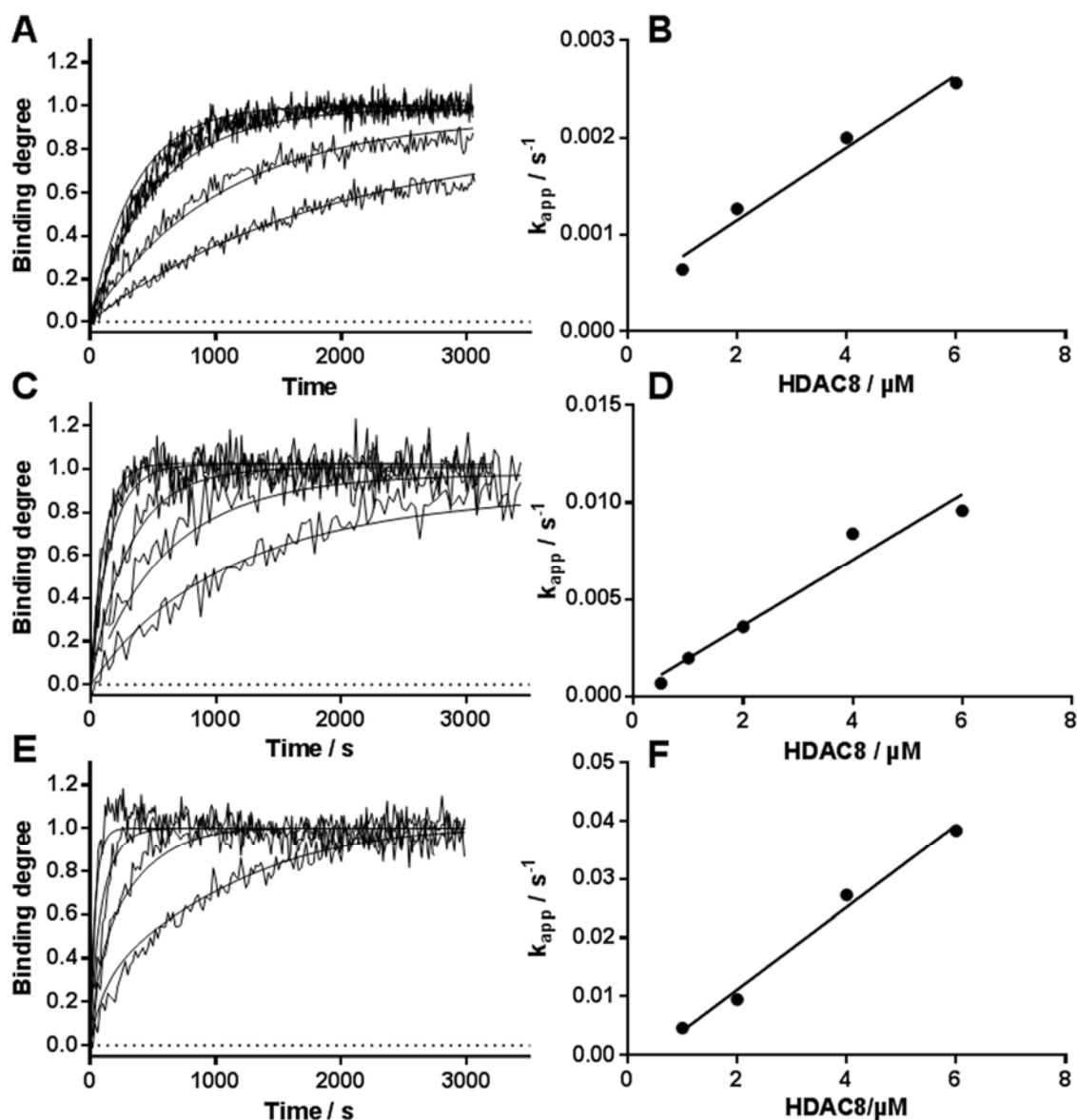


**Figure 4** Association kinetics of 200nM DBD-ligands to varying concentrations of HDAC8. The left panels show experimental time courses and smooth curves from Global Fit Analysis to the most likely binding model (A), C) one-step and E) CS). The panels on the right hand side show plots of corresponding apparent rate constants from 1-exponential fits versus applied HDAC8 concentration. A) / B) refer to DBD-ligand **8**, C) / D) to **9** and E) / F) to **10**.



## Kinetically selective HDAC8 inhibitors

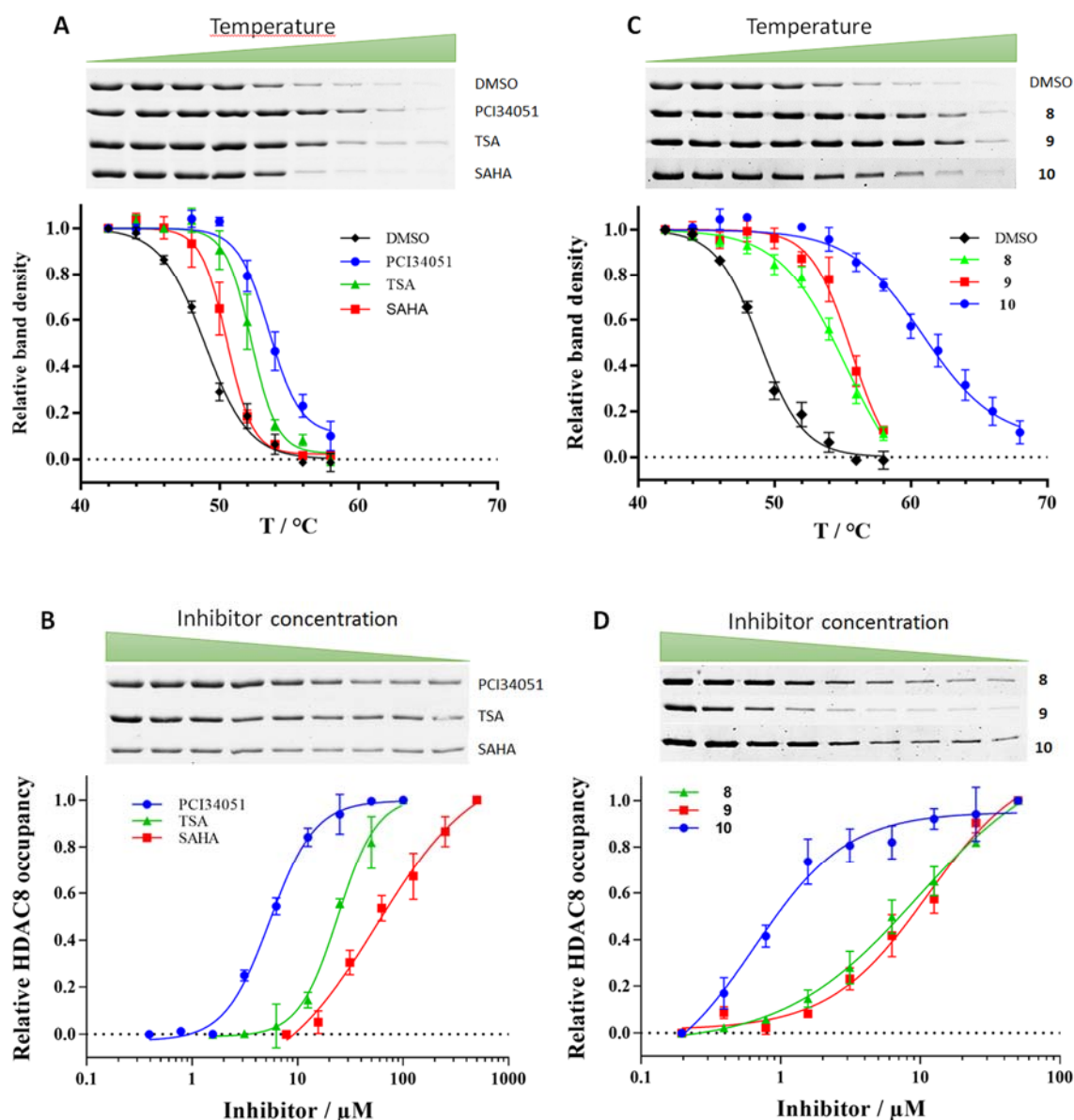


**Figure 5** Thermal stabilization of HDAC8 upon binding of standard inhibitors (A and B) and indicated DBD-probes (C and D) in assay buffer. In A) and C) the thermal denaturation of HDAC8 is shown in the absence (DMSO) and in the presence of 100  $\mu\text{M}$  of various substances for different temperatures. The optimal temperature with maximal difference in band intensities is chosen for each inhibitor to be kept constant in the corresponding dose-response curves below (B and D). The chosen temperature is 50  $^{\circ}\text{C}$  for all inhibitors except **10** in B) and D) and 54  $^{\circ}\text{C}$  for **10** in D). The relative HDAC8 occupancy is calculated from the intensity of the HDAC8 band in the corresponding gel indicating protein that is protected against thermal denaturation in the presence of increasing inhibitor concentrations. Data points represent mean and standard deviation of independent experiments,  $n=3$ .

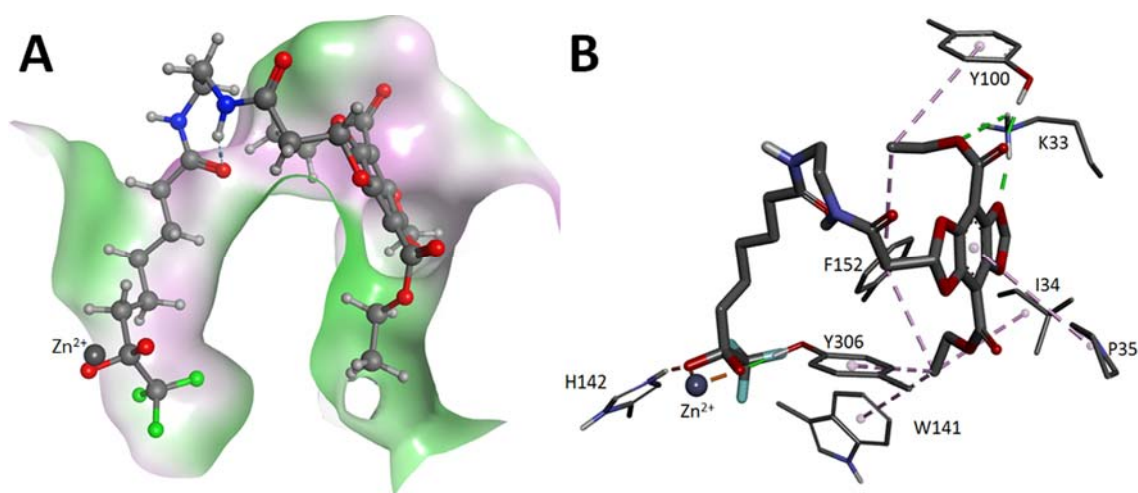


**Figure 6** Best docking pose of **10** in HDAC8 (based on PDB-ID 1T64). A) Cross-section of active site (left) and allosteric pocket (right) filled with **10**. The surface of the binding pockets is colored by hydrophobicity (green: lipophilic, white: neutral, magenta: hydrophilic). B) Ligand interaction with target residues. H-bonds: green, metal-complexation: orange, alkyl-alkyl/pi interactions: magenta.

## Supplementary Material

## Selection of the most likely binding mechanism for DBD-ligands to HDAC8:

**Tab. S1** Global fit analysis of DBD-ligands applying the one-step-binding model

Rate constants	<b>8</b>	<b>9</b>	<b>10</b>
<b>Global Fit Analysis</b>			
$k_1 / M^{-1}s^{-1}$	452 ± 3	1930 ± 40	4400 ± 100
$k_{-1} / s^{-1}$	(6.1 ± 0.6) * 10 <sup>-5</sup>	(5.3 ± 9.6) * 10 <sup>-5</sup>	(1.0 ± 0.1) * 10 <sup>-4</sup>
RT / h	4.3 ± 0.5	5 ± 9	2.8 ± 0.3
<b>Experimental Data</b>			
$k_{on\_app} / (M^{-1}s^{-1})$	374±4	1690±20	7040±530
RT / h *	1.9 ± 0.1	3.3 ± 0.5	> 25

\*competitive displacement kinetics, RT: residence time = 1/ $k_{-1}$

In case of a one-step-binding mechanism,  $k_1$  (global fit) should agree with  $k_{on\_app}$ . For this model, there is only for **8** and **9** a reliable agreement between fitted and experimental data.

**Tab. S2** Error sum of Squares of global data fit of indicated model to data sets of binding kinetics of DBD-ligands 8, 9 and 10 to HDAC8.

Model	<b>8</b>	<b>9</b>	<b>10</b>
One-step	<b>2.7</b>	<b>3.4</b>	3.2
IF	2.7	3.4	3.2
CS	2.7	3.4	<b>2.5</b>

The one-step model has two fit parameters, whereas IF- and CS-model have 4 parameters. The most likely models are highlighted in red. For 8 and 9 there is no improvement in terms of error sum of squares from the simple one-step-binding model (2 parameter) to the more complex IF- and CS-models (4 parameter). Thus, the one-step model appears to be most likely. In contrast, the error sum of square for the CS-model of the binding kinetics of 10 is significantly lower than for the other models. In this case, Akaike's information criterion (Akaike, 1974) and F test were used to calculate the probability for the most likely model:

## Compare models with the corrected Akaike's Information Criteria

	1-schritt	CS
<b>Sum-of-squares</b>	3.2	2.446
<b>Number of data points</b>	700	700
<b>Number of parameters</b>	2	4
<b>Akaike's Information Criteria (corrected, AICc)</b>	-3765.52	-3949.55
<b>Probability model is correct</b>	<0.01%	>99.99%
<b>Difference in AICc</b>	184.04	

CS has a lower AICc than 1-schritt so is more likely to be the correct model.

## Compare models with F test

Model	SS	DF
1-schritt (null)	3.2	698
CS (alternative)	2.446	696
Difference	0.754	2
Percentage Difference	30.83%	0.29%
Ratio (F)	107.27	
P value	<0.0001	

If *1-schritt* (the null hypothesis) were true, there would be a 0.00% chance of obtaining results that fit CS (the alternative hypothesis) so well.

Since the P value is less than the traditional significance level of 5%, you can conclude that the data fit significantly better to CS than to *1-schritt*.

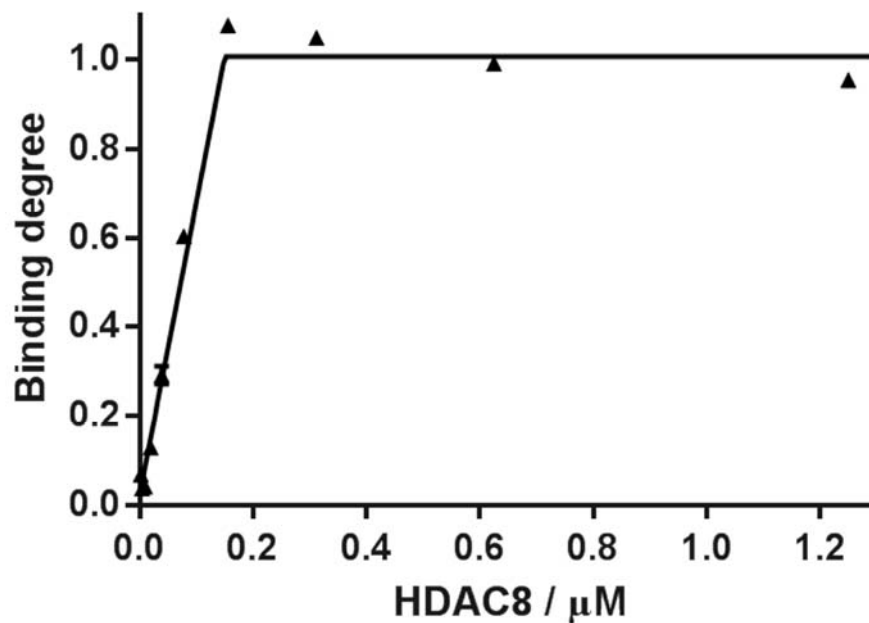
Note that the F test assumes that *1-schritt* is a simpler case of CS. If this is not the case, you should ignore the F test results.

**Table S3** Docking results of **10** to different crystal structures of HDAC8

PDB-ID	GBVI/WSA dG Score	Metal complexation	H-bonds	Hydrophobic interactions
1T69 (closed)	-23	bidentate	H142, Y306, G151, D101	F207, F208, H180, P273
1T64 (sub-open)	-25	bidentate	H142, Y306, Y100, K33	Y100, F152, Y306, W141, I34, P35
1VKG (wide-open)	-21	bidentate	H142, Y306, K202	M274, C275

**Table S4** IC<sub>50</sub>-values of reference compounds against HDAC8 (see Fig. 1):

Compound	IC <sub>50</sub> / $\mu\text{M}$
SAHA	5.8 $\pm$ 0.4
Trichostatin A (TSA)	0.41 $\pm$ 0.03
PCI-34051	0.027 $\pm$ 0.002

**Figure S1** Active site titration of 200nM compound **10** with HDAC8 indicating stoichiometric binding and completely binding active enzyme.

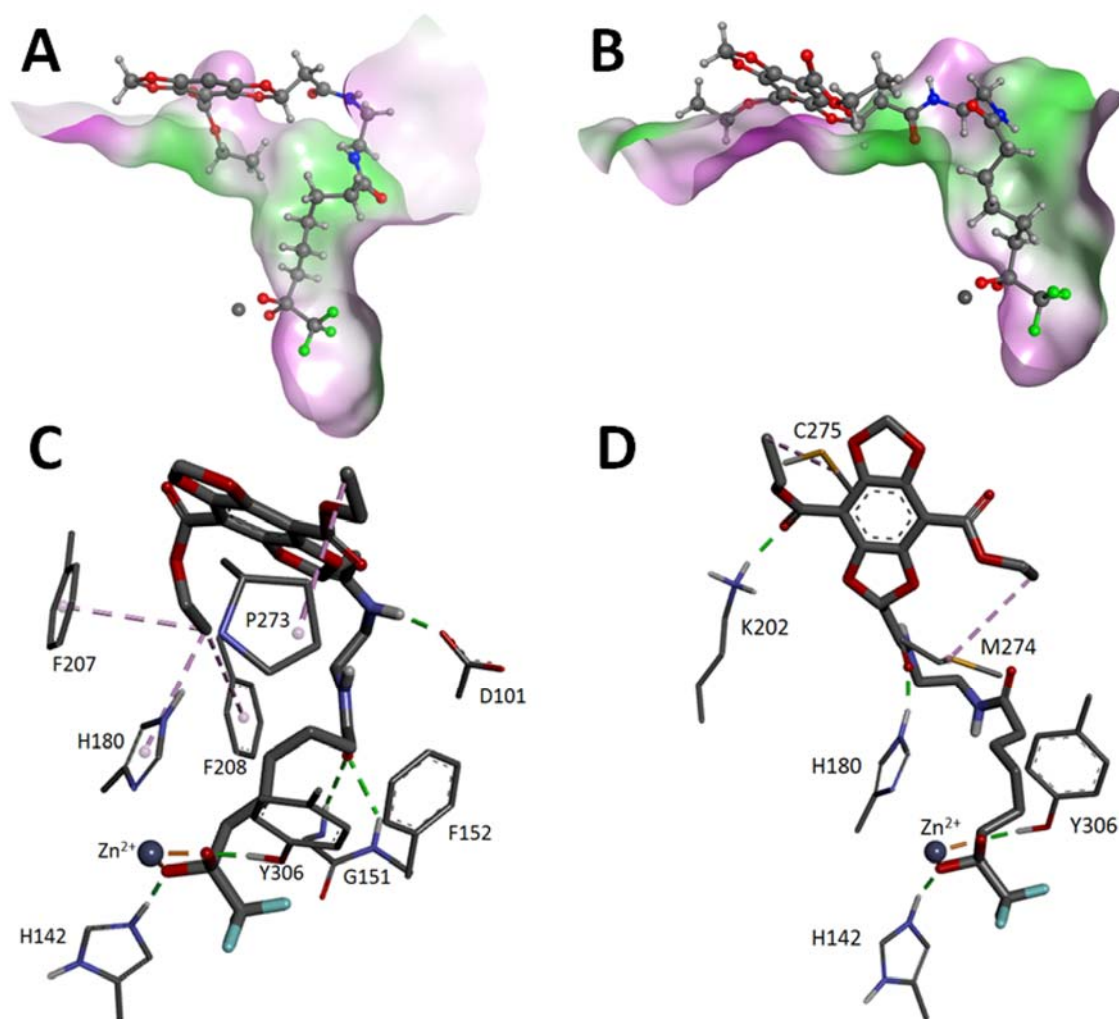


**Figure S2** Best docking poses of **10** in closed (A/C) and wide-open HDAC8 (B/D). The surface of the binding pockets (A/B) is colored by hydrophobicity (green: lipophilic, white: neutral, magenta: hydrophilic). Ligand interaction (C/D) with target residues are colored as follows: H-bonds: green, metal-complexation: orange, alkyl-alkyl/pi interactions: magenta.

## Kinetically selective HDAC8 inhibitors

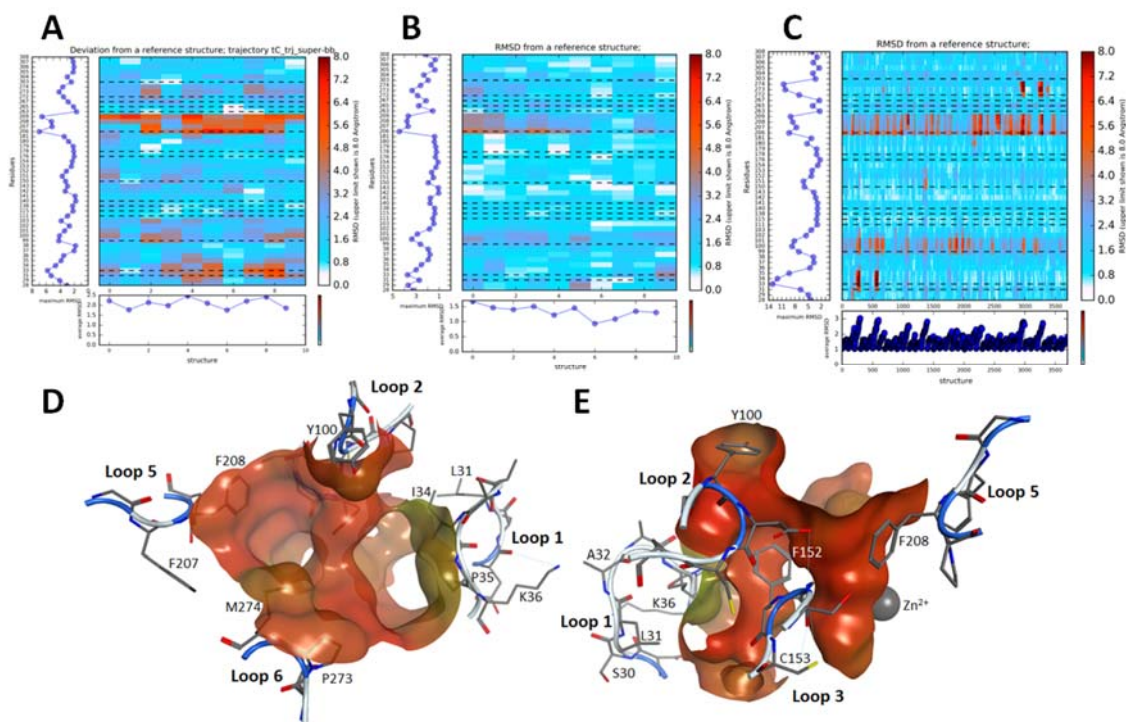


**Figure S3** Binding site flexibility of HDAC8. A) tCONCOORD-TRAPP analysis (Stank *et al.*, 2017). B) RIplig-TRAPP analysis. C) L-RIP-TRAPP analysis. The red regions denote high and white/light blue regions low deviations of the respective residue from the reference structure (PDB-ID: 1T64). D) Top view and E) side view of both binding pockets with surrounding amino acids of enhanced flexibility. The surface of the binding pockets is colored according to B-factors (B-factor of 10 corresponds to red and 35 to green).

### Kinetically selective HDAC8 inhibitors

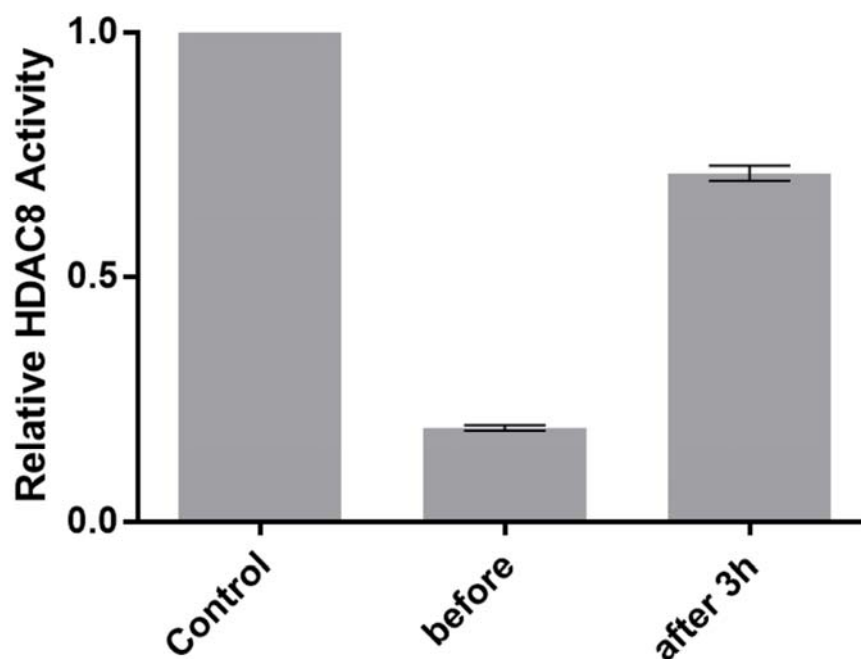


**Figure S4** Dialysis of a preformed complex between HDAC4 and compound **10**. Relative enzyme activity of preformed complexes between HDAC8 and indicated compounds before and after 3h dialysis against assay buffer at 4<sup>0</sup>C. The control, free HDAC8, was used to normalize the measured enzyme activity. Shown are means and standard errors, n=3.

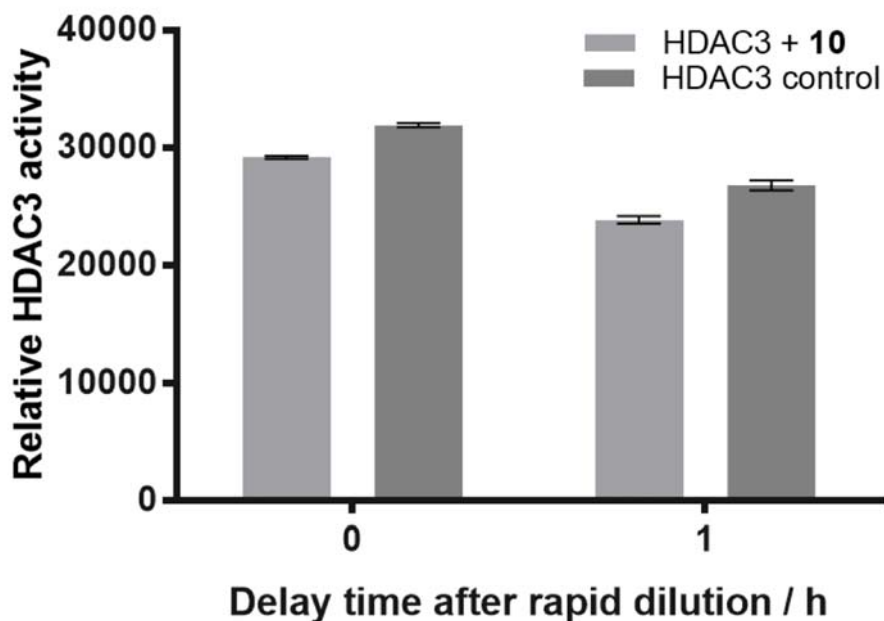


**Figure S5** Rapid dilution of complex between HDAC3 and **10**. 600 nM **10** and about 100 nM HDAC3 were incubated for 1 h at 4<sup>0</sup>C before rapid 1:100 dilution. The HDAC3



control contained no inhibitor. The enzyme activity was determined right after and 1 h after rapid dilution according to the standard assay protocol. The fluorescence of the AMC product is a measure of the relative HDAC3 activity and was measured with indicated delay time after rapid dilution. The data show that **10** dissociates faster than the dilution and assay time of about 30 min.

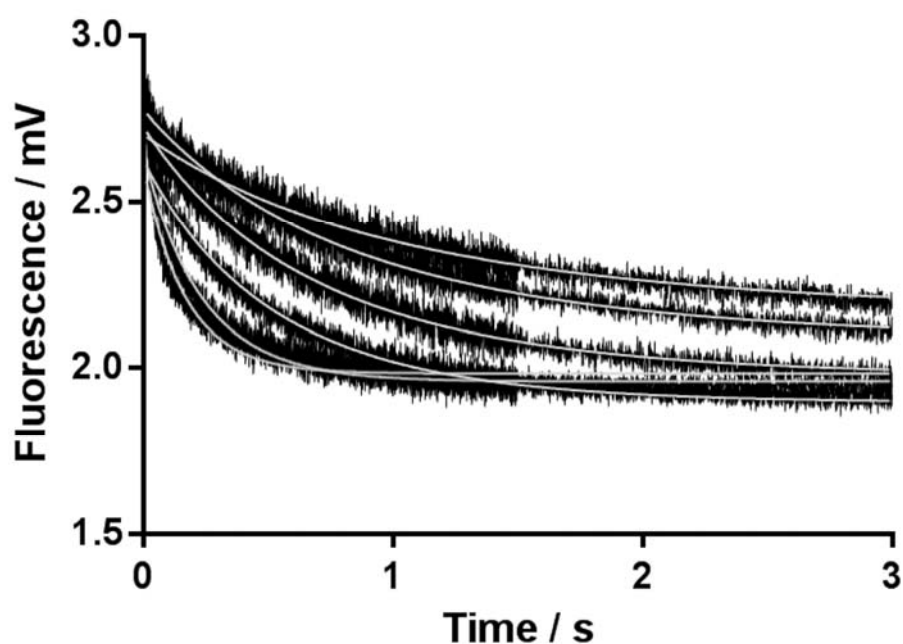


**Figure S6** Stopped-Flow-Kinetics of PCI-34051 binding to HDAC8. 300nM binding active HDAC8 were mixed with 0.3, 0.5, 0.7, 1.0, 2.5 and 3.5  $\mu\text{M}$  of the inhibitor. The intrinsic tryptophan fluorescence of HDAC8 (Exc. 285, Em.  $> 300$  nm) is quenched by PCI-34051. The fluorescence is measured as voltage of the photomultiplier in mV and plotted versus time. 98100 data points were analyzed simultaneously using global fit analysis and COPASI program. The association and dissociation rates of PCI-34051 from HDAC8 were determined to be  $1.7 \cdot 10^6 \text{ M}^{-1}\text{s}^{-1}$  and  $0.26 \text{ s}^{-1}$ , respectively. Slightly different offset values were considered by corresponding individual fit parameters.

## References

- Akaike, H. (1974). A New Look at the Statistical Model Identification. *IEEE Transactions on Automatic Control* *19*, 716-723.
- Stank, A., Kokh, D. B., Horn, M., Sizikova, E., Neil, R., Panecka, J., Richter, S. and Wade, R. C. (2017). TRAPP webserver: predicting protein binding site flexibility and detecting transient binding pockets. *Nucleic Acids Res.*

---

**Titel:**

Using design of experiment to optimize enzyme activity assays

**Autoren:**

Niklas Jänsch, Felix Colin, Michael Schröder, Franz-Josef Meyer-Almes

**Bibliographische Daten:**

ChemTexts (doi.org/10.1007/s40828-019-0095-2)

**Zusammenfassung:**

In dieser Laborübung lernen Studenten die Anwendung der statistischen Versuchsplanung (DOE) zur Optimierung eines Trypsin-Aktivitätstests unter Verwendung des künstlichen Substrats N $\alpha$ -Benzoyl-L-Arginin-p-Nitroanilid (BAPNA). Der Ansatz des Response Surface Modeling (RSM) wird genutzt, um die kombinierten Auswirkungen relevanter Faktoren auf die Hemmung von Trypsin durch den kompetitiven Inhibitor Benzamidin zu planen und zu bewerten. Die RSM-Matrizes und Statistiken werden mit kommerzieller Software erstellt. Die experimentellen Daten werden mit der Michaelis-Menten-Theorie verglichen. Die vorhergesagten Werte stimmen gut mit den experimentellen Daten überein. Die umfassende Analyse der Daten bietet einen tiefen Einblick in die Beziehung zwischen Substrat, Inhibitorkonzentration und Assay-Empfindlichkeit im Kontext des Hochdurchsatz-Wirkstoffscreenings. Die Datenanalyse zeigt auch unerwartete, aber erklärbare Wechselwirkungen zwischen dem Substrat und dem pH-Wert in dem angewandten Enzymaktivitätstest. Die kombinierte Planung, Durchführung und Analyse praktischer Experimente zeigt, dass DOE ein hervorragendes Werkzeug ist, um die Beziehung zwischen verschiedenen Parametern, die die Enzymaktivität beeinflussen, zu untersuchen und funktionale Enzymaktivitätstests in einer Vielzahl von Anwendungen zu optimieren.



# Using design of experiment to optimize enzyme activity assays

Niklas Jansch<sup>1</sup> · Felix Colin<sup>1</sup> · Michael Schröder<sup>1</sup> · Franz-Josef Meyer-Almes<sup>1</sup>

Received: 10 October 2019 / Accepted: 29 October 2019 / Published online: 13 November 2019  
© Springer Nature Switzerland AG 2019

## Abstract

This laboratory exercise teaches students the application of design of experiments (DOE) for optimizing a trypsin activity assay using the artificial substrate  $N_\alpha$ -benzoyl-L-arginine-*p*-nitroanilide (BAPNA). The response surface modeling (RSM) approach is exploited to design and evaluate the combined effects of relevant factors on the inhibition of trypsin by the competitive inhibitor benzamidine. RSM matrices and statistics are generated using commercial software. Experimental data are compared with Michaelis–Menten theory. The predicted values are in good agreement with the experimental data. The comprehensive analysis of data provides deep insight into the relationship between substrate, inhibitor concentration, and assay sensitivity in the context of high-throughput drug screening. Data analysis reveals also unexpected but explainable interactions between the substrate and the pH value in the applied enzyme activity assay. The combined design, performance, and analysis of practical experiments demonstrates that DOE is an excellent tool to explore the relationship between several parameters affecting the enzyme activity and to optimize functional enzyme activity assays in a variety of applications.

**Keywords** RSM · DOE · Michaelis–Menten · Competitive inhibitors · Assay development · High-throughput screening

## Introduction

The statistical design of experiments (DOE) was originally developed to optimize agricultural processes [1], but it soon evolved into a broadly applicable method for process and product optimization in academia and industry, e.g., pharma, automotive, and semiconductor industry [2–4]. DOE can be used to reduce costs and greatly enhance the efficiency of knowledge gain in scenarios with many influencing factors and potential interactions between each other. Among other areas of application, DOE is well established in drug discovery [5]. Nowadays, drug discovery is mainly driven by high-throughput screening (HTS) of large drug libraries with a million and more different chemical entities and can be applied to each druggable protein. By performing suboptimal assays, it is easy to miss potential hits or to identify misleading compounds. To avoid false positive and false negative hits it is of utmost importance to optimize the used assay protocol [6]. For the establishment of an optimized

assay with high sensitivity for active compounds of interest, a successive optimization of the involved factors (e.g., pH, temperature, substrate concentration, enzyme concentration, etc.) is necessary. The classic variation of only one single factor at a time neglects possible interaction between the factors and may lead to inconsistent results. These interactions can only be taken into account by investigating the combination of factors. However, the number of all possible combinations of several levels of three or more factors, also called full factorial design, can easily exceed the manageable workload and costs. Therefore, it is highly recommended to use specialized software for the DOE to narrow down the number of experiments on the basis of statistical arguments. The selection of factor and level combinations is simultaneously optimized for the subsequent statistical data analysis. To ensure this, DOE and data analysis are usually integral components of the same DOE software package. Data analysis provides a model and quality parameters which describe the experimental data and allow for the prediction of the target quantity, e.g., assay sensitivity, depending on significant influencing factors such as reagent concentrations. With this procedure the impact of several factors and, most importantly, interactions of these factors with each other can be elucidated.

✉ Franz-Josef Meyer-Almes  
franz-josef.meyer-almes@h-da.de

<sup>1</sup> Department of Chemical Engineering and Biotechnology,  
University of Applied Sciences Darmstadt, Haardtring 100,  
64295 Darmstadt, Germany

Training in our “Chemical Engineering and Biotechnology” Master’s program includes a practical DOE course to support scientific thinking and convey the knowledge and skills required to optimize assays and processes in academia and as well in an industrial environment. This is exemplified by a trypsin enzyme activity assay used to detect inhibitors. Experimental data of enzyme inhibition are compared with the Michaelis–Menten theory. In the last part of the practical course, the students use their deeper understanding of the Michaelis–Menten theory to discuss the highly relevant question of how to optimize the sensitivity of an assay for industrial HTS of compound libraries for new drug candidates.

## Theoretical background

Optimizing a particular analytical procedure using DOE is carried out by collecting data of a limited number of experiments. The main goal is to optimize a particular and carefully defined response quantity by a minimum of required experiments to also optimize the demand for the applied resources, e.g., time, man power, number of experimental animals, amount of reagents. In many cases the number of relevant variables that influence the response variable, or simply the response, can be narrowed down by referring to the literature or personal experience. The remaining 2–4 variables of a system, referred to as the factors of the study, are varied simultaneously at a limited number of factor levels to define a set of experiments in an approach called response surface modeling (RSM) [7]. This kind of experimentation is especially useful when the most influential factors and factor interactions are not known. Two factors interact with each other if the effect of one depends on the level of the other. Usually, factor interactions are caused by real physical or chemical effects. The levels of the factors are chosen to cover the presumed experimental space. Several design schemes, such as Box–Behnken [8], central composite [9], or mixed designs have been described that are used to create a balanced design for the contribution of each factor and provide a statistically reduced number of informative experiments. In the practical course, a D-optimal design [10] is chosen to match the number of experiments that are workable on a micro titer plate in parallel. These designs allow great flexibility in the specifications of a particular problem. D-optimal designs are straight optimizations based on a chosen optimality criterion and the model that will be fit. The MODDE (Sartorius) software calculates the D-efficiency of several design variants based on the number of practicable experiments. The design with greatest D-efficiency is supposed to provide maximum information. Experimental designs usually contain several replicates of an experiment, where all factor levels are set to the mean value in the center

of the explored experimental space, also referred to as the center point. The replication of the center point is necessary for the estimation of the experimental error and assumed to represent the error of the entire covered experimental space. It is good practice in DOE to randomize the order of experiments to avoid that the effect of external variability, such as room temperature or who performs the experiment, coincides with the effect of a factor. Before data analysis, systematic and statistical outliers have to be eliminated from the data set. Systematic outliers may come from pipetting errors or effects that interfere with the measurement technology, e.g., precipitation during absorbance measurements. Statistical outliers can easily be recognized in the residuals normal probability plot offered by MODDE software. The plot displays the cumulative normal probability against the normalized residuals (difference between response and corresponding value of the model function). The plot allows one to easily verify that the residuals are normally distributed, if the data points follow close to a straight line, which is a prerequisite of further statistical analysis. Statistical outliers clearly deviate from the normal probability line and usually with more than three standard deviations from the model function. The model function describes the dependency of the response on factors and factor interactions that are represented by the product of the factors multiplied by a corresponding parameter (Eq. 1). In order to enable the modulation of curved response surfaces with maxima and minima, quadratic terms may also be included in the model function. A general model function for the hypothetical factors  $X_1$  and  $X_2$  looks like

$$Y = b_0 + b_1X_1 + b_2X_2 + b_{12}X_1X_2 + b_{11}X_1^2 + b_{22}X_2^2 \quad (1)$$

where  $Y$  is the response,  $b_x$  is the parameter, and  $X_{1/2}$  are the factors.

The quality of the resulting model function can be assessed by calculating the coefficient of determination ( $R^2$ ) and the model predictive power ( $Q^2$ ) from sum of square expressions:

$$R^2 = 1 - \frac{\sum_{i=1}^N (y_i - \hat{y}_i)^2}{\sum_{i=1}^N (y_i - \bar{y})^2} \quad Q^2 = 1 - \frac{\sum_{i=1}^N (y_i - \hat{\hat{y}}_i)^2}{\sum_{i=1}^N (y_i - \bar{y})^2} \quad (2)$$

where  $N$  is the number of experiments,  $y_i$  is the response,  $\bar{y}$  is the mean response,  $\hat{y}_i$  is the fit value, and  $\hat{\hat{y}}_i$  is the predicted left-out response value.

$R^2$  describes how well the model fits the current data. A value of 1 equals a perfect model and 0 means that there is only noise.  $Q^2$  describes how well the model will predict new data.  $R^2$  should not exceed  $Q^2$  by more than 0.2–0.3 for a good model.

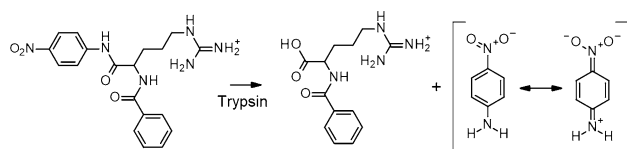


**Fig. 1** Hydrolysis of BAPNA substrate by trypsin. The released *p*-nitroaniline can be photometrically measured at 405 nm

## Experimental section

As a practical example of the application of DOE, a common enzyme assay for the serine protease trypsin is used. Trypsin catalyzes the hydrolysis of the artificial substrate *N*<sub>α</sub>-benzoyl-L-arginine-*p*-nitroanilide (BAPNA) releasing the chromogenic product *p*-nitroaniline (Fig. 1). The formation of *p*-nitroaniline can easily be measured photometrically at 405 nm using a common microplate reader. The slope of the time-dependent product formation is used as a stable measure of the enzyme activity.

## DOE using the software mode

For the examination of changes in enzyme activity affected by different factor combinations, the software MODDE (Sartorius Stedim Biotech, Aubagne, France; <https://umetrics.com/product/modde-pro>) is used. At first, an RSM design is developed including enzyme and substrate concentrations as well as pH as factors. The pH is varied between 7.0 and 8.0 using 200 mM 3-(*N*-morpholino)propanesulfonic acid (MOPS) buffer solution. The enzyme concentration is varied between 10 and 20 μg/mL and the substrate concentration between 1 and 4 mM, in order to ensure Michaelis–Menton conditions of substrate excess and generate a measurable linear increase of *p*-nitroaniline concentration (Fig. 1)

## Execution of experiments

On the basis of the generated RSM, a pipetting pattern for the measurement of enzyme activity in the presence and in the absence of the competitive trypsin inhibitor benzamidine is created. The factors are varied as suggested by the software using a D-optimal design (Fig. 2). The order of the experiments is randomized to avoid potential distortions from external influences. At first ultrapure water, buffer, and the enzyme are pipetted into 8-well microtiter strips (NUNC MTP-Strips immune module F8 Maxisorb NUNC 469949) with a final volume of 200 μL and then equilibrated for 10 min at room temperature. Typically, 40–48 experiments with different and randomized factor combinations including 6–7 center points with identical conditions to determine the random error are performed by each team of students. The reaction is started by the

Exp No	Run Order	pH	Trypsin	BAPNA	Abs. Diff.	Rel. Diff.
1	12	7	10	100	0.55	42.2
10	4	7.5	20	100	1.54	49.5
11	23	8	20	100	1.82	52.8
12	43	8	20	100	1.87	53.4
13	27	7	10	200	0.95	38.8
14	26	8	10	200	1.35	44.8
15	2	7.5	15	200	1.82	43.3
16	44	7.5	15	200	1.92	45.3
17	9	7	20	200	1.41	33.8
18	33	8	20	200	2.56	43.8
19	35	7	10	300	1.31	40.9
2	28	7	10	100	0.59	47.9
20	19	8	10	300	2.43	51.7
21	14	7.5	15	300	1.58	30.6
22	31	7	20	300	1.92	31.6
23	38	7.5	20	300	2.90	38.7
24	13	8	20	300	2.97	37.6
25	32	7	10	400	0.74	21.8
26	8	7	10	400	1.22	32.0
27	29	7.5	10	400	2.13	41.4
28	40	7.5	10	400	1.79	37.4
29	22	8	10	400	2.22	41.8
3	41	7.5	10	100	0.87	50.7
30	21	8	10	400	2.16	39.2
31	24	7	15	400	1.82	31.3
32	16	8	15	400	2.50	33.6
33	15	7	20	400	2.15	28.5
34	11	7	20	400	1.76	24.9
35	42	7.5	20	400	3.10	33.3
36	1	8	20	400	N.D.	N.D.
37	3	8	20	400	N.D.	N.D.
38	7	7	15	300	1.53	32.7
39	20	7.5	15	200	1.72	42.4
4	18	8	10	100	0.88	50.0
40	39	7.5	15	200	1.73	41.0
41	25	7.5	15	200	1.52	38.4
42	10	7.5	15	200	1.50	39.4
43	30	7.5	15	200	1.80	42.7
44	17	7.5	15	200	1.85	43.7
5	5	8	10	100	1.09	56.5
6	6	7	15	100	0.81	43.9
7	37	8	15	100	1.35	49.6
8	34	7	20	100	1.03	42.1
9	36	7	20	100	1.23	47.3

**Fig. 2** Worksheet of D-optimal design for three factors (pH, trypsin concentration, and BAPNA concentration). The trypsin levels are given as final concentrations in μg/mL and the BAPNA levels are in μM. The measured responses are already filled out. The absolute difference is given as  $\Delta\Delta E_{405} \times 10,000/s$  and the relative difference as ratio of the absolute difference and the activity in the absence of inhibitor in percent. N.D. not determined

addition of substrate. For the measurements in the presence of the inhibitor, the water volume is reduced in favor of added 100 μM benzamidine. This concentration is equal to the IC<sub>50</sub> of benzamidine to trypsin and is determined by the students prior to the DOE experiments by measuring the enzyme activity from a serial dilution of the inhibitor. The enzyme activity is determined by measuring the absorbance of *p*-nitroaniline product at 405 nm for 10 min at 1-min intervals using a TECAN GENios reader. All experiments are performed in triplicate.

## Data analysis and interpretation

For the evaluation of the experiments, the slope of product formation ( $\Delta E_{405}/s$ ) is calculated and multiplied by  $10^4$  to obtain values that are better suited for subsequent data analysis. In addition, besides the slope, which represents the initial velocity of substrate conversion, two further responses are defined: the absolute and the relative inhibition. For the calculation of the absolute inhibition, the slope of the inhibited reaction is subtracted from that of the reaction without inhibitor at exactly the same factor and level combination. The percentage relative inhibition is calculated by dividing the absolute inhibition by the slope of the reaction in the absence of inhibitor multiplied by 100. The observed values for each reaction are entered into the worksheet of the DOE software for subsequent statistical data analysis. The data are analyzed according to the following procedure:

1. Systematic and technical errors, e.g., from obviously inaccurate pipetting or turbidity are removed.
2. Statistic errors are identified through residual (difference between data and fit model) normal probability plots (N-plot). Outliers are supposed to deviate from linear behavior and to be outside of a  $\pm 3$  interval of deleted studentized residuals from the model function and are removed.
3. Coefficient plots are used to interpret and analyze interactions of the factors. A factor is regarded as significant if the factor effect is greater than its error. The model function is optimized by removing all non-significant factors and terms. Typically, this step increases the predictability of the model.
4. For the estimation of the model quality, the parameters  $R^2$ ,  $Q^2$ , model validity, and the reproducibility are calculated. High values implicate a good model.  $R^2$  is the coefficient of determination and describes how well the model fits the data.  $Q^2$  is a measure for the predictive power of the model and provides the percentage variation of the response predicted by the model according to cross validation. It tells one how well the model predicts new data. The model validity is an important parameter that is defined within the MODDE software. Values below 0.25 indicate lack of fit of the model. Finally, the reproducibility is given, which indicates the variation of the response under the same conditions at the center points. A reproducibility of approximately 1.0 means that the replicate values of the response at the center point are identical under the same conditions.
5. For further model evaluation, the observed versus predicted plot can be consulted. This plot displays the observed versus the predicted values of the response. With a good model all points will fall on the 1:1 line.

## Results and discussion

The application of DOE is exemplified by an enzyme activity assay for the protease trypsin with and without the competitive inhibitor benzamidine at its  $IC_{50}$  concentration. The relative inhibition is defined as the percentage of inhibited enzyme and the absolute inhibition as the difference between inhibited and uninhibited enzyme activity. Before data analysis, the data set has to be cleansed and freed from outliers. First, two experiments with obvious pipetting errors (wrong total volume) were removed from a data set of 40 experiments with different factor and level combinations. Then four further statistical outliers were removed, because the corresponding residuals deviated significantly from the expected linear behavior of the N-probability plot. After the removal of the outliers, the normalized residuals for the absolute and relative inhibition varied by less than three standard deviations and showed linear behavior indicating that the data are normally distributed around the model function, which is a prerequisite for a sound statistical analysis. Figure 3 shows the residual N-probability plot for both responses, absolute and relative inhibition.

The coefficient plots show different relative factor effects on the response values absolute and relative inhibition (Fig. 4). The factor pH shows a positive linear and negative quadratic term in both model functions for absolute and relative inhibition. This constellation suggests a maximum response for this factor in the model function. Other factor effects are opposite, e.g., trypsin (Try) and BAPNA (BAP). To increase the predictive power of the models, the non-significant terms were removed from both model functions (Fig. 4).

After reduction, model functions with excellent predictive power were obtained for both response values, which is reflected by a high correlation between observed and predicted data and coefficients of determination of 0.96 for absolute and 0.87 for relative inhibition, which describe how well the model function fits the data (Fig. 5). This is confirmed by  $Q^2$ , which accounts for the fraction of variation of the response that can be predicted by the model ( $Q^2 = 0.93$  for absolute and  $Q^2 = 0.78$  for relative inhibition). The software also indicates lack of fit, which suggests that a significant factor could have been missed in the data analysis. The parameter model validity calculated by MODDE indicates no lack of fit, because the values are larger than 0.25. However, the informative value of this parameter is limited for mathematical reasons if the reproducibility approaches 100%, as observed for absolute inhibition. In this case  $R^2$  and  $Q^2$  must also be considered. Since the model for absolute inhibition predicts the data splendidly, a lack of fit can be excluded.

With untrained students, good models are usually derived only for absolute inhibition. Therefore, the following data

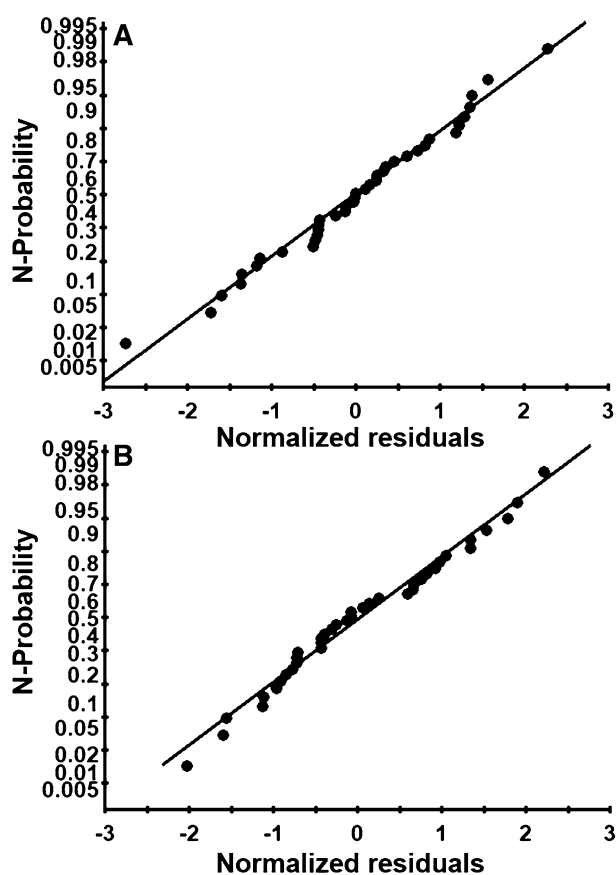


**Fig. 3** N-probability plot of studentized residuals from the model function for absolute (a) and relative inhibition (b)

analysis focuses mainly on the better model. Nevertheless, trends of factor effects, particularly the substrate concentration, are still usable in most cases. Substrate and trypsin concentrations show strong positive effects, which are trivial, because both factors accelerate substrate turnover, increasing the absolute difference between enzyme activity in the presence and absence of benzamidine. In addition, both factors show a significant synergistic effect on the response (or positive interaction term) indicating the physical interaction between enzyme and substrate. Similarly, pH shows a positive linear and negative quadratic effect on absolute inhibition suggesting the existence of a maximum in the model function. The pH optimum appears in the contour surface diagram between about 7.8 and 8.0 in agreement with a reported optimum between pH 7 and 9 under different assay conditions [11] (Fig. 6). The contour diagram is particularly suited to visualize factor interactions, e.g., pH and BAPNA concentration. The effect of BAPNA becomes stronger with higher pH values (Fig. 6). Significant interactions between factors as revealed by the coefficient plot usually have an underlying chemical or physical reason. A plausible explanation is that higher pH values shift the equilibrium

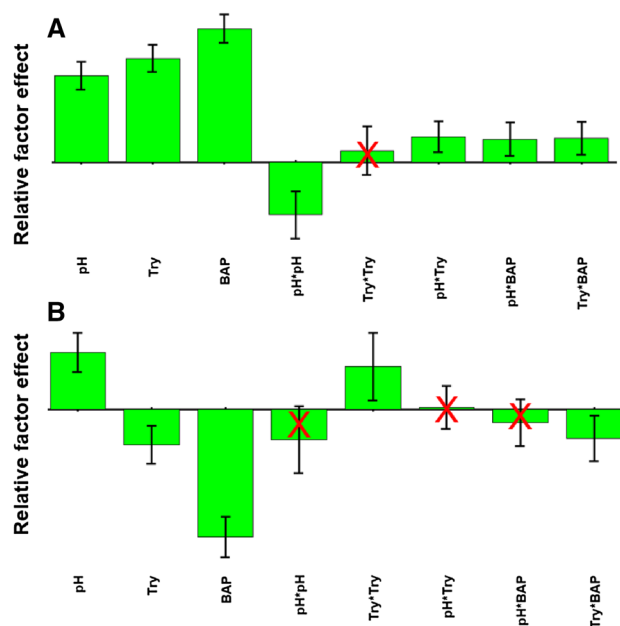


**Fig. 4** Coefficient plot that shows the relative impact of factors on the response absolute (a) and relative inhibition (b). Try and BAP denote the factors trypsin and BAPNA. The product of two factors represents interactions between the corresponding factors and squared factors are quadratic terms that enable maxima or minima in the model function. Red crosses denote non-significant model terms that are removed from the model functions

between protonated and deprotonated *p*-nitroaniline product to the deprotonated form. The amino group has a stronger +M effect than the ammonium group and causes stronger absorption at 405 nm due to more pronounced mesomerism (Fig. 1). More signal means greater difference between the enzyme activities in the absence and in the presence of inhibitor, which is defined as absolute inhibition. The positive effect of the interaction between trypsin and pH is probably due to a more effective deprotonated enzyme at higher pH.

The substrate concentration has the strongest influence on both responses (Fig. 4). At first it seems surprising that the substrate concentration has an opposite effect on absolute and relative inhibition (Fig. 7). Since benzamidine is a competitive inhibitor of trypsin, the expectation of the students before the experiments is usually that increasing concentrations of substrate should lead to somehow less inhibition, which is only observed with the response relative inhibition. To better understand this apparently contradictory result, the data are compared with data simulated using Eqs. 3 and 4 in the absence and presence of inhibitor according to the Michaelis–Menten theory (Fig. 8a, b).  $V_{\max}$  was assumed to be 1.0, and  $K_M$  is chosen to be 940  $\mu\text{M}$  [12]. For simplicity,  $K_i$  is assumed to equal the used  $\text{IC}_{50}$  concentration of benzamidine.



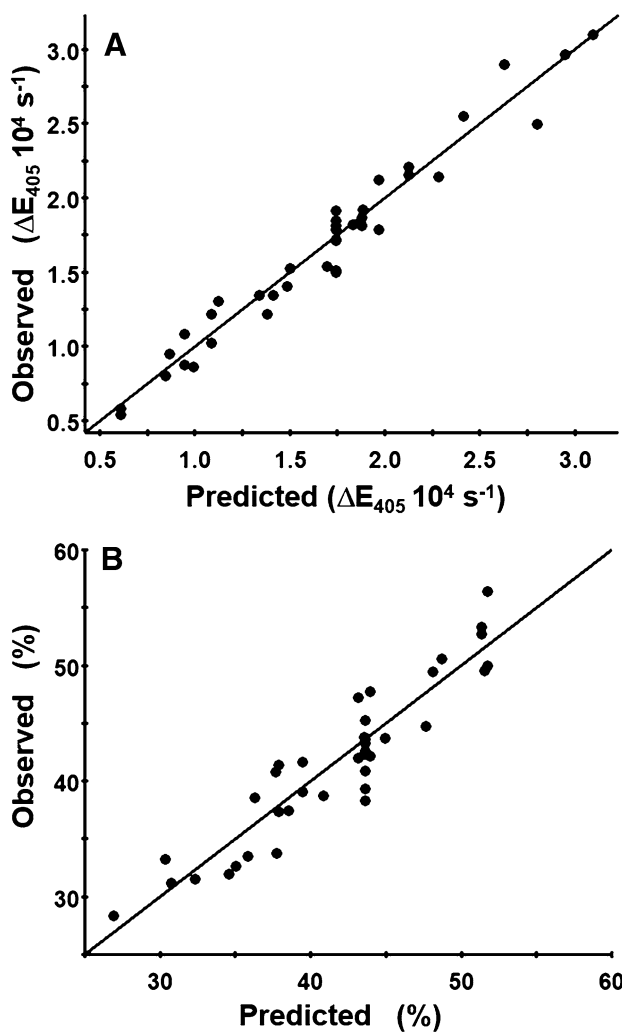


**Fig. 5** Observed versus predicted plots for absolute (a) and relative (b) inhibition. The absolute inhibition has the unit of the measured signal that is the change of absorbance at 405 nm multiplied by  $10^4$  and divided by time, while relative inhibition is in percent with regard to enzyme activity in the absence of inhibitor

$$v_o = \frac{v_{\max} \times [S]}{K_M + [S]} \tag{3}$$

$$v = \frac{v_{\max} \times [S]}{[S] + K_M \left( \frac{[I]}{K_i} \right)} \tag{4}$$

In fact, both simulated responses decrease with substrate concentrations at concentrations greater than  $2000 \mu\text{M}$  (Fig. 8b). However, looking at the substrate concentration range that is covered by the experiment ( $0\text{--}400 \mu\text{M}$ ) the opposite factor effect on the responses absolute and relative inhibition becomes obvious in agreement with the experimental data (Fig. 7).

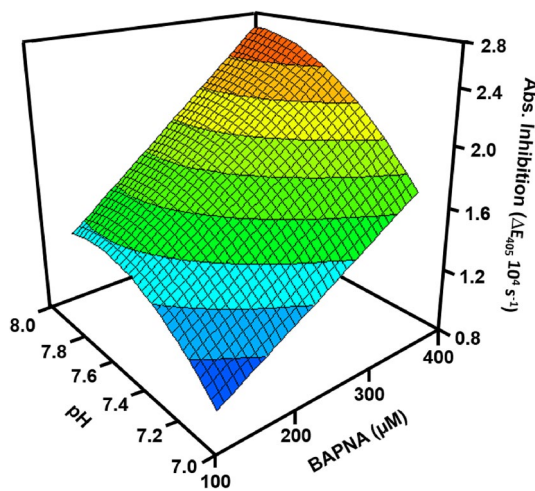


**Fig. 6** Contour plot of the model function showing the interaction between pH and substrate concentration regarding the response absolute inhibition. The trypsin concentration is  $15 \mu\text{g/mL}$

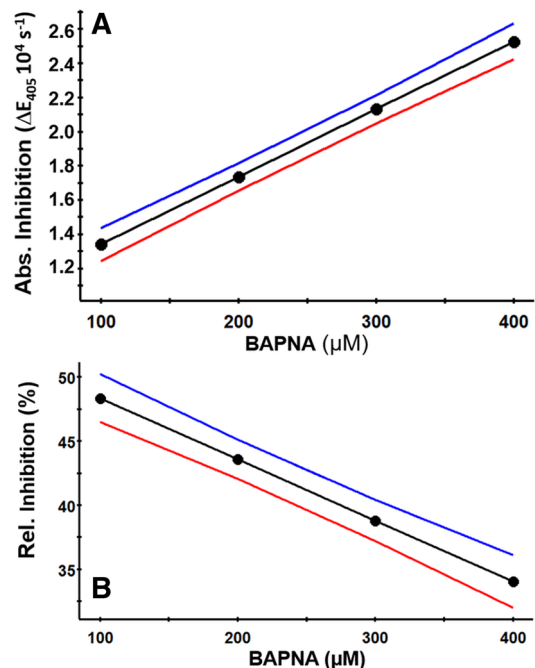


**Fig. 7** Prediction plots for model functions for absolute (a) and relative (b) inhibition. The black dots are predicted values assuming pH 7.5 and  $c(\text{trypsin}) = 15 \mu\text{g/mL}$ . Blue lines denote the upper and red lines the lower limit of 95% confidence intervals

Because benzamidine is a competitive inhibitor, the substrate is able to displace the inhibitor with increasing concentrations and the equilibrium is shifted progressively to the enzyme–substrate complex which results in a steady decrease of relative inhibition starting with theoretical 50% at zero substrate concentration (Fig. 8b). In contrast, the

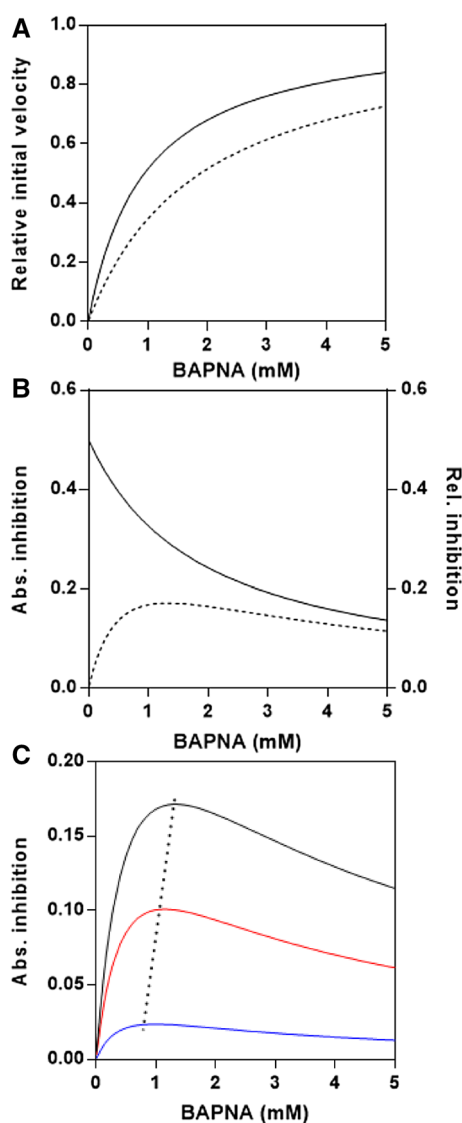


**Fig. 8** Simulated Michaelis–Menten data in the absence (solid line) and in the presence of inhibitor at  $IC_{50}$  concentration (dashed line) (a).  $V_{max}$  was chosen to be 1 and  $K_M=0.94$  mM [12]. The binding constant of the inhibitor was assumed to equal the determined  $IC_{50}$  value of 100  $\mu$ M to a first approximation. Absolute and relative inhibition as a function of substrate concentration calculated from the Michaelis–Menten data (b). Absolute inhibition in the presence of different inhibitor concentrations ( $IC_{50}$  black line,  $0.5 IC_{50}$  red line, and  $0.1 IC_{50}$  blue line) (c). The dotted line in c illustrates the shift of maximum absolute inhibition to lower substrate concentrations when smaller inhibitor concentrations are applied

absolute inhibition increases at substrate concentrations below 1 mM (Fig. 8b). The maximum of absolute inhibition occurs at a substrate concentration of approximately  $K_M$ , when the  $IC_{50}$  concentration inhibitor is applied. At this concentration the biggest difference can be measured between enzyme activity in the absence and the presence of inhibitor. However, screening assays should be sufficiently sensitive for lower concentrations of weak compounds, since

novel pharmacophores often have low activity and must be optimized by means of medicinal chemistry. But such new chemical entities are of greatest interest, because they enable freedom to operate and filing new patents. Therefore, the impact of lower inhibitor concentrations on the response absolute inhibition was analyzed (Fig. 8c). There are essentially two consequences: first, the difference between enzyme activity in the absence and presence of inhibitor becomes smaller; and second, the maximum shifts to lower substrate concentration when the inhibitor concentration is decreased. Therefore, the task of assay optimization is seeking a compromise between a well-performing signal at higher substrate concentrations and sensitivity to identify weak inhibitors at lower substrate concentrations. This is reflected by substrate concentrations between  $1/3$  and  $1 K_M$ , which are usually chosen for HTS campaigns.

## Conclusion

Statistical design of experiments is a well-established method in a broad variety of applications. Here, we present a practical course for master's students on this subject. The students learn the basics and the general use of DOE and apply the method to the optimization of an enzyme activity assay with special emphasis on pharmaceutical HTS. The students learn to identify and remove systematic technical and statistical outliers and dissect the influence of pH, trypsin concentration, and substrate concentration on the absolute and relative inhibition of the enzyme. Data analysis reveals the most important factors and factor interactions. The seemingly contradictory opposite dependency of absolute and relative inhibition is resolved by a comparison of experimental data with simulated data based on Michael–Menten theory. In the last part, simulated data are used to provide expectations about the best substrate concentration for a sensitive screening assay. On the basis of experimental data and simulations, the students get a quantitative comprehension about the most adequate substrate concentration, which must be carefully chosen on the basis of a trade-off between performance in terms of measurement signal, in our example absolute inhibition, and sensitivity for compounds with low inhibitory activity. The acquired knowledge provides not only deep insight in the world of drug discovery but also serves as a solid basis for the optimization of processes and products in many other application areas.

## References

1. Snedecor GW (1956) Statistical methods applied to experiments in agriculture and biology, 5th edn. Iowa State University Press, Ames

2. Mason RL, Gunst RF, Hess JL (2003) *Statistical design and analysis of experiments: with applications to engineering and science*, vol 474. Wiley, New York
3. John PW (1998) *Statistical design and analysis of experiments*. SIAM, Philadelphia
4. Rekab K, Shaikh M (2005) *Statistical design of experiments with engineering applications*. CRC, Boca Raton
5. Tye H (2004) Application of statistical ‘design of experiments’ methods in drug discovery. *Drug Discov Today* 9(11):485–491. [https://doi.org/10.1016/S1359-6446\(04\)03086-7](https://doi.org/10.1016/S1359-6446(04)03086-7)
6. Coussens NP, Sittampalam GS, Guha R, Brimacombe K, Grossman A, Chung TDY, Weidner JR, Riss T, Trask OJ, Auld D, Dahlin JL, Devanaryan V, Foley TL, McGee J, Kahl SD, Kales SC, Arkin M, Baell J, Bejcek B, Gal-Edd N, Glicksman M, Haas JV, Iversen PW, Hoepfner M, Lathrop S, Sayers E, Liu H, Trawick B, McVey J, Lemmon VP, Li Z, McManus O, Minor L, Napper A, Wildey MJ, Pacifici R, Chin WW, Xia M, Xu X, Lal-Nag M, Hall MD, Michael S, Inglese J, Simeonov A, Austin CP (2018) Assay guidance manual: quantitative biology and pharmacology in preclinical drug discovery. *Clin Transl Sci* 11(5):461–470. <https://doi.org/10.1111/cts.12570>
7. Box GE, Draper NR (1987) *Empirical model-building and response surfaces*. Wiley, New York
8. Box GE, Behnken DW (1960) Some new three level designs for the study of quantitative variables. *Technometrics* 2(4):455–475
9. Massart DL, Vandeginste BG, Buydens L, De Jong S, Lewi PJ, Smeyers-Verbeke J, Mann CK (1998) *Handbook of chemometrics and qualimetrics: part A*. *Appl Spectrosc* 52:302A
10. de Aguiar PF, Bourguignon B, Khots M, Massart D, Phan-Thau-Luu R (1995) D-optimal designs. *Chemometr Intell Lab Syst* 30(2):199–210
11. Sipos T, Merkel JR (1970) Effect of calcium ions on the activity, heat stability, and structure of trypsin. *Biochemistry* 9(14):2766–2775. <https://doi.org/10.1021/bi00816a003>
12. Erlanger BF, Kokowsky N, Cohen W (1961) The preparation and properties of two new chromogenic substrates of trypsin. *Arch Biochem Biophys* 95:271–278. [https://doi.org/10.1016/0003-9861\(61\)90145-x](https://doi.org/10.1016/0003-9861(61)90145-x)

**Publisher’s Note** Springer Nature remains neutral with regard to jurisdictional claims in published maps and institutional affiliations.

---

## Methionine 274 Is Not the Determining Factor for Selective Inhibition of Histone Deacetylase 8 (HDAC8) by L-Shaped Inhibitors

### **Autoren:**

Niklas Jänsch, Kim Leoni Lang, Franz-Josef Meyer-Almes

### **Bibliographische Daten:**

International Journal of Molecular Sciences (doi.org/10.3390/ijms231911775)

### **Zusammenfassung:**

HDAC8 ist ein wichtiges Ziel in mehreren Indikationsbereichen, darunter Neuroblastomen bei Kindern. Es wurden mehrere Isoenzym-selektive Inhibitoren von HDAC8 mit L-förmigen Strukturen entwickelt. Eine theoretische Studie legt nahe, dass Methionin 274 (M274) als "Schalter" fungieren könnte, der eine transiente Bindungstasche steuert, die bei der Bindung von L-förmigen Inhibitoren induziert wird. Diese Hypothese wurde in dieser Studie experimentell untersucht. Die Thermostabilität und Funktionalität von HDAC8-Wildtyp und mutierten Varianten mit ausgetauschtem M274 wurden mit biophysikalischen Methoden analysiert. Darüber hinaus wurde die Bindungskinetik von L-förmigen und linearen Referenzinhibitoren dieser HDAC8-Varianten bestimmt, um die Art der Interaktion aufzuklären. Der Austausch von M274 hat einen erheblichen Einfluss auf die Enzymaktivität, ist aber nicht der entscheidende Faktor für die selektive Erkennung von HDAC8 durch L-förmige Inhibitoren.



Article

# Methionine 274 Is Not the Determining Factor for Selective Inhibition of Histone Deacetylase 8 (HDAC8) by L-Shaped Inhibitors

Niklas Jänsch, Kim Leoni Lang and Franz-Josef Meyer-Almes \*

Department of Chemical Engineering and Biotechnology, University of Applied Sciences Darmstadt, Haardtring 100, 64295 Darmstadt, Germany

\* Correspondence: franz-josef.meyer-almes@h-da.de

**Abstract:** HDAC8 is an important target in several indication areas including childhood neuroblastoma. Several isozyme selective inhibitors of HDAC8 with L-shaped structures have been developed. A theoretical study has suggested that methionine 274 (M274) would act as a “switch” that controls a transient binding pocket, which is induced upon binding of L-shaped inhibitors. This hypothesis was experimentally examined in this study. The thermostability and functionality of HDAC8 wildtype and mutant variants with exchanged M274 were analyzed using biophysical methods. Furthermore, the binding kinetics of L-shaped and linear reference inhibitors of these HDAC8 variants were determined in order to elucidate the mode of interaction. Exchange of M274 has considerable impact on enzyme activity, but is not the decisive factor for selective recognition of HDAC8 by L-shaped inhibitors.

**Keywords:** HDAC inhibitors; binding selectivity; thermo stability; HDAC8 muteins



**Citation:** Jänsch, N.; Lang, K.L.; Meyer-Almes, F.-J. Methionine 274 Is Not the Determining Factor for Selective Inhibition of Histone Deacetylase 8 (HDAC8) by L-Shaped Inhibitors. *Int. J. Mol. Sci.* **2022**, *23*, 11775. <https://doi.org/10.3390/ijms231911775>

Academic Editors: Wolfgang Sippl and Hany S. Ibrahim

Received: 13 September 2022

Accepted: 28 September 2022

Published: 4 October 2022

**Publisher's Note:** MDPI stays neutral with regard to jurisdictional claims in published maps and institutional affiliations.



**Copyright:** © 2022 by the authors. Licensee MDPI, Basel, Switzerland. This article is an open access article distributed under the terms and conditions of the Creative Commons Attribution (CC BY) license (<https://creativecommons.org/licenses/by/4.0/>).

## 1. Introduction

Epigenetic regulation by acetylation and deacetylation of proteins is an important mechanism by which living cells control essential cellular processes. Initial observations have indicated that histones can be acetylated and thereby modulate chromatin structure and gene expression. This has stimulated comprehensive research focusing on the actors responsible for posttranslational modifications and especially the acetylation of histones. The acetylation state of histones and other proteins in cells is reversible and depends on a dedicated balance of acetylation maintained by acetyltransferases and deacetylation by the action of histone deacetylases. Proteome analyses revealed that protein acetylation is not focused on histone class, but rather involves thousands of proteins in all cellular compartments, suggesting that acetylation is a common mechanism by which cellular processes are controlled, very similar to protein phosphorylation [1,2] Therefore, it is no surprise that deregulation of protein acetylation is associated with multiple diseases, including cancer [3–5] as probably the most important indication area, and also neurological and neurodegenerative diseases [6,7] Human histone deacetylase 8 (HDAC8) is a zinc-dependent member of HDAC class I, which deacetylates numerous substrates in the nucleus and cytoplasm [8–10], and is a proven target for childhood neuroblastoma [11]. Selective inhibition of HDAC8 caused strong anti-neuroblastoma effects without toxicity in xenograft mouse models [11]. This observation stimulated the development of several selective HDAC8 inhibitors (Figure 1).

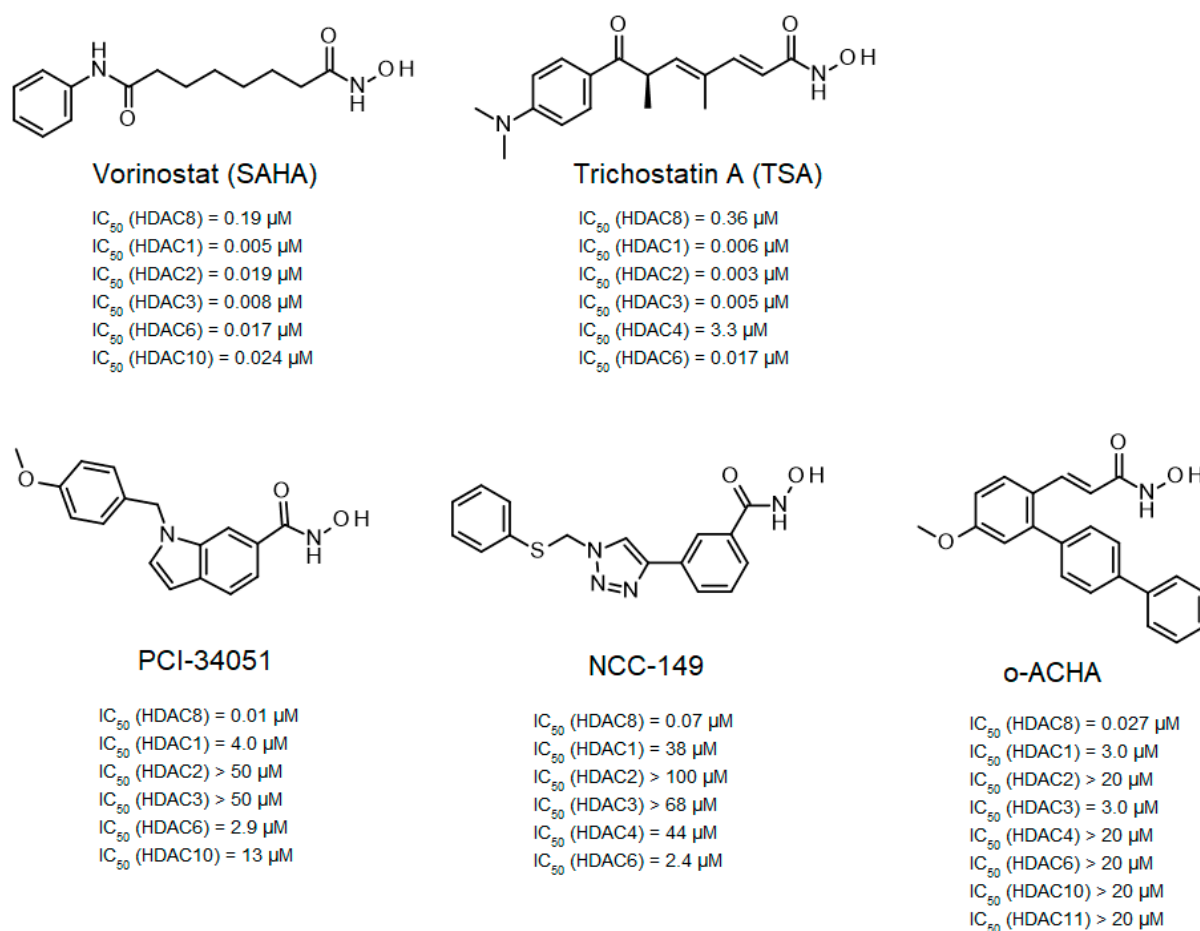


**Figure 1.** Structures of linear and L-shaped HDAC inhibitors used in this study. IC<sub>50</sub>-values of SAHA and PCI-34051 are from Balasubramanian et al. [12], NCC-149 from Suzuki et al. [13], and o-ACHA from Huang et al. [14].

Among the first inhibitors found to have extraordinary selectivity for HDAC8 were PCI-34051 and NCC-149 [12,13]. The hydroxamic acid PCI-34051 has an IC<sub>50</sub>-value of 10 nM and a selectivity more than 200-fold higher than other HDAC isozymes. Consequently, PCI-34051 has been the most commonly used reference compound for studying the biological role of HDAC8 in cellular systems [11,15–17]. Huang et al. developed branched ortho-aryl-N-hydroxycinnamides as HDAC8-selective inhibitors, including o-ACHA which inhibits HDAC8 with an activity similar to PCI-34051 and has antiproliferative effects against several cancer cell lines [14]. In contrast, most linear hydroxamic acid HDAC inhibitors, including clinically approved suberoylanilide hydroxamic acid (SAHA, vorinostat) and trichostatin A (TSA), are unspecific pan-inhibitors effecting more or less all zinc-dependent HDACs. It appears that many HDAC8-selective inhibitors have L-shaped forms [12,13,18,19]. This particular aspect was investigated in a comprehensive study by Marek et al., who showed that HDAC8-selective inhibitors adopt an L-shaped conformation when binding to a HDAC8-specific pocket between Y306 and the L1 and L6 loops [20]. Crystal structures of complexes between selective inhibitors and HDAC8 from *Schistosoma mansoni* (smHDAC8) showed preferential molecular interactions with the catalytic tyrosine (corresponding to Y306 in human HDAC8) and the L6 loop, which is more flexible than the L1 loop. Although HDAC8 from *Schistosoma mansoni* (smHDAC8) shares only 41% sequence identity with human HDAC8, both structures show a very high degree of overlap, and the active site differs only by one amino acid in the L6 loop, where H292 in smHDAC8 corresponds to M274 in human HDAC8. L-shaped inhibitors show very similar binding

poses in wildtype smHDAC8 and “humanized” mutant variant smHDAC8<sub>H292M</sub> [20]. In other HDAC isozymes, a L1–L6 lock sterically prevents L-shaped inhibitor binding, which might explain why L-shaped inhibitors preferentially bind to HDAC8. In a computational study using flexible docking and molecular dynamics simulations, Yao et al. suggested that the flexibility of methionine 274 (M274) and the L-shaped structure of inhibitors might be the most important determinants for selective inhibition of HDAC8 [21]. Binding of L-shaped inhibitors was proposed to induce a conformational change of M274 from flipped-out to flipped-in conformation, which should open the HDAC8-selective pocket. In other HDAC isozymes, methionine is replaced by leucine, which lacks the flexibility of M274 in molecular dynamics simulations. Consequently, L-shaped inhibitors were assumed to be unable to induce opening of the selectivity pocket between the L1 and L6 loops [21]. Since selective L-shaped inhibitors bind in very similar poses to wildtype smHDAC8 and smHDAC8<sub>H292M</sub> in crystal structures, where the critical H292 is exchanged with methionine [20], it appears disputable whether the postulated function of this amino acid as a pivotal switch to control the exposure of the selective sub-pocket would be the determining mechanism for selective HDAC8 inhibition. To clarify the role of M274 in isozyme-selective HDAC8 inhibition, we performed a comprehensive series of experiments to investigate the functionality, thermostability, and ligand binding of human HDAC8 wildtype and mutant variants. herein the experiments, M274 was exchanged by either leucine, which is conserved among most other human HDAC isozymes, or alanine, which is thought to impose less steric restrictions and, therefore, should resemble a permanently open and well accessible HDAC8-selective sub-pocket.

## 2. Results and Discussion

More than 80 crystal structures of HDAC8 (54 human and 30 from *Schistosoma mansoni*) have been obtained in complex with a variety of inhibitors. However, no diffractable crystals have been obtained from the apo-enzyme, which has been attributed to the extraordinary flexibility of HDAC8 [22]. Ligand binding and enzyme activity of HDAC8 have been shown to depend largely on the flexibility of the neighboring loops [23–28]. The high malleability of the binding region allows the accommodation of ligands that are highly chemically and structurally divergent, including SAHA [25], PCI-34051 [20], tropolones [29], largazole analogs [26], 1,3-benzo-thiazine-2-thiones [17], meta-substituted benzhydroxamic acids [18], and so-called linkerless HDAC8 inhibitors [19]. Crystal structures of HDAC8 complexes with non-selective linear inhibitors showed no participation of M274 during side pocket formation [25]. By analyzing crystal structures of L-shaped inhibitors bound to smHDAC8 from *Schistosoma mansoni*, a special selective binding pocket was observed between the catalytic tyrosine and the L1–L6 loop [20]. A computational study suggested that this selective binding pocket is a transient binding pocket, which opens upon binding of L-shaped inhibitors, and is controlled by movement of M274 [21]. Moreover, this structural change was not observed when M274 was replaced by leucine in the same computational study, leading to the hypothesis that M274 is the key factor responsible for selective HDAC8 inhibition [21].

To address this important research question, mutant variants of human HDAC8 were generated using site-directed mutagenesis, where M274 was exchanged either against leucine, which is conserved in all other human zinc-dependent HDACs with exception of HDAC10 (Figure 2), or against alanine, which was chosen because of its small side chain. We measured the impact of these two mutations on the substrate conversion of the artificial substrate Boc-Lys(Ac)-AMC, using the assay developed by Werbeck et al. (Figures 3 and S1) [30,31].

The catalytic efficiency of the human wildtype HDAC8 (HDAC8<sub>wt</sub>) was determined to be  $24 \pm 3 \text{ M}^{-1} \text{ s}^{-1}$ , in agreement with the value measured by Kunze et al. under comparable conditions ( $38 \pm 4 \text{ M}^{-1} \text{ s}^{-1}$ ) [31]. By exchanging M274 to leucine, the catalytic efficiency decreased about 10-fold to a value of  $2.3 \pm 0.1 \text{ M}^{-1} \text{ s}^{-1}$ , and an exchange to alanine yielded an even higher drop of catalytic efficiency down to a value of  $0.4 \pm 0.01 \text{ M}^{-1} \text{ s}^{-1}$ ,

which was only about 1% compared with HDAC8<sub>wt</sub> activity (Figure 3D, Table S1). To check whether this dramatic change in enzyme activity was caused by changes to the structural integrity and stability of the enzyme, we analyzed thermal protein denaturation using differential scanning fluorimetry (Figure 4). There was no significant difference in protein stability between HDAC8<sub>wt</sub> and HDAC8<sub>M274L</sub>, and only slightly less stability of HDAC8<sub>M274A</sub> compared with HDAC8<sub>wt</sub>, indicating that the overall structural integrity of HDAC8<sub>wt</sub> was essentially unaffected by M274L and M274A exchanges (Figure 4A–C).

L6 loop		
	<b>smHDAC8</b>	<b>CLAT--DPHRI</b>
	<b>HDAC8</b>	<b>TIAG--DP<b>M</b>CS</b>
class I	<b>HDAC1</b>	<b>SLSG--DRLGC</b>
	<b>HDAC2</b>	<b>SLSG--DRLGC</b>
	<b>HDAC3</b>	<b>SLGC--DRLGC</b>
	<b>HDAC4</b>	<b>AVEGHPTPLGG</b>
class IIa	<b>HDAC5</b>	<b>AVEGHLSP LGG</b>
	<b>HDAC7</b>	<b>AAEGHPAP LGG</b>
	<b>HDAC9</b>	<b>ALEGHTPP LGG</b>
class IIb	<b>HDAC6-CD2</b>	<b>AARG--DPLGG</b>
	<b>HDAC10</b>	<b>SAIG--DPEGO</b>
class IV	<b>HDAC11</b>	<b>ILEG--DRLGG</b>

**Figure 2.** Multiple sequence alignment of the L6 loop across all human zinc-dependent HDAC isozymes and smHDAC8 from *Schistosoma mansoni*. M274 of human HDAC8 is highlighted in bold and red.

The dramatic differences in catalytic efficiencies reflect altered substrate recognition and turnover numbers, and might also have been caused by subtle structural changes of the active site. More specifically, M274 appears to be important for the recognition and turnover of the artificial substrate Boc-Lys(Ac)-AMC, and is probably an important determinant for the spectrum of HDAC8-specific substrates in vivo.

Next, we investigated how the exchange of M274 to leucine and alanine impacted the binding behavior of a selection of commonly used and well-studied linear inhibitors (SAHA, TSA), as well as L-shaped inhibitors (PCI-34051, NCC-149, and o-ACHA), which are known to be HDAC8-selective [20]. We measured IC<sub>50</sub> values of selected inhibitors against HDAC8<sub>wt</sub> and mutant variants HDAC8<sub>M274L</sub> and HDAC8<sub>M274A</sub> (Table S2). Interestingly, linear and L-shaped inhibitors showed very similar inhibition patterns against all HDAC8 variants (Figure 5B). To our surprise, the IC<sub>50</sub> values between HDAC8<sub>wt</sub> and HDAC8<sub>M274L</sub> showed no significant differences (Figures 5 and S2).

This observation contradicted the postulation of a computational study which suggested that leucine instead of methionine is unable to act as a switch that opens a side pocket for the binding of HDAC8-selective L-shaped inhibitors [21]. We anticipated that the replacement of methionine by the smaller amino acid alanine in HDAC8<sub>M274A</sub> would create a constitutively open HDAC8-selective pocket between the L1- and L6-loop, with facilitated access for L-shaped inhibitors. Contrary to our expectation, IC<sub>50</sub>-values of all inhibitors, no matter whether linear or L-shaped, were about 10-fold higher than for HDAC8<sub>wt</sub> or HDAC8<sub>M274L</sub> (Figures 5B and S2), suggesting enforced hydrophobic interactions between inhibitors and M274. These hydrophobic interactions might also be formed when M274 is replaced by leucine with a similar hydrophobic side chain, but not by the much smaller alanine at this position. These findings clearly show that M274 is involved in general inhibitor binding, but disprove a pivotal role for M274 as a “switch” for the selective inhibition of HDAC8 by L-shaped inhibitors.

To support the observations made by IC<sub>50</sub> measurements, we tested for thermal stabilization of all HDAC8 variants in the presence of linear and L-shaped inhibitors (Figure 5). Thermal shifts were calculated by the difference between the first and second melting events. We assumed that the second melting event involved the ligand-stabilized



protein, because this event only occurs in the presence of a ligand (Figures 4D and S3). The first melting event was mainly unaffected by ligand addition, and resulted in the value for the protein without ligand. In agreement with the  $IC_{50}$  results, we saw no differences in the thermal shifts of HDAC8<sub>wt</sub> or HDAC8<sub>M274L</sub> in the presence of inhibitors, whether L-shaped or linear (Figures 4E and S2). Furthermore, we confirmed the increase in  $IC_{50}$  for the HDAC8<sub>M274A</sub> variant, which showed smaller thermal shifts. HDAC8<sub>M274A</sub> is about 4–6 °C less stabilized by ligand addition than either the wild type or the leucine mutant variant. These results support the enzyme activity data that was obtained, and demonstrate that the interaction between HDAC8<sub>M274A</sub> and inhibitors was weakened with respect to HDAC8<sub>wt</sub>.

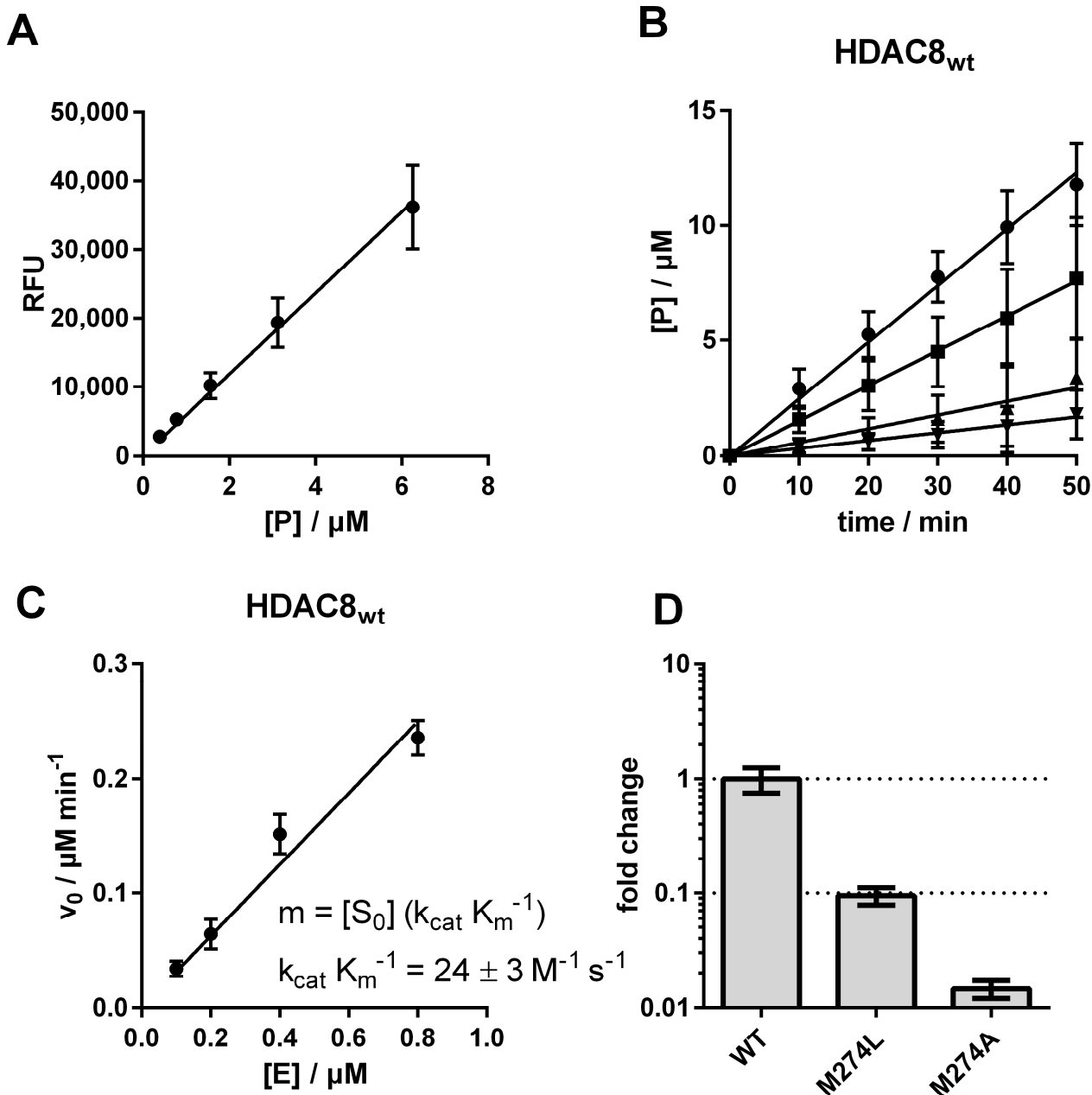


**Figure 3.** Determination of catalytic efficiencies for HDAC8. (A) Product calibration using free AMC. (B) Progress curves for the conversion of 200  $\mu\text{M}$  of the artificial substrate Boc-Lys(Ac)-AMC by  $\bullet$  0.8  $\mu\text{M}$ ,  $\blacksquare$  0.4  $\mu\text{M}$ ,  $\blacktriangle$  0.2  $\mu\text{M}$ , and  $\blacktriangledown$  0.1  $\mu\text{M}$  HDAC8<sub>wt</sub>. (C) Plot of initial velocity against enzyme concentration. (D) Comparison of the catalytic efficiencies. Data show mean values and standard deviations,  $n \geq 3$ .

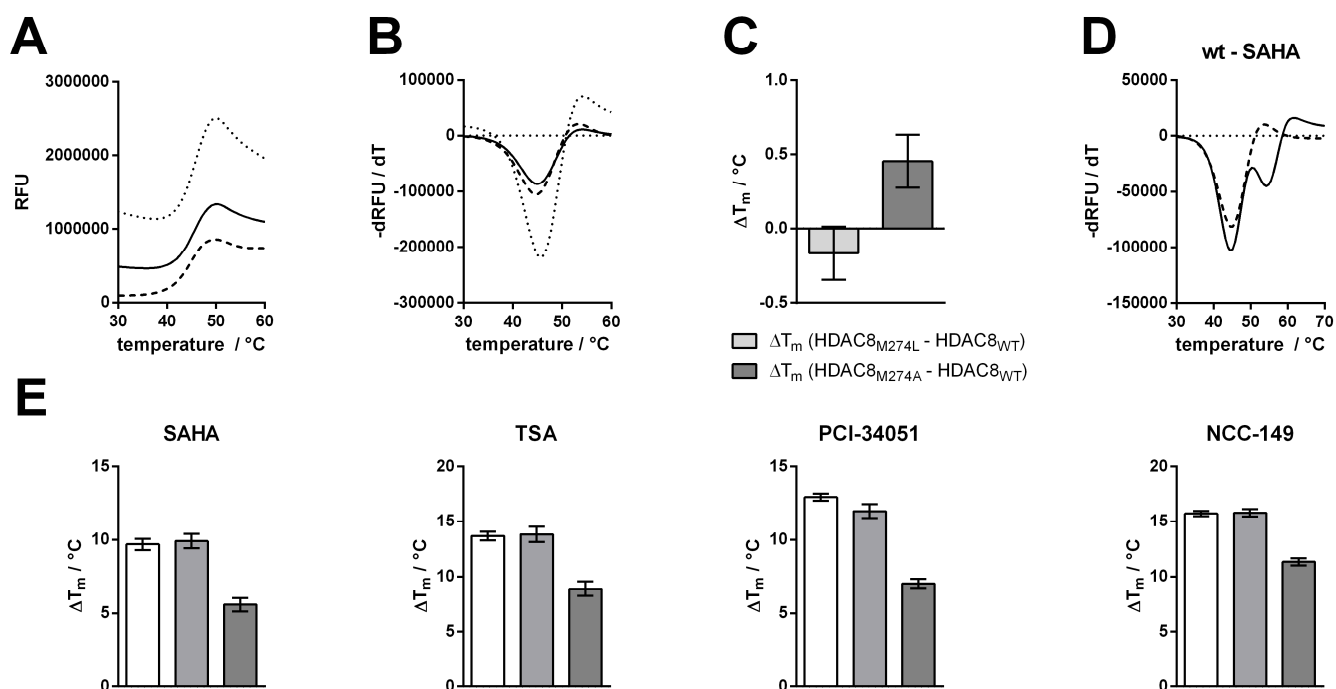


**Figure 4.** Determination of protein melting points and thermal shift assay. (A) Raw fluorescence data for the thermal denaturation of HDAC8<sub>wt</sub> (meshed line), HDAC8<sub>M274L</sub> (solid line), and HDAC8<sub>M274A</sub> (dotted line). (B) First derivative for the thermal denaturation of HDAC8<sub>wt</sub> (meshed line), HDAC8<sub>M274L</sub> (solid line), and HDAC8<sub>M274A</sub> (dotted line). (C) Comparison of  $T_m$  values between the mutant variants and the wild type. (D) Thermal shift assay showing unbound HDAC8<sub>wt</sub> (meshed line) and SAHA-bound HDAC8<sub>wt</sub> (solid line). (E) Thermal shifts for SAHA, TSA, PCI-34051, and NCC-149 for HDAC8<sub>wt</sub> (white bar), HDAC8<sub>M274L</sub> (light gray bar), and HDAC8<sub>M274A</sub> (dark gray bar). For the thermal shift assay, 12.5  $\mu$ M HDAC8 and 125  $\mu$ M of indicated inhibitor were used. Data show mean values and standard deviations,  $n \geq 3$ .

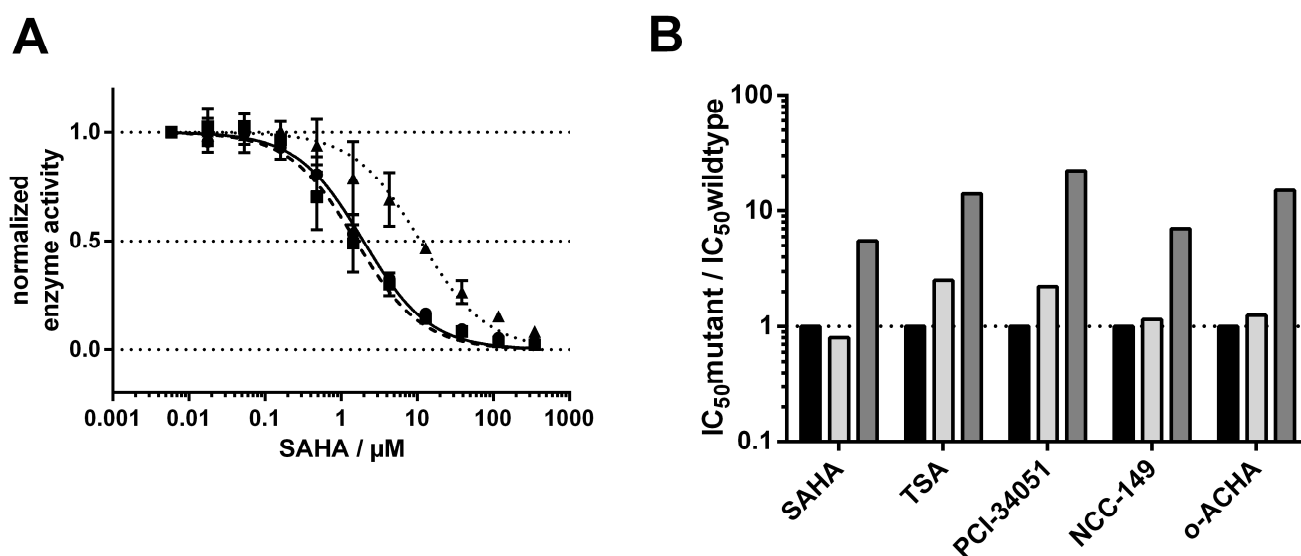


**Figure 5.** IC<sub>50</sub> determination and comparison. (A) Dose-response curve for the IC<sub>50</sub> determination of SAHA for HDAC8<sub>wt</sub> (●, solid line), HDAC8<sub>M274L</sub> (■, meshed line), and HDAC8<sub>M274A</sub> (▲, dotted line). (B) Comparison of IC<sub>50</sub> values for different linear and L-shaped inhibitors for HDAC8<sub>wt</sub> (black bar), HDAC8<sub>M274L</sub> (light gray bar), and HDAC8<sub>M274A</sub> (dark gray bar).

Taken together, the data show that M274 is not the sole determining factor for selective binding of L-shaped inhibitors to HDAC8. In particular, M274 does not control the exposure of the HDAC8-selective pocket.

We further investigated the accessibility of the binding pocket by using stopped-flow experiments, and measured the rate constants for the binding of representative linear (TSA) and L-shaped (NCC-149) inhibitors to HDAC8<sub>wt</sub> and HDAC8<sub>M274A</sub>. Because the active site of HDAC8 is flanked by three tryptophane residues, it is possible to measure a decrease in intrinsic fluorescence upon binding of a ligand to the active site. In theory, and under the assumption that M274 acts a gatekeeper for a transient binding pocket, the rate of the interaction depends on the movement of M274. Therefore, the interaction must be slower for HDAC8<sub>wt</sub> than for the HDAC8<sub>M274A</sub> mutant variant in which the postulated transient binding pocket is supposed constitutively open. Similar to the enzyme activity and protein stabilization experiments, there were no qualitative differences between the binding kinetics of linear and L-shaped inhibitors to HDAC8<sub>wt</sub> and HDAC8<sub>M274A</sub>. However, we observed faster association rates for the binding of the inhibitors TSA and NCC-149 to HDAC8<sub>wt</sub>, compared with binding to HDAC8<sub>M274A</sub>, which was in contrast to our expectations noted above (Figures 6 and S4). Thus, the association rate seems to reflect the lower affinity of all investigated inhibitors to HDAC8<sub>M274A</sub> compared with HDAC8<sub>wt</sub>, and does not support the suggestion of M274 barring the access of L-shaped inhibitors to the HDAC8-selective sub-pocket.

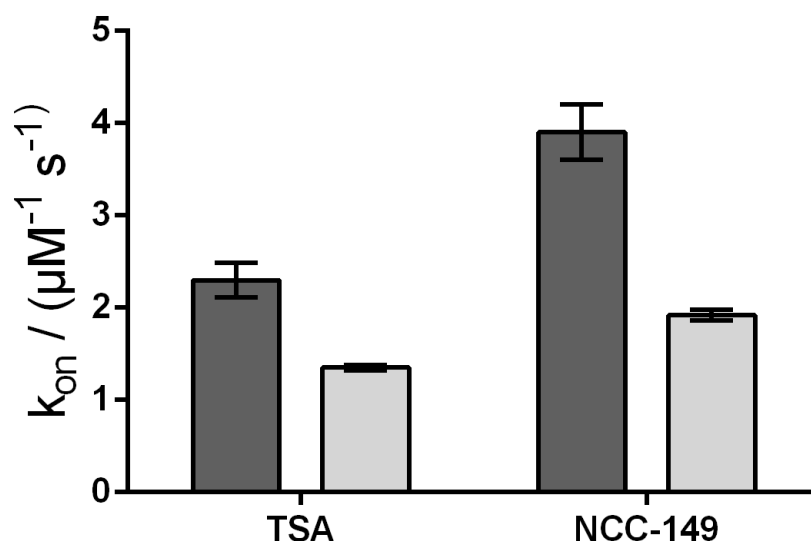


**Figure 6.** Comparison of the rate constants of association for TSA and NCC-149 between HDAC8<sub>wt</sub> (dark gray bars) and HDAC8<sub>M274A</sub> (light gray bars). Rate constants were determined by stopped-flow kinetics.

#### *Flexibility around Binding Pocket of HDAC8*

The extraordinary flexibility of loops around the active site is a specific feature of HDAC8. Different ligands induce alternative conformations of the L1 and L2 loop flanking the active site [25,26]. The active site binding pocket in an HDAC8-inhibitor complex can change from a narrow channel (PDB-ID 1T69), to a sub-open conformation with a second transient pocket (PDB-ID 1T64), to a structure with a wide open funnel-shaped pocket (PDB-ID 1VKG). Along with the L1 and L2 loop, the flipping of the F152 sidechain is one of the main characteristics in the dynamic interconversion between HDAC8 conformations [25,32]. Recently deposited crystal structures of HDAC8–ligand complexes show that L-shaped inhibitors induce a pronounced flip of the F152 side chain, and M274 also appears to be flexible and to interact with a ligand in some cases (e.g. PDB-IDs 6ODA, 6ODB, 6ODC).

To gain more insight in the possible role of M274 as a molecular switch controlling the opening of the transient HDAC8 sub-pocket between L1 and L6 loops, 11 representa-

tive crystal structures of human HDAC8 and the “humanized” HDAC8 from *Schistosoma mansoni* were analyzed to assess the structural conservation of amino acids flanking the active site pocket, including P273 and M274 from the L6 loop. This analysis revealed a low average RMSD value of 0.389 Å over 10 conserved amino acids flanking the active site pocket (Figures S5 and S6), indicating that the positions of these amino acids are highly defined. However, the analysis also indicates some flexibility around the binding pocket of HDAC8, in agreement with previous studies [26,28]. As expected, a closer look at distinct amino acids revealed that the positions of catalytic and, particularly, zinc-chelating amino acids remained almost unchanged, whereas those flanking the hydrophobic binding tunnel and the L6 loop showed more flexibility (Table S3). This is in agreement with numerous observations about the high malleability of the binding site in HDAC8 [26,27]. M274 in the L6 loop demonstrates structural deviations similar to those of F152 in the canonical binding tunnel (Table S3). In similar crystal structures of HDAC8 from *Schistosoma mansoni* (smHDAC8), L-shaped inhibitors have been found to bind into the HDAC8-selective sub-pocket between the L1–L6 loop and the catalytic tyrosine. The hydroxamate group of PCI-34051 chelates the catalytic zinc ion, and the methoxyphenyl head group forms Pi–Pi interactions with Y341 (Y306 in human HDAC8) and also H292. Furthermore, the methoxy group forms non-polar contacts with the sidechain of P291 in the L6 loop [20]. If H292 is exchanged by methionine corresponding to M274 in human HDAC8, the binding mode of PCI-34051 shows only minor changes, particularly regarding contact with the L6 loop. However, the ligand retains non-polar contact with P291 and also with the sidechain of M292 (alias M274) [20]. The crystal structure of smHDAC8<sub>H292M</sub> (PDB-ID: 6HSF) is tetrameric. Interestingly, a superimposition of the four monomers gives another impressive argument for the intrinsic flexibility and adaptability to ligands of the HDAC8-selective pocket (Figure S5). The PCI-34051 ligand and the methyl group of M292 show different orientations in different monomers. The distances between the methyl carbon atoms of M292 among the four monomers vary between 0.24 and 2.2 Å. Notably, the methyl group of M292 in chain A of this crystal structure points to the closer oriented ligand, while the methyl group of M292 in chain C is moved away from the more distant ligand, demonstrating that the ligand does not necessarily push the methyl group aside (Figure S5B). To rationalize this observation, we inserted PCI-34051 ligands from chains A and C in the crystal structure of smHDAC8<sub>H292M</sub> (PDB-ID: 6HSF) into the 3D structure of human HDAC8 (PDB-ID: 1T67), and performed subsequent energy minimization to optimize the binding poses within the selective HDAC8 binding pocket between L1–L6 loops and Y306. Notably, the methyl-group in the sidechain of M274 was not pushed away by the ligand but seemed to be attracted, coming into proximity with the ligand (Figure 7).

The orientation of the methyl group towards the ligand facilitates non-covalent hydrophobic interactions, which have been observed in crystal structures of smHDAC8<sub>H292M</sub> in complex with PCI-34051 [20]. These results support our experimental data, which are in agreement with the suggestion of attracting hydrophobic interactions between M274 and active site binding inhibitors.

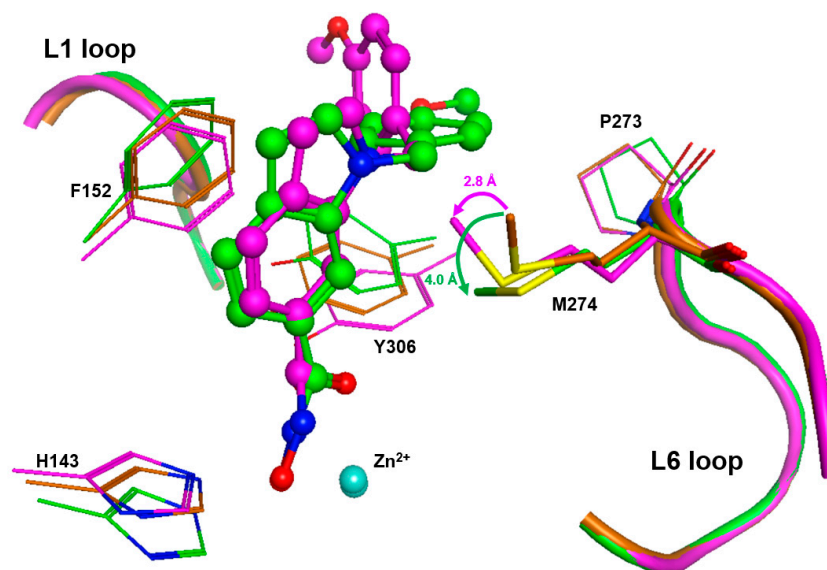


**Figure 7.** Close-up view of the binding pocket of human HDAC8. The unchanged conformation of HDAC8 (PDB-ID: 1T67, brown) is superimposed onto energy-minimized complex structures between HDAC8 (PDB-ID: 1T67) and PCI-34051 ligands (ball and sticks), with starting poses taken from tetrameric PDB-ID: 6HSF, chain A (green) and chain C (magenta). L1 and L6 loops are shown as tubes with the same color code. The catalytic zinc ions are displayed as cyan spheres. After some arrangement of the side chains of neighboring amino acids, PCI-34051 fits well into the selective HDAC8 pocket between Y306 and L1–L6 loops. Interestingly, the methyl group of M274 is not pushed away by the ligands, but is rather attracted, coming into proximity with the hydrophobic groups of the ligand.

### 3. Materials and Methods

#### 3.1. Recombinant Protein Production, Purification, and Mutant Variant Generation

pET14b vector (Novagen, EMD Millipore, Burlington, MA, USA) containing codon-optimized human HDAC8, fused to a n-terminal His6-SUMO tag, was used to express HDAC8 in *E. coli* BL21 (DE3) (New England Biolabs, Ipswich, MA, USA). Cells were grown in autoinduction media at 30 °C overnight, then harvested by centrifugation for 10 min at 8000× *g* and 4 °C. Cells were resuspended in lysis buffer (pH 8.0, 150 mM KCl, 50 mM Tris, 5 mM imidazole, 5 mM DTT, and 5 µg/mL DNaseI) and lysed by sonication. Lysates were clarified by centrifugation at 18,000× *g* and 4 °C for 30 min, then passed through a 0.45 µm PVDF syringe filter unit. Chromatography was conducted on a ÄKTA pure FPLC system (GE Healthcare). A 5 mL prepacked cComplete His tag purification column was equilibrated with 5 cv of IMAC buffer A (pH 8.0, 150 mM KCl, 50 mM Tris, and 5 mM imidazole), then the lysate was pumped over the column and washed with 10 cv IMAC buffer A. Protein was eluted using a step gradient with IMAC buffer B (pH 8.0, 150 mM KCl, 50 mM Tris, 75 mM imidazole). Fractions containing His6-SUMO-HDAC8 were pooled and 10 µg/mL His6 tagged SUMO protease was added whilst dialyzing against AIC buffer A (pH 7.0, 25 mM Tris, 50 mM NaCl) at 4 °C overnight. The dialysate was conducted to a second IMAC to remove His6-SUMO tag and His6-SUMO protease. Flow-through that contained HDAC8 was concentrated and further purified using a strong anion exchange column (MiniChrom Toyopearl GigaCap Q-650M, 5 mL, Tosoh Bioscience GmbH) and eluted with a linear gradient using AIC buffer B (pH 7.0, 25 mM Tris, 1 M NaCl). Fractions containing HDAC8 were pooled, concentrated to 1.5 mL, and 5 mM DTT was added to prevent oxidation. The final purification step included size exclusion chromatography with a HiLoad 16/600 Superdex 75 pg column (GE Healthcare, Chicago, IL, USA) equilibrated with SEC buffer (pH 8.0, 150 mM KCl, 50 mM Tris, 5% glycerol, 1 mM TCEP). The fractions containing HDAC8 were collected, concentrated, adjusted to 20 mg/mL, flash frozen with liquid nitrogen, and stored at −80 °C. Typical yields using this protocol were about 0.4%

(mass wet cell pellet/mass protein) for the wildtype HDAC8. Primers used for point mutations are listed in Table S4.

### 3.2. Michaelis-Menten Parameters

Catalytic efficiencies were determined following the protocol by Werbeck et al. [30]. The indicated concentration of HDAC8 was mixed with 200  $\mu\text{M}$  Boc-Lys(Ac)-AMC in MAL buffer (pH 8.0, 50 mM Tris, 137 mM NaCl, 2.7 mM KCl, 1 mM  $\text{MgCl}_2$ , 1 mg/mL BSA) at 20 °C. Immediately after mixing the enzyme with substrate, 50  $\mu\text{L}$  of the reaction mixture was removed and added to 50  $\mu\text{L}$  developer solution (500  $\mu\text{M}$  SAHA, 5 mg/mL trypsin in MAL buffer) for the measurement of a blank. Then, 50  $\mu\text{L}$  aliquots were removed at 10, 20, 30, 40, 50 min and added to 50  $\mu\text{L}$  developer solution. After the final timepoint, the measuring signal was developed for 15 min at 30 °C. Measurements were performed using a Pherastar fluorescence plate reader with a coumarin filter module. RFU for each timepoint were subtracted from RFU at 0 min and product concentration was calculated using external calibration of free AMC. Product concentration in  $\mu\text{M}$  was plotted against time in min, and the slope was calculated in GraphPad Prism using linear regression starting at 0/0 to yield initial velocity  $v_0$ . Then  $v_0$  was plotted against enzyme concentration and slope was again forced to go through 0/0, and was divided by initial substrate concentration to yield catalytic efficiency  $k_{\text{cat}}/K_{\text{m}}$ .

### 3.3. Protein Melting Points and Ligand Induced Thermal Stabilization

Protein melting curves were generated using the Quant Studio 5 real-time PCR system (Thermo Fisher Scientific, Waltham, MA, USA) and SYPRO orange dye. For that purpose, 0.5 mg/mL HDAC8 (12.5  $\mu\text{M}$ ) was mixed with a 10-fold concentration of SYPRO orange and 125  $\mu\text{M}$  of the indicated inhibitor in SEC buffer, then preincubated for 1 h at 30 °C. Samples were heated using a linear gradient of 0.015 °C/s. Plotted curves represent the mean of three independent measurements.

### 3.4. $\text{IC}_{50}$ Determination

Enzyme activity assay was executed in assay buffer (25 mM Tris-HCL pH 8.0, 50 mM NaCl, and 0.001 % (*v/v*) pluronic F-68) in half area 96-well black microplates (Greiner Bio-One, Solingen, Germany). For  $\text{IC}_{50}$  determination, 10 nM HDAC8 was preincubated for 1 h with a serial dilution of the indicated compounds. The enzyme reaction was initiated by the addition of 20  $\mu\text{M}$  Boc-Lys(TFA)-AMC (Bachem, Bubendorf, Switzerland). After substrate conversion at 30 °C for 1 h, the reaction was stopped by adding 1.67  $\mu\text{M}$  suberoylanilide trifluoromethylketone (SATFMK). The deacetylated substrate was cleaved with 0.42 mg/mL trypsin to release fluorescent 7-amino-4-methylcoumarin (AMC, Amsterdam, The Netherlands), which was detected with a microplate reader (PHERAstar FS or BMG LABTECH) with fluorescence excitation at 360 nm and emission at 460 nm.  $\text{IC}_{50}$  values were calculated by generating dose-response curves in GraphPad Prism, and fitting those to a 4-parameter fit model.

### 3.5. Stopped-Flow Kinetics

Binding kinetics were measured using a BioLogic SFM3000 Stopped-Flow instrument, by mixing 0.5  $\mu\text{M}$  HDAC8 with the indicated inhibitor concentrations in SEC buffer. Stopped-Flow was operated in fluorescence mode, and time-dependent change in tryptophane fluorescence was monitored over the course of 1 s with a data interval of 500 ns. Excitation wavelength was set to 281 nm with a 320 nm high pass cut-off filter. The output filter was set to 1 ms and voltage to 600. Kinetics were measured at 25 °C. Binding of inhibitors decreases the tryptophane fluorescence of HDAC8<sub>wt</sub> and mutant variants.

### 3.6. Flexibility Analysis

Eleven crystal structures of human HDAC8 in complex with different ligands (PDB-IDs 1T64, 1T67, 1T69, 1VGK, 1W22, 2V5W, 2V5X, 3F0R, 3F07, 3SFF, 5DC6), along with the

crystal structure of smHDAC8<sub>H292M</sub> from *Schistosoma mansoni* (PDB-ID 6HSF), were loaded into MOE 2020 software (Chemical Computing Group ULC, Montreal, QC, Canada) and superimposed after sequence alignment. Alignment and RMSD calculations were based on 10 conserved active site amino acids: H142, H143, F152, D178, H180, F208, D267, P273, M274 and Y306 (numbering according to human HDAC8). MOE 2020 was also employed to create the heatmap of pairwise RMSD values between these amino acids for all PDB entries. Where necessary, binding poses were energy minimized within a radius of 10 Å around the ligand, using MOE 2020 and applying an AMBER 14 forcefield.

#### 4. Conclusions

The development of isozyme-selective HDAC inhibitors is challenging because of the sequentially and structurally highly conserved active site. Recently, a HDAC8-selective side pocket between the L1 and L6 loop was identified, which is required for the binding of L-shaped HDAC8-selective inhibitors [20]. M274 is located in the L6 loop and is unique to HDAC8, since all other human zinc-dependent HDACs except HDAC10 have a leucine at this position (Figure 2). Moreover, a computational study postulated that M274 acts as a switch to open the HDAC8-selective side pocket as an essential mechanism for selective HDAC8 inhibition [21].

In this experimental study we investigated the role of M274 for substrate and inhibitor recognition, using several HDAC8 mutant variants and a combination of biochemical and biophysical methods. Replacing M274 by leucine or alanine led to a dramatic drop in catalytic efficiency, demonstrating the important role of this amino in substrate recognition and turnover. However, HDAC8<sub>wt</sub> and HDAC8<sub>M274L</sub>, which represent the active site of most other zinc-dependent HDACs, showed very similar inhibitor binding behavior for unselective linear and selective L-shaped inhibitors. Therefore, M274 is not the single and pivotal determinant for selective HDAC8 inhibition. Binding of all investigated inhibitors to HDAC8<sub>M274A</sub> with a constitutively open HDAC8-selective pocket was less potent and slower compared with binding to HDAC8<sub>wt</sub>. This finding suggests an attracting hydrophobic interaction between M274 and active site binding inhibitors, which cannot be formed with the much smaller sidechain of alanine at this position.

In summary, M274 is important for catalytic efficiency, and its hydrophobic side chain can interact with active site binders. However, M274 does not serve as the decisive factor to control the opening of a transient HDAC8-selective pocket enabling preferential binding of L-shaped inhibitors to HDAC8.

**Supplementary Materials:** The following supporting information can be downloaded at: <https://www.mdpi.com/article/10.3390/ijms231911775/s1>.

**Author Contributions:** Conceptualization, F.-J.M.-A.; Data curation, N.J.; Formal analysis, N.J.; Funding acquisition, F.-J.M.-A.; Investigation, N.J. and K.L.L.; Supervision, F.-J.M.-A.; Writing—original draft, N.J.; Writing—review & editing, F.-J.M.-A. All authors have read and agreed to the published version of the manuscript.

**Funding:** This research was supported by the LOEWE priority program TRABITA, State of Hesse, Germany (to FJMA).

**Data Availability Statement:** All supporting information is provided in the submitted Supplementary Materials.

**Conflicts of Interest:** The authors declare no conflict of interest.

#### References

1. Choudhary, C.; Kumar, C.; Gnad, F.; Nielsen, M.L.; Rehman, M.; Walther, T.C.; Olsen, J.V.; Mann, M. Lysine acetylation targets protein complexes and co-regulates major cellular functions. *Science* **2009**, *325*, 834–840. [[CrossRef](#)] [[PubMed](#)]
2. Scholz, C.; Weinert, B.T.; Wagner, S.A.; Beli, P.; Miyake, Y.; Qi, J.; Jensen, L.J.; Streicher, W.; McCarthy, A.R.; Westwood, N.J.; et al. Acetylation site specificities of lysine deacetylase inhibitors in human cells. *Nat. Biotechnol.* **2015**, *33*, 415–423. [[CrossRef](#)] [[PubMed](#)]

3. Goutas, D.; Theocharis, S.; Tsourouflis, G. Unraveling the Epigenetic Role and Clinical Impact of Histone Deacetylases in Neoplasia. *Diagnostics* **2021**, *11*, 1346. [[CrossRef](#)] [[PubMed](#)]
4. Sun, Y.; Lu, F.; Sun, Y.; Yue, S.; Wang, Y. Histone Deacetylase Inhibitors in Cancer Therapy. *Curr. Top. Med. Chem.* **2018**. [[CrossRef](#)]
5. Chakrabarti, A.; Melesina, J.; Kolbinger, F.R.; Oehme, I.; Senger, J.; Witt, O.; Sippl, W.; Jung, M. Targeting histone deacetylase 8 as a therapeutic approach to cancer and neurodegenerative diseases. *Future Med. Chem.* **2016**, *8*, 1609–1634. [[CrossRef](#)]
6. Wang, X.; Liu, J.; Zhen, J.; Zhang, C.; Wan, Q.; Liu, G.; Wei, X.; Zhang, Y.; Wang, Z.; Han, H.; et al. Histone deacetylase 4 selectively contributes to podocyte injury in diabetic nephropathy. *Kidney Int.* **2014**, *86*, 712–725. [[CrossRef](#)]
7. Mielcarek, M.; Zielonka, D.; Carnemolla, A.; Marcinkowski, J.T.; Guidez, F. HDAC4 as a potential therapeutic target in neurodegenerative diseases: A summary of recent achievements. *Front. Cell. Neurosci.* **2015**, *9*, 42. [[CrossRef](#)]
8. Deardorff, M.A.; Bando, M.; Nakato, R.; Watrin, E.; Itoh, T.; Minamino, M.; Saitoh, K.; Komata, M.; Katou, Y.; Clark, D.; et al. HDAC8 mutations in Cornelia de Lange syndrome affect the cohesin acetylation cycle. *Nature* **2012**, *489*, 313–317. [[CrossRef](#)]
9. Wilson, B.J.; Tremblay, A.M.; Deblois, G.; Sylvain-Drolet, G.; Giguère, V. An acetylation switch modulates the transcriptional activity of estrogen-related receptor alpha. *Mol. Endocrinol.* **2010**, *24*, 1349–1358. [[CrossRef](#)]
10. Olson, D.E.; Udeshi, N.D.; Wolfson, N.A.; Pitcairn, C.A.; Sullivan, E.D.; Jaffe, J.D.; Svinkina, T.; Natoli, T.; Lu, X.; Paulk, J.; et al. An unbiased approach to identify endogenous substrates of “histone” deacetylase 8. *ACS Chem. Biol.* **2014**, *9*, 2210–2216. [[CrossRef](#)]
11. Rettig, I.; Koeneke, E.; Trippel, F.; Mueller, W.C.; Burhenne, J.; Kopp-Schneider, A.; Fabian, J.; Schober, A.; Fernekorn, U.; von Deimling, A.; et al. Selective inhibition of HDAC8 decreases neuroblastoma growth in vitro and in vivo and enhances retinoic acid-mediated differentiation. *Cell Death Dis.* **2015**, *6*, e1657. [[CrossRef](#)] [[PubMed](#)]
12. Balasubramanian, S.; Ramos, J.; Luo, W.; Sirisawad, M.; Verner, E.; Buggy, J.J. A novel histone deacetylase 8 (HDAC8)-specific inhibitor PCI-34051 induces apoptosis in T-cell lymphomas. *Leukemia* **2008**, *22*, 1026–1034. [[CrossRef](#)] [[PubMed](#)]
13. Suzuki, T.; Muto, N.; Bando, M.; Itoh, Y.; Masaki, A.; Ri, M.; Ota, Y.; Nakagawa, H.; Iida, S.; Shirahige, K.; et al. Design, synthesis, and biological activity of NCC149 derivatives as histone deacetylase 8-selective inhibitors. *ChemMedChem* **2014**, *9*, 657–664. [[CrossRef](#)]
14. Huang, W.J.; Wang, Y.C.; Chao, S.W.; Yang, C.Y.; Chen, L.C.; Lin, M.H.; Hou, W.C.; Chen, M.Y.; Lee, T.L.; Yang, P.; et al. Synthesis and biological evaluation of ortho-aryl N-hydroxycinnamides as potent histone deacetylase (HDAC) 8 isoform-selective inhibitors. *ChemMedChem* **2012**, *7*, 1815–1824. [[CrossRef](#)] [[PubMed](#)]
15. Dasgupta, T.; Antony, J.; Braithwaite, A.W.; Horsfield, J.A. HDAC8 Inhibition Blocks SMC3 Deacetylation and Delays Cell Cycle Progression without Affecting Cohesin-dependent Transcription in MCF7 Cancer Cells. *J. Biol. Chem.* **2016**, *291*, 12761–12770. [[CrossRef](#)]
16. Hsieh, C.L.; Ma, H.P.; Su, C.M.; Chang, Y.J.; Hung, W.Y.; Ho, Y.S.; Huang, W.J.; Lin, R.K. Alterations in histone deacetylase 8 lead to cell migration and poor prognosis in breast cancer. *Life Sci.* **2016**, *151*, 7–14. [[CrossRef](#)]
17. Wolff, B.; Jansch, N.; Sugiarto, W.O.; Fruhschulz, S.; Lang, M.; Altintas, R.; Oehme, I.; Meyer-Almes, F.J. Synthesis and structure activity relationship of 1, 3-benzo-thiazine-2-thiones as selective HDAC8 inhibitors. *Eur. J. Med. Chem.* **2019**, *184*, 111756. [[CrossRef](#)]
18. Heimburg, T.; Kolbinger, F.R.; Zeyen, P.; Ghazy, E.; Herp, D.; Schmidtkunz, K.; Melesina, J.; Shaik, T.B.; Erdmann, F.; Schmidt, M.; et al. Structure-Based Design and Biological Characterization of Selective Histone Deacetylase 8 (HDAC8) Inhibitors with Anti-Neuroblastoma Activity. *J. Med. Chem.* **2017**, *60*, 10188–10204. [[CrossRef](#)]
19. KrennHrubec, K.; Marshall, B.L.; Hedglin, M.; Verdin, E.; Ulrich, S.M. Design and evaluation of ‘Linkerless’ hydroxamic acids as selective HDAC8 inhibitors. *Bioorg. Med. Chem. Lett.* **2007**, *17*, 2874–2878. [[CrossRef](#)]
20. Marek, M.; Shaik, T.B.; Heimburg, T.; Chakrabarti, A.; Lancelot, J.; Ramos Morales, E.; Da Veiga, C.; Kalinin, D.V.; Melesina, J.; Robaa, D.; et al. Characterization of histone deacetylase 8 (HDAC8) selective inhibition reveals specific active site structural and functional determinants. *J. Med. Chem.* **2018**. [[CrossRef](#)]
21. Yao, P.; Gao, Q.; Wang, Y.; Yao, Q.; Zhang, J. Mechanistic Exploration of Methionine 274 Acting as a “Switch” of the Selective Pocket Involved in HDAC8 Inhibition: An in Silico Study. *ChemMedChem* **2021**, *16*, 1933–1944. [[CrossRef](#)] [[PubMed](#)]
22. Dowling, D.P.; Gantt, S.L.; Gattis, S.G.; Fierke, C.A.; Christianson, D.W. Structural Studies of Human Histone Deacetylase 8 and Its Site-Specific Variants Complexed with Substrate and Inhibitors. *Biochemistry* **2008**, *47*, 13554–13563. [[CrossRef](#)] [[PubMed](#)]
23. Decroos, C.; Christianson, N.H.; Gullett, L.E.; Bowman, C.M.; Christianson, K.E.; Deardorff, M.A.; Christianson, D.W. Biochemical and Structural Characterization of HDAC8 Mutants Associated with Cornelia de Lange Syndrome Spectrum Disorders. *Biochemistry* **2015**, *54*, 6501–6513. [[CrossRef](#)]
24. Decroos, C.; Bowman, C.M.; Moser, J.-A.S.; Christianson, K.E.; Deardorff, M.A.; Christianson, D.W. Compromised Structure and Function of HDAC8 Mutants Identified in Cornelia de Lange Syndrome Spectrum Disorders. *ACS Chem. Biol.* **2014**. [[CrossRef](#)]
25. Somoza, J.R.; Skene, R.J.; Katz, B.A.; Mol, C.; Ho, J.D.; Jennings, A.J.; Luong, C.; Arvai, A.; Buggy, J.J.; Chi, E.; et al. Structural snapshots of human HDAC8 provide insights into the class I histone deacetylases. *Structure* **2004**, *12*, 1325–1334. [[CrossRef](#)] [[PubMed](#)]
26. Decroos, C.; Clausen, D.J.; Haines, B.E.; Wiest, O.; Williams, R.M.; Christianson, D.W. Variable active site loop conformations accommodate the binding of macrocyclic largazole analogues to HDAC8. *Biochemistry* **2015**, *54*, 2126–2135. [[CrossRef](#)] [[PubMed](#)]
27. Deschamps, N.; Simões-Pires, C.A.; Carrupt, P.-A.; Nurisso, A. How the flexibility of human histone deacetylases influences ligand binding: An overview. *Drug Discov. Today* **2015**, *20*, 736–742. [[CrossRef](#)] [[PubMed](#)]



28. Jansch, N.; Meyners, C.; Muth, M.; Kopranovic, A.; Witt, O.; Oehme, I.; Meyer-Almes, F.J. The enzyme activity of histone deacetylase 8 is modulated by a redox-switch. *Redox Biol.* **2019**, *20*, 60–67. [[CrossRef](#)] [[PubMed](#)]
29. Ononye, S.N.; VanHeyst, M.D.; Oblak, E.Z.; Zhou, W.; Ammar, M.; Anderson, A.C.; Wright, D.L. Tropolones as lead-like natural products: The development of potent and selective histone deacetylase inhibitors. *ACS Med. Chem. Lett.* **2013**, *4*, 757–761. [[CrossRef](#)]
30. Werbeck, N.D.; Shukla, V.K.; Kunze, M.B.A.; Yalinca, H.; Pritchard, R.B.; Siemons, L.; Mondal, S.; Greenwood, S.O.R.; Kirkpatrick, J.; Marson, C.M.; et al. A distal regulatory region of a class I human histone deacetylase. *Nat. Commun.* **2020**, *11*, 3841. [[CrossRef](#)]
31. Kunze, M.B.; Wright, D.W.; Werbeck, N.D.; Kirkpatrick, J.; Coveney, P.V.; Hansen, D.F. Loop interactions and dynamics tune the enzymatic activity of the human histone deacetylase 8. *J. Am. Chem. Soc.* **2013**, *135*, 17862–17868. [[CrossRef](#)] [[PubMed](#)]
32. Brunsteiner, M.; Petukhov, P.A. Insights from comprehensive multiple receptor docking to HDAC8. *J. Mol. Model.* **2012**, *18*, 3927–3939. [[CrossRef](#)] [[PubMed](#)]

---

## 6 Danksagung

---

Zum Abschluss ist es nun soweit mich bei all den Menschen zu bedanken, welche mich während dieser intensiven Zeit begleiteten, für mich da waren und mich bei der Anfertigung dieser Arbeit auf allen Ebenen unterstützen.

Zunächst möchte ich mich ausdrücklich bei Herrn Prof. Dr. Meyer-Almes für das in mich gesetzte Vertrauen, die mir zugetragene forschende Gestaltungsfreiheit und die äußerst angenehme und offene Zusammenarbeit in den letzten Jahren bedanken.

Des Weiteren bedanke ich mich bei Herrn Prof. Dr. Harald Kolmar, welcher mir im Rahmen der kooperativen Promotionsplattform zwischen Hochschule Darmstadt und Technischer Universität Darmstadt die Möglichkeit zur Promotion ermöglichte und für die Übernahme des Referates.

Zusätzlich möchte ich meinen Dank der Graduiertenorganisation Ingenium der TU Darmstadt aussprechen, dessen Finanzierung das Fundament für diese Arbeit legte.

Nicht zu vergessen sei an dieser Stelle, dass diese Arbeit ohne die Unterstützung all der Mitglieder der Arbeitsgruppe Meyer-Almes und der damaligen Arbeitsgruppe Fuchsbauer nicht zustande gekommen wäre. Deswegen gilt mein besonderer Dank den Laboringenieuren Michael Schröder und Ulrike Becher, meinen Kollegen Anita Anderl, Norbert Jüttner, David Fiebig, Benjamin Wolff, Christian Meyners, Markus Schweipert, Anton Frühauf sowie meinen Bacheloranden Oki Wisely Sugiarto, Aleksandra Koprancic, Ewelina Wozny, Tina Öhlmann, Sidra Basheer, Charlotte Deszczyk, Linh Ngoc Lai und Kim Leoni Lang.

Ein herzlicher Dank gilt meinen engen Freunden die immer ein offenes Ohr für mich hatten und mir zur Seite standen vor allen meiner Freundin Maraike. Danke für deinen bedingungslosen Rückhalt, deine Unterstützung und deine motivierenden Worte, welche mich bis zum Abschluss dieser Arbeit brachten.

Mein ganz besonderer Dank gilt meinem Bruder Manuel, dessen kreative Ader mich schon frühzeitig inspirierte und einen großen Bestandteil an meinem Wirken hat. Sowie meinen Eltern Ute und Bernd, die mich auf allen Wegen stets unterstützt haben und mir durch Ihren bedingungslosen Rückhalt ermöglichten mein Leben uneingeschränkt zu gestalten. Vielen Dank an euch.

---

## 7 Erklärungen

---

### Erklärung laut Promotionsordnung

#### **§8 Abs. 1 lit. c der Promotionsordnung der TU Darmstadt**

Ich versichere hiermit, dass die elektronische Version meiner Dissertation mit der schriftlichen Version übereinstimmt und für die Durchführung des Promotionsverfahrens vorliegt.

#### **§8 Abs. 1 lit. d der Promotionsordnung der TU Darmstadt**

Ich versichere hiermit, dass zu einem vorherigen Zeitpunkt noch keine Promotion versucht wurde und zu keinem früheren Zeitpunkt an einer in- oder ausländischen Hochschule eingereicht wurde. In diesem Fall sind nähere Angaben über Zeitpunkt, Hochschule, Dissertationsthema und Ergebnis dieses Versuchs mitzuteilen.

#### **§9 Abs. 1 der Promotionsordnung der TU Darmstadt**

Ich versichere hiermit, dass die vorliegende Dissertation selbstständig und nur unter Verwendung der angegebenen Quellen verfasst wurde.

#### **§9 Abs. 2 der Promotionsordnung der TU Darmstadt**

Die Arbeit hat bisher noch nicht zu Prüfungszwecken gedient.

Darmstadt,

---

Niklas Jansch

---

## ERKLÄRUNG ZUM EIGENANTEIL AN DEN VERÖFFENTLICHUNGEN

Im Folgenden ist aufgelistet, mit welchem Anteil ich an den Veröffentlichungen beteiligt war.

Mein Anteil an der folgenden Veröffentlichung beträgt 40% mit geteilter Erst-Autorenschaft. Mein Beitrag bemisst sich an folgenden Tätigkeiten:

- Ideengebung und Literaturrecherche
- Klonierung von HDAC4 Mutanten
- Produktion und Aufreinigung von HDAC4
- Messung von Michaelis-Menten Parametern
- Bestimmung von IC<sub>50</sub>-Werten
- Datenauswertung und Verfassen von Teilen der Publikation

### [1] Mechanistic Insights into Binding of Ligands with Thiazolidinedione Warhead to Human Histone Deacetylase 4

Schweipert, S.; **Jänsch, N.**; Upadhyay, N.; Kalpana, T.; Wozny, E.; Basheer, S.; Wurster, E.; Müller, M.; Ramaa, C.S.; Meyer-Almes, F.J.

Pharmaceuticals ([doi.org/10.3390/ph14101032](https://doi.org/10.3390/ph14101032))

Mein Anteil an der folgenden Veröffentlichung beträgt 20%. Mein Beitrag bemisst sich an folgenden Tätigkeiten:

- Produktion und Aufreinigung von HDAC8
- Testung von Enzymaktivität und Bestimmung von IC<sub>50</sub>-Werten
- Datenauswertung und Verfassen von Teilen der Publikation

### [2] Assessment of Tractable Cysteines for Covalent Targeting by Screening Covalent Fragments

Petri, L.; Ábrányi-Balogh, P.; Imre, T.; Pálffy, G.; Perczel, A.; Knez, D.; Hrast, M.; Gobec, M.; Sosič, I.; Nyíri, K.; Vértessy, B.G.; **Jänsch, N.**; Desczyk, C.; Meyer-Almes, F.J.; Ogris, I.; Golič Grdadolnik, S.; Giacinto Iacovino, L.; Binda, C.; Gobec, S.; Keserü, G.M.

ChemBioChem ([doi.org/10.1002/cbic.202000700](https://doi.org/10.1002/cbic.202000700))

Mein Anteil an der folgenden Veröffentlichung beträgt 33%. Mein Beitrag bemisst sich an folgenden Tätigkeiten:

- Produktion und Aufreinigung von HDAC8
- Testung von Enzymaktivität und Bestimmung von IC<sub>50</sub>-Werten

### [3] Discovery of novel N-substituted thiazolidinediones (TZDs) as HDAC8 inhibitors: in-silico studies, synthesis, and biological evaluation

Upadhyay, N.; Tilekar, K.; **Jänsch, N.**; Schweipert, M.; Hess, J. D.; Henze Macias, L.; Mrowka, P.; Aguilera, R. J.; Choe, J.Y.; Meyer-Almes, F. J.; Ramaa, C. S.

Bioorganic Chemistry ([doi.org/10.1016/j.bioorg.2020.103934](https://doi.org/10.1016/j.bioorg.2020.103934))

---

Mein Anteil an der folgenden Veröffentlichung beträgt 80% mit Erst Autorenschaft. Mein Beitrag bemisst sich an folgenden Tätigkeiten:

- Ideengebung und Literaturrecherche
- Klonierung von HDAC8-Mutanten
- Produktion und Aufreinigung von HDAC8
- Probenvorbereitung für Massenspektrometrie von HDAC8-Fragmenten
- Entwicklung EMSA
- Bestimmung der thermischen Stabilität von HDAC8
- Bestimmung von IC<sub>50</sub>-Werten
- Datenauswertung und Verfassen von Teilen der Publikation

#### [4] Switching the Switch: Ligand Induced Disulfide Formation in HDAC8

Jänsch, N.; Sugiarto, W.O.; Muth, M.; Koprancic, A.; Desczyk, C.; Ballweg, M.; Kirschhöfer, F.; Brenner-Weiss, G.; Meyer-Almes, F. J.

Chemistry – A European Journal (doi.org/10.1002/chem.202001712)

Mein Anteil an der folgenden Veröffentlichung beträgt 33%. Mein Beitrag bemisst sich an folgenden Tätigkeiten:

- Produktion und Aufreinigung von HDAC8
- Testung von Enzymaktivität und Bestimmung von IC<sub>50</sub>-Werten

#### [5] Discovery of 5-naphthylidene-2,4-thiazolidinedione derivatives as selective HDAC8 inhibitors and evaluation of their cytotoxic effects in leukemic cell lines

Tilekar, K.; Upadhyay, N.; Jänsch, N.; Schweipert, M.; Mrowka, P.; Meyer-Almes, F. J.; Ramaa, C. S. Bioorganic Chemistry (doi.org/10.1016/j.bioorg.2019.103522)

Mein Anteil an der folgenden Veröffentlichung beträgt 50%. Mein Beitrag bemisst sich an folgenden Tätigkeiten:

- Produktion und Aufreinigung von HDAC8
- Testung von Enzymaktivität und Bestimmung von IC<sub>50</sub>-Werten
- Bestimmung der thermischen Stabilität von HDAC8

#### [6] Synthesis and structure activity relationship of 1,3-benzo-thiazine-2-thiones as selective HDAC8 inhibitors

Wolff, B.; Jänsch, N.; Sugiarto, W.O.; Frühschulz, S.; Lang, M.; Altintas, R.; Oehme, I.; Meyer-Almes, F. J. European Journal of Medicinal Chemistry (doi.org/10.1016/j.ejmech.2019.111756)

Mein Anteil an der folgenden Veröffentlichung beträgt 80% mit Erst Autorenschaft. Mein Beitrag bemisst sich an folgenden Tätigkeiten:

- Bestimmung von Enzymaktivitäten
- Datenauswertung und Verfassen von Teilen der Publikation

#### [7] Using design of experiment to optimize enzyme activity assays

Jänsch, N.; Colin, F.; Schröder, M.; Meyer-Almes, F. J.

ChemTexts (doi.org/10.1007/s40828-019-0095-2)

---

Mein Anteil an der folgenden Veröffentlichung beträgt 50%. Mein Beitrag bemisst sich an folgenden Tätigkeiten:

- Produktion und Aufreinigung von HDAC8
- Testung von Enzymaktivität und Bestimmung von IC<sub>50</sub>-Werten

**[8] Thiocarbonyl Surrogate via Combination of Potassium Sulfide and Chloroform for Dithiocarbamate Construction**

Tan, W.; **Jänsch, N.**; Öhlmann, T.; Meyer-Almes, F. J.; Jiang, X.  
Organic Letters (doi.org/10.1021/acs.orglett.9b02784)

Mein Anteil an der folgenden Veröffentlichung beträgt 50%. Mein Beitrag bemisst sich an folgenden Tätigkeiten:

- Ideengebung und Literaturrecherche
- Klonierung von HDAC8-Mutanten
- Produktion und Aufreinigung von HDAC8
- Probenvorbereitung für Massenanalytik
- Bestimmung von IC<sub>50</sub>-Werten
- Datenauswertung und Verfassen von Teilen der Publikation

**[9] Covalent inhibition of histone deacetylase 8 by 3,4-dihydro-2H-pyrimido[1,2-c][1,3]benzothiazin-6-imine**

Muth, M.; **Jänsch, N.**; Kopranovic, A.; Krämer, A.; Wössner, N.; Jung, N.; Kirschhöfer, F.; Brenner-Weiss, G.; Meyer-Almes, F. J.  
Biochimica et Biophysica Acta (BBA) – General Subjects (doi.org/10.1016/j.bbagen.2019.01.001)

Mein Anteil an der folgenden Veröffentlichung beträgt 80% mit Erst Autorenschaft. Mein Beitrag bemisst sich an folgenden Tätigkeiten:

- Ideengebung und Literaturrecherche
- Klonierung von HDAC8-Mutanten
- Produktion und Aufreinigung von HDAC8
- Entwicklung EMSA
- Bestimmung von IC<sub>50</sub>-Werten
- Messen von CD-Spektren
- Bestimmung der thermischen Stabilität von HDAC8
- Datenauswertung und Verfassen von Teilen der Publikation

**[10] The enzyme activity of histone deacetylase 8 is modulated by a redox-switch**

**Jänsch, N.**; Meyners, C.; Muth, M.; Kopranovic, A.; Witt, O.; Oehme, I.; Meyer-Almes, F. J.  
Redox Biology (doi.org/10.1016/j.redox.2018.09.013)

Mein Anteil an der folgenden Veröffentlichung beträgt 40%. Mein Beitrag bemisst sich an folgenden Tätigkeiten:

- Produktion und Aufreinigung von HDAC8
- Bestimmung der thermischen Stabilität von HDAC8

**[11] Kinetically selective and potent inhibitors of HDAC8**

Schweipert, M.; **Jänsch, N.**; Sugiarto, WO.; Meyer-Almes, F. J.  
Biological Chemistry (doi.org/10.1515/hsz-2018-0363)

---

Mein Anteil an der folgenden Veröffentlichung beträgt 50% mit Erst Autorenschaft. Mein Beitrag bemisst sich an folgenden Tätigkeiten:

- Ideengebung und Literaturrecherche
- Produktion und Aufreinigung von HDAC8
- Probenvorbereitung für Massenspektrometrie von HDAC8-Fragmenten
- Entwicklung kinetischer Reaktivitätsassay

**[12] 3-Chloro-5-Substituted-1,2,4-Thiadiazoles (TDZs) as Selective and Efficient Protein Thiol Modifiers**

**Jänsch, N.;** Frühauf, A.; Schweipert, M.; Debarnot, C.; Erhardt, M.; Brenner-Weiss, G.; Kirschhöfer, F.; Jasionis, T.; Capkauskaite, E.; Zubriene, A.; Matulis, D.; Meyer-Almes, F. J.

ChemBioChem (doi.org/10.1002/cbic.202200417)

Mein Anteil an der folgenden Veröffentlichung beträgt 80% mit Erst Autorenschaft. Mein Beitrag bemisst sich an folgenden Tätigkeiten:

- Ideengebung und Literaturrecherche
- Klonierung von HDAC8-Mutanten
- Produktion und Aufreinigung von HDAC8
- Bestimmung von IC<sub>50</sub>-Werten
- Bestimmung der thermischen Stabilität von HDAC8
- Messung von Michaelis-Menten Parametern
- Entwicklung *stopped-flow-assay*

**[13] Methionine 274 Is Not the Determining Factor for Selective Inhibition of Histone Deacetylase 8 (HDAC8) by L-Shaped Inhibitors**

**Jänsch, N.;** Lang, K. L.; Meyer-Almes, F. J.

International Journal of Molecular Sciences (doi.org/10.3390/ijms231911775)

---

## ERKLÄRUNG ZUR BEGUTACHTUNG DER VERÖFFENTLICHUNGEN

Prof. Dr. Harald Kolmar  
Referent

Prof. Dr. Franz-Josef Meyer-Almes  
Korreferent

Weder Referent (Prof. Dr. Harald Kolmar) noch Korreferent (Prof. Dr. Franz-Josef Meyer-Almes) der vorliegenden kumulativen Doktorarbeit waren an der Begutachtung nachstehender Veröffentlichungen beteiligt:

**[1] Mechanistic Insights into Binding of Ligands with Thiazolidinedione Warhead to Human Histone Deacetylase 4**

Schweipert, S.; **Jänsch, N.**; Upadhyay, N.; Kalpana, T.; Wozny, E.; Basheer, S.; Wurster, E.; Müller, M.; Ramaa, C.S.; Meyer-Almes, F.J.

Pharmaceuticals (doi.org/10.3390/ph14101032)

**[2] Assessment of Tractable Cysteines for Covalent Targeting by Screening Covalent Fragments**

Petri, L.; Ábrányi-Balogh, P.; Imre, T.; Pálffy, G.; Perczel, A.; Knez, D.; Hrast, M.; Gobec, M.; Sosič, I.; Nyíri, K.; Vértessy, B.G.; **Jänsch, N.**; Desczyk, C.; Meyer-Almes, F.J.; Ogris, I.; Golič Grdadolnik, S.; Giacinto Iacovino, L.; Binda, C.; Gobec, S.; Keserű, G.M.

ChemBioChem (doi.org/10.1002/cbic.202000700)

**[3] Discovery of novel N-substituted thiazolidinediones (TZDs) as HDAC8 inhibitors: in-silico studies, synthesis, and biological evaluation**

Upadhyay, N.; Tilekar, K.; **Jänsch, N.**; Schweipert, M.; Hess, J. D.; Henze Macias, L.; Mrowka, P.; Aguilera, R. J.; Choe, J.Y.; Meyer-Almes, F. J.; Ramaa, C. S.

Bioorganic Chemistry (doi.org/10.1016/j.bioorg.2020.103934)

**[4] Switching the Switch: Ligand Induced Disulfide Formation in HDAC8**

**Jänsch, N.**; Sugiarto, W.O.; Muth, M.; Koprancovic, A.; Desczyk, C.; Ballweg, M.; Kirschhöfer, F.; Brenner-Weiss, G.; Meyer-Almes, F. J.

Chemistry – A European Journal (doi.org/10.1002/chem.202001712)

**[5] Discovery of 5-naphylidene-2,4-thiazolidinedione derivatives as selective HDAC8 inhibitors and evaluation of their cytotoxic effects in leukemic cell lines**

Tilekar, K.; Upadhyay, N.; **Jänsch, N.**; Schweipert, M.; Mrowka, P.; Meyer-Almes, F. J.; Ramaa, C. S.

Bioorganic Chemistry (doi.org/10.1016/j.bioorg.2019.103522)

**[6] Synthesis and structure activity relationship of 1,3-benzo-thiazine-2-thiones as selective HDAC8 inhibitors**

Wolff, B.; **Jänsch, N.**; Sugiarto, W.O.; Frühschulz, S.; Lang, M.; Altintas, R.; Oehme, I.; Meyer-Almes, F. J.

European Journal of Medicinal Chemistry (doi.org/10.1016/j.ejmech.2019.111756)

**[7] Using design of experiment to optimize enzyme activity assays**

**Jänsch, N.**; Colin, F.; Schröder, M.; Meyer-Almes, F. J.

ChemTexts (doi.org/10.1007/s40828-019-0095-2)



---

**[8] Thiocarbonyl Surrogate via Combination of Potassium Sulfide and Chloroform for Dithiocarbamate Construction**

Tan, W.; Jäsch, N.; Öhlmann, T.; Meyer-Almes, F. J.; Jiang, X.  
Organic Letters (doi.org/10.1021/acs.orglett.9b02784)

**[9] Covalent inhibition of histone deacetylase 8 by 3,4-dihydro-2H-pyrimido[1,2-c][1,3]benzothiazin-6-imine**

Muth, M.; Jäsch, N.; Koprancovic, A.; Krämer, A.; Wössner, N.; Jung, N.; Kirschhöfer, F.; Brenner-Weiss, G.; Meyer-Almes, F. J.  
Biochimica et Biophysica Acta (BBA) – General Subjects (doi.org/10.1016/j.bbagen.2019.01.001)

**[10] The enzyme activity of histone deacetylase 8 is modulated by a redox-switch**

Jäsch, N.; Meyners, C.; Muth, M.; Koprancovic, A.; Witt, O.; Oehme, I.; Meyer-Almes, F. J.  
Redox Biology (doi.org/10.1016/j.redox.2018.09.013)

**[11] Kinetically selective and potent inhibitors of HDAC8**

Schweipert, M.; Jäsch, N.; Sugiarto, W.O.; Meyer-Almes, F. J.  
Biological Chemistry (doi.org/10.1515/hsz-2018-0363)

**[12] 3-Chloro-5-Substituted-1,2,4-Thiadiazoles (TDZs) as Selective and Efficient Protein Thiol Modifiers**

Jäsch, N.; Frühauf, A.; Schweipert, M.; Debarnot, C.; Erhardt, M.; Brenner-Weiss, G.; Kirschhöfer, F.; Jasionis, T.; Capkauskaitė, E.; Zubriene, A.; Matulis, D.; Meyer-Almes, F. J.  
ChemBioChem (doi.org/10.1002/cbic.202200417)

**[13] Methionine 274 Is Not the Determining Factor for Selective Inhibition of Histone Deacetylase 8 (HDAC8) by L-Shaped Inhibitors**

Jäsch, N.; Lang, K. L.; Meyer-Almes, F. J.  
International Journal of Molecular Sciences (doi.org/10.3390/ijms231911775)

---

Referent  
(Prof. Dr. Harald Kolmar)

---

Korreferent  
(Prof. Dr. Franz-Josef Meyer-Almes)